DAUS 2026

Drones and Unmanned Systems

Proceedings

2nd International Conference on Drones and Unmanned Systems (DAUS' 2026)

25-27 February 2026, Salzburg, Austria

IFSA

Drones and Unmanned Systems

Proceedings of the 2nd International Conference on Drones and Unmanned Systems (DAUS' 2026)

25-27 February 2026
Salzburg, Austria

Edited by
Dr., Prof. Sergey Y. Yurish
International Frequency Sensor Association,
Barcelona, Spain

IFSA Publishing

Sergey Y. Yurish, *Editor*
Drones and Unmanned Systems
DAUS' 2026 Conference Proceedings

E-mail (for orders and customer service enquires): ifsa.books@sensorsportal.com

Visit our Home Page on http://www.sensorsportal.com

ISBN: 978-84-09-82031-3
BN-20260219-XX
BIC: TRP

Contents

Foreword

These proceedings present the peer-reviewed contributions of the *2nd International Conference on Drones and Unmanned Systems (DAUS' 2026)*, held on 25–27 February 2026 in Salzburg, Austria.

The volume is intended as a concise snapshot of current research and engineering practice in unmanned and autonomous platforms—covering enabling technologies, methods, experimental validation, and application case studies that move the field toward safer, more capable, and more scalable deployments.

The papers collected in this volume highlight both foundational research and application-driven innovation. Readers will find contributions addressing, among others, drone-enabled inspection and non-destructive testing, cooperative navigation and payload transport, formation flight and multi-agent control, resilient communications and private 5G networking, airborne deconfliction testbeds, synthetic aperture radar concepts, security topics including jamming/spoofing analysis, and simulation environments for next-generation autonomy. Together, these works demonstrate a shared objective: to make unmanned systems more capable, more trustworthy, and more deployable—with safety, robustness, and societal benefit kept firmly in view.

On behalf of the organizing bodies, I would like to thank the authors for their valuable submissions, the reviewers for their careful assessments and constructive recommendations, and the committee members for their commitment to delivering a rigorous and engaging technical program. I hope this volume serves as a practical reference for ongoing work and as an invitation to new collaborations that advance drones and unmanned systems in research, industry, and society.

Prof., Dr. Sergey Y. Yurish,
DAUS' 2026 Conference Chairman

(001)

Active Thermographic Inspection System Integrated on a Drone Platform

Shashank Pant, Stephane Brunet, Dmitrii Klishch, Gurpreet Singh and Marc Genest
Aerospace Research Centre, National Research Council Canada, Ottawa, Ontario, K1A 0R6, Canada
E-mail: shashank.pant@nrc-cnrc.gc.ca

Summary: This paper reports recent advancements in developing a drone-based active thermographic inspection system for detecting hidden structural defects in aerospace components. Building on previous work, the drone platform was redesigned to reduce weight, enhance safety, and incorporate a lightweight, synchronized optical–thermal camera system controlled via a Raspberry Pi. The impact of propeller downwash on thermal measurements was experimentally assessed, showing measurable cooling effects but no reduction in defect detectability. An image processing workflow was developed to stabilize optical video to reduce influence of drone vibration. All tested algorithms, except for Good Features to Track (GFTT), achieved effective stabilization by successfully tracking all selected features across the optical video frames. Future efforts will focus on camera calibration, integration with the drone's autopilot, and both laboratory and field trials to validate system performance under real-world conditions, with the ultimate goal of enabling autonomous drone-based active thermography inspections.

Keywords: Drone-based inspection, Active thermography, Image processing, Automation.

1. Introduction

Drone-based optical and infrared (IR) inspections are widely used in various industrial applications including aerospace [1], agriculture [2], construction [3], infrastructure [4], among others [5-7]. These systems enable rapid, remote, optical and thermal data acquisition to support applications such as crop health monitoring, structural integrity assessment, and detection of anomalies for preventive maintenance. In terms of drone-based IR inspection, passive thermography is commonly used, which relies on natural thermal contrast between the background and the area of interest to detect anomalies [8]. While effective for identifying surface issues such as heat loss, moisture ingress, or material defects, passive thermography is limited in detecting hidden or subsurface anomalies. Active thermography addresses this limitation by using a controlled external heat source to induce a thermal response in the material of interest. Analysis of the thermal behaviour enables the identification of hidden anomalies that are not detectable through visible imaging or passive IR techniques [9].

A drone equipped with an active thermography system has the potential to autonomously fly and perform inspections, enabling cost effective, efficient and remote detection of subsurface defects. However, several technical challenges must be addressed to make this capability practical. These include the integration of a suitable heating source onto the drone's platform, ensuring image stabilization to compensate for drone motion, understanding the effects of propeller-induced airflow on thermal measurements, and optimizing the system's weight and power requirements to maintain desired flight performance. Overcoming these obstacles is essential to realizing a fully functional airborne active thermography inspection system.

The primary objective of this ongoing research is to address the current lack of commercially available drone-based active thermography inspection system by developing one. Expanding on the previous work by the authors [10], this paper presents several key advancements, including a comprehensive redesign of the drone, an analysis of propeller downwash effects, the integration of a lightweight camera system, and the assessment of image stabilization techniques applied to data captured by the new camera system.

2. Drone Redesign

In the previous setup [10], a custom drone was designed and built, featuring an integrated on-board heating system consisting of four 250-watt halogen lamps, along with thermal and optical camera systems, as shown in Fig. 1.

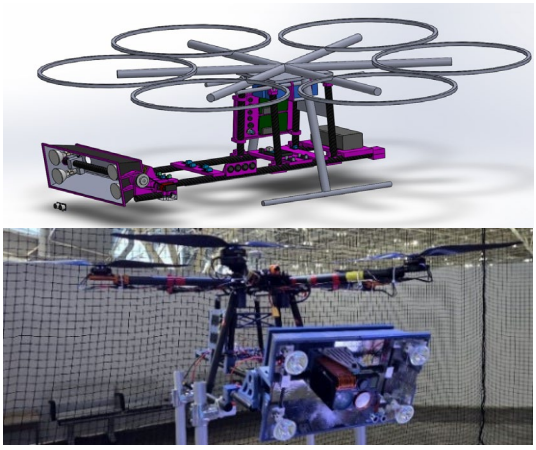

Fig. 1. Previous drone with on-board heating source, Top: computer aided design (CAD) model, Bottom: actual prototype.

The on-board heating lamps provided sufficient thermal energy for detecting hidden damage; however, several design limitations were identified. The thermal/optical camera system was relatively heavy weighing approximately 680 grams, also the reflector weighing 380 grams offered no added benefit; however, both were contributing to the added weight. Furthermore, a propeller shroud was required to prevent unintended collisions between the drone blades and the inspected structure. Based on these findings, the drone was subsequently redesigned and constructed, with the updated design shown in Fig. 2.

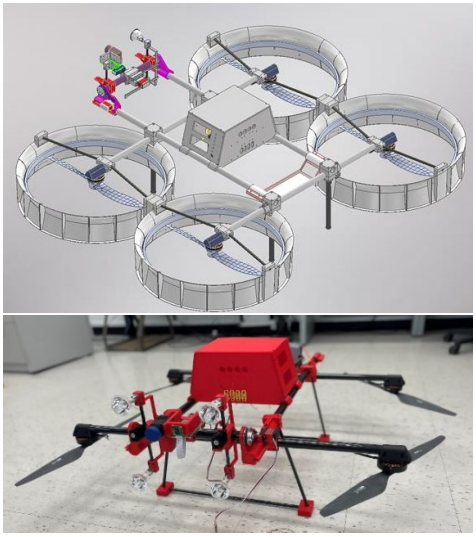

Fig. 2. Image of the redesigned drone, Top: CAD model, Bottom: actual prototype without the propeller guard.

The updated design also consists of a new thermal (Evidir alpha) and optical (IMX296-MIPI) camera system. Combined they weigh less than 200 grams, providing significant weight saving compared to the previous design. Both the optical and the thermal cameras were synchronized and controlled using Raspberry Pi for further expansion.

3. Effect of Propeller Downwash

This experiment was conducted in a laboratory environment on a composite panel shown in Fig. 4, which contained simulated delamination and impact damage. Four 250-watt heating lamps were positioned approximately 45.7 cm (18 inches) from the panel, a distance determined to be optimal in previous experiments. The lamps were turned on for 20 seconds and the overall temperature was monitored for 60 seconds. The experiments were first performed with the drone's propellers off and then repeated with the drone's propellers on, result of which is shown in Fig. 3. As expected, propeller downwash was found to modify the thermal profile by lowering the peak temperature between 1 to 2 °C. However, post-processed data exhibited that impact damage and delaminations in the composite panel remained detectable under both propeller-on and propeller-off conditions, an example of which is shown in Fig. 3 for impact damage. More details on this part of the experiment can be found in [11].

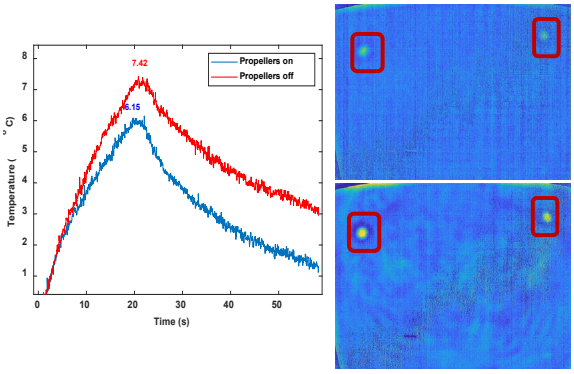

Fig. 3. Example of temperature profile (left) over impacted surface and processed 1st principal component thermography images under propeller-on (top right) and propeller-off (bottom right) conditions. Detected impact damages in the processed images are highlighted with red boxes.

4. Image Processing

Image processing is a critical step in the post-processing of drone-based active thermography data. The workflow involves extracting images after the heating phase from the acquired video feed, stabilizing them, and then performing detailed analysis. To develop and test the image processing methodology, an experiment was conducted, where part of the drone's heating and camera system was mounted on a fixed frame, as shown in Fig. 4.

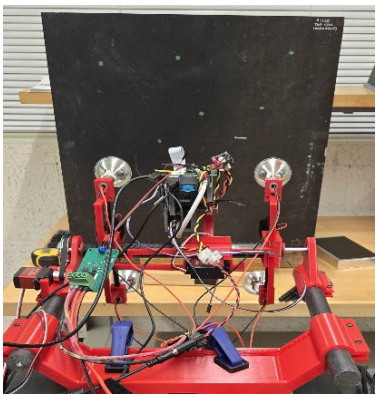

Fig. 4. Experimental setup for acquiring thermal and optical video feed during heating and cooling phases.

Similar to the previous case, the heating lamps were located ~45.7 cm (18 inches) away from the panel and were switched on for roughly 20 seconds to heat the structure. Thermal and optical data were captured during the heating phase and for approximately

50 seconds afterward, during the cooling phase. Thermal data were captured at a resolution of 640×480 pixels, and optical at 1280×720 pixels, both recorded at 25 frames per second. To simulate drone vibrations, the fixture holding the camera system was manually shaken during both the heating and cooling periods. First, a post-processing script was developed to detect the start and end of the heating cycle by analyzing the percentage of white pixels in the captured optical video feed, an example of which is shown in Fig. 5.

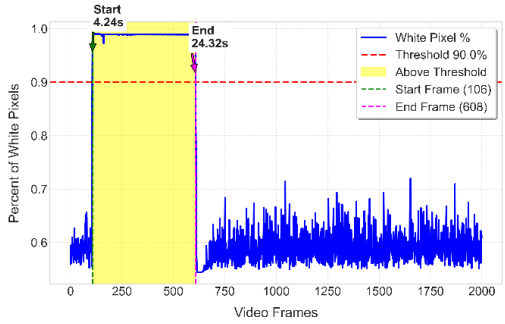

Fig. 5. Plot illustrating the start and end of the heating cycle.

For subsequent analysis, only the video segment recorded after the completion of heating cycle was used. Since active thermography relies on monitoring changes in pixel temperature over time, even slight movements can introduce noise into the results [9]. To address this, the stabilization method described in [12] was applied to the optical videos. Several feature extractions and tracking algorithms were evaluated, including: Oriented FAST and Rotated BRIEF (ORB) [13], Accelerated-KAZE (AKAZE) [14], BRISK [15], and Good Features to Track (GFTT) [16]. A mask was applied to user-selected regions to isolate features for tracking. The parameters of the feature extractors were adjusted to detect small, low-contrast features. Fig. 6 shows the detected features with and without the mask. For stabilization purposes, only the features detected within the masked areas were tracked.

Overall, all feature extraction and tracking algorithms, except for GFTT, successfully tracked the desired features within the masks across all video frames. GFTT failed to track features in some frames, resulting in missed frames during the video stabilization process. It was also observed that the optical and thermal cameras had very different fields of view despite being equidistance from the panel, and the raw images from the new thermal camera exhibited some distortions, as shown in Fig. 7, highlighting the need for further refinement and calibration.

5. Future Work

Future work will focus on calibrating both optical and thermal camera images, enabling stabilization data from the optical feed to be applied directly to the thermal images. The camera system will be integrated with the drone's autopilot, and controlled laboratory experiments will be conducted to simulate drone-induced vibrations, allowing for a thorough evaluation of the drone-mounted camera system's ability to detect and characterize hidden structural defects. Following laboratory validation, field trials will be conducted on aircraft structures in two phases. First, the drone will be mounted on a fixed test rig to obtain stable, repeatable measurements. Once optimal performance is achieved in this controlled setup, free-flight tests will be carried out to evaluate real-world performance, environmental resilience, and operational efficiency. Insights from these studies will aid in refinement of stabilization algorithms, optimization of camera setups, and enhancement of flight control strategies –ultimately aiming to automatically detect structural anomalies during inspections.

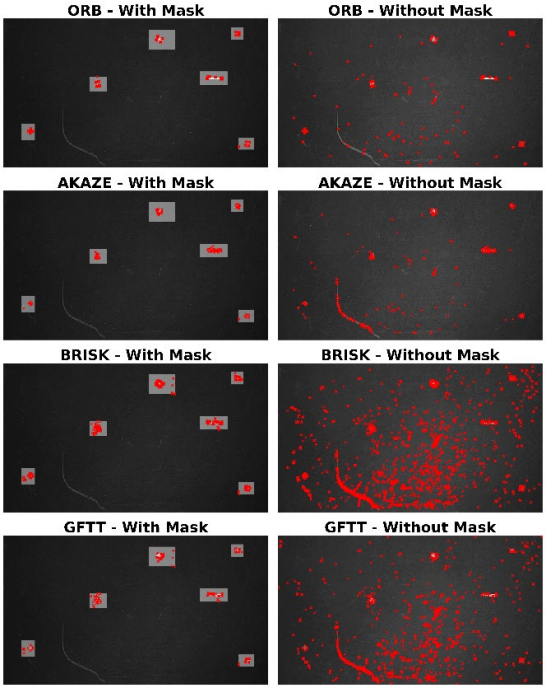

Fig. 6. Images displaying the keypoints identified by the feature extractor, both with and without the use of masks.

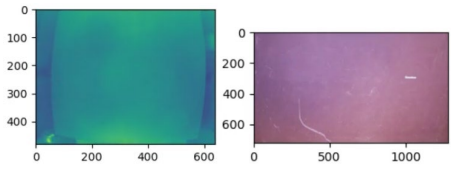

Fig. 7. Image extracted from thermal (left) and optical (right) video frame, size in pixels.

6. Conclusion

This paper presents continuing progress toward realizing a fully functional, autonomous, drone-based

active thermographic inspection system for aerospace applications. The redesigned platform successfully integrated a lightweight synchronized optical-thermal camera system. Experimental evaluation confirmed that subsurface defects remain detectable under both propeller-on and propeller-off conditions, despite altered thermal profiles. An image processing workflow was developed to detect the heating and cooling phases. The extracted video feed following the heating cycle was further analyzed using image stabilization techniques to mitigate drone-induced vibration. It was observed that, despite being positioned at the same distance from the panel, the optical and thermal cameras had notably different fields of view, and the raw thermal images exhibited some distortions, highlighting the need for further refinement. Upcoming integration with drone's autopilot system, along with planned laboratory and field trials, will enable a comprehensive evaluation of system performance in both controlled and real-world environments. These developments will position this drone-based active thermography system as a promising tool for automated inspection to improve maintenance efficiency and reduce inspection costs in aerospace and other industrial sectors.

Acknowledgement

The authors would like to acknowledge the Canadian Department of National Defence for funding this research.

References

[1]. D. A. Rodríguez, C. L. Tafur, P. F. M. Daza, J. A. V. Vidales, et al., Inspection of aircrafts and airports using UAS: A review, *Results in Engineering*, Vol. 22, 2024, 102065.

[2]. G. Dutta, P. Goswami, Application of drone in agriculture: A review, *International Journal of Chemical Studies*, Vol. 8, Issue 5, 2020, pp. 181-187.

[3]. H. Liang, S.-C. Lee, W. Bae, J. Kim, et al., Towards UAVs in construction: Advancements, challenges, and future directions for monitoring and inspection, *Drones*, Vol. 7, Issue 3, 2023, 202.

[4]. P. Nooralishahi, C. Ibarra-Castanedo, S. Deane, F. López, et al., Drone-based non-destructive inspection of industrial sites: A review and case studies, *Drones*, Vol. 5, Issue 4, 2021, 106.

[5]. S. Vergura, Criticalities of the outdoor infrared inspection of photovoltaic modules by means of drones, *Energies*, Vol. 15, Issue 14, 2022, 5086.

[6]. S. Jordan, J. Moore, S. Hovet, J. Box, et al., State-of-the-art technologies for UAV inspections, *IET Radar, Sonar & Navigation*, Vol. 12, Issue 2, 2018, pp. 115-164.

[7]. S.-J. Heo, W. S. Na, Review of drone-based technologies for wind turbine blade inspection, *Electronics*, Vol. 14, Issue 2, 2025, 269.

[8]. Y. Ma, Z. Zeng, Z. Luo, N. Tao, et al., Current challenges and advancements of aerial thermography for outdoor structural health monitoring: A review, *IEEE Sensors Journal*, Vol. 25, Issue 12, 2025, pp. 21000-21016.

[9]. S. Pant, M. Genest, C. Ibarra-Castanedo, N. P. Avdelidis, et al., Inspection of a helicopter blade using drone-based active thermography, *Proceedings of SPIE*, Vol. 12535, 2023, 1253509.

[10]. S. Pant, M. Genest, D. Klishch, C. Ibarra-Castanedo, et al., Development of drone-based active thermographic inspection system, in *Proceedings of the 1st International Conference on Drones and Unmanned Systems (DAUS'25)*, 2025, pp. 27-29.

[11]. M. Genest, S. Pant, D. Klishch, Influence of propeller downwash on drone-based active infrared thermographic inspection, *Proceedings of SPIE*, Vol. 13054, 2025, 130540G.

[12]. S. Pant, P. Nooralishahi, N. P. Avdelidis, C. Ibarra-Castanedo, et al., Evaluation and selection of video stabilization techniques for UAV-based active infrared thermography application, *Sensors*, Vol. 21, Issue 5, 2021, 1604.

[13]. OpenCV, ORB (Oriented FAST and Rotated BRIEF), https://docs.opencv.org/4.x/d1/d89/tutorial_py_orb.html

[14]. OpenCV, AKAZE local features matching, https://docs.opencv.org/4.x/db/d70/tutorial_akaze_matching.html

[15]. OpenCV, BRISK feature detector, https://docs.opencv.org/4.x/de/dbf/classcv_1_1BRISK.html

[16]. OpenCV, Shi-Tomasi corner detector, https://docs.opencv.org/3.4/d4/d8c/tutorial_py_shi_tomasi.html

(003)

Digital Twin-Driven Multistorey Mapping with Cooperative Micro Aerial Vehicles

Tianxiong Zhang, Victor Victor and Uwe Aßmann
Chair of Software Technology, Technische Universität Dresden, Dresden, Germany
E-mail: tianxiong.zhang@tu-dresden.de

Summary: Micro aerial vehicle (MAV) swarms have strong potential for indoor mapping. However, most studies adopt a single-altitude strategy, which flies all MAVs at the same height, flattening the vertical structure and limiting the map's expressiveness. They also often lack a unified interface for real-time interaction and state monitoring. To address these gaps, we propose a digital twin-driven, multi-MAV, multistorey mapping pipeline that operates with minimal sensing. The system consists of a Digital Twin-based Controller, a Mapping Service, and a Digital Twin Web Service. The Mapping Service integrates a Map Bug exploration policy and a Downwash Avoidance policy, and leverages a Single Map Merge Service together with a TF Broadcaster to organize altitude layers and their spatial frames. We validate the approach in a physical indoor testbed. The pipeline enables multiple MAVs to capture complementary, height-dependent environmental features and produce layered indoor maps, while the digital twin provides real-time, interactive supervision of mission execution and vehicle states.

Keywords: Mapping, Digital twin, Swarm, Micro Aerial Vehicle (MAV), Unmanned Aerial Vehicle (UAV), Drone.

1. Introduction

With the rapid development of micro aerial vehicles (MAVs), their applications have attracted increasing attention, ranging from property surveillance [1] and search-and-rescue operations [2] to gas leak localization [3]. Among these applications, indoor mapping is a key capability, as it enables exploration of potentially hazardous indoor environments without exposing humans to risk. Owing to their small size, MAVs are highly agile and can operate safely in confined spaces without interfering with human activities.

However, the limited battery capacity of such platforms results in short operational time, making it difficult for a single MAV to complete complex missions independently. This limitation motivates multi-MAV cooperation, which can significantly reduce mission time and improve system robustness compared to single-vehicle operation [4]. At the same time, the strict payload constraints of MAVs prevent the use of complex sensing suites, introducing additional challenges for indoor mapping.

The Crazyflie platform, as a representative MAV, has been widely adopted in indoor autonomy and multi-agent systems. Several studies have explored indoor mapping using Crazyflie MAVs [5]. Nevertheless, most existing approaches rely on a single-altitude mapping strategy, in which all MAVs maintain the same flight height throughout exploration. As a result, the generated maps are typically limited to planar 2D representations, which fail to capture variations in vertical structure and cannot explicitly encode height information [6-9]. In addition, prior work often lacks a digital twin framework that synchronizes control states with perception outcomes [10], and therefore does not provide a unified interface for real-time interaction and continuous monitoring of MAV states for human operators [2, 3, 11].

Therefore, in this work, we employ Crazyflies and propose a digital twin-driven multistorey mapping pipeline that supports minimal sensing as a low-cost and scalable prototype. The proposed pipeline establishes a bidirectional closed loop between data and control, enabling tight coupling between mapping, monitoring, and task execution. Fig. 1 illustrates the Crazyflie MAVs during the mapping mission.

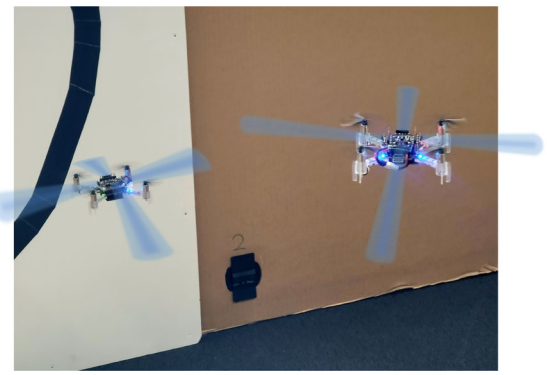

Fig. 1. MAVs performing a multistorey mapping mission in a real-world unknown environment (multi-ranger deck's FOV in blue).

In summary, the main contributions of this work are as follows:

1) We introduce a swarm exploration strategy with low memory and computational requirements, enabling multiple MAVs to autonomously explore environments at different height layers without relying on external localization infrastructure.

2) We design a digital twin service based on RESTful APIs that provides real-time visualization of

MAV behaviors and system states. By abstracting high-level MAV tasks into unified HTTP endpoints, the proposed approach offers a platform- and network-independent control interface.

3) We validate the proposed pipeline through multiple experimental scenarios. The results demonstrate that the MAVs can reliably perform mapping tasks at different height layers, achieving over 90 % improvement in coverage compared to conventional single-layer 2D mapping approaches.

2. Methods

The main limitation of MAVs lies in their limited payload capacity. In this work, each MAV is equipped with four single-beam 2D range sensors, oriented forward, backward, left, and right, with a maximum sensing range of 4 m. We assume that all MAVs can obtain pose estimates within a shared global reference frame, and reliable communication is available. Under these assumptions, this paper focuses on the digital twin-driven integration of multistorey mapping and task control-monitoring, rather than on localization methods or drift correction algorithms themselves.

2.1. System Overview

The proposed system pipeline with the Crazyflie MAV platform is illustrated in Fig. 2. The hardware setup consists of Crazyflie 2.1 MAVs equipped with a Multi-Ranger deck for local mapping and a Flow deck for onboard odometry and height estimation.

At the beginning of a mission, the physical MAVs establish communication with ROS 2, using Crazyswarm2 as the middleware. Subsequently, the Digital Twin Web Service launches a dedicated Mapping Service web monitor for each MAV, enabling operators to observe the MAV's behavior and state in real time through a browser interface. In parallel, a digital twin-based controller is instantiated for each MAV, allowing motion commands to be issued via HTTP requests.

The Mapping Service operates as a task-level component within the Digital Twin Web Service and integrates two lightweight algorithms: a Map Bug-based exploration algorithm for navigating unknown areas and a Downwash Avoidance algorithm to mitigate aerodynamic interference. The Mapping Service further relies on two supporting services. The Single Map Merge Service combines maps generated by multiple MAVs operating at the same height layer, while the TF Broadcaster publishes independent coordinate frames for different altitude layers. By assigning each MAV to a predefined height, a layered spatial perception structure is formed. Since each MAV acquires only planar 2D range measurements, the environment representation is encoded as occupancy grid maps.

Finally, the motion references computed by the Mapping Service are fed back to the Digital Twin Web Service and forwarded to the digital twin-based controller to execute physical control of the MAVs. The controller is implemented as a finite-state machine (FSM) that abstracts low-level motion into high-level behaviors, thereby simplifying MAV control and ensuring consistency between the digital twin and physical execution.

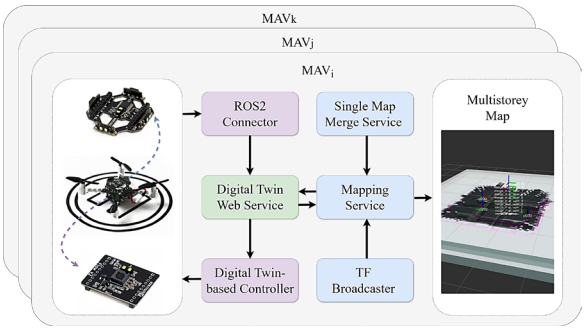

Fig. 2. Overview of the pipeline. The box color indicates the sub-system each component belongs to: Mapping (blue), control (purple), and digital twin (green).

2.2. Digital Twin-Based Controller

The proposed digital twin-based controller introduces an FSM as the core control layer of each MAV to define common behaviors and to synchronize task execution with system scheduling.

As shown in Fig. 3, a dual-domain FSM is designed at the controller level to jointly manage the lifecycle of software services and the physical execution flow of the MAV.

In the software lifecycle domain, the controller follows a standard OSGi-style lifecycle, progressing through the states INSTALLED → RESOLVED → STARTING → ACTIVE → STOPPING. Control interfaces are exposed only when the controller is in the ACTIVE state, during which continuous interaction with the physical MAV is maintained. The remaining states are reserved for dependency resolution, initialization, and resource cleanup.

In the physical task domain, MAV behavior is abstracted into a cyclic execution flow: IDLE → HOVERING → FLYING / MAPPING → HOVERING → LANDING → IDLE. Mapping is modeled as a task-level substate embedded within the motion-related states, enabling modular abstraction and structured control of MAV behaviors.

2.3. Multistorey Mapping

To enable multistorey mapping, two complementary algorithms are employed: Map Bug and Downwash Avoidance. The Map Bug algorithm provides each MAV with a wall-following capability [2], allowing autonomous exploration of unknown environments. The exploration strategy is formulated as an FSM, as illustrated in Fig. 4. Similar to classical

bug-based methods [12-14], the MAV switches between motion primitives to follow environmental boundaries and progressively explore free space while maintaining simplicity and low computational cost.

To be specific, this FSM uses a front range and a lateral (side) range to maintain a desired offset d_{ref} from a wall while safely negotiating corners.

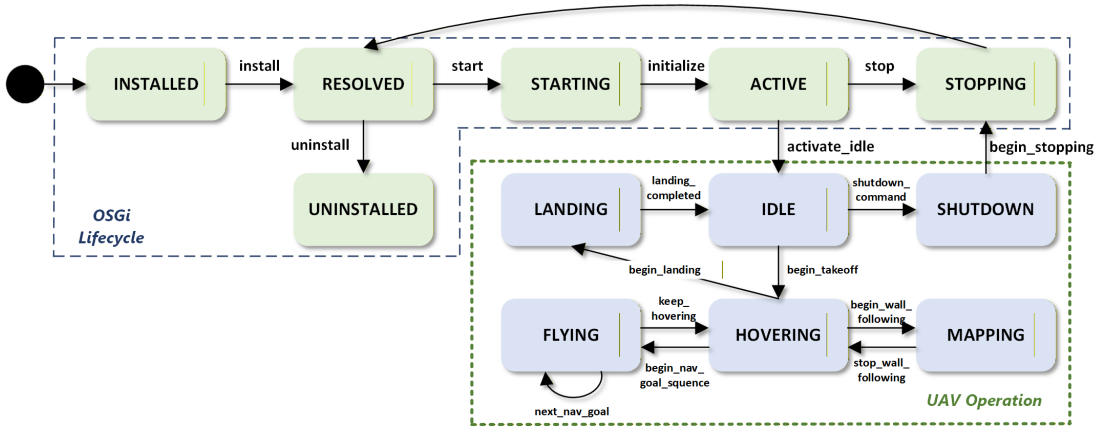

Fig. 3. FSM used in the controller.

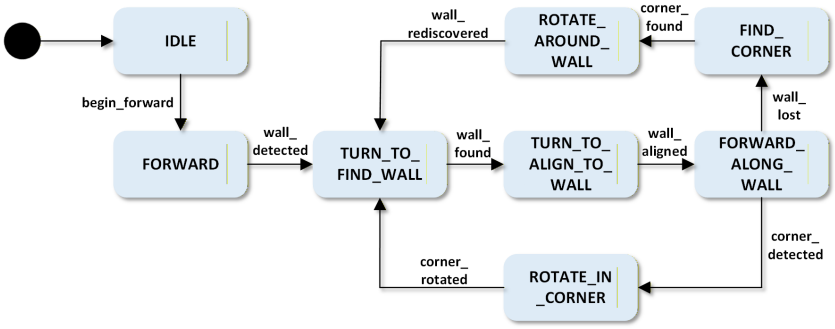

Fig. 4. FSM of the Map Bug algorithm.

At initialization, the controller stores the current heading as the reference ψ_{prev} and selects the follow-side $s \in \{+1, -1\}$ (left/right). The drone first moves forward in the FORWARD state. When the front range becomes smaller than the safety threshold $d_{\text{ref}} + \varepsilon_r$, the controller switches to TURN_TO_FIND_WALL and performs a pure yaw scan with angular velocity $\omega = s * \omega_{max}$. Once both the front and side range beams detect the wall simultaneously within a geometric bound of a $\pi/4$, the wall bearing is estimated using the ratio of the two range measurements. The controller then enters TURN_TO_ALIGN_TO_WALL and rotates until the heading error with respect to the estimated wall direction falls below ε_θ, then the system transitions to FORWARD_ALONG_WALL, where the drone moves forward with $v_x = v_{max}$ while a bounded lateral velocity v_y is applied to regulate the lateral distance error $|side - d_{ref}|$.

While in the FORWARD_ALONG_WALL state, corner situations are handled by two event-based conditions. (1) Inner corners are detected when the front range satisfies $front < d_{ref} + \varepsilon_r$, indicating an obstacle directly ahead. In this case, the drone stores the current heading ψ_{prev}, and performs an in-place rotation until $|wrap(\psi - \psi_{prev})| \approx \theta_{corner}$. After completing the turn, the controller returns to the wall-alignment behavior. (2) Outer corners are detected when the lateral range suddenly increases (i.e., $side > \text{def} + \Delta$), indicating the end of the current wall. The drone first executes a short alignment/search maneuver and then performs a smooth outer-corner turn. The turning motion follows the same lateral control law as wall following, but with the curvature gain reduced by k_{corner} to ensure a smooth transition. Range/angle buffers $(\varepsilon_r, \varepsilon_\theta)$ ensure stable, seamless transitions.

The above algorithms enable autonomous exploration for each MAV. However, given the limited sensing capability, each MAV must operate at a designated altitude to construct occupancy grid maps at different height levels, which together form a multistorey map. This layered operation introduces an additional challenge: the downwash effect generated by the propellers of higher-altitude MAVs can significantly disturb MAVs flying below [15]. Due to their low mass, MAVs are particularly sensitive to

such airflow disturbances, which may lead to instability or mission failure.

To address this issue, we design a Downwash Avoidance algorithm that explicitly prevents MAVs from entering unsafe vertical proximity.

Algorithm: Downwash Avoidance.

Input: P_{self}, P_{peer}, ranges R, params (R_{xy}, H_{gap})
Output: V = (v_x, v_y, yaw_{rate}) or *NULL*

conflict ← nearest peer with $d_{xy} < R_{xy}$ and $0 < dz \leq H_{gap}$
if conflict and idle then $home_{xy} \leftarrow current_{xy}$; lateral_sign ← side_with_max_clearance(R); enter AVOID
if AVOID then $v_y \leftarrow$ lateral_sign·v_{avoid}; $v_x \leftarrow$ backoff_if_front_blocked(R); $yaw_{rate} \leftarrow 0$;
if conflict_cleared() then enter RETURN and keep $home_{xy}$
if RETURN then (v_x, v_y) ← guidance_to($home_{xy}$) with speed_limit and safety_clamps(R); if at_home() then exit mode
otherwise return NULL

This algorithm augments the Map Bug algorithm with a minimalist two-mode supervisor driven by a downwash trigger. A conflict is declared for the nearest peer whose horizontal overlap and vertical offset satisfy

$$d_{xy} = \sqrt{(x_{self} - x_i)^2 - (y_{self} - y_i)^2} \leq R_{xy}, \quad (1)$$

$$0 < (z_i - z_{self}) \leq H_{gap}, \quad (2)$$

where d_{xy} is the horizontal distance between the ego drone and peer i, and R_{xy} is the horizontal overlap threshold for declaring proximity. H_{gap} is the downwash vertical gap threshold.

When triggered, the drone records a home point in the plane and enters AVOID, executing a zero-yaw lateral sidestep $v_y = \pm v_{avoid}$ toward the side with larger measured clearance (from r_{left}, r_{right}), with an optional short back-off in v_x if the front range is constrained, while yaw is held at zero to keep the behavior predictable and sensor-consistent. Once no peer satisfies the downwash condition, the supervisor switches to RETURN, guiding back to the saved home point. The mode exits upon proximity to home, after which wall following resumes.

To construct occupancy grid maps across different height levels, two core services are required: the TF Broadcaster and the Single Map Merge Service.

The TF Broadcaster enables the system to correctly represent multistorey maps by dynamically publishing an independent coordinate frame (child frame) for each height layer. The inter-layer height H_{layer} can be manually configured. By publishing frames for different layers and offsetting them along the z-axis according to the predefined layer height, planar occupancy grids can be visualized in a vertically layered manner, explicitly capturing structural information at different heights.

The Single Map Merge Service is responsible for merging occupancy grids when multiple MAVs operate at the same height layer. The service continuously monitors each MAV's altitude and assigns it to a discretized layer index. It then listens for local grid maps from the MAVs and, once sufficient data for a given layer is collected, aligns map boundaries and merges the grids at the cell level. The merged map is subsequently published layer by layer, providing a consistent representation of the environment for further processing or visualization.

The final output is expressed as a layered map set:

$$Map_{layered} = \{M_{h1}, M_{h2}, \ldots, M_{hn}\}, \quad (3)$$

where each M_{hn} captures height-specific structures from its unique sensing perspective.

2.4. Digital Twin Web Service

To enable real-time visualization and interactive control of MAV task execution during multistorey mapping, this work implements a Digital Twin Web Service based on a RESTful API, supporting both state monitoring and behavior control.

For state monitoring, the service provides live visualization of each MAV's Controller FSM and Mapping FSM. Upon startup, each MAV is assigned a dedicated Web Service instance and unique access ports (e.g., cf231 → 8080 & 9090, cf232 → 8081 & 9091), allowing operators to observe individual MAVs on the web interface. All state transitions are dynamically updated in the digital twin dashboard in real time.

For behavior control, the system implements a mechanism to trigger explicit FSM transitions via standard HTTP requests (e.g., activate_idle, begin_takeoff, begin_landing). These requests immediately drive the corresponding physical actions of the MAV while maintaining synchronized FSM states, thereby closing the control loop. The interface is network-agnostic, deployable on any accessible server, and enables cross-platform, remote task issuance, facilitating integration with other systems.

3. Experiments

To validate the proposed approach, experiments were conducted in a real-world setup. We first built a 2 m × 2.15 m cardboard-based physical testbed and designed two test scenarios within this environment, as shown in Fig. 5.

Experiments involved up to two MAVs due to spatial and hardware limitations. The MAVs were assigned flight altitudes of 0.4 m and 0.65 m, with a

navigation speed of 0.2 m/s and a yaw (spin) speed of 0.5 rad/s. A safety distance of 0.5 m to obstacles was maintained. The complete set of experimental parameters is summarized in Table 1.

Fig. 5. Test environment: (a) Scenario 1 – no obstacles; (b) Scenario 2 – a 0.48 m obstacle placed at the center.

Table 1. Parameter configuration for experiments.

Parameter	Value (m)
Map resolution	0.05
Global map size	5 × 5
R_{xy}	0.2
H_{gap}	0.5
Ranger Value Buffer	0.2
H_{layer}	0.15

Fig. 6 shows the multistorey mapping results. At the beginning of the experiment, the MAVs were randomly placed within the testbed. Since we rely on relative positioning rather than an external localization system, the initial positions of the MAVs were set to share a common reference frame.

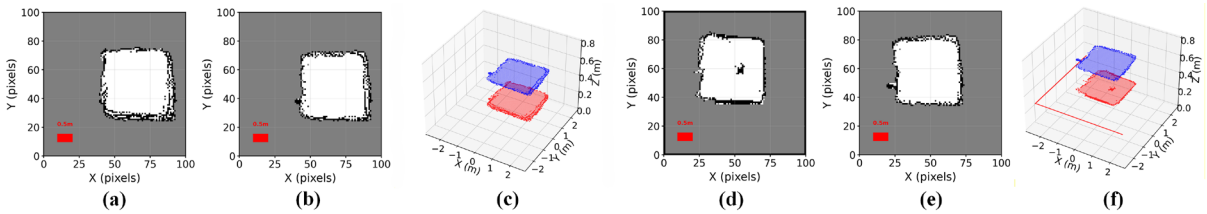

Fig. 6. Multistorey mapping results: (a) Layer 0 of scenario 1 - height 0.3 m; (b) Layer 1 of scenario 1 - height 0.6 m; (c) 3D layered map of scenario 1; (d) Layer 0 of scenario 2 - height 0.3 m; (e) Layer 1 of scenario 2 - height 0.6 m; (f) 3D layered map of scenario 2.

The MAVs then took off, reached their respective height layers, and started constructing the occupancy maps for each layer. The results demonstrate that the MAVs successfully captured the structure of the environment and completed the mapping for both height layers. The measured distances between walls are accurate, as indicated by the 0.5 m scale in the figure. Some diffuse edges appear in the map contours, which is expected because the position estimates rely solely on onboard filtering. The Crazyflies use an EKF based on flow deck and IMU data, which accumulates error over time and is sensitive to environmental factors.

Fig. 6(d)-(f) shows the results for Scenario 2, where a 0.48 m rectangular obstacle was added to the environment. This obstacle impacts the mapping of Layer 0. The results show that the MAV flying at Layer 0 captured the obstacle, while the MAV at Layer 1, flying above the obstacle, generated a different map. This demonstrates the intended effect of the proposed approach: generating distinct maps for different height layers in indoor environments with obstacles at varying heights. Fig. 7(a) compares single-layer and dual-layer maps in terms of coverage: the dual-layer map increases coverage by 92.9 % and the number of explored cells by 91.6 %, indicating richer environmental representation. Fig. 7(b) compares the coverage between single-layer and dual-layer maps in this scenario, showing an increase of 102.4 % in coverage and 97.1 % in the number of explored cells.

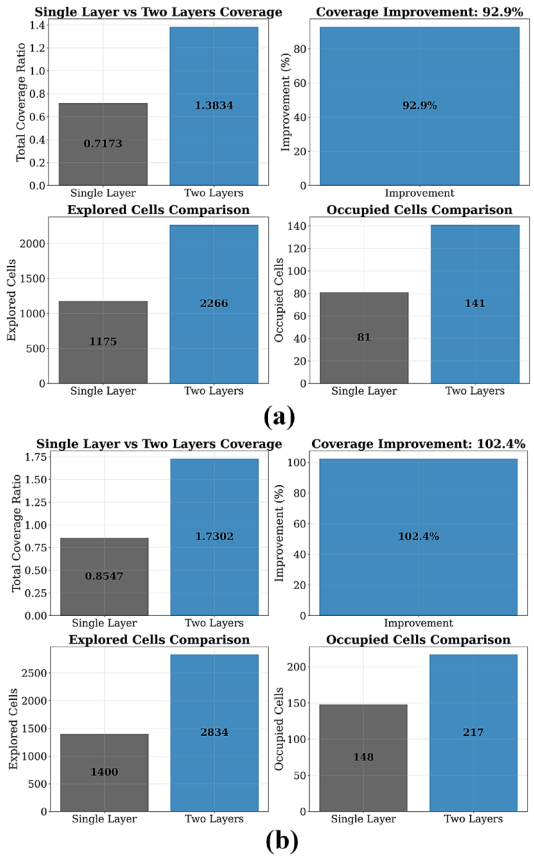

Fig. 7. Comparison of single-layer and dual-layer maps in terms of coverage and number of explored cells. (a) Scenario 1; (b) Scenario 2.

Fig. 8 shows the Digital Twin Web Service interface. Each MAV is associated with two web pages, displaying the real-time status of the MAV's Controller FSM and Map Bug FSM, respectively. This setup enables the operator to monitor the behavior of each MAV in real time, enhancing situational awareness during mission execution.

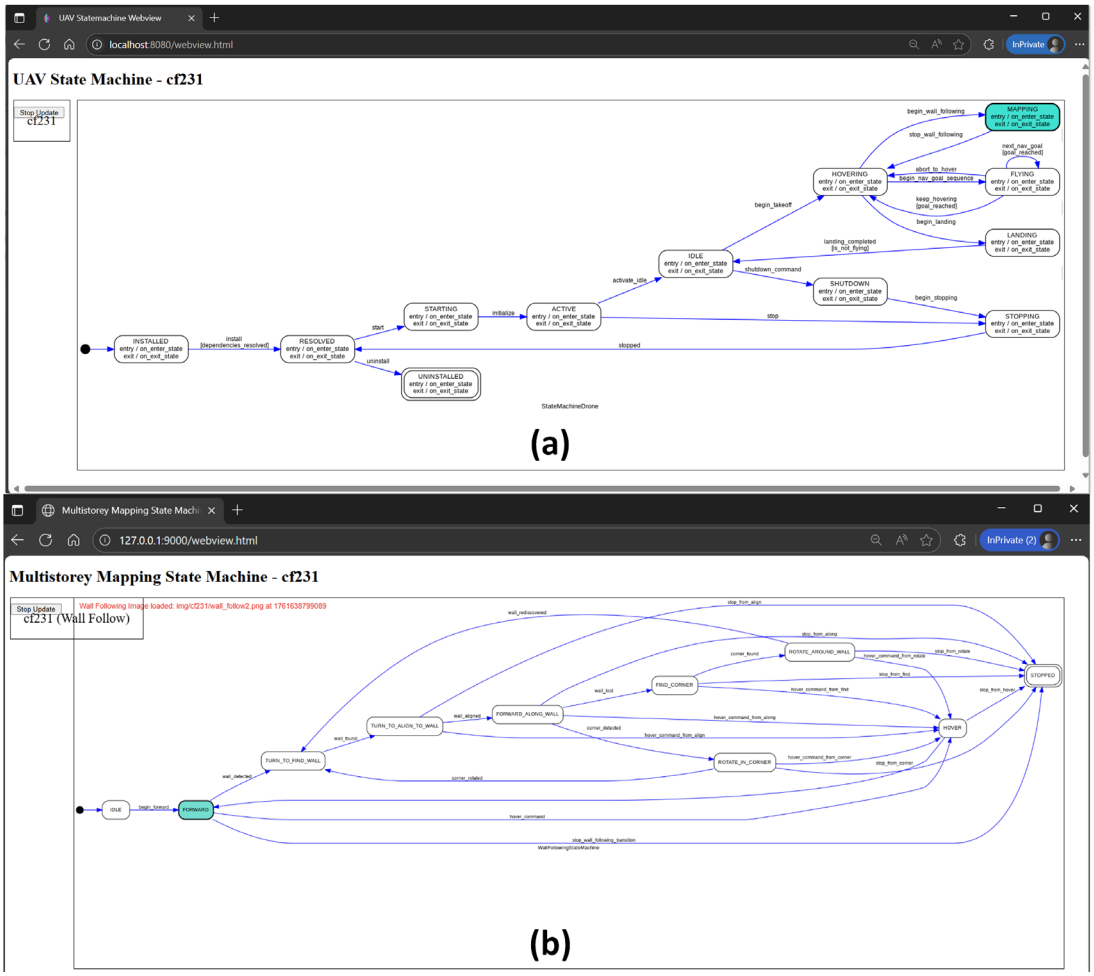

Fig. 8. Screenshot of Digital Twin Web Service. (a) Real-time web page of the Digital Twin-based Controller FSM; (b) Real-time web page of the Multistorey Mapping FSM.

4. Discussion

Localization Accuracy: The proposed approach does not rely on external positioning systems. The experiments use only the Flow Deck and the onboard IMU for pose estimation. Consequently, the resulting maps are less precise compared to methods that employ high-accuracy external systems (e.g., motion capture). Drift in the Flow Deck and IMU may cause slight deviations in map boundaries. Additionally, manually setting the initial positions of the MAVs can introduce small errors. However, the method's independence from external localization allows MAVs to operate in completely unknown environments without pre-installed infrastructure, broadening its applicability.

Swarm size: Due to spatial constraints, the experiments were conducted with only two MAVs simultaneously. This does not imply that the method is limited to this size; the proposed framework is highly scalable. By simply adding additional MAV IDs in the system, more MAVs can be synchronized for multistorey mapping.

Exploration Algorithm: The Map Bug algorithm is used for exploration of unknown environments. It is easy to implement and requires minimal computational resources, making it suitable for MAVs. However, its performance may be limited in more complex or cluttered environments. Future work will focus on developing more flexible and robust exploration strategies.

Layered Perception Benefits: Experiments show that different altitude layers capture complementary structural features. For example, the lowest layer reveals floor-level obstacles and base structures, while higher layers expose shelf-level or hanging-object profiles invisible to lower MAVs. This demonstrates that a layer-separated perception stack enhances spatial interpretability, particularly in complex indoor environments.

5. Conclusions

In this work, we present a digital twin-based multistorey mapping pipeline for an indoor environment using multiple MAVs. The Digital Twin Web Service provides real-time visualization and an interactive control interface of MAV task execution, closing the loop between the digital model and physical system. The proposed controller leverages an FSM as the core control layer to define general MAV behaviors, enabling coordinated task scheduling and behavior synchronization. For the Mapping Service, we integrate Map Bug and Downwash Avoidance algorithms to support autonomous exploration at different altitude layers. Combined with the Single Map Merge Service and TF Broadcaster, the system enables the construction of occupancy maps across multiple height layers. Experiments conducted in a physical testbed demonstrate that MAVs can effectively capture environmental information at different heights and generate multistorey maps, highlighting the potential advantages of using MAV swarms for complex indoor mapping tasks.

Acknowledgements

This research was funded by the German Research Foundation (DFG) as part of RTG-AirMetro, grant number GRK 2947/1, 508591287, and the European Social Fund (ESF Plus) and the German Federal State of Saxony within the project ProSECO (100687967).

References

[1]. M. Saska, V. Vonásek, J. Chudoba, J. Thomas, et al., Swarm distribution and deployment for cooperative surveillance by micro-aerial vehicles, *Journal of Intelligent & Robotic Systems*, Vol. 84, Issue 1, 2016, pp. 469-492.

[2]. K. N. McGuire, C. De Wagter, K. Tuyls, H. J. Kappen, et al., Minimal navigation solution for a swarm of tiny flying robots to explore an unknown environment, *Science Robotics*, Vol. 4, Issue 35, 2019, eaaw9710.

[3]. B. P. Duisterhof, S. Li, J. Burgués, V. J. Reddi, et al., Sniffy Bug: A fully autonomous swarm of gas-seeking nano quadcopters in cluttered environments, in *Proceedings of the IEEE/RSJ International Conference on Intelligent Robots and Systems (IROS'21)*, 2021, pp. 9099-9106.

[4]. D. Jaisinghani, T. U. Rehman, R. Mulkey, S. Pandey, et al., IoT in the air: Thread-enabled flying IoT network for indoor environments, in *Proceedings of the IEEE International Conference on Pervasive Computing and Communications Workshops and other Affiliated Events (PerCom Workshops'23)*, 2023, pp. 142-147.

[5]. T. Zhang, D. Grzelak, M. Lindner, S. H. S. Bukkapatnam, et al., A bigraph-based digital twin for multi-UAV landing management, *Drones*, Vol. 8, Issue 9, 2024, 464.

[6]. P. Arias-Perez, A. Gautam, M. Fernandez-Cortizas, M. G. P. Sanchez-Sierra, et al., Exploring unstructured environments using minimal sensing on cooperative nano-drones, *IEEE Robotics and Automation Letters*, Vol. 9, Issue 7, 2024, pp. 6378-6385.

[7]. V. Niculescu, T. Polonelli, M. Magno, L. Benini, Ultra-lightweight collaborative mapping for robot swarms, *arXiv*, 2024, arXiv:2407.03136.

[8]. J. Markdahl, M. Vikgren, TinySLAM-based exploration with a swarm of nano-UAVs, *arXiv*, 2023, arXiv:2309.02834.

[9]. T. Samavedula, S. Mohapatra, S. K. Nayak, Mini Mapper: Cost-effective indoor mapping and navigation using nano drone, in *Proceedings of the 17th International Conference on COMmunication Systems and NETworks (COMSNETS'25)*, 2025, pp. 1377-1379.

[10]. T. Zhang, D. Grzelak, W. Zhao, M. Lindner, et al., A review on the construction, modeling, and consistency of digital twins for advanced air mobility applications, *Drones*, Vol. 7, Issue 9, 2023, 576.

[11]. C. Friess, V. Niculescu, T. Polonelli, M. Magno, et al., Fully onboard SLAM for distributed mapping with a swarm of nano-drones, *IEEE Internet of Things Journal*, Vol. 11, Issue 20, 2024, pp. 32363-32380.

[12]. K. N. McGuire, G. C. H. E. de Croon, K. Tuyls, A comparative study of bug algorithms for robot navigation, *Robotics and Autonomous Systems*, Vol. 121, 2019, 103261.

[13]. L. Lamberti, L. Bompani, V. J. Kartsch, M. Rusci, et al., Bio-inspired autonomous exploration policies with CNN-based object detection on nano-drones, in *Proceedings of the Design, Automation & Test in Europe Conference & Exhibition (DATE'23)*, 2023, pp. 1-6.

[14]. E. Magid, E. Rivlin, CautiousBug: A competitive algorithm for sensory-based robot navigation, in *Proceedings of the IEEE/RSJ International Conference on Intelligent Robots and Systems (IROS'04)*, 2004, pp. 2757-2762.

[15]. P. P. Neumann, P. Hirschberger, M. Bartholmai, Influence of rotor downwash on vertically displaced nanobots in flight, *Materials Today: Proceedings*, Vol. 32, 2020, pp. 108-111.

(004)

Cooperative UAV Payload Transport with Autonomous Navigation

Alice James, Avishkar Seth, Endrowednes Kuantama, Subhas Mukhopadhyay, Richard Han
Macquarie University, Advanced Drone Systems Research Centre, Sydney, NSW 2109, Australia
Tel.: + 61 (02) 9850 7111
E-mail: alice.james@mq.edu.au

Summary: This paper investigates cooperative payload delivery using multi-agent uncrewed aerial vehicles equipped with a self-balancing tray and a trajectory-planning algorithm. We aim to address the challenges of localization and navigation in cooperative aerial manipulation under GPS-denied conditions. We introduce a robust visual-inertial localization system and an adaptive navigation approach using a global leader algorithm to achieve stable and precise load transportation. Our system utilizes a 3-degree end effector for precise movement and a novel ROS-based inter-UAV communication strategy to ensure tight coordination. The SBT mechanism effectively balances the load, maintaining stable flight dynamics with low vibration levels less than 0.5 m/s^2. The system demonstrated superior performance, with deviations of less than 0.2 meters for curved paths and less than 0.1 meters for straight paths, at a constant flight speed of 3 m/s. These results, validated through autonomous flight experiments, confirm the system's effectiveness in achieving precise navigation and stable payload transportation.

Keywords: Cooperative UAVs, Payload transport, Load stabilisation, Visual-inertial odometry, Multi-agent control, GPS-denied navigation, ROS.

1. Introduction

Cooperative aerial robotics holds immense potential in various research applications, including exploration [1], disaster response [2], and logistics [3], where flexibility and agility are crucial. Applying uncrewed aerial vehicles (UAVs) to automate logistics and transportation can significantly reduce costs, increase efficiency, and alleviate the burden on ground infrastructure. Furthermore, their maneuverability and three-dimensional movement capabilities make them particularly effective for aerial manipulation tasks, offering substantial benefits across numerous applications [4]. However, despite these advantages, optimizing these systems presents several challenges, particularly in enhancing communication, localization, navigation, and mechanical adaptability to improve performance in complex environments [5, 6].

In our previous work, we explored cooperative payload transportation using two UAVs, aiming to overcome the limitations of pull-based systems by enabling two independent drones to maintain payload stability collaboratively [7, 8]. This led to the development of the Self-Balancing Tray (SBT), a push-based mechanism supported by a three-degree-of-freedom end-effector (3-DEE) gimbal on each UAV, with a control system that demonstrated strong stability during cooperative transport tasks. In this work, we focus on localisation and adaptive navigation for cooperative UAV load transport using a leader–follower configuration, mechanically connected through an upgraded 3-DEE servo mechanism, as shown in Fig. 1. The objective is to ensure that the follower UAV can track the leader's motion without detaching the SBT. Tests are conducted using three motion patterns (straight, circular, and curved) to evaluate maximum deviation and adaptive adjustment.

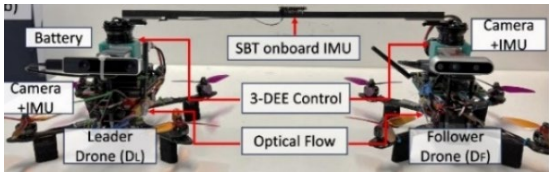

Fig. 1. Cooperative UAV: New configuration.

The system integrates visual–inertial odometry (VIO) via a tracking camera with an onboard inertial measurement unit (IMU), enabling real-time state estimation through direct communication with the onboard computer. This configuration removes the need for external systems such as motion capture and relies solely on reliable, lightweight onboard sensing and computation. To evaluate performance, experiments are conducted with the UAVs interfaced to a ground control station, using TCPROS (the default communication protocol in ROS) to manage data exchange between distributed components. The contributions of this work are as follows:
1. Visual–inertial localisation: An onboard tracking camera with IMU enables flexible UAV localisation.
2. Adaptive navigation: A global leader algorithm enables dynamic leader assignment, improving navigation flexibility and system responsiveness.
3. Inter-UAV communication: A ROS node-based communication method ensures reliable, precise distance maintenance between quadrotors.

2. Problem Formulation

Accurate localization and positioning pose significant challenges in cooperative robot control across diverse environments. Recent research has examined system performance in indoor [9], outdoor

environments using combinations of stereo vision, IMU, and UWB [10], [11], and GPS-denied settings [1]. Technologies such as motion capture (MOCAP) [12-14], OptiTrack [15], ultra-wideband (UWB) [16-18], and visual–inertial odometry (VIO) [19] are widely used for precise UAV indoor positioning and control in laboratory conditions. A vision-based approach for cable-suspended cooperative transportation has localised vehicles relative to each other using artificial markers [20]. Other vision-based studies focus on multi-vehicle coordination and planning while overlooking transportation problems that require simultaneous coordination and manipulation of structures [21]. Most experiments rely heavily on external MOCAP systems, making improved onboard perception essential.

In cooperative leader–follower UAV systems, some models operate without inter-UAV communication [20, 12], while others use decentralised control supported by sensing-based communication [22, 23]. Methods such as real-time dynamic programming [24] and centralised architectures [25, 19] highlight the importance of robust communication for effective coordination. The proposed approach integrates VIO using a tracking camera and onboard IMU to enable accurate localization and positioning. This sensing system operates within a distributed ROS framework, providing reliable onboard computation and inter-UAV communication.

2.1. Cooperative Aerial Manipulation Model

The cooperative lift system is engineered for ease of detachment, flight stability, and minimal interference with quadcopter maneuverability. This is achieved through a 3-DEE mechanism comprising three servos arranged in a gimbal configuration to enable precise motion along all three rotational axes. Each UAV connects to the self-balancing tray (SBT) through magnetically coupled attachment points in a push-based configuration, as shown in Fig. 1. These detachable connections promote compatibility with standard multi-rotor platforms and support scalability for multi-UAV cooperation. The SBT is equipped with onboard sensors that monitor its orientation and transmit balance data to the connected UAVs. To visualise and analyse its motion, a carbon fibre rod is used to represent the SBT's movement across multiple directions. This setup demonstrates the SBT's ability to maintain a level orientation while both drones follow pre-defined paths with varying shapes. The system architecture comprises two quadcopters, each with a frame size of 295 mm × 295 mm, supported by 2300 KV motors and equipped with 5-inch propellers. Each UAV is equipped with a Jetson Nano onboard computer, a downward-facing optical flow sensor with an integrated time-of-flight (ToF) rangefinder for altitude control, a flight controller, and a tracking camera with an IMU for accurate localisation and navigation. The 3-DEE system connects each UAV to the SBT via magnetic joints, maintaining system stability while enabling quick detachment. The SBT position is continuously monitored and communicated to ensure a balanced payload orientation throughout cooperative flight.

The cooperative UAV control system for the two drones, the Leader (D_L) and the Follower (D_F), is designed to ensure synchronized flight and reliable communication between them. The system architecture is illustrated in the block diagram shown in Fig. 2. The D_L processes SBT position data, including IMU readings and coordinate information (d_{SBT}, x, y). Communication between the UAVs is managed through the MAVROS framework, where the leader functions as the ROS PRIMARY and the follower as the ROS REPLICA. The leader's MAVROS node handles ROS camera pose updates $(P_L(x))$, executes guided flight commands, and transforms the vision frame into the MAVROS coordinate frame. This information is then transmitted to the follower's mavros node, which uses it to update its flight pose $(P_F(x))$, allowing the follower to maintain a stable hover while tracking the leader's path. An Extended Kalman Filter (EKF) is used to initialize and continuously update the home parameters, orientation, and velocities (V_x, V_y) for both drones. This ensures that the follower accurately mirrors the leader's position and movement, maintaining the formation $D_L = D_F = (x, y, V_x, V_y)$. The cooperative control strategy, supported by real-time data exchange and coordinated control, maintains system stability and synchronization throughout flight.

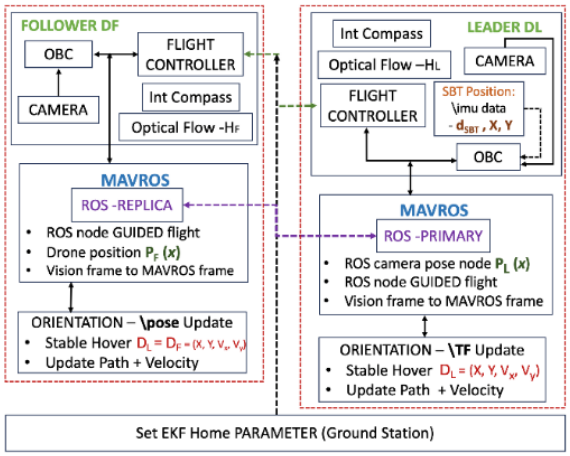

Fig. 2. System flow for the leader and follower drone.

The scope of this research focuses on cooperative UAV localisation and navigation during hover and translational movement, excluding take-off and landing phases. All drones and the ground control station are connected via a 2.4 GHz Wi-Fi router using a star network configuration, where the follower drone subscribes to data broadcast by the leader. The 3-DEE system used to stabilise the SBT is based on prior work [7, 8] and is tuned for flight with servo angle limits of ±40° for pitch and yaw, and ±30° for roll.

2.2. Localization and Navigation Methods

The cooperative control system utilizes a visual pose transform for two drones, where D_L delegates its orientation information to the D_F. The SBT connects the two drones, maintaining stability and balance through the path. The pre-planned paths (curve, circular, and straight) are used to test the feasibility of the cooperative control mechanism. The leader drone, equipped with an orientation sensor (camera and IMU) and an altitude sensor (H_L), communicates the necessary adjustments to the follower drone, ensuring synchronized attitude and movement, as shown in Fig. 3(a) along the designated paths. The distance (d_{SBT}) between the drones is maintained throughout the flight to demonstrate the effectiveness of the 3-DEE control system and the robustness of the SBT under varying flight conditions.

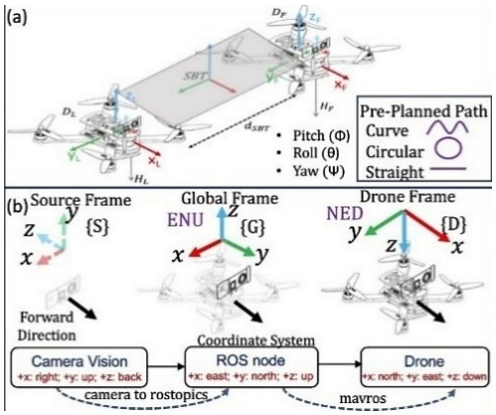

Fig. 3. Coordinate: (a) localization; (b) VIO Tracking.

The coordinate transformation process, essential for integrating VIO tracking with drones for indoor non-GPS flights, is illustrated in Fig. 3(b). The system starts with the camera vision coordinate system, denoted as the Source Frame S, where the axes are defined as (+X(right),+Y(up),+Z(back)). This data is converted to the ROS node coordinate system, or Global Frame G, which aligns with the ENU (East-North-Up) convention: (+X(east), +Y(north), +Zup). The final transformation is into the Drone Coordinate System, or Drone Frame D, adhering to the NED (North-East-Down) convention: (+X(north), +Y(east), +Z(down)). In practice, these transforms yield the VIO pose metric used to generate MAVROS guidance setpoints (ψ_L in Eq. (6) and $v_F = v_L + K_p e_p$ in Eq. (7)).

The mathematical model for the cooperative control system incorporates each drone's velocity, state vector, and position. The control algorithm enables direct movement in the x and y directions by adjusting rotational dynamics, while maintaining a fixed inter-drone distance to support the SBT. It accounts for pitch, roll, and yaw angles to transform angular body rates $[x \quad y \quad z]^T$ into Euler rates, using the computed angular velocity v. As described in [7], the coordinated control relies on the net system behaviour defined as $D_{\text{total}} = D_T$, where synchronized drone orientations are critical. Using Euler's rotational formulas, each drone's attitude is derived from the combined effects of four rotors and associated dynamics to compute the resultant movement angle. Eq. 1 in models the swarm's collective rotation for lifting the SBT, where c and s represent the cosine and sine of the rotation angle, respectively.

$$D_T = \begin{bmatrix} c\theta_{D_T}c\psi_{D_T} & c\theta_{D_T}s\psi_{D_T} & -s\theta_{D_T} \\ s\psi_{D_T}s\theta_{D_T}c\psi_{D_T} - c\phi_{D_T}s\psi_{D_T} & c\phi_{D_T}c\psi_{D_T} + s\phi_{D_T}s\theta_{D_T}s\psi_{D_T} & s\phi_{D_T}c\theta_{D_T} \\ c\phi_{D_T}s\theta_{D_T}c\psi_{D_T} + s\phi_{D_T}s\psi_{D_T} & s\theta_{D_T}c\phi_{D_T}c\psi_{D_T} - s\phi_{D_T}s\psi_{D_T} & -s\phi_{D_T}c\theta_{D_T} \end{bmatrix} \quad (1)$$

Visual navigation uses radial fisheye camera data to project 3D points, determining pose and depth. Path models describe the leader drone's movement along a sine wave and a straight path, with the follower maintaining a lateral offset. The system utilizes an EKF and a PID controller to refine state estimations and minimize errors, thereby ensuring precise coordination during flight. For the radial fisheye lens' in the camera used the relationship between a 3D point and its image projected can be described in Eq. (1), wherein $r(\theta)$ is the radial distance on the image plane, θ is the angle between the incoming ray and the optical axis and k is the focal length and distortion characteristics.

$$\begin{cases} r(\theta) = k \cdot \theta \\ d = r_l - r_r \\ Z_{cam} = \dfrac{f \cdot b}{d} \end{cases} \quad (2)$$

The disparity d is calculated as the difference between corresponding pixel coordinates from the two horizontally aligned fisheye cameras, denoted as left r_l and right r_r. Given the baseline distance b between the cameras and the focal length f, the depth Z_{cam} of a point in the scene is estimated using these parameters. The three-dimensional projection of point $P = (X, Y, Z)^T$ in the camera vision coordinate system to the fisheye image plane is modelled as Eq. (3). In the experiments, VIO is provided by an onboard tracking camera with an IMU (Intel RealSense T265), which contains a stereo fisheye pair; Eq. (2)–(3) describes this internal stereo geometry. The control loop does not use raw disparity/depth directly; it consumes the camera's metric VIO pose/velocity outputs (published to MAVROS/ROS) for leader–follower guidance and distance regulation.

$$\begin{bmatrix} x' \\ y' \end{bmatrix} = k \cdot \theta \cdot \frac{1}{\sqrt{x^2 + y^2 + z^2}} \begin{bmatrix} x \\ y \end{bmatrix} \quad (3)$$

The curve and circular path leader-follower model defines the leader UAV's trajectory as a sine wave in the horizontal plane, where A and B represent the amplitude and frequency, respectively. The variable x denotes the horizontal position, and B_x sets the phase, determining the y-coordinate along the path. Increasing B increases the frequency, producing more oscillations within the same distance. The leader UAV follows this sine wave at a fixed altitude, adjusting its yaw to align with the path. The leader's position P_L is given by Eq. (4). The velocity of the leader UAV will be tangent to the path represented in Eq. (5).

$$P_L(x) = \begin{bmatrix} x \\ y \\ h_L \end{bmatrix} = \begin{bmatrix} x \\ Asin(B_x) \\ h_L \end{bmatrix}, \quad (4)$$

$$V_L(x) = \frac{d}{dx} P_L(x) = \begin{bmatrix} 1 \\ ABcos(B_x) \\ 0 \end{bmatrix}, \quad (5)$$

$$\psi_L(x) = atan2(ABcos(B_x), 1), \quad (6)$$

$$V_F(x) = V_L(x) + K_P(P_F(x) - P_L(x)) \quad (7)$$

Aligning the leader's yaw angle $\psi_{L(x)}$ with the path can be represented using Eq. 6. The term $AB\cos(B_x)$ represents the y-component of the velocity, while the constant 1 represents the x-component, ensuring proper orientation. The arctan2 function accurately determines the angle, accounting for both components to maintain an efficient path following. The follower UAV traces the same path as the leader while maintaining a lateral offset to preserve the SBT distance. Its velocity vector aligns with that of the leader and is adjusted to compensate for positional errors, as shown in Eq. (7). Both UAVs use identical onboard autopilot controllers; our contribution generates MAVROS setpoints, and the follower pose-tracks the leader's broadcasted guidance for coordinated lift.

2.3. Navigation Algorithm

The D_L continuously estimates the goal distance and SBT angles using VIO. It transmits the planned trajectory, odometry data, and the SBT pose to the follower through ROS primary replica communication. To ensure accurate path following, the leader performs a reverse cross-check by comparing the follower's received coordinates, referred to as the *CheckPost*, and calculates the positional error. The total distance D_{total} between the leader and follower is computed using the Euclidean distance formula. If either the *CheckPost* error or D_{total} exceeds predefined thresholds, the leader activates an adaptive control mode to correct the follower's trajectory. Otherwise, it continues guiding the follower using VIO pose updates, ensuring synchronized and accurate motion. As shown in Fig. 2, the D_L is assigned based on the topics it publishes. It computes its orientation and the SBT position, plans the path, and transmits this data through the MAVROS ROS PRIMARY node. In the experiments reported, (D_L) is designated pre-flight and remains the leader for the entire run; no in-flight leader reassignment/handover is performed. Here, "adaptive" refers to the threshold-triggered correction mode used by followers rather than role switching. Visual navigation data is sent to MAVROS to support guided flight. The D_F receives updates through the MAVROS ROS REPLICA node and adjusts its position and orientation to maintain formation and leader's path.

3. Experimental Validation

3.1. Software Calibration and Algorithm Tests

The calibration of the visual-inertial camera addresses significant noise and drift caused by IMU sensor bias, scale factor instability, and gyroscope error, thereby improving distance accuracy, re-localization, and pose tracking. Calibration is performed using the Kalibr toolbox under controlled conditions, with a focus on intrinsic camera parameters and IMU noise modelling. As shown in Fig. 4, the results show clear improvements: x-axis measurements become more linear and closely follow the ground truth, while z-axis drift is substantially reduced. Although y-axis drift increases slightly, it exhibits a more consistent pattern, allowing for better compensation during pose estimation. The three pre-planned flight paths are first tested in simulation, as shown in Fig. 5. The D_L maintains a steady trajectory along the x-axis, ranging from approximately -1.5 to 3.0 meters, at an altitude between 2.6 and 3.4 meters.

The D_F initially deviates but corrects its path, achieving final alignment with a mean positional error of 0.2 meters. In the circular and curved paths, the D_L navigates a multi-turn path ranging from -1.0 to 4.0 meters along the x-axis and -2.0 to 2.0 meters along the y-axis. In both circular and curved scenarios, the D_F adjusts its trajectory after initial deviation, maintaining mean positional errors of 0.15 meters and 0.25 meters.

These simulation results demonstrate that the cooperative drone system, utilizing visual-inertial feedback, effectively maintains formation and accurately follows the leader drone's path across different flight patterns.

3.2. VIO Navigation Model

The system is evaluated in a real-world indoor environment using physical flight path tests. Camera and IMU pose information are initialized through

MAVROS and visualized in RVIZ. Specific MAVROS topics are selected to publish position estimates from the camera, including /mavros/vision_pose, /mavros/local_position, and /mavros/global_position. These topics provide essential pose and position data. Simultaneously, the camera outputs odometry and pose information through the /camera/camera_odom and /camera/camera_pose topics. All data streams are coordinated using the /tf topic, which manages transformations between coordinate frames, particularly between camera_odom_frame and camera_pose_frame. The transformed data is visualized in RVIZ, illustrating the spatial relationship between the frames, while terminal outputs provide detailed values for rotation and translation. This setup ensures precise localization and mapping. The leader drone publishes these topics, and the follower drone subscribes to this data.

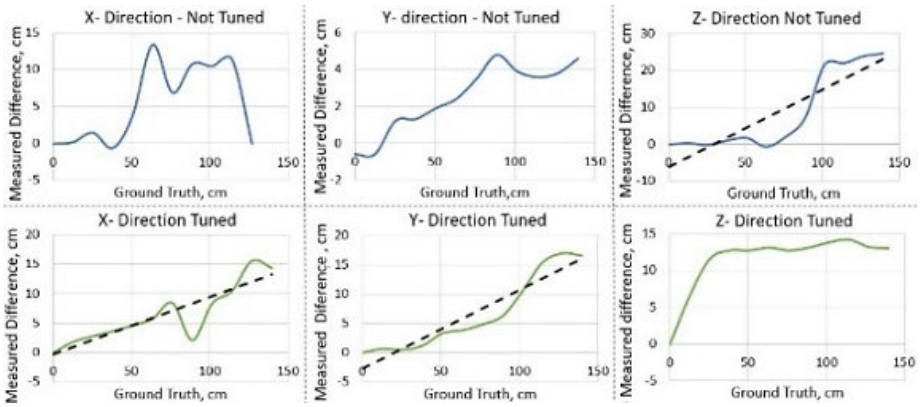

Fig. 4. T265 Tracking Camera Untuned and Tuned axis readings.

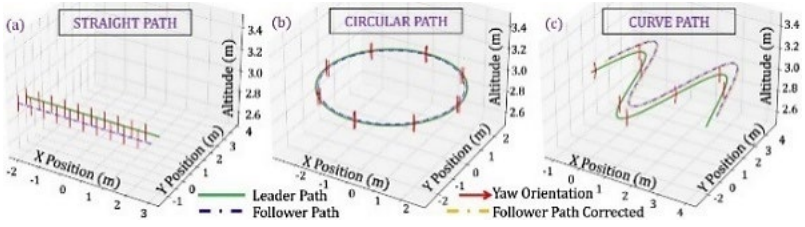

Fig. 5. Leader Follower navigation simulation results.

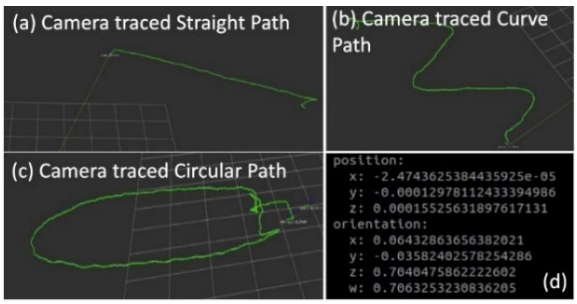

Fig. 6. VIO navigation model verification: (a) straight path; (b) circular path; (c) curve path; (d) sample pose/odom data.

Fig. 6(a) illustrates the camera tracing a straight path, shown by a green line, to verify the model's accuracy in linear motion tracking. Fig. 6(b) displays the camera's trajectory along a curved path, testing the model's ability to handle complex, non-linear movements. Fig. 6(c) depicts a circular path traced by the camera, evaluating the model's performance in repetitive and closed-loop movements. Fig. 6(d) presents a sample of pose and odometry data, providing specific coordinates and orientation of the camera at a given point. This data is crucial for assessing the precise position and orientation of the camera during navigation. Overall, we validate the reliability and accuracy of the VIO navigation model in performing complex patterns. Across all test paths, the position update rate is consistently maintained at 50 Hz, supporting real-time tracking. The performance metrics of the cooperative drone system using visual navigation are presented in Table 1. The straight path shows the best overall performance, achieving 28 FPS, 15 ms latency, and 2.1 cm position error.

Table 1. Visual Navigation Performance Metrics

Path Type	Update Rate (Hz)	FPS	Latency (ms)	Error (cm)
Circular	50	22	30	6.8
Curve	50	21	27	5.2
Straight	50	28	15	2.1

The positional error values represent the system's deviation from the planned trajectory for both the leader and follower drones i.e. the RMS Euclidean tracking error between each UAV's local position estimate and its commanded trajectory setpoint. The circular and curved paths show slightly reduced performance. The circular path records 22 FPS, 30 ms latency, and a 6.8 cm error, while the curved path achieves 21 FPS, 27 ms latency, and a 5.2 cm error. These results significantly improve upon preliminary test performance, which typically ranged between 30–40 Hz update rates, latencies below 50 ms, and positional errors within 10 cm.

5. Results and Discussion

The test is conducted by flying two drones carrying the SBT in an indoor environment at low speeds, approximately 3–5 m/s. The flight log results for circular, curved, and straight paths over ten iterations are shown in Fig. 7. These logs, based on acceleration and angular velocity data, illustrate the synchronization between the leader drone (blue) and the follower drone (red). In the circular path, the drones maintain a consistent radius with position errors within ±0.2 m and an average deviation of approximately 0.1 m, indicating strong coordination. For the curved path, the follower successfully tracks the leader through complex turns, with position errors within ±0.2 m and an average deviation of about 0.15 m. The straight path demonstrates the highest precision, with position errors below ±0.1 m and 0.05 m average deviation.

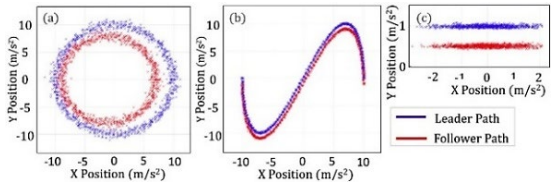

Fig. 7. Flight path verification: (a) circular; (b) curve; (c) straight.

The plots in Fig. 8 show the roll (Y-axis) and pitch (X-axis) rates of the leader and follower drones in radians per second (rad/s). The leader (green) and follower (red) closely track the desired roll rate (blue), with deviations within ±0.5 rad/s, indicating sync.

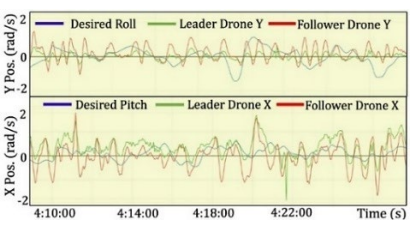

Fig. 8. Position and tracking error along the X and Y axis.

Pitch rates similarly follow the desired trajectory, with deviations within ±0.4 rad/s. Although the follower exhibits periodic oscillations, they remain within acceptable bounds, supporting stable flight. These results confirm synchronized orientation between the drones, enabling balanced payload transport and consistent flight dynamics. The IMU data from the BLE sensor mounted on the SBT during a circular trajectory flight is illustrated in Fig. 9. The tray is cooperatively lifted by two drones. Over the 40-second duration, vibrations along the X, Y, and Z axes remain minimal, indicating balanced system.

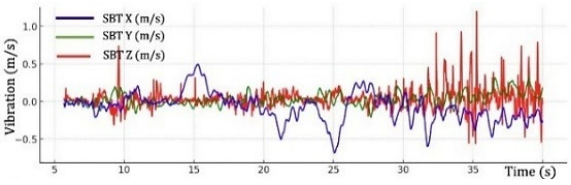

Fig. 9. Vibration across the X, Y and Z axis of the SBT inertial frame.

The Y-axis shows the least deviation, while occasional spikes in the X and Z axes remain within acceptable limits, confirming effective vibration damping and payload stabilization.

6. Conclusions

This paper presents a cooperative UAV system for precise load transportation using visual-inertial navigation and a global leader algorithm. The system maintains a 50 Hz position update rate across all path types, achieving 28 FPS, 15 ms latency, and a 2.1 cm position error on the straight path. Circular and curved paths record 22 FPS and 21 FPS, with latencies of 30 ms and 27 ms, and errors of 6.8 cm and 5.2 cm, respectively, exceeding typical visual navigation performance benchmarks. The ROS-based inter-UAV communication ensures tight coordination, with flight logs across ten iterations showing deviations within ±0.2 m for circular and curved paths, and below ±0.1 m for the straight path. The SBT stabilizes the payload effectively, with vibrations constrained below 0.5 m/s^2 on X and Y axes and below 0.2 m/s^2 on Z. These results confirm the system's capability for accurate, synchronized, and stable cooperative flight, supporting its application in precision-driven aerial transport tasks. In future work, the system will be tested at higher flight speeds and with more than two drones to evaluate its robustness and scalability under increased dynamic conditions. Further evaluation will quantify communication robustness and VIO recovery behaviour under controlled disturbances.

References

[1]. X. Zhou, X. Wen, Z. Wang, Y. Gao, et al., Swarm of micro flying robots in the wild, *Science Robotics*, Vol. 7, Issue 66, 2022, eabm5954.

[2]. M. Petrlik, P. Petracek, V. Kratky, T. Musil, et al., UAVs beneath the surface: Cooperative autonomy for subterranean search and rescue in DARPA SubT, *Field Robotics*, Vol. 3, Issue 1, 2023, pp. 1-68.

[3]. D. K. D. Villa, A. S. Brandao, M. Sarcinelli-Filho, A survey on load transportation using multirotor UAVs, *Journal of Intelligent & Robotic Systems*, Vol. 98, Issue 2, 2020, pp. 267-296.

[4]. J. Mendoza-Mendoza, L. Alvarez-Icaza, J. C. Herrera-Lozada, Snake aerial manipulators: A review, *IEEE Access*, Vol. 8, 2020, pp. 28222-28241.

[5]. S.-J. Chung, A. A. Paranjape, P. Dames, S. Shen, et al., A survey on aerial swarm robotics, *IEEE Transactions on Robotics*, Vol. 34, Issue 4, 2018, pp. 837-855.

[6]. S. C. Barakou, A. T. Tzes, K. K. Vayanos, Real-time applicable cooperative aerial manipulation: A survey, in *Proceedings of the International Conference on Unmanned Aircraft Systems (ICUAS'23)*, 2023, pp. 1076-1083.

[7]. A. James, N. R. Chowdhury, Cooperative drone payload delivery with self-balancing tray, in *Proceedings of the International Conference on Advanced Robotics and Mechatronics (ICARM'24)*, 2024, pp. 25-30.

[8]. A. James, N. R. Chowdhury, Cooperative drone delivery via push-based lift with payload stabilization, in *Proceedings of the 10th Workshop on Micro-Aerial Vehicle Networks, Systems, and Applications (DroNe'24t)*, 2024, pp. 31-36.

[9]. G. Li, G. Loianno, Nonlinear MPC for cooperative transportation with multiple quadrotors, in *Proceedings of the IEEE/RSJ International Conference on Intelligent Robots and Systems (IROS'23)*, 2023, pp. 3165-3171.

[10]. K. Klausen, T. I. Fossen, T. A. Johansen, Cooperative control for multirotors transporting an unknown suspended load, *IEEE Transactions on Control Systems Technology*, Vol. 28, Issue 2, 2020, pp. 653-660.

[11]. H. Yu, Y. Li, Y. Zhang, Z. Chen, CSLAM and GPS based navigation for multi-UAV cooperative transportation, *Lecture Notes in Computer Science*, Vol. 11742, 2019, pp. 315-325.

[12]. P.-X. Wu, H. Huang, Y.-H. Liu, Cooperative transportation of UAVs without inter-UAV communication, *IEEE/ASME Transactions on Mechatronics*, Vol. 28, Issue 4, 2023, pp. 2340-2351.

[13]. S. Kim, S. Choi, H. J. Kim, Cooperative aerial manipulation using multirotors with multi-DOF robotic arms, *IEEE/ASME Transactions on Mechatronics*, Vol. 23, Issue 2, 2018, pp. 702-713.

[14]. M. Zhao, T. Anzai, F. Shi, X. Chen, et al., Versatile articulated aerial robot DRAGON, *The International Journal of Robotics Research*, Vol. 42, Issue 4-5, 2023, pp. 214-248.

[15]. J. S. Furtado, H. B. Resende, F. O. Moraes, P. L. Brito, Comparative analysis of OptiTrack motion capture systems, in Proceedings of the Congress of National Mechanical Engineering (K. L. Cavalca, F. G. Dedini, Eds.), *Springer, Cham*, 2018, pp. 363-371.

[16]. W. Shule, K. Al-Makhlasawy, F. Xinyu, A. A. A. El-Latif, UWB-based localization for multi-UAV and heterogeneous multi-robot systems, *Procedia Computer Science*, Vol. 175, 2020, pp. 357-364.

[17]. Y. Han, K. Liu, Y. Lee, H. S. Lee, A novel cooperative localization method based on IMU and UWB, *Sensors*, Vol. 20, Issue 2, 2020, 456.

[18]. A. Masiero, F. Fissore, A. Guarnieri, F. Pirotti, et al., A comparison of UWB and motion capture UAV indoor positioning, International Archives of the Photogrammetry, *Remote Sensing and Spatial Information Sciences*, Vol. XLII-2/W13, 2019, pp. 471-476.

[19]. G. Loianno, V. Kumar, Cooperative transportation using small quadrotors with monocular vision and inertial sensing, *IEEE Robotics and Automation Letters*, Vol. 3, Issue 2, 2018, pp. 680-687.

[20]. M. Gassner, T. Cieslewski, D. Scaramuzza, Dynamic collaboration without communication, in *Proceedings of the IEEE International Conference on Robotics and Automation (ICRA'17)*, 2017, pp. 5196-5202.

[21]. M. Saska, V. Vonásek, T. Krajník, L. Přeučil, Deployment of groups of unmanned micro aerial vehicles in GPS-denied environments, *Autonomous Robots*, Vol. 41, Issue 4, 2017, pp. 919-944.

[22]. M. Tognon, H. A. Tello-Chavez, E. Gasparin, Q. Sablé, et al., Aerial co-manipulation with cables: Internal force for equilibria, stability, and passivity, *IEEE Robotics and Automation Letters*, Vol. 3, Issue 3, 2018, pp. 2577-2583.

[23]. C. Gabellieri, M. Tognon, D. Sanalitro, A. Franchi, Force-based collaboration in swarms, *Swarm Intelligence*, Vol. 14, Issue 1, 2020, pp. 57-82.

[24]. A. Mohiuddin, T. H. Tran, Y. M. S. Zweiri, D. Gan, Dual-UAV payload transportation via real-time dynamic programming, *Drones*, Vol. 7, Issue 3, 2023, 188.

[25]. C. Masone, M. Tognon, A. Franchi, Cooperative transportation of a payload using quadrotors: A reconfigurable cable-driven parallel robot, in *Proceedings of the IEEE/RSJ International Conference on Intelligent Robots and Systems (IROS'16)*, 2016, pp. 1623-1630.

(005)

Deep Reinforcement Learning-Based UAV Recovery Using a Mobile Manipulator with a Magnetic Gripper

Y. Kim [1], J. Lee [1] and H.-S. Yoon [2]
[1] DGIST, Interdisciplinary Engineering, 333 Techno jungang-daero, Daegu, Korea
[2] DGIST, Division of Intelligent Robot, 333 Techno jungang-daero, Daegu, Korea
Tel.: + 82 53 785 4662
E-mail: hsyoon@dgist.ac.kr

Summary: This study proposes a mid-flight recovery system to address the limitations of conventional net-based methods, which can cause damage to fixed-wing unmanned aerial vehicles (UAVs) during retrieval. To safely and efficiently recover UAVs approaching at high-speed, we present a switching magnetic gripper-based recovery system mounted on a mobile manipulator platform. The proposed approach overcomes the restricted workspace of stationary recovery systems and enables dynamic interaction with fast-moving UAVs. For the generation of recovery behaviors, a model was developed using the Soft Actor-Critic (SAC) algorithm, a representative method in deep reinforcement learning (DRL). The trained model effectively learns UAV motion dynamics to achieve reliable recovery operations. Training and evaluation were conducted in a PyBullet simulation environment. The experimental results demonstrate that the proposed system successfully captures fixed-wing UAVs, indicating its potential to complement and enhance existing UAV recovery methods.

Keywords: UAV Recovery System, Deep reinforcement learning, Mobile manipulator, Magnetic gripper, Soft actor critic.

1. Introduction

Unmanned fixed-wing aerial vehicles (UAVs) are widely employed in surveillance, reconnaissance, and logistics missions, requiring reliable recovery mechanisms for repeated operation and maintenance. Conventional recovery systems, including net-, hook-, and rope-based mechanisms, rely on passive recovery and deceleration, often imposing substantial impulsive loads on the airframe and reducing structural integrity [1]. Although recent shipborne recovery studies have attempted to mitigate these effects through aerodynamic configuration and trajectory optimization, such approaches remain constrained by passive mechanical capture principles and limited adaptability under uncertain approach conditions [1].

At the same time, advances in control and optimization have motivated learning-based methods for dynamic recovery and guidance. Deep reinforcement learning (DRL) has demonstrated strong performance in continuous control tasks, with algorithms such as Soft Actor-Critic (SAC) offering sample-efficient and stable policy learning under stochastic dynamics [2]. In recovery and guidance problems, Zero-Effort Miss (ZEM) and Zero-Effort Velocity (ZEV) concepts have been shown to improve terminal-phase precision by explicitly accounting for relative motion dynamics [3]. Policy-gradient-based methods, including Proximal Policy Optimization (PPO) and recurrent extensions, have also been explored to address temporal dependencies, though often with increased sensitivity to reward sparsity and training instability [4, 5].

Robotic manipulation has recently been investigated as a means of active mid-air recovery. While fixed-base manipulators and vision-guided catching systems have demonstrated feasibility in controlled environments, their limited workspace and alignment tolerance restrict application to low-speed fixed-wing UAVs. Furthermore, most learning-based recovery studies focus on low-speed quadrotor platforms, leaving mid-flight recovery of fast-approaching fixed-wing UAVs largely unexplored.

In this context, the present study investigates a mid-flight recovery framework using a mobile manipulator equipped with a switching magnetic gripper. By integrating explicit aerodynamic modeling, simplified magnetic coupling, and a SAC-based controller augmented with ZEM-inspired guidance terms, the proposed approach enables adaptive recovery while reducing mechanical stress during capture.

2. Methods

The methodology is divided into three subsections: Hardware Design, Simulation Environment, and Learning Framework.

2.1. Hardware Design

The system was configured to capture a rapidly approaching fixed-wing UAV (2.5 kg, 15 m/s) with minimal impact force. To reduce relative velocity, a mobile robot was modeled with 2 degrees of freedom (DOF) motion. On top of the mobile platform, a 1-DOF lifting column and a 6-DOF manipulator were integrated. A magnetic gripper with a rated adhesion force of 200 N was installed at the manipulator end-effector.

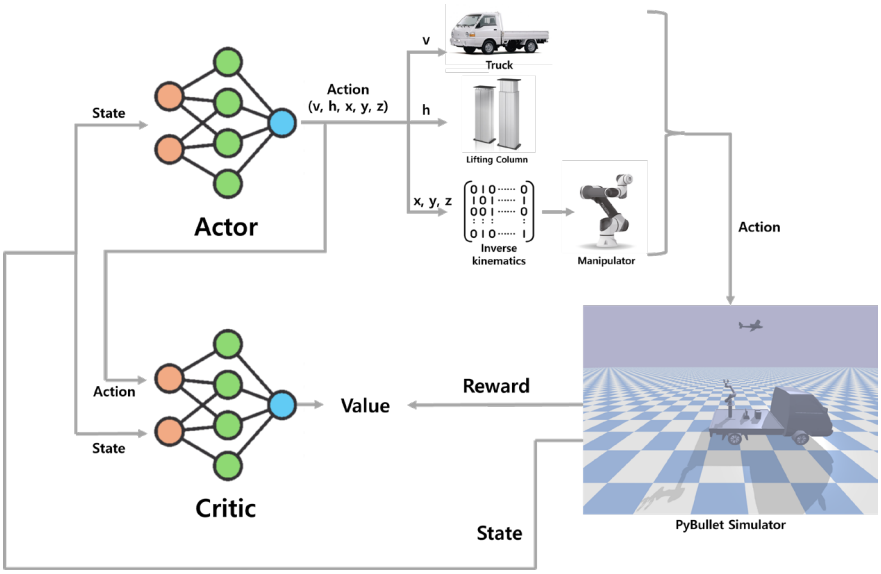

Fig. 1. Multi-Head Network Structure.

2.2. Simulation Environment

The simulation environment was implemented in PyBullet. As PyBullet lacks native lift modeling, aerodynamic lift was computed explicitly using a lift equation.

Magnetic coupling between the UAV and gripper was represented as a dipole–plate force, considering only translational motion since the end-effector orientation remains fixed.

A curriculum learning scheme improved generalization: the UAV's trajectory and orientation were randomized in proportion to the success rate.

2.3. Learning Framework

The UAV recovery control policy was trained with the Soft Actor–Critic (SAC) algorithm [2] for sample-efficient continuous control. The policy adopted a multi-head network (see Fig. 1).

The reward function (see Table 1) encouraged smooth, aligned recovery by rewarding proximity and directional alignment while penalizing excessive relative velocity. A Zero-Effort Miss (ZEM) bonus [3] enhanced precision.

The observation space included UAV position, velocity, and orientation across multiple temporal frames (0, 5, 10, 15-frame history).

3. Results

The proposed Multi-Head SAC framework successfully accomplished the UAV recovery task, as illustrated in Fig. 2. Comparative evaluations were conducted against Vanilla SAC, GRU-based PPO (GRU-PPO), and TD3 with a Hindsight Experience Replay buffer (TD3+HER) under identical simulation conditions, with 20 trials per method. All approaches except GRU-PPO achieved a 100 % success rate. Among them, the Multi-Head SAC demonstrated the highest inference performance, achieving 89 FPS (no GUI) on an RTX 4070 laptop, indicating its suitability for real-time recovery tasks.

Table 1. Reward Function

Item	Function	Weight
d	$\|P_{UAV} - P_{EE}\|$	
δd	$0.99\ d_{prev} - d_{now}$	5
D	$\|P_{UAV} - P_{Prev\_EE}\|$	
Δ	$0.99\ D_{now} - d_{now}$	$tanh\,\Delta + 0.3\,\Delta$
s_{rel}	$\|v_{UAV} - v_{EE}\|$	
δs_{rel}	$0.99\ s_{prev} - s_{now}$	0.5
Align	$cos\angle(v_{rel}, P_{rel})$	1
ZEM	$d + v_{rel}t_{go} + \frac{1}{2}gt_{go}^2$	$\begin{cases} +1\ ZEM < 0.1 \\ 0\ otherwise \end{cases}$

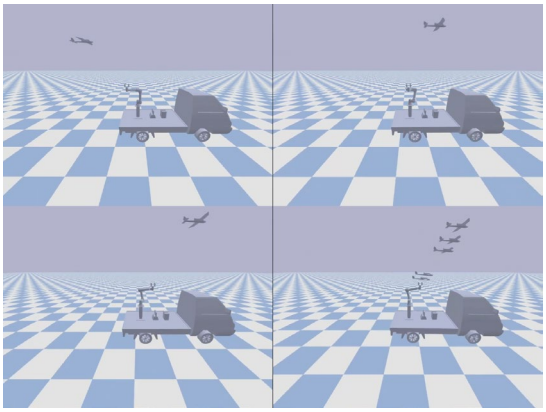

Fig. 2. Frame Sequence Montage of UAV Recovery

Impact analysis showed that the average impulse imparted on the UAV during capture was

approximately 2.75 kg·m/s, remaining within the structural tolerance of small fixed-wing airframes. This reduction was achieved by actively tracking the incoming UAV and lowering the relative capture velocity to approximately 1 m/s. In contrast, conventional net- or hook-based recovery systems rely on passive deceleration from cruise speeds exceeding 15 m/s, which typically induces higher impulsive loads.

Table 2. Multi-Head SAC Hyperparameters.

Name	Value
Learning Rate	0.0003
Batch Size	512
Tau	0.005
gamma	0.98
Train Frequency	1
Entropy Coefficient	0.2
Buffer Size	1000000

While the proposed approach improves impact mitigation and recovery adaptability, it introduces additional system complexity due to the use of a mobile platform, a multi-DOF manipulator, and learning-based control. Consequently, the framework is most suitable for applications in which airframe protection and reusability are prioritized over hardware and computational simplicity.

4. Conclusions

This study presented a deep reinforcement learning based UAV recovery framework using a mobile manipulator equipped with a magnetic gripper. The proposed system demonstrated efficient mid-flight capture of fixed-wing UAVs by reducing the relative velocity to approximately 1 m/s at impact – significantly mitigating structural stress compared to net or hook-based methods, which typically involve deceleration within 1 s and impact speeds exceeding 15 m/s. Overall, the results suggest that the proposed approach offers a promising alternative for mid-air UAV recovery, improving safety, reusability, and operational robustness of fixed-wing aerial systems.

Acknowledgements

This work was supported by the Future Challenge Defense Technology Research and Development Program through the Agency for Defense Development (ADD) grant funded by the Defense Acquisition Program Administration (DAPA) in 2025(No.915134201)

This research was supported by Korea Ministry of Science and ICT. (Grant Number: 25-IT-02)

References

[1]. L. Chu, F. Gu, X. Du, M. Zhang, et al., Aerodynamic configuration and control optimization for a novel horizontal-rope shipborne recovery fixed-wing UAV system, *Aerospace Science and Technology*, Vol. 137, 2023, 108253.

[2]. T. Haarnoja, A. Zhou, P. Abbeel, S. Levine, Soft actor-critic: Off-policy maximum entropy deep reinforcement learning with a stochastic actor, in *Proceedings of the 35th International Conference on Machine Learning (ICML'18)*, 2018, pp. 1861-1870.

[3]. Y. Gong, Y. Guo, Y. Lyu, G. Ma, et al., Hybrid zero-effort-miss/zero-effort-velocity guidance for powered descent phase, *Journal of Guidance, Control, and Dynamics*, Vol. 47, Issue 5, 2024, pp. 1026-1037.

[4]. J. Schulman, F. Wolski, P. Dhariwal, A. Radford, et al., Proximal policy optimization algorithms, *arXiv*, 2017, arXiv:1707.06347.

[5]. C. Igl, K. Ciosek, M. Li, R. T. McAllister, et al., Deep variational reinforcement learning for POMDPs, in *Proceedings of the 35th International Conference on Machine Learning (ICML'18)*, 2018, pp. 2117-2126.

[6]. D. Kalashnikov, J. Varley, Y. Chebotar, B. Swanson, R. Jonschkowski, C. Finn, S. Levine, K. Hausman, MT-Opt: continuous multi-task robotic reinforcement learning at scale, *arXiv*, 2021, arXiv:2104.08212, 2021.

[7]. M. Hausknecht, P. Stone, Deep recurrent Q-learning for partially observable MDPs, in *Proceedings of the AAAI Fall Symposium Series*, Arlington, Virginia, USA, 9-11 November 2015, pp. 73-80.

(007)

Experimental Evaluation of a Fuel Cell Hybrid Propulsion System for a Fixed-Wing UAV

Jong-Bo Shin [1], Hae-In Kim [1], Seung-Gon Kim [2] and Jae-Sung Bae [3]
[1] Korea Aerospace University, Department of Smart Air Mobility, Goyang, Republic of Korea
[2] Korea Aerospace University, Department of Smart Drone Engineering, Goyang, Republic of Korea
[3] Korea Aerospace University, Department of Aeronautical and Astronautical Engineering, Goyang, Republic of Korea
Tel.: +82-2-300-0102
E-mail: jsbae@kau.ac.kr

Summary: Fuel cells generate electricity through an electrochemical reaction between hydrogen and oxygen. Although fuel cells offer high energy density and eco-friendly characteristics, they exhibit relatively low power density, resulting in slow transient response and challenges in maintaining stable power output. To overcome these limitations, this study experimentally evaluated the applicability of a hybrid propulsion system combining a fuel cell and a Li-Po battery for a fixed-wing UAV. The hybrid system, consisting of an air-cooled polymer electrolyte membrane fuel cell (PEMFC) and a 12S Li-Po battery, was ground-tested in a configuration identical to that used on the fixed-wing UAV. The findings indicated that the system maintained stable power output under varying load conditions, exhibited distinct power-sharing behavior, and demonstrated clear thermal responsiveness and reliable transient response. These results confirm the technical feasibility and operational potential of the fuel-cell-based hybrid propulsion system for fixed-wing UAV applications.

Keywords: Fixed-wing UAV, Fuel cell, PEMFC, Hybrid system performance.

1. Introduction

In recent years, there has been a growing demand for UAV propulsion systems capable of achieving long-endurance and sustainable flight operations [1]. Lithium battery-based electric propulsion systems are environmentally friendly and have a relatively simple system architecture. However, their low energy density limits flight endurance and operational range [1, 2]. In particular, increasing the battery capacity to achieve longer missions leads to an increase in overall weight, resulting in reduced efficiency [2].

To overcome the limitations of lithium battery-based electric propulsion systems, hydrogen fuel cells have been considered as an alternative power source [3]. Even though hydrogen fuel cells provide high energy density and environmentally friendly operation, they have limitations in responding to dynamic load variations and maintaining stable output [2, 4].

To address these issues, this study applies a hybrid propulsion system that combines a polymer electrolyte membrane fuel cell (PEMFC) with a Li-Po battery.

In the proposed hybrid system, the fuel cell supplies the baseline power during long-duration operation, while the battery compensates for transient peak loads and rapid load variations, thereby improving output stability, response characteristics, and overall power system efficiency [5].

In this study, ground-based experiments were conducted to experimentally verify the applicability of a fuel-cell based hybrid propulsion system for fixed-wing UAVs. For the ground-based experiments, the propulsion system was implemented to replicate the actual propulsion configuration of a fixed-wing UAV, allowing a realistic evaluation of its performance.

Previous research on fuel-cell-based hybrid propulsion systems has primarily focused on small UAV platforms.

In contrast, this study implements and evaluates a PEMFC–Li-Po battery hybrid propulsion system on a scaled fixed-wing UAV platform under representative mission load profiles, with emphasis on real-time power-sharing behavior, load-following characteristics, and output and thermal stability.

2. Configuration of the Hybrid Propulsion System

2.1. Airframe Overview

A fixed-wing unmanned aerial vehicle (UAV) platform, a 35 %-scale model of the Columbia 400, was employed to integrate the fuel-cell-based hybrid propulsion system. The aircraft adopts a low-wing configuration, which offers advantages over mid- and high-wing layouts in accommodating heavy components, such as hydrogen storage vessels, beneath the fuselage. This configuration also enhances stability during ground roll by lowering the aircraft's center of gravity.

2.2. Configuration of the Hybrid Propulsion System

In this study, the hybrid propulsion system consists of a fuel cell and a Li-Po battery, and its overall schematic is presented in Fig. 1. The system is divided into three main subsystems: the propulsion, power, and storage systems. The propulsion subsystem comprises a motor, an electronic speed controller (ESC), and a capacitor. The power subsystem includes the fuel cell and the battery, whereas the storage subsystem consists of a high-pressure hydrogen vessel.

The hybrid system was configured such that the fuel cell supplies the primary power during steady operation, while the Li-Po battery supplements the power demand when the required power exceeds the rated output of the fuel cell or during transient operating conditions.

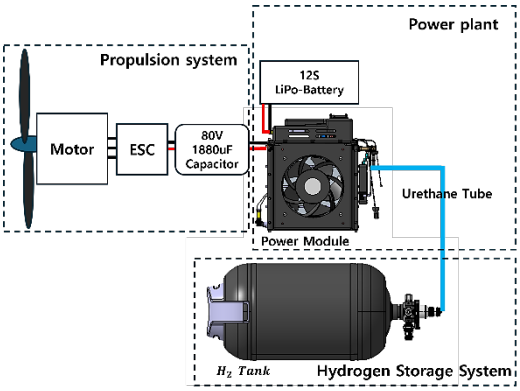

Fig. 1. Schematic configuration of the Hybrid Propulsion System.

This hybrid system enhances the overall system stability, transient response, and operational efficiency.

2.3. Mission Profile

Based on the mission profile of the fixed-wing UAV, a performance analysis was performed, and short-term (15 min) and long-term (75 min) mission load profiles were established to evaluate the hybrid system's response characteristics under simulated flight conditions.

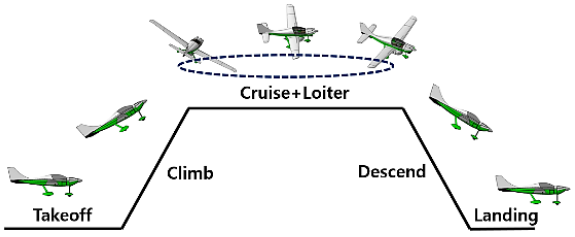

Fig. 2. Fixed-Wing UAV Mission Profile.

The mission load profiles, defined in terms of the time-varying electrical power demand and represented as power versus time, are shown in Figs. 3 and 4.

They comprise five sequential flight phases: takeoff, climb, cruise, descent, and landing.

In the cruise phase of the long-duration mission profile, transient acceleration segments were incorporated to represent realistic load variation patterns.

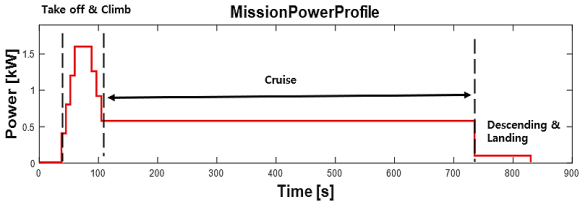

Fig. 3. Short-term Mission Load Profile

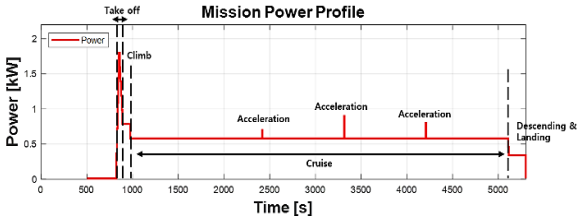

Fig. 4. Long-term Mission Load Profile

2.4. Results of Hybrid Propulsion System Ground Test

The short-duration ground test results corresponding to the mission load profile are presented in Fig. 5, while the long-duration test results are shown in Fig. 6. The correlation between the imposed electrical load demand and the measured output power indicates that the hybrid system maintained stable load-following behavior, even though the electrical load was applied through manual throttle control.

During transient peak-load conditions, the system sustained stable power output, confirming the hybrid system's ability to deliver high power, effectively respond to dynamic load variations, and exhibit distinct power-sharing characteristics between the fuel cell and the battery.

These observed power-sharing characteristics show that the battery supplemented the power demand during transient or peak load conditions, consistent with the inherent electrical behavior of the fuel cell system. In the short-duration test, the fuel cell stack temperature reached a maximum of 46 °C and then gradually decreased during the cruise phase, exhibiting a smooth and stable thermal response.

In the long-duration operation test, the fuel cell alone continuously supplied primary power throughout the 4140 s cruise phase, demonstrating the long-term operational stability of the fuel-cell-based power system.

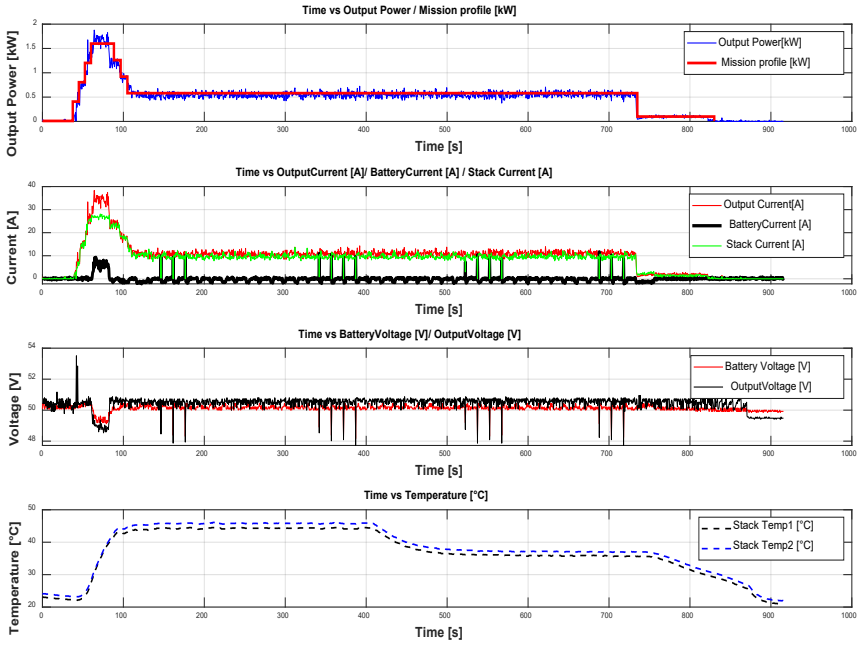

Fig. 5. Short-term Test Results of the Hybrid Propulsion System (Power, Current, Voltage, and Temperature Responses).

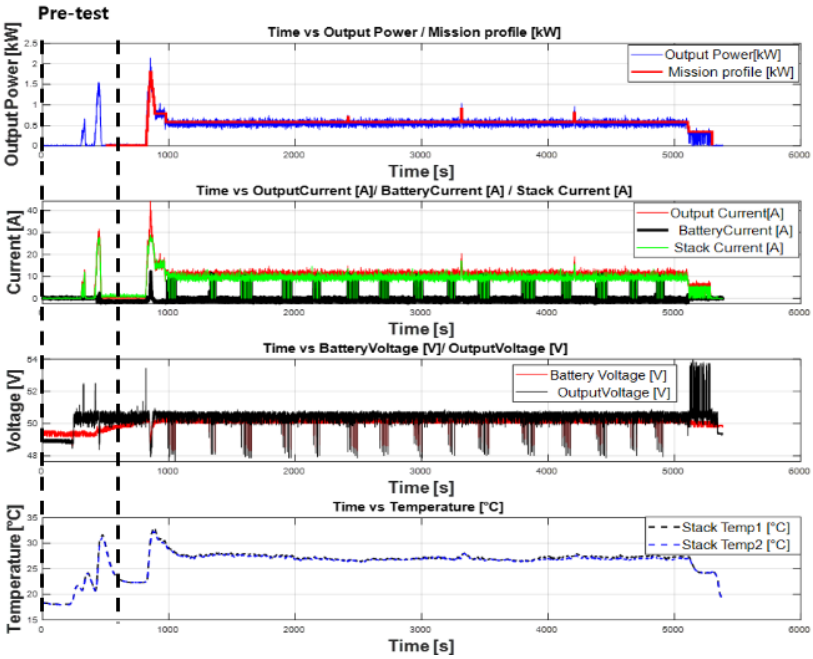

Fig. 6. Long-term Test Results of the Hybrid Propulsion System (Power, Current, Voltage, and Temperature Responses).

The stack temperature exhibited distinct thermal behavior with respect to load changes – rising under higher loads and decreasing as the load was reduced. During the steady-state cruise phase, the stack temperature stabilized at approximately 28 °C. Since PEMFC performance is sensitive to operating temperature, the limited variation in stack temperature indicates that the fuel cell operated within a stable thermal range, preventing performance degradation during the mission.

3. Conclusion

In this study, short and long-duration operation tests were conducted on a fuel-cell–Li-Po battery hybrid propulsion system.

The results showed that the system maintained stable power output under dynamic load conditions and revealed distinct power-sharing behavior between the fuel cell and the battery.

Moreover, the hybrid system demonstrated stable load-following performance in response to the mission

load profile. During the cruise phase of both the short- and long-duration tests, the fuel cell independently provided steady power, while the battery compensated during purging, overload, and transient conditions, thereby ensuring overall output stability.

Based on the ground test results, appropriate inlet configuration will be required for flight testing, as the cooling performance of the air-cooled fuel cell system depends on inlet geometry and flight conditions.

These results confirm the long-term operational feasibility of the fuel-cell hybrid propulsion system and its potential applicability to fixed-wing UAVs. The findings of this study provide fundamental data for the practical implementation of fuel-cell hybrid propulsion systems in UAVs and contribute to the development of effective operational strategies. Furthermore, these results provide the basis for flight tests.

Acknowledgements

This paper is research supported by the Ministry of Trade, Industry and Energy (A major activities of 2024 Industry Academia Cooperation: Aviation and defense SW professional Education) and Ministry of Land, Infrastructure and Transport (MOLIT) of the Korean government through the Korea Agency for Infrastructure Technology Advancement (KAIA) under the project “Development of a Certification System for Hydrogen Fuel Cell-Based Propulsion Systems for Small Aircraft” (RS-2023-00243094).

References

[1]. D. F. M. Santos, R. B. Ferreira, D. S. Falcão, A. M. F. R. Pinto, Evaluation of a fuel cell system designed for unmanned aerial vehicles, *Energy*, Vol. 253, 2022, 124151.

[2]. D. Verstraete, A. Gong, D. C. Lu, J. L. Palmer, Experimental investigation of the role of the battery in the AeroStack hybrid, fuel-cell-based propulsion system for small unmanned aircraft systems, *International Journal of Hydrogen Energy*, Vol. 40, Issue 3, 2015, pp. 1598-1606.

[3]. A. Gong, D. Verstraete, Design and bench test of a fuel-cell/battery hybrid UAV propulsion system using metal hydride hydrogen storage, in *Proceedings of the 53rd AIAA/SAE/ASEE Joint Propulsion Conference*, 2017, 4629.

[4]. C. Yang, S. Moon, Y. Kim, A fuel cell/battery hybrid power system for an unmanned aerial vehicle, *Journal of Mechanical Science and Technology*, Vol. 30, Issue 5, 2016, pp. 2379-2385.

[5]. A. Savvaris, Y. Xie, K. Malandrakis, M. Lopez, et al., Development of a fuel cell hybrid-powered unmanned aerial vehicle, in *Proceedings of the 24th Mediterranean Conference on Control and Automation (MED’16)*, 2016, pp. 1110-1115.

(008)

Development of an Autonomous Formation Flight System Based on Distributed Multi-Agent Control

J. W. Choi [1] and Y. H. Choi [2*]
[1] University of Korea Aerospace, Department of Artificial Intelligence, 76, Hanggongdaehak-ro, Deogyang-gu, Goyang-si, Gyeonggi-do, Republic of Korea
[2] University of Korea Aerospace, Department of Smart Drone Engineering, 76, Hanggongdaehak-ro, Deogyang-gu, Goyang-si, Gyeonggi-do, Republic of Korea
Tel.: + 82-2-300-0254
E-mail: jwmc_1118@kau.kr

Summary: The utilization of unmanned aerial vehicles (UAVs) for reconnaissance and surveillance has been rapidly increasing in recent years. To effectively monitor wide areas, extensive research has focused on the cooperative operation of multiple UAVs, emphasizing path planning and formation control. This study proposes a path planning method for a leader UAV and a distributed formation-flight system in which follower UAVs maintain formation relative to the leader. The leader UAV employs a vector field algorithm to efficiently fly near the designated multi-waypoints, while the follower UAVs use bearing information to maintain the desired formation relative to the leader. The proposed algorithm was validated through Simulation-in-the-Loop (SITL) experiments conducted in the ROS and Gazebo environments. The simulation results demonstrate that the UAVs successfully maintain the desired formation while passing near the designated multi-waypoints.

Keywords: Path planning, Formation control, Leader-follower, Multi-agent.

1. Introduction

In recent years, the frequency of wars and civil conflicts around the world has led to a rapid increase in the use of Unmanned Aerial Vehicles (UAVs) for military operations such as reconnaissance, surveillance, and search missions [1, 2]. Conversely, technologies for Counter-UAV (C-UAV) operations are also being actively developed in response [3, 4].

As UAV technologies continue to advance, their mission domains are expanding, and the precision and complexity of their tasks are significantly increasing. To ensure stability and reliability in mission execution under these conditions, operating a swarm of multiple UAVs has become more essential than relying on a single UAV.

The leader-follower structure [5, 6] is one of the representative approaches to UAV swarm operations. For autonomous mission execution, the leader typically requires research on path planning through the mission area, while the followers must be controlled to form and maintain a formation relative to the leader.

2. Methodology

The leader UAV is assumed to follow a nonholonomic model, and the follower UAVs are modeled as holonomic systems.

2.1. Path Planning for Leader

For reconnaissance and search missions, multi-waypoints are designated instead of a single target location, allowing the UAV to sequentially visit each point and survey the surrounding area. Accordingly, the leader UAV utilizes the vector field described in Fig. 1, Eq. (1) and Eq. (2) to navigate through the assigned waypoints.

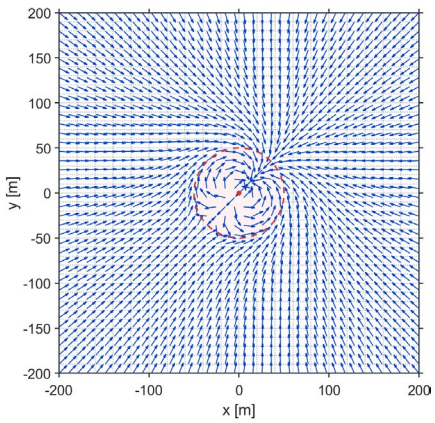

Fig. 1. Vector field for multi-waypoint guidance.

$$V_r = a\cos\theta - \frac{R^2}{r^2}\cos\theta - \left(exp\left(v * \frac{r}{R}\right) - 1\right), \quad (1)$$

$$V_\theta = -a\sin\theta - \frac{R^2}{r^2}\sin\theta, \quad (2)$$

where a and v are coefficients, θ represents the direction from the current waypoint toward the next waypoint, and R is the turning radius of the leader. The coefficients a and v are determined following the approach proposed by Lee [7].

The leader UAV is assumed to move at a constant speed. It is guided toward the waypoint using a proportional (P) controller based on the vector field direction at the current position. When the distance between the UAV and the current waypoint becomes less than or equal to 1 m, the waypoint is updated to the next one.

2.2. Formation Control for Followers

Let the set of agents be $V = \{1, 2, \dots, n\}$, and the set of connectivities be $E \subseteq V \times V$. The communication topology among n agents can then be represented as $G = (V, E)$. If agent i receives information from agent j, this relationship can be expressed as $(i, j) \in E$. The set of neighboring agents from which agent i receives information is defined as $N_i = \{j \in V : (i, j) \in E\}$.

The bearing vector that agent i obtains from its neighbor agent j is defined as follows in Eq. (3).

$$\boldsymbol{g}_{ij} = \frac{\boldsymbol{p}_j - \boldsymbol{p}_i}{\|\boldsymbol{p}_j - \boldsymbol{p}_i\|}, \forall (i, j) \in E \tag{3}$$

Using the bearing vector $\boldsymbol{g}_{ij}$, the orthogonal projection matrix $\boldsymbol{P}_{\boldsymbol{g}_{ij}}$ can be denoted as in Eq. (4).

$$\boldsymbol{P}_{\boldsymbol{g}_{ij}} = \boldsymbol{I}_d - \boldsymbol{g}_{ij}\boldsymbol{g}_{ij}^T \tag{4}$$

The desired formation $G(\boldsymbol{p}^*)$ satisfies the constraints given in Eq. (5) and Eq. (6).

$$\frac{\boldsymbol{p}_j^*(t) - \boldsymbol{p}_i^*(t)}{\|\boldsymbol{p}_j^*(t) - \boldsymbol{p}_i^*(t)\|} = \boldsymbol{g}_{ij}^*, \forall (i, j) \in E, \tag{5}$$

$$\boldsymbol{p}_l^*(t) = \boldsymbol{p}_l(t) \tag{6}$$

To enable a single follower to track the leader, a virtual leader-based formation system was designed as illustrated in Fig. 2.

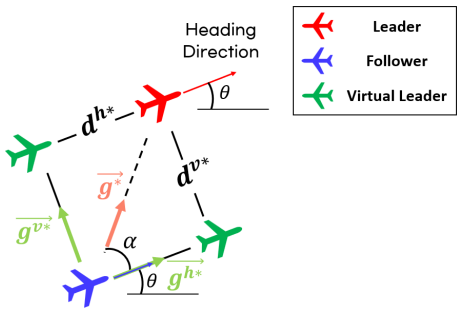

Fig. 2. Virtual leader-based formation system.

In the leader's body-fixed frame, this system generated two virtual leaders: one positioned at a distance d^{h*} along the leader's direction of motion, and the other at a distance d^{v*} in the orthogonal direction. These virtual leaders serve as reference points that determine the follower's position based on bearing constraints with two virtual leaders. The desired bearing vectors from the follower to the virtual leaders are given by $\boldsymbol{g}^{h*} = [1\ 0]^T, \boldsymbol{g}^{v*} = [0\ 1]^T$. Under these constraints, the virtual leader aligned with the motion direction determines the forward position of the follower, while the perpendicular virtual leader determines its lateral position.

To control follower UAVs, each follower receives the position of its leader, and the corresponding controller [8] is designed as follows in Eq. (7) ~ Eq. (8).

$$\boldsymbol{v}_i = -\boldsymbol{R}_{\theta_i}^T \boldsymbol{R}_l \sum_{j \in N_i} \boldsymbol{P}_{\boldsymbol{g}_{ij}^*} \boldsymbol{R}_l^T (\boldsymbol{p}_j - \boldsymbol{p}_i) + \boldsymbol{q}_i, \tag{7}$$

$$\dot{\boldsymbol{q}}_{f_i} = \boldsymbol{R}_l \boldsymbol{R}_{\theta_i} \boldsymbol{R}_{\theta_i}^T \boldsymbol{R}_l \sum_{j \in N_i} \boldsymbol{P}_{\boldsymbol{g}_{ij}^*} \boldsymbol{R}_l^T (\boldsymbol{p}_j - \boldsymbol{p}_i), \tag{8}$$

where $\boldsymbol{v}_i$ is the commanded velocity of the follower UAV, $\boldsymbol{R}_{\theta_i}, \boldsymbol{R}_l$ denote the rotation matrices of the follower UAV and its corresponding leader, respectively.

The heading control of each follower UAV is designed to align its heading with that of its leader, using a proportional (P) controller referenced to the leader's heading angle.

3. Simulation

To validate the proposed virtual leader-based bearing formation system, a Simulation-in-the-Loop (SITL) experiment was conducted in the ROS (Robot Operating System) and Gazebo environment (Fig. 3, Fig. 4).

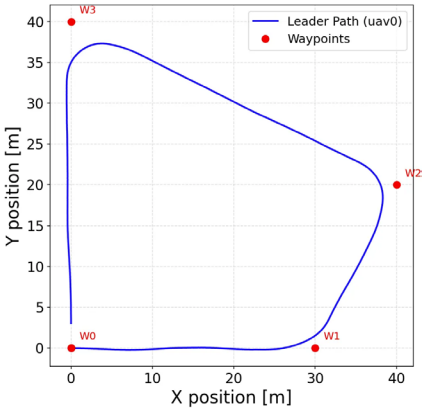

Fig. 3. Leader UAV's trajectory result.

4. Conclusions

This paper proposes a virtual leader-based bearing formation system for performing reconnaissance missions using multiple UAVs. Through simulation, it is confirmed that the leader UAV effectively passes

near the designated waypoints, and the follower UAVs maintain a V-shaped formation along the leader.

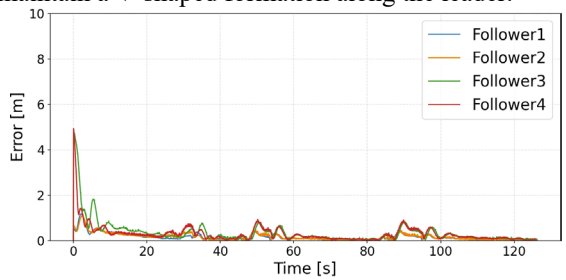

Fig. 4. Follower UAV's formation tracking error result.

Acknowledgements

This paper is research supported by the Ministry of Trade, Industry and Energy (A major activities of 2024 Industry-Academia Cooperation: Aviation and defense SW professional Education)

References

[1]. W. Liu, T. Zhang, S. Huang, K. Li, A hybrid optimization framework for UAV reconnaissance mission planning, *Computers & Industrial Engineering*, Vol. 173, 2022, 108653.

[2]. W. Y. H. Adoni, S. Lorenz, J. S. Fareedh, R. Gloaguen, et al., Investigation of autonomous multi-UAV systems for target detection in distributed environment: Current developments and open challenges, *Drones*, Vol. 7, Issue 4, 2023, 263.

[3]. S. Samaras, E. Diamantidou, D. Ataloglou, N. Sakellariou, et al., Deep learning on multi-sensor data for counter UAV applications – A systematic review, *Sensors*, Vol. 19, Issue 21, 2019, 4837.

[4]. M. Sherman, S. Shao, X. Sun, J. Zheng, Counter UAV swarms: Challenges, considerations, and future directions in UAV warfare, *IEEE Wireless Communications*, Vol. 31, Issue 2, 2024, pp. 190-196.

[5]. H. Su, Z. Yang, S. Zhu, C. Chen, Bearing-based formation maneuver control of leader–follower multi-agent systems, *IEEE Control Systems Letters*, Vol. 7, 2023, pp. 1554-1559.

[6]. Z. Tang, R. Cunha, T. Hamel, C. Silvestre, Bearing leader–follower formation control under persistence of excitation, *IFAC-PapersOnLine*, Vol. 53, Issue 2, 2020, pp. 5671-5676.

[7]. J. Lee, S. Park, Pre-simulation-based autonomous landing approach by vector field for fixed-wing UAVs, *International Journal of Aeronautical and Space Sciences*, Vol. 24, Issue 1, 2023, pp. 166-172.

[8]. J. Choi, Y. Choi, Development of a bearing-based distributed control method for UAV formation tracking and obstacle avoidance, *Aerospace*, Vol. 12, Issue 11, 2025, 1013.

(009)

Advanced Unmanned Vehicle Systems for Port Security

R. Company [1], J. M. Higón [1], A. Laguna [1], M. Gabarda [1], D. Severinsen [2], S. Contorno [2], F. Pérez [3] and A. García [3]

[1] Fundación Valenciaport, Muelle del Turia s/n., 46024 Valencia, Spain
[2] Lemvos GmbH, Am Mittleren Moos 48, 86167 Augsburg, Germany
[3] FAV Innovation and Technologies, Escritor Rafael Ferreres 2, 46013 Valencia, Spain
Tel.: + 34 674 744 080
E-mail: rcompany@fundacion.valenciaport.com

Summary: Underwater threats represent an increasing challenge to maritime safety and port security, demanding advanced solutions beyond traditional monitoring and inspection methods. This paper presents the development and field testing of a 5G-enabled USV designed to enhance situational awareness and operational resilience against underwater risks in port environments. The study was conducted at the Port of Valencia, one of Europe's most advanced smart ports equipped with a 5G Standalone (SA) network. By combining high-speed, low-latency communications with sensing technologies (including sonar modules, optical cameras, and environmental sensors) the proposed system enables real-time data exchange, remote operation, and continuous monitoring across surface and subsurface domains. Experimental trials validated the USV's ability to detect submerged objects, support emergency response, and perform inspection and environmental monitoring tasks under stable 5G connectivity. These results demonstrate how the integration of unmanned surface platforms with next-generation communication networks can significantly strengthen the capacity to detect, assess, and mitigate underwater threats under teleoperated conditions.

Keywords: Port security, Underwater monitoring, Autonomous systems, Unmanned vehicles (UUV, USV, UAV), Smart ports, Artificial intelligence, Maritime surveillance, Sensor fusion, 5G communications.

1. Introduction

Ensuring underwater security is a critical component of maintaining safe and continuous port operations. The Port of Valencia, one of the busiest and most technologically advanced ports in Europe, faces daily challenges related to vessel traffic management, infrastructure maintenance, and the prevention of unauthorized underwater activities. Traditional monitoring methods, such as diver inspections or fixed sensors, often provide limited coverage and slow response times in dynamic maritime environments.

To address these challenges, recent advances in autonomous systems and smart port technologies have introduced innovative solutions that integrate multiple sensing and surveillance platforms. By combining Unmanned Underwater Vehicles (UUVs), Unmanned Surface Vehicles (USVs), and Unmanned Aerial Vehicles (UAVs), ports can implement a coordinated, multi-domain situational awareness framework. Supported by 5G communications and AI-based detection algorithms, these systems enable continuous monitoring, faster anomaly detection, and enhanced decision-making at the port command and control centre.

Within this context, the Lemvos autonomous platform represents a significant advancement in port security operations. Its integration with existing infrastructure and sensor networks provides a scalable and adaptive approach to maritime surveillance. Autonomous operation reduces human exposure to risk while increasing efficiency in inspection and monitoring tasks. The following sections present experimental results and operational tests conducted at the Port of Valencia, including an analysis of performance metrics and detection capabilities.

2. State-of-the-Art

Technologies are advancing rapidly, and with them, so are the methods employed by smugglers to threaten ports worldwide. A notable example is the series of incidents reported along the Galician coast involving narco-submarines transporting tons of illegal substances [1]. Consequently, port security systems must evolve to incorporate new technologies capable of detecting and countering such sophisticated threats. Today, a variety of advanced technologies are employed in maritime surveillance and port protection, as summarized in Table 1 and Table 2.

All these systems and sensors can be integrated and processed using advanced data fusion and AI-based analytics to provide comprehensive situational awareness. An illustrative example of the application of these technologies in port security is the Port of Singapore, a global leader in the deployment of USVs for maritime protection.

Since 2023, the Republic of Singapore Navy has operated the MARSEC USV, a 16.9-meter, 30-ton vessel equipped with radar, optical sensors, and an autonomous Collision Detection and Collision Avoidance (CDCA) system. In January 2025, these vessels began fully uncrewed patrols, operating alongside manned ships to enhance surveillance and enable rapid response in the busy Singapore Strait [2].

Table 1. Robotic Systems for Port Surveillance and Security.

Type	Definition
USV [2]	Small or medium-sized autonomous vessels that navigate the water surface using GPS and onboard sensors. They can be remotely controlled or operate independently along predefined routes.
ROV (Remotely Operated Vehicle) [3]	Underwater robots tethered to a control station via cable, allowing precise maneuvering and continuous video transmission. They can operate at greater depths than divers and carry tools or manipulators.
AUV (Autonomous Underwater Vehicle) [4]	Fully autonomous underwater robots capable of long-duration missions without real-time human control. Equipped with sonar, cameras, and navigation systems to map and inspect underwater environments.
UAV [5]	Aerial platforms equipped with optical, infrared, or multispectral cameras, capable of real-time data transmission and autonomous flight patterns. They can cover large areas quickly and operate in locations that are difficult or dangerous for humans.

Table 2. Sensor and Detection Technologies Used in Port Security.

Type	Definition
FLS (Forward Looking Sonar) [3]	A sonar system that sends sound waves forward to create real-time images of the underwater environment ahead of a vessel, helping to detect and avoid obstacles.
SSS (Side-Scan Sonar)	A sonar device that emits sound pulses to both sides of a vessel to produce high-resolution images of the seabed and underwater objects.
Cameras [3-4]	Optical sensors that capture visual, infrared, or thermal images. They are used for continuous observation and documentation of port areas.
Hydrophone	An underwater acoustic sensor that detects, records, and analyses sounds in the water, such as those produced by marine life or machinery.
AIS (Automatic Identification System)	An electronic system that automatically transmits and receives data about a vessel's identity, position, speed, and route to improve navigation and tracking.
LIDAR (Light Detection and Ranging)	A remote sensing technology that uses laser light to measure distances and generate precise 3D models or maps of surfaces and surroundings.

3. Port of Valencia

The Port of Valencia is Spain's main maritime hub and one of the most advanced ports in Europe, recognized for its strong commitment to digitalization and sustainability. It connects key trade routes between Europe, Africa, Asia, and the Americas and has positioned itself as a reference in smart port development through early adoption of automation and communication technologies.

Fundación Valenciaport, the innovation and research arm of the Port Authority, leads numerous projects focused on port logistics, digital transformation, and maritime security. Within this framework, the Foundation coordinated the experimental activities presented in this paper.

The port area is covered by a 5G Standalone (SA) network, providing high-speed and low-latency communication that enables real-time monitoring, control, and data exchange for autonomous maritime systems. Complementing this infrastructure, a fibre-optic backbone ensures stable, high-capacity connectivity between the test sites and the control centres. The LEMVOS USV trials were conducted in the Xità dock and service basin, providing realistic port conditions to assess 5G coverage, navigation performance, and sonar-based inspection capabilities.

4. Methodology

4.1. System Architecture

The LM450 USV (Fig. 1) employs the AutomatePro platform as its onboard computation and control unit. The system operates on Jetson Linux 36.3 (Ubuntu 22.04 LTS base) with an NVIDIA PREEMPT_RT kernel, ensuring deterministic scheduling and low-latency response for mission-critical control loops.

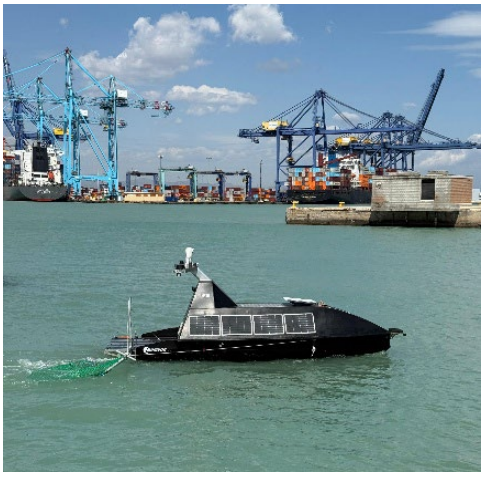

Fig. 1. LEMVOS USV performing tests at the Port of Valencia.

4.1.1. Hardware Platform

AutomatePro integrates an NVIDIA Jetson Orin Nano 8GB System-on-Module (SOM), which provides GPU-accelerated computing capabilities suitable for

real-time sensor processing and future AI/ML features. The system includes onboard monitoring, enabling real-time diagnostics of connected sensors and peripherals.

4.1.2. Software Architecture

The software stack is based on Robot Operating System (ROS) 2 Humble Hawksbill, which provides a standardized middleware framework for distributed sensor integration, data communication, and system orchestration. ROS 2's Data Distribution Service (DDS) middleware enables efficient publish-subscribe communication patterns between system components, facilitating modular development and scalability. All software components are containerized using Docker, enabling isolated execution environments, simplified deployment procedures, and enhanced system reliability. Custom NVIDIA kernel modifications were implemented to ensure seamless integration between the Jetson module and the AutomatePro.

4.1.3. Communication Infrastructure

The platform leverages 5G cellular connectivity to establish high-bandwidth, low-latency communication. This enables the following.

- Real-time Video Streaming: H.264 compressed video transmission at configurable bitrates;
- WebSocket-based Data Visualization: Bidirectional communication protocol enabling real-time sensor telemetry display and remote command execution through web-based control interfaces;
- Command and Control: Low-latency transmission of navigation commands.

The camera driver implements H.264 compression, significantly reducing data transmission requirements while maintaining sufficient image quality for surveillance and inspection tasks. This optimization is particularly critical for sustained operations over cellular networks where bandwidth availability may vary.

4.1.4. System Monitoring and Diagnostics

Comprehensive system health monitoring is implemented through continuous telemetry collection across multiple subsystems as:

- Power System Monitoring: Generator status, battery voltage/current, and fuel levels;
- Navigation Subsystems: GNSS signal quality metrics;
- Computing Resources: CPU/GPU utilization, memory usage, thermal states, and storage capacity;

All monitoring data is published through ROS 2 topics and logged for post-mission analysis, enabling predictive maintenance and performance optimization.

4.2. Sensor Integration

Modern port surveillance relies on multi-sensor integration to achieve continuous situational awareness across both surface and subsurface domains. The LM450, equipped with the AutomatePro onboard controller, supports modular payload configurations that enable adaptive mission profiles. In the current configuration, two primary sensing modules are employed: a Pan–Tilt–Zoom (PTZ) camera and a Ping DSP 3DSS scan sonar.

4.2.1. PTZ Camera

The PTZ camera provides dynamic optical surveillance suitable for wide-area monitoring in port environments. Its ability to pan, tilt, and zoom enables both panoramic situational awareness and detailed inspection of specific surface targets. When integrated with AutomatePro's mission software, the system supports automated object tracking and event detection, enhancing over-surface port-security operations by identifying and following vessels, personnel, or other moving objects within restricted areas.

4.2.2. Ping DSP 3DSS Sonar

The Ping DSP 3DSS SSS extends the LM450's detection capabilities below the waterline, providing continuous subsurface monitoring (Fig. 2). Mounted on the LM450's hull, the 3DSS delivers high-resolution volumetric imaging of underwater structures and objects, even in turbid or low-visibility conditions where optical sensors are ineffective. In a port-security context, this integration enables the detection of potentially hazardous or illicit underwater objects, such as narcotics pods, magnetic attachments, or diver intrusions, thereby enhancing the overall safety and integrity of the port environment.

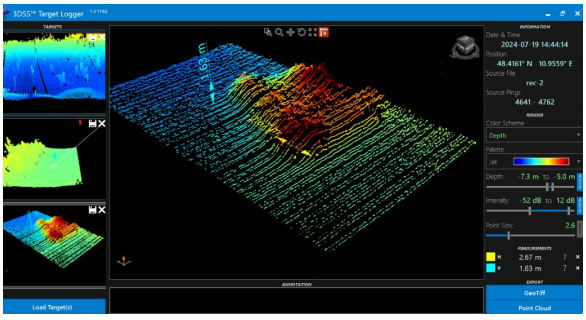

Fig. 2. Ping DSP User Interface.

5. Tests and Results

During tests carried out at Valenciaport harbour, the Fundación Valenciaport team did a dedicated measurement campaign using an USV equipped with a 5G signal UE configured to analyse the most significant network parameters. The USV navigated through various areas of the port waters, continuously recording key radio parameters including Signal-to-Noise Ratio (SINR), Physical Cell Identity (PCI), Reference Signal Received Power (RSRP), and Reference Signal Received Quality (RSRQ). The resulting data enabled the generation of a detailed 5G coverage map of the port area, serving both as validation of the private 5G network deployment and as a reference for future optimization efforts.

To enhance the interpretability of this massive amount of network data, FAVIT developed an Immersive Decision Support System (IDSS). Instead of relying on raw data logs, the system processes 5G KPIs (SINR, RSRP) in real-time and projects them as a geospatial heatmap overlaid on the port's digital twin (Fig. 3). This immersive visualization allows operators to intuitively identify 'shadow zones' or areas with optimal connectivity (>25 dB SINR) for high-bandwidth operations.

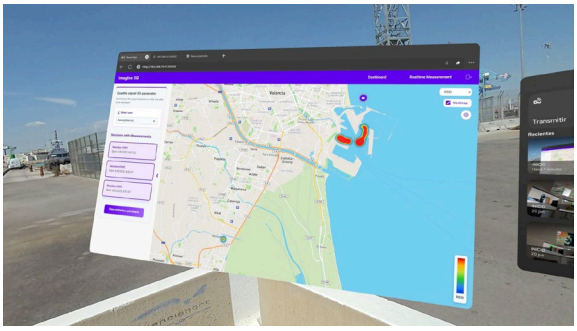

Fig. 3. Immersive Decision Support System (IDSS) interface displaying real-time 5G coverage heatmaps (SINR/RSSI) over the Port of Valencia map.

By integrating these 5G coverage layers directly into the command interface, the system significantly reduces the operator's cognitive load. This ensures that during critical missions, such as the remote piloting of the USV for the subsequent Search and Rescue (SAR) trials, the pilot can proactively maintain the vessel within the optimal 5G footprint, guaranteeing the stability of the critical Full HD video uplink required for emergency response.

The LEMVOS USV was deployed to evaluate its capabilities in supporting rapid response operations. During the trials, the USV autonomously launched rescue buoys and smart lifejackets toward individuals in the water, while concurrently transmitting Full HD video streams to enable remote monitoring. The demonstrations validated the potential of 5G-enabled USVs to facilitate early accident signalization, enhance situational awareness for port authorities, and support time-critical rescue efforts with low latency and high reliability.

Moreover, a study was conducted using the sonar device integrated into the USV. This sonar can generate a three-dimensional point cloud, which enables the visualization of any object located on the seabed, attached to a ship's hull, or along dock walls for maintenance tasks such as crack detection. During the tests carried out at the Port of Valencia, bathymetric surveys were performed on the seabed of two docks within Valenciaport, specifically at the Xità dock and the service basin. The results revealed a higher concentration of sediments in one area compared to the other; however, no weighted objects were detected on the seabed.

To further validate the sonar detection performance under controlled conditions, an additional experiment was carried out at approximately 6 m depth using the Customs boat (Fig. 4). A dummy cylindrical object (Ø 200 mm × 600 mm), representing a typical narcotics tube, was magnetically attached to a flat steel panel suspended from the boat (Fig. 5). The sonar system successfully detected the object, with reflection intensity providing a clear and consistent visualization (Fig. 6). The measured sonar signature indicated an apparent object length of 0.71 m, representing approximately 20 % deviation from the actual 0.6 m physical length (Fig. 7).

Fig. 4. Customs boat.

Fig. 5. Dummy narcotics tube magnetically attached to a flat steel panel representing a hull.

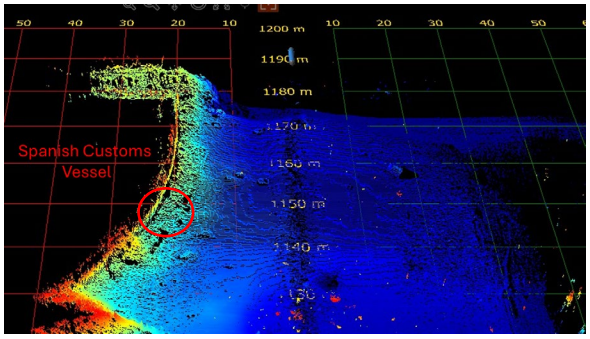

Fig. 6. Sonar image with the bottle attached to the hull.

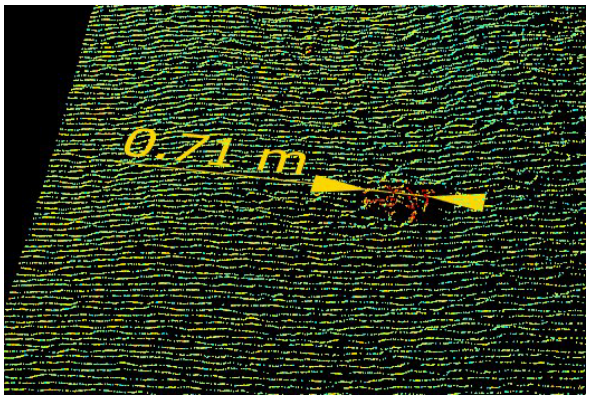

Fig. 7. Measurement results of the dummy narcotic tube.

Although detection performance may vary depending on the hull material and geometry, these trials confirmed that cylindrical shapes are acoustically favourable targets. Different shapes were tested in a lakebed, a plastic box and 8 mm diameter ropes were successfully detected (Fig. 8).

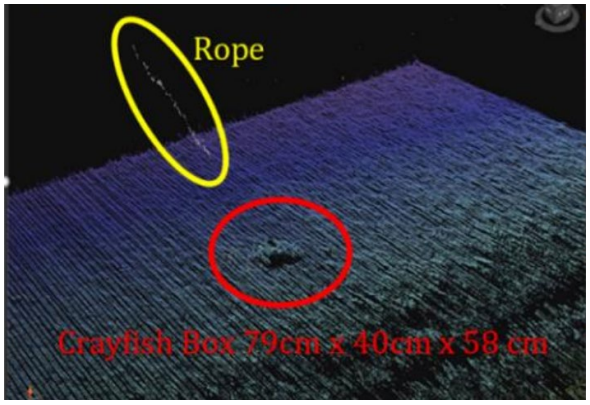

Fig. 8. Sonar image with different objects.

Table 3 shows that most sonar KPIs were achieved. Although the detection range was lower than target, it has minimal operational impact, while the higher scan rate improves overall system performance.

Table 3. Sonar rapid hull scan KPIs vs actual performance achieved.

KPI	Achieved Performance	Comments
Scan Rate	50 m/min	Scan Rates up to 100 m/min are expected to be possible with further testing
Object Detection Size (Diameter)	200 mm	Detection of ropes down to 8 mm diameter possible, with lower reliability
Object Detection Size (Length)	600 mm	Detection of 500 mm length is expected to be possible within some conditions
Detection Range	22 m	Results beyond 25-30 m range have more noise and are not as clear. Operationally having a detection range of 22 m instead of 50 m will have little to no negative effect

6. Future Implementations

While the current deployment focuses on teleoperated navigation mode, the platform architecture is designed to support future autonomous capabilities through advanced sensor fusion algorithms.

6.1. Sensor Fusion

The system implements a multi-sensor localization framework combining GNSS positioning with inertial odometry. For future autonomous operations, an Extended Kalman Filter (EKF) will be deployed to fuse GNSS measurements, IMU data, and Visual Inertial Odometry (VIO) to achieve robust, high-frequency state estimation even during GNSS signal degradation.

The dual-antenna RTK-GNSS configuration provides absolute heading measurements independent of magnetic sensors, thereby eliminating susceptibility to magnetic disturbances. This design ensures consistent orientation estimation in environments where magnetic interference compromise IMU readings.

6.2. Autonomous Navigation

The NVIDIA Jetson Orin platform provides GPU acceleration suitable for deploying Deep Neural Network (DNN) models for future enhancements as:

- Image Segmentation: Semantic segmentation of water surfaces for free-path detection and path planning;

- Object Detection: Real-time identification and tracking of vessels, and floating objects using convolutional neural network.

These capabilities will extend the system's autonomy level from current human-supervised operations to fully autonomous mission execution.

These modules are envisioned as inputs to future autonomous navigation and path-planning pipelines. However, no neural network training, inference benchmarks, dataset evaluation, or autonomy performance results are presented in this paper.

7. Conclusions

Underwater control technologies significantly enhance port security, as monitoring systems, such as sonar radars, underwater cameras, and acoustic sensors, allow for the precise detection of intrusions, submerged objects, and potential structural risks. This continuous and detailed surveillance capability helps reduce the likelihood of accidents and improves the efficiency of emergency responses to situations such as leaks, sabotage, or sinkings, thereby ensuring a safer and more controlled port environment.

The experimental results obtained at the Port of Valencia confirm that the proposed system architecture is technically feasible and operationally effective in real-world port conditions. The LEMVOS USV demonstrated reliable navigation, robust 5G coverage, and sonar-based object detection capabilities.

Future developments should focus on expanding the system's autonomy through advanced AI-based sensor fusion, object recognition, and route planning algorithms. The incorporation of machine learning models for anomaly detection and predictive maintenance will further strengthen resilience and reduce human intervention.

Acknowledgment

This work has been carried out as part of the Horizon Europe projects SMAUG [6] and UnderSec [7].

References

[1]. J. Romero Doniz, Aparece un nuevo narcosubmarino en Galicia, en el interior de la ría de Arousa, *La Voz de Galicia*, 14 March 2023 (in Spanish).

[2]. G. Dominguez, Singapore: Making waves – Singapore's navy looks to the future, *Asia-Pacific Defence Reporter*, Vol. 48, Issue 4, 2022, pp. 33-36.

[3]. A. Cardaillac, M. Ludvigsen, Camera-sonar combination for improved underwater localization and mapping, *IEEE Access*, Vol. 11, 2023, pp. 123070-123079.

[4]. S. Tani, F. Ruscio, M. Bresciani, A. Caiti, R. Costanzi, Stereo vision system for autonomous ship hull inspection, *IFAC-PapersOnLine*, Vol. 55, Issue 31, 2022, pp. 375-380.

[5]. G. Gomathy, G. Prabakaran, K. Livisha, S. Parasuram, R. A. Raj, Drone surveillance integrated with machine learning for enhanced port management, in *Proceedings of the International Conference on Communication, Computing and Internet of Things (IC3IoT'24)*, 2024, pp. 1-6.

[6]. SMAUG Project, Smart Maritime And Underwater Guardian (SMAUG), https://smaug-horizon.eu/

[7]. UnderSec Project, https://www.undersec-project.eu/

(010)

A Study on the Effect of Air Compressor Configuration on Proton Exchange Membrane Fuel Cells System for Aviation

Ju Won Jang [1] and Seung-Gon Kim [2]
[1] Department of Space Systems Convergence Korea Aerospace University,
76, Hanggongdaehak-ro, Deogyang-gu, Goyang-si, Republic of Korea
[2] Department of Smart Drone Engineering Korea Aerospace University,
76, Hanggongdaehak-ro, Deogyang-gu, Goyang-si, Republic of Korea
Tel.: + 82 1087915224
E-mail: jjw9821@kau.kr

Summary: As global efforts to achieve carbon neutrality accelerate, the aviation sector is actively developing electric propulsion systems to replace conventional internal combustion engines. Among these, the Proton Exchange Membrane Fuel Cells (PEMFCs) has been recognized as a promising electric propulsion technology due to its high efficiency and reliability. However, at high altitudes, the reduced atmospheric pressure decreases the oxygen partial pressure at the cathode, resulting in lower cell potential and overall output performance. To address this issue, this study compares the characteristics of single-stage and two-stage air compressor configurations under atmospheric conditions at an altitude of 25000 ft. The single-stage compressor compensates for performance loss by increasing the active area and number of cells, while the two-stage compressor maintains oxygen partial pressure close to standard atmospheric. The findings of this study are expected to contribute to the efficient design of air management systems for hydrogen-electric propulsion aircraft.

Keywords: Hydrogen-electric propulsion aircraft, Proton exchange membrane fuel cells (PEMFCs), Air compressor, Oxygen partial pressure.

1. Introduction

The aviation sector accounts for approximately 2–3 % of global carbon emissions, but its share is expected to grow significantly in the future as aviation demand continues to rise alongside technological advancements [1, 2]. Therefore, decarbonizing aviation is recognized as a key challenge for achieving net-zero climate goals.

Against this background, the aviation sector has been developing electric propulsion systems as alternatives to conventional internal combustion – based systems to achieve zero carbon emissions. Among these, the Proton Exchange Membrane Fuel Cells (PEMFCs**)** has been recognized as a promising next-generation propulsion technology due to its high efficiency and reliability [3].

$$H_2 \rightarrow 2H^+ + 2e^-, \quad (1)$$

$$\frac{1}{2}O_2 + 2H^+2e^- \rightarrow H_2O \quad (2)$$

The PEMFC is an eco-friendly energy source that generates electricity through the electrochemical reaction of hydrogen and oxygen, with water as the only byproduct [3]. It also boasts advantages such as high energy density, excellent fuel efficiency, and low operating temperatures, attracting significant attention as an aviation propulsion system [3].

However, aviation PEMFCs face various environmental constraints as altitude increases. Among these, the low atmospheric pressure at high altitudes reduces the partial pressure of oxygen within the fuel cell, potentially degrading the stack's electrochemical reactivity and power output performance [4]. Therefore, optimizing the design and configuration of the air compressor is crucial to ensure sufficient oxygen supply under aircraft flight conditions.

In this paper, the characteristics of single-stage and two-stage air compressor configurations were compared and analyzed to address the reduction in PEMFC output caused by decreased oxygen partial pressure in high-altitude environments. The single-stage compressor system increased the active area and number of cells to compensate for output reduction due to decreased oxygen partial pressure and analyzed the resulting output-to-weight ratio characteristics. The two-stage compressor system was evaluated in terms of its power consumption and overall system efficiency while maintaining the oxygen partial pressure at a level like that of PEMFC operation under standard atmospheric conditions. Through this analysis, an appropriate air compressor configuration suitable for aviation PEMFC systems was derived.

2. System Configuration

The aircraft selected as the subject of this study is Dornier 228. The Dornier 228 was converted into a hydrogen-electric aircraft by installing the ZA600 fuel cell power pack developed by ZeroAvia and demonstrated stable operational performance through a total of 12 test flights. The Dornier 228 has a service ceiling of up to 25000 ft, and the ZA600 is a 600 kW

PEMFC propulsion system consisting of three power packs [5]. Therefore, this study determined a suitable air compressor for a single ZA600 power pack under atmospheric conditions at an altitude of 25000 ft. Fig. 1 presents a schematic diagram of an aviation PEMFC air supply system. Table 1 and Table 2 present the specifications of the Dornier 228 aircraft and the ZA600 single power pack, respectively. Table 3 presents the atmospheric conditions at 25000 ft [6].

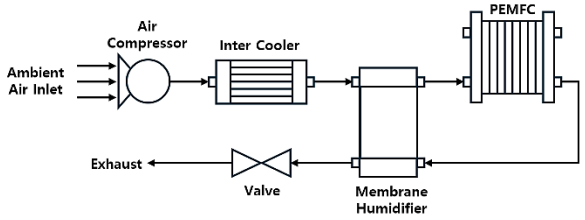

Fig. 1. Schematic diagram of an aviation PEMFC air supply system.

Table 1. Specifications of Dornier 228.

Parameter	Value
Capacity	19 Passengers
Power Plant	2 * Turboprop, 579 kW each
Service Ceiling (ft)	25000

Table 2. Specifications of ZA600 single PEMFC power pack.

Parameter	Value
Max Continuous Power (kW)	200
Operating Voltage (V)	910 – 570
Operating Current (A)	0 - 300
Cell Numbers	2 * 455
Dimension (mm)	580 * 492 * 902
Weight (kg)	140

Table 3. Air properties at 25000 ft.

Parameter	Value
Temperature (°C)	-34.5
Pressure (Pa)	37600
Density (kg/m^3)	0.549
Viscosity (Pa·s)	$1.539 \cdot 10^{-5}$

Under the atmospheric conditions at 25000 ft, the single-stage compressor system was configured to supply air to the cathode at an inlet pressure of 1 bar, while the two-stage compressor system was designed to deliver air at 2 bar. Achieving a cathode inlet pressure of 1 bar requires a compression ratio of approximately 2.66, whereas a target pressure of 2 bar requires a total compression ratio of approximately 5.32. For the two-stage compressor configuration, the total compression ratio was equally distributed between stages, resulting in a per-stage compression ratio of approximately 2.31.

3. Effect of Altitude on PEMFCs Voltage

The net power output of the PEMFC system with respect to pressure variation is calculated by subtracting the power consumption of the air supply compressor from the fuel cell stack power, as expressed in Eq. (3).

$$P_{net} = P_{stack} - P_{comp} \quad (3)$$

3.1. PEMFCs Power Modeling

The PEMFCs stack power is defined as the product of the fuel cell current, the cell voltage, and the number of cells, as presented in Eq. (4). The cell voltage is determined by subtracting the activation, ohmic, and concentration overpotentials from the reversible voltage, as given in Eq. (5) [7].

$$P_{stack} = V_{cell} \cdot I \cdot N_{cell}, \quad (4)$$

$$V_{cell} = E_{th} - V_{act} - V_{ohm} - V_{conc} \quad (5)$$

The output voltage of a PEMFC depends on the partial pressures of the reaction gases. This relationship can be theoretically expressed by the Nernst equation, as shown in Eq. (6) [4].

$$E_{th} = E^0 + \frac{RT}{2F} ln\left(\frac{p_{H_2}(p_{o_2})^{\frac{1}{2}}}{p_{H_2O}}\right), \quad (6)$$

where E is the cell potential, E^0 is the standard reversible voltage, R is gas constant, T is the temperature, F is Faraday's constant, and p_{H_2}, p_{o_2}, p_{H_2O} are the partial pressures of hydrogen, oxygen, and water vapor, respectively.

$$p_{o_2} = p_{Total} \cdot x_{O_2} \quad (7)$$

The partial pressure of oxygen (p_{O_2}) is expressed as the product of the total pressure (p_{Total}) and the oxygen mole fraction (x_{O_2}) [4]. As flight altitude increases, atmospheric pressure decreases. As seen from Eq. (6), a decrease in oxygen partial pressure reduces the cell potential, lowering the overall voltage of the PEMFCs. In addition, lower air pressure intensifies both activation and concentration losses, since reduced oxygen partial pressure slows the electrode reaction kinetics and limits oxygen diffusion within the PEMFCs [4, 7]. Consequently, these combined effects further reduce the cell voltage under high-altitude operating conditions.

3.2. Effect of Altitude on PEMFCs Voltage

Equation (8) calculates the compressor power consumption required for isentropic air compression as

a function of the compression ratio and mass flow rate [8].

$$P_{comp} = \frac{\dot{m}_{air} \cdot c_p \cdot T_{in}}{\eta_{comp}} \left[\left(\frac{P_{out}}{P_{in}} \right)^{\frac{\gamma-1}{\gamma}} - 1 \right] \quad (8)$$

The air mass flow rate is determined from the oxygen consumption of the fuel cell reaction, the operating current, and the number of cells [6]

$$\dot{m}_{air} = \frac{S_{O_2}}{r_{O_w}} \frac{M_{air}}{4F} \cdot I \cdot N_{cell} \quad (9)$$

As altitude increases, the reduction in ambient pressure leads to a higher required compression ratio to maintain the target cathode inlet pressure, resulting in increased compressor power consumption and a reduction in net PEMFC system output.

4. Conclusion

This study focuses on evaluating the effects of altitude on PEMFC performance and comparing single-stage and two-stage air compressor systems. It is expected that maintaining higher oxygen partial pressure through a two-stage configuration will mitigate voltage losses and enhance the efficiency of aviation PEMFC systems. The outcomes of this study will contribute to the design optimization of air supply systems for hydrogen-powered aircraft.

Acknowledgements

This paper is research supported by the Ministry of Land, Infrastructure and Transport (MOLIT) of the Korean government through the Korea Agency for Infrastructure Technology Advancement (KAIA) under the project “Development of a Certification System for Hydrogen Fuel Cell-Based Propulsion Systems for Small Aircraft” (RS-2023-00243094). And this paper is research supported by the Ministry of Trade, Industry and Energy (A major activity of 2024 Industry-Academia Cooperation: Aviation and defense SW professional Education [RS-2024-00412499]).

References

[1]. D. S. Lee, D. W. Fahey, A. Skowron, M. R. Allen, et al., The contribution of global aviation to anthropogenic climate forcing for 2000 to 2018, *Atmospheric Environment*, Vol. 244, 2021, 117834.

[2]. X. Xiong, X. Song, A. Kaygorodova, K. Wang, Aviation and carbon emissions: Evidence from airport operations, *Journal of Air Transport Management*, Vol. 109, 2023, 102383.

[3]. B. Wang, D. Zhao, T. Li, W. Liang, Current technologies and challenges of applying fuel cell hybrid propulsion systems in unmanned aerial vehicles, *Progress in Aerospace Sciences*, Vol. 116, 2020, 100620.

[4]. J. W. Pratt, J. Brouwer, G. S. Samuelsen, Performance of proton exchange membrane fuel cell at high-altitude conditions, *Journal of Propulsion and Power*, Vol. 23, Issue 2, 2007, pp. 313-319.

[5]. ZeroAvia, Flight testing, https://zeroavia.com/flight-testing/

[6]. J. Jang, J. Choi, H. Jeong, Designing a waste heat recovery heat exchanger for polymer electrolyte membrane fuel cell operation in medium-altitude unmanned aerial vehicles, *Energies*, Vol. 17, Issue 6, 2024, 1362.

[7]. R. O’Hayre, S. W. Cha, W. G. Colella, F. B. Prinz, Fuel Cell Fundamentals, *Wiley*, Hoboken, 2016.

[8]. S. Gelfi, A. G. Stefanopoulou, J. T. Pukrushpan, H. Peng, Dynamics of low-pressure and high pressure fuel cell air supply systems, in *Proceedings of the American Control Conference*, 2003, pp. 2049-2054.

(011)

Control Law Design for Stall Recovery of a Fighter Configuration Unmanned Aerial Vehicle

Jaehun Yu [1] and Sanghyuk Park [2]
[1] Korea Aerospace University, Department of Smart Aviation Mobility, Goyang, Republic of Korea
[2] Korea Aerospace University, Department of Aerospace Engineering, Goyang, Republic of Korea
Tel.: +82 93780470
E-mail: yujh535@kau.kr

Summary: This study proposes a stall maneuver control law for a fighter-configuration unmanned aerial vehicle, enabling automatic stall entry and recovery. The control law is designed based on a high-angle-of-attack aerodynamic model, which incorporates aerodynamic coefficients reflecting the characteristics of a fighter-configuration aircraft and employs the wing-element method. The proposed control law allows the aircraft to maintain its attitude during stall flight and subsequently recover stably to cruise flight. The aircraft enters stall by increasing pitch attitude. In the stall condition, roll attitude is controlled by differential horizontal tails, and yaw motion is suppressed by anti-spin. Stall recovery restores angle of attack, airspeed, and attitude through pitch-rocking and pull-up maneuvers. The proposed control law is validated through flight experiments.

Keywords: Fighter configuration UAV, Automated stall maneuver, Stall recovery, Wing-strip-theory.

1. Introduction

The onset of stall leads to a rapid reduction in lift, attitude stability, and the effectiveness of the main wing control surfaces. Furthermore, abrupt motions during stall conditions may induce excessive transient responses, resulting in reduced controllability of the aircraft. The aircraft may consequently loss attitude stability or significant altitude loss during stall recovery attempts.

A fighter-configuration aircraft is capable of preserving a portion of lift even in stall [1]. Accordingly, the design of a stall-control law requires an aerodynamic model that reflects these aerodynamic characteristics.

To ensure stable recovery from stall conditions, a control law that can maintain the attitude in the stall condition is required. Stall recovery requires control laws to recover the angle of attack, velocity, and attitude. The aircraft should first restore the angle of attack and airspeed, and then sequentially recover the attitude.

In this study, a high angle of attack aerodynamic model is developed, and a control law is designed to maintain attitude stability under stall. The stall recovery procedure is formulated using pitch rocking and pull-up maneuvers. The proposed flight control law is verified through flight experiments using an F-22 RC scaled aircraft.

2. Aerodynamic Modeling

The aerodynamic computation in the high-angle-of-attack region is conducted by wing-strip theory. The aircraft is divided into elements, and the total aerodynamic forces and moments are obtained by integrating the forces and moments from each element. In the wing element method, aircraft angular motions induce different effective angles of attack for each element. The variation in aerodynamic forces as a function of the angle of attack at each element enables the representation of dynamic aerodynamic effects [2]. In this study, the wing elements are composed of a total of six elements: left and right main wings, horizontal tail, and rudder.

The aerodynamic computation in the high angle of attack region requires aerodynamic coefficients C_L, C_D, C_M. In this study, aerodynamic coefficients are evaluated using the approximate model [3] proposed by Christopher and Traub's lift model [4] according to the sweep angle of the leading edge. However, the original approximation model exhibits errors in the cruise angle of attack range. Accordingly, the approximate model is refined by incorporating AVL analysis results within the angle-of-attack range corresponding to cruise flight. The estimated aerodynamic coefficients C_L, C_D, C_M are presented in Fig. 1.

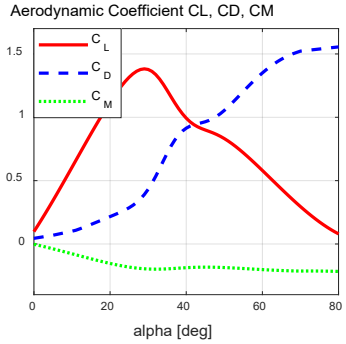

Fig. 1. Aerodynamic coefficient under High angle of attack.

3. Stall Flight Control Law

3.1. Trim Analysis and Linearization

The aircraft dynamic model performs trim analysis for a constant thrust command and elevator deflection. Linear models are derived by linearizing at the trim point. These linear models incorporate angle-of-attack–dependent aerodynamic characteristics and are used for the design of stall flight control laws.

In this study, control law design and flight experiments are conducted under a static stability margin 0 % condition. Trim analysis under this condition indicates that stall occurs at an angle of attack of approximately 26 degrees. At the maximum elevator -30 deg, the aircraft converges to an angle of attack of 41 deg, a pitch attitude of 12 deg, an air speed of 11 m/s.

3.2. Stall Attitude Controller

The longitudinal controller controls the pitch attitude angle using the elevator. The inner loop of the attitude controller consists of an angle of attack damper, a pitch rate damper, and a z-axis non-acceleration controller. Pitch attitude control operates in the pre-stall region, and after stall, the elevator is gradually increased to its maximum deflection to maintain a high angle of attack.

The lateral controller controls the roll attitude angle through differential deflection of the left and right horizontal tails. The inner loop of the attitude controller includes a roll rate damper. The lateral controller remains active throughout the entire stall flight envelope. For roll attitude control, a minimum control surface deflection is ensured, while any remaining available deflection range of the horizontal tail after longitudinal control is additionally exploited.

In the post-stall, yaw stability is ensured through the application of an anti-spin maneuver. In angle-of-attack regions where aerodynamic drag exceeds lift, aileron deflections generate yawing moments that dominate over rolling moments. Consequently, the yaw motion occurs in a direction opposite to that observed in the pre-stall. Using these aerodynamic characteristics, yaw motion is suppressed in the high angle of attack by actuating differential deflections of the aileron and flap as a function of yaw rate.

The control gains designed for each linearized model are scheduled as a function of the angle of attack to reflect the stall characteristics.

During stall maneuvers, when the aircraft pitch attitude becomes high or nose-down, roll-attitude feedback control becomes ineffective. Accordingly, roll attitude control is formulated to track a reference vector $\hat{k}_{ref}$ in the NED (North–East–Down) coordinate frame, representing the desired roll attitude.

The roll control command is generated based on the error e_ϕ, between the aircraft z-axis vector and the reference vector [5]. The roll attitude is controlled so that the vector error e_ϕ is eliminated.

3.3. Stall Recovery Maneuver

The aircraft enters the stall by increasing its pitch attitude while maintaining a constant thrust command. The elevator is deflected to its maximum angle to sustain a high angle of attack, and the roll attitude is controlled to remain level. Yaw stability is ensured by an anti-spin that utilizes the ailerons and inner flaps.

Subsequently, the aircraft recovers from stall through pitch rocking maneuver [6] and pull-up maneuver [5]. The pitch rocking maneuver induces pitch angular motion through elevator. The aircraft generates an appropriate pitch response to lower the nose and restores the angle of attack and airspeed.

The aircraft performs a pull-up maneuver to appropriately raise the nose when it is directed downward. A z-axis non-acceleration command is generated to raise the nose along a semicircular trajectory with diameter ΔH.

The z-axis normal-acceleration command is derived from the centripetal acceleration formulation and is expressed as a function of the aircraft airspeed, the diameter of the circular trajectory, and the position on the circular trajectory. The generated command is constrained according to the limits defined by the V–N envelope. The diameter ΔH of the circular trajectory is selected such that the commanded z-axis normal acceleration remains within the allowable margins of the V–N envelope.

The equations for estimating the position along the semi-circular trajectory and the z-axis specific-acceleration command for nose-up motion are summarized in Eqs. (1)–(2). A schematic overview of the pull-up maneuver is presented in Fig. 2.

$$\dot{\chi} = \frac{1}{V_{air}}(g\cos\chi - A_z), \tag{1}$$

$$A_{z_{cmd}} = g\cos\chi - \frac{2V_{air}^2}{\Delta H} \tag{2}$$

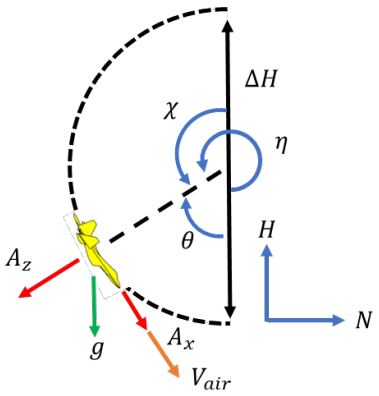

Fig. 2. Schematic of Pull up maneuver.

4. Stall Flight Experiment

The stall maneuver algorithm is validated through flight experiments using F-22 RC-scaled aircraft. The flight experiments were conducted on the runway of Korea Aerospace University under a 0 % static stability margin, with a total of 15 flight tests performed. In this paper, a representative case is presented, the corresponding flight test data are shown in Fig. 3, and the flight trajectory is illustrated in Fig. 4.

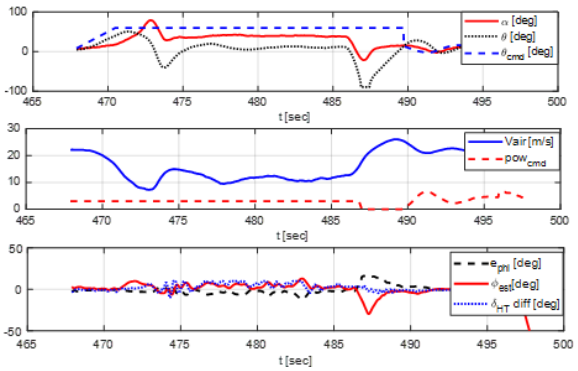

Fig. 3. Stall flight response.

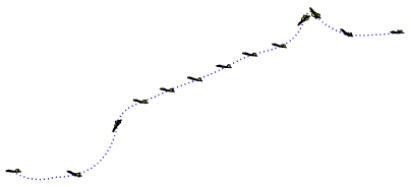

Fig. 4. Stall flight trajectory.

The aircraft enters stall by increasing the pitch attitude while maintaining a constant thrust command. After the angle of attack reaches a maximum of 80 deg, the stall is sustained by maintaining a large elevator deflection. While maintaining the stall, the aircraft converged to an angle of attack of 39 deg, a pitch attitude of 12 deg, an altitude rate of −4 m/s, and an airspeed of 11 m/s.

The aircraft maintains its attitude through roll attitude control using differential horizontal tail and anti-spin. Subsequently, the aircraft recovers its angle of attack and airspeed through a pitch-rocking and recovers its attitude through a pull-up, returning to level flight.

5. Conclusions

This study proposes a flight control law that enables a fighter-configuration aircraft to automatically enter and safely recover from stall condition.

After the aircraft enters the stall, a control law is designed to ensure stable attitude regulation. Attitude control maintains roll attitude through differential horizontal tail, and yaw stability is ensured through an anti-spin. The controller is designed based on linearized models corresponding to the stall condition, and then gain scheduling is performed.

Subsequently the aircraft recovered from the stall through pitch-rocking and pull-up maneuvers. The control gains for the pitch rocking maneuver are designed based on an aerodynamic model that encompasses the stall regime. Furthermore, attitude recovery is structured as a procedure in which a pull-up maneuver is executed following pitch rocking, enabling a safe transition from the stall condition to cruise flight.

The proposed stall maneuver control law was verified through flight experiments conducted under the static-stability-margin 0 %. The flight-test results demonstrated that the converged angle of attack, pitch attitude, and airspeed in the stall closely matched the trim analysis results, thereby validating the reliability of the designed aerodynamic model.

Acknowledgements

This work was supported by the Korea Agency for Infrastructure Technology Advancement (KAIA) grant funded by the Ministry of Land, Infrastructure and Transport (MOLIT) (Grant RS-2024-00444205).

This research was conducted with the support of the Korea Institute for Advancement of Technology funded by the government (Ministry of Trade, Industry and Energy) (Project No. P0023691, The training course for an expert-to-be building up in the Urban Air Mobility).

References

[1]. Sutrisno, T. A. Rohmat, S. B. Wibowo, S. Iswahyudi, Vortex dynamics study of the canard deflection angles' influence on the Sukhoi Su-30-like model to improve stall delays at high AoA, *Aerospace*, Vol. 7, Issue 3, 2020, 23.

[2]. J. M. Brandon, Dynamic stall effects and applications to high performance aircraft, in *Proceedings of the AGARD Conference on High-Lift System Aerodynamics (AGARD-CP-515)*, 1993, Paper 26.

[3]. C. Jouannet, P. Krus, Modeling of unsteady aerodynamic characteristics of delta wings, in *Proceedings of the 23rd Congress of the International Council of the Aeronautical Sciences (ICAS'02)*, 2002, pp. 273.1-273.9.

[4]. L. W. Traub, Extending the leading-edge suction analogy to nonslender delta wings, *Journal of Aircraft*, Vol. 55, Issue 5, 2018, pp. 2174-2177.

[5]. S. Park, Autonomous aerobatics on commanded path, *Aerospace Science and Technology*, Vol. 18, Issue 1, 2012, pp. 64-74.

[6]. C. Kim, B. Hwang, D. Jung, S. Kim, et al., A study on prevention control law of aircraft departure at high angle of attack, *Journal of the Korean Society for Aeronautical & Space Sciences*, Vol. 33, Issue 7, 2005, pp. 85-91 (in Korean).

(012)

RCS-Based Wing Shape Optimization of a Delta-Wing UAV

Yeong Jin Son [1], Dong Kyun Im [2] and Kyoung Jin Jung [3]
[1] Dept. of Mechanical and Aeronautical Systems Engineering, Cheonju University, Aerodynamic Design Optimization Laboratory, 298 Daeseong-ro Cheongwon-gu, Cheongju-si, Republic of Korea
[2] Dept. of Aeronautical and Mechanical Engineering, Cheonju University, Aerodynamic Design Optimization Laboratory, 298 Daeseong-ro Cheongwon-gu, Cheongju-si, Republic of Korea
[3] Agency for Defense Development, Republic of Korea
Tel.: + 82 1025706377, +82 1064172915
E-mail: mark0923@cju.ac.kr, aeroperf@naver.com

Summary: This study presents an open-source aero-stealth design exploration framework for a low-observable cranked-lambda delta-wing UAV. Inboard and outboard leading-edge sweep angles are used as design variables, while an upper bound on an average radar cross section metric is imposed as a constraint. Aerodynamic performance is evaluated with OpenVSP and VSPAERO by computing lift-to-drag ratio over an angle-of-attack range. Stealth performance is assessed with PyPOFacets electromagnetic scattering analysis to estimate average RCS over multiple observation directions. The analyses are coupled through an automated workflow that shares a single geometry definition and consistently aggregates objectives and constraints, reducing errors from manual file handling and data conversion. A multi-objective optimization loop executed in RCE maps trade-offs and generates candidate designs for conceptual-stage decision making.

Keywords: Delta-wing UAV, Radar Cross Section (RCS), Optimization, Low observability.

1. Introduction

UAV operational scopes have expanded to include missions such as intelligence, surveillance and reconnaissance, strike, electronic warfare, long-endurance loitering, penetration, and evasion, which has strengthened survivability requirements. As a result, integrated capabilities that simultaneously achieve aerodynamic efficiency, propulsion performance, and low observability are increasingly required [1]. Detection avoidance is a key design requirement affecting mission success probability and loss rate in hostile environments [2]. Because radar scattering is strongly governed by airframe geometry and external configuration and often conflicts with aerodynamic performance [3], aerodynamic metrics and RCS should be considered concurrently from the early configuration design phase. Delta-wing planforms are attractive for UAVs due to structural simplicity, efficient internal volume utilization, and high-angle-of-attack maneuverability, but sweep angle significantly influences both L/D and RCS through changes in aerodynamic characteristics and scattering geometry. This aero–stealth coupling limits the reliability of single-discipline design approaches, requiring coupled aerodynamic and RCS analyses under a consistent geometry definition and unified conditions. To reduce time and procedural errors from manual tool chaining, an automated MDO workflow integrating geometry generation, aero/RCS evaluation, result aggregation, and iterative optimization is adopted, typically implemented via process integration and design optimization frameworks enabled by advances in computing and software capabilities [4].Hu et al. proposed a multidisciplinary design optimization strategy for the conceptual design of a tailless unmanned combat aerial vehicle, considering aerodynamic performance, stealth characteristics, and structural constraints. They adopted a two-level architecture (system/subsystem) and optimized global external shape variables at the system level [5]. Zhou et al. proposed an adjoint-based scattering sensitivity analysis for three-dimensional aero-stealth optimization. They computed RCS gradients efficiently using scattering sensitivities and demonstrated the feasibility of concurrent aerodynamic–RCS optimization [6]. Bae et al. developed a multidisciplinary conceptual design workflow for an air-to-ground guided missile by integrating DATCOM-based aerodynamic analysis with PoFacets-based RCS evaluation [7]. This study investigates a delta-wing UAV by using the inboard and outboard sweep angles as design variables with a span limit as a geometric constraint. Aerodynamic performance is evaluated in OpenVSP to obtain the lift-to-drag ratio, while electromagnetic scattering analysis in PyPOFacets provides an average RCS metric. The aero–stealth trade-off is explored via multi-objective optimization using an automated workflow that enforces a unified geometry definition, thereby reducing inconsistencies and aggregation errors across toolchains. By integrating geometry generation, aerodynamic and RCS evaluations, result aggregation, and iterative optimization, the study presents a reproducible open-source procedure for concurrent aero–stealth design exploration.

2. Analysis Tool

2.1. RCE

RCE is an open-source distributed process-integration platform that registers heterogeneous design and analysis tools as components and connects their input–output relationships into executable workflows. Users define tool dependencies and execution order via a graphical interface, while RCE supports running components across networked nodes. During execution, RCE centrally collects and manages generated data to ensure traceability, post-processing, and reproducibility of iterative runs.

2.2. OpenVSP

OpenVSP is an open-source project released in 2012 under the NASA Open Source Agreement (NOSA) version 1.3. It is a parametric aircraft geometry modeling tool that generates three-dimensional geometric models by defining aircraft shapes using engineering parameters. The generated geometry can be exported to various formats suitable for engineering analyses and subsequently used in downstream simulations. OpenVSP also provides the VSPAERO aerodynamic solver, which enables aerodynamic analysis of the defined configuration. In addition to the graphical user interface, users can automate geometry generation and analysis workflows through scripting and API-based control.

2.3. Radar Cross Section Calculation Program

This study calculated the radar cross section of a delta-wing unmanned aerial vehicle using the PyPOFacets code, which is a Python implementation of the existing POFacets [8]. Fundamentally, PyPOFacets is based on the Physical Optics (PO) approximation method, identical to POFacets, and evaluates the monostatic RCS by integrating the incident and scattered electromagnetic field behavior for each triangular element. The Physical Optics technique approximates the surface current induced on an object's surface based on the given incident electromagnetic field and boundary conditions to calculate the scattered electromagnetic field. This approach assumes electromagnetic reflection phenomena on a perfectly conductive surface, where the surface current (J_s) is expressed as in Equation (1) based on the relationship between the incident magnetic field (H_i) and the surface normal vector n. In this PO-based formulation, edge diffraction is not explicitly modeled, and its contribution may become important for certain aspect angles where scattering is dominated by edges

$$J_s = 2n \times H_i, \quad (1)$$

where n denotes the unit normal vector of the object's surface, and Hi represents the incident magnetic field. The scattered electric field (E_s) induced by the surface current defined in this manner can be used to express the radar cross section (RCS) as the ratio of the scattered electric field (E_s) to the incident electric field (E_i), as shown in Equation (2).

$$RCS(m^2) = \lim_{\gamma \to \infty} 4\pi r^2 \frac{|E_s|^2}{|E_i|^2} \quad (2)$$

This equation represents the intensity of the electromagnetic wave reflected from the object toward the observation point. The radar cross section (RCS) is expressed in decibel-square meters (dBsm), and its relationship with the physical cross-sectional area (m²) is given as follows.

$$RCS(dBsm) = 10 \log_{10} \left[\frac{RCS(m^2)}{1m^2} \right] \quad (3)$$

3. Analysis

3.1. Reference Model

The baseline configuration is the cranked-lambda-wing UAV planform proposed as a low-observable geometry in [9], which is adopted as the reference model. The cited work notes that this planform is relatively underrepresented in the literature and is relevant to application contexts associated with armed flying-wing platforms such as the X-47B. The authors also report advantages in low observability and aerodynamic efficiency, supporting its representativeness for the present study, which concurrently considers aerodynamic performance and RCS. The geometric specifications and analysis conditions are summarized in Table 1 and Table 2, respectively. Aerodynamic validation follows the experimental and numerical results reported in [9]. The baseline geometry is shown in Fig. 1.

3.2. Aerodynamic Analysis

In this study, a low-fidelity aerodynamic analysis was conducted on a delta-wing unmanned aerial vehicle using the VSPAERO module of OpenVSP.

Table 1. Geometry Dimensions.

Parameter	Value
Wing Area, S	0.145 m²
Wing Span	0.75 m
Aspect Ratio	3.879
Inboard Sweep Angle	58°
Outboard Sweep Angle	40°
Airfoil Profile	NACA 641212

Table 2. Aerodynamic Analysis Conditions.

Parameter	Value
Velocity	30 m/s
Angle of Attack	0°~40° (5°)
Reynolds Number	5.75×10^5

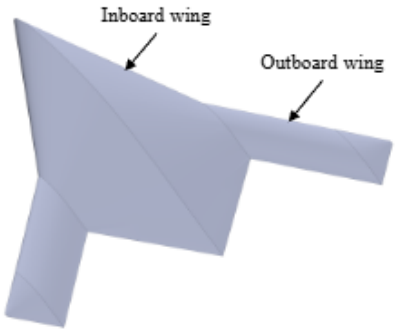

Fig. 1. Reference Geometry.

VSPAERO is based on the Vortex Lattice Method, which calculates lift and induced drag, and is widely used during the conceptual design phase due to its relatively fast computation and simple setup. The lift coefficient, drag coefficient, and lift-to-drag ratio were calculated at angles of attack ranging from 0° to 40° in 5° increments, and the comparison with reference data is illustrated in Fig. 2 to Fig. 4. The reliability of the simulation results was assessed by comparing them with experimentally derived reference data reported in the literature. As a result, the lift coefficient showed a similar trend to the reference values across the entire range, with good agreement within approximately ±10 % error in the low angle-of-attack region below 10°. In terms of drag coefficient, the results were comparable up to 10°, but under high angle-of-attack conditions above 15°, the OpenVSP predictions tended to underestimate the drag compared to the reference data. This discrepancy is attributed to structural limitations of the VLM method, which does not account for viscous effects or flow separation [10]. Consequently, the lift-to-drag ratio was also overestimated due to this drag underprediction, with deviations of approximately ±15–20 % observed in the high angle-of-attack range. Therefore, the analysis results are considered to fall within an acceptable level of accuracy given the inherent limitations of low-fidelity methods.

3.3. RCS Analysis

RCS analysis was performed using a PyPOFacets-based code by specifying the sweep conditions for frequency, azimuth angle, and elevation angle, as summarized in Table 3. The operating frequency was set to 1e10 Hz, corresponding to 10 GHz. The azimuth angle was swept from 0° to 360° with a 1° increment. The elevation angle was fixed at 90°, representing a side-looking condition, and the full-azimuth RCS pattern was obtained. The RCS results presented in this section were computed for each azimuth angle and are reported in dBsm. Fig. 5 shows the polar plot of the azimuth-swept RCS for the baseline model. The baseline RCS exhibits a strong directional dependency, with the scattering intensity varying significantly with azimuth angle. The maximum RCS was 0.62 dBsm, indicating the presence of a peak at a specific azimuth angle where scattering is amplified. The minimum RCS was −47.34 dBsm, implying that a deep null occurs at certain azimuth angles where scattering is substantially reduced. The mean RCS was −20.24 dBsm, representing the overall average scattering level over the full azimuth range. The dynamic range between the maximum and minimum values was 47.96 dB, suggesting that detectability can vary markedly depending on the observation azimuth. Therefore, the low-observability performance of the baseline model should be evaluated not only using the mean value but also by considering the existence of azimuth sectors associated with elevated RCS and the magnitude of the peak RCS.

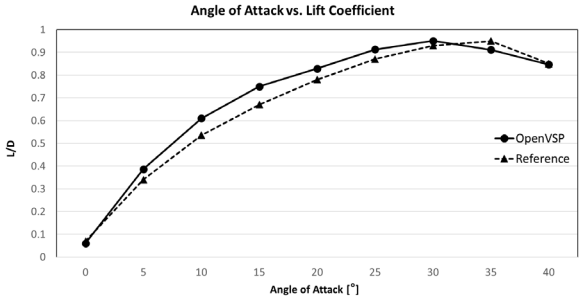

Fig. 2. Lift Coefficient (OpenVSP vs Reference).

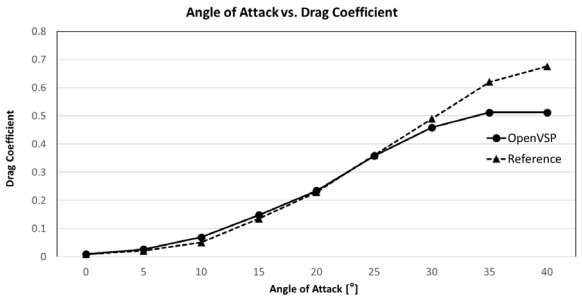

Fig. 3. Drag Coefficient (OpenVSP vs Reference).

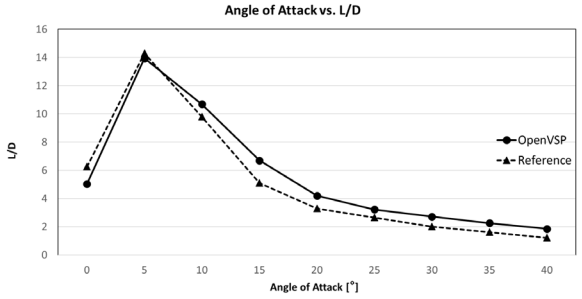

Fig. 4. Lift to Drag Ratio (OpenVSP vs Reference).

Table 3. RCS Analysis Conditions

Parameter, Unit	Value
Frequency, Hz	1.0×10^{10}
Correlation Length, m	1
Standard Deviation, m	0
Azimuth Start Angle, deg	0
Azimuth End Angle, deg	360
Azimuth Step, deg	1
Elevation Start Angle, deg	90
Elevation End Angle, deg	90
Elevation Step, deg	1

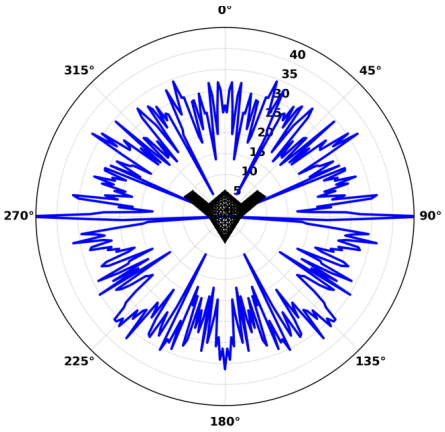

Fig. 5. Azimuth-Swept RCS Polar Plot.

3.4. Building the RCE Framework

To repeatedly evaluate aerodynamic performance and radar scattering characteristics under an identical geometric definition, an RCE-based automated framework was established (Fig. 6). The optimization component generates the design variables, namely the inboard and outboard sweep angles. The OpenVSP geometry-generation component updates the baseline configuration using the specified sweep-angle combination. The VSPAERO aerodynamic-analysis component computes the aerodynamic performance metrics for the updated geometry. In parallel, an STL model is exported from the same geometry. The STL model is passed to the PyPOFacets-based RCS analysis component. The RCS analysis is performed using the identical STL. The mean RCS and the maximum RCS are then computed. These two analysis results are then fed back to the optimization component through the RCE data-transfer structure for iterative exploration. This workflow automates the handling of differing input formats and result aggregation across analysis tools, thereby reducing procedural errors and enabling a stable search of the aerodynamic–RCS trade-off. For the optimization, Dakota's multi-objective genetic algorithm was adopted. Table 4 summarizes the objective functions, constraints, design variables, and search ranges used to define the optimization problem. The objective functions were set to maximize the mean lift-to-drag ratio averaged over multiple angles of attack and to minimize the mean RCS computed over a specified observation-angle range. The mean lift-to-drag ratio was selected as an objective because maximizing L/D at a single design point can degrade performance under other operating conditions [11]. Averaging L/D across multiple conditions mitigates performance variation and serves as a robust indicator representative of overall aerodynamic efficiency. Because RCS varies significantly with azimuth and elevation angles, the mean RCS was used as an objective to avoid excessive sensitivity to localized spikes at specific angles while still reflecting the overall detectability level within the observation-angle region of interest. However, since an average metric can mask peak exposure at certain angles, the maximum RCS was additionally imposed as a constraint to exclude designs exhibiting excessively increased peaks in particular viewing directions [12]. The design variables were defined as the inboard sweep angle and outboard sweep angle. Sweep angle is a key planform parameter that strongly affects both subsonic drag and radar scattering characteristics. Separating the inboard and outboard regions enables independent control of planform alignment and the chord and area distributions. This separation is beneficial for balancing the aerodynamic–stealth trade-off. Based on prior delta- and lambda-planform UAV cases, inboard leading-edge sweep is generally above 40°. Outboard sweep is typically milder, ranging from the teens to the mid-40° range. Accordingly, the search ranges were set to 40–63° for the inboard sweep and 10–45° for the outboard sweep [13].

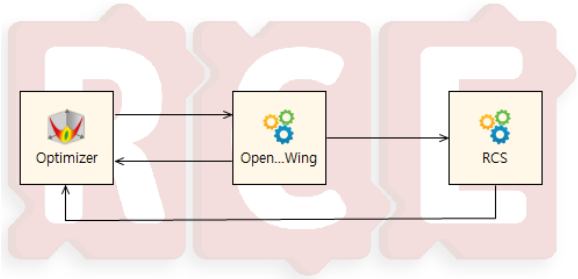

Fig. 6. Configuration of the RCE Workflow for Optimization, Aerodynamic and RCS Analysis

Table 4. Optimization Problem Definition.

Problem Definition	Parameter	Range
Objective	LD Avg	Maximize
Objective	RCS Avg	Minimize
Constraints	RCS Max	-40~-20 dBsm
Design Variable	Inboard Sweep	40°~63°
Design Variable	Outboard Sweep	10°~45°

3.5. Optimization Results

Fig 7 shows the convergence behavior of the optimization, confirming stable progress toward the

final solution. As a result of the optimization, the inboard sweep angle decreased from 58.0° to 52.0°, and the outboard sweep angle decreased from 40.0° to 35.15°. Table 5 presents the performance metric comparison. Under this change, the aerodynamic performance exhibited a limited variation, with the average lift-to-drag ratio increasing from 5.6218 to 5.6512 by 0.0294. In contrast, the RCS performance improved substantially. The maximum RCS was reduced from 0.62 dBsm to −19.71 dBsm, corresponding to a decrease of 20.33 dB, and the mean RCS was reduced from −20.24 dBsm to −30.6597 dBsm, corresponding to a decrease of 10.42 dBsm. The pattern comparison in Fig. 8 also confirms that, under the same condition, the optimized configuration exhibits a lower scattering level over the entire azimuth range and that spike-like dominant peaks are suppressed. In this study, the reason why the reduced sweep angles led to RCS reduction is that RCS is governed not simply by the magnitude of the sweep angle itself, but by the effective projected geometry and edge alignment formed in the radar observation direction, as well as the resulting distribution of scattering directions. The present result compares azimuth-dependent scattering under 10 GHz and θ = 90°. For the optimized configuration, changes in the alignment of the leading edge and outer planform edges alleviate the geometric conditions that previously produced a strong reflected component toward the radar receiving direction at specific azimuth angles, and the scattering energy is redistributed toward a broader set of directions. As a result, strong specular components and localized peaks in the side-observation condition are suppressed, leading to a reduction in the mean RCS.

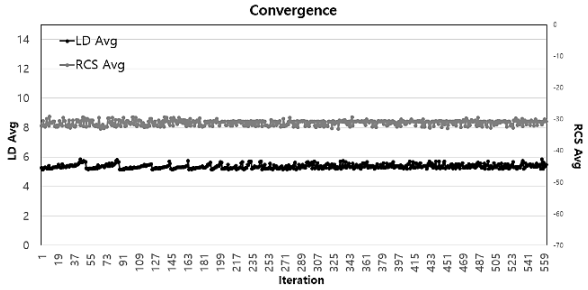

Fig. 7. Optimization Convergence.

Table 5. Performance Metric Comparison.

Parameter	Reference	Optimization
Inboard Sweep	58°	52°
Outboard Sweep	40°	35.15°
LD AVG	5.621838266	5.641221
RCS AVG	-20.24 dBsm	-30.67 dBsm
RCS Max	0.62 dBsm	-19.71 dBsm

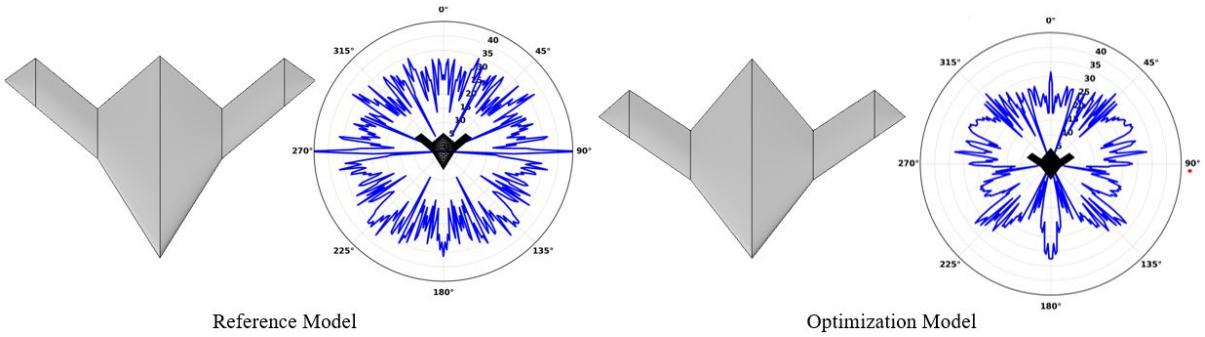

Fig. 8. Reference and Optimized Configurations with RCS Patterns.

4. Conclusion

This study presents an open-source integrated aero–stealth design exploration workflow for a low-observable cranked-lambda delta-wing UAV, enabling coupled evaluation and optimization of aerodynamic performance and radar cross section (RCS). OpenVSP/VSPAERO-based aerodynamic analysis and PyPOFacets-based RCS analysis were linked through an RCE-based automated process, allowing performance metrics to be computed consistently and evaluated iteratively under a unified geometry definition. The optimization was performed by selecting the inboard and outboard leading-edge sweep angles as design variables and imposing an upper bound on the maximum RCS as a constraint. As a result, the inboard sweep angle decreased by 6° and the outboard sweep angle decreased by 4.85°.

Aerodynamic performance improved slightly, with the average lift-to-drag ratio increasing by approximately 0.2. In contrast, stealth performance improved substantially, with the maximum RCS reduced by 20.33 dBsm and the mean RCS reduced by 10.42 dBsm. The RCS pattern comparison also indicates an overall reduction in scattering levels across azimuth angles and suppression of spike-like dominant peaks, which qualitatively agrees with the reduced reflected component toward the radar receiving direction and the redistribution of scattering energy due to changes in effective projected geometry and edge alignment in the radar observation direction. Overall, the results demonstrate that sweep-angle

adjustments can increase aerodynamic performance while achieving meaningful RCS reduction, and the proposed automated workflow provides a reproducible basis for exploring the trade-off between aerodynamic efficiency and low observability at the conceptual design stage. This framework can be extended by incorporating additional design variables, applying higher-fidelity analysis methods, and evaluating broader operational conditions.

Acknowledgements

This paper is based on research supported by the Ministry of Trade, Industry and Energy (A major activities of 2025 industry-academia cooperation: aviation and defense SW professional education).

References

[1]. H. Karali, G. Inalhan, A. Tsourdos, Advanced UAV design optimization through deep learning-based surrogate models, *Aerospace*, Vol. 11, Issue 8, 2024, 669.

[2]. C. Yuan, D. Ma, Y. Jia, L. Zhang, Stealth unmanned aerial vehicle penetration efficiency optimization based on radar detection probability model, *Aerospace*, Vol. 11, Issue 7, 2024, 561.

[3]. C. Thoulon, G. Roge, O. Pironneau, Gradient-based aero-stealth optimization of a simplified aircraft, *Fluids*, Vol. 9, Issue 8, 2024, 174.

[4]. H. Díaz, L. F. Alarcón, C. Mourgues, S. García, Multidisciplinary design optimization through process integration in the AEC industry: Strategies and challenges, *Automation in Construction*, Vol. 73, 2017, pp. 102-119.

[5]. T. Hu, X. Yu, Aerodynamic stealthy structural multidisciplinary design optimization of unmanned combat air vehicle, *Chinese Journal of Aeronautics*, Vol. 22, Issue 4, 2009, pp. 380-386.

[6]. L. Zhou, J. Huang, Z. Gao, W. Zhang, Three-dimensional aerodynamic stealth optimization based on adjoint sensitivity analysis for scattering problem, *AIAA Journal*, Vol. 58, Issue 6, 2020, pp. 2702-2715.

[7]. H. Bae, K. Lee, J. Jeong, D. Sang, et al., 500 lbs-class air-to-surface missile design by integration of aerodynamics and RCS, *Journal of the Korean Society for Aeronautical and Space Sciences*, Vol. 40, Issue 2, 2012, pp. 184-191 (in Korean).

[8]. C. Chagas, PyPOFacets repository, https://github.com/claytonchagas/PyPOFacets

[9]. H. Aleisa, K. Kontis, M. Nikbay, Low observable uncrewed aerial vehicle wind tunnel model design, manufacturing, and aerodynamic characterization, *Aerospace*, Vol. 11, Issue 3, 2024, 216.

[10]. C. N. D. Sheridan, D. D. V. Pham, S. K. S. Whiteside, Evaluation of VSPAERO analysis capabilities for conceptual design of aircraft with propeller-blown wings, in *Proceedings of the AIAA AVIATION Forum*, 2021, 2510.

[11]. Z. Lyu, J. R. R. A. Martins, Aerodynamic design optimization studies of a blended-wing-body aircraft, *Journal of Aircraft*, Vol. 51, Issue 5, 2014, pp. 1604-1617.

[12]. S. M. Vaitheeswaran, T. S. Gowthami, S. Prasad, B. Yathirajam, Monostatic radar cross section of flying wing delta planforms, *Engineering Science and Technology, an International Journal*, Vol. 20, Issue 2, 2017, pp. 467-481.

[13]. R. K. Nangia, M. E. Palmer, A comparative study of four UCAV wing layouts – High speed aero performance & stability considerations, in *Proceedings of the 25th Congress of the International Council of the Aeronautical Sciences (ICAS'06)*, 2006, Paper 2006-3.7.2.

(013)

Design and Implementation of a Servo Motor Control Library for Drone Control Systems

Jinyoung Lee [1] and Sungwook Cho [2]
[1] Cheongju University, Department of Mechanical and Aeronautical Systems Engineering, 298 Daeseong-ro, Cheongwon-gu, Cheongju-si, Chungbuk, South Korea
[2] Cheongju University, Department of Aeronautical and Mechanical Engineering, 298 Daeseong-ro, Cheongwon-gu, Cheongju-si, Chungbuk, South Korea
Tel.: + 82 43 229 7948
E-mail: swcho84@cju.ac.kr

Summary: This paper presents the design and implementation of a lightweight servo-motor control library for unmanned aerial vehicle (UAV) actuation systems using a USB–CAN interface and a time-structured dual-loop scheduling architecture. The proposed framework focuses on reliable command transport, packet integrity, and telemetry parsing under periodic real-time constraints rather than implementing a host-side closed-loop controller. A custom AA–55 CAN framing protocol is employed to ensure deterministic frame synchronization, error detection, and continuous parameter monitoring. The control architecture operates with a nominal 50 ms command transmission cycle and a configurable telemetry polling cycle, enabling consistent actuation and stable feedback acquisition under Linux-based environments. Experimental validation on a ground-based servo test bench demonstrates high consistency between reference commands and measured actuator response, with deviations remaining within the resolution limits of the telemetry interface. The modular design allows seamless integration with ROS 2 and embedded UAV subsystems such as gimbals and control-surface actuators. The results indicate that the proposed library provides a practical and extensible transport-layer foundation for robust, low-latency multi-axis UAV actuation systems.

Keywords: Servo motor control, CAN communication protocol, Real-time control loop, Concurrent process scheduling, Modular software framework.

1. Introduction

Servo motors play a critical role in modern unmanned aerial vehicles (UAVs), serving as the primary actuation mechanisms for gimbals, payload stabilization systems, and aerodynamic control surfaces. The responsiveness and stability of these actuators directly influence flight safety, sensing accuracy, and mission effectiveness, particularly in scenarios involving rapid target tracking or dynamic environmental disturbances [1, 2].

Conventional UAV architectures typically rely on pulse-width modulation (PWM)-based servo interfaces or high-level middleware frameworks, such as ROS-based actuator controllers and UAVCAN (Cyphal) networks, to abstract low-level communication and device management. While these solutions offer strong ecosystem support and ease of integration, they often limit direct access to transport-layer timing, packet integrity, and feedback synchronization mechanisms. As a result, the host system has limited visibility into communication jitter, frame loss, or telemetry desynchronization, which can degrade actuator reliability under high-frequency command updates or bandwidth-constrained conditions [3].

In practice, many UAV actuation systems operate in a hybrid configuration where the servo controller performs internal closed-loop control (e.g., PID or field-oriented control), while the host system is responsible for generating reference commands and interpreting telemetry feedback. In such cases, the overall system performance is strongly influenced by the reliability and temporal structure of the communication layer rather than the control algorithm itself. This observation motivates the development of a lightweight transport- and scheduling-oriented servo control library that explicitly addresses packet framing, command arbitration, and bounded-latency telemetry acquisition.

This paper proposes a USB–CAN-based servo-motor control framework that emphasizes deterministic frame synchronization, time-structured command scheduling, and modular software architecture. Instead of introducing a new control law, the proposed library focuses on ensuring that reference commands and sensor feedback are delivered in a consistent and verifiable manner under non-real-time Linux environments. A custom AA–55 CAN framing protocol is adopted to provide explicit frame boundary detection, payload validation, and structured parsing of both integer and floating-point telemetry parameters.

2. Related Work

UAV actuator control frameworks can be broadly categorized into three classes: PWM-based servo interfaces, middleware-driven CAN networks, and custom transport-layer implementations.

2.1. PWM-Based Servo Control

Traditional UAV platforms commonly use PWM signals to drive hobby-grade or industrial servo motors. This approach benefits from simplicity and wide hardware compatibility, but it provides limited telemetry capability and minimal error detection. Feedback such as position, current, or temperature is typically unavailable or requires additional sensor wiring. Furthermore, PWM-based systems lack inherent packet integrity verification or frame synchronization, making them less suitable for high-reliability or safety-critical UAV applications [2].

2.2. Middleware and CAN-Based Frameworks

Modern UAV ecosystems increasingly adopt CAN-based communication standards such as UAVCAN (Cyphal) and ROS 2 actuator interfaces. These frameworks provide structured message definitions, node discovery, and strong support for distributed systems. ROS 2, in particular, enables integration with control pipelines, simulation environments, and behavior-based architectures. However, these systems often abstract away low-level transport details, such as serial buffering behavior, frame boundary handling, and host-side scheduling policies. As a result, precise characterization of communication latency and jitter is difficult without modifying the middleware stack [4, 5].

2.3. Positioning of the Proposed Approach

The proposed library occupies a complementary position between low-level PWM actuation and full middleware-based CAN frameworks. Rather than replacing UAVCAN or ROS-based control architectures, it provides a transport-layer foundation that emphasizes explicit frame synchronization and reconstruction from raw byte streams, host-side timing control and arbitration between command and telemetry traffic, and lightweight integration with higher-level frameworks such as ROS 2 or embedded flight-control companions.

In this sense, the library is designed to serve as a diagnostic, prototyping, and integration tool for UAV actuation systems where transparency of communication behavior and bounded-latency feedback are critical. While middleware-based frameworks provide rich ecosystem support, their abstraction of transport-layer behavior limits direct control over timing, buffering, and frame reconstruction, which are essential for characterizing communication-induced delays and jitter.

From a system evaluation perspective, these differences directly influence achievable update rates, closed-loop stability margins, and the observability of failure modes under high bus utilization or intermittent telemetry loss. In experimental settings, the ability to explicitly control frame timing and inspect intermediate communication states enables repeatable benchmarking of latency distributions, jitter bounds, and command–telemetry interaction effects that are often obscured in fully abstracted middleware stacks.

To make these conceptual and practical distinctions explicit and comparable, the following analysis maps the proposed design choices to representative UAV actuation frameworks in terms of interface modality, telemetry richness, frame integrity, timing control, and system integration complexity. This comparison highlights the trade-offs between integration convenience, real-time observability, and transport-layer transparency that motivate the proposed approach.

Table 1. Comparison of UAV Actuation Frameworks.

Feature	PWM-Based Servo	UAVCAN / Cyphal	ROS-Based Controllers	Proposed Library
Interface type	PWM	CAN	CAN / middleware	USB–CAN (aa–55)
Telemetry support	Limited / none	Rich	Rich	Rich (pos/vel/current/temp)
Frame integrity	None	Crc / protocol-level	Middleware-level	Explicit sof/eof + payload validation
Host timing control	Minimal	Abstracted	Abstracted	Explicit dual-loop
Update rate control	Fixed	Configurable	Configurable	User-defined (20–200 hz configurable)
Integration complexity	PWM	CAN	CAN / middleware	USB–CAN (aa–55)
Ros 2 compatibility	Limited / none	Rich	Rich	Rich (pos/vel/current/temp)

3. System Architecture

3.1. Overall Design

The proposed system is composed of two primary software components: a command and communication server and a graphical monitoring interface. The architecture is designed to separate real-time serial communication from user interaction and high-level command generation, thereby minimizing timing interference and improving modularity. Fig. 1 shows the overall architecture of the proposed USB–CAN

servo control framework. The control layer schedules periodic command transmission and telemetry parsing using thread-safe queues. The communication layer performs AA–55 frame reconstruction and TX/RX logging from a continuous serial byte stream. The USB–CAN interface encodes and decodes CAN frames and handles serial buffering and signal conversion. Telemetry feedback is returned from the servo motor unit as C4/C6 CAN frames, enabling structured monitoring of position, velocity, current, and system status.

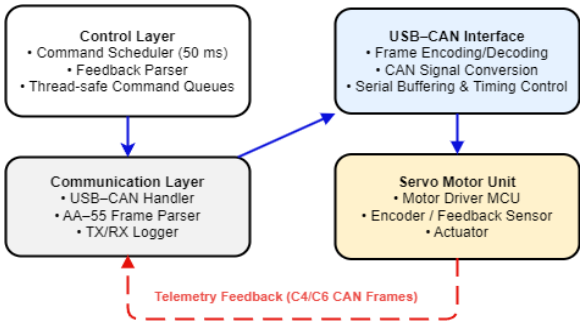

Fig. 1. Architecture of Servo-Motor Control library.

The server component maintains exclusive access to the serial USB–CAN interface and is responsible for generating CAN frames using the AA–55 protocol, scheduling command and telemetry traffic, reconstructing incoming frames from the continuous serial byte stream, parsing telemetry data into engineering units, and broadcasting logs and status information to all connected clients. External clients, including both a command-line interface and a graphical user interface (GUI), communicate with the server through a UNIX domain socket, which allows multiple monitoring or control tools to attach to the same communication backend without introducing contention on the serial port.

3.2. Software Layering

The system is structured into four functional layers that separate user interaction, scheduling, communication, and data interpretation to improve modularity and timing robustness. The application layer provides command generation and real-time visualization of actuator states, including position, velocity, current, power, and temperature, and supports scripted step and sweep inputs for experimental evaluation. The control and scheduling layer enforce periodic task execution, arbitrates between high-priority actuation commands and background telemetry polling, and maintains actuator stability through a keep-alive mechanism. The communication layer manages CAN frame construction and serial transmission over the USB–CAN interface, while the parsing and logging layer reconstructs complete frames from the serial byte stream, decodes payloads into engineering units, and records all TX/RX activity for performance analysis. This modular design enables seamless integration with embedded UAV companion computers and external frameworks such as ROS 2.

3.3. Command Arbitration & Keep-Alive Strategy

To prevent interference between telemetry polling and high-priority actuation commands, the system employs a simple arbitration policy. Background parameter requests are suspended whenever a user command is being transmitted or when the time since the last command is below a predefined threshold. This approach reduces bus contention and ensures that time-critical commands are delivered without delay.

A periodic keep-alive mechanism retransmits the most recent valid position command when the system remains idle for a specified interval. This strategy prevents servo drift and unintended torque release that may occur if the actuator controller interprets a prolonged communication gap as a stop condition.

4. AA–55 CAN Frame Structure

4.1. Frame Structure Overview

The proposed library employs a lightweight, byte-oriented framing protocol, referred to as the AA–55 format, to encapsulate CAN payloads over a continuous USB serial stream. This design enables explicit frame boundary detection, payload validation, and deterministic reconstruction under variable buffering conditions. Each frame is delimited by a Start-of-Frame (SOF) marker and an End-of-Frame (EOF)marker, allowing the receiver to resynchronize even in the presence of byte loss or partial reads. The general structure of an AA–55 frame is defined as:

$$F = \{SOF, CMD, ID, LEN, D_{0..N-1}, CHK, EOF\}, \quad (1)$$

where SOF and EOF are fixed sentinel bytes (0xAA and 0x55, respectively), CMD denotes the command or response type, ID identifies the target actuator or parameter group, LEN specifies the payload length, $D_{0..N-1}$represents the CAN data field, and CHK is a host-side validation field used to detect malformed or corrupted frames.

4.2. Field Definition Table

Table 2 details the field-level composition of the AA–55 frame. The use of fixed sentinel bytes for the SOF and EOF fields enables explicit frame boundary detection and rapid resynchronization under partial reads or byte loss. The CMD and ID fields jointly define both the semantic category of the message and the target actuator or parameter group, allowing a unified representation of motion commands and telemetry requests within a single frame format. The

LEN field provides structural consistency checking by constraining the expected payload size, while the DATA field encapsulates CAN-compatible payloads such as position, velocity, current, and system status. Finally, the CHK field implements a lightweight host-side validation mechanism that complements CAN-level error detection, enabling early rejection of malformed frames before higher-level processing.

Table 2. AA-55 Frame Format.

Field	Size (Bytes)	Description
SOF	1	Start-of-frame marker (0xAA)
CMD	1	Command or response identifier (e.g., motion command, telemetry request, feedback type)
ID	1	Target device or parameter group identifier
LEN	1	Length of payload field
DATA	N	CAN payload (position, velocity, current, status, etc.)
CHK	1	Payload validation byte (host-side consistency check)
EOF	1	End-of-frame marker (0x55)

4.3. Frame Reconstruction Algorithm

Incoming data are processed as an asynchronous serial byte stream. The receiver maintains a sliding window buffer and performs frame reconstruction through a finite-state parsing process. The algorithm detects the SOF marker, accumulates subsequent bytes until a valid EOF marker is observed, and verifies the structural consistency of the frame based on the LEN and CHK fields. Frames that fail validation are discarded, and the parser immediately re-enters the SOF search state, ensuring bounded recovery time under corrupted or misaligned input.

Fig. 2 show a Control and communication state machine of the proposed USB–CAN actuation library. The system transitions from an idle state to a scheduling phase upon receiving external commands, where arbitration and timing control determine priority between actuation and telemetry traffic. Outgoing commands are encoded into AA–55 frames and transmitted via the USB–CAN interface to the servo motor unit. Incoming telemetry frames are reconstructed using explicit SOF/EOF synchronization and lightweight validation before being parsed into engineering units and broadcast to connected clients. A keep-alive mechanism closes the loop by periodically returning control to the scheduler, enabling consistently bounded command updates and continuous system monitoring.

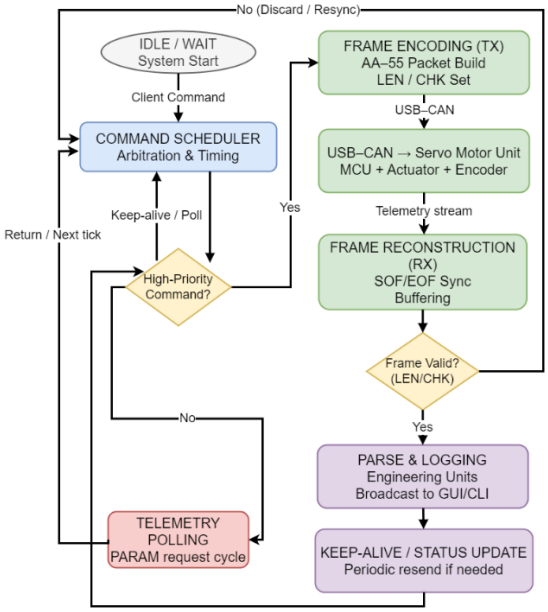

Fig. 2. Control and communication state machine of the proposed USB–CAN actuation library.

4.4. Timing Model and Communication Performance

$$T_{rt} = T_{tx} + T_{usb} + T_{can} + T_{servo} + T_{rx} \quad (2)$$

The round-trip latency T_{rt} is modeled as the sum of the host-side transmission scheduling delay T_{tx}, USB serial buffering and driver latency T_{usb}, CAN bus transmission time T_{can}, internal servo processing delay T_{servo}, and host-side reception and parsing time T_{rx}. This decomposition enables explicit attribution of latency variance to transport, bus, and actuator subsystems.

$$T_c = 50\,ms, T_t \in [80\,ms, 100\,ms], \quad (3)$$

where T_c denotes the command update period of the actuation loop and T_t denotes the telemetry polling period used to acquire periodic state feedback from the servo motor unit.

$$L = t_{rx}^{telemetry} - t_{rx}^{command}, \quad (4)$$

where $t_{rx}^{command}$ is the host-side timestamp at which an actuation command is transmitted, and $t_{rx}^{telemetry}$ is the timestamp of the first valid telemetry frame confirming actuator response.

$$R = \frac{N_c \cdot S_c + N_t \cdot S_t}{T}, R < R_{max}, \quad (5)$$

where N_c and N_t denote the number of command and telemetry frames transmitted within the observation

window T, S_c and S_t represent the corresponding frame sizes in bytes, and R_{max} is the maximum allowable bus utilization to prevent communication saturation.

$$\sigma_L = \sqrt{\frac{1}{N}\sum_{i=1}^{N}(L_i - \mu_L)^2}, \quad (6)$$

where L_i denotes the measured end-to-end latency of the i-th trial, μ_L is the mean latency over N measurements, and σ_L quantifies the timing jitter of the communication and scheduling framework.

5. Experimental Results and Discussion

5.1. Actuation Performance and Tracking Accuracy

The actuation capability of the proposed library was validated through a multi-step response experiment. Target positions were incrementally increased from 0° to 360° to evaluate the system's tracking precision across a wide angular range. As illustrated in the top panel of Fig. 3, the measured position demonstrates exceptional alignment with the reference commands. The library achieved a high level of steady-state consistency, with a final position of 360.003° recorded at the end of the experiment. This corresponds to a deviation that remains within the effective resolution and quantization limits of the telemetry and encoder interface, exceeding the design requirement of 0.5 %. Such consistency is attributed to the reliable command delivery of the REPEAT strategy, which prevents potential torque release or position drift by periodically refreshing the actuator's internal setpoints. Furthermore, the synchronized analysis of speed and current profiles provides insight into the control stability. During each position transition, the measured speed rose smoothly without excessive oscillation, while the current profile exhibited transient peaks corresponding to the torque required for acceleration, followed by immediate stabilization upon reaching the target. This indicates that the AA-55 protocol's telemetry parsing effectively captures the actuator's dynamic behavior in real-time, allowing the host system to verify not only the final position but also the mechanical health and load conditions of the UAV actuation system.

5.2. Jitter and Reliability Analysis

The timing determinism of telemetry acquisition was evaluated by analyzing the reception intervals of 1000 telemetry frames. Fig. 4 illustrates the communication jitter characteristics under a nominal polling configuration in the range of 80–100 ms. As depicted in the histogram of Fig. 4. (a), the telemetry intervals are distributed around a mean of 80.26 ms, reflecting the effects of non-deterministic Linux scheduling and USB serial buffering. Although the standard deviation was measured at 51.09 ms, the distribution confirms that the majority of frames are captured within a predictable operating window, which is sufficient to maintain consistent actuator monitoring in transport-layer-driven control architectures. The scatter plot in Fig. 4(b) further visualizes the temporal stability of these intervals. While occasional latency spikes occur, the proposed AA–55 framing protocol successfully prevented data corruption by ensuring byte-level resynchronization and payload validation. This resilience ensures that the high-level control logic consistently receives valid state feedback, decoupling host-side timing variability from physical actuation reliability. During all experimental trials, estimated bus utilization remained below the saturation threshold R_{max}, and no frame drops or telemetry loss events were observed, confirming stable operation under the evaluated command and polling rates. In this implementation, Rmax was conservatively defined as 50 % of the nominal CAN bus bandwidth to avoid saturation under worst-case burst conditions.

6. Conclusion

In this paper, we designed and implemented a lightweight servo-motor control library tailored for UAV systems using a USB-CAN interface. By adopting a time-structured dual-loop scheduling architecture and a custom AA-55 framing protocol, we addressed the challenges of reliable command transport and telemetry parsing in a non-real-time Linux environment. Experimental validations demonstrated that the proposed system achieves high actuation consistency, with steady-state deviations remaining within the sub-0.01 % range at a 360° rotation, as constrained by the resolution of the telemetry and encoder interface. Although the host-side communication exhibited a jitter of approximately 51 ms under non-real-time Linux scheduling, the robust framing and keep-alive retransmission strategies ensured continuous feedback delivery and prevented frame loss or command starvation. This library provides a practical and scalable solution for drone developers requiring transparent and reliable actuator monitoring without the overhead of complex real-time operating systems.

Acknowledgement

1. This paper is based on research supported by the Ministry of Trade, Industry and Energy (A major activities of 2025 industry-academia cooperation: aviation and defense SW professional education).

2. The current research was supported by the Space Challenge Program funded by the Korea government (Korea AeroSpace Administration, KASA) (RS-2022-NR067041).

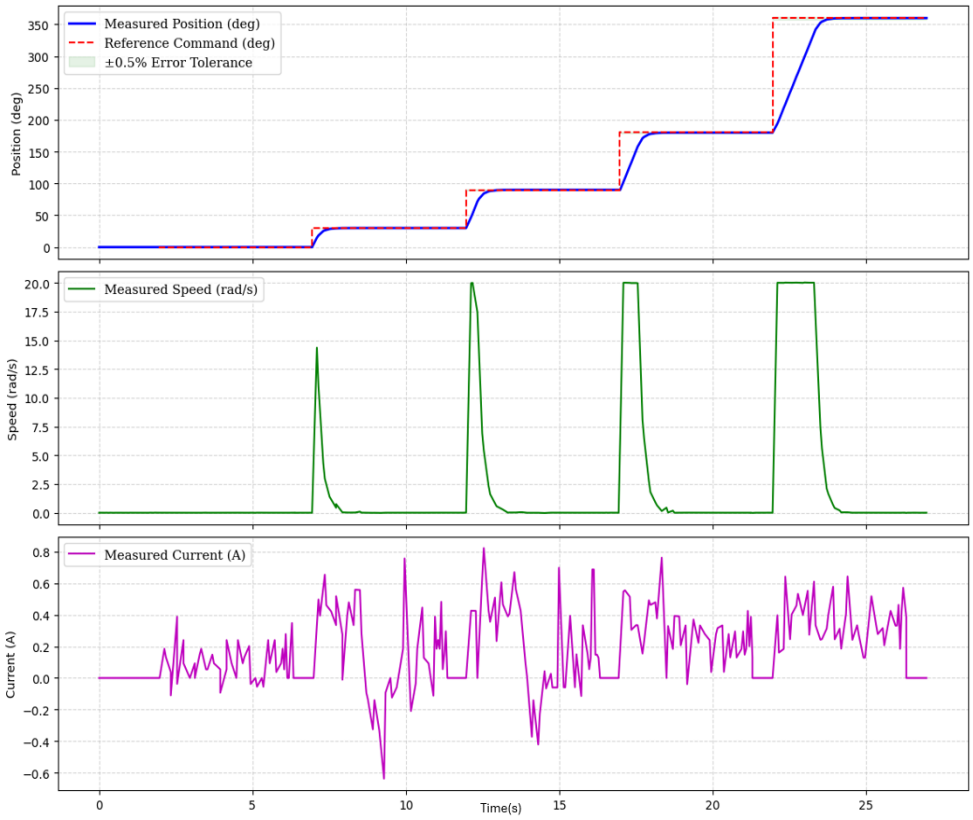

Fig. 3. Experimental results of multi-step response: Time-synchronized position, velocity, and current profiles.

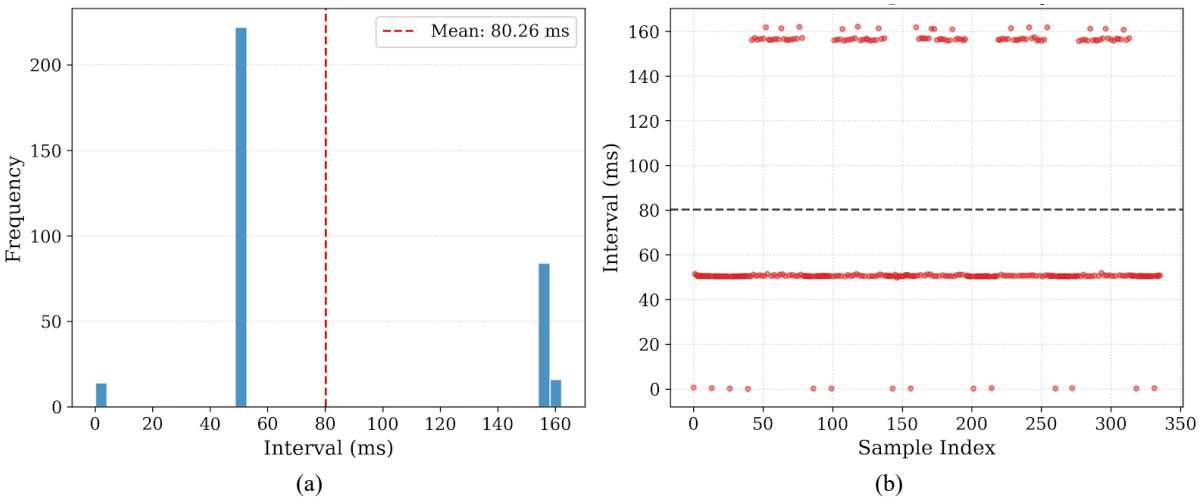

Fig. 4. Statistical analysis of telemetry reception intervals: Histogram (a) and temporal distribution (b).

References

[1]. C. Anastasopoulos, G. Tsourveloudis, K. Dalamagkidis, Design of a real-time test bench for UAV servo actuators, in *Proceedings of the International Conference on Unmanned Aircraft Systems (ICUAS'18)*, 2018, pp. 1224-1231.

[2]. J. Sharma, R. Kumar, A. Nayyar, Robust PID control of single-axis gimbal actuator via UAV platform, *IFAC-PapersOnLine*, Vol. 53, Issue 1, 2020, pp. 113-118.

[3]. E. M. Coates, S. W. Wischmeyer, D. T. Alemnji, G. E. Droge, et al., Toward nonlinear flight control for fixed-wing UAVs: System architecture, field experiments, and lessons learned, *IEEE Access*, Vol. 10, 2022, pp. 48753-48766.

[4]. T. Kronauer, J. Pohlmann, M. Matthé, T. Smejkal, et al., Latency analysis of ROS2 multi-node systems, in *Proceedings of the 19th ACM Conference on Embedded Networked Sensor Systems (SenSys'21)*, 2021, pp. 329-330.

[5]. Y. Ye, Z. Nie, X. Liu, X. Wu, et al., ROS2 real-time performance optimization and evaluation, *Chinese Journal of Mechanical Engineering*, Vol. 36, 2023, 144.

(014)

Policy and Institutional Drivers of UAV Innovation Ecosystems under Economic Security Constraints

K. Miwa [1] and K. Sumikura [2]
[1] Science Techonology and Innovation Policy Program, National Graduate Institute for Policy Studies (GRIPS),7-22-1 Roppongi, Minato-ku, Tokyo 106-8677, Japan
[2] National Graduate Institute for Policy Studies (GRIPS), 7-22-1 Roppongi, Minato-ku, Tokyo 106-8677, Japan
Tel.: + 81-3-6439-6000
E-mail: doc24055@grips.ac.jp

Summary: Unmanned Aerial Vehicles (UAVs) have emerged as a central dual-use technology at the intersection of national security, industrial policy, and civilian innovation. Under intensifying economic security constraints – such as export controls, procurement rigidity, and research-security regulations – countries have adopted divergent institutional approaches to UAV development. This study examines how such constraints shape national UAV innovation ecosystems by focusing on the direction and intensity of civil–military knowledge flows.

Using a large-scale bibliometric dataset of approximately 180000 UAV-related publications indexed in Scopus (2001–2025), this paper constructs indicators of Military-to-Civil (M2C) and Civil-to-Military (C2M) citation flows as proxies for knowledge absorption and reconfiguration across domains. These indicators are interpreted alongside observed shifts in the international diffusion of attack-capable UAVs, which transitioned from U.S.–Israeli dominance in the early 2000s to China- and Turkey-centered export-oriented models in the late 2010s.

The results suggest that UAV diffusion and the deepening of national innovation capabilities do not necessarily coincide, but are mediated by institutional configurations shaping civil–military knowledge flows. Countries differ markedly in how civilian knowledge is absorbed into military capability, how operational feedback is institutionalized, and how export access interacts with innovation incentives. The paper identifies several ecosystem patterns – hybrid, absorptive, wartime-adaptive, and institutionally constrained – and discusses implications for Japan as it seeks to strengthen its UAV innovation ecosystem under economic security constraints. By linking bibliometric evidence with observed diffusion patterns, the study provides an empirically grounded perspective on how institutional design mediates the relationship between dual-use innovation and national security objectives under economic security constraints.

Keywords: UAV innovation, Dual-use technology, Economic security, Innovation ecosystems, Civil–military knowledge flow, Bibliometric analysis.

1. Introduction

Unmanned Aerial Vehicles (UAVs) have rapidly diffused across both military and civilian domains, becoming emblematic of contemporary dual-use technologies. In the military domain, UAVs support intelligence, surveillance, reconnaissance, and precision strike missions; in the civilian domain, they enable disaster response, infrastructure inspection, logistics, agriculture, property tax assessment and environmental monitoring. As geopolitical competition intensifies, however, UAV-related technologies have increasingly been subject to economic security policies, including export controls, research-security regimes, and procurement restrictions [1, 2]. This perspective aligns with the concept of "weaponized interdependence," which highlights how states leverage control over global economic and technological networks to exert strategic influence through regulatory and access-based mechanisms [2]. In this context, UAVs represent a particularly instructive case, as their development depends on a wide range of civilian technologies – such as sensors, communications, artificial intelligence, and autonomous control – while simultaneously being embedded in highly regulated military and security frameworks. This dual character makes UAV innovation especially sensitive to institutional arrangements governing procurement, testing, export, and civil–military collaboration, reflecting long-standing insights that innovation emerges from iterative interactions between military demand, civilian research, and institutional contexts rather than linear technology transfer [3, 4].

Rather than treating wars or geopolitical shocks as direct causal variables, this study focuses on how such events coincide with observable structural changes in UAV diffusion patterns. This perspective is consistent with prior research emphasizing that the impact of military-related innovation depends less on technological capability itself than on institutional mechanisms that enable absorption, feedback, and iterative learning [5, 6].

As illustrated in Fig. 1, the international diffusion of attack-capable UAVs (including MALE-type UCAVs and loitering munitions (e.g., Harpy-type systems)) has shifted from an early U.S.–Israel–led, high-performance and state-centric model in the 2000s to more export-oriented and rapidly adaptive models centered on China and Turkey from the mid-2010s

onward [7]. This assessment draws on the CNAS Drone Proliferation Dataset, which systematically documents cross-national transfers and adoption of armed UAVs and loitering munitions since the early 2000s. In this study, the dataset is used not to evaluate platform performance, but to identify shifts in supplier structure and diffusion patterns, highlighting how access conditions and export orientation have reshaped the global UAV landscape [7]. This shift suggests that access conditions and institutional configurations, rather than platform performance alone, have become increasingly influential in shaping UAV innovation trajectories.

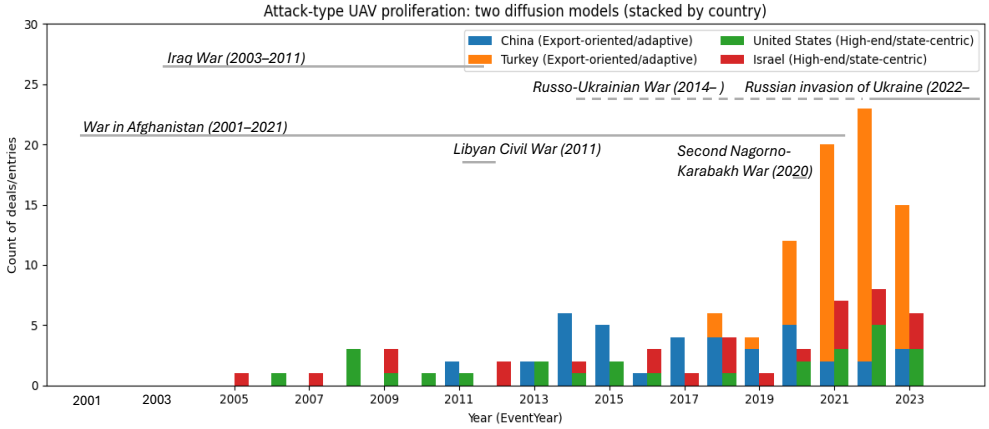

Fig. 1. Attack-type UAV proliferation: two diffusion models (stacked by country).

Importantly, this transformation does not imply a simple decline in technological sophistication. Rather, it reflects a reconfiguration of innovation ecosystems in which export accessibility, development speed, and the ability to incorporate operational feedback increasingly shape competitive advantage. The observed diffusion shift therefore raises questions about how different institutional environments enable or constrain learning processes within national UAV ecosystems.

2. Research Questions and Analytical Perspective

Innovation in dual-use technologies such as UAVs is increasingly shaped by institutional configurations that govern how knowledge moves between civilian and military domains. In this context, an innovation-ecosystem perspective enables analysis of how complementarities among policies, organizations, and knowledge-production systems jointly influence national innovation outcomes [8].

This study addresses three research questions:

- **RQ1:** How do levels and directions of civil–military knowledge flows (M2C and C2M) differ across major UAV-producing countries?
- **RQ2:** How does the international shift in attack-capable UAV diffusion align with changes in these knowledge-flow patterns?
- **RQ3:** What implications do these patterns suggest for Japan's UAV innovation ecosystem under economic security constraints?

These research questions are motivated by the observation that innovation outcomes in dual-use domains cannot be fully explained by R&D investment levels or technological capability alone. Instead, the interaction between institutional constraints and knowledge circulation plays a decisive role in shaping how technologies evolve from experimental systems into operational capabilities.

Accordingly, wars and geopolitical crises are not treated as direct causal variables, but as institutional shocks that reconfigure procurement speed, testing environments, and feedback mechanisms. These changes are assumed to manifest indirectly through shifts in observable knowledge flows between civilian and military research domains.

3. Data and Methodology

3.1. Bibliometric Dataset

The analysis draws on approximately 180000 UAV-related publications indexed in Scopus between 2001 and 2025. Publications are classified into military, civilian, and dual-use categories based on title, abstract, and keyword filters.

This time span allows for the observation of both long-term structural trends and shorter-term discontinuities associated with major geopolitical events, while mitigating the influence of short-lived fluctuations in publication activity.

3.2. Knowledge-Flow Indicators

Military-related, civilian-related, and dual-use literatures were identified using separate

keyword-based filters applied to titles, abstracts, and author keywords in Scopus. These filters were implemented as rule-based queries using OR conditions, rather than proportional thresholds of term frequency. This approach reflects the mixed terminology commonly used in UAV-related research, particularly in dual-use contexts.

The three literature sets were defined independently and are not mutually exclusive. As a result, some publications appear in more than one set, indicating the coexistence of civilian and military contexts within the same research output. Such overlaps were not removed, as the objective of this study is not to assign documents to exclusive categories, but to examine directional citation relationships between civilian-related and military-related bodies of literature.

Based on these literature sets, two directional citation indicators were constructed. Directional knowledge flows are defined strictly from the perspective of the citing publication. Civil-to-Military (C2M) citation flows capture instances in which publications associated with military-related literature cite publications associated with civilian-related literature, indicating military learning and knowledge absorption from civilian research (often interpreted as a "spin-on" pattern). Conversely, Military-to-Civil (M2C) citation flows capture citations from civilian-related literature to military-related literature, indicating that civilian research draws upon knowledge originating in military-related research (often interpreted as a "spin-off" pattern). These directed citation links serve as proxies for the direction and intensity of knowledge circulation across civilian and military domains, without implying direct technology transfer or causal effects. Rather than treating publication counts as the primary object of analysis, this study focuses on patterns of directional citation relationships between literature sets. Accordingly, C2M and M2C flows are interpreted as indicators of knowledge reconfiguration at the ecosystem level, rather than as measures of technological output, performance, or causal impact.

3.3. Comparative Framework

The bibliometric results are compared across major UAV-producing countries – United States, China, Israel, Turkey, Ukraine, and Japan – and interpreted alongside observed changes in the global diffusion of attack-capable UAV platforms.

4. Results

4.1. Global Trends

Globally, UAV-related publications have increased steadily since the early 2000s, with particularly rapid growth after 2014. Civilian-oriented publications dominate in volume, reflecting the expansion of commercial drone markets and enabling technologies such as AI, sensors, and autonomy.

While overall publication volumes have expanded, the orientation of knowledge production has changed markedly over time. As shown in Fig. 2, the ratio of military-oriented to civilian-oriented UAV publications has declined across most countries, indicating a long-term transition toward civilian-led knowledge production. This trend reflects the growing importance of commercial technologies – such as sensors, autonomy, and AI – as foundational inputs to UAV development. Fig. 2 also includes additional countries beyond the core cases examined in this study, in order to situate the focal countries within broader global trends in the orientation of UAV-related knowledge production. An important exception to this global trend is Ukraine, where military-oriented UAV publications have increased since the mid-2000s, diverging from the broader shift toward civilian-led knowledge production observed in most other countries.

Citation analysis reveals a substantial increase in C2M flows over time, while M2C flows exhibit more heterogeneous patterns across countries.

4.2. Structural Break Analysis of Proliferation Dynamics

To further examine temporal changes in UAV diffusion, this study applies structural break analysis to annual proliferation data of armed UAVs and loitering munitions from 2000 to 2023. A two-regime Poisson mean-shift model identifies a clear breakpoint around 2018, after which the annual number of proliferation events increases sharply from an average of 2.7 to 24.8 events (Fig. 3(a)).

In addition, a mean-shift model applied to the annual supplier share of China and Turkey detects a distinct breakpoint around 2012, where the average share rises from near zero to 0.52 (Fig. 3(b)).

Together, these results indicate a staged transformation in UAV diffusion dynamics, in which changes in supplier structure precede the subsequent acceleration of proliferation volume.

4.3. Cross-National Differences

Taken together, these trends suggest that the civilian domain has become a primary source of technological inputs for UAV development, while military research increasingly focuses on system integration, operational concepts, and mission-specific applications.

Beyond publication volumes, countries differ substantially in how civilian and military knowledge domains interact. Fig. 4 illustrates the evolution of M2C and C2M citation flows across major UAV-producing countries from 2000 to 2025. Fig. 4 demonstrates that while C2M flows increase across all major UAV-producing countries, M2C flows vary

substantially, indicating asymmetric patterns of knowledge absorption and spillover across national innovation ecosystems. The results indicate that C2M flows have increased globally, while M2C flows remain uneven, suggesting asymmetric patterns of knowledge absorption and spillover across national innovation ecosystems [9]. These trends are interpreted as ecosystem-level learning patterns rather than direct technology transfer.

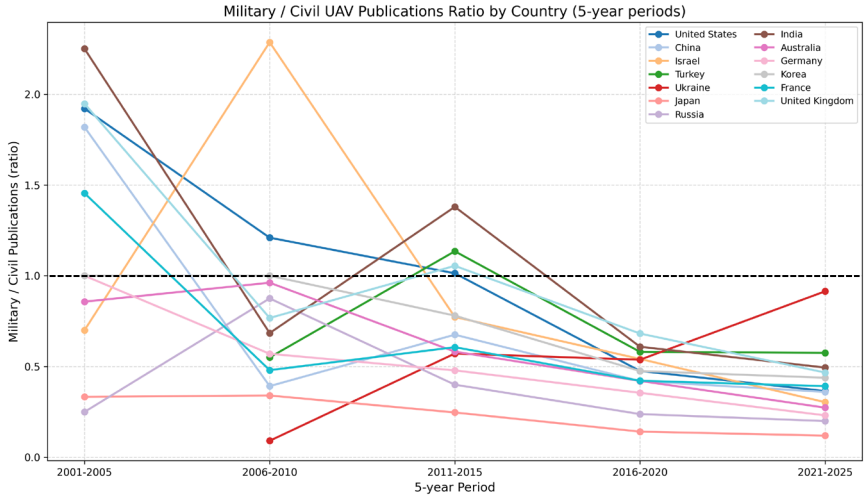

Fig. 2. Military/Civil UAV Publications Ratio by Country (5-year periods).

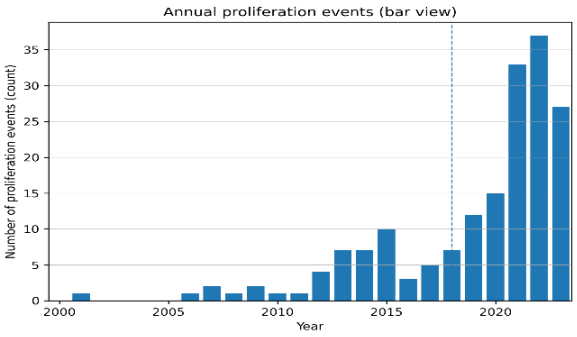

(a) Annual proliferation events (COUNT), 2000–2023

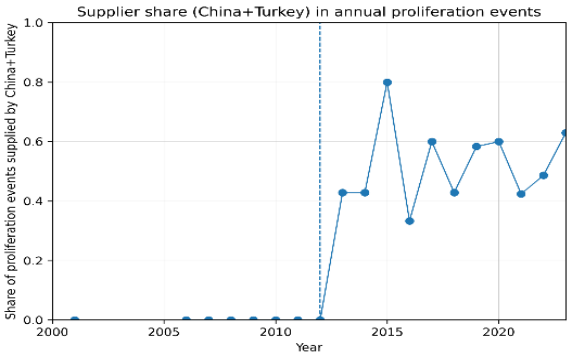

(b) Supplier share of China and Turkey, 2000–2023

Fig. 3. Structural breaks in global UAV proliferation dynamics (2000–2023).

Distinct national patterns emerge:

United States: High publication volume and a strong civilian research base, combined with persistent military engagement. C2M flows are substantial, reflecting effective absorption of civilian technologies; however, procurement processes and institutional transition mechanisms remain comparatively slow, potentially limiting the speed at which innovations are operationalized.

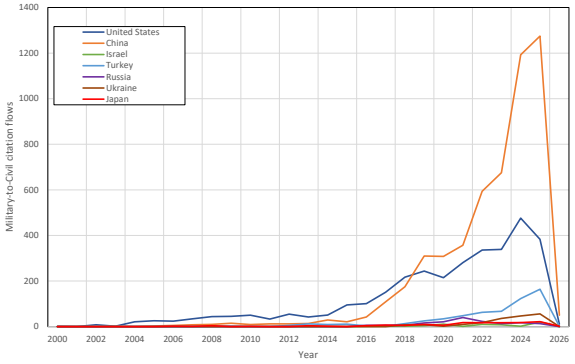

(a) M2C citation flows

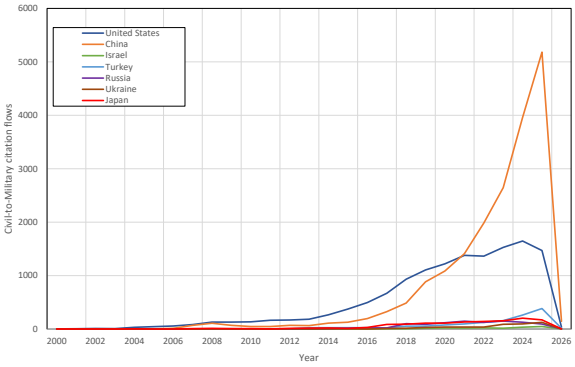

(b) C2M citation flows

Fig. 4. M2C and C2M citation flows in UAV-related research (2001–2025).

China: Large and rapidly growing C2M flows, consistent with an absorptive ecosystem that integrates civilian research into military capability under centralized coordination.

Israel: Tightly integrated, defense-oriented ecosystem characterized by close coupling between military demand, domestic defense firms, and civilian R&D institutions. Balanced civil–military knowledge circulation is reinforced by institutionalized learning mechanisms, including rapid feedback from operational deployment and long-standing procurement–industry linkages.

Turkey: Comparatively moderate publication volume combined with rapidly increasing C2M flows, reflecting an ecosystem shaped by fast development and iteration cycles, close state–industry coordination, and export-oriented deployment strategies that incentivize rapid capability refinement through operational use.

Ukraine: Wartime-adaptive innovation ecosystem marked by a sharp rise in military-oriented research and intensified C2M flows following conflict escalation, driven by accelerated testing, battlefield feedback, and the temporary relaxation of institutional constraints on civil–military collaboration under wartime conditions.

Japan: Predominantly civilian-oriented research output, supported by strong industrial capabilities in enabling technologies. However, bidirectional knowledge circulation remains limited, suggesting that institutional arrangements – rather than technological constraints – impede the transformation of civilian research into sustained military and industrial capabilities.

5. Interpretation: Innovation Ecosystems under Constraint

5.1. Trajectory-Based Typology of UAV Innovation Ecosystems

Fig. 5 synthesizes cross-national differences in research orientation and knowledge circulation by plotting the military–civil publication ratio and the relative balance of C2M and M2C citation flows, based on time-series data aggregated in five-year intervals from 2001 to 2025. Countries for which data are unavailable for parts of the period are excluded from the plot.

The figure captures not only cross-sectional differences in the levels of these indicators, but also their persistence, direction of change, and responsiveness to institutional and geopolitical shocks discussed in the preceding section. Accordingly, the resulting typology does not represent a static classification at a specific point in time, but rather ideal-typical outcomes of distinct temporal trajectories shaped by different institutional and geopolitical conditions. The ecosystem types should therefore be understood as analytical models rather than fixed or permanent national characteristics.

Based on Fig. 5, national innovation ecosystems are classified into four types according to two primary criteria: research orientation, as indicated by the military–civil publication ratio, and the direction of knowledge circulation, as indicated by the relative balance between C2M and M2C citation flows.

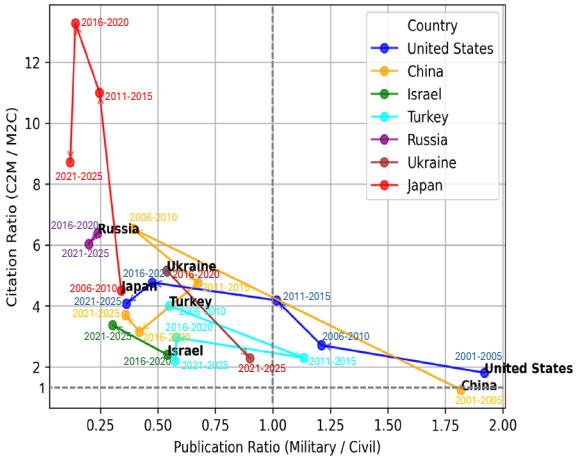

Fig. 5. Trajectory-based typology of UAV innovation ecosystems based on publication orientation and civil–military knowledge flows (2001–2025)

Based on Fig. 5, national innovation ecosystems are classified into four types according to two primary criteria: research orientation, as indicated by the military–civil publication ratio, and the direction of knowledge circulation, as indicated by the relative balance between C2M and M2C citation flows.

1. Hybrid ecosystems (e.g., United States) combine a strong civilian research base with sustained military absorption, as reflected in persistent C2M flows. However, these systems exhibit relatively limited M2C feedback, suggesting institutional rigidity in procurement and diffusion despite long-term stability in research orientation.

2. Absorptive ecosystems (e.g., China) are characterized by a sustained dominance of C2M flows and a rising military orientation over time, indicating large-scale and systematic integration of civilian knowledge into military systems across the observation period.

3. Wartime-adaptive innovation ecosystems (e.g., Ukraine) display pronounced temporal shifts following major geopolitical shocks, with rapidly increasing military orientation and intensified C2M flows. These patterns reflect the temporary relaxation of institutional constraints and accelerated iteration driven by operational feedback during wartime.

4. Institutionally constrained ecosystems (e.g., Japan) exhibit a persistent civilian research orientation alongside comparatively weak and stable C2M and M2C flows over time, indicating limited cross-domain knowledge circulation despite the availability of civilian knowledge, reflecting institutional constraints on civil–military interaction.

These four ecosystem types do not represent static classifications at a specific point in time. Rather, they capture the outcomes of temporal trajectories that countries have followed under different institutional and geopolitical conditions. Accordingly, these ecosystem types should not be interpreted as fixed or inherent national characteristics, but as ideal-typical models reflecting distinct paths of evolution.

5.2. Answers to the Research Questions

The findings presented in this section provide explicit answers to the research questions posed in Section 2.

Regarding RQ1, the analysis reveals substantial cross-national variation in both research orientation and the direction of civil–military knowledge flows. While C2M flows increase across most countries over time, the balance between C2M and M2C differs markedly, reflecting distinct national patterns of knowledge absorption and feedback.

With respect to RQ2, the results indicate that shifts in global UAV diffusion and supplier structures are systematically aligned with differences in these knowledge-flow trajectories. Countries characterized by sustained or accelerating C2M dominance exhibit more rapid integration of civilian knowledge into military systems, whereas others display persistent institutional frictions.

Finally, in response to RQ3, the Japanese case demonstrates that constraints on UAV innovation stem less from technological capability than from institutional arrangements governing knowledge circulation. This suggests that reforms targeting procurement, civil–military interfaces, and export frameworks are central to enhancing ecosystem performance under economic security constraints.

6. Policy Implications and Conclusion

For Japan, the findings suggest that the central challenge lies not in the absence of technological capability but in the institutional design governing knowledge circulation.

In particular, export control frameworks have long functioned as a central institutional constraint on knowledge and technology circulation in defense-related domains. Under Japan's Three Principles on Transfer of Defense Equipment and Technology, overseas transfers were historically restricted to five non-lethal categories, reflecting a postwar pacifist orientation.

Recent political developments, however, indicate a potential shift, as the ruling Liberal Democratic Party and Japan Innovation Party have agreed to propose abolishing this five-category rule from fiscal 2026. If implemented, this reform would represent a significant recalibration of Japan's export control regime and could enable more dynamic civil–military technology exchange and defense industrial development, provided appropriate safeguards are maintained [10].

From a policy perspective, these findings imply that strengthening the UAV innovation ecosystem under economic security constraints may require the following measures:

- Faster and more adaptive procurement and testing mechanisms;
- Institutionalized pathways for bidirectional civil–military knowledge exchange;
- Export and transfer frameworks that support learning incentives without undermining security objectives.

This study does not claim causal identification, but identifies systematic correspondences in observed patterns. This study contributes to debates on dual-use innovation by demonstrating how civil–military knowledge flows can serve as early indicators of ecosystem reconfiguration under economic security constraints. By focusing on knowledge circulation rather than technological performance alone, the analysis offers a framework for comparing national innovation ecosystems in sensitive technology domains. Future research should integrate institutional, industrial, and procurement-level indicators to more causally assess how policy interventions affect ecosystem resilience and long-term capability development.

References

[1]. OECD, OECD Science, Technology and Innovation Outlook 2018: Adapting to Technological and Societal Disruption, *OECD Publishing*, Paris, 2018.

[2]. H. Farrell, A. L. Newman, Weaponized interdependence: How global economic networks shape state coercion, *International Security*, Vol. 44, Issue 1, 2019, pp. 42-79.

[3]. N. Rosenberg, Critical issues in science policy research, *Science and Public Policy*, Vol. 18, Issue 6, 1991, pp. 335-346.

[4]. D. J. Teece, Explicating dynamic capabilities: The nature and microfoundations of (sustainable) enterprise performance, *Strategic Management Journal*, Vol. 28, Issue 13, 2007, pp. 1319-1350.

[5]. D. C. Mowery, Military R&D and innovation, Chapter 28, in Handbook of the Economics of Innovation (B. H. Hall, N. Rosenberg, Eds.), *Elsevier*, 2010, pp. 1219-1256.

[6]. V. W. Ruttan, Is War Necessary for Economic Growth? Military Procurement and Technology Development, *Oxford Univ. Press*, New York, 2006.

[7]. Center for a New American Security (CNAS), Drone proliferation dataset, https://www.cnas.org/publications/reports/drone-proliferation

[8]. R. Adner, R. Kapoor, Value creation in innovation ecosystems: How the structure of technological interdependence affects firm performance in new technology generations, *Strategic Management Journal*, Vol. 31, Issue 3, 2010, pp. 306-333.

[9]. A. Gilli, M. Gilli, Why China has not caught up yet: Military-technological superiority and the limits of

imitation, *International Security*, Vol. 43, Issue 3, 2019, pp. 141-189.
[10]. Ministry of Foreign Affairs of Japan (MOFA), Three principles on transfer of defense equipment and technology, https://www.mofa.go.jp/press/release/press22e_000010.html

(015)

A Study on System Modeling Techniques for Power Analysis of Hydrogen Fuel Cell Based C-172R Aircraft

Youyoung Yang, JeongHwan Oh, JunSeong Lee, SungSu Kim and KwangHyun Lee
MOASOFT Co., Ltd, Seoul, 05770, Republic of Korea
Tel.: +82-24203203
E-mail: yyyang@moasoftware.co.kr

Summary: This study presents a system-level modeling framework and mission-profile-based power analysis for a hydrogen fuel cell–battery hybrid electric propulsion system applied to a retrofitted Cessna 172R aircraft, referred to as the C-172RHX. Motivated by global efforts toward carbon-neutral aviation, hydrogen-electric propulsion has emerged as a promising alternative for small and regional aircraft. Despite active demonstrations worldwide, system-level evaluations under realistic operational conditions remain limited. To address this gap, a unified powertrain model integrating the fuel cell stack, battery, power distribution unit, inverter, and electric motor is developed. Using a mission profile derived from the aircraft's Pilot Operating Handbook, the model quantifies power flow, energy consumption, and power-split characteristics across all flight phases. The results provide insights for component sizing, safety assessment, and thermal management strategies, and support future certification frameworks for hydrogen-electric aircraft. This work contributes to advancing zero-emission aviation technologies.

Keywords: Hydrogen fuel cell, Hybrid electric propulsion, Retrofitted light aircraft, System modeling techniques, Power demand analysis, Mission profile.

1. Introduction

Global aviation is entering a transitional phase as international policy frameworks increasingly emphasize the achievement of carbon neutrality by 2050. Despite ongoing improvements in aircraft efficiency and operational practices, aviation remains difficult to decarbonize due to its dependence on high energy-density fuels and the amplified climate impact of high-altitude emissions. Coupled with steady growth in global air traffic demand, these factors suggest that incremental technological improvements alone are unlikely to achieve long-term emission reduction targets [1, 2].

Among the proposed alternatives, hydrogen has emerged as a promising aviation energy carrier owing to its high gravimetric energy density and the potential for zero-carbon operation at the point of use. In particular, hydrogen fuel cell–based electric propulsion systems offer high electrochemical efficiency and inherent compatibility with electric powertrains, making them attractive for small- and medium-scale aircraft where battery-electric propulsion is limited by specific energy constraints [3-5].

Recent research has explored hydrogen-powered aircraft concepts primarily at the conceptual and preliminary design level, addressing fuel cell sizing, hydrogen storage integration, and aircraft-level performance trade-offs [6, 7]. In parallel, studies on electric and hybrid-electric propulsion have highlighted the importance of mission-based power and energy analysis for early-stage feasibility assessment, particularly in identifying peak power requirements and hybridization strategies across different flight phases [8, 9].

Comprehensive reviews have further emphasized the need for integrated system modeling and energy management to evaluate hybrid-electric propulsion architectures under realistic operating conditions [10]. Nevertheless, much of the existing literature remains component-centric, often neglecting the coupled power and energy dynamics of complete propulsion systems [11].

Moreover, system-level investigations focusing on the retrofit of certified CS-23 light aircraft are still limited. Existing studies typically address conceptual feasibility or small experimental platforms, while explicit validation against certified aircraft performance data and flight manuals is frequently omitted [12-14]. Such baseline validation is essential to assess whether hydrogen-electric propulsion systems can realistically reproduce conventional aircraft performance and to support future certification-oriented studies [15].

In this context, the present study investigates a hydrogen-electric conversion of the certified Cessna 172R, designated C-172RHX, in which the conventional reciprocating engine is replaced by a hydrogen fuel cell–battery hybrid electric propulsion system. This work develops a system-level power and energy analysis framework and performs a mission-profile-based assessment of propulsion power demand and energy consumption by integrating baseline performance data from the C-172R Pilot's Operating Handbook with models of the fuel cell system, high-voltage battery, power distribution unit, inverter, and electric motor. The results aim to support early-stage design and feasibility assessment of hydrogen fuel cell–battery hybrid propulsion systems for retrofitted light aircraft.

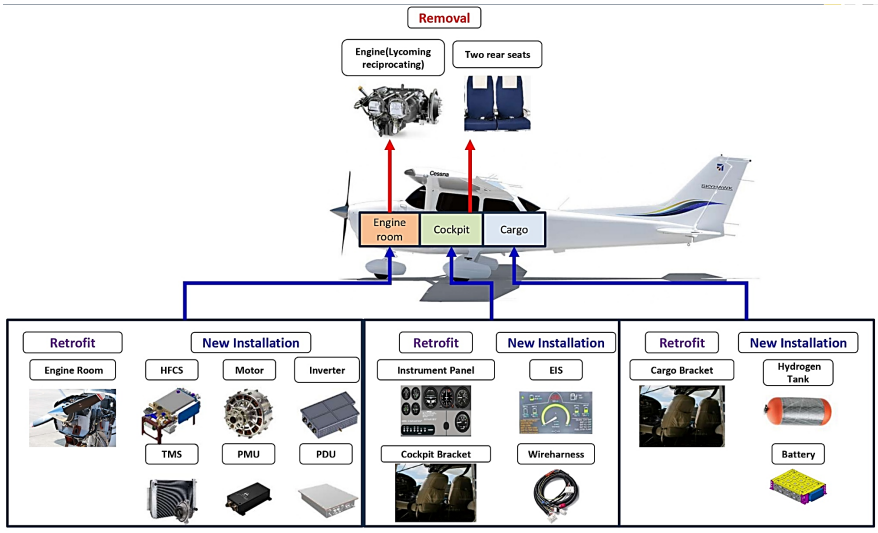

Fig. 1. Retrofitted Configuration of the C-172RHX Hydrogen–Electric Propulsion System.

2. System Modeling Framework

This study develops a system-level modeling framework for a hydrogen fuel cell–battery hybrid electric propulsion system retrofitted to a certified Cessna 172R aircraft, hereafter referred to as C-172RHX. The framework is intended to evaluate mission-dependent power demand, energy consumption, and power-sharing characteristics under realistic operational constraints, rather than to address detailed controller design or component-level optimization.

The propulsion architecture adopts a regulated high-voltage DC bus configuration. A hydrogen fuel cell system serves as the primary energy source, providing a continuous output power of 70 kW and a peak power of 90 kW for durations exceeding 5 min. Compressed gaseous hydrogen is stored at 700 bar with a total onboard mass of 6.3 kg. A lithium-ion battery system with a usable energy capacity of 26.8 kWh supplements the fuel cell by supplying transient peak power up to 120 kW (≥ 3 min) and absorbing excess power when charging is permitted. Key component ratings and constraints of the C-172RHX powertrain are summarized in Table 1.

Electrical power from the fuel cell and battery is interfaced through a power distribution unit (PDU), which regulates the DC bus voltage at 360 V and distributes power to the propulsion inverter and onboard electrical loads. The PDU is sized for a maximum output power of 150 kW with a nominal efficiency of 95 %. The inverter–motor assembly delivers up to 130 kW of shaft power to a fixed-pitch propeller.

Mission-based power demand is defined using representative C-172R operational data for taxi, takeoff, climb, cruise, and descent phases. Propulsion power demand is expressed at the shaft level, while continuous electrical loads of 3.2 kW are supplied throughout the entire mission. This formulation enables a direct comparison between available electrical power and phase-dependent demand envelopes.

A supervisory, rule-based energy management strategy is employed to allocate power between the fuel cell and battery while respecting power limits, state-of-charge thresholds, and hydrogen availability. The strategy prioritizes fuel cell operation near its nominal continuous rating during steady phases and assigns the battery to support transient peak demands or to maintain battery state-of-charge within predefined bounds. The logic of the energy management system is illustrated in Fig. 2 and is intended to represent realistic operational behavior without introducing optimization-based control complexity.

Table 1. Key Component Ratings and Constraints of the C-172RHX Powertrain.

Component	Parameter	Value
Fuel Cell System	Output Voltage	250~400 VDC
	Continuous power	70 kW
	Peak power	90 kW (≥ 5 min)
	Hydrogen storage	6.3 kg (2.1 kg × 3, 700 bar, Type 4)
Battery System	Type	Li-ion
	Output Voltage	240~403.2 VDC
	Energy capacity	26.8 kWh
	Peak power	120 kW (≥ 3 min)
Power Distribution Unit (PDU)	Input voltage	240~403.2 VDC
	Output voltage	360 VDC
	Max output power	150 kW
	Efficiency	95 %
Inverter & Motor	Max propulsion power	130 kW
	Efficiency	97 %, 91 %
Energy Management System	Control strategy	Rule-based

Algorithm 1 Energy Management Algorithm for the Fuel Cell–Battery Hybrid Powertrain

Input:
P_{Demand} (kW), SoC_{BAT} (%), $SoH2$ (%), K_{chg}, $FC_{\text{State}} \in \{0, 1\}$
Output:
P_{FC} (kW), P_{BAT} (kW; + discharge, − charge)
Constants:
$P_{\text{FC,Cons}} = 70$ kW, $P_{\text{FC,Max}} = 90$ kW,
$P_{\text{Land}} = 30$ kW, $P_{\text{PDU,Max}} = 150$ kW
$SoH2_{\text{min}} = 10\%$,
$SoC_{\text{BAT,Min}} = 25\%$, $SoC_{\text{BAT,Cut}} = 20\%$,
$SoC_{\text{BAT,Max}} = 95\%$, $SoC_{\text{BAT,tar}} = 100\%$,
$P_{\text{BAT,DisMax}} = 120$ kW, $P_{\text{BAT,ChgMax}} = 32$ kW

$FC_{\text{Avail}} \leftarrow (FC_{\text{State}} = 1) \wedge (SoH2 > SoH2_{\text{min}})$
$P_D \leftarrow \min(P_{\text{Demand}}, P_{\text{PDU,Max}})$
if $\neg FC_{\text{Avail}}$ **then**
  $P_D \leftarrow \min(P_D, P_{\text{Land}})$
  $P_{\text{FC}} \leftarrow 0$
  $P_{\text{BAT}} \leftarrow \text{sat}(P_D, 0, P_{\text{BAT,DisMax}})$
  return
end if
if $SoC_{\text{BAT}} \leq SoC_{\text{BAT,Cut}}$ **then**
  $P_D \leftarrow \min(P_D, P_{\text{Land}})$
  $P_{\text{FC}} \leftarrow \text{sat}(P_D, 0, P_{\text{FC,Max}})$
  $P_{\text{BAT}} \leftarrow P_D - P_{\text{FC}}$
  $P_{\text{BAT}} \leftarrow \text{sat}(P_{\text{BAT}}, -P_{\text{BAT,ChgMax}}, 0)$
  return
end if
$P_{\text{FC,cmd}} \leftarrow P_{\text{FC,Cons}} + K_{\text{chg}}(SoC_{\text{BAT,tar}} - SoC_{\text{BAT}})$
$P_{\text{FC}} \leftarrow \text{sat}(P_{\text{FC,cmd}}, 0, P_{\text{FC,Max}})$
$P_{\text{BAT}} \leftarrow P_D - P_{\text{FC}}$
if $P_{\text{BAT}} \geq 0$ **then**
  $P_{\text{BAT}} \leftarrow \text{sat}(P_{\text{BAT}}, 0, P_{\text{BAT,DisMax}})$
else
  $P_{\text{BAT}} \leftarrow \text{sat}(P_{\text{BAT}}, -P_{\text{BAT,ChgMax}}, 0)$
end if
if $SoC_{\text{BAT}} \leq SoC_{\text{BAT,Min}}$ **then**
  if $P_{\text{BAT}} > 0$ **then**
    $P_{\text{FC}} \leftarrow \text{sat}(P_D, 0, P_{\text{FC,Max}})$
    $P_{\text{BAT}} \leftarrow P_D - P_{\text{FC}}$
    if $P_{\text{BAT}} \geq 0$ **then**
      $P_{\text{BAT}} \leftarrow \text{sat}(P_{\text{BAT}}, 0, P_{\text{BAT,DisMax}})$
    else
      $P_{\text{BAT}} \leftarrow \text{sat}(P_{\text{BAT}}, -P_{\text{BAT,ChgMax}}, 0)$
    end if
  end if
end if
return

Fig. 2. Energy Management Algorithm for the Fuel Cell–Battery Hybrid Powertrain.

3. Mission Profile and Power Demand Analysis

Mission-based power demand analysis was performed using a representative operational profile of the Cessna 172R, consisting of taxi, takeoff, climb, cruise, and descent phases. The reference mission includes a 4-min climb to a cruise altitude of 2000 ft, followed by a 60-min cruise and a 5-min descent, resulting in a maximum flight duration of 69 min. The corresponding altitude and propulsion power demand profiles are illustrated in Fig. 3.

During taxi, takeoff, and climb, the required propulsion power reaches up to 130 kW, exceeding the continuous power rating of the fuel cell system. Under these transient conditions, the battery system supplements the fuel cell to satisfy peak power demand while respecting component power limits. During steady cruise, the propulsion power demand stabilizes at 69.2 kW, corresponding to approximately 58 % of maximum power at a cruise speed of 99 KTAS. This operating point is intentionally selected to align with the nominal continuous rating of the fuel cell system.

The resulting power allocation between the fuel cell and battery over the reference mission is shown in Fig. 4. The fuel cell supplies the majority of the steady-state propulsion power, operating near its continuous rating, while the battery primarily provides transient peak power support and absorbs excess power during low-demand phases. The fuel cell power contribution is determined by referencing experimentally obtained voltage–current–power characteristics of the fuel cell system, whereas the battery compensates for short-term deviations between instantaneous power demand and the fuel cell operating point.

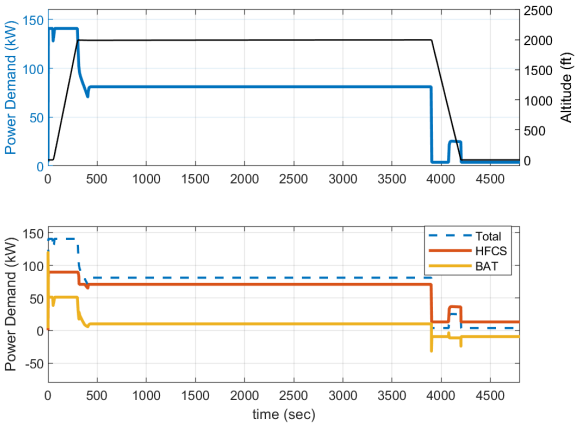

Fig. 3. Mission Profile and Corresponding Power Demand of the C-172RHX.

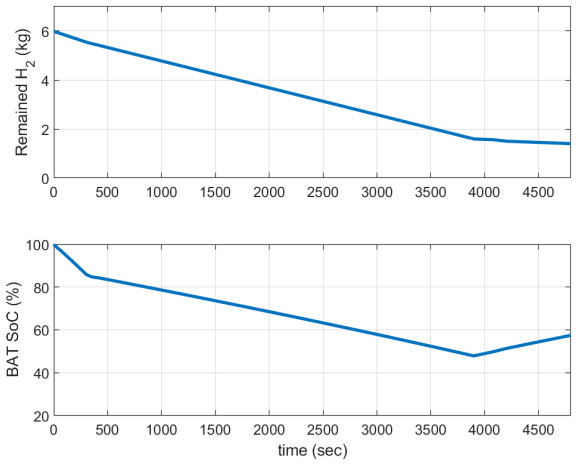

Fig. 4. Power Split between Fuel Cell and Battery during the Reference Mission.

Key mission-level parameters and performance metrics are summarized in Table 2. Component ratings and onboard energy quantities, including maximum propulsion power and total stored energy, are defined from the assumed system specifications. In contrast, the hydrogen consumption during cruise is estimated using experimentally measured fuel cell performance maps evaluated at the corresponding cruise power level. Based on this approach, the estimated cruise hydrogen consumption ranges from 4.1 to 4.6 kg/h for the selected operating condition. Continuous electrical loads of 3.2 kW, representing avionics and auxiliary systems, are supplied throughout the entire mission and are included in the overall power balance.

Table 2. Summary Mission Power, Energy, and Hydrogen Consumption Metrics.

Parameter	Value	Unit	Remarks
Maximum propulsion power	130	kW	
Cruise power	69.2	kW	58 % power @ 2000 ft
Cruise speed	99	KTAS	
Total onboard energy	133.2	kWh	Fuel cell + battery
Fuel cell energy contribution	113.2	kWh	From 6.3 kg H_2
Battery energy contribution	26.8	kWh	
Total hydrogen mass	6.3	kg	Stored
Estimated cruise H_2 consumption	4.1-4.6	kg/h	From FC map
Maximum flight time	68	min	Reference mission
Continuous electrical loads	3.2	kW	Avionics & auxiliaries

These results provide a quantitative, system-level assessment of mission-dependent power demand, energy utilization, and hydrogen consumption for a hydrogen fuel cell–battery hybrid propulsion system applied to a CS-23 class light aircraft. The analysis demonstrates that the proposed powertrain configuration can satisfy realistic mission requirements while maintaining operational margins consistent with experimentally observed fuel cell performance.

4. Conclusions

This study presented a system-level modeling and mission-based power analysis of a hydrogen fuel cell–battery hybrid electric propulsion system retrofitted to a certified Cessna 172R aircraft (C-172RHX). By integrating component-level specifications with experimentally obtained fuel cell performance maps and representative mission profiles, the proposed framework enables a transparent assessment of propulsion power demand, energy utilization, and hydrogen consumption under realistic operational conditions.

The results demonstrate that the hybrid powertrain can satisfy mission-dependent power requirements of a CS-23 class light aircraft while maintaining operational margins. Transient peak demands during taxi, takeoff, and climb are effectively supported by the battery system, whereas steady-state cruise operation is predominantly sustained by the fuel cell near its nominal continuous rating. The estimated cruise hydrogen consumption, derived from experimental fuel cell data, indicates that the selected onboard hydrogen storage capacity is sufficient for the defined reference mission.

Future work will extend the present analysis to include thermal management effects, dynamic fuel cell response, and fault and degradation scenarios relevant to certification considerations. In addition, further experimental validation and sensitivity studies with alternative mission profiles and power management strategies will be conducted to support the development of hydrogen-electric propulsion systems for light aircraft.

Acknowledgements

This research was supported by the Ministry of Land, Infrastructure and Transport and the Korea Agency for Infrastructure Technology Advancement (KAIA) under the project ‘Development of Certification Framework and Safety Verification Technologies for Small Aircraft Equipped with Hydrogen Fuel-Cell Propulsion Systems’ (Project No. RS-2023-00246686).

References

[1]. National Academies of Sciences, Engineering, and Medicine, The Carbon Dioxide Challenge Facing U.S. Aviation and Paths to Achieve Net-Zero Emissions by 2050, *The National Academies Press*, Washington, DC, 2023.

[2]. M. Braun, W. Grimme, K. Oesingmann, Pathway to net zero: Reviewing sustainable aviation fuels, environmental impacts and pricing, *Journal of Air Transport Management*, Vol. 117, 2024, 102578.

[3]. M. A. Patel, R. Braun, M. Gohardani, Comprehensive investigation on hydrogen and fuel cell technology in the aviation and aerospace sectors, *Progress in Aerospace Sciences*, Vol. 104, 2019, pp. 1-30.

[4]. J. H. Lee, M. Kim, S. Park, Sustainable aviation – Hydrogen is the future, *Aerospace Science and Technology*, Vol. 128, 2022, 107755.

[5]. A. Khandelwal, B. Karakaya, M. F. Hasan, Hydrogen-powered aircraft: Fundamental concepts, key technologies, and environmental impacts, *Renewable and Sustainable Energy Reviews*, Vol. 175, 2023, 113182.

[6]. G. L. M. Vonhoff, Conceptual design of hydrogen fuel cell aircraft, Master’s Thesis, *Delft University of Technology*, Delft, 2021.

[7]. M. C. Massaro, S. Pramotto, P. Maroccolo, A. H. A. Monteverde, et al., Optimal design of a hydrogen-powered fuel cell system for aircraft applications, *Energy Conversion and Management*, Vol. 306, 2024, 118318.

[8]. J. Hu, J. D. Booker, Preliminary sizing of electric-propulsion powertrains for concept aircraft designs, *Designs*, Vol. 6, Issue 5, 2022, 90.

[9]. H. Liu, Y. Yao, J. Wang, T. Yang, et al., Energy management and system design for fuel cell hybrid unmanned aerial vehicles, *Energy Science & Engineering*, Vol. 10, Issue 10, 2022, pp. 3987-4006.

[10]. F. Yu, J. Chen, P. Gao, Y. Kong, et al., A review of hybrid-electric propulsion in aviation: Modeling methods, energy management strategies, and future prospects, *Aerospace*, Vol. 10, Issue 3, 2023, 214.

[11]. A. Kuśmierek, C. Galiński, W. Stalewski, Review of the hybrid gas–electric aircraft propulsion systems versus alternative systems, *Progress in Aerospace Sciences*, Vol. 141, 2023, 100927.

[12]. O. K. Keles, I. Hakyemez, M. Bagriyanik, O. Kalenderli, A study on power system retrofit for Cessna-172S aircraft by using hydrogen fuel cell and battery hybrid, *IEEE Access*, Vol. 12, 2024, pp. 84485-84497.

[13]. C. Svensson, Hydrogen fuel cell aircraft for regional travel, Master's Thesis, *Chalmers Tekniska Högskola*, Gothenburg, 2024.

[14]. T. Donateo, A. Ficarella, L. Lecce, Preliminary design of a retrofitted ultralight aircraft with a hybrid electric fuel cell power system, *Journal of Physics: Conference Series*, Vol. 2716, 2024, 012028.

[15]. The Cessna Aircraft Company, C-172R Pilot's Operating Handbook, *Cessna Aircraft Company*, Wichita, 1996.

(016)

On the Potential of Public Network Dual-Use for Medium Altitude Long Endurance Remotely Piloted Aircraft Systems (MALE RPAS)

Gunnar Schneider [1], Michael Rachner [1], Jan Bauer [2] and Bertram Schütz [1,3]
[1,2] Fraunhofer FKIE, [1] Communication Systems, [2] Cyber Analysis & Defense, 53177 Bonn, Germany
[3] Hochschule Osnabrück, Institute of Management and Technology, 49809 Lingen, Germany
E-mail: {gunnar.schneider, michael.rachner, jan.bauer, bertram.schuetz}@fkie.fraunhofer.de

Summary: Medium Altitude Long Endurance (MALE) Remotely Piloted Aircraft Systems (RPASs) operate at an altitude of approximately 12 km with a long operational life up to 40 h. In Terms of efficiently transmitting sensor and situation information, a robust and broadband communication link is crucial for enabling new applications such as transmission of high-definition ISR (Intelligence, Surveillance, Reconnaissance) data. Traditional tactical data links offer high robustness but deliver low data rates and incur high costs per node, making scaling distributed sensor networks difficult. This work aims to assess whether the civilian communication technologies can meet the requirements of MALE RPASs in a tactical environment, using the NATO Anglova scenario as a representative example. To this end, we analyze the extent to which the European Aviation Network and 5G-Non-Terrestrial Networks can be used and represent an open, cost-effective alternative to open up new operational possibilities – in particular through the dual use of civilian technologies with applications in sensor and communication relay payloads. Our results indicate significant potential for civil-driven technologies, although further detailed modeling and field testing are required.

Keywords: MALE RPAS, UAV, Dual use, 5G-NTN, SATCOM, European Aviation Network (EAN).

1. Introduction

Medium Altitude Long Endurance (MALE) Remotely Piloted Aircraft Systems (RPASs) are systems that can operate at an altitude of 12 km with long flight times over long ranges. But can tactical communication links cover the current use cases of MALE RPAS? The type of communication with autonomous systems such as MALE RPAS significantly determines their purpose and possible applications. Widely available, reliable broadband communication enables MALE RPASs to gain new operational relevance. This could be achieved through suitable sensor or communication payloads. Tactical data links often have the characteristic of being highly robust in tactical scenarios, but they have a lower data rate [1] and usually generate high monetary costs per node and in operation. This also has an impact on distributed sensor networks with a high number of nodes that may be located on the ground or at sea, for example, and need to be connected via flying relay nodes. If, in the future, a large number of sensors can be quickly integrated into a situational picture in a tactical environment, new capabilities in the field of communication can be created through the dual use of civilian technologies.

The EAN and 5G-Non-Terrestrial Networks (NTN) are promising technologies for MALE RPASs. These are mainly based on the 3GPP mobile communications standard, which can be used both terrestrial and via satellite. The mobile communications sector is a growing market in which technology is developing rapidly [2] and advancing into new areas such as satellite communications. Because EAN and 5G-NTN are open, standardized technologies with a large market [2], they are widely used and less expensive than tactical links. The aim of this Paper is to present the two technologies EAN and 5G-NTN in connection with their use in a MALE RPAS using the *Anglova* scenario as an example. The NATO IST-124 Anglova [3] scenario provides the tactical context in which a MALE RPAS can operate. Section 2 focuses in particular on the technical differences between the systems in terms of data rate and frequency, as well as the effects of the different satellite positions of the two systems. The MALE RPAS is also presented in order to derive the parameters for a tactical scenario. The parameters for radio links resulting from the use of the MALE RPAS are presented in Section 3 and compared with the radio systems presented. Section 4 then presents a tactical use case. The use of civilian communication technologies in a heterogeneous communication system can result in MALE RPAS payloads whose communication requirements exceed what can be achieved with existing communication solutions. A summary with an outlook can be found in the conclusion (Section 5).

2. Commercial Mobile Systems for Aviation Application

The EAN [4] is widely used in civil aviation, offering broadband Internet access to aircraft. Passengers can connect to the Internet via onboard Wi-Fi, assuming the aircraft is equipped for EAN. The advent of 5G introduces new possibilities, including standardized non-terrestrial deployment. The 5G-NTN standard includes satellite coverage, allowing standard 5G devices to connect via satellite to the 5G network.

This enhances coverage in previously underserved areas, such as maritime and aerial regions.

2.1. Properties of MALE RPASs

The MALE RPAS, an EU PESCO project development [5], is a tactical remote-controlled flight platform. It operates at altitudes up to 12 km with speeds between up to 500 km/h and a flight duration up to 40 h and can carry payloads of up to 2300 kg [6]. Systems that meet this definition are the Airbus Eurodrone and the U.S. MQ-9 Reaper drone by General Atomics [7].

2.2. Scenario

The *Anglova* scenario, defined by the NATO IST-124 Research Task Group, involves Vignette 1, where fixed-wing UAVs (Unmanned Aerial Vehicles) are connected via satellite and Ultra High Frequency (UHF) links, see Fig. 1. The Harvest UAV's goal is to gather sensor data and centrally deliver it to the headquarter (HQ). This scenario employs multiple radio systems, including High Frequency (HF), Very High Frequency (VHF), UHF, and Satellite Communication (SATCOM), with plans to incorporate 4G and 5G [8].

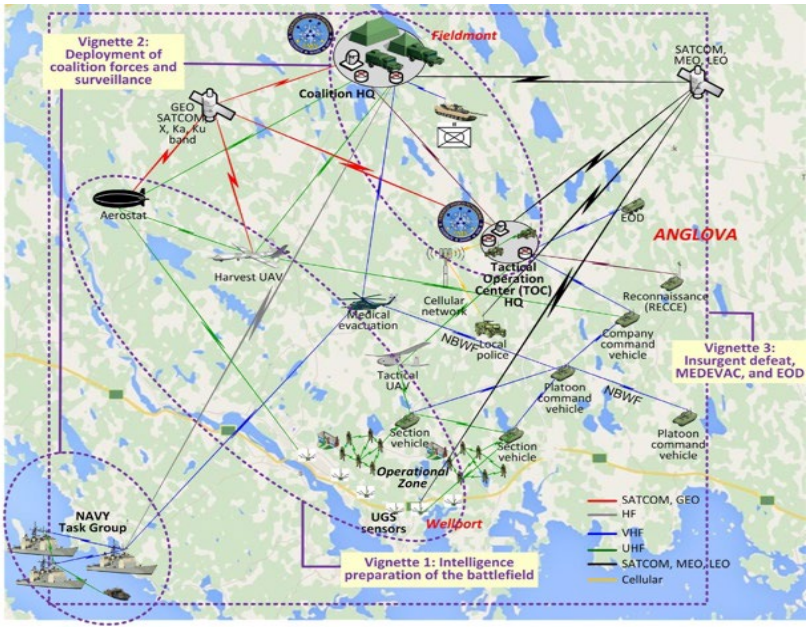

Fig. 1. NATO IST-124 reference scenario *Anglova* (cf. [3]).

In this paper, the Anglova scenario serves as the foundation for enhancing it with extra communication systems. In Vignette 1, sensor nodes are intended to gather monitoring data. The network gateways feature a Beyond Line-of-Sight (BLOS) channel. The majority of data is relayed via the harvesting UAV to the coalition headquarter (CHQ).

2.3. European Aviation Network (EAN)

The EAN offers Internet access to commercial aircraft across Europe using two communication technologies: a terrestrial Long Term Evolution (LTE) network and a satellite system. The LTE network, operated by Deutsche Telekom AG, consists of over 300 ground base stations, providing coverage up to 150 km per cell [9]. The satellite system, supported by the Viasat "Hellas Sat 3" satellite, ensures connectivity in maritime and remote areas. Aircraft are equipped with separate terminals for LTE and SATCOM [10].

Fig. 2 illustrates the EAN network structure, showing how the aircraft connect via the Complementary Ground Component (CGC) and Mobile Satellite Service (MSS). The CGC includes onboard transponders and ground base stations linked to a core network. The satellite terminal facilitates communication with a ground station through the satellite relay. Both networks integrate at the "Meet Me Point," establishing the link to the Internet and the Internet Service Provider (ISP).

a) *Terrestrial Communication:* As mentioned before, the terrestrial components of the EAN use LTE technology. Adjustments to the Radio Access Network (RAN) are necessary to accommodate aircraft speeds up to 1200 km/h, causing frequency shifts up to about 2.4 kHz. CGC terminals on the aircraft must compensate for these shifts. For the communication, LTE Band 65 is used. At an altitude of 8000 m, the network achieves full coverage. Base stations operate with a transmission power of 80 W, and antennas are directed upwards [12].

The CGC system consists of over 300 base stations, covering the European area as illustrated in Fig. 3 [13]. Key features of the EAN include a data rate peaking at 75 Mbit/s, latency under 100 ms (typically 20–70 ms), seamless availability over land and water due to SATCOM, and a range of 150 km per cell under the CGC system connection.

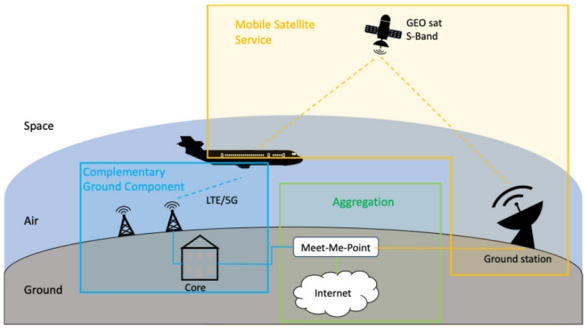

Fig. 2. EAN architecture (cf. [11]).

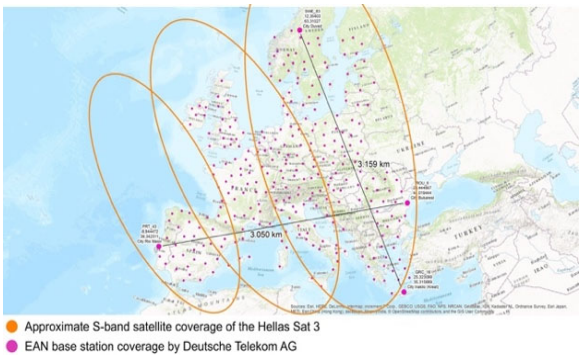

Fig. 3. EAN coverage by Deutsche Telekom AG and Viasat (cf. [10, 13]).

The terrestrial network's capacity can be increased by densifying cell deployment, reducing the cell size to maximize bandwidth. CGC terminals onboard aircraft have enhanced transmission power of 5 W, compared to typical terminals at 0.2 W [12, 14]. The CGC terminal antenna is mounted under the aircraft to maintain a Line-of-Sight (LOS) connection with ground base stations.

b) *Satellite Connection:* The Viasat "Hellas Sat 3" satellite provides EAN with satellite access via MSS. It is an S-band multi-beam satellite in geostationary orbit at 39 °E [15, 16], launched in 2017 [17]. Bandwidths for S-band communication are allocated as 2×15 MHz. The "Hellas Sat 3" operates within the frequency ranges of 1980–1995 MHz for Earth-to-Space communication and 2170–2185 MHz for Space-to-Earth communication [18]. A detailed overview of the satellite characteristics can be found in [17]. Regulations specify that frequencies may be used for in-flight communication from a minimum altitude of 1000 m [18]. The "Hellas Sat 3" covers the European area, as illustrated in Fig. 3. Satellite connections are primarily utilized in regions not covered by the CGC, mainly maritime zones. The satellite is connected to a ground station via a feeder link. The data can then be forwarded to the meeting point via the ground station. The aircraft are connected to the satellite via an onboard terminal, mounted on the aircraft's roof.

2.4. 5G-NTN

5G-NTN, part of the 3rd Generation Partnership Project (3GPP)'s 5G standard specification, aims to provide global 5G services by connecting earth-based devices via NTN infrastructure. As defined by 3GPP, NTN includes space-borne (Geosynchronous Equatorial Orbit (GEO), Medium Earth Orbit (MEO), Low Earth Orbit (LEO)) or airborne nodes (Unmanned Aircraft System (UAS), High-altitude Platform System (HAPS)) integrated into the network either as transparent or regenerative payload architectures [19]. Using the NTN node as a relay between the device and satellite gateway denotes a transparent payload architecture, whereas if the node has its own base station, it is a regenerative payload architecture. The standard specifies that commercial devices can operate within these networks. 5G-NTN debuted with initial studies in Release 15, while requirements for transparent payload architecture were specified in Releases 17 and 18 [20]. The most recent 3GPP Release, Release 19, finalized in October 2025, specifies the requirements for regenerative payload architectures in 5G-NTN systems.

a) *Specifications:* Initial frequency ranges for 5G-NTN were specified in Releases 17 and 18. FR1-NTN spans 410–7125 MHz, and FR2-NTN covers 17300–30000 MHz. The complete list of 5 G-NTN bands can be found in [21].

In terms of coverage, 3GPP's report TR23.737 calculates the number of satellites needed for global coverage from a geographical point of view [22]. At 800 km altitude, 80 LEO satellites can achieve continuous global coverage. Satellite beam diameters vary between 100–1000 km for non-GEO satellites and 200–3500 km for GEO satellites [19], requiring regulatory and operational adjustments, also addressed in TR23.737 [22].

3GPP defines target data rates for scenarios like "Airplane connectivity," where up to 360 Mbps downlink and 180 Mbps uplink should be available [23]. The authors of [24] simulated 5G-NTN-LEO throughput for S-band and Ka-band connections using 30 MHz and 400 MHz bandwidths, respectively, yielding maximum rates of 16 Mbps (S-band) and 190 Mbps (Ka-band) per cell user.

Delay and Doppler shift are critical due to satellite distances and speeds, also addressed in the 3GPP standard. In the 3GPP report [23], the Round-Trip Time (RTT) for 5G-NTN-LEO and 5G-NTN-GEO is calculated as the sum of the individual signal propagation times over the channel, with an additional 5 ms added for each direction. These 5 ms are defined in the report as one-way network latency.

Consequently, the maximum latency for a 5G-NTN-LEO transmission is 70 ms, while the minimum latency is 22 ms. In contrast, 5G-NTN-GEO experiences significantly higher latencies, ranging from 490 ms to 570 ms, due to much greater distances.

Maximum Doppler shift values are detailed in report [19], specified in parts per million (ppm). Maximum frequency shift depends on satellite altitude, with 24 ppm at 600 km and 21 ppm at 1200 km for LEO links, translating to 48 kHz and 42 kHz shift at 2 GHz. GEO-satellite links have a lower maximum shift of 0.93 ppm, equating to 1860 Hz at 2 GHz.

b) *5G-NTN Implementations:* Initial 5G-NTN implementations prioritize continuous connectivity and seamless coverage. The transparent architecture approach is being adopted as it is independent of signal type, allowing existing satellite technology to remain unchanged [27]. Following the first successful 5G connectivity tests in 2023, during which Vodafone and AST SpaceMobile established a 5G voice call via the low-orbit satellite BlueWalker 3, both companies have formed a joint venture named SatCo to act as a dedicated satellite service provider for mobile communications. Table 1 lists the existing frequencies ranges of BlueWalker 3 and provides a comparison with the 5G bands they would match. SatCo is planning the launch of the satellite-based communication service in early 2026. The planned European constellation will incorporate a comprehensive command switch functionality to ensure operational control and compliance with European oversight and security requirements. In addition to supporting commercial mobile broadband, the system will provide capabilities for Public Protection and Disaster Relief (PPDR), thereby enhancing communication and coordination among European emergency services in line with the EU Critical Communication System (EUCCS) framework [28].

Table 1. Bluewalker 3 frequency ranges, cf. [25].

Service Description	Frequency Range	NR-band [26]
Service Links (Earth-to-Space)	846.5–849 MHz	n5
	845–846.5 MHz	n5
	788–798 MHz	n14
Service Links (Space-to-Earth)	891.5–894 MHz	n5
	890–891.5 MHz	n5
	758–768 MHz	n14
Gateway/Feeder Links (Earth-to-Space)	47.2–50.2 and 50.4–51.4 GHz	n262
Gateway/Feeder Links (Space-to-Earth)	37.5–42.0 and 42.0–42.5 GHz	n260

3. Radio Links for MALE RPAS

To effectively use communication systems for MALE RPAS, they must meet key requirements outlined in Section 2.1: Maintain connectivity at UAV speeds up to 500 km/h, ensure seamless handovers in networks with multiple base stations or relays, and guarantee continuous coverage in the operational area. These criteria are crucial for reliable communication in MALE RPAS operations.

3.1. Communication Requirements

A distinction must be made between terrestrial and satellite-based communication for a MALE RPAS-type UAV communication system. Key parameters to evaluate include:

- **Distance/Coverage**: In general, the drone must have the necessary equipment to meet the link budget requirements for a successful link between satellite or ground stations [29]. Seamless coverage is necessary in the drone's operational area, achievable through a heterogeneous approach that combines multiple technologies to increase coverage. Available infrastructure and the size of the area to be covered depend on the scenario.
- **Data Rate**: The data rate is crucial to the application for which the drone is being considered. High data rates are essential for many sensors and should be ensured through high-bandwidth communication technologies.
- **Delay**: In satellite communication, the signal propagation time between the drone and the communication node is significantly affected by the satellites' varying orbital altitudes [19]. This can lead to particularly long signal propagation times, which are examined in detail in Section 3.2. Fig. 4 provides a general overview of signal propagation time as a function of distance, with the propagation speed of the signal equivalent to that of light.
- **Velocity**: Besides long signal propagation times in satellite communication, Doppler effects are also critical for communication requirements. The system must accommodate the drone's, the base station's, and the satellite's relative velocity to each other to maintain a stable connection. The frequency shift f_d is given by **Equation (1)** and is presented in [30]. Let c denote the speed of light, f_0 the original (carrier) frequency, and v_r the velocity.

$$f_d = \frac{c}{c - v_r} f_0 - f_0 \tag{1}$$

- **Reliability**: Network reliability is crucial in a tactical context, as availability directly impacts the operational capability of systems and the reliability of information. Civilian network systems, with their centralized structure, present a single point of failure despite technical redundancies. They have a centralized core that makes them vulnerable.

EAN and 5G are designed for speeds up to 1200 km/h [19]. Techniques for compensating frequency shifts in these technologies are essential

[31]. EAN, especially with CGC, has adjusted the LTE air interface to facilitate speed compensation.

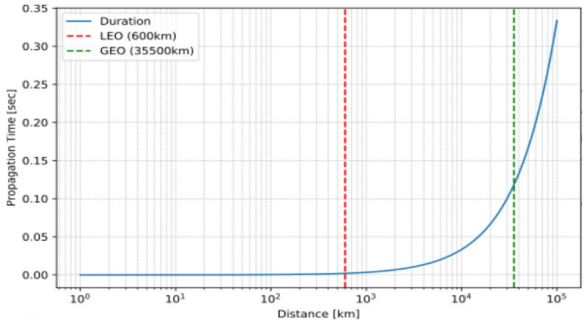

Fig. 4. Signal propagation time vs. distance.

3.2. Comparison of Communication Systems

Both 5G-NTN and EAN provide terrestrial components and satellite-based parts that have been used in civil applications or have been successfully tested. It is conceivable to use only the terrestrial components to supplement a tactical satellite system, as terrestrial use offers scaling advantages over satellite systems. System performance can be enhanced by adding more cells on the ground.

In addition to weighing up which technology can be used by the EAN, a comparison is also made between the EAN CGC, 5G-NTN-LEO, and 5G-NTN-GEO. Fig. 5 compares the RTT of CGC, 5G-NTN-LEO, and 5G-NTN-GEO satellite communication technologies. The lower edge of the color-coded blocks indicates the minimum RTT, and the upper edge represents the maximum RTT. 5G-NTN-LEO and GEO refer to the transparent payload architecture defined by 3GPP, with RTT values derived from 3GPP definitions [23]. For 5G-NTN-LEO, including an additional 5 ms per direction, maximum latency reaches 70 ms, while minimum latency is 22 ms. The CGC system exhibits similar latencies, ranging from 20 ms to 70 ms. In contrast, 5G-NTN-GEO experiences significantly higher latencies from 490 ms to 570 ms. EAN also uses satellite technology with latencies exceeding 500 ms in GEO orbit [32]. Notably, latency in GEO satellite transmissions is mainly due to signal propagation time, with processing latencies having less impact. Initial performance tests with OpenAirInterface (OAI) Core and RAN for 5G-NTN-GEO transmission runtimes have been conducted, establishing a connection between two Software-Defined Radios (SDRs) and a GEO satellite, measuring average latencies around 553 ms [33].

4. Use Case for Civilian Cellular Networks in Military Operations

The EAN systems and 5G-NTN technology can complement MALE RPAS systems by enabling broadband, low-latency connections. In the *Anglova* scenario Vignette 1, a MALE RPAS can serve as a harvester, assuming sensor network communications are integrated as a payload into the system, allowing sensor data to be collected and sent to the CHQ. EAN and 5G-NTN can act as a redundant link alongside tactical data links, enabling the transmission of more data over time and ensuring lower latencies for data fusion purposes if needed. Unlike tactical waveforms, civilian communication technologies are not particularly resistant to jamming and are comparatively more vulnerable [34]. Fig. 6 illustrates the connection of these systems with MALE RPAS, utilizing EAN through terrestrial mobile radio and a satellite connection in the S-band, together with 5G-NTN as a second SATCOM. Communication is routed to service providers via a gateway, facilitating data transfer to the CHQ [35].

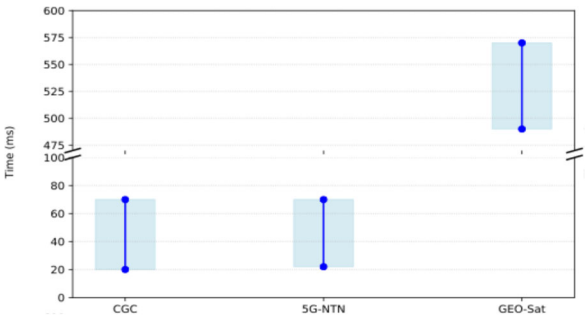

Fig. 5. RTT comparison of the signal delay between EAN-CGC, 5G-NTN and GEO SATCOM [23, 32].

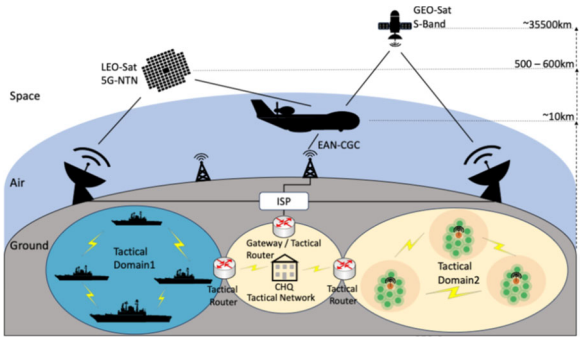

Fig. 6. EAN and 5G network concept with MALE RPAS in *Anglova* context.

Large distance variations lead to increased Free Space Loss (FSL) [36, 37], affecting components in various communication technologies and causing runtime differences. Signal propagation can reach several hundred milliseconds, as shown in Fig. 4, with the shortest latency achievable via EAN-CGC. Fast communication methods enable swift trans-mission to the CHQ, accessible via a gateway for quicker data availability. High-speed data transmission allows the interconnection of multiple sensors, enhancing situational awareness. MALE RPASs have versatile

applications, serving as flying communication nodes or sensor payloads, with the possibility of a combined payload. EAN offers advantages with its compact CGC terminal design.

4.1. Sensors as a Payload Concept

A sensor payload can include various sensors, such as a radar sensor. The sensor specifies the communication requirements, such as latency and data rate. The sensor data can also be processed at a network edge integrated into the MALE RPAS and transmitted cyclically rather than continuously. The payload can then be connected using 5G-NTN and EAN.

4.2. Communication as a Payload Concept

To supplement the communication needed for MALE RPAS operation, it can act as a communication node. Its high flight altitude enables broader communication coverage, enhancing ships or buoy nodes at sea with MALE RPAS payloads [38], thereby extending terrestrial system ranges [37]. Delay Tolerant Networking (DTN) mechanisms [39] can transport large data volumes, utilizing various cyclic systems [40], [41]. Other communication systems can also be integrated here, making 5G-NTN and EAN part of a heterogeneous network.

5. Conclusion

This paper explores the potential use of EAN and the new 5G-NTN standard with the MALE RPAS, detailing their characteristics. Terrestrial connections with the EAN CGC offer high data rates and low latency, with performance enhanced by additional base stations. EAN's integration in the near future with 5G is expected to increase capacity even further. The 3GPP is standardizing 5G-NTN to enable satellite communication with standard mobile devices, aiming to globally expand mobile networks through satellites, enhancing connectivity in underserved regions. Despite high attenuation in satellite communication, these systems are effective in LOS conditions. Successful initial 5G-NTN tests were conducted using AST's BlueWalker 3 satellite. The commercial satellite service is scheduled to launch in early 2026. The current and future availability of broadband technology is promising for UAV operations, with standardizing and expanding civil technology allowing terminal compactness to complement tactical data links. Using the example of the *Anglova* scenario in combination with MALE RPAS, we were able to show that dual use of civil technologies as a supplement to tactical functions enables new applications. Large sensor networks can thus be implemented economically. Both the connection of payloads with sensors and the connection of communication payloads in heterogeneous networks could be realized in this way. These broadband communication networks build the basis for UAV swarm applications [39]. Once the first 5G-NTN satellite service becomes commercially available, further research and field trials can be conducted to gain deeper insights into the performance of 5G-NTN with unmanned systems.

References

[1]. C.-H. Kao, Performance analysis of a JTIDS/ Link-16-type waveform transmitted over slow, flat Nakagami fading channels in the presence of narrowband interference, Master's Thesis, *Naval Postgraduate School*, Monterey, 2008.

[2]. Z. Lesjak, Telecommunications industry statistics (overview for 2025), https://tridenstechnology.com/ telecommunications-industry-statistics/

[3]. NATO Research Task Group, Annex A – Operational Perspective for IST-124, *NATO*, 2015.

[4]. Viasat, European Aviation Network, https://www.europeanaviationnetwork.com

[5]. PESCO, Permanent Structured Cooperation (PESCO) homepage, https://www.pesco.europa.eu/

[6]. Airbus, Eurodrone - Large Long Endurance RPAS, https://mediaassets.airbus.com/pm_38_684_684139-8cl7d5e96t.pdf

[7]. General Atomics Aeronautical, MQ-9A Block 5, https://www.gaasi.com/images/products/aircraft_systems/pdf/2509_MQ-9A-BLK-5_E.pdf

[8]. N. Suri, E. Benvegnu, M. Tortonesi, C. Stefanelli, et al., A realistic military scenario and emulation environment for experimenting with tactical communications and heterogeneous networks, in *Proceedings of the International Conference on Military Communications and Information Systems (ICMCIS'16)*, 2016, pp. 1-8.

[9]. Deutsche Telekom, Viasat und Deutsche Telekom erweitern die Breitbandabdeckung des europäischen Flugnetzes im Mittelmeerraum, https://www.telekom.com/de/medien/medieninformationen/detail/eanantennen-fuer-zypern-1061678

[10]. Deutsche Telekom, Neue Breitbandplattform für Europas Luftverkehr, https://www.telekom.com/ resource/blob/320650/bc04329c06edfd7e191d6aa9c077c29e/dl-150929-datenblatt-data.pdf

[11]. EoPortal, Components of EAN, https://www.eoportal.org/satellitemissions/ean#components-of-ean

[12]. Heise Online, Internet über den Wolken, https://www.heise.de/select/ct/2017/4/1487004422221162

[13]. Deutsche Telekom, Images and media center, https://www.telekom.com/en/media/mediacenter/images

[14]. Heise Online, Kurz erklärt: European Aviation Network (EAN), https://www.heise.de/select/ix/ 2018/6/1527383594474949

[15]. A. Sebayang, Das schnelle Flugzeug-Internet wird Realität, https://www.golem.de/news/ka-ku-und-ean-s-band-das-schnelle-flugzeug-internet-wird-realitaet-1705-127309-2.html

[16]. Hellas Sat, Hellas Sat 3 - Satellite communication & connectivity solutions, https://www.hellassat.net/ coverage/hellas-sat-3/

[17]. Thales Group, Hellas Sat 3 / Inmarsat S European Aviation Network (EAN), https://www.thalesgroup.com/en/worldwide/space/press-release/hellas-sat-3-inmarsat-s-european-aviation-network-ean-communication

[18]. Bundesnetzagentur, Inmarsat-Geschäftsmodell "European Aviation Network (EAN)" im MSS 2 GHz-Frequenzbereich, Amtsblattmitteilung Nr. 66/2018, *Bundesnetzagentur*, 2018, pp. 1-4.

[19]. Solutions for NR to support non-terrestrial networks (NTN), Technical Report TR 38.821 V16.2.0, *3GPP*, 2021.

[20]. G. Masini, How we reached a common vision on the architecture for 5G non-terrestrial networks in 3GPP Rel19, https://www.ericsson.com/en/blog/2024/10/ntn-payload-architecture

[21]. User Equipment (UE) radio transmission and reception; Part 5: Satellite access Radio Frequency (RF) and performance requirements, Technical Specification TS 38.101-5 V18.7.0, *3GPP*, 2024.

[22]. Study on architecture aspects for using satellite access in 5G, Technical Report TR 23.737 V17.0.0, *3GPP*, 2021.

[23]. Service requirements for the 5G system; Stage 1, Technical Specification TS 22.261 V18.15.0, *3GPP*, 2024.

[24]. J. Sedin, L. Feltrin, X. Lin, Throughput and capacity evaluation of 5G New Radio non-terrestrial networks with LEO satellites, in *Proceedings of the IEEE Global Communications Conference (GLOBECOM'20)*, 2020, pp. 1-6.

[25]. AST & Science LLC, FCC Form 442 File No. 1059-EX-CN-2020 BlueWalker 3 non-geostationary satellite updated technical annex, 2020, https://fcc.report/ELS/AST-Science-LLC/1059-EX-CN-2020/248967

[26]. NR; Base Station (BS) radio transmission and reception, Technical Specification TS 38.104 V18.7.0, *3GPP*, 2024.

[27]. R. Stuhlfauth, 5G NTN startet durch: NR-NTN und IoT-NTN, *HF-Praxis*, Issue 3, 2024, pp. 42-46. https://www.beam-verlag.de/fachartikel-hf-technik/aerospace-defence/ (in German)

[28]. Vodafone, Vodafone and AST SpaceMobile announce new EU satellite constellation, https://www.vodafone.com/news/newsroom/technology/vodafone-ast-space-mobile-announce-european-sovereign-satellite-operations-centre

[29]. M. Uko, R. C. Palat, S. J. Macmull, E. T. Matson, Link budget design for integrated 5G-LEO communication applications, in *Proceedings of the IEEE International Conference on Consumer Electronics – Taiwan (ICCE-TW'19)*, 2019, pp. 1-2.

[30]. S. Han, W. Shin, J.-H. Kim, Beam size design for LEO satellite networks with Doppler shift characteristics, in *Proceedings of the 13th International Conference on Information and Communication Technology Convergence (ICTC'22)*, 2022, pp. 924-926.

[31]. A. K. Meshram, P. K. Bishoyi, M. G. S. Sri, S. S. S. Yadav, et al., Doppler effect mitigation in LEO-based 5G non-terrestrial networks, in *Proceedings of the IEEE Globecom Workshops (GC Wkshps'23)*, 2023, pp. 311-316.

[32]. European Aviation Network, EAN factsheet: Benefits at a glance (PDF), https://www.telekom.com/resource/blob/573766b5820f07e7fbcb1b4ce41b94a/dl-ean-factsheet-data.pdf

[33]. F. Völk, D. W. Matolak, U.-C. Fiebig, Field trial of a 5G non-terrestrial network using OpenAirInterface, *IEEE Open Journal of Vehicular Technology*, Vol. 3, 2022, pp. 243-250.

[34]. Y. Arjoune, S. Faruque, Smart jamming attacks in 5G New Radio: A review, in *Proceedings of the 10th Annual Computing and Communication Workshop and Conference (CCWC'20)*, 2020, pp. 1010-1015.

[35]. C. Barz, F. Quinkert, Advanced security gateways for heterogeneous tactical ad hoc networks, in *Proceedings of the International Conference on Military Communications and Information Systems (ICMCIS'15)*, 2015, pp. 1-6.

[36]. H. T. Friis, A note on a simple transmission formula, *Proceedings of the IRE*, Vol. 34, Issue 5, 1946, pp. 254-256.

[37]. G. Schneider, M. Goetz, I. Nissen, Sea trial measurements of LTE and HF performance for underwater network extension, in *Proceedings of the IEEE 49th Conference on Local Computer Networks (LCN'24)*, 2024, pp. 1-6.

[38]. G. Schneider, M. Goetz, I. Nissen, Design and implementation of a gateway buoy for the Underwater-IoT, in *Proceedings of the IEEE 48th Conference on Local Computer Networks (LCN'23)*, 2023, pp. 1-6.

[39]. M. C. A. Baltzer, G. Schneider, I. Nissen, Meaningful human control over swarms in ISTAR, in *Proceedings of the IEEE 50th Conference on Local Computer Networks (LCN'25)*, 2025, pp. 1-7.

[40]. Y. Kato, T. Sugiyama, New drone's flight path proposal to reduce information delivery time in DTN, in *Proceedings of the 13th International Conference on Information and Communication Technology Convergence (ICTC'22)*, 2022, pp. 1251-1253.

[41]. K. Fall, A delay-tolerant network architecture for challenged internets, in *Proceedings of the Conference on Applications, Technologies, Architectures, and Protocols for Computer Communications (SIGCOMM'03)*, 2003, pp. 27-34.

(018)

Improving Crisis Response with a Combined Air Picture and Collaborative Mission Planning

G. Schwoch, J. Bethge, N. Peinecke and J. Rieke
German Aerospace Center (DLR), Institute of Flight Guidance, Lilienthalplatz 7,
38108 Braunschweig, Germany
E-mail: gunnar.schwoch@dlr.de

Summary: Disaster events pose significant challenges for crisis management, including limited access to communication, inaccessible areas, possibly outdated data, and hazardous transportation. The RESITEK (*Resiliente Technologien für den Katastrophenschutz*; Resilient technologies for crisis management) project addresses these issues by integrating DLR's capabilities into a comprehensive shared operational and situational picture system to support crisis response agencies in Germany. Based on end user interviews, the system addresses the lack of real-time, shared situational awareness, and particularly the coordination of manned and unmanned aircraft. Leveraging the European U-space framework, the system provides flight authorisation, geo-awareness, and traffic information services, while a conflict detection and resolution module ensures safe operations. A collaborative mission planning module distributes heterogeneous resources using optimisation and coverage algorithms. The common operational and situational picture aggregates data from U-space, ADS-B/ADS-L, radar, and other sensors and data sources, presenting a modal, scalable interface that highlights impending intrusions and other risks. The goal is to provide a robust and adaptable solution that can be scaled depending on the severity of the events, ultimately saving lives and reducing the impact of disasters. Effective communication and situational awareness are key components of this system.

Keywords: Crisis management, Mission planning, Traffic fusion, Common operational and situational picture, First responders, Unmanned aircraft systems, UAS, drones, U-space.

1. Introduction

The RESITEK (*Resiliente Technologien für den Katastrophenschutz*; Resilient technologies for crisis management) project has the goal of combining the capabilities and technologies of the German Aerospace Center (DLR) in crisis management to improve crisis response in general and, in the scope of this work, with the application of a combined air picture and a collaborative mission planning technique. The need for this is derived from interviews with actual end users in crisis management, i.e. public and private response agencies, such as firefighting units or first aid agencies. The needs have been collected in a qualitative manner and showed, in this scope, the lack of a combined air picture for a complete situational awareness during crisis response. Previous crisis events showed conflicting airspace users, such as the threat of uncrewed units (e.g., drones) to crewed helicopters. Notably, the drones were deployed in an uncoordinated way, but not of malicious intent, but simply unknown to other airspace users.

The main objective is to develop an integrated data and visualisation system that enables efficient capture, planning, and execution of responses during catastrophic events. This system is able to collect, analyze, and facilitate decisions based on relevant data.

The project, in addition to the above functions, addresses several key areas of focus, including space weather, which has a significant impact on both human populations and energy infrastructure. Additionally, the project aims to enhance the resilience of electrical grids by developing "island" networks that can function independently in the event of a disaster. To improve mobility in crisis situations the use of electric vehicles for transportation, access, and emergency services is investigated. These mentioned key areas, however, are not within the scope of this publication.

The system will also incorporate advanced technologies for communication and navigation, allowing response teams to coordinate effectively and efficiently. A key component is the development of a modular and adaptable common operational and situational picture (COSP) that can be easily expanded or modified to accommodate changing scenarios and user requirements. This COSP requires input from various sources, along with services and functionalities that enable the comprehensive and classified view on units, resources and statuses. To achieve this, the collected needs from end users have been translated into system components, where possible and applicable. Core parts of the result are the combined air picture with a mission planning module, and the COSP itself. While the mission planning module makes use of certain services from the European U-space concept, cooperative search pattern algorithms and conflict detection and resolution (CDR), the COSP integrates information from uncooperative traffic detection and the combined air picture to present a scalable, modal interface that unifies a multitude of data. The architecture, as developed and deployed in the frame of the RESITEK project and this publication, is presented in Fig. 1. Blue boxes represent actual screens with a human machine interface (HMI), while white boxes represent services or modules.

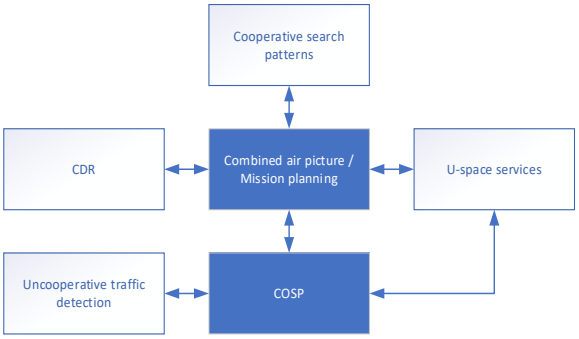

Fig. 1. Combined air picture and COSP architecture.

A comprehensive live demonstration of the system will take place, showcasing its capabilities with various response vehicles, including both manned and unmanned aircraft, and may be presented in future work.

2. State of the Art and End User Needs

State of the art in crisis management varies widely across the entities involved in crisis response, even within the same country. For example, there is no common understanding of the terms common operational picture (COP), common situational picture (CSP) or common operational and situational picture (COSP). The term COSP is used in this publication. Different perspectives exist on COSP as a process, product, or operating environment [1]. Further, crisis response units are not centralized and have their own local solutions, covering their needs and expectations on the one hand, but offering no standardized connectivity to other response units. To get an understanding of the actual needs and applied techniques, the RESITEK project team conducted selected interviews with relevant German end users. The interviews were based on a standardized interview guideline, which was created following principles from Helfferich [2]. An important part of this guideline is the introduction of a “background” in the beginning of the interview to set the scene. Relevant time periods for the crisis reaction and potential means of crisis reaction are asked, followed by questions for proposed measures. Finally, the expert opinion on missing or inadequately utilised technologies is requested.

The interviewed end users were active employees or volunteers of firefighting units, police, infrastructure providers (electricity, water), and municipalities of selected German regions around the cities Aachen and Braunschweig. Ultimately, a total of 22 (out of 29 identified possible end users) were contacted. Twelve of the organisations (approx. 55 %) gave their informal consent to participate in interviews, and nine interviews were successfully conducted (approx. 40 % of the end users initially contacted). Due to data protection rules, names and direct citations cannot be provided. The responses have been categorized based on qualitative content assessment introduced in [3] and are presented in a generalised and anonymised way in the following.

Through the interviews, a qualitative statement regarding the time periods was stated to be position updates of resources in intervals of maximum 30 seconds, and daily map updates. Real-time information on visual information from sensors, e.g. thermal imagery gathered by drones, have been deemed beneficial.

Consequently, the interviewees have stated that the constant availability of resources is key for a quick and efficient reaction in crisis situations. Dedicated and specialised training of personnel, volunteers and crisis management units has been proposed as a concrete measure.

Finally, when asked about missing or inappropriately used technology, it turned out that many end users rely on analogue methods, such as maps, pen and paper, and telephone communication. Live video streams, aerial images updated on a daily basis, the deployment of mobile radars to get a combined air picture, and heterogeneous airborne resources (small to large drones as well as crewed helicopters for person transport) have been indicated as beneficial. In more detail, the following technologies or techniques with the indicated added value have been mentioned in the interviews.

- Live video streams: Enable rapid situation assessment and decision-making;
- Up-to-date aerial maps: Provide a detailed situation assessment for large-scale operations;
- Satellite images (e.g. Copernicus[1]): Real-time representation of disaster scenarios such as floods or fires;
- Drones: Useful for situation assessment, search for persons, and supply of remote areas;
- Helicopters: Area search, water rescue, and hazard removal;
- Mobile radar systems: Improvement of airspace observation.

Considering the identified gaps and missing technology, the RESITEK project, in the scope of this research, focused on the development, adaptation and integration of mission planning components for efficient deployment of aerial resources, and the creation of a combined air picture by integration of data from several sources.

3. Mission Planning and Cooperative Search Patterns

In RESITEK a coordinated mission planning for all ground and airborne resources is one of the key factors.

[1] Earth observation component of the European Union’s Space programme [4].

This is accomplished using a two-fold approach with the following objectives:

1. Keep track of position, tasks and predicted trajectory of every unit as well as its intended and unintended interaction with all other units;
2. Plan a strategic cooperative mission for all involved response vehicles under restrictions from cooperative units and replan missions and trajectories based on detected conflicts or non-cooperative traffic.

The first objective is achieved by collecting positions and tasks of all involved manned and unmanned units and presenting them in a common air picture. Moreover, non-cooperative traffic (see section 6), when detected, complements the operational and situational picture and supplements the first objective. Additionally, planned trajectories from the second objective are displayed in the same aerial picture providing an overview of the – constantly monitored and updated – positions, tasks and predictions. This results in an aerial picture, which unifies the positions of all cooperative and non-cooperative units, as well as the assigned tasks and planned trajectories from cooperative units. It supports the response units gaining and holding air situational awareness.

The second objective is achieved using current vehicle positions and abilities (energy level, payload, camera aperture, etc.) to efficiently distribute and split the assigned tasks between the cooperative vehicles as shown in Fig. 2.

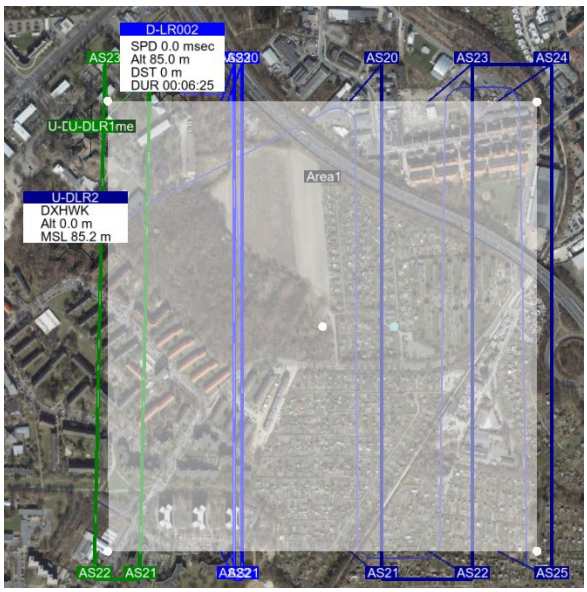

Fig. 2. Mission planning for mapping with multiple (heterogeneous) drones.

The tasks can be assigned by an operator from an HMI which also displays the air picture. Since the air picture holds all necessary information, a central task assignment and mission planning is the obvious choice. This strategic mission planning generates coordinated and conflict-free trajectories. These trajectories are displayed likewise in the common air picture. For instance, mapping of an area might be assigned to multiple heterogenous response vehicles to complete the task more quickly. To that aim, conflict-free waypoint lists or trajectories covering the whole area are planned.

The strategic mission plan results from solving a central optimization problem with respect to the overall time needed, the number of vehicles used, the overall distance and some constraints ensuring conflict free trajectories or waypoint lists. The planned flight routes and distances depend on the different camera aperture angles, cruise speeds and flight heights of each vehicle, leading to approximately the same estimated flight time of each vehicle. The splitting of the overall area and the starting lines as well as the number of units are an output of the optimization. Subsequently, a boustrophedon algorithm [5] plans the individual routes and waypoints for each vehicle, taking into account parameters such as the flight altitude or the camera aperture to calculate the coverage area and the distance between the boustrophedon lines. Moreover, using a simple approximation the algorithm checks if the turning radius between two boustrophedon lines is flyable with the given vehicle type (i.e. fixed-wing or multicopter drones) and the desired cruise speed. If necessary, the distance between two following boustrophedon lines is adapted or the order of the lines is changed. The resulting mission and its planned waypoint list for each vehicle is shown in Fig. 2.

Applying safety margins to detected non-cooperative vehicle positions, assigning new tasks or detected conflicts requires replanning of the strategic mission plan or a new tactical mission. This replanning is enabled using conflict detection and resolution (Section 4) or U-space services (introduced in Section 5). Taking into account safety margins and priorities between manned and unmanned vehicles the interaction between all detected units is constantly monitored and conflict-free.

Regarding the second objective, the cooperative mission planning allows not only mapping, but other tasks as well. The resulting trajectories are calculated or replanned to be conflict-free using already given knowledge as described in Sections 4 and 5. Supported tasks in crisis response may be:

- the setup of no-fly zones;
- mapping of an area to gain a situational picture of the crisis area;
- search and rescue tasks to:
  - find injured people;
  - get in contact with them and providing information;
  - make a first aid response by bringing them water or first aid kits;
  - lead people out to a landing spot or a safe location;
  - guide an ambulance to the emergency site in cases of obstructed or otherwise inaccessible paths.

- following and assessing the status of streets, rails and bridges;
- checking the condition of buildings and other relevant infrastructure;
- checking connectivity to the global system for mobile communication, give warnings, or even re-establish communication for specific areas.

Other services in the crisis management are often unseen and regard conflict detection and resolution, complying geo-zones or chosen no-fly zones, information consolidation to generate an overall situational picture, and rules for avoiding manned and unmanned conflicts and ensure large safety margins.

4. Conflict Detection and Resolution

In RESITEK, CDR plays a role in the following main areas:

First, every cooperative unit involved in the crisis relief operation has to coordinate itself with other units. Apart from the usual strategic decisions accomplished in the mission planning, situations may occur where one unit comes in conflict with another cooperative one, e.g., due to delays in mission execution or non-nominal situations.

Second, it must be considered that potential conflicts between a response unit and other airspace users not under mission control occur, such as additional response units which are not connected to a global crisis management system, or even unregistered private drones. Although keeping non-cooperative traffic away from the crisis area should be an overall goal, it may happen that non-cooperative drones or aircraft enter the mission area. In that case CDR can be the last resort to avoid hazardous situations and maintain the original objectives of the crisis relief mission.

Third, the conflict detection is also extended to detect intrusions of airspace users into restricted areas. This results in the possibility to define no-fly zones to enclose the mission area (as presented in Section 5 and depicted in Fig. 4 later on) or protect sensitive infrastructure within the mission area, for example critical infrastructure or populated regions not requiring aerial support, thus limiting the risk to people.

Due to heterogeneous aircraft in crisis response, there cannot be a general rule to resolve conflicts. Priority management can help to preserve safety in the air and on the ground, especially when human actors are involved. For example, although the response units in the air might be understood as priority units compared to private and leisure aircraft, a helicopter with a pilot onboard must have priority over an unmanned aircraft. Thus, a crisis management system needs to implement an internal weighted priority system which then can be used for resolution advisories or automated conflict resolution. Aircraft with humans onboard may have priority over unmanned aircraft, and search and rescue activities may come before general mapping tasks.

Selected situations where a conflict detection can assist the response units are depicted in Fig. 3.

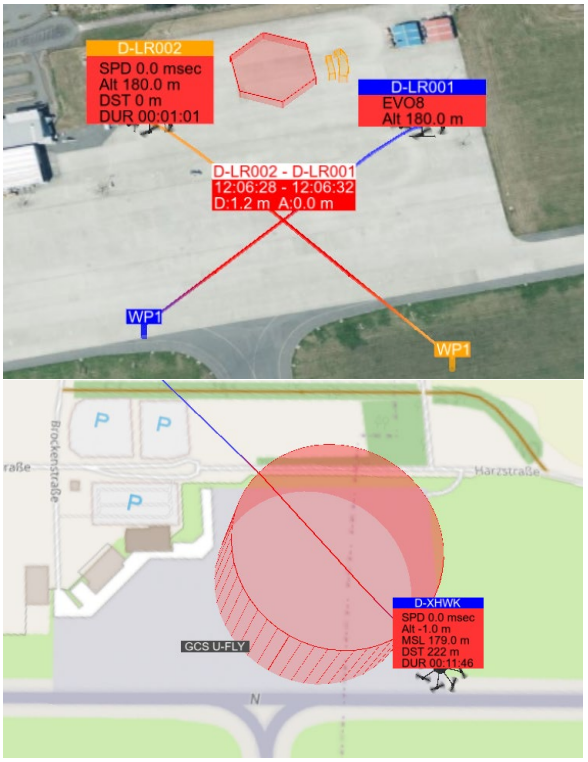

Fig. 3. Conflict detection between cooperative users (top) and geozones (bottom).

To enable CDR functionality, a system resembling the civil U-space concept has been implemented. U-space, as the European vision of an unmanned traffic management system, offers a variety of potential services, which can be exploited to enable the discussed functionalities, as presented in the following.

5. U-Space Services as Enabler

The implemented combined air picture is based on the U-space concept, introduced by EU Regulation 2021/664 [6] and the corresponding implementing regulations in Member States. The aim of this regulation is to enable the establishment of a U-space ecosystem (consisting of an airspace, necessary infrastructure, and offered services) for unmanned aircraft systems (UAS), or drones, in particular in low altitudes, which can be operated in large numbers with a high degree of automation. To this end, a U-space offers U-space services, provided by a certified provider (U-space Service Provider, USSP). Four services are defined as mandatory by the regulation (see below). The regulation states that the four mandatory services must be offered in any U-space. In addition to these mandatory services, optional services may be offered, most notably (and the only ones

mentioned in the current regulation) the *conformance monitoring service* (monitoring the adherence to an approved flight plan) and the *weather service* (offering weather information). The way these services should act is further refined in the Applicable Means of Compliance and Guidance Material (AMC/GM) [7] issued by the European Union Aviation Safety Agency (EASA).

If a U-space is already available in the crisis area, the corresponding services can be used, potentially enriched with additional functionality, such as a priority concept. In the other case, a dedicated crisis U-space can be established, focusing on the required functionality. As the application of such U-space services in a crisis context is not the main use case of the regulation, it can be assumed that an operator from a response unit may carry out special missions in accordance with the privileges of emergency response units and thus might deploy these services independently, sometimes even non-conforming to the regulation if required from a practical view. Thus, the presented concept in the following, although it may use the regulatory wording, might not always be conforming to the regulation and/or the AMC/GM. The operationalisation of emergency privileges, as an important but complex topic, is out of scope of this publication.

The *UAS flight authorisation service* (based on Article 10 of Regulation 2021/664 [6]) reviews the operator's flight plan request and approves or rejects it based on the conditions of the flight and other authorized flights. In most cases, the flight plan is approved or rejected due to conflicts in the flight path. Once the USSP receives the flight request from the UAS operator, it checks whether there is any overlap in the four dimensions (three-dimensional position plus time) of the planned flight path. If there are no conflicts, the USSP approves the UAS operator's flight request. If the USSP detects a conflict in the planned flight path in the conflict scenario, the USSP cannot grant the flight approval. The flight plan is only authorized once the USSP confirms that there is no conflict with the planned flight path. Not required by current regulation, a USSP might include a proposal for an approvable alternative flight plan in the future.

The *geoawareness service* (based on Article 9 of Regulation 2021/664 [6]) ensures, among other things, that flights are only conducted in authorised areas. No-fly zones are areas closed for safety reasons such as presence of segregated traffic or sensible infrastructures. The geo-zones thus support safety, data protection and environmental aspects. In a crisis context in particular, they can also be used to protect the aircraft in the crisis area from external participants and to ensure that external regular traffic is not affected negatively. The geo-zones are divided into different types: excluded, restricted and unrestricted geo-zones. While excluded zones can be used to protect a mission area from intruding traffic and restricted zones can limit the access to a certain type of airspace user, the principle of unrestricted areas can be created to manage the traffic in the mission area.

Fig. 4 depicts a small mission area that is protected by excluded zones (red areas), while a search pattern mission is created inside the mission area. In this way, no external traffic adhering to geoawareness rules, can enter the mission area and disturb the crisis response operation. Further, the geoawareness service also gives the UAS operator a warning when the flight plan or the current position of the UAS is threatening to leave the mission area.

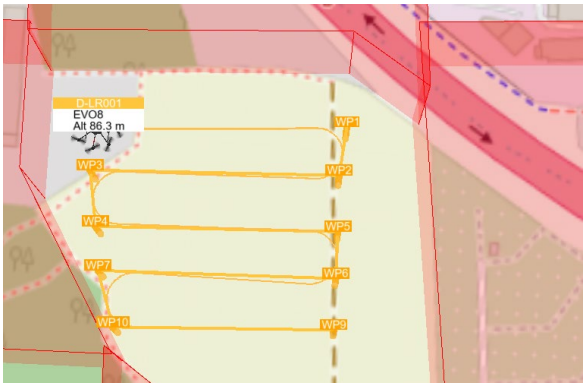

Fig. 4. Search pattern in a mission area protected by excluded geo-zones (red).

The *traffic information service* and the *network identification service* (based on Articles 8 and 11 of Regulation 2021/664 [6]) help manage the response units available for the crisis relief operation in an efficient and safe manner, assuming integrated information of the current air traffic picture of cooperative aircraft as well as surrounding traffic not managed by the system. The UAS operator receives the aggregated data of the USSP, which can then be displayed in a ground control station for managing the own traffic, for example. Further, the traffic information service and the network identification service provide an important knowledge about cooperative traffic, required for the following steps of detecting non-cooperative traffic (Section 6) and creating a common operational and situational picture (Section 7).

6. Detection of Unauthorized, Non-Cooperative Traffic

Unauthorized traffic, in this scope, is defined as airspace users that enter into or remain in the area under crisis management. On the other side, non-cooperative traffic is defined as airspace users that are not equipped with transponders or similar technology and thus do not actively transmit their positions to U-space services or other airspace users. Entering the area under crisis management may happen intentionally or unintentionally. For example, unauthorized traffic may be present in case of onlookers but also in case of uninformed responders.

Non-cooperative airspace participants that do not actively report their positions to a traffic management system or other airspace users impose a bigger risk to the operation, as they need to be detected first and would not show up on cooperative systems in the first place. In case the traffic is cooperative (in this case: making themselves conspicuous) it is relatively easy to identify and manage risks imposed by these.

Thus, it is crucial to detect and discriminate non-cooperative aircraft from other cooperative aircraft that are part of the crisis responders. In this context it is assumed that crisis responders are cooperative, that is, equip their aircraft with transponders or make them otherwise visible for the local U-space, e.g., by using DRI (direct remote identification) [8], ADS-L [9], or using proprietary telemetry broadcast, and thus available through the traffic information service described in Section 5. Further, it is assumed that detection systems for air traffic are available, e.g., ground-based radar, Lidar, or acoustic sensing. That way, non-cooperative traffic will be characterized by the fact that it is detected by detection systems only, while being unknown to U-space. This opens the opportunity to identify "own" units in contrast to non-cooperative traffic. The objects recognized by sensors can be compared with the data from U-space on the basis of various criteria. As described in Fig. 5, in addition to the position, there are information about the direction of movement and speed. If applicable, classification can also be relevant. Depending on the sensor system, the data is processed differently and can provide information ranging from raw data to already classified objects (e.g. birds, cars, aeroplanes, people, etc.).

In the presented system all detected traffic will be fused and compared to traffic known to U-space to identify non-cooperative aircraft. Another possibility of non-conformant aircraft is an approved flight plan in U-space, but e.g. a massive deviation from a planned trajectory or flight area. This can be of importance especially when no conformance monitoring service is available. Further, intent of such traffic will be fused and compared to traffic known to U-space to identify non-cooperative aircraft to identify possible risks for the crisis operation. This functionality might be based on the advanced U-space service for *tactical conflict detection* as described in the U-space CONOPS edition 4 [10].

One challenge in data association is the relatively low update rates of U-space and sensors, which in combination with the potentially high agility of an unknown UAS can lead to relatively large position deviations. When modifying the route to avoid unexpected traffic, conservatively estimated distances to unknown participants must be maintained. To get more precise results, a comprehensive multi-target fusion filter (indicated as tracking and prediction in Fig. 5) with the ability to predict the current status could be used. Details on the fusion approach, association logic, track management, or uncertainty handling is topic to future research.

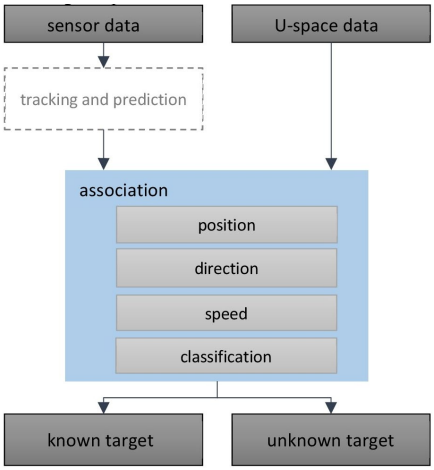

Fig. 5. Data association process of sensor and U-space data.

7. Common Operational and Situational Picture

The common operational and situational picture (COSP) plays a crucial role in crisis management. We refer to the underlying mental model of the users as a COSP while the technology to evoke the COSP will be called a COSP System (COSPS).

There is no univocal definition of the COSP term [11], and different perspectives exist on COSP as a process, product, or operating environment [12]. From the various definitions given in these publications the following common implications can be drawn:

1. A COSP is a special case of a shared mental model (SMM) [13];
2. Elements of a COSPS can be different for different participants (heterogeneous COSPS), or identical (homogeneous COSPS), depending on the purpose;
3. A COSPS can be centralized or networked, depending on the kind of dataflow available;
4. Known situational awareness displays can be part of a heterogeneous COSPS but by itself do not represent a COSPS. For example, a detect and avoid (DAA) display can be used to avoid traffic in a situation that involves other air traffic, but since its use is not limited in time and space, it is not a COSPS on its own;
5. A COSPS can be made entirely of parts that – by itself – are not COSPS;
6. COSPS can have a hierarchical architecture:
   a. They start from a layer of distributed, scattered sensors and singular data points;
   b. These are aggregated in a layer of databases, containing partly processed and fused data points;
   c. These can be further aggregated in a layer of commonly available higher-order databases ("data warehouse");
   d. The final layer comprises HMIs that present selected information to the user.

7. Networked COSPS do not necessarily have a hierarchical structure. Instead, they may actively re-distribute portions of data on demand or on occurrence in a peer-to-peer fashion. Thus, peer-to-peer networked COSPS may have a lower latency (presenting more up-to-date data) but have the risk of providing inconsistencies to individual agents.

Establishing such a COSP is realized by providing access to a server that is available to all participants. The software running on the sever is designed to address both, the growing threat of non-cooperative drones in the airspace, and the common awareness about own units, as well as other important features, in detail:

- Positions of all own units, including sensors and, if available, field teams;
- The system status of each own system component, including sensors and data sources;
- The operation parameters of sensors, including field of view and bearing;
- Positions and velocity vectors of air traffic, if available;
- Possible dangers arising from other drones, e.g., arising from entering protected zones.

The system is developed with the following principles in mind:

1. *Scalability and adaptiveness*: The information shall be displayed on various platforms such as wall projections, table displays, desktop stations, laptops, mobile devices;
2. *Expectability*: The symbology used is aimed to be intuitive by following examples from existing systems, ensuring that users can quickly understand the information presented;
3. *Modality and Relevance*: Information is available on request, but important data for the current function or mission is "pushed" to the user's attention, minimising distractions and maximising effectiveness.

These principles are realised by providing a server-based core application that allows to open remote displays on every device in the same network in a browser application.

Data shall be integrated from a number of available systems and sensors, including U-space services, transponders like AIS (Automatic Identification System), ADS-B (Automatic Dependent Surveillance – Broadcast) and ADS-L (Automatic Dependent Surveillance – Light) [9], and mobile clients. Mobile clients allow to interact with field teams using chat functionality, and by sending markers and coordinates directly. Possible risks, predictions and classifications provided by other systems can be integrated and displayed quickly by utilizing industry standards, e.g. WMS (Web Map Service), WFS (Web Feature Service) [14], and SAPIENT [15].

An example of a COSP implementation can be seen in Fig. 6, making use of a wide-screen display with multi-touch capabilities. The situation in the bottom image shows a drone that has been classified as a threat since it is about to intrude the protected zone. The position of the drone is shown on a digital moving map (Fig. 7) that also depicts the extent of the protected zone (shown as a red framed area). The user can see the time to intrusion (tti) and the distance to intrusion (dti) when activating the drone symbol. In a similar fashion more information is available in other parts of the HMI.

Fig. 6. Example of a COSP implementation on a display table.

Fig. 7. A symbology for a drone about to enter a protected zone.

The performance of the COSP outlined in this publication heavily depends on the number, technical implementation, processing capability and accuracy of sensors and data sources integrated. We have shown that it is relatively straight-forward to integrate further sensors, for example. Future test campaigns will have to show which combination of sensor technologies with U-space-services turns out to be most efficient in terms of latency, update rate, false-alarm rates and scalability with traffic volume.

8. Conclusion and Outlook

The RESITEK project demonstrates that crisis response can substantially benefit from a combined air picture. By utilising U-space infrastructure, the project provides real-time flight authorisation, geo-awareness,

and traffic information, thereby addressing both cooperative and non-cooperative aircraft. The conflict detection and resolution (CDR) engine, using a priority-based weighting system, supports the mission in presence of unexpected traffic, while the mission-planning module allocates heterogeneous assets efficiently across strategic and tactical layers.

The Common Operational and Situational Picture (COSP) serves as the perceptual backbone, presenting a scalable, modal interface that unifies sensor feeds, U-space data, and field-team inputs. This holistic view satisfies the end user-derived requirements for rapid, accurate situational awareness and supports replanning and risk assessment.

Future investigations may address the implications an existing U-space with active traffic in the crisis area might have, and if an exclusive use for crisis response is required in such cases. Additional future work will refine the multi-target fusion for non-cooperative traffic detection, and validate the system in large-scale live demonstrations. RESITEK lays a foundation for resilient, interoperable crisis management, where diverse stakeholders share a common, real-time operational picture, thereby enhancing safety, efficiency, and adaptability during catastrophic events. The presented systems play a key role in the management of such events.

References

[1]. K. Steen-Tveit, B. E. Munkvold, From common operational picture to common situational understanding: An analysis based on practitioner perspectives, *Safety Science*, Vol. 142, 2021, 105381.

[2]. C. Helfferich, Leitfaden- und Experteninterviews, Chapter 55, in Handbuch Methoden der empirischen Sozialforschung (N. Baur, J. Blasius, Eds.), *Springer VS*, Wiesbaden, 2022, pp. 669-686 (in German).

[3]. P. Mayring, Qualitative Inhaltsanalyse: Grundlagen und Techniken, *Beltz*, Weinheim, 2022 (in German).

[4]. European Union, About Copernicus, https://www.copernicus.eu/en/about-copernicus

[5]. H. Choset, Coverage of known spaces: The boustrophedon cellular decomposition, *Autonomous Robots*, Vol. 9, Issue 3, 2000, pp. 247-253.

[6]. Commission Implementing Regulation (EU) 2021/664 of 22 April 2021 on a regulatory framework for the U-space, *European Commission*, 2021.

[7]. Acceptable means of compliance and guidance material to Regulation (EU) 2021/664 on a regulatory framework for the U-space, *European Union Aviation Safety Agency*, 2022.

[8]. Commission Implementing Regulation (EU) 2019/947 of 24 May 2019 on the rules and procedures for the operation of unmanned aircraft, *European Commission*, 2019.

[9]. European Union Aviation Safety Agency, ADS-L 4 service description (SRD860), 2024, https://www.easa.europa.eu/en/downloads/142821/en

[10]. U-space ConOps and architecture (Edition 4), *CORUS-XUAM Consortium*, 2023.

[11]. J. Wolbers, K. Boersma, The COP as collective sensemaking, *Journal of Contingencies and Crisis Management*, Vol. 21, Issue 4, 2013, pp. 186-199.

[12]. J. Copeland, Emergency response: Unity of effort through a common operational picture, Strategy Research Project, *U.S. Army War College*, Carlisle Barracks, 2008.

[13]. C. A. Bolstad, M. R. Endsley, Shared mental models and shared displays: An empirical evaluation of team performance, in *Proceedings of the Human Factors and Ergonomics Society Annual Meeting*, Vol. 43, Issue 3, 1999, pp. 369-373.

[14]. Open Geospatial Consortium, OGC standards, https://www.ogc.org/standards/

[15]. BSI Group, BSI Flex 335 v2.0:2024-03 - SAPIENT network of autonomous sensors and effectors – Interface control document – Specification, *The British Standards Institution*, 2024.

(019)

Hydrogen-Rich 3D-Printed Gyroid Lattice LEO Satellite Composites for Cosmic Ray Attenuation

Seunghyeon Kang [1], Chaehwan Lim [2], Jaewon Shim [2], Woomin Cho [2,3,4], Hyunung Oh [2,3] and Youngwoo Nam [1,2]

[1] Interdisciplinary Program in Space Systems Engineering, Aerospace University, Korea
[2] Graduate School of Aerospace and Mechanical Engineering, Aerospace University, Korea
[3] Department of Smart Air Mobility, Aerospace University, Korea
[4] Department of Future & Smart Construction Research, Institute of Civil Engineering and Building Technology, Korea
Tel.: + 82 10-3834-9516
E-mail: ywnam@kau.ac.kr

Summary: Protecting electronic devices in low Earth orbit (LEO) from cosmic radiation and harsh environmental factors, such as atomic oxygen (AO), UV radiation, and vacuum, remains a critical challenge in the New Space era. This study presents a lightweight, radiation-shielding sandwich composite fabricated via Fused Deposition Modeling (FDM) 3D printing. The composite utilizes a polyetheretherketone (PEEK) gyroid core structure filled with polyethylene (PE) to enhance shielding performance by increasing the hydrogen content. The outgassing test confirmed the composite's robust thermal and vacuum stability, with a TML of 0.08 %. Furthermore, proton irradiation experiments and NASA OLTARIS simulations demonstrated that higher PE fill ratios significantly improved shielding efficacy, outperforming conventional aluminum at an equivalent areal density. The developed PEEK/PE composites exhibit excellent additive manufacturability and show significant promise as a protective solution for satellite electronics.

Keywords: Low Earth Orbit (LEO), Satellite, Radiation shielding, 3D printing, TPMS structure, Gyroid lattice structure, Polymer.

1. Introduction

The growth of the space industry and the transition into the New Space era have led to the significant expansion of small and low Earth orbit (LEO) satellite constellations, often by private companies such as SpaceX's Starlink. These systems increasingly rely on commercial off-the-shelf (COTS) components to reduce costs. However, COTS devices are particularly vulnerable to the LEO space environment, which includes high-energy protons and electrons trapped by Earth's magnetic field, galactic cosmic rays (GCR), and solar energetic particles (SEP). This vulnerability can lead to component failures or shortened mission lifespans [1], with reported mission failure rates as high as 41 % within one year [2]. Therefore, effective radiation shielding is essential. In LEO unmanned systems such as small satellites and distributed satellite swarms, where on-orbit maintenance or replacement is not feasible, enhanced radiation robustness of onboard electronics is a critical requirement.

Fused deposition modeling (FDM), an additive manufacturing (AM) method that utilizes thermoplastic filaments, offers several significant advantages, including low cost, design flexibility, rapid fabrication, and the ability to form integrated structures. According to the Bethe–Bloch equation, materials with a high Z/A ratio (atomic number to mass number) exhibit superior radiation dose reduction. Hydrogen, possessing the highest Z/A ratio, is the most effective element for radiation shielding; however, its direct application is limited owing to handling difficulties and safety concerns [3]. Consequently, thermoplastic polymers with high hydrogen content are widely investigated as practical alternatives [4]. The purpose of this study is to design an effective radiation-shielding sandwich composite for LEO satellites. To achieve this, we developed a hydrogen-rich FDM composite and verified its LEO durability and radiation shielding properties.

2. Materials and Methods

2.1. Materials

Polyether ether ketone (PEEK) and polyethylene (PE) were chosen as thermoplastic polymers for FDM-based manufacturing. PEEK was selected for its high mechanical strength and excellent thermal stability, making it suitable for load-bearing structural components. Meanwhile, PE was chosen for its high hydrogen content, which provides effective radiation shielding against high-energy charged particles. The PEEK structures were fabricated using a 3D printer at an extrusion temperature of 420 °C. To further enhance radiation attenuation, polyethylene (PE) was introduced as a filler material within the internal voids of the printed gyroid structures. In addition, hexagonal boron nitride (h-BN) nanoparticles, known for their high neutron capture cross section and thermal stability, were incorporated as a functional filler to

improve neutron attenuation performance without compromising the mechanical integrity of the composite.

2.2. Outgassing Testing

The Total Mass Loss (TML) test of the composite proposed in this study was conducted in accordance with the ASTM E-595 standard. According to the specification, the specimen mass ranged from 100 to 300 mg. Before testing, the specimens were preconditioned in a temperature and humidity chamber at 23 °C and 50 % relative humidity for 24 hours. Subsequently, they were exposed to a high vacuum environment of 10^{-6} Torr at 125 °C for 24 hours. The TML value was determined by measuring the specimen mass before and after exposure to the test solution.

2.3. Space Radiation Experiment

The radiation shielding performance of the composite proposed in this study was evaluated using the MC-50 cyclotron facility at the Korea Institute of Radiological & Medical Sciences (KIRAMS). Proton beams with an energy of 50 MeV were irradiated onto the specimens, and the shielding performance was subsequently analyzed.

2.4. Space Radiation Analysis

Radiation shielding performance was evaluated using NASA OLTARIS for a circular low Earth orbit (550 km, 51.6°) with a mission duration of 365 days. The radiation environment included galactic cosmic rays (BO-20, solar minimum) and trapped protons (AP9). Shielding effectiveness was assessed in terms of tissue dose for different gyroid configurations.

3. Results and Discussion

3.1. Outgassing Testing

Outgassing characteristics were evaluated using PEEK specimens fabricated by FDM 3D printing. The tests were performed in accordance with ASTM E595, using standardized specimens weighing approximately 200 mg. For space applications, a total mass loss (TML) below 1.0 % is generally required. The results showed that the FDM-fabricated PEEK specimens exhibited a TML of 0.08 %, satisfying the qualification criteria for space-use materials. This confirms that the 3D-printed PEEK face sheets exhibit low-outgassing behavior under vacuum and thermal conditions relevant to LEO environments.

3.2. Space Radiation Experiment

The results of the space radiation experiment showed that radiation shielding performance improved as polyethylene (PE) filling content increased. All polymer-based specimens demonstrated higher shielding efficiency than aluminum at the same areal density.

4. Conclusions and Future Works

In this study, a radiation shielding structure was developed to protect onboard electronic components in satellites from the space radiation environment. The 3D-printed PEEK exhibited excellent resistance to outgassing under high-vacuum conditions, and the radiation shielding performance of the composite was found to be superior to that of conventional aluminum at an equivalent areal density. Future work will focus on evaluating the structural integrity of the gyroid architecture through mechanical property assessments to verify its suitability for practical aerospace applications.

Acknowledgment

This paper is research supported by the Ministry of Trade, Industry and Energy (A major activities of 2024 Industry-Academia Cooperation: Aviation and defense SW professional Education).

This work was supported by Korea Research Institute for defense Technology planning and advancement (KRIT) grant funded by the Korea government (DAPA(Defense Acquisition Program Administration)) (KRIT-CT-22-040, Heterogeneous Satellite Constellation based ISR Research Center, 2022).

References

[1]. P. S. Winokur, G. K. Lum, M. R. Shaneyfelt, F. W. Sexton, et al., Use of COTS microelectronics in radiation environments, *IEEE Transactions on Nuclear Science*, Vol. 46, Issue 6, 1999, pp. 1494-1503.

[2]. M. Tafazoli, A study of on-orbit spacecraft failures, *Acta Astronautica*, Vol. 64, Issue 2-3, 2009, pp. 195-205.

[3]. J. H. Cha, Y. Kim, S. K. S. Kumar, C. Choi, et al., Ultra-high-molecular-weight polyethylene as a hypervelocity impact shielding material for space structures, *Acta Astronautica*, Vol. 168, 2020, pp. 182-190.

[4]. S. Guetersloh, C. Zeitlin, L. Heilbronn, J. Miller, et al., Polyethylene as a radiation shielding standard in simulated cosmic-ray environments, *Nuclear Instruments and Methods in Physics Research B*, Vol. 252, Issue 2, 2006, pp. 319-332.

(020)

Data Offloading for Mobile Unmanned Systems – Evaluation of Throughput and Latency in a Private 5G Network

B. Schuetz [1,2], F. Bott [1], R. Holling [1], O. Stenzel [1], J. Bauer [2] and S. Greiser [1]
[1] Osnabrück University of Applied Sciences, Faculty of Management, Culture and Technology, Kaiserstraße 10c, 49809 Lingen (Ems), Germany
[2] Fraunhofer Institute for Communication, Information Processing and Ergonomics FKIE, Zanderstraße 5, 53177 Bonn, Germany
E-mail: bertram.schuetz@hs-osnabrueck.de, s.greiser@hs-osnabrueck.de

Summary: This paper investigates data offloading for mobile unmanned systems in private 5G networks. The presented evaluation is based on real-world measurements in a modernized industrial facility, using an unmanned ground vehicle. Our results indicate that the service requirements for uplink and downlink throughput are mostly met, while latency is still partially an issue for real-time data offloading and online processing.

Keywords: Unmanned systems, Mobile robotics, Data offloading, 5G private networks, Real-world measurements.

1. Introduction & Motivation

With its promise of low latency and high throughput, 5G New Radio (NR) yields exciting potential for the future of industry, mobile robotics, and unmanned systems. This paper targets especially the use case of data offloading for online processing. Thereby, a fast, wireless network, e.g., 5G, is used to transport sensor data to a server, which then conducts resource-intensive calculations and returns the results in real-time. Such an approach can save space, weight, energy, and cost by replacing CPU and GPU capabilities of mobile systems with edge-near cloud solutions. One prominent use case is the calculation of precise Visual Simultaneous Localization and Mapping (VLSAM) combined with a high-resolution Light Detection and Ranging (LiDAR). An exemplary system setup for this approach is shown in Fig. 1, where the collected LiDAR data of an Unmanned Ground Vehicle (UGV) is offloaded via the 5G NR system to a Data Processing Server (DPS) for online processing and an associated Network Attached Storage (NAS) for further data analysis. While data offloading seems very promising, sufficient wireless throughput and low latency is critical to ensure real-time capability. Thus, since the network conditions are the limiting factor, this paper investigates the concept by presenting and analyzing measurements of private 5G network throughput and latency in a challenging real-world environment.

2. Related Work & Contribution

Since the introduction of 5G NR, several performance measurements and evaluations have been published. Especially prominent is the early work by Rappaport, et al. [1]. Newer results are presented by Ghourtani, et al. [2], whereas a comprehensive survey on 5G channel measurements and models is presented in [3], which references the most important public-cations in the field. A comprehensive survey on edge computing and data offloading in general was published by Qui et al. [4]. 5G-specific literature on the topic is presented by Pham et al. [5] and Di Lorenzo et al. [6].

This paper contributes to this field by giving novel insights into the current state-of-the-art of 5G NR performance and service requirements compliance [7], with the goal to increase the scientific community's assessment of its potential for data offloading. One unique characteristic of the presented results is the deployment of a commercial-grade 5G NR system, produced by Ericsson, in a large, modernized industrial indoor facility. Such an environment yields much potential for automation and mobile robotics, yet it is very challenging for wireless communication, due to the facility's size and steel construction. In comparison, most analyzed data sets mentioned in the survey by Wang et al. [3], were collected in labs or smaller facilities, often using prototypical network infrastructure.

To support future research, all data is made available under: https://doi.org/10.5281/zenodo.18465652.

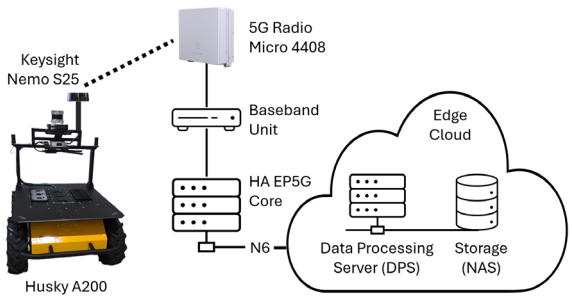

Fig. 1. Overview of the used network architecture for UGV data offloading via 5G NR to an edge-near cloud.

3. System Setup

This section summarizes the system setup, including the test area, the used UGV, and the 5G NR network system.

3.1. Test Area

The private 5G campus network of the Faculty of Management, Culture and Technology of the Osnabrück University of Applied Sciences is hosted in a modernized industrial facility. Originally, the area was a central railway repair workshop, which was converted into a university campus. Within the large hall, several buildings were constructed to house labs, seminar rooms, and offices. Due to the still existing large steel structures, which are characteristic of such workshops, the environment is rather challenging for radio signal propagation and network deployment. Fig. 2 shows an image along the long central axis of the main hall and a floorplan, which also includes the buildings within the hall.

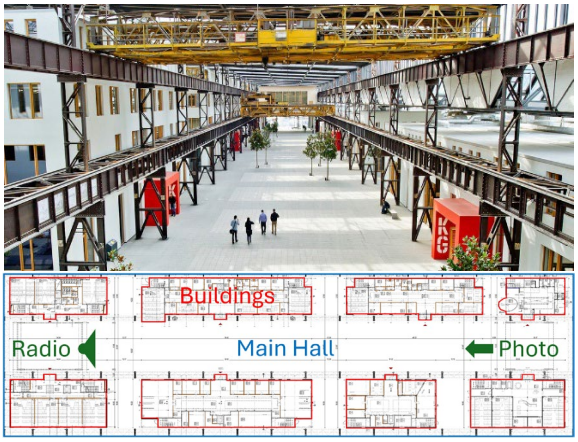

Fig. 2. Test area and floorplan Campus Lingen, photo taken along length axis (green arrow), cf. https://www.hs-osnabrueck.de/en/study/student-life/campus/

3.2. Unmanned System Platform

A Clearpath Robotics Husky A200 UGV was selected as the reference system. The Husky A200 was chosen because it is a widely available off-the-shelf platform and deploys several sensor types, which are interesting for data offloading. These sensors include especially a multi-layer 3D LiDAR, a stereo and depth camera, an RTK system, and several IMUs.

To conduct the 5G network throughput measurements, a Keysight Nemo Handy [8] was attached to the Husky at 1 m above floor height. The Nemo Handy is essentially a Samsung Galaxy S25, which is flashed with a custom Keysight firmware and application. Together with the Nemo Outdoor Playback data analysis software, this enables reliable, professional network measurements, especially for 5G private networks.

3.3. 5G Network System

To enable efficient data offloading in a private 5G network, the unmanned system must be connected with the Data Processing Server (DPS) and the Network Attached Storage (NAS) via the local 5G infrastructure, as illustrated in Fig. 1. The used system is an Ericsson Private 5G (EP5G) network, which is operated on the 3.7-3.8 GHz frequency band (n78). For the conducted measurement campaign, a single Ericsson Micro Radio 4408 was deployed. While our full-scale 5G network is planned to use multiple radio units for optimal coverage, the choice of a single radio for this evaluation was made to simplify the experiment parameters, create challenging link conditions, and avoid cell handovers. The radio dot was attached to a large tripod on a balcony within the central hall of the facility, cf. Fig. 2, at a height of 11.275 m above the pavement. The heading was aligned along the length axis of the building, looking down at 35°. The wattage was set to 4×250 mW. To avoid any impact from virtualization, a dedicated bare metal server was used as DPS, which is connected via an N6 interface. A condensed summary of the network system is shown in the following Table 1.

Table 1. Configuration 5G NR Network.

Component	Product	Configuration / Connection
Core Hardware	DELL Server R640	2×SFP28, 25 GbE with OM3, l = 5 m
Core Software	Ericsson EP5G	Release 25.81
Baseband Unit	BBU 6651	TDD Pattern: 2-DDSU / 2-10:2:2
Radio	Ericsson Mirco Radio 4408	4×250 mW, Fiber OS2 9/125, l = 200 m
Data Processing Server	DELL PowerEdge R6515	Ubuntu Server 24.04 LTS, 1×SFP28, 25 GbE with OM3, l = 5 m
Switching	FS S5850-48B8C-PE	FS OS 7.4.8, 48×SFP28 + 8×QSFP28

4. Measurements & Evaluation

The main research question of the presented evaluation is whether the data offloading demand can be satisfied by the 5G network. Therefore, measured data rate demands of the UGV will be presented, analyzed, and compared to the statistical distribution of the measured 5G throughput. The evaluation also analyzes latency measurements to assess if the 3GPP latency service requirements [7] are met and if the delays are low enough to enable real-time operation.

4.1. Data Offloading Demand UGV

To quantify the data rate, which an unmanned system demands to offload to a processing server, a

two-minute test drive was conducted with the reference UGV. Thereby, a ROS 2 bag of all relevant sensor data is saved and later analyzed. The resulting data rate demands are presented in Table 2.

Table 2. Measured RoS2 data rates of reference UGV (Clearpath HUSKY A200), cf. Section 3.2.

Data Source	Product	Data Rate [Mbit/s]
Stereo RGB Camera	Stereolabs ZED 2i	10.958
Depth Camera	Stereolabs ZED 2i	5.481
Multi-Layer 3D-LiDAR	Ouster OS1 32 Gen2 (1024 points @20 Hz)	12.523
IMU	Fix position Vision Sensor Fusion RTK2	0.509
Combined	all above	**29.471**

It has to be noted that we only consider the payload data rates here. Usually, the DPS would run a ROS 2 subscriber or a streaming service, such as Apache Kafka, to offload the data. Thus, additional network and control overhead would occur. Since the amount overhead depends heavily on the protocols, we note an evaluation of network overhead for future work.

4.2. 5G Throughput & Latency

Detailed 5G throughput and latency measurements were conducted using the Nemo Handy [8], which was attached to the UGV at a height of 1 m above the floor, cf. Section 3. For the throughput measurements, an iperf3 server was hosted on the DPS, while an iperf3 client ran in TCP mode on the Nemo Handy. The latency (one-way delay) is approximated using half the Round-Trip Time (RTT) of ICMP Pings from the UGV to the server. The results of these measurements are visualized on the maps in Figs. 3-5. The following evaluation analyzes the statistical distribution of the data. Therefore, Figs. 6, 7, and 9 show Empirical Cumulative Distribution Functions (ECDFs) and regular Boxplots of the data.

Downlink Throughput: Due to the focus on data offloading for online processing, our evaluation mainly analyzes the uplink and latency measurements. Thus, in short, here are the condensed findings regarding downlink throughput distribution, which is shown in Fig. 6:

- The median downlink throughput in the hall is 599.8 Mbit/s, with a lower quartile of 378.5 Mbit/s and an upper quartile of 958.6 Mbit/s;
- In the buildings, a median of 145.2 Mbit/s was achieved, with a lower quartile of 111 Mbit/s and an upper quartile of 247 Mbit/s;
- The medians and lower quartiles reside far above the UGVs' combined data rate demand of 29 Mbit/s, cf. Table 2. While usually the uplink throughput to a server is critical for data off-loading, this high downlink throughput enables fast machine-to-machine streaming via 5G.

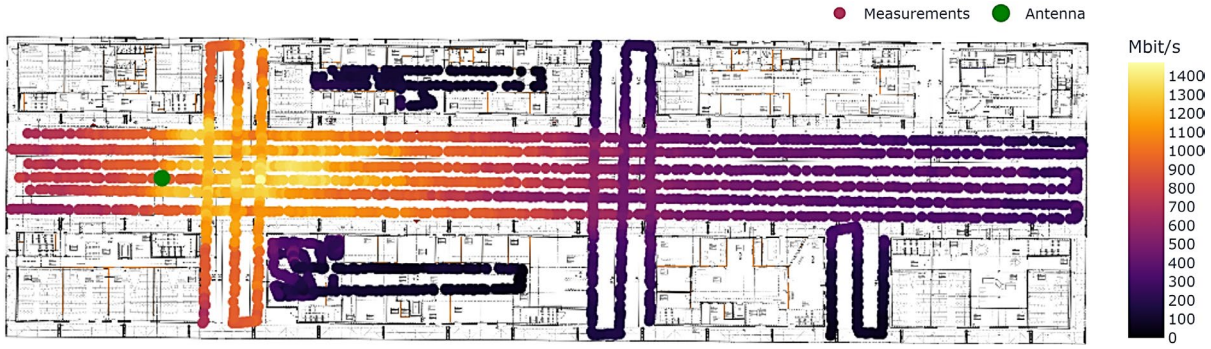

Fig. 3. Measured iperf3 TCP Throughput 5G Downlink in Mbit/s.

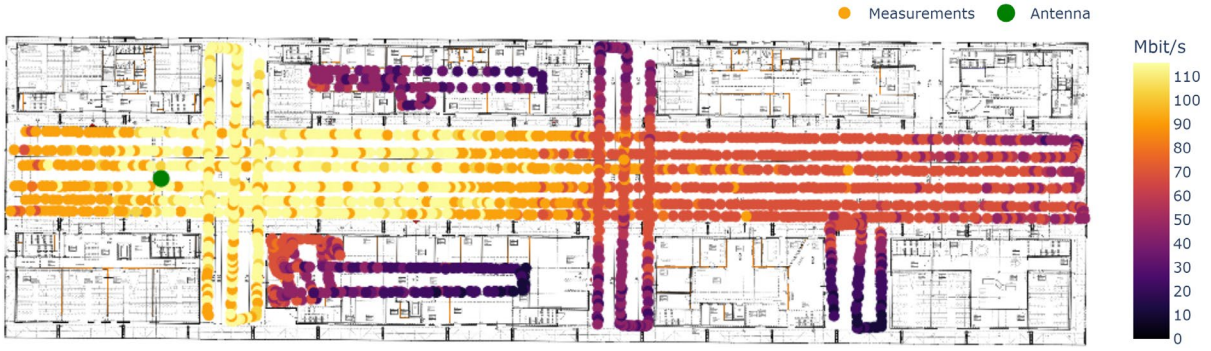

Fig. 4. Measured iperf3 TCP Throughput 5G Uplink in Mbit/s.

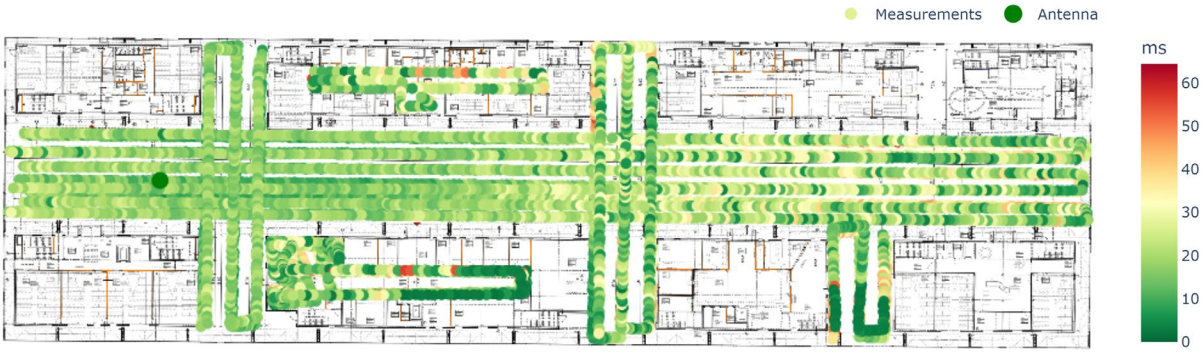

Fig. 5. Measured latency (one-way-delay) in ms, using ICMP Ping RTT/2.

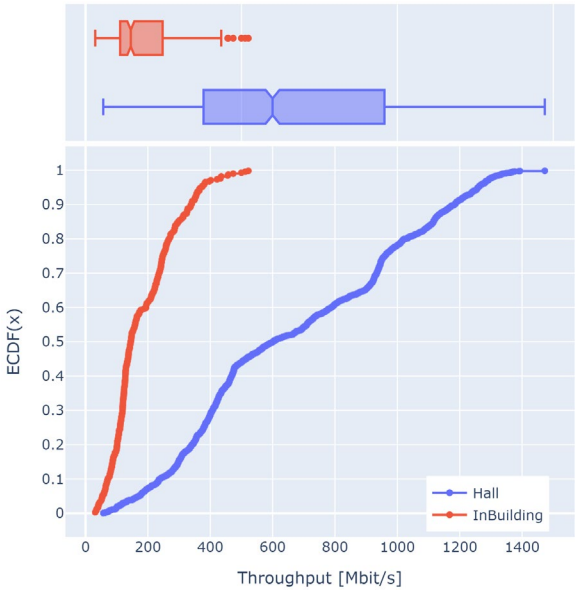

Fig. 6. ECDF and Boxplot of measured iperf3 TCP Throughput 5G Downlink in Mbit/s.

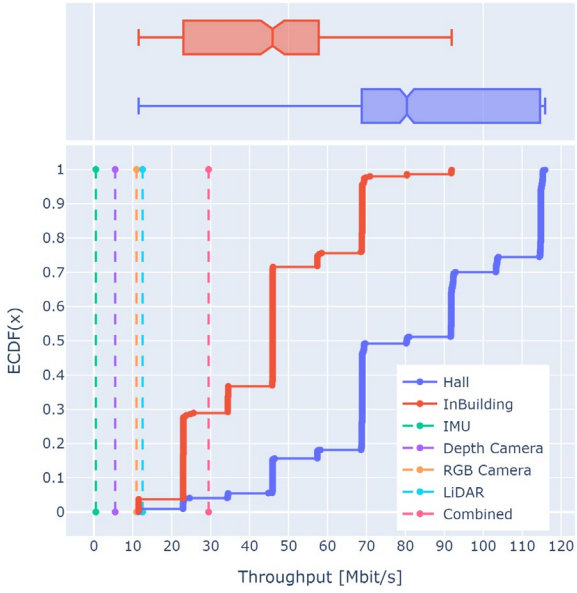

Fig. 7. ECDF and Boxplot of measured iperf3 TCP Throughput 5G Uplink in Mbit/s.

Uplink Throughput: Sufficient uplink throughput is the critical key for real-time data offloading and online processing. The uplink throughput distribution of the 5G measurements is shown in Fig. 7, which shows:

- The median downlink throughput in the hall is 80.4 Mbit/s, with a lower quartile of 68.8 Mbit/s and an upper quartile of 114.6 Mbit/s;
- In the buildings, the median is at 45.9 Mbit/s, with a lower quartile of 23.0 Mbit/s and an upper quartile of 57.8 Mbit/s.

Compared to the measured data rate demands, cf. Table 2, which are represented by the vertical lines in Fig. 7, the following key takeaways can be identified:

- The IMU and depth camera data rate demand can be always satisfied;
- In the main hall, the LiDAR and RGB camera demand is satisfied in 99.9 percent of positions and still in 94 percent in the buildings;
- The combined data rate demand is satisfied in 96 percent of measurement positions in the hall and in 71 percent of positions in the buildings.

One interesting finding is the stepped nature of the uplink throughput, seen in Fig. 7. The reason for these steps is the automatic selection of the used Modulation and Coding Scheme (MCS) in the 5G NR waveform. This explanation is in line with the findings of Rappaport et al. [1] and Ghourtani, et al. [2]. Given the fundamental inverse-square law of wireless communication, the reception power sinks drastically with distance. Thus, the Signal-to-noise and interference Ratio (SNIR) decreases, which results in an increased Block Error Rate (BLER). This finally forces the NR waveform to select a more robust MCS, sacrificing throughput for robustness. To further investigate this phenomenon, Fig. 8 shows the correlation between throughput and Euclidean distance to the radio for the main hall measurements.

The data points in the buildings have no line of sight (LOS) by default, and, thus, are excluded here. The points are colored depending on the existence of a LOS, which was calculated using simple 3D models of the buildings in the main hall. For future work, it is very interesting to create a more precise 3D model, which also includes smaller obstacles, like the steel beams and trees, which are visible in the photo in Fig. 2. Notice, since fitting a function for TCP

throughput over distance is a complex task, the depicted trendline simply uses the Locally WEighted Scatterplot Smoothing (LOWESS) to visualize the trend. The trendlines not only highlight the expected throughput decline with increasing distance, but the slope difference also clearly indicates a stronger decline if the LOS is blocked. In general, electromagnetic waves can overcome a blocked LOS by transmitting through an obstacle or bending around it using diffraction. Since the buildings are made of reinforced concrete and the frequency of 3.8 GHz is rather high, transmission and diffraction are unlikely. Thus, a possible explanation is the impact of multi-path reflections within the hall, especially at the roof, which spans across the whole facility.

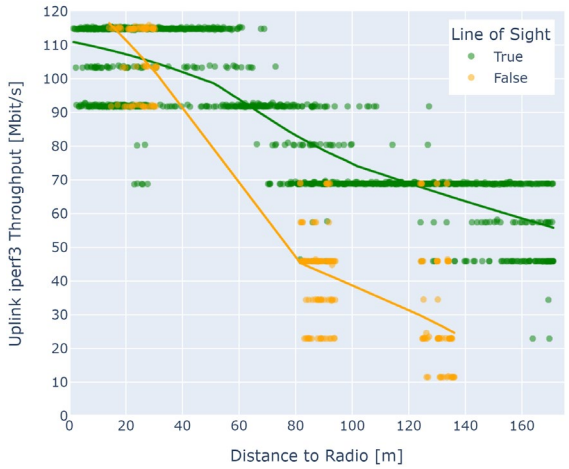

Fig. 8. Correlation uplink throughput to distance, colored by existence of line of sight. Main hall measurements only.

Latency: While uplink throughput is usually the critical key performance indicator for data offloading, real-time systems also require low latency. This is especially important if time-critical functions shall be calculated by the data processing server, e.g., VSLAM. Fig. 9 shows the latency distribution in ms, approximated using half the RTT of ICMP Pings from the UGV through the 5G infrastructure to the server and back. The vertical lines indicate the 3GPP service requirements for the low-latency, high-reliability scenarios, cf. [7, Table 7.2.2-1]. Analyzing the data, which is shown in Fig. 9, highlights the following key takeaways:

- In the main hall, the median latency is 19 ms, with a lower quartile of 26 ms and an upper quartile of 13.5 ms;
- The median latency only slightly increases to 21 ms in the buildings, but a higher variance leads to a lower quartile of 11.4 ms and an upper quartile of 32.375 ms;
- The targeted 60 ms 3GPP service requirement for Process Automation would be always achieved. This also applies to the 100 ms latency target for remote operation of Underwater UAVs, discussed in our DAUS 2025 paper [10];
- The 30 ms latency requirement for Intelligent Transport Systems is achieved in 83 percent of positions in the hall, and 70 percent in the buildings;
- For Discrete Automation, the ambitious goal of 10 ms latency can only be satisfied in 13 percent of data samples in the hall and in 22 percent in the buildings.

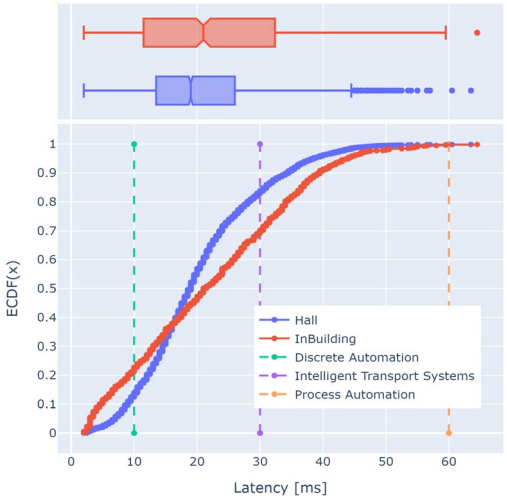

Fig. 9. ECFD and Boxplot of measured latency (one-way delay) in ms, using ICMP Ping RTT/2 approximation, the vertical lines represent the 3GPP 5G latency service requirements, cf. [7, Table 7.2.2-1].

5. Conclusion & Future Work

As shown by the presented evaluation, based on real-world measurements, the 5G service requirements for uplink and downlink throughput are mostly met, while latency is still partially an issue for real-time data offloading and online processing. The most important numbers for this use case are the presented median uplink throughputs of 80.4 Mbit/s in the hall and 45.9 Mbit/s in the buildings. Given some variance, this leads to a 96 percent satisfaction of the UGVs data offload demand in the hall and 71 percent in the buildings, cf. Fig. 7. The service requirements regarding latency instead are only satisfied partially, e.g., the 30 ms latency requirement for Intelligent Transport Systems is only achieved 83 percent of time in the hall and 70 percent in the buildings cf. Fig. 9.

For future work, we plan to extend the measurements to our full network configuration with multiple radios, thus, also evaluating the impact of handovers. Also, it is very interesting to create a high-resolution 3D model of the test area and use our measurements to evaluate the accuracy of modern Ray Tracing-based 5G signal propagation simulators, such as NVIDIA Sionna RT [11]. This approach would enable novel capabilities for unmanned systems, such as site-specific, communication-aware path planning, which is especially challenging in multi-robot scenarios.

Acknowledgements

We want to thank the Lower Saxony Ministry for Economic Affairs, Labour, Transport and Digitalisation for the funding of the 5G network, and the Talent Academy Smart Factory & Products of Osnabrück University of Applied Science for supporting this research.

References

[1]. T. S. Rappaport, G. R. MacCartney, M. K. Samimi, S. Sun, Wideband millimeter-wave propagation measurements and channel models for future wireless communication system design, *IEEE Transactions on Communications*, Vol. 63, Issue 9, 2015, pp. 3029-3056.

[2]. M. R. Ghourtani, S. K. A. R. R. Boddireddy, J. J. Xiao, M. Di Renzo, Link-level evaluation of uplink cell-free MIMO in 5G NR over frequency-selective channels, *IEEE Open Journal of the Communications Society*, Vol. 6, 2025, pp. 632-649.

[3]. C.-X. Wang, J. Bian, J. Sun, W. Zhang, et al., A survey of 5G channel measurements and models, *IEEE Communications Surveys & Tutorials*, Vol. 20, Issue 4, 2018, pp. 3142-3168.

[4]. T. Qiu, J. Chi, X. Zhou, Z. Ning, et al., Edge computing in industrial internet of things: Architecture, advances and challenges, *IEEE Communications Surveys & Tutorials*, Vol. 22, Issue 4, 2020, pp. 2462-2491.

[5]. Q.-V. Pham, F. Fang, V. N. Ha, M. J. Piran, et al., A survey of multi-access edge computing in 5G and beyond: Fundamentals, technology integration, and state-of-the-art, *IEEE Access*, Vol. 8, 2020, pp. 116974-117017.

[6]. S. Barbarossa, S. Sardellitti, P. Di Lorenzo, Communicating while computing: Distributed mobile cloud computing over 5G heterogeneous networks, *IEEE Signal Processing Magazine*, Vol. 31, Issue 6, 2014, pp. 45-55.

[7]. Service requirements for the 5G system; Stage 1, Technical Specification TS 22.261 version 15.9.0 Release 15, *3GPP*, 2019.

[8]. Nemo Handy measurement solution, https://www.keysight.com/at/de/product/NTH50047B/nemo-handy-handheld-measurement-solution.html

[9]. Clearpath Robotics, Husky A200 User Manual, https://www.clearpathrobotics.com/wp-content/uploads/2013/02/Husky-A200-UGV-UserManual-0.12.pdf

[10]. M. Bauer, P. Taras, A. Zeman, Investigating the impact of communication delays and bandwidth restrictions on remote operations of unmanned systems, in *Proceedings of the 1st International Conference on Drones and Unmanned Systems (DAUS'25)*, 2025, pp. 13-19.

[11]. NVIDIA, Introduction to Sionna RT, https://nvlabs.github.io/sionna/rt/tutorials/Introduction.html

(021)

STRIDE – Simulation Testbed for Real-Time In-Flight Deconfliction Experiments

L. Carlén Eriksson, E. Persson, M. Ekström, C. Ahlberg and B. Çürüklü
Mälardalen University, Department of Engineering Sciences, Universitetsplan 1, 72123 Västerås, Sweden
Tel.: + 46(0)21-101300
E-mail: lennie.carlen.eriksson@mdu.se

Summary: The safe integration of multiple unmanned aerial vehicles (UAVs) into shared airspace requires tactical deconfliction methods that ensure separation in both space and time while remaining compatible with the non-prescriptive European U-space regulatory framework. This paper presents a modular and algorithm-agnostic testbed for experimental evaluation of on-board tactical deconfliction within a Z-volume in U-space, where airspace occupancy is defined in four dimensions. The testbed integrates the PX4 flight stack, ROS 2, and the Gazebo simulation environment to support timing-aware trajectory planning, execution, and decentralised conflict detection under realistic vehicle dynamics and communication conditions. A dual-layer communication architecture is employed, combining global mission management over cellular networks with local peer-to-peer broadcast inspired by ADS-L for cooperative traffic awareness. Each UAV maintains a local discretised 4D airspace representation and performs short-horizon motion prediction using uncertainty-aware contingency volumes that account for state estimation error, communication delay, and prediction uncertainty. Simulation and flight experiments demonstrate that the prescribed entry and exit times are met with successful decentralised conflict detection and avoidance without collisions.

Keywords: Multi-UAV, U-space, Traffic detection, Traffic collision, Traffic deconfliction.

1. Introduction

To safely integrate an increasing number of Unmanned Aerial Vehicles (UAVs) into shared airspace, new traffic management systems are required. In Europe, U-space provides such a framework, defining functional requirements for traffic information, tactical conflict detection, and conflict resolution within the Z-volume [1], [2]. In this context, each UAV operates according to a 4D operational volume where every spatial cell is associated with an entry and exit time, and safe separation must therefore be maintained in both space and time.

Existing multi-UAV research platforms treat time primarily as an internal parameter for trajectory execution rather than as an explicit dimension for conflict detection and resolution. Such an approach limits their suitability for evaluating onboard tactical deconfliction under U-space Z-volume assumptions, where entry/exit timing and temporal separation are fundamental requirements.

This paper presents a modular and algorithm-agnostic testbed for experimental evaluation of onboard tactical deconfliction in U-space Z-volumes. The testbed combines a real flight stack, decentralised peer-to-peer communication, time-dependent 4D trajectory execution, and a mission manager. A baseline deconfliction method is implemented to validate testbed functionality. However, comparative algorithm evaluation is left for future work.

The main contribution is the testbed architecture itself, which enables repeatable evaluation in both simulation and physical flight through native 4D trajectory execution with prescribed entry and exit times. Experimental results demonstrate decentralised conflict detection and avoidance under communication delay while maintaining temporal and spatial separation.

2. Background

The European U-space framework establishes the regulatory and conceptual basis for the integration of unmanned aircraft into shared airspace. At the regulatory level, Commission Implementing Regulation (EU) 2021/664 defines functional service requirements for traffic information and conflict resolution while deliberately avoiding prescriptive technical or architectural choices [3]. At the conceptual level, the SESAR U-space Concept of Operations [2] provides a common operational interpretation of these requirements, introducing concepts such as tactical deconfliction, 4D trajectory intent, cooperative information exchange, and Z-volume operations.

Together, the regulation and the SESAR Concept of Operations define what capabilities are required, but not how capabilities are to be implemented. Responsibility for safety assurance remains with the Unmanned Aerial System (UAS) operator, and implementation-level design choices are intentionally left open. As a result, the implementation and evaluation of onboard tactical deconfliction depend on experimental assessment under defined assumptions rather than on compliance with prescribed technical solutions.

The following subsections summarize the regulatory assumptions and conceptual foundations

relevant to this work and motivate the need for a dedicated evaluation environment.

2.1. Regulatory Context

The U-space regulatory framework specifies functional requirements for traffic information and conflict resolution services while remaining neutral with respect to technical implementation. Regulation (EU) 2021/664 defines service obligations for U-space operations but does not prescribe specific algorithms, separation minimum, discretisation methods, or performance metrics for tactical deconfliction [3]. Instead, concepts such as safe separation, 4D trajectory intent, and Z-volume operations are defined at a conceptual level, with responsibility for safety assurance assigned to the UAS operator rather than to a specific system architecture.

EASA Acceptable Means of Compliance and Guidance Material further clarify that multiple technical solutions may be used to meet these functional requirements. On-board Detect-and-Avoid capabilities are acknowledged as a valid means of compliance, especially in latency-critical situations or under degraded communication conditions, while leaving implementation details to the system designer [4].

2.2. U-Space Tactical Deconfliction

U-space tactical deconfliction is not restricted to a centralised implementation. While the regulatory framework requires that conflict resolution services be provided, it does not prescribe whether tactical deconfliction is performed by external U-space services or on-board the UAV [3]. U-space operational concepts explicitly allow centralised, on-board, and hybrid approaches, reflecting different assumptions regarding communication availability, automation level, and allocation of responsibility [2].

2.3. Peer-to-Peer Communication

The U-space framework does not mandate direct communication between UAS, but neither does it restrict the use of local peer-to-peer information exchange to support on-board functions. The regulatory framework remains neutral with respect to communication architectures and does not require that all traffic information used for tactical deconfliction be mediated by **external** U-space services [3]. Locally available cooperative traffic information therefore constitutes a permissible input for on-board tactical deconfliction, particularly in scenarios where low latency or robustness to communication degradation is required.

U-space operational concepts assume the availability of cooperative traffic information for in-flight conflict detection and resolution, without prescribing how such information is exchanged [2]. This includes the possibility of direct information exchange between nearby airspace users as a complement to U-space services. From an aviation perspective, such cooperative local broadcast mechanisms are conceptually aligned with an Automatic Dependent Surveillance Light (ADS-L) style surveillance, in which dependent state information is shared directly between participants to support situational awareness and tactical separation [5]. ADS-L traffic messages include a global time-stamp indicating when the state information was generated on-board the transmitting UAV, while communication is based on contention-driven broadcast and does not provide deterministic delivery latency [5].

2.4. Z-Volume Representation and Discretisation

In U-space, a Z-volume is defined as a volume of airspace with specific access conditions and service requirements but does not prescribe how such volumes are to be represented internally by UAS or U-space services. The regulatory framework specifies functional requirements related to traffic information and conflict resolution while remaining neutral with respect to airspace discretisation, spatial and temporal resolution, or trajectory representation [3]. Similarly, U-space operational concepts introduce the use of 4D trajectory intent and prediction for conflict detection but do not define a standardized discretisation of Z-volumes or separation parameters [2].

In this work, the Z-volume is represented using an internal discretized spatiotemporal model to support on-board prediction and tactical deconfliction. The discretisation is used as an implementation-level representation and is not intended to describe a regulatory or standardized Z-volume structure. Each UAS maintains a local 4D representation of the surrounding airspace based on cooperative state information and its own planned trajectory. This representation is used to evaluate predicted separation over a finite horizon and to trigger local replanning when conflicts are detected.

The spatial and temporal resolutions of the discretisation are selected based on assumptions regarding vehicle dynamics, communication update rates, and on-board computational resources. These parameters are introduced to enable repeatable experimental evaluation of on-board local deconfliction within a distributed multi-UAV system, rather than to define operational separation requirements or U-space compliance criteria.

2.5. Motivation for a Dedicated Testbed

Existing multi-UAV research platforms support time-parameterised trajectory generation and tracking, primarily to ensure smooth control, synchronisation, and coordinated motion. Representative examples

include the MRS UAV System developed at Czech Technical University (CTU) in Prague [6] and other PX4[2]- and Robot Operating system (ROS[3])-based multi-UAV research stacks, such as Aerostack2 [7]. In these systems, time is typically used as an internal parameter for trajectory execution rather than as an explicit constraint. As a result, trajectories are not represented with required times of arrival, nor is time treated as an important dimension for conflict detection and resolution.

In comparison, U-space concepts assume 4D trajectory intent within the Z-volume, where tactical deconfliction depends on the predicted occupancy of airspace volumes over time [2]. As discussed in Section 2.2, the regulatory framework permits on-board deconfliction as a valid architectural option from time-critical conflicts or degraded connectivity. Section 2.3 further establishes that ADS-L style peer-to-peer communication provides a suitable mechanism for cooperative state exchange in such scenarios. Evaluating on-board tactical deconfliction under these assumptions requires control over arrival times, entry and exit timing for the volumes, as well as temporal separation. This methodological gap motivated the development of a dedicated testbed designed to support timing-aware trajectory planning and on-board local deconfliction for repeatable evaluation in both simulation and real flight.

3. Implementation

The proposed testbed, as described in Fig. 1, is a modular simulation and control framework designed for testing and evaluating multi-UAV coordination and tactical conflict resolution within the Z-volume in U-space. The testbed integrates the PX4 flight stack[1], ROS2[4] and the Gazebo[5] simulation environment, allowing realistic modelling of UAV dynamics such as multi-rotor control, environmental physics and inter-vehicle communication in both simulation and on physical platforms, with the ability to log any data produced in the system. The testbed supports coordinated multi-UAV operations, mission planning, trajectory generation and tactical deconfliction.

The testbed uses a global and local communication architecture. The global layer connects UAVs to a web-based Mission Management Tool (MMT) for mission planning, assignment, progress reporting, and data retrieval over cellular networks [8, 9]. The local layer provides peer-to-peer communication over a wireless local area network, where each UAV broadcasts its position, velocity, identification, and operational priority while listening to similar messages from nearby UAVs. The distributed exchange allows each UAV to maintain local situational awareness and perform tactical deconfliction without centralised control.

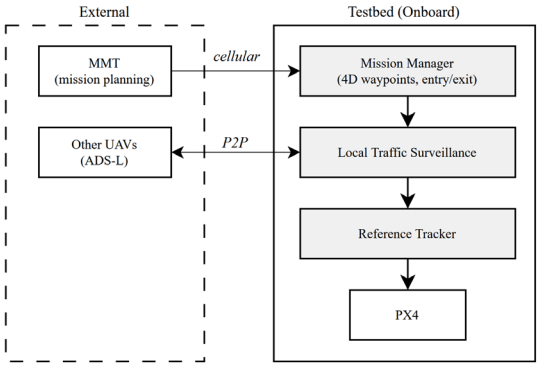

Fig. 1. Flowchart describing the testbed. Arrows indicate data flow.

The mission manager transforms global waypoints into local coordinates and generates flight plans adapted to constraints on position, velocity, and acceleration. Trajectories can be regenerated when conflicts or changing conditions are detected. The reference tracker follows the planned trajectories and allows different tracking algorithms and control schemes to be compared within the same architecture.

The Local Traffic Surveillance system enables decentralised detection and avoidance of potential conflicts based on local prediction and protected airspace evaluation by using a broadcast and a listener function. To perform on-board traffic deconfliction, each UAV evaluates conflicts from its own perspective, using ADS-L–style broadcast messages received from nearby UAVs. Broadcast messages contain identification, global position, velocity, priority, and a global time-stamp indicating when the data was generated on-board the transmitting UAV. Acceleration can be estimated at the listener by differentiating consecutive velocity updates using their associated time-stamps. Using these inputs, each UAV predicts the short-term motion of surrounding UAVs over a prediction horizon and compares it with its own planned trajectory. The predicted relative position between two UAVs is computed using a constant-acceleration model. Within a prediction horizon, the relative position between two UAVs is computed as in equation (1).

$$r(t) = r_0 + v_r t + \frac{1}{2} a_r t^2, \quad (1)$$

where r_0 and v_r are the relative position and velocity at the current time, and a_r is the relative acceleration estimated from consecutive velocity broadcasts using their time-stamps.

4. Experimental Evaluation

The testbed architecture was evaluated in both simulation and full-scale physical flight experiments,

[2] https://docs.px4.io/main/en/ros2/
[3] www.ros.org
[4] https://github.com/ros2
[5] https://gazebosim.org/home

while the tactical deconfliction functionality was assessed exclusively within the simulation environment. By applying the regulatory context from Section 2.1 to this work, the safety thresholds, discretisation strategies, and performance metrics adopted are introduced as implementation-level parameters for evaluating on-board local deconfliction in a multi-UAV system, operating within a U-space Z-volume.

4.1. Timing Accuracy Experiment

To evaluate the path-following functionality in a Z-volume, an experiment was set up where an UAV's ability to follow specified entry and exit times was tested. To validate the testbed, an acceptable time range was set to $\pm 1000\ ms$ of the desired exit time. To test the timing accuracy, 10 different paths were created with lengths varying from 10 m to 1000 m together with 5 varied sets of required entry and exit times for all the paths. All paths were dynamically feasible for the UAV within the required time constraints. The velocity and acceleration constraints applied along the x-, y-, and z- axis in the experiments were $v_{max} = [10.0,10.0,5.0]\ m/s$ and $a_{max} = [2.0,2.0,2.0]\ m/s^2$. Wind was also simulated in varying directions to test the reference tracker's ability to follow the trajectory.

4.2. Multi-UAV Conflict Scenario

To verify the testbed's ability to implement prediction and avoidance algorithms within a Z-volume, an experiment was performed. In the experiment, five multi-rotor UAVs operated in an urban environment derived from geographic data for an area near Västerås, Sweden. Each of the five UAVs was assigned a number designation between 1 to 5. The number also represents which priority they have for tactical deconfliction. The priority decides who should perform the collision avoidance maneuver. Higher numbers always avoid smaller numbers. Fixed priorities are used to simplify evaluation and ensure deterministic conflict resolution. Investigating adaptive or rule-based priority assignment is left for future work. Each of the UAVs has paths assigned to it and each path segment has an entry time and an exit time. The paths are setup so that the UAVs fly between two points, where each of the points represents a starting position and goal position for the path segment. A visual description of the experimental setup can be seen in Fig. 2.

For conflict evaluation, a time-varying safety contingency volume is constructed around each trajectory position within a prediction horizon by combining the UAV footprint with margins accounting for bounded state estimation error, communication delay, and short-term prediction uncertainty. The resulting contingency volume is defined as the sum of these terms, as shown in equation (2). Prediction uncertainty is modelled as a horizon-dependent growth term. A conflict is detected if the predicted separation distance between two UAVs is within the contingency volume at any point within the prediction horizon, which then triggers local replanning. The contingency volume used for conflict detection is defined as:

$$R(t) = R_{phys} + R_{est} + R_{com} + R_{pred}(t), \quad (2)$$

where R_{phys} represents the UAV's footprint, R_{est} is the bounds estimation uncertainty, R_{com} is the communication delay, and $R_{pred}(t)$ represents the prediction uncertainty growth over the prediction horizon.

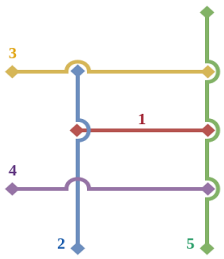

Fig. 2. Experimental setup. Each colour represents a path a UAV flies back and forth. Each arc in the path represents expected avoidance behaviour. The number assigned to each path represents both the UAV's priority and its numerical designation. Every UAV was flying at the same reference altitude.

Communication delay is accounted for using the message age, derived from the difference between the local time and the time-stamp included in the received broadcast, resulting in an additional buffer term defined in equation (3). The communication-related buffer is calculated as:

$$R_{com} = \| v \| \Delta t_{age} + \frac{1}{2} a_{max} \Delta t_{age}^2, \quad (3)$$

where Δt_{age} is the age of the last received state update, computed from the difference between the local time and the time-stamp provided in the ADS-L message. v is the reported velocity, and a_{max} is an upper limit on acceleration.

The prediction logic follows established approaches in decentralised multi-robot collision avoidance, where short-horizon motion prediction is combined with uncertainty-aware safety margins through inflated safety volumes to account for bounded state uncertainty and prediction error [10]. A similar modelling principle is employed in aviation risk assessment frameworks such as the Specific Operations Risk Assessment (SORA), where contingency and operational volumes are defined by expanding the flight volume to account for deviations from the planned trajectory due to uncertainty, delays, and abnormal conditions [11]. Together, these approaches motivate the use of additive safety buffers around predicted UAV trajectories for decentralised conflict detection.

Using these equations, it is possible to predict collisions. To verify the functionality of the testbed, an ego-centric method described in equation (4) is used for collision prediction, where overlapping contingency volumes do not necessarily trigger a deconfliction event. It works from the perspective of UAV i where a conflict is detected if the predicted position of another UAV j lies within the protected airspace of UAV i:

$$\left\|\hat{p}_j(t) - \hat{p}_i(t)\right\| < R_i(t) \quad (4)$$

To verify the testbed's ability to support replanning of a trajectory, a method inspired by T. Baca, where a z-axis offset was applied to the reference trajectory of the MPC tracker [12], was implemented. In this experiment the reference trajectory of the MPC tracker is not altered. Instead, the time-dependent trajectory is altered. From one UAV's perspective, when one or more collisions are predicted with lower priority UAVs, the time for the first and last positions within the contingency volume is saved. Between these time samples an offset is added to the z-axis. The offset is calculated by subtracting the height difference between the UAVs from the height of the contingency volume. When these new points in time are created, a new trajectory calculation is performed, which take the current time, the two avoidance points and the exit time of the Z-volume into consideration.

5. Results

The results in this work assess architectural and algorithmic feasibility under defined assumptions, rather than proposing standardized U-space separation criteria.

The timing accuracy experiment evaluated the ability for a UAV to follow 4D trajectories with a t_{entry} and a t_{exit}. The duration is calculated by $T = t_{exit} - t_{entry}$. The experiment found that the max deviation $\Delta T = \left\|T_{actual} - T_{planned}\right\|$ was $\Delta T = 170\,\text{ms}$ on a path length of $1000\,m$ for $T_{planned} = 300\,s$. The average deviation T_{avg} for all the tested scenarios was $T_{avg} = 90\,ms$.

The results for the multi-UAV conflict scenario, in which the experiment setup is visualized in Fig. 2, can be seen in Table 1 and describes the five UAVs and their corresponding performance and minimal separation distance to other UAVs. The number for each UAV also corresponds to the priority. An UAV with higher priority number must avoid UAVs with lower priority numbers. The resulting maximum deviation between the entry and exit times was negligible. Table 1 shows that no collisions occurred and all the predicted collisions could be solved by replanning once. The lowest minimal separation for all the UAVs was $7.91\,m$. The difference between the calculated minimum deviation between UAVs is due to GPS noise and an offset in the sampling rate.

Table 1. The results from the perspective of 5 different UAVs using a broadcaster at 1Hz. Cells without numbers show combinations where the UAVs were outside of each other's broadcasting range.

UAV	Paths	Predicted collisions	Trajectory replanned	Minimum separation distance				
				UAV 1	UAV 2	UAV 3	UAV 4	UAV 5
1	40	0	0		8.4 m	56.73 m	56.72 m	11.61 m
2	20	11	11	8.38 m		9.32 m	8.03 m	-
3	20	9	9	56.73 m	9.37 m		-	9.3 m
4	20	8	8	29.2 m	7.91 m	-		61.87 m
5	10	14	14	11.64 m	-	9.29 m	61.83 m	

6. Conclusions

This paper presents a modular and algorithm-agnostic testbed for the experimental evaluation of on-board tactical deconfliction within a Z-volume in U-space context.

The primary contribution is the design of the framework, which combines an established flight stack, communication, time-dependent trajectory execution, and prediction-based conflict detection and avoidance. The framework enables repeatable and systematic evaluations in both simulation and on physical UAV platforms.

The results of the timing accuracy experiment confirmed the ability to follow U-space 4D trajectories in a Z-volume with set entry and exit times. Sub-second time deviations were achieved, which confirmed the ability to evaluate U-space concepts based on 4D trajectories.

The multi-UAV conflict scenario showed that the testbed supported decentralised prediction and avoidance while handling communication delays by taking message age into consideration, instead of using a deterministic latency. The predicted collisions were resolved through local replanning while also maintaining safe separation distances.

This work does not propose a standardized solution for separation or tactical deconfliction within U-space. Instead, it presents a possibility to evaluate tactical deconfliction methods within the U-space regulations. The testbed enables comparisons between different prediction and avoidance methods within the same architectural context.

Future work will expand the testbed to evaluate adaptive priority handling and build a tighter integration with external U-space services for the implementation of hybrid centralised–decentralised deconfliction solutions. Additional work will also

focus on evaluating different tactical deconfliction and prediction solutions, both in simulation and on real UAV platforms.

References

[1]. C. Barrado, M. Boyero, L. Brucculeri, G. Ferrara, et al., U-Space concept of operations: A key enabler for opening airspace to emerging low-altitude operations, *Aerospace*, Vol. 7, Issue 3, 2020, 24.

[2]. U-space Concept of Operations (ConOps), Fourth Edition, SESAR 3 Joint Undertaking, 2023, https://www.sesarju.eu/node/4544

[3]. Commission Implementing Regulation (EU) 2021/664 of 22 April 2021 on a regulatory framework for the U-space, *European Commission*, 2021.

[4]. Acceptable means of compliance and guidance material to Regulation (EU) 2021/664 on a regulatory framework for the U-space, Issue 1, European Union Aviation Safety Agency, 2022, https://www.easa.europa.eu/en/downloads/137398/en

[5]. Technical specification for ADS-L on SRD-860, Issue 2, *European Union Aviation Safety Agency*, 2024.

[6]. T. Bača, M. Petrlík, M. Vrba, V. Špurný, et al., The MRS UAV system: Pushing the frontiers of reproducible research, real-world deployment, and education with autonomous unmanned aerial vehicles, *Journal of Intelligent and Robotic Systems*, Vol. 102, 2021, 26.

[7]. M. Fernandez-Cortizas, M. Molina, P. Arias-Perez, R. Perez-Segui, et al., Aerostack2: A software framework for developing multi-robot aerial systems, *IEEE Robotics and Automation Letters*, Vol. 9, Issue 3, 2024, pp. 2383-2390.

[8]. A. E. Ameri, V. G. Lindgren, B. Çürüklü, R. Fresco, et al., A user interface for supervision of missions in the multi-UAV context using text-to-speech, in *Proceedings of the 12th International Conference on Human-Agent Interaction (HAI'24)*, 2024, pp. 402-403.

[9]. A. E. Ameri, B. Miloradovic, B. Çürüklü, A. V. Papadopoulos, et al., Interplay of human and AI solvers on a planning problem, in *Proceedings of the IEEE International Conference on Systems, Man, and Cybernetics (SMC'23)*, 2023, pp. 3166-3173.

[10]. H. Zhu, B. Brito, J. Alonso-Mora, Decentralized probabilistic multi-robot collision avoidance using buffered uncertainty-aware Voronoi cells, *Autonomous Robots*, Vol. 46, Issue 2, 2022, pp. 401-420.

[11]. Specific Operations Risk Assessment (SORA), Main Body, Version 2.5, *Joint Authorities for Rulemaking on Unmanned Systems (JARUS)*, 2024.

[12]. T. Bača, D. Hert, G. Loianno, M. Saska, et al., Model predictive trajectory tracking and collision avoidance for reliable outdoor deployment of unmanned aerial vehicles, in *Proceedings of the IEEE/RSJ International Conference on Intelligent Robots and Systems (IROS'18)*, 2018, pp. 6753-6760.

(022)

An Integrated Process for UAS Available Airspace Evaluation Based on Multi Criteria Decision-Making

Geon Woo Kim, and Hui Yang Kim
Department of Advanced Air Transportation of Korea Aerospace University,
76, Hanggongdaehak-ro, Deogyang-gu, Goyang-si, Republic of Korea
Tel.: +82-10-6416-5555
E-mail: ggw0915@naver.com

Summary: UAS operating at low altitudes must account for multiple constraints, such as ground population exposure and obstacles including buildings. Accordingly, this study proposes a UAS available airspace evaluation process that incorporates four primary constraints by using multi-criteria decision-making. In particular, two types of geofences are implemented to ensure safe separation from obstacles, while the integration of dynamic population data and altitude-dependent geofence constraints enables a more realistic estimation of airspace usability in dense urban settings. Finally, a case study is performed in Yeongdeungpo-gu, Seoul, to evaluate the available airspace ratio across different altitudes. The proposed process quantitatively assesses multiple constraints and identifies practically usable airspace for UAS operations in complex urban environments.

Keywords: Unmanned aircraft system, Available airspace evaluation, Ground risk, Geofence.

1. Introduction

As the use of Unmanned Aircraft Systems (UAS) continues to expand across various sectors, their operations in urban environments are expected to grow accordingly. Low-altitude UAS flights must account for multiple operational constraints, including ground population exposure and physical obstacles such as buildings.

This study aims to identify airspace in which UAS can operate safely under varying flight altitudes and time periods. The proposed method integrates four primary constraints – Important National Facilities, airspace restrictions, ground risk, and obstacles – to determine available airspace.

2. Methodology

This study applies a Multi-Criteria Decision-Making (MCDM) process that integrates four key criteria for evaluating available airspace. As shown in Fig. 1, the process first assesses airspace restrictions and Important National Facilities, and then incorporates ground risk and geofencing to determine the usable airspace.

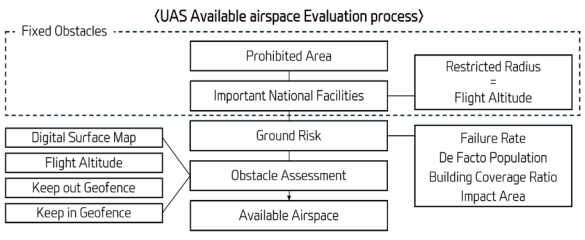

Fig. 1. UAS Available Airspace Evaluation Process.

2.1. Airspace and Important National Facilities

Among the airspace categories classified by purpose of use, Prohibited Areas are defined as regions where flight is forbidden due to safety, national defense, or other public concerns. In these areas, UAS operations are restricted to maintain safety and prevent potential security risks.

Important National Facilities, as defined in the United Defense Act of the Republic of Korea, are sites whose damage or destruction would pose serious risks to national security or public safety. To avoid such risks, UAS operations should be restricted in their vicinity. The restricted radius applied in this study follows the Specific Operations Risk Assessment (SORA) approach, which assigns a safety radius corresponding to the UAS flight altitude [1].

2.2. Ground Risk

Unlike conventional air traffic that operates at higher elevations, UAS flying in low-level airspace must consider their potential impact on people on the ground. To quantitatively assess this impact, ground risk within the target region, as defined in Equation (1), was evaluated.

$$\lambda_{fatality} = \lambda_{fatal\ accident} \times N_{people} \times P_{\text{Fatal|Impact}} \quad (1)$$

Here, $\lambda_{\text{fatality}}$ denotes the probability of a fatality involving a third party on the ground, while $\lambda_{\text{fatal accident}}$ represents the probability of a fatal accident. $P_{\text{Fatal|Impact}}$ indicates the probability of a fatality given a collision between the aircraft and a person. The number of people exposed to a fatal accident, N_{people}, is calculated as shown in Equation (2).

$$N_{people} = D_{population} \times F_{exposure} \times A_{impact} \quad (2)$$

Here, $D_{\text{population}}$ represents the population within each grid cell, F_{exposure} denotes the proportion of people exposed to risk, and A_{impact} refers to the impact area. If the calculated ground risk is lower than the Target Level of Safety (TLS), operations within the area are permitted. The TLS for ground risk was set to 10^{-6}, as suggested in the SORA [1].

2.3. Obstacles

To model the actual flight environment, building heights were combined with terrain elevation to generate a Digital Surface Map (DSM) of the study area. Two types of geofences were applied to assess airspace [2]. The Keep-out geofence creates a safety radius around buildings, while the Keep-in geofence excludes airspace narrower than 2r to account for aircraft position error r. Assuming constant-altitude flight, airspace segments rendered inaccessible by the Keep-in geofence were closed.

3. Case Study

A case study was conducted in Yeongdeungpo-gu, Seoul, to verify the applicability of the proposed process. Table 1 presents the parameters used in the case study. The case study was conducted using a DJI MATRICE 400. $\lambda_{fatal\ accident}$ was set to 5×10^{-6} by referencing the Bayesian UAS failure model proposed by Peng Han [3], and $P_{\text{Fatal|Impact}}$ was set to 1 following the study by Breunig, which analyzed the relationship between kinetic energy and fatality probability [4]. $D_{population}$ was estimated by allocating de facto population at the census output area level provided by the Seoul Metropolitan Government to grid cells. During the preprocessing stage, it was assumed that no population exists in river areas; therefore, the population was randomly distributed within non-river areas. $F_{exposure}$ was estimated using the building coverage ratio of each grid cell. The population corresponding to the proportion of building area relative to the grid area was assumed to be located indoors and to be fully protected from impact with the aircraft. Melnyk [5] derived the relationship between aircraft mass and impact area as

$$A_{impact} = m \times 0.220464 \quad (3)$$

where m denotes the aircraft mass. Based on this relationship, A_{impact} was set to 3.5 m^2 in this study. The buffer distance for keep-out geofences was determined based on the work of Oh [6], with 15 m applied to buildings lower than 60 m and 30 m applied to buildings exceeding 60 m in height. In addition, a vertical buffer of 30 m above the building height was applied in accordance with ICAO guidelines. A keep-in geofence was additionally defined to account for the positional uncertainty of the aircraft. However, as no empirically validated references are available regarding the magnitude of UAS positioning errors in this context, the radius of the keep-in geofence was assumed to be 5 m in this study.

Table 1. Parameters used in case study.

Spatiotemporal Background			
Date	Time		Height
Aug 20, 2025	14:00		120 m
Ground Risk			
Aircraft		MTOW	
DJI MATRICE 400		15.8 kg	
$\lambda_{fatal\ accident}$	$P_{\text{Fatal\|Impact}}$		A_{impact}
5×10^{-6}	1		3.5 m^2
Geofence			
Under 60 m	Over 60 m	Position Error	Vertical Separation
15 m	30 m	5 m	30 m

Fig. 2 presents the available airspace at an altitude of 120 m at 2:00 p.m. on August 20. Fig. 3 illustrates the variation in the available airspace ratio with changes in altitude. According to the figure, two key observations can be identified. First, a sharp increase in the available airspace ratio is observed at an altitude of 90 m. An increase in the available airspace ratio indicates a reduction in operational constraints; therefore, this altitude can be considered a potential threshold for defining a minimum safe flight altitude in complex urban environments.

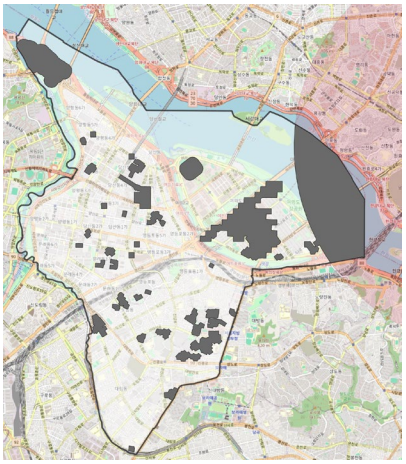

Fig. 2. 120 m airspace analysis on August 20, 14:00.

Second, a slight decrease in the available airspace ratio is observed below 90 m. This pattern is attributed to the method used in this study to define the restricted radius around Important National Facilities. Under this altitude, even with increasing altitude, the constraints imposed by obstacles do not change significantly.

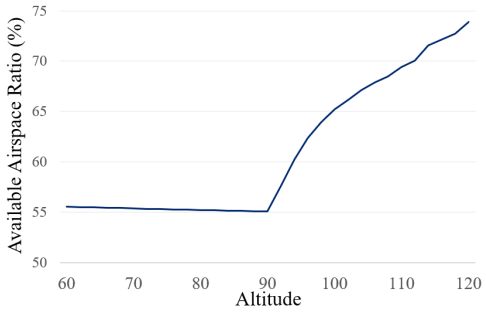

Fig. 3. Variation in available airspace by altitude(R).

4. Conclusions

This study presented an evaluation process for determining available airspace for UAS operations by integrating four major safety constraints. The proposed process combines building heights and terrain elevation and applies keep-in and keep-out geofences that account for aircraft positional uncertainty, thereby removing infeasible areas and deriving operationally realistic available airspace. Considering these characteristics, this study employed an elimination method, one of the non-compensatory MCDM approaches, which is suitable for available airspace analysis problems where safety constraints play a dominant role.

However, while the adopted approach is effective for safety-based decision-making, several limitations remain. Since all constraints are eliminated based on identical reference criteria, it is difficult to directly reflect operator-specific preferences. In addition, due to the lack of reliable aircraft failure rate data and precise measurements of positional uncertainty, some parameters were determined based on assumptions. Applying identical geofence requirements across all scenarios, despite potential variations depending on flight speed or aircraft type, also constitutes a limitation of this study.

Future research will extend this work by addressing path planning and allocation problems within the available airspace derived from the proposed process, incorporating user preferences and weighting schemes. The ultimate goal is to develop UAS route planning algorithms that ensure safety while simultaneously considering operational efficiency and mission objectives.

Acknowledgements

This paper is research supported by the Ministry of Trade, Industry and Energy (A major activities of 2024 Industry-Academia Cooperation: Aviation and defense SW professional Education).

References

[1]. Guidance on Specific Operations Risk Assessment (SORA), Version 2.5, *Joint Authorities for Rulemaking on Unmanned Systems (JARUS)*, 2024.

[2]. J. Cho, Y. Yoon, How to assess the capacity of urban airspace: A topological approach using keep-in and keep-out geofence, *Transportation Research Part C: Emerging Technologies*, Vol. 92, 2018, pp. 137-149.

[3]. P. Han, X. Yang, Y. Zhang, L. Yan, Quantitative ground risk assessment for urban logistical unmanned aerial vehicle (UAV) based on Bayesian network, *Sustainability*, Vol. 14, Issue 9, 2022, 5733.

[4]. J. Breunig, J. Forman, A. Lacher, M. Weibel, Risk-based approach for small unmanned aircraft systems, Technical Report MTR170425, *The MITRE Corporation*, 2018, pp. 14-15.

[5]. R. Melnyk, D. Schrage, V. Volovoi, D. Mavris, A third-party casualty risk model for unmanned aircraft system operations, *Reliability Engineering and System Safety*, Vol. 124, 2014, pp. 105-116.

[6]. S. H. Oh, Y. J. Yoon, Urban drone operations: A data-centric and comprehensive assessment of urban airspace with a Pareto-based approach, *Transportation Research Part A: Policy and Practice*, Vol. 182, 2024, 104033.

(023)

Geolocation of UAV Communication Jammers via Deep Learning-Based Signal Classification on LEO SIGINT Constellation

C. Jung and Z. Yoon
Korea Aerospace University, Department of Artificial Intelligence, 76 Hanggongdaehak-ro,
Deogyang-gu Goyang-City, Geonggi-do, 10540, South Korea
Tel.: + 82 1091384029
E-mail: chanhee1126@kau.kr

Summary: The increasing deployments of small UAVs in modern conflicts and near critical infrastructure has amplified the importance of Counter-UAV (C-UAV) systems. While communication jamming of UAV control frequencies (2.4/5.8 GHz ISM band, S-band)is a primary defense, the jammers themselves become high-priority Electronic Warfare (EW) targets. Rapid detection and geolocation of these jammers are vital for operational superiority. This paper proposes a comprehensive system for geolocating ground-based jammers using a Low Earth Orbit (LEO) SIGINT satellite constellation. We developed a MATLAB-Python hybrid simulation framework, incorporating realistic orbital dynamics, to validate the system. This paper demonstrates the performance of an integrated approach that combines Deep Learning for signal classification with a Dual-Hypothesis Extended Kalman Filter (EKF) algorithm for precise geolocation, offering a robust solution for geolocating terrestrial EW threats.

Keywords: UAV (Unmanned Aerial Vehicle), Jamming, Deep learning, EKF (Extended Kalman Filter), Geolocation, Signal Classification, SIGINT (Signal Intelligence).

1. Introduction

In modern society, securing superiority in the electromagnetic spectrum is essential across various domains, and recent conflicts have further highlighted the growing importance of EW (Electronic Warfare). In particular, jammer signals that can disrupt critical assets such as GPS and military communication systems are emerging as a serious threat. To effectively counter such threats, it is essential to identify jammer signals and rapidly determine the location of the jammer.

Furthermore, as the threat of UAV escalates over battlefields and near critical infrastructure, jamming attacks targeting these drones are now a primary consideration for Counter-UAV (C-UAV) operations. The war in Ukraine is a stark example. Early in the conflict, Russian EW forces were reportedly highly effective, with some reports claiming they neutralized up to 90 % of Ukraine's UAV through sophisticated jamming [1]. This pervasive EW environment has forced both sides into a rapid cycle of adaptation, highlighting that control of the spectrum is central to the drone war.

This research proposes a system to identify these jamming signals and estimate the jammer's location by utilizing the constellation orbital ephemeris of the **Hawkeye 360** signal intelligence (SIGINT) satellites. This paper presents an integrated geolocation framework that combines a Deep Learning model for robust signal classification and a Dual-Hypothesis Extended Kalman Filter (EKF) algorithm [2] for precise location estimation.

2. System Model and Simulation Framework

This study constructed a simulation environment by referencing the mission profiles of operational satellites, such as the Hawkeye 360 constellation. The satellites are assumed to fly in a LEO formation of three, acquiring Time Difference of Arrival (TDOA) and Frequency Difference of Arrival (FDOA) information. The target signal was set as a non-cooperative communication jammer, and the specific simulation parameters are shown in Table 1.

The original signal source utilizes an OFDM-modulated signal, which is commonly employed in UAV communications. To simulate jamming environment, three representative jammer types– Chirp, Wideband, and Tone-were superimposed onto the original signal. The resulting I/Q Constellation Diagram for each signal type are presented in Fig. 1. To replicate realistic satellite reception, the signal data was further processed by incorporating Free Space Path Loss (FSPL), Doppler effects, and Additive White Gaussian Nois e(AWGN).

Table 1. Simulation Parameters.

Parameter	Value
Orbit Model	LEO (575 km)
Target Freq	2.4 GHz, S-band
Jamming Signal Waveform	Chirp, Wideband, Tone
Channel Model	FSPL + Doppler + AWGN

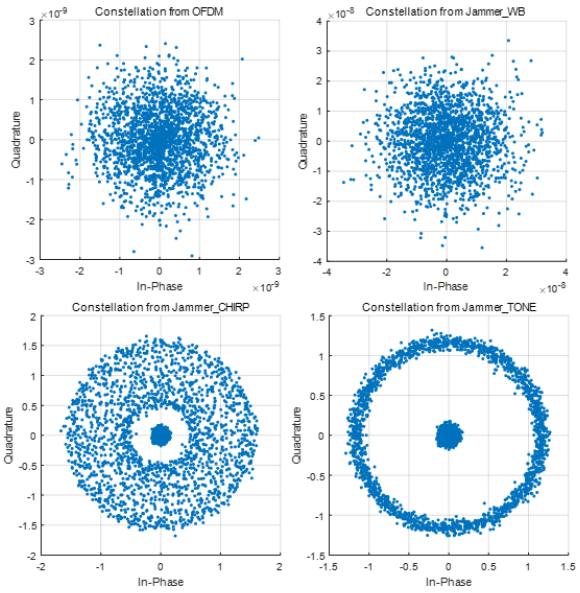

Fig. 1. Constellation Diagram.

3. Methodology

The proposed framework adopts a hybrid simulation architecture that integrates a MATLAB-based environment with a Python-based deep learning pipeline. MATLAB is used to generate signal data and to model satellite orbital dynamics, while Python is employed for signal classification using deep learning model. The overall system flow is illustrated in Fig. 2.

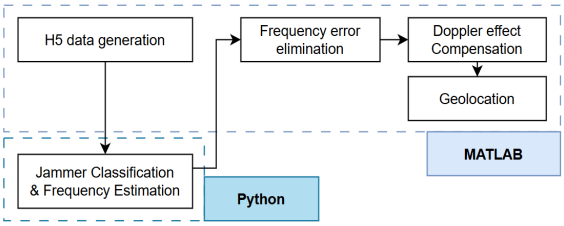

Fig. 2. Hybrid System Architecture.

3.1. Simulation Scenario

The objective of the simulation is to estimate the location of a jammer that neutralizes the communication signals of a UAV, based on data collected by SIGINT satellites. The scenario is implemented using a drone as a representative example of a UAV. As depicted in Fig. 2, the primary objective is to geolocate the jammer by assuming the satellites can successfully intercept the jammer's signal at the same time it is disrupting the drone's operation. The target UAV jammers were simulated in diverse operational environments, including ground-based stationary units and high altitude mobile platforms.

In this study, a simulation was conducted by designing an EW scenario where three SIGINT satellites collect signals from a UAV communicating via OFDM modulation for the purpose of geolocation. The jammer power levels were configured with a base JNR of 10-30 dB, incorporating dynamic biases and a 1.5 dB standard deviation to simulate realistic interference. Signals were collected at a measurement interval of 1 second by a LEO satellite constellation with a baseline determined by their orbital states.

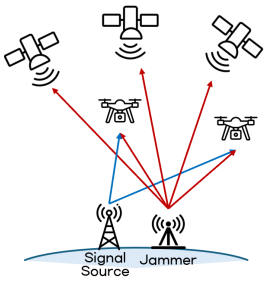

Fig. 3. UAV Jammer Scenario.

3.2. Signal Classification Using CNN-LSTM

The jammer signal data generated in MATLAB (in HDF5 format) is fed into a CNN-LSTM model within the Python environment [3]. Jammer signals exhibit distinct frequency change patterns over time. Therefore, CNN is utilized to extract time-frequency features from the spectrogram, and the LSTM learns the sequential (time-series) features.

The signal processing begins with a preprocessing stage where the PhaseFeatures module extracts amplitude, phase, and phase derivative values from each signal segment to facilitate precise classification. The model employs a multi-scale approach utilizing parallel branches with varying kernel sizes, allowing it to effectively identify both phase variations between pulses and distinct frequency modulation trends for each signal type. The classifier was trained to categorize signals into four distinct class: OFDM_Clean, Jammer_WB, Jammer_TONE, Jammer_CHIRP. As demonstrated in the Confusion Matrix in Fig. 4, the proposed model successfully identified and distinguished all four categories.

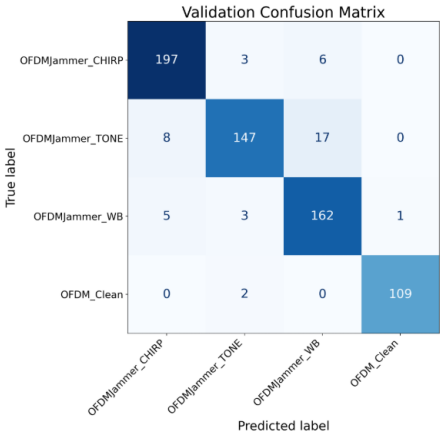

Fig. 4. Validation Confusion Matrix.

Table 2. Classification Report.

Class	OFDM	CHIRP	WB	TONE
F1-score	0.99	0.95	0.91	0.90
Accuracy	0.93			

Following signal classification, the center frequency of the interference signal is estimated through FFT-based peak detection. This estimated frequency, along with the classification confidence scores, is exported in JSON format and subsequently passed to the MATLAN-based geolocation module.

3.3. Geolocation Algorithm Using EKF

Geolocation methods based on TDOA inherently suffers from an ambiguity problem that generates false locations. There is a significant risk of filter divergence if the initial estimate is far from the true location. To enhance measurements robustness, the reference satellite is not fixed. Instead, at each processing step, the satellite with the highest peak is dynamically set as the reference through cross-correlation operations among the three satellites. Since orbital information is obtained via TLE, it was observed that the estimation error using a fixed reference satellite was at least 1.5 times larger than that of the dynamic configuration when calculating basic TDOA/FDOA. The detailed comparison is presented in Fig. 5. Based on these results, dynamic reference satellite assignment is adopted to improve geolocation accuracy.

To address the inherent ambiguity of TDOA-based geolocation, a Dual-Hypothesis Tracking algorithm is employed, as illustrated in the flowchart in Fig. 6. Mode number of one to two are candidate of signal source's location.

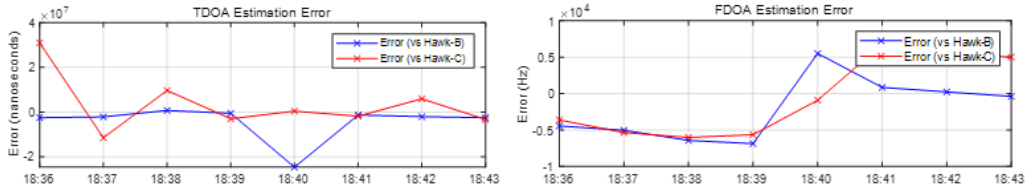

(a) Dynamic reference satellite assignment

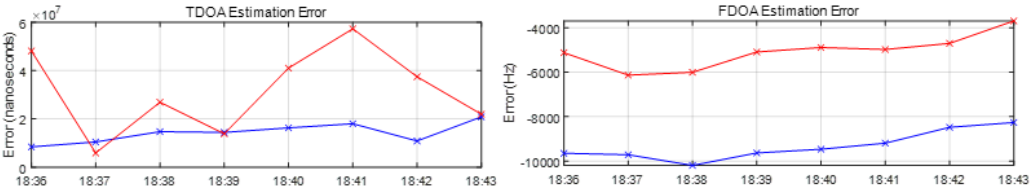

(b) Fixed reference satellite assignment

Fig. 5. Comparison of TDOA/FDOA estimation error.

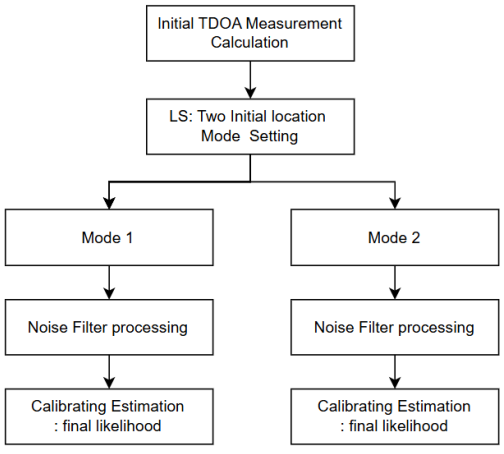

Fig. 6. Flowchart of EKF Geolocation Algorithm.

The core of the proposed algorithm is an EKF that defines the three-dimensional position of the signal source as the state vector $X = [x, y, z]^T$ and performs state estimation in the ECEF coordinate system. For the state dynamics model, a static model is adopted under the assumption that the target signal source is stationary or moving at a low velocity, with residual position uncertainty modeled through the process noise. The TDOA measurement equation h(x) is defined as a nonlinear function of the range differences between the signal source and the satellites. This equation is linearized using the Jacobian matrix H, composed of the differences between unit vectors directed toward each satellite, to establish the observation model. The equations used are as follows:

$$x_k = Fx_{k-1} + w_k,\ w_k \sim N(0, Q_k), \quad (1)$$

$$y_k = h(x_k) + v_k,\ v_k \sim N(0, R_k), \quad (2)$$

$$H_k = \left[\frac{\partial h(x)}{\partial x}\right]_{x=\hat{x}_{k|k-1}} = \begin{bmatrix} (u_{sat1} - u_{Ref})^T \\ (u_{sat2} - u_{Ref})^T \end{bmatrix}, \quad (3)$$

$$R_k = \sum_{j=1}^{N_{sat}} \psi_j \cdot \overline{R_{J,k}} \cdot \psi_j^T + R_{weight}\ [4], \quad (4)$$

$$\mu_{k,m} = \frac{p(z_k|m)\mu_{k-1,m}}{\sum_{j=1}^{M} p(z_k|j)\mu_{k-1,j}} [2] \quad (5)$$

The algorithm operates in the following stages:

Initialization: An optimization is performed on the initial TDOA measurements to establish two candidate location modes (the initial hypotheses) that minimize the error. Rather than relying on a single measurement pulse, a multi-pulse cost function is constructed using measurements collected over two to four pulses. This cost function is defined as the residual between the predicted range differences, derived from satellite positions at each pulse, and the corresponding measured TDOA values.

To find the global minimum of the highly nonlinear cost function, multiple seed points are uniformly distributed over the Earth's surface, and numerical optimization is performed from each seed location. The resulting candidate solutions are then clustered to remove redundancies based on their mutual distances, and the top two points with the lowest cost function values are ultimately selected as the initial hypothesis candidates. An equal initial probability of 0.5 is assigned to each hypothesis at the start of the filtering process.

Parallel Filtering: Two independent EKFs are executed concurrently. Each filter assumes its corresponding hypothesis represents the true location and independently updates its state estimates. The state covariance matrix is updated using Joseph Form, which is adopted to enhance the numerical stability of the filtering process. In addition, the process noise covariance (Q) is modeled using two parallel configurations-a static model (Q_{static}) and a moving model (Q_{moving})-to account for potential target mobility. The measurement noise covariance (R) adopts an adaptive structure in which measurement weights are dynamically adjusted based on the signal-to-noise (SNR) of the received signal. By employing this adaptive noise model in noisy environments, filter divergence can be mitigated even in the presence of anomalous measurement noise. Furthermore, individual noise models are constructed for each satellite to maximize the filter's convergence rate by incorporating weights into the calculations even in cases of unfavorable geometric configurations.

Probability Update: As the satellites move along their orbit, the likelihood of each hypothesis representing the true location is computed in real-time-based on the residual between newly acquired measurements and the corresponding filter predictions. The likelihood is computed according to Bayes' theorem by incorporating the statistical distributions associated with each hypothesis and the corresponding measurement residuals. The updated hypothesis probabilities are subsequently used as weighting factors to form a weighted sum of the candidate position estimates, yielding the final estimated location of the signal source. This multi-hypothesis based EKF framework ensures both the accuracy and robustness of the geolocation estimate, even in the presence of initialization errors or variations in the signal environment.

4. Results

The performance of proposed multi-hypothesis EKF is presented in Fig. 7. The input datasets consist of the clean OFDM signal and three corresponding jamming affected signals types. Across all four scenarios, the system achieved a final geolocation error of less than 650 m. In addition to the final accuracy, the proposed algorithm exhibited stable convergence behavior of candidate hypotheses. As shown in the probability transition plots, the filter consistently identified the correct location mode among the two initial hypotheses within a short observation window.

Furthermore, the adaptive noise models for Q and R allowed the filter to maintain robust performance even under severe interference from wband, chirp, and tone jammers.

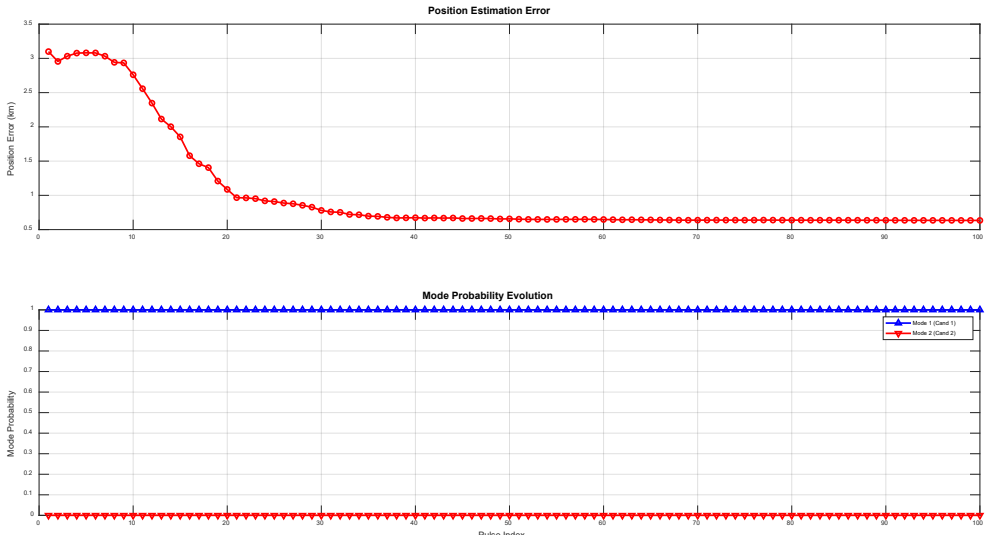

(a) OFDM

Fig. 7 (a). Results of Geolocation.

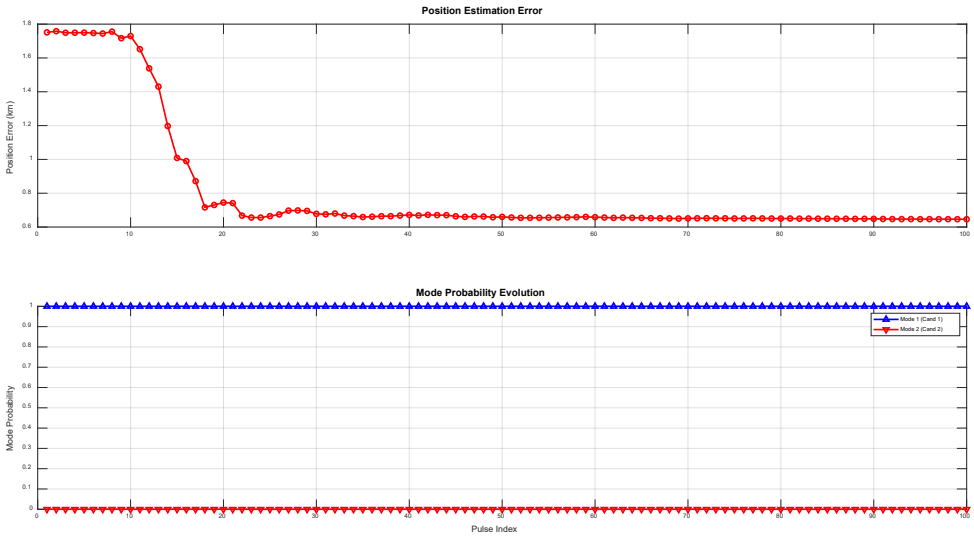

(b) OFDM with WB

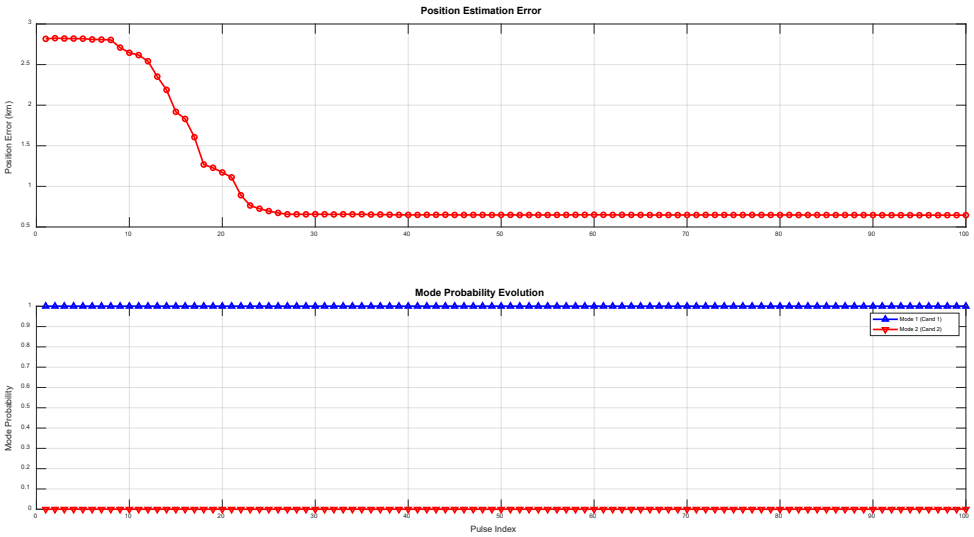

(c) OFDM with CHIRP

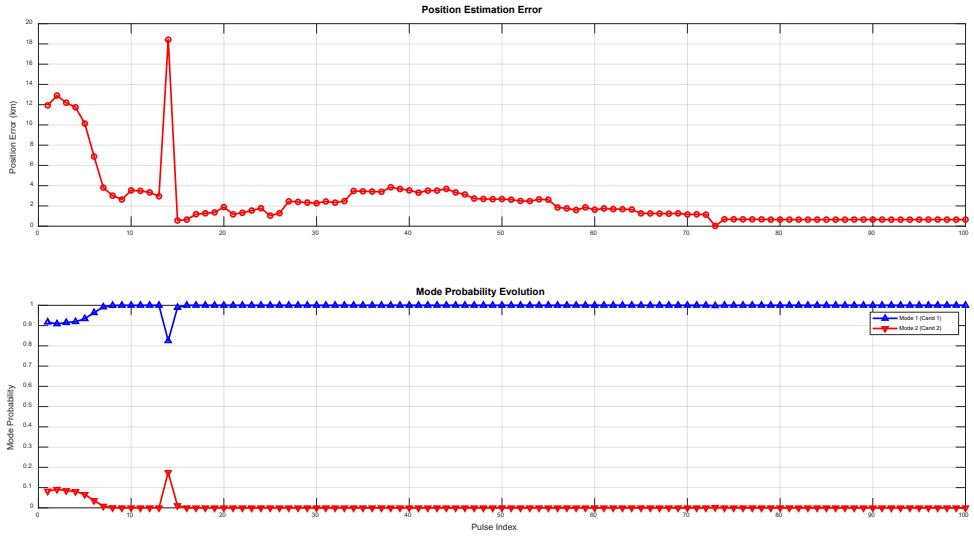

(d) OFDM with TONE

Fig. 7 (b-d). Results of Geolocation.

5. Conclusion

In this work, a simulation framework was proposed for a satellite-based geolocation system utilizing a LEO constellation is presented. The framework is designed to operate in jamming environments by the integration of deep learning-based signal classification and a dual-hypothesis EKF.

Simulation results show that the proposed system effectively identified and classifies various jammer signals types, providing essential signal parameters for the subsequent geolocation process. The dual-hypothesis algorithm successfully resolves the inherent initial position ambiguity associated with TDOA-based geolocation. By dynamically selecting reference satellites and employing adaptive noise models, the jammer's location estimates consistently conve with an error margin on the order of several hundred meters. When compared to a conventional single-hypothesis EKF which often suffers from filter divergence when the initial estimate is far from the truth.

Overall, the results indicate that the integrated approach of deep learning-based signal classification with an adaptive multi-hypothesis EKF significantly improves the robustness of satellite-based geolocation. The proposed framework provides a robust foundation for future SIGINT missions and satellite-based anti-UAV jammer localization strategies in complex EW environments.

Acknowledgements

"This paper is research supported by the Ministry of Trade, Industry and Energy (A major activities of 2024 Industry-Academia Cooperation: Aviation and defense SW professional Education)."

Reference

[1]. D. Axe, Russia's electronic-warfare troops knocked out 90 percent of Ukraine's drones, Forbes, 2022, https://www.forbes.com/sites/davidaxe/2022/12/24/russias-electronic-warfare-troops-knocked-out-90-percent-of-ukraines-drones/

[2]. D. Simon, Optimal State Estimation: Kalman, H∞, and Nonlinear Approaches, *Wiley*, Hoboken, 2006.

[3]. J. Jang, J. Choi, Y. Yoon, A deep learning-based automatic modulation classification method on SDR platforms, *Journal of IKEEE*, Vol. 26, Issue 4, 2022, pp. 45-53.

[4]. J. Khalife, Z. M. Kassas, A static reduced-order multiple-model adaptive estimator for noise identification, *IEEE Transactions on Aerospace and Electronic Systems*, Vol. 59, Issue 3, 2023, pp. 2672-2686.

(024)

Hybrid Distillation with CoT Guidance for Edge-Drone Control Code Generation

Yizhan Feng [1,4], Hichem Snoussi [1,4], Yuhang Wang [2], Jing Teng [2], Abel Cherouat [3,4] and Tian Wang [5]

[1] UR-LIST3N, University of Technology of Troyes, Troyes, France
[2] Institute of Artificial Intelligence, North China Electric Power University, Beijing, China
[3] UR-GAMMA3, University of Technology of Troyes, Troyes, France
[4] EUt+, Data Science Lab, European Union
[5] Institute of Artificial Intelligence, Beihang University, Beijing, China
E-mail: hichem.snoussi@utt.fr

Summary: With large language models demonstrating significant potential in code generation tasks, their application to onboard control of resource-constrained Unmanned Aerial Vehicles has emerged as an important research direction. However, a notable contradiction exists between the high resource consumption of large models and the real-time, lightweight requirements of UAV platforms. This paper proposes an integrated approach that combines knowledge distillation, chain-of-thought guidance, and supervised fine-tuning for UAV multi-SDK control tasks, aiming to efficiently transfer complex reasoning and code generation capabilities to smaller models. Firstly, a high-quality dataset covering various mainstream UAV SDKs is constructed, featuring instruction-code-reasoning chains, and incorporates counterfactual negative samples for data augmentation, guiding the model to learn the end-to-end logic from instruction parsing to code generation. Secondly, leveraging DeepSeek-Coder-V2-Lite quantized via QLoRA as the teacher model, and based on a hybrid black-box and white-box distillation strategy, high-quality chain-of-thought soft labels are generated. These are combined with a weighted cross-entropy loss using hard labels to transfer complex reasoning capabilities to the smaller student model. Finally, through prompt tuning engineering optimized for the UAV control scenario, the model's performance on core tasks such as SDK type recognition and function call matching is enhanced. Experimental results indicate that the distilled lightweight model (parameters≤1B) maintains high code generation accuracy while achieving significant improvements in deployment and inference efficiency, effectively demonstrating the feasibility and superiority of our approach in achieving precise and lightweight intelligent control for UAVs.

Keywords: Large language models, Drone, Knowledge distillation, Chain-of-thought, Lightweight.

1. Introduction

Large language models have achieved breakthrough progress in the field of natural language processing, and their powerful language understanding and generation capabilities are rapidly penetrating critical areas such as robotics and autonomous driving [1, 2]. For instance, the ChatGPT has attracted widespread attention due to their strong general-purpose capabilities [3]; the DeepSeek series has become an important open-source choice owing to its excellent overall performance and advantages in long-context handling [4]; the Llama series demonstrates significant potential in specific domain applications thanks to its open ecosystem and extensive community fine-tuned versions [5]; and the Qwen series offers a full-stack model family ranging from large-scale to lightweight versions, excelling particularly in code understanding and tool calling [6]. These models collectively push the boundaries of technology, providing a rich foundation of models for downstream applications. In the context of UAV applications, researchers have begun exploring the use of LLMs for high-level task planning, natural language interaction, and the automatic generation of control code, opening up new possibilities for creating more intelligent and user-friendly autonomous UAV systems [7].

However, directly deploying the most advanced large models on resource-constrained UAV edge devices poses severe challenges. These models typically contain tens or hundreds of billions of parameters, demanding extremely high computational power, memory, and energy consumption. In contrast, UAV platforms are constrained by size, weight, and power limitations, resulting in limited onboard computing capacity. Consequently, most current research remains within a "ground-side" paradigm, where powerful LLMs running on cloud servers or ground stations perform asynchronous task planning and analysis, sending resultant commands to the UAV [8]. This mode is inevitably hampered by network latency, bandwidth instability, and data privacy risks, making it difficult to meet the requirements for low-latency, high-reliability control tasks such as real-time obstacle avoidance and dynamic path planning for UAVs.

To break through this bottleneck and enable real-time intelligent control with LLMs on UAV onboard platforms, model lightweighting techniques have become crucial. Knowledge Distillation (KD) has emerged as an effective model compression method

[9, 10]. Its core idea follows a "teacher-student" framework, transferring the knowledge encapsulated within a large, complex pre-trained "teacher model" to a lightweight "student model". The classical KD process often introduces a temperature parameter into the SoftMax function to generate smoothed "soft labels". These soft labels contain not only the teacher model's confidence in the correct category but also reveal richer knowledge, such as similarity relationships between different categories, offering far more instructive value than original "hard labels". The training objective for the student model is a weighted combination of two loss functions: one is the distillation loss, consistent with traditional supervised learning but based on the teacher's soft labels, typically measured using Kullback-Leibler divergence to quantify the distribution difference between the student's output and the teacher's soft labels; the other is the student loss, based on the ground-truth labels [10]. Through this joint optimization, the student model can learn not only specific task knowledge but also mimic the generalization "thinking" of the teacher model, thereby maintaining performance close to the teacher's even with a significant reduction in parameters [11, 12].

The Chain-of-Thought (CoT) technique is key to enhancing the multi-step reasoning abilities of large models [13]. The core of CoT lies in simulating human thinking processes. Through specific prompt engineering techniques, it guides the model to explicitly generate a sequence of intermediate reasoning steps before producing the final answer. For example, when faced with a composite mathematical word problem, CoT guides the model to first decompose the problem, gradually compute intermediate results, and finally arrive at the answer, rather than performing direct end-to-end output. This approach breaks down complex reasoning tasks into more manageable sub-problems, significantly improving the model's accuracy not only in tasks like arithmetic, commonsense reasoning, and symbolic manipulation but also greatly enhancing the interpretability and controllability of the model's decision-making process, as errors can be traced to specific steps [14]. The methodology has evolved to include the Program of Thoughts—an approach that translates natural language reasoning steps into executable code to enhance computational accuracy, thus enabling adaptation to more complex reasoning scenarios.

Fortunately, several mainstream LLMs (e.g., DeepSeek, Llama, Qwen) have been open-sourced, and lightweight versions specifically optimized for code generation tasks have been released, providing a preliminary model foundation for deployment on resource-constrained devices. Our preliminary research work [15, 16] has already validated the feasibility of deploying these code-optimized lightweight LLMs for multi-task UAV control in simulated environments. However, discrepancies exist between simulation environments and the real physical world. Furthermore, to adapt to the wide variety of UAV SDKs with their respective unique features, and to meet the stringent requirements of small platforms with extremely limited computational resources, deeper compression and targeted fine-tuning of these existing LLMs are still necessary. Therefore, this paper proposes a collaborative optimization framework integrating knowledge distillation and chain-of-thought reasoning. It aims to further compress the model while precisely transferring the complex multi-step reasoning capabilities from the teacher model to the student model, ultimately realizing a lightweight onboard model suitable for various UAV platforms, capable of real-time code generation and interactive control.

2. Methodology

We propose a knowledge distillation framework for UAV control tasks, comprising three core stages: 1. construction of a high-quality chain-of-thought instruction dataset based on multiple mainstream UAV SDKs; 2. a hybrid distillation strategy to transfer complex reasoning capabilities from a teacher model to a lightweight student model; and 3. the fine-tuning integrated with prompt engineering to further enhance instruction adherence and code generation performance. The overall framework of the proposed method is illustrated in Fig. 1.

In the data construction phase for UAV control, we build a large-scale, high-quality multi-SDK instruction dataset. Data sources cover official Python API documentation from eight mainstream UAV SDKs: TelloPy, olympe, MAVSDK, AirSDK, Skydio, dronekit, mavproxy, and Wingtra, ensuring the model's adaptability to diverse hardware platforms and software ecosystems. Dataset construction adopts a multi-level annotation strategy: automatically generating basic instruction-code pairs from API documentation, enhancing them with detailed chain-of-thought reasoning processes through the teacher model, and finally conducting manual verification to ensure data quality. Each training sample strictly follows the <instruct-think-code> triplet structure, where natural language instructions simulate real operational scenarios requiring composite tasks involving 3-5 API calls; the thought chain elaborately demonstrates the complete reasoning process from instruction parsing, SDK selection, function call sequence determination to parameter validation; the final code implementation strictly adheres to each SDK's syntax specifications and incorporates comprehensive exception handling mechanisms. This structured data ensures the model learns the end-to-end closed-loop logic from semantic understanding to code generation. Furthermore, inspired by counterfactual distillation research [17], we employ multi-perspective CoT technology to enhance model robustness. Specifically, through prompt engineering, we guide the teacher model to generate both positive CoT and negative CoT (counterarguments for incorrect options), enabling the model to understand task logic from both positive and

negative angles, thereby enhancing its comprehension of causal relationships.

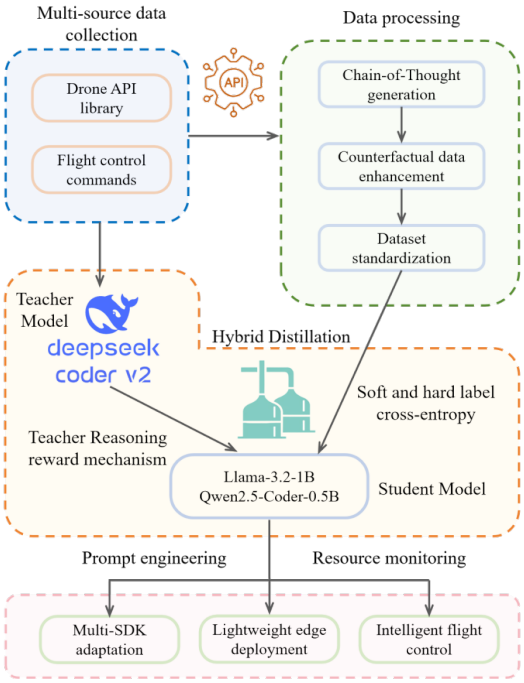

Fig. 1. Overview of the proposed methodological framework.

In the model selection and distillation strategy phase, to meet the stringent lightweight requirements of UAV onboard platforms, this work selects two types of high-performance, low-parameter open-source models as student bases: Llama-3.2-1B-Instruct and Qwen2.5-Coder-0.5B-Instruct [5, 6]. The teacher model employs DeepSeek-Coder-V2-Lite fine-tuned with QLoRA quantization. QLoRA is an efficient fine-tuning technique that significantly reduces memory footprint while maintaining model performance through low-rank adaptation and gradient backpropagation optimization, making it particularly suitable for resource-constrained edge computing scenarios [18]. DeepSeek-Coder-V2 is a large language model specifically designed for code generation tasks, employing a mixture-of-experts architecture and code-specific training corpus. Its lite version substantially reduces computational requirements while maintaining powerful code capabilities [19]. We combine the flexibility of black-box distillation with the precision of white-box distillation to maximize knowledge transfer efficiency. Black-box distillation utilizes the teacher model to generate high-quality CoT reasoning processes as soft labels, employing SoftMax functions to produce smoothed probability distributions, which enables the student model to learn the teacher's decision-making process. Meanwhile, white-box distillation aligns the intermediate representations of teacher and student models by minimizing the mean squared error between hidden states, allowing the student model to learn richer semantic representations.

In the fine-tuning optimization phase, this study incorporates prompt engineering methods to enhance fine-tuning effectiveness. Prompt engineering significantly influences model output quality and generalization capability through careful design of input templates and instruction formats. We design structured prompt templates that explicitly specify SDK types, API functions, and parameter constraints. The fine-tuning process focuses on three core tasks: SDK type identification, function call matching, and parameter integrity verification. Throughout the training process, we continuously monitor key metrics including loading time, inference speed, and resource utilization, ensuring the model meets real-time control requirements.

3. Experiments

To comprehensively evaluate the effectiveness of the proposed large model distillation method for UAV control tasks, the experiments were conducted on a desktop environment equipped with an NVIDIA RTX 4090 GPU. Training stability is the foundation for ensuring reproducible model performance. Throughout the training process, the final training loss of the Llama-3.2-1B model stabilized below 0.5, while the Qwen2.5-Coder model's loss converged below 0.8, both showing a stable and consistently decreasing trend without significant fluctuations. At the token level, the models achieved an accuracy of over 80 % on the entire training set. These results demonstrate that the hybrid distillation and counterfactual data augmentation strategy effectively guides the small models in learning knowledge from the teacher model, leading to a robust training process with good convergence.

The results for efficient inference optimization are significant. As shown in Table 1, the distilled small models (≤1 Bparameters) achieved an order-of-magnitude inference acceleration, with a generation speed reaching 400-595 tokens/s, far exceeding the speed of the teacher model (9.85 tokens/s). In terms of loading time, the optimized models were significantly shortened relative to their baseline versions. The loading time for the Qwen_0.5B_Counter was as low as 1.71 s, fully meeting the real-time requirement for rapid startup in UAV systems. Regarding memory usage, the peak GPU memory footprint of all distilled models was controlled within 5.1 GB, and the system runtime memory increase remained stable at a low level of approximately 1.4 GB. This metric fully demonstrates that the distilled models satisfy the stringent resource constraints of UAV onboard platforms.

The incorporation of counterfactual samples has also endowed the models with the ability to identify infeasible instructions. In specialized tests, for instructions beyond their capability scope, the models could accurately recognize them and return appropriate prompt messages (e.g., Current SDK does not support this function), rather than generating erroneous code or

invalid operations. This error-handling mechanism significantly enhances the reliability and safety of the model in practical applications, avoiding potential flight risks caused by erroneous instructions.

Table 1. Model resource efficiency performance.

Model	Loading Time (s)	Generation Speed (tokens/s)	GPU Memory (GB)	Runtime Increase (GB)
QLoRA-DeepSeek	19.15	9.85	10.54	2.20
Llama-1B (Baseline)	12.74	586.82	4.43	1.45
Qwen-0.5B (Baseline)	6.17	400.91	5.03	1.40
Llama-1B-Counter	2.39	595.6	4.3	1.43
Qwen-0.5B-Counter	1.71	400.93	5.08	1.42

4. Conclusion

We propose a LLM distillation method for UAV control tasks. By integrating hybrid distillation, chain-of-thought guidance, and counterfactual data augmentation, it has successfully transferred the complex reasoning and code generation capabilities of large models to lightweight models with fewer than 1B parameters. Experimental results indicate that the distilled models achieve an effective balance between performance and efficiency, the training process is stable, functional coverage is comprehensive, and the models support end-to-end tasks across multiple SDKs. More importantly, the resource efficiency of the models is significantly improved, with markedly reduced loading times, inference speeds meeting real-time control requirements, and minimal GPU memory and RAM usage, fully satisfying the stringent constraints of UAV onboard platforms. This study provides a feasible technical solution for deploying large models on resource-limited UAV edge devices, enabling real-time and reliable human-machine interactive intelligent control in complex scenarios.

Acknowledgements

This work has been partially funded by BPI DreamScanner project.

References

[1]. A. Vaswani, N. Shazeer, N. Parmar, J. Uszkoreit, et al., Attention is all you need, in *Proceedings of the 31st International Conference on Neural Information Processing Systems (NIPS'17)*, 2017, pp. 5998-6008.

[2]. S. H. Vemprala, R. Bonatti, A. Bucker, A. Kapoor, ChatGPT for robotics: Design principles and model abilities, *IEEE Access*, Vol. 12, 2024, pp. 55682-55696.

[3]. J. Schulman, B. Zoph, C. Kim, et al., ChatGPT: Optimizing language models for dialogue, OpenAI Blog, 2022, https://openai.com/blog/chatgpt

[4]. D. Guo, Q. Zhu, D. Yang, Z. Xie, et al., DeepSeek-Coder: When the large language model meets programming--The rise of code intelligence, *arXiv*, 2024, arXiv:2401.14196.

[5]. H. Touvron, T. Lavril, G. Izacard, X. Martinet, et al., LLaMA: Open and efficient foundation language models, *arXiv*, 2023, arXiv:2302.13971.

[6]. J. Bai, S. Bai, Y. Chu, Z. Cui, et al., Qwen technical report, *arXiv*, 2023, arXiv:2309.16609.

[7]. F. Zeng, W. Gan, Y. Wang, N. Liu, et al., Large language models for robotics: A survey, *arXiv*, 2023, arXiv:2311.07226.

[8]. S. Liu, L. Liu, J. Tang, B. Yu, et al., Edge computing for autonomous driving: Opportunities and challenges, *Proceedings of the IEEE*, Vol. 107, Issue 8, 2019, pp. 1697-1716.

[9]. C. Buciluǎ, R. Caruana, A. Niculescu-Mizil, Model compression, in *Proceedings of the 12th ACM SIGKDD International Conference on Knowledge Discovery and Data Mining*, 2006, pp. 535-541.

[10]. G. Hinton, O. Vinyals, J. Dean, Distilling the knowledge in a neural network, *arXiv*, 2015, arXiv:1503.02531.

[11]. V. Sanh, L. Debut, J. Chaumond, T. Wolf, DistilBERT, a distilled version of BERT: smaller, faster, cheaper and lighter, *arXiv*, 2019, arXiv:1910.01108.

[12]. X. Jiao, Y. Yin, L. Shang, X. Jiang, et al., TinyBERT: Distilling BERT for natural language understanding, in Findings of the Association for Computational Linguistics: EMNLP 2020 (T. Cohn, Y. He, Y. Liu, Eds.), *Association for Computational Linguistics*, *Online*, 2020, pp. 4163-4174.

[13]. J. Wei, X. Wang, D. Schuurmans, M. Bosma, et al., Chain-of-thought prompting elicits reasoning in large language models, in *Proceedings of the 36th International Conference on Neural Information Processing Systems (NeurIPS'22)*, 2022, pp. 24824-24837.

[14]. H. Lightman, V. Kosaraju, Y. Burda, H. Edwards, et al., Let's verify step by step, in *Proceedings of the Twelfth International Conference on Learning Representations (ICLR'24)*, 2024.

[15]. Y. Feng, H. Snoussi, J. Teng, et al., Large language models to enhance multi-task drone operations in simulated environments, in *Proceedings of the 1st International Conference on Drones and Unmanned Systems (DAUS'25)*, 2025, pp. 212-218.

[16]. Y. Feng, H. Snoussi, J. Teng, et al., Large language model-based multi-task UAVs-towards distilled real-time interactive control, in *Proceedings of the International Conference on Unmanned Aircraft Systems (ICUAS'23)*, 2023, pp. 114-118.

[17]. T. Feng, Y. Li, L. Chenglin, et al., Teaching small language models reasoning through counterfactual distillation, in *Proceedings of the Conference on Empirical Methods in Natural Language Processing (EMNLP'24),* 2024, pp. 5831-5842.

[18]. T. Dettmers, A. Pagnoni, A. Holtzman, L. Zettlemoyer, QLoRA: Efficient finetuning of quantized LLMs, in *Proceedings of the 37th International Conference on Neural Information Processing Systems (NeurIPS'23)*, 2023, pp. 10088-10115.

[19]. Q. Zhu, D. Guo, Z. Shao, D. Yang, et al., DeepSeek-Coder-V2: Breaking the barrier of closed-source models in code intelligence, *arXiv*, 2024, arXiv:2406.11931.

(025)

Multi-Frequency, Multi-Direction Array Optimization for Acoustic Drone Localization

N. Itare, J.-H. Thomas and K. Raoof
Laboratoire d'Acoustique de l'Université du Mans (LAUM), UMR 6613,
Institut d'Acoustique – Graduate School (IA-GS), CNRS, Le Mans Université, France
E-mail: nathan.itare@univ-lemans.fr

Summary: This preliminary study aims at presenting a multi-objective optimization of a microphone array in the context of the localization of a drone using 4 microphone arrays by triangulation. In order to fully cover the aerial space, the arrays used need to be optimized in their directivity. This is realized with an algorithm called NSGA II, which is applied on a specific structure of array, that can optimize its directivity for multiple frequencies and directions. This algorithm enables us to consider several array candidates that have different compromises in terms of main lobe area or secondary lobe discrimination. The resulting candidates are tested with simulations and characterized with their DOA root mean squared error across different directions and for several signal-to-noise ratios.

Keywords: Drone localization, Microphone array, Genetic algorithm, Multi-objective optimization.

1. Introduction

Drone localization is necessary in the context of dealing with situations where drones are identified as a threat. This localization can be realized using the noise produced by the propellers using microphone arrays. The use of microphone arrays combined with the knowledge of the particular acoustic signature of an UAV enables us to locate it by using specific signal processing techniques. Generally, most techniques using microphone arrays yield only the direction of arrival (DOA) of a source [1]. To complete the localization, it is therefore possible to use triangulation techniques by combining several DOAs [2]. This preliminary study uses 4 microphone arrays to perform triangulation and aims at optimizing the directivity of the arrays with a multi-objective optimization algorithm in order to fully cover the aerial space.

The technique used to obtain the DOA for one array is called the Time-Frequency Representation (TFR) method [3]. This technique is based on the delay and sum beamforming combined with an energy calculation on chosen components of its spectral representation. The chosen components correspond to the drone signature which enables us to increase the signal to noise ratio.

Since beamforming is used and that most of the energy of the drone lies in low frequency, then the main lobe obtained after the computation of beamforming is quite large. Additionally, in high frequency, secondary lobes can appear and make difficult the distinction of the true source. It is therefore necessary to optimize the directivity of the array taking into account multiple frequencies and multiple directions.

Genetic algorithms are well suited to face the microphone placement problem. Multiple algorithms exist and have different complexities along with advantages and disadvantages [4]. The NSGA-II algorithm [5] is chosen in our study for its fast convergence, the fact that it is a well-tested algorithm and that it requires few parameters. This study is a continuation of [3] with significant differences in two areas. In [3], only one direction and frequency are considered with one objective function for the optimization. With the use of NSGA-II, two or more objective functions can be used. A solution is evaluated for each objective and the algorithm favours the best one using a non-dominated sorting technique. In this work, the defined functions consider multiple directions and frequencies. The rest of the paper is organized as follows. Section 2 explains the parameters of the optimization. Section 3 presents some optimization results. Section 4 describes how the arrays are evaluated and show some array performance. Section 5 concludes and gives some perspectives.

2. Parameters of Optimization

2.1. Array Structure and Disposition

The array structure used for localization is the same that the one in [3]. The array contains 10 microphones, one microphone at the center and three microphones on each branch corresponding to the axes of a 3D cartesian coordinate system.

As described in the introduction, 4 microphone arrays are used via a triangulation process. In order to fully cover the aerial space, one array is placed at the center and three are placed on a circle with a radius determined by the maximum length of cable available.

Given the disposition of microphones in one array, each array's directivity can be optimized between -45° and 135° in azimuth and for elevations between 0 and 70°. All these directivities are optimized in steps of 15°.

2.2. Frequencies Used for Localization

The largest spacing possible between two microphones is 1.2 m which gives a low frequency of around 200 Hz. Smallest spacings between microphone arrays are 0.02 m which gives a high frequency bandpass of around 8.5 kHz. Given that most of the energy is in low frequencies, the directivity is chosen to be optimized for [250 500 2000] Hz frequencies.

2.3. Objective Functions

Two objective functions can be proposed so that we can visualize the solutions in a pareto front. The first objective is a combination of main lobe areas for different frequencies and the second is a combination of maximum sidelobe levels (MSL). The main lobe area $S_{-3\,dB}$ is defined as the area above -3 dB of the main lobe level. This area can be computed using a solid angle defined as:

$$\iint_{S_{-3\,dB}} \cos\theta \, d\theta \, d\varphi, \tag{1}$$

with θ the elevation and φ the azimuth. The MSL is defined here as the difference between the main lobe level and the sidelobe level. Since NSGA-II is normally set to minimize objective functions, then the opposite of the MSL combination is defined as the second objective function. The two objective functions are defined as:

$$f_1 = \sum_{i=1}^{N_f} w_{f1,i} \cdot \frac{mean_\Omega\,(area(f_i))}{\max\limits_{\Omega}\,(area(f_i))}, \tag{2}$$

$$f_2 = -\sum_{i=1}^{N_f} w_{f2,i} \cdot \frac{mean_\Omega\,(MSL(f_i))}{\max\limits_{\Omega}\,(MSL(f_i))}, \tag{3}$$

with $w_{f1,i}$ and $w_{f2,i}$ the weights used to give more importance to specific frequencies. The main lobe area needs to be more reduced in low frequency and less in high frequency. Therefore, the weights w_{f1} can be defined as: [1 0.5 0.3] in relation to the three selected frequencies. The MSL needs inversely to be optimized more in high frequency. The weights w_{f2} are defined as [0.3 0.5 1]. $mean_\Omega$ and max_Ω are respectively the mean and maximum across all directions Ω. $area(f_i)$ and $MSL(f_i)$ are the main lobe area and MSL for the frequency f_i chosen among the frequencies defined in Section 2.2. The MSL values are used in the linear domain in equations 2 and 3, as well as during optimization, but they are presented in decibels in Figs. 1 and 2.

2.4. NSGA II Parameters

The optimization is performed with a population of 50 individuals and 1000 generations. Simulated binary crossover and polynomial mutation are used as genetic operators. The crossover probability is 0.9 and the mutation one is 0.1. The distribution indices for crossover and mutation are respectively $\eta_c = 12$ and $\eta_m = 18$ which control the spread of the offspring around the parents [5]. As defined in Section 2.2, variables can take values in the range [0.02, 1.2] with a step size of 0.02. Since both genetic operators give continuous values, each modified variable is projected onto the nearest value in the feasible set, which ensures that bound and discretization constraints are always satisfied. Binary tournament selection is used to generate offsprings with a mating pool size of half the population.

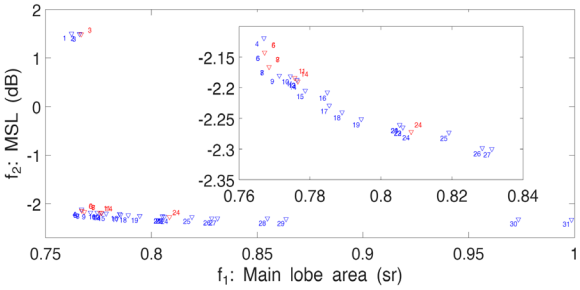

Fig. 1. Pareto front of the multi-objective optimization.

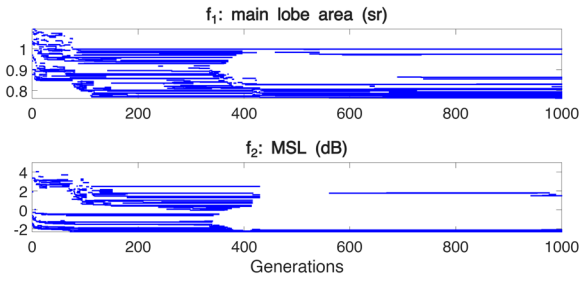

Fig. 2. Evolution of the two objective functions with generations.

3. Optimization Results

Optimization results are presented with the pareto front of the last generation in Fig. 1. The horizontal and vertical axis correspond to the first and second objective functions. After getting rid of duplicate arrays, 31 arrays remain as seen in this figure.

The evaluation of both objective functions is performed simultaneously for each individual and takes on average 0.728 s, based on measurements over 50 randomly generated individuals. Computations were performed on an Intel i7-8665U CPU with 16 GB RAM. This computation time mainly depends on the number of frequencies, the number of source directions, the spherical grid resolution, and the number of microphones. Parallelization over source directions using `parfor` in MATLAB® was employed to reduce the evaluation time per individual.

Fig. 2 shows the behavior of the two objective functions along generations. A fast convergence is observed during the first 120 generations. The main lobe area converges between 0.75 and 1 sr and the MSL between -2 and 2.5 dB. After 420 generations, the main lobe area converges mainly between 0.76 and 0.82 sr; the MSL between -2.3 and -2.1 dB. Afterward, only small variations occur and the algorithm is stopped at 1000 generations due to the associated computational cost and the marginal improvements observed beyond this point.

4. Evaluation of the Optimized Arrays

All the arrays optimized showed in the pareto front need to be compared in order to choose one or several final candidates. This is done by performing DOA localization with a simulated drone signal. Each array is then evaluated with its angular RMSE in azimuth and elevation. The simulated drone signal is the same as the one used in [6] with 2800 points, the fundamental frequency f_0 = 75 Hz, and 85 harmonics (until 6375 Hz). The drone signal is simulated with a free-field propagation model and beamforming is performed with a far-field model. The tested directions are the same as the optimized directions ranging from -45° to 135° in azimuth and from 0° to 70° in elevation with a 15° step. White noise is added to the simulated drone signal and the simulation is performed with a signal-to-noise ratio (SNR) from -10 dB to 10 dB with a step of 5 dB and also at 20 dB. Beamforming is computed with 2048 points and 10 harmonics are selected with the TFR method. The varying width of each harmonic is defined as the width of a pass-band filter with a quality factor of Q = 5. Harmonics are selected using a pitch tracking algorithm [6] computed between 150 Hz and 350 Hz, with 5 harmonics and 8192 for the Fast Fourier transform. All bins inside the defined frequency interval are selected for energy calculation in the TFR method. Since f_0 is constant throughout the trajectory, the selected frequencies representative of the drone's signature are the same.

A first set of evaluation can be performed with a low angular resolution for beamforming and a low number of realizations (30) to eliminate several arrays. The RMSE in azimuth and elevation averaged over SNRs for each array are shown in Fig. 3. Elevation errors averaged over SNRs are below 0.7° for all arrays. Azimuth errors averaged over SNRs are higher than elevation ones and few arrays yield errors close to 0.75°. Taking a threshold of 0.79° in azimuth, 8 arrays can be selected for a more accurate assessment. This second evaluation is performed with 100 realizations and a resolution of (0.1°, 0.1°) in azimuth and elevation respectively for beamforming. Their azimuth and elevation RMSE mean across SNR are also shown in Fig. 3.

Fig. 4 presents the angular RMSE vs SNR for arrays selected after the first set of evaluation. Only the 5 best arrays are shown for the sake of clarity. Arrays 3 and 14 yields the best results in azimuth as can be seen also in Fig. 3. In the pareto front (Fig. 1) arrays 3 and 14 have very different MSL but their main lobe areas are very low. Beamforming shows an error around 0.92° in azimuth and 0.44° in elevation from –5 dB of SNR (Fig. 4).

The link between this type of error and the full position error can be evaluated with a triangulation simulation. A source is simulated with the same model as the DOA assessment with an azimuth of 50° and an elevation varying with the source getting farther away. The distance of the source from the center array goes from 50 m to 350 m and the source starts on the ground (elevation = 0°). Triangulation is performed with 4 arrays, one at the center, the others on a 13 m circle placed at $\left[\frac{\pi}{6}, \frac{5\pi}{6}, -\frac{\pi}{2}\right]$. Array 14 is taken for this simulation. An error of 0.92° in azimuth and 0.44° in elevation is introduced to all arrays. Fig. 5 shows the results of this simulation with an error lower than 1 m for a source at 50 m. For a source at 350 m the position error is between 3 m and 5 m.

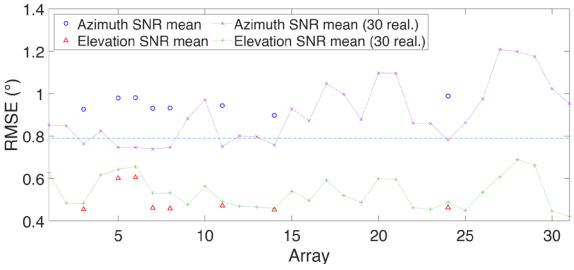

Fig. 3. Azimuth and elevation RMSE mean across SNRs for each optimized array for both evaluation sets. The dotted line is the threshold for array selection.

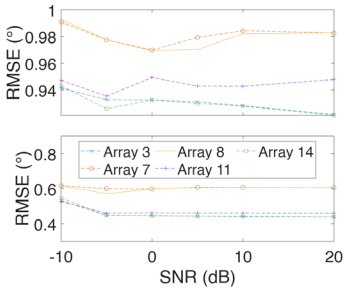

Fig. 4. RMSE vs SNR in azimuth (top) and elevation (bottom) for the 5 best arrays selected.

5. Conclusions

This preliminary study explores the optimization of a microphone array with a particular structure in the context of drone localization performed using triangulation of several DOAs. The multi-objective genetic algorithm NSGA II is an interesting algorithm that enables us to perform a multi-direction and multi-frequency optimization. Two objective functions are defined taking into account the main lobe area and the sidelobes in the directivity pattern for several

frequencies and directions. Once optimized, all the arrays can be visualized on a pareto front for comparison. The arrays can also be evaluated with simulations of DOA localization and be compared in terms of angular RMSE vs SNR. The results presented in this study show that two array yields the best performance in terms of RMSE particularly in azimuth. Errors obtained are close to 0.92° in azimuth and 0.44° which yields positions errors close between 3 and 5 m for a source at 350 m.

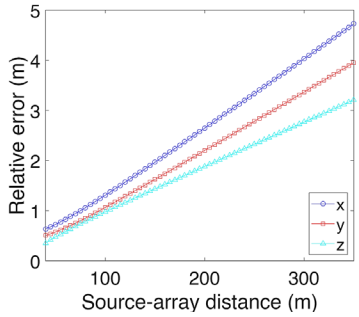

Fig. 5. Relative position error vs source-array distance for DOAs error of 0.92° in azimuth and 0.44° in elevation.

Acknowledgements

The authors thank the Agence Nationale de la Recherche for funding this work (ANR-23-ASM2-0008).

References

[1]. X. Yan, A. K. Shakya, A. Kumar, G. Pillai, et al., UAV detection and tracking in urban environments using passive sensors: A survey, *Applied Sciences*, Vol. 13, Issue 20, 2023, 11320.

[2]. A. K. Agrawal, Localization using angle-of-arrival (AoA) triangulation, in *Proceedings of the International Workshop on Environmental Sensing Systems for Smart Cities (ESSC'25)*, 2025, pp. 14-19.

[3]. N. Itare, J.-H. Thomas, K. Raoof, Genetic algorithm-based acoustic array optimization for estimating UAV DOA using beamforming, *Drones*, Vol. 9, 2025, 149.

[4]. A. Konak, D. W. Coit, A. E. Smith, Multi-objective optimization using genetic algorithms: A tutorial, *Reliability Engineering & System Safety*, Vol. 91, Issue 9, 2006, pp. 992-1007.

[5]. K. Deb, S. Agrawal, A. Pratap, T. Meyarivan, A fast elitist non-dominated sorting genetic algorithm for multi-objective optimization: NSGA-II, *Lecture Notes in Computer Science*, Vol. 1917, 2000, pp. 849-858.

[6]. N. Itare, J.-H. Thomas, K. Raoof, T. Blanchard, Acoustic estimation of the direction of arrival of an unmanned aerial vehicle based on frequency tracking in the time-frequency plane, *Sensors*, Vol. 22, Issue 11, 2022, 4021.

[7]. S. A. Zahorian, H. Hu, A spectral/temporal method for robust fundamental frequency tracking, *The Journal of the Acoustical Society of America*, Vol. 123, Issue 6, 2008, pp. 4559-4571.

(026)

Certification Strategies and Planning for Hydrogen Fuel Cell-Powered Normal Category Aircraft in Korea

Hyunjin Jung, Unyul Baek and Yonghoon Choi
Korea Institute of Aviation Safety Technology, 155-30, Robo land-ro, Seo-gu, Incheon, Republic of Korea
Tel.: + 82 32-727-5812
E-mail: hjjung@kiast.or.kr

Summary: Hydrogen fuel cell–powered aircraft are emerging as a promising zero-emission solution for future aviation. Their certification remains challenging due to fundamental differences from conventional internal combustion engine–based systems. Key challenges include hydrogen storage and supply, high-voltage electrical architectures, and safety considerations not fully addressed by existing airworthiness standards, particularly Part 23 for normal category airplanes.
This study reviews the regulatory background and certification scope for hydrogen-powered aircraft and proposes certification strategies and a planning framework tailored to the Korean regulatory environment. The study highlights the limitations of conventional engine-based certification approaches and emphasizes the application of Part 23 supplemented by hydrogen-specific Special Conditions in accordance with §21.16. A stepwise certification approach addressing both component-level and aircraft-level compliance is proposed, aligned with international certification trends led by the FAA and EASA, to support the safe introduction of hydrogen-powered normal category aircraft in Korea.

Keywords: Hydrogen fuel cell aircraft, Normal airplane, Supplemental type certificate, Korea airworthiness standard.

1. Introduction

The International Civil Aviation Organization (ICAO) has introduced the Carbon Offsetting and Reduction Scheme for International Aviation (CORSIA) to mitigate carbon emissions from the aviation sector. As a result, the global aviation industry is accelerating its transition away from conventional fossil fuel–based propulsion systems toward zero-emission or low-carbon propulsion technologies. Within this context, hydrogen fuel cell–powered propulsion systems have emerged as a promising candidate for next-generation aircraft propulsion, as they produce no carbon dioxide emissions during operation.

However, hydrogen fuel cell propulsion systems exhibit fundamentally different architectural and functional characteristics compared to conventional fossil fuel-based engines. In particular, the use of high-pressure hydrogen storage, the potential for hydrogen leakage and fire hazards, and the operation of high-voltage electrical power systems introduce new safety considerations that are not explicitly addressed by existing airworthiness standards. Consequently, the current certification requirements, especially those established under Part 23 for normal category airplanes, are insufficient to comprehensively address the safety aspects associated with hydrogen-powered aircraft.

In Korea, the Aviation Safety Act and its associated regulatory framework likewise do not provide explicit definitions or dedicated certification requirements for hydrogen-powered aircraft or hydrogen fuel cell propulsion systems. Under these circumstances, the applicability of existing airworthiness standards must be carefully evaluated, and a structured certification strategy that accounts for the unique characteristics and hazards of hydrogen fuel cell propulsion systems is required.

Accordingly, this study proposes certification strategies and a planning framework to support the safe introduction of hydrogen fuel cell–powered aircraft within the Korean regulatory environment.

2. Certification Strategies Analysis

2.1. Certification Scope and Applicability for Hydrogen-Powered Aircraft

Hydrogen fuel cell propulsion systems operate aircraft by generating electrical power through an electrochemical reaction between hydrogen and oxygen and supplying the generated power to an electric motor that drives a propeller. A hydrogen fuel cell propulsion system typically consists of a fuel supply system (hydrogen), fuel cell stacks, mechanical balance-of-plant subsystems including thermal and water management systems, and electrical balance-of-plant subsystems such as power conversion and power control units.

However, the current Korean Aviation Safety Act does not provide explicit definitions or dedicated airworthiness requirements for hydrogen-powered aircraft or hydrogen fuel cell propulsion systems. Consequently, when an applicant applies for a type certificate in accordance with §21.17(a)(1), compliance must be demonstrated with the applicable airworthiness standards in effect on the date of application, such as Part 23 or Part 25, depending on the aircraft category.

Nevertheless, hydrogen fuel cell propulsion systems exhibit fundamentally different characteristics and design philosophies compared to conventional

internal combustion engines. As a result, existing airworthiness standards alone are insufficient to fully address the unique safety considerations associated with hydrogen fuel cell propulsion, including hydrogen storage, fuel supply, and high-voltage electrical systems. Accordingly, as provided under §21.16, it is necessary to establish dedicated Special Conditions to incorporate safety requirements that specifically address the novel and unusual features of hydrogen fuel cell propulsion systems into the certification basis.

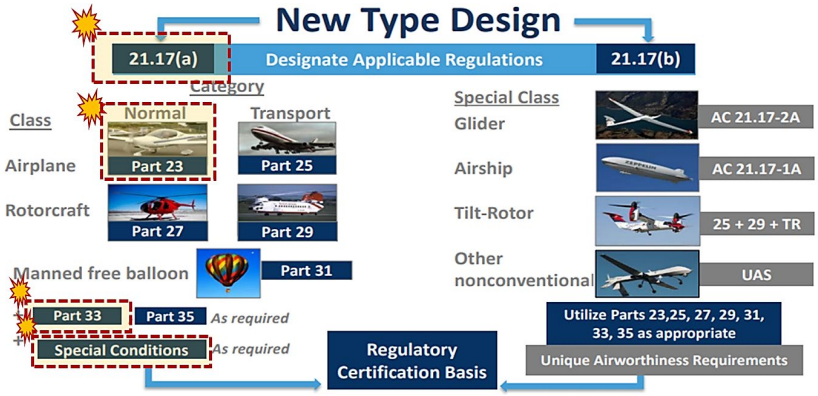

Fig. 1. Architectures of HFC System on Aircraft [1].

2.2. Certification Approach Based on Hydrogen-Powered Aircraft

When applying a hydrogen fuel cell propulsion system to an aircraft, defining the appropriate certification scope represents a critical starting point in the certification process. Existing airworthiness standards, such as Part 23, establish safety requirements at the aircraft level, while Part 33 addresses certification requirements for aircraft engines.

Unlike conventional internal combustion engines, hydrogen fuel cell propulsion systems comprise multiple subsystems, including electric motors, fuel cell stacks, and hydrogen storage and supply systems. Due to this distributed and electrically driven architecture, hydrogen fuel cell propulsion systems do not readily fit within the traditional definition of an "engine" as assumed under Part 33. As a result, there are inherent structural and functional limitations in classifying hydrogen fuel cell propulsion systems within the conventional engine certification framework.

2.3. Certification Strategy and Planning Framework for Korea

For small airplanes equipped with hydrogen fuel cell propulsion systems, the certification approach should be based on the application of Part 23 airworthiness standards, supplemented by the establishment of Special Conditions to address novel hazards and system characteristics. Major propulsion system elements, including fuel cell stacks, hydrogen storage systems, and hydrogen supply systems, should demonstrate compliance with the applicable safety requirements in accordance with §23.2505, Function and Installation.

These components are first shown to comply with the applicable requirements at the component or subsystem level prior to installation. Following installation, compliance is subsequently verified at the aircraft level against the relevant Part 23 airworthiness standards. This stepwise certification approach enables the assurance of safety at both the system component level and the overall aircraft level, thereby maintaining certification consistency and system integration integrity.

Furthermore, Special Conditions provide a regulatory mechanism to address safety aspects that are not explicitly covered by existing Part 23 requirements, such as high-pressure hydrogen storage, electrical arcing associated with high-voltage systems, and hazards related to hydrogen leakage and fire. Accordingly, the establishment of a certification basis combining Part 23 with hydrogen-specific Special Conditions allows the unique characteristics of hydrogen fuel cell propulsion systems to be appropriately reflected within the airworthiness framework.

In parallel, major aviation authorities, including the FAA and EASA, have established international collaborative working groups to support the certification of hydrogen-powered aircraft and have proposed phased certification roadmaps [2] based on hazard identification, safety assessment, and regulatory gap analysis. In the initial phase, experience is accumulated through the use of Special Conditions and a limited number of certification projects, while mid- to long-term efforts focus on the development of dedicated airworthiness standards and certification procedures for hydrogen-powered aircraft.

Accordingly, the certification strategy for hydrogen-powered aircraft in Korea should maintain alignment with these international regulatory trends, while establishing a phased certification plan that reflects national regulatory constraints, testing capabilities, and infrastructure readiness.

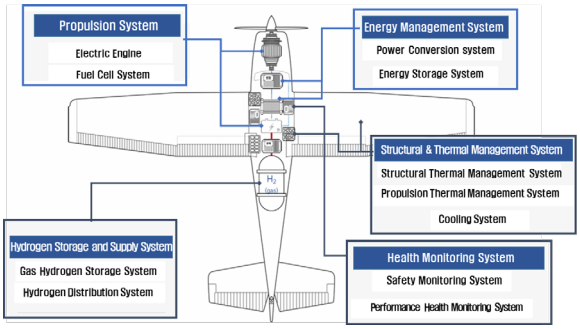

Fig. 2. Certification Approach of Aircraft with HFC.

3. Conclusions

This study examined the background for reviewing certification requirements and the definition of the certification scope for hydrogen-powered aircraft, and proposed a certification approach for small airplanes equipped with hydrogen fuel cell propulsion systems. The study confirmed that the certification of hydrogen fuel cell propulsion systems should be based on the Part 23 airworthiness standards, supplemented by the establishment of Special Conditions to appropriately address the novel design characteristics that differ from those of conventional internal combustion engines.

The proposed certification framework provides a foundational structure that enhances international regulatory alignment while improving the feasibility of domestic implementation within the Korean certification environment. However, ongoing research activities may reveal ambiguities or gaps in detailed certification procedures, indicating the need for further clarification of Special Conditions and the associated means of compliance.

Accordingly, it is necessary to identify and address these procedural issues through future mock certification exercises and validation activities, thereby establishing a safe and effective certification framework for hydrogen-powered aircraft and ensuring continued harmonization with international airworthiness standards.

Acknowledgements

This research was supported by the Ministry of Land, Infrastructure and Transport (MOLIT) of the Republic of Korea and the Korea Agency for Infrastructure Technology Advancement (KAIA) through the 2023 R&D program entitled “Development of Certification System and Safety demonstration technology for Normal Airplane with HFCPS” (Grant No. RS-2023-00246686).

References

[1]. 14 CFR Part 21 - Certification procedures for products and articles, *Federal Aviation Administration*, 2024.
[2]. J. Castillo, C. Fotache, H. Leadbetter, EASA certification roadmap on H2, in *Proceedings of the International Workshop on Certification of Hydrogen Applications in Aviation*, 2024.

(027)

Effects of Center-of-Gravity Offset on the Gust Response of a Tandem Helicopter

Hyugjin Song and Moonsung Cho
Korea Aerospace University, Department of Aerospace Engineering,
76, Hanggongdaehak-ro, Deogyang-gu, Goyang-si, Gyeonggi-do, Republic of Korea
E-mail: mscho@kau.ac.kr

Summary: Modern UAVs perform a variety of missions – such as wildfire detection – that require low-speed flight or hovering, making them vulnerable to external disturbances like gusts. In addition, when wings or various payloads are added to extend range or enhance mission capability, an offset may occur between the center of gravity (CG) and the center of thrust (CT) of the lift rotors. This study investigates the gust-response behavior of a simple tandem-helicopter UAV when such CG–CT offsets are present. Using an analytical method, we derive the influence of the offset on vehicle stability through stability-derivative formulation and eigenvalue-based analysis. A numerical approach is also developed to simulate gust-response behavior by combining the flight dynamic equations with an oblique-flow propeller model based on Blade Element Momentum Theory (BEMT). Our results show that the numerical model can efficiently capture CG-offset effects under dynamic gust conditions – cases that cannot be described by the analytical method – without relying on high-fidelity, high-cost CFD. Finally, we outline future research directions for extending the analysis to aircraft with more complex geometries.

Keywords: Gust, Unmanned aerial vehicle (UAV), Tandem helicopter, Center of gravity, Center of thrust, Hovering, Flight stability.

1. Introduction

From Vertical Takeoff and Landing (VTOL) UAVs [1] to aerial robotic platforms equipped with manipulator arms [2], many modern UAV missions involve hovering in low-speed flight regimes, where wind gusts significantly affect performance. For example, wildfire-monitoring drones must withstand turbulent flows generated by fire-induced thermal plumes [3].

As UAV use increases, the integration of various payloads – such as cameras and sensors – and the development of wing-assisted configurations to expand range have become common. These factors introduce the possibility of an offset between the aircraft's center of gravity (CG) and the lift-rotor center of thrust (CT).

In this study, we analyze how CG–CT offset affects the gust-response behavior of a tandem-helicopter UAV during low-speed or hovering flight. Considering the full aerodynamic interactions of a winged UAV is complex, we begin with a simplified configuration: a tandem helicopter using a longitudinal 3-DOF dynamic model and a propeller thrust-variation model under gusts. We then examine how gust type and aircraft parameters influence the resulting gust response.

2. Methods

2.1. Analytical Method

We first perform a mathematical analysis of flight stability in the presence of a CG–CT offset. A linearized state-space model is constructed using small-perturbation theory. Gust-induced variations in thrust and horizontal drag are modeled using the advance ratio (μ) and rotor inflow ratio (λ).

Thrust coefficient is defined:

$$C_T = \frac{1}{2}\sigma a\left[\frac{1}{3}\theta\left(1+\frac{3}{2}\mu^2\right)-\frac{1}{2}\lambda\right], \quad (1)$$

where σ is a blade solidity, θ is a blade pitch angle at 75 % span of the balde.

In plane force coefficient is defined:

$$C_H = \frac{a\sigma}{2}\left(\frac{\mu c_{d0}}{2a}+\frac{1}{3}a_1\theta-\frac{3}{4}\lambda a_1+\frac{1}{2}\mu\theta\lambda+\frac{1}{4}\mu a_1^2\right), \quad (2)$$

where c_{d0} is a 0 degree angle of attack drag coefficient, and a_1 is a flapping coefficient of the blade defined from [4].

Induced velocity is defined:

$$\left(\frac{v_i}{v_h}\right)^4+\left(\frac{V}{v_h}\right)^2\left(\frac{v_i}{v_h}\right)^2 = 1, \quad (3)$$

where v_h is an induced velocity of propeller when hovering. V is an inflow velocity normal to the disk.

From the linearized model, stability derivatives are derived, enabling eigenvalue-based analysis of dynamic properties such as natural frequency and damping ratio [5].

Linearized state-space equation is defined:

$$\begin{bmatrix}\Delta\dot{z}\\ \Delta\dot{w}\\ \Delta\dot{x}\\ \Delta\dot{u}\\ \Delta\dot{\theta}\\ \Delta\dot{q}\end{bmatrix} = \begin{bmatrix}0 & 1 & 0 & 0 & 0 & 0\\ 0 & Z_w & 0 & 0 & 0 & 0\\ 0 & 0 & 0 & 1 & 0 & 0\\ 0 & 0 & 0 & X_u & -g & X_q\\ 0 & 0 & 0 & 0 & 0 & 1\\ 0 & 0 & 0 & M_u & 0 & M_q\end{bmatrix}\begin{bmatrix}\Delta z\\ \Delta w\\ \Delta x\\ \Delta u\\ \Delta\theta\\ \Delta q\end{bmatrix} \quad (4)$$

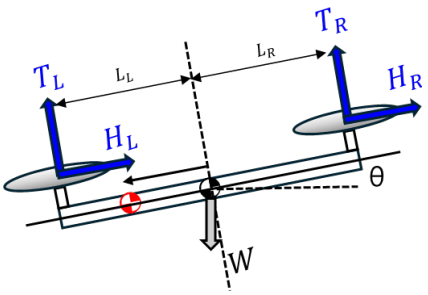

Fig. 1. Free body diagram of Tandem helicopter.

The influence of CG–CT offset on these stability derivatives is examined at trim, highlighting how aft rotor arm lengths affect gust response. For this purpose, root finding algorithm was used to find the rpm, thrust, and drag of the propeller when in trim state according to low-speed flight speed. CG offset ratio is a normalized value obtained by dividing the offset distance by the arm distance. (The parameters of propeller are defined: air density = 1.225 kg/m^3, Radius = 0.258, Lift slope of blade = 2π, Pitch angle at 75 % span = 0.3025 (rad). The mass of helicopter = 1.18 kg and Moment of inertia = 0.0625 kgm^2).

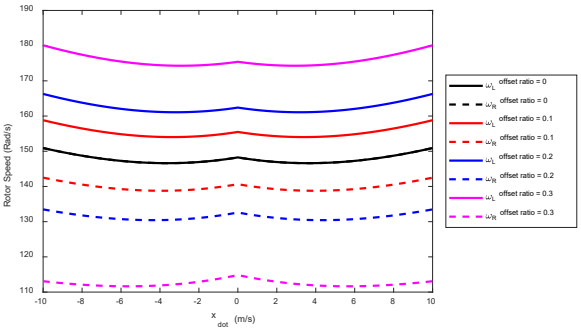

Fig. 2. Trim analysis of Tandem helicopter by varying offset ratio and forward speed.

CG offset ratio is defined:

$$r_{offset} = \frac{\Delta X_{CG}}{L}, \quad (5)$$

where ΔX_{CG} is a deviated distance[m] of CG from CT, L is original arm length which is L = 0.45 m.

Left side propeller arm is defined:

$$L_L = (1 - r_{offset}) * L \quad (6)$$

Right side propeller arm is defined:

$$L_R = (1 + r_{offset}) * L \quad (7)$$

For open loop analysis, small perturbation theory was used to induce small disturbances in the state variables of the trim state and derive stability derivatives. This analysis reveals which translational or rotational stability derivatives most strongly contribute to gust-induced instabilities induced by propeller aerodynamics. It was found that the degree to which the aircraft's z-direction disturbance generates a moment increases due to the CG offset, M_w. This suggests that the CG offset causes a difference in propeller RPM, and that propellers with different RPMs show different sensitivities to disturbances.

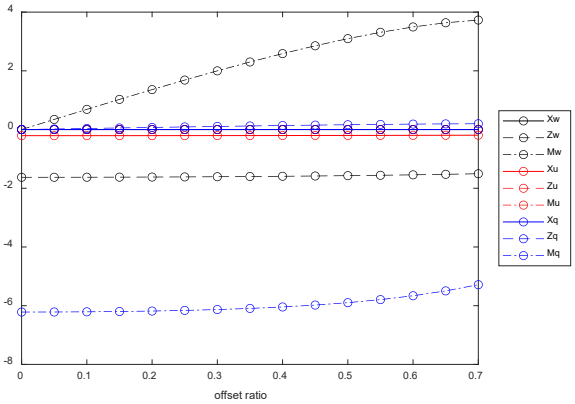

Fig. 3. Longitudinal stability derivatives of a tandem helicopter with different CG offset ratios.

The eigenvalues of the system were analyzed, and for longitudinal behavior, the s1, s2, and s3 modes were analyzed. s1 is eigenvalue of z-directional translational motion, s2 is eigenvalue of x-directional motion, which is more damped. s3 is eigenvalue of x-directional and pitch coupled motion, as the offset ratio increased, damping decreased.

2.2. Numerical Method

Since the analytical approach cannot fully capture dynamic gusts – such as horizontally and vertically varying gusts – it is insufficient for modeling realistic rotor–gust interactions. Dynamic gusts induce time-varying differences in the inflow seen by the fore and aft rotors, which static models cannot represent. Furthermore, existing models assumed that the induced velocity was constant along the azimuth, but in reality, when a gust of wind blows against a propeller, the induced velocity varies along the azimuth. This can be expressed using the Pitts and Peters model [6]. Additionally, when a horizontal gust blows, the retrieving area of the propeller generates aerodynamic force in the post stall area, and for this purpose, the post stall aerodynamics of the airfoil were applied. The blade's airfoil geometric information used chord distribution, pitch angle distribution, and zero-lift angle of attack distribution of APC 10X4.7 propeller [7].

Analytical models also cannot incorporate controller behavior (e.g., PID control), nor can they capture thrust and drag variations arising from vehicle motion because they consider only the trim point.

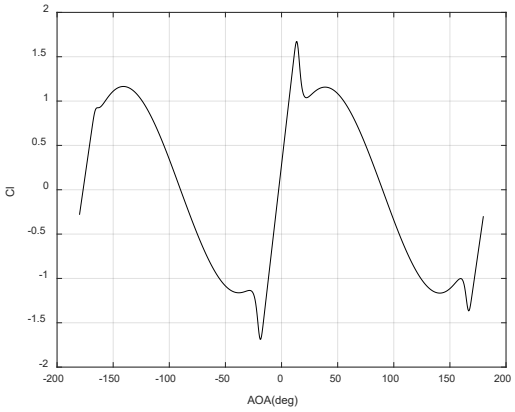

Fig. 4. Full angle of attack (-180~180 deg) lift coefficient.

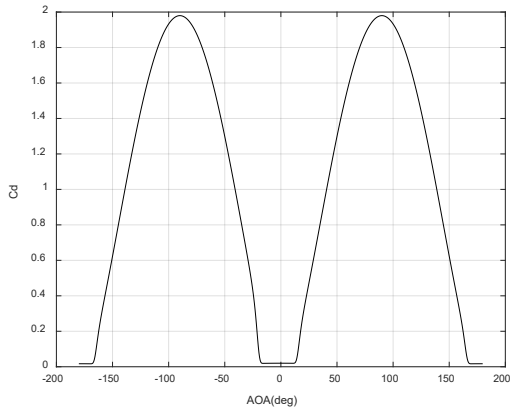

Fig. 5. Full angle of attack (-180~180 deg) drag coefficient.

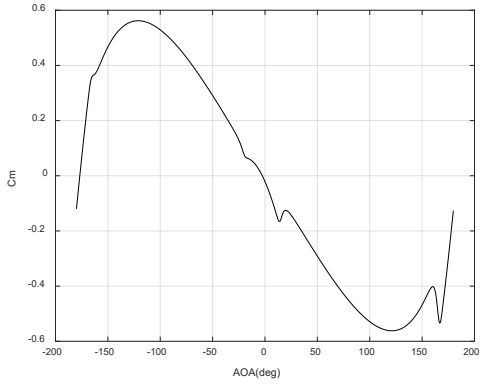

Fig. 6. Full angle of attack (-180~180 deg) pitching moment coefficient.

Therefore, we develop a numerical simulation framework capable of modeling dynamic gusts, onboard control systems, and the UAV's relative motion within the wind field. To avoid the high computational cost of CFD, we adopt a fast propeller–gust interaction model based on oblique-flow BEMT (Blade Element Momentum Theory), which computes aerodynamic forces for arbitrary inflow angles. BEMT method can be utilized by using the root finding algorithm, finding an induced velocity that matches the thrust induced using momentum theory and the thrust induced using the blade element method.

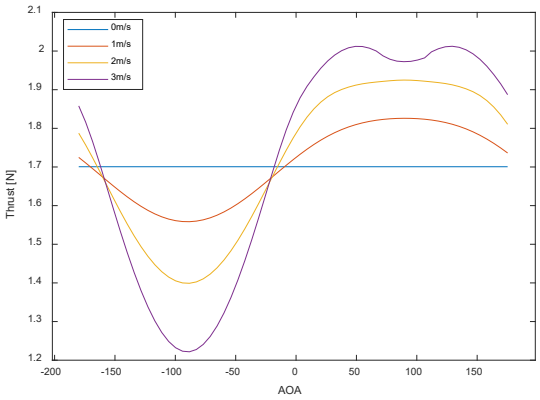

Fig. 7. Thrust variation according to inflow angle, wind velocity and angle of attack[deg] (3000 RPM).

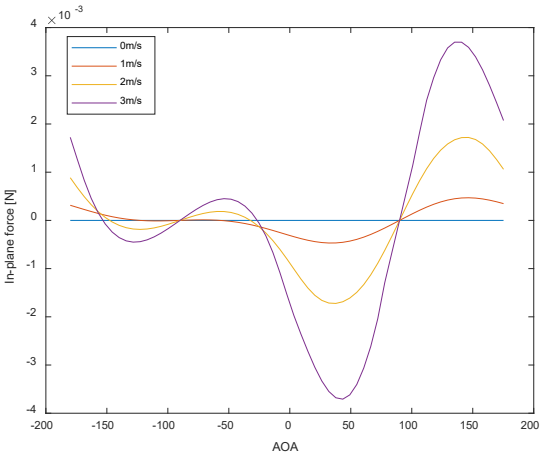

Fig. 8. In plane force variation according to inflow angle, wind velocity and angle of attack[deg] (3000 RPM)

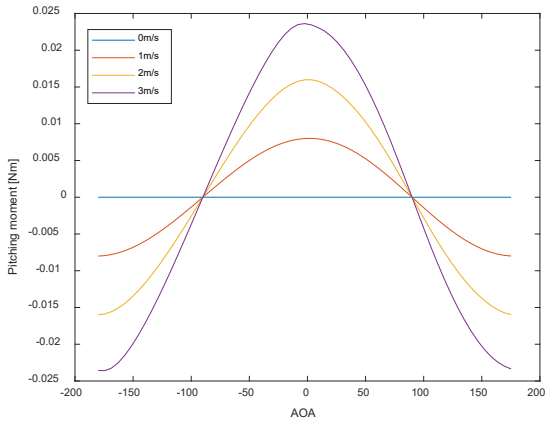

Fig. 9. Pitching moment variation according to inflow angle, wind velocity and angle of attack[deg] (3000 RPM).

A 3-DOF flight-dynamics model is used to compute vehicle motion, updating the flow velocity

incident on each rotor. A closed-loop control system, similar to those implemented in autopilots, is integrated. Because CG shifts create asymmetric rotor arm lengths that may cause oscillation, control allocation is adapted to the fore–aft arm-length difference to model only designed (not uncertain) offsets [8]. The UAV controller uses a PID controller, with the inner loop controlling the pitch angle and the outer loop controlling the X and Z directions. The gain value was obtained through trial and error method (PID gains: $KP_x = 100, KI_x = 100, KD_z = 10, K\,P_z = 100, KI_z = 100, KD_z = 10, KP_\theta = 10, KI_\theta = 20, KD_\theta = 10$).

3. Results and Discussion

The analytical stability-derivative approach alone cannot fully describe the offset effects under dynamic gust conditions compared to numerical solution. For linear systems without closed loops, it was analyzed that the damping coefficient of the system decreases as the offset ratio increases, but the vibration characteristics could not be determined because there was no imaginary region pole. Numerical simulations show that the vehicle's motion couples strongly with the gust field, altering gust stability beyond what static stability derivatives can predict. The gusts that change over time were modeled using a sine curve. The wind speed was set to 2 m/s and the period to 5 seconds.

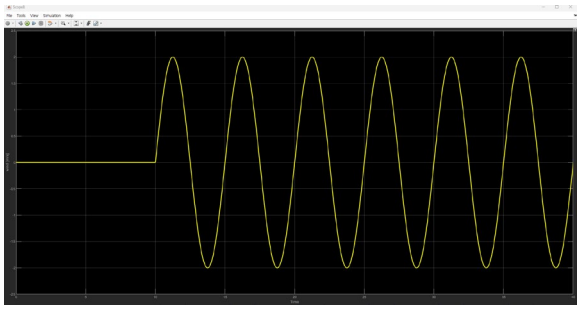

Fig. 10. Pitching moment variation according to inflow angle and angle of attack (3000 RPM).

Numerical simulation results using the BEMT and Pitts and Peters models showed that the rotor's gust sensitivity varied depending on the CG offset ratio, resulting in a significant increase in pitching and translational oscillation. Additionally, the proposed numerical method enables efficient simulation of moving-gust scenarios without relying on computationally expensive CFD by using look up table.

For horizontal gust, as the CG offset increases, additional small vibrations are observed in addition to the wind-induced vibration period, which appears to be due to differences in sensitivity to gusts entering the blades due to differences in propeller RPM. The difference in behavior in the Z direction was not affected by the CG offset, and as the CG offset ratio increased, the amplitude of the X direction and pitching motions became larger. This was similar to the effect on the X direction motion mode and pitching motion mode, as analyzed in the linear state space equation.

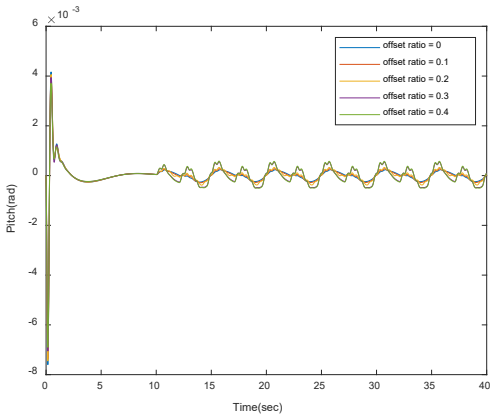

Fig. 11. Pitch behavior when subjected to horizontal gusts with a wind speed of 2 m/s and a period of 5 seconds.

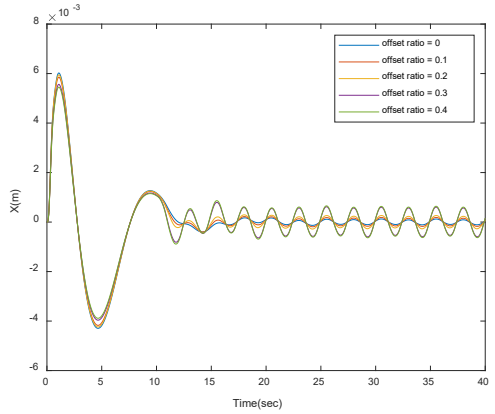

Fig. 12. X directional behavior moment variation according to inflow angle and angle of attack (3000 RPM).

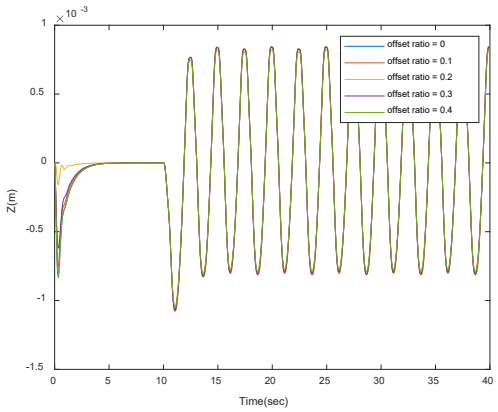

Fig. 13. Z directional behavior moment variation according to inflow angle and angle of attack (3000 RPM).

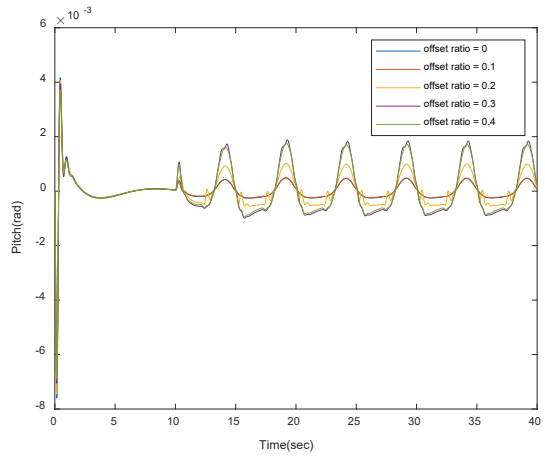

Fig. 14. Pitch directional behavior when subjected to vertical gusts with a wind speed of 2 m/s and a period of 5 seconds.

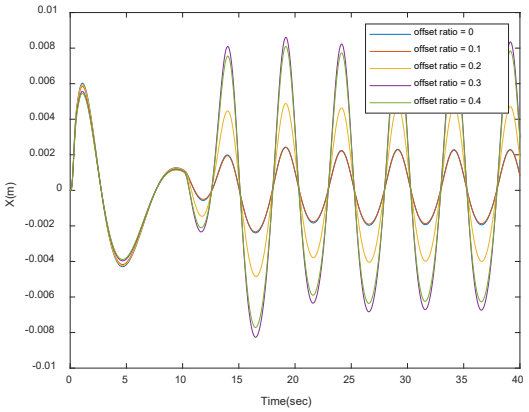

Fig. 15. X directional behavior when subjected to vertical gusts with a wind speed of 2 m/s and a period of 5 seconds.

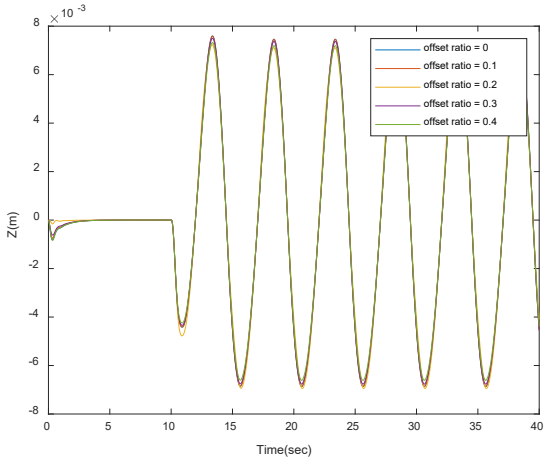

Fig. 16. Z directional behavior when subjected to vertical gusts with a wind speed of 2 m/s and a period of 5 seconds.

When vertical gusts change over time, the amplitudes of the X-direction motion and the pitching motion increase more noticeably as the offset ratio increases. In addition, differences in the rotor gust sensitivity according to RPM create an asymmetric pitching motion vibration.

In conclusion, even though the controller was designed to account for the variation in rotor arm length due to the center of gravity shift through control allocation, it was not able to control the differences in the sensitivity of the rotor's aerodynamics to gusts. Significant increases in wind speed or offset ratio can lead to significant vibrations in vertical gusts. However, when air enters the blade vertically, especially from below, more complex aerodynamics, such as vortex ring states, may need to be considered.

Future work will incorporate wing and fuselage aerodynamic effects under gusts using post-stall models for wing's airfoil [8] and potential-flow-based fuselage aerodynamics [10], allowing full-envelope predictions across wide ranges of angle of attack and sideslip. Realistic turbulence fields such as the von Kármán gust model [11] and strip-theory-based turbulence loads [12] will also be implemented.

Acknowledgements

This paper is research supported by the Ministry of Trade, Industry and Energy (A major activities of 2024 Industry – Academia Cooperation: Aviation and defense SW professional Education)

References

[1]. F. Li, W. Song, B. Song, J. Jiao, Dynamic simulation and conceptual layout study on a quad-plane in VTOL mode in wind disturbance, *International Journal of Aerospace Engineering*, Vol. 2022, 2022, 3549293.

[2]. K. Kondak, K. Krieger, A. Albu-Schäffer, M. Schwarz, et al., Closed-loop behavior of an autonomous helicopter equipped with a robotic arm for aerial manipulation tasks, *International Journal of Advanced Robotic Systems*, Vol. 10, Issue 2, 2013, 145.

[3]. D. Moura, J. P. A. Sobral, et al., Autonomous targeting system for a firefighting drone-compensation for wind disturbance, Master's Thesis, *Universidade de Coimbra*, Coimbra, 2021.

[4]. A. R. S. Bramwell, G. Done, D. Balmford, Rotor aerodynamics in forward flight, Chapter 4, in Bramwell's Helicopter Dynamics (A. R. S. Bramwell, et al., Eds.), *Elsevier*, Oxford, 2001, pp. 94-133.

[5]. J. F. Whidborne, A. P. Mendez, A. Cook, Effect of rotor tilt on the gust rejection properties of multirotor aircraft, *Drones*, Vol. 6, Issue 10, 2022, 305.

[6]. W. Khan, M. Nahon, A propeller model for general forward flight conditions, *International Journal of Intelligent Unmanned Systems*, Vol. 3, Issue 2/3, 2015, pp. 72-92.

[7]. UIUC Propeller Database, https://mselig.ae.illinois.edu/props/propDB.html

[8]. A. R. Kumutham, D. K. Pratihar, A. K. Deb, Impact of CoM placement on quadcopter's performance and controller development, in *Proceedings of the 36th Conference of Open Innovations Association (FRUCT'24)*, 2024, pp. 331-336.

[9]. B. Montgomerie, Methods for root effects, tip effects and extending the angle of attack range to +- 180 deg., with application to aerodynamics for blades on wind turbines and propellers, Technical Report FOI-R--1338--SE, *Swedish Defence Research Agency (FOI)*, 2004.

[10]. H. J. Allen, Estimation of the forces and moments acting on inclined bodies of revolution of high fineness ratio, Technical Report NACA-RM-A9I26, *National Advisory Committee for Aeronautics*, 1949.

[11]. K. Cole, A. Wickenheiser, Spatio-temporal wind modeling for UAV simulations, *arXiv*, 2019, arXiv:1909.00067.

[12]. M. Selig, Modeling full-envelope aerodynamics of small UAVs in realtime, in *Proceedings of the AIAA Atmospheric Flight Mechanics Conference*, 2010, 7635.

(028)

Kalman-Conditioned Action Chunking Transformers for Dynamic Object Grasping Toward Aerial Recovery Systems

Jiyeon Koo, Eunseom Pyo and Andrew Jaeyong Choi
Gachon University, School of Computing, 1342 Seongnam-daero, Sujeong-gu, Seongnam-si, Gyeonggi-do, Republic of Korea
Tel.: + 82 1090045267
E-mail: halo1225@gachon.ac.kr

Summary: Autonomous aerial recovery systems require robust grasping capabilities for targets exhibiting dynamic and partially observable motion. In particular, recovering unmanned aerial vehicles or airborne objects involves significant state uncertainty caused by sensor noise, occlusions, and unpredictable dynamics. This work presents a belief-augmented manipulation framework as a foundational study toward aerial recovery systems. We introduce a Belief-Augmented Action Chunking Transformer that integrates state estimates and uncertainty information into the policy input. A Kalman filter is used to extract belief representations from visual tracking data, which are provided to the policy at the episode level. Experiments conducted using real robot datasets demonstrate that incorporating belief information improves policy robustness in dynamic object grasping tasks.

Keywords: Dynamic object grasping, Belief state, Imitation learning, Motion uncertainty, Aerial recovery, Robotic arm manipulation.

1. Introduction

The increasing deployment of unmanned aerial vehicles (UAVs) in aerospace, defense, and civilian applications has highlighted the importance of reliable aerial recovery systems [1]. Scenarios such as mid-air vehicle capture, autonomous landing assistance, and reusable aerial platforms require the ability to safely and accurately grasp or intercept targets that are in motion. These targets often exhibit irregular dynamics and are observed under limited sensing conditions, making aerial recovery a challenging problem in autonomous systems.

From a robotics perspective, aerial recovery can be decomposed into three core components: visual perception of a moving target, state estimation under uncertainty, and generation of manipulation actions based on the estimated state. Among these, dynamic object grasping under partial observability remains a fundamental challenge. Visual observations are inherently noisy and incomplete due to motion blur, occlusions, latency, and changing viewpoints, which leads to significant uncertainty in target state estimation.

Recent advances in imitation learning and transformer-based policies, such as Action Chunking Transformers (ACT), have shown promising results in robotic manipulation by learning long-horizon action sequences from demonstrations [2]. However, these approaches typically treat observations as deterministic inputs and do not explicitly account for uncertainty in the perceived state [3]. As a result, their performance can degrade in dynamic environments where object motion and sensing uncertainty play a critical role.

Before addressing fully irregular and highly dynamic aerial targets, it is essential to study grasping policies that can handle temporally evolving object states while explicitly considering uncertainty. This work focuses on dynamic object grasping as a prerequisite for aerial recovery systems, assuming structured but time-varying target motion. By addressing this intermediate problem, we aim to establish a robust policy framework that can later be extended to more complex aerial recovery scenarios.

To this end, we propose a Belief-Augmented Action Chunking Transformer, which extends the ACT framework by incorporating belief representations derived from state estimation. A Kalman filter is employed to estimate the target's position, velocity, and associated uncertainty from visual tracking data [4]. The resulting belief vector is injected into the policy input, enabling the model to condition its actions on both estimated states and uncertainty.

2. Belief-Augmented ACT Architecture

2.1. Belief Vector Definition

In this study, we propose a belief-augmented architecture (Fig. 1) based on the Action Chunking Transformer (ACT) for dynamic object grasping, where observation uncertainty is explicitly incorporated through an additional belief token. The original ACT predicts future action sequences using visual observations and robot states; however, in dynamic environments where the object's position and velocity change rapidly, making stable decisions based on a single observation remains challenging.

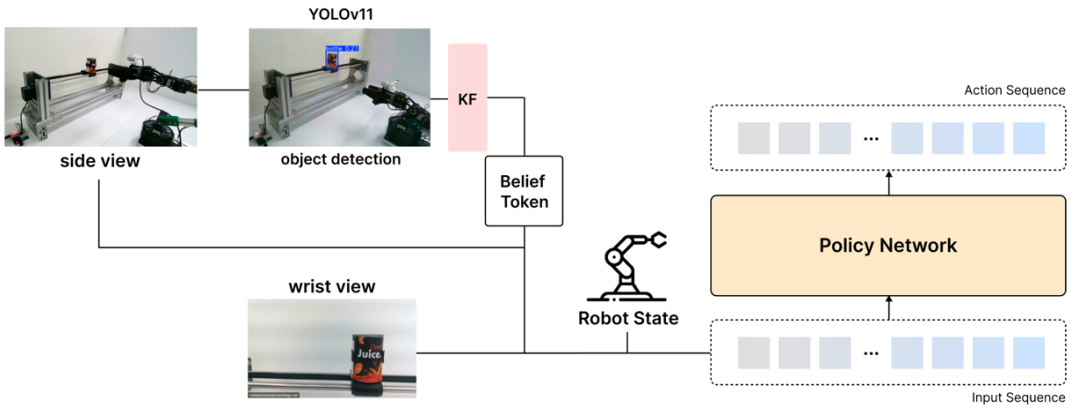

Fig. 1. System architecture of the Kalman-Conditioned Action Chunking Transformers.

To address this limitation, we define a belief vector that represents the object state and its uncertainty estimated via a Kalman filter, and introduce it as an additional input token to the Transformer encoder. The belief vector is composed of the following six-dimensional state:

$$b = [u_f, v_f, \dot{u}_f, \dot{v}_f, \sigma_u, \sigma_v] \quad (1)$$

This belief vector simultaneously captures the dynamic characteristics of the object and the confidence of the observation, reflecting a minimal set of state information required for rapid decision-making under limited sensing conditions, such as those encountered in aerial unmanned vehicle recovery scenarios.

2.2. Extension of ACT Input Structure

The defined belief vector is provided to the Transformer encoder as a single token, in the same manner as image feature tokens and robot state tokens. Through the self-attention mechanism, this belief token is integrated with visual information and robot states, enabling the model to learn correlations among different modalities.

As a result, the policy is able to generate actions by jointly considering not only the current observation of the object but also its dynamic motion trends and estimation confidence, leading to more stable and informed action generation in dynamic grasping tasks [5].

3. Dataset Construction and Training Method

A robot grasping dataset was constructed using the LeRobot dataset format for dynamic object grasping. Data were collected with a Leader–Follower WidowX robotic system (Fig. 2), where grasping demonstrations executed by the leader robot were replicated and recorded by the follower robot. Each data sample consists of multi-view camera images, robot joint states, action sequences, and a belief vector.

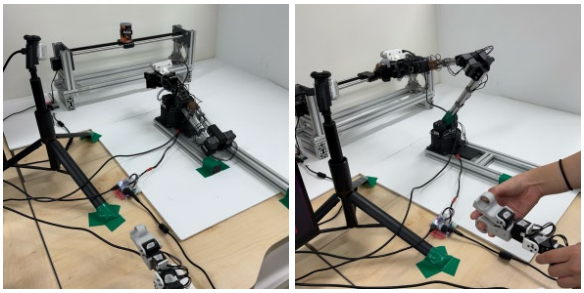

Fig. 2. Leader-Follower hardware setup for demonstration data collection.

The belief vector is computed at the episode level and assigned uniformly to all frames within the same episode to reduce frame-level estimation noise and ensure stable training. The proposed Belief-Augmented ACT is trained using the original ACT training pipeline without structural modifications, while maintaining the same input format during both training and inference.

4. Experimental Results

As shown in Table 1, a comparative experiment was conducted against the conventional Baseline ACT policy on a recovery task involving a dynamically moving object.

Table 1. Comparison of recovery performance between policies.

Policy Type	Trials	Number of Successes	Success Rate (%)
Baseline ACT	50	5	10.0
Belief-Augmented ACT	50	13	26.0

All experiments were performed under identical environmental conditions and initial settings, and each policy was evaluated over a total of 50 independent trials.

The Baseline ACT policy successfully recovered the target object in 5 out of 50 trials, achieving a success rate of approximately 10 %. In contrast, the proposed Belief-Augmented ACT policy achieved 13 successful recoveries out of 50 trials, corresponding to a success rate of approximately 26 %. This represents an improvement of more than 2.6× compared to the baseline ACT policy.

The observed performance gain can be attributed to the incorporation of belief information, which explicitly encodes not only the estimated object position and velocity but also the associated estimation uncertainty. By leveraging this additional information, the policy is able to make more reliable action decisions in dynamic environments. In particular, the proposed approach demonstrated more stable recovery behavior under observation noise and irregular object motion.

5. Conclusions

This paper presented a Belief-Augmented Action Chunking Transformer (ACT) framework for dynamic object grasping as a preliminary study toward aerial recovery systems for unmanned aerospace platforms. By incorporating a belief vector containing the object's estimated position, velocity, and uncertainty obtained via a Kalman filter, the proposed policy explicitly accounts for observation uncertainty in dynamic environments. Experimental results showed that the proposed method outperformed the baseline ACT in recovery success rate, demonstrating the effectiveness of uncertainty-aware state representation.

While this study focuses on relatively simple dynamic objects, the proposed approach provides a scalable foundation for aerial recovery tasks involving irregular and unpredictable motion [6]. Future work will extend this framework to more realistic aerial scenarios and investigate online belief updates for improved robustness.

References

[1]. F. Ruggiero, V. Lippiello, A. Ollero, Aerial manipulation: A literature review, *IEEE Robotics and Automation Letters*, Vol. 3, Issue 3, 2018, pp. 1957-1964.

[2]. T. Z. Zhao, V. Kumar, S. Levine, C. Finn, Learning fine-grained bimanual manipulation with low-cost hardware, *arXiv*, 2023, arXiv:2304.13705.

[3]. J. A. Bagnell, An invitation to imitation, Technical Report CMU-RI-TR-15-08, *Carnegie Mellon University*, 2015.

[4]. R. E. Kalman, A new approach to linear filtering and prediction problems, *Journal of Basic Engineering*, Vol. 82, Issue 1, 1960, pp. 35-45.

[5]. A. Posadas-Nava, et al., Action chunking with transformers for image-based spacecraft guidance and control, *arXiv*, 2025, arXiv:2509.04628.

[6]. H. C. Cheung, H. Yu, G. Loianno, Aerial grasping with soft aerial vehicle using disturbance observer-based model predictive control, *arXiv*, 2024, arXiv:2409.14115.

(029)

Distributed UAV-SAR: A Distributed Drone-Based Synthetic Aperture Radar System for the Investigation and Demonstration of Novel Applications, Imaging Algorithms and Future Spaceborne Radar Concepts

S. V. Baumgartner, L. L. Lamberti, S. J. Sanchez Urresta, V. Mustieles Pérez, T. Börner, M. Villano and G. Krieger
German Aerospace Center (DLR), Microwaves and Radar Institute,
Muenchener Str. 20, 82234 Wessling, Germany
Tel.: +49 8153 28 2321
E-mail: stefan.baumgartner@dlr.de

Summary: In this paper DLR's distributed multi-static drone-borne synthetic aperture radar (SAR) system "Distributed UAV-SAR" is introduced and some technical details are presented. The system consists of several octocopters, each equipped with a custom-build and reconfigurable software defined multi-channel SAR sensor and a localization unit with integrated radar synchronization capabilities. For single-pass and multi-baseline interferometric and tomographic radar applications the octocopters need to fly safely in close formation with pre-defined and controlled three-dimensional distances to each other. For coherent multi-static SAR imaging the radar clocks of the spatially distributed SAR sensors have to be synchronized. The methods used for formation flight control and radar clock synchronization are also briefly discussed in the paper. The Distributed UAV-SAR system is currently under development and will be operational in the second half 2026.

Keywords: Radar, Synthetic aperture radar, Multi-static radar, Distributed radar, UAS, Multi-agent, Formation flying.

1. Introduction

A powerful and established remote sensing technology for Earth observation with applications in the field of environmental and infrastructure monitoring, disaster response and climate science is synthetic aperture radar (SAR) [1]. SAR is able to provide information with high spatial resolution about the Earth's surface and even subsurface, independent of daylight, weather conditions and cloud cover.

Distributed SAR systems promise, especially in the context of NewSpace SAR, to overcome the size, weight and power constrains that limit single-platform implementations and also enable new operation paradigms, including scalable resolution, increased swath width, adaptive acquisition, enhanced revisit times and improved robustness through redundancy.

Furthermore, distributed SAR enables technologies like multi-baseline single-pass across-track interferometry for the generation of accurate digital elevation models, as well as single-pass radar tomography and holography for three-dimensional (3D) imaging, e.g., for measuring vertical forest structures or even for the detection and imaging of buried objects (cf. Fig. 1) [2].

Conventionally, new techniques, algorithms and concepts for spaceborne SAR are investigated and demonstrated by using airborne radar systems before they are implemented on spacecrafts. However, especially for bi- and multi-static acquisitions such an approach could very quickly become expensive and the flight planning, coordination and synchronization of the formation flying aircrafts quite complex.

The availability of powerful off-the-shelf unmanned aerial vehicles (UAVs), advances in the miniaturization and the high availability of relatively low-cost off-the-shelf radio frequency hardware have motivated us to build up the Distributed UAV-SAR system.

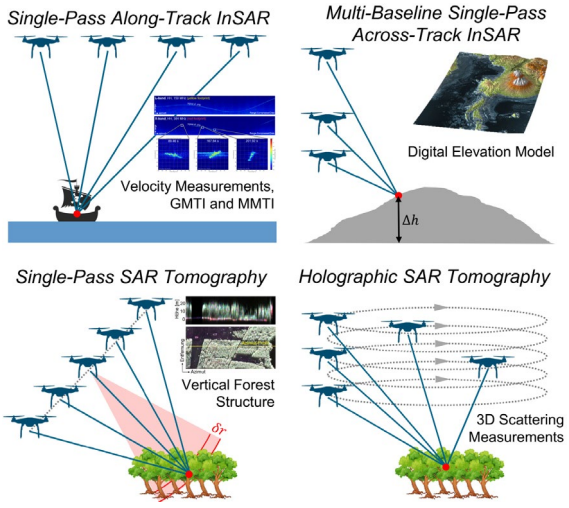

Fig. 1. Examples for multi-platform single-pass radar acquisition geometries.

Our primary goal is to use this system for the investigation and demonstration of novel radar applications, novel multi-static radar imaging algorithms and novel radar concepts.

2. System Overview

In Fig. 2 a high-level overview of the Distributed UAV-SAR system is shown. Currently it consists of 3 MK-U25 octocopter platforms, which allow for flight times of up to 30 min (including 6 kg payload) with an additional 10 % battery reserve remaining. During radar data acquisition a platform speed of 10 m/s over ground is envisaged. These parameters allow for imaging a scene of ≥1 km² during a single flight at an altitude of 120 m above ground. The system is scalable and not limited to just three UAVs.

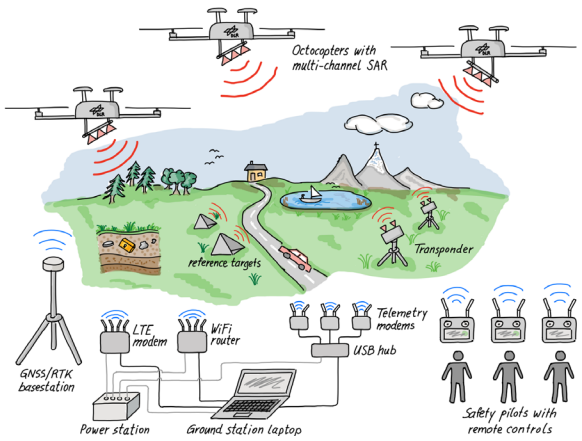

Fig. 2. Distributed UAV-SAR system overview.

3. Radar Instrument and LRSU

A block diagram of the payload is shown in Fig. 3. For multi-static radar operation, the most important parts are the digital multi-channel radar (red) and the localization and radar synchronization unit (LRSU, green).

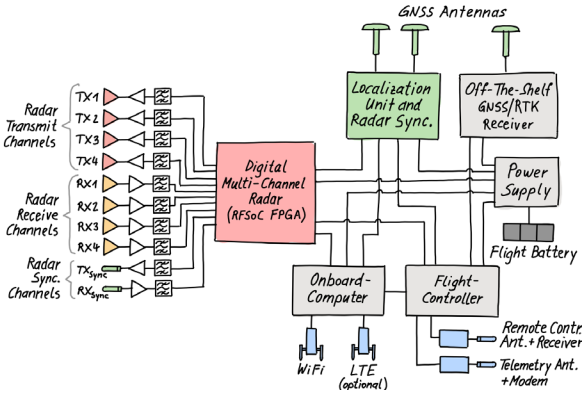

Fig. 3. Block diagram of a part of the octocopter payload.

The core of the radar sensor is an off-the-shelf RFS oC (Radio Frequency System-on-Chip) [3]. In this device the radio frequency (RF) unit is integrated so that only a few external hardware components are required for building up a powerful and reconfigurable software defined multi-channel SAR. High-frequency radar signal generation, down conversion to baseband and analog-to-digital conversion is done directly inside the RFS oC.

Radar synchronization of spatially distributed radars, which inherently do not share the same local oscillator, is challenging and plays a key role for coherent multi-static processing. Due to hardware tolerances the oscillators on each radar have different frequency and phase offsets which have to be compensated. For this the LRSU synchronizes the start time of the pulses of each radar using the GNSS PPS signal. Additionally, the radars periodically exchange and store synchronization pulses, which are used in post-processing for fine synchronization with a required time accuracy of ≤ 10.5 ps [3].

4. Formation Flying

For the acquisition geometries shown in Fig. 1 the octocopters have to fly safely in close formation with pre-defined 3D distances. For accurate real-time distance control onboard computers are connected to the flight controllers (cf. Fig. 4). The control software is running directly on the onboard computers which can communicate with each other over Wi-Fi. Different control strategies are currently under investigation by using Software in the Loop (SITL) simulations taking into account disturbances caused by wind and gusts.

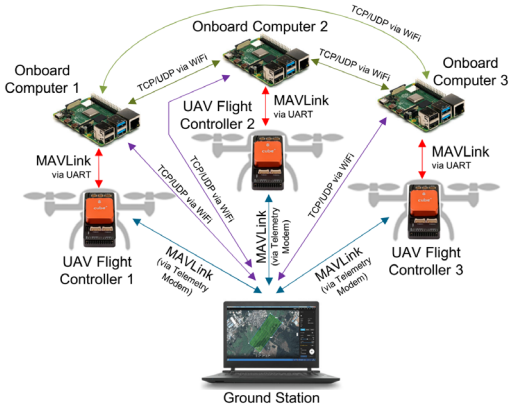

Fig. 4. Architecture for formation flight control.

5. Conclusion

DLR's Distributed UAV-SAR was introduced and some technical details were presented. The system is currently under development and it will be operational in the second half of 2026.

References

[1]. A. Moreira, P. Prats-Iraola, M. Younis, G. Krieger, et al., A tutorial on synthetic aperture radar, *IEEE*

Geoscience and Remote Sensing Magazine, Vol. 1, Issue 1, 2013, pp. 6-43.

[2]. A. Moreira, P. Prats-Iraola, M. Nannini, G. Dani, Spaceborne multi-baseline synthetic aperture radar (SAR) imaging, in *Proceedings of the IEEE International Geoscience and Remote Sensing Symposium (IGARSS'23)*, 2023, pp. 345-348.

[3]. L. Lamberti, S. Baumgartner, G. Krieger, Distributed UAV-SAR: System concept overview and error model, in *Proceedings of the Kleinheubach Conference*, 2024, pp. 1-4.

(030)

Beyond the Ring: A Multi-Agent Reinforcement Learning Framework for Attack and Defense Intelligence in Drone Soccer

Chansoo Son and Andrew Jaeyong Choi
Gachon University, School of Computing, 1342 Seongnam-daero, Sujeong-gu, Seongnam-si, Gyeonggi-do, Republic of Korea
Tel.: + 82 1042827773
E-mail: thsct01@gmail.com

Summary: Multi-agent reinforcement learning (MARL) provides a framework for interacting agents, and policy-gradient methods such as Proximal Policy Optimization have achieved strong performance in autonomous drone racing. However, most advances target single-UAV tasks and do not capture tightly coupled attack–defense interactions in drone sports or competitive multi-UAV scenarios. This paper presents Beyond the Ring, a competitive MARL framework for attack and defense intelligence in drone soccer. Using NVIDIA Isaac Lab, we build a rulebook-faithful 3D environment where an attacking quadrotor must fly through a ring-shaped goalpost and return to its start region, while a defending quadrotor must reach and hold a defensive point and attempt to block the attacker. The interaction is modeled as a zero-sum game with dense and event-based rewards combined via exponential moving-average normalization. Self-play MAPPO with Elo and cross-play evaluation shows monotonic improvement, robust generalization, and suggests extensions to onboard AI pilots and decoy strategies.

Keywords: Multi-agent reinforcement learning, Drone-soccer, Quadrotor, Zero-sum games, Competitive self-play, UAV AI pilot, Isaac Lab.

1. Introduction

Multi-agent reinforcement learning (MARL) provides a unified framework for sequential decision-making with multiple interacting agents [1]. On the single-agent side, Proximal Policy Optimization (PPO) [2] and deep policies have enabled champion-level autonomous drone racing, robust sim-to-real transfer and agile flight near platform limits [3–6], highlighting deep RL as an AI pilot for UAVs – yet mostly in single-UAV settings. In MARL, benchmarks such as SMAC, FightLadder and VolleyBots [7–9] have advanced evaluation and coordination studies, but they do not capture the ring-centered attack–defense dynamics of drone soccer, where multiple UAVs interact around a shared 3D structure under realistic constraints.

This work introduces *Beyond the Ring*, a competitive MARL framework for drone soccer with physically realistic quadrotor dynamics. We study a two-agent attack–defense game implemented in NVIDIA Isaac Lab, following the FIDA rulebook for ring geometry and nominal agent placement [10]. The interaction is cast as a zero-sum MARL problem, with policies trained via self-play MAPPO and evaluated using Elo and cross-play analysis [4, 5, 7–9].

2. Drone-Soccer Simulation Environment

Fig. 1 summarizes the overall task structure, observation and action interfaces, reward design and the competitive MARL training pipeline.

Fig. 2, the drone-soccer environment is built on NVIDIA Isaac Lab to support high-throughput GPU simulation of two quadrotor agents. The geometric layout and game rules follow the FIDA drone-soccer rulebook [10], including the ring diameter, goal height and nominal locations of the attacker and defender.

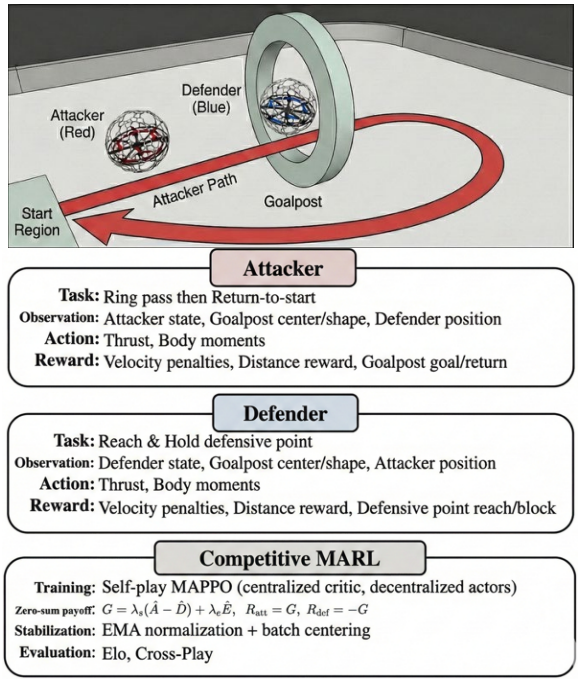

Fig. 1. Overview of the drone-soccer scenario, agent interfaces and competitive MARL pipeline.

2.1. Scenario, Interfaces and Training Overview

Fig. 1 overviews the drone-soccer scenario and competitive MARL pipeline. A circular ring-shaped goalpost is fixed in the arena, with an attacker (red) that must fly through the ring and return to its starting region and a defender (blue) that must hold a defensive point near the ring and block the attacker's approach; the ring geometry follows the official drone-soccer specifications [10], and drone initial poses are randomly perturbed around rulebook-based spawns. Each agent receives a compact observation of its own state, the ring and task targets, and uses a shared 4D continuous action space with one thrust and three body-moment commands. Rewards combine velocity penalties, distance-based shaping and event bonuses/penalties for ring passes, return, holding, blocks, crashes and violations, and are merged into a scalar game return G, with $R_{\text{att}} = G$and $R_{\text{def}} = -G$, defining a zero-sum game trained with self-play Multi-Agent PPO and evaluated using Elo rating and cross-play matches. We set shaping weights to provide dense guidance for approach/positioning while keeping event terms as the decisive objective signal, and we add ring-centric penalties to suppress degenerate behaviors such as ring-hugging, wrong-direction entry, and illegal inside-ring defense. To stabilize self-play under non-stationary opponents and mixed dense/sparse rewards, each reward component is standardized using EMA mean/variance before forming G, with optional batch centering; this normalization primarily improves training stability and reduces sensitivity to weight tuning, and it can indirectly benefit final performance by preventing collapse.

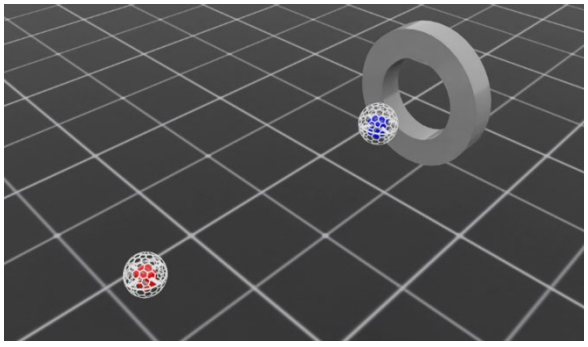

Fig. 2. Drone Soccer RL Environment in NVIDIA Isaac Lab.

3. Experimental Results

In our experiments, we train populations of attacker and defender policies under the proposed zero-sum formulation and periodically save policy snapshots. Fig. 3 shows the resulting Elo trends for both roles. The Elo ratings increase steadily over training, which indicates that self-play discovers progressively stronger strategies rather than cycling among exploitable behaviors. Fig. 4 presents cross-play WinRate and ScoreRate matrices between attacker and defender generations. Newer attackers systematically dominate older defenders, while updated defenders are more resilient against early attackers.

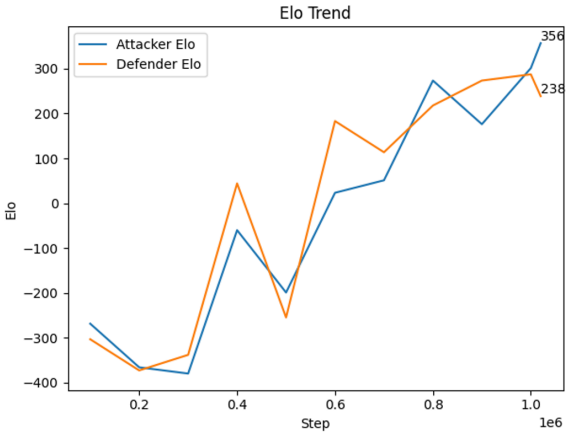

Fig. 3. Elo ratings and cross-play WinRate.

WinRate is defined as the fraction of evaluation episodes that end in an attacker win. We compute it as the number of attacker wins divided by the sum of attacker wins, draws, and attacker losses. An attacker win corresponds to completing a successful ring pass followed by return to the start region before the episode terminates. A defender win corresponds to preventing attacker success under the evaluation rules, for example by achieving a valid defensive hold for the required duration, triggering an effective block that terminates the episode, forcing a crash, or reaching the time limit without the attacker completing the success condition. A draw is recorded when neither side satisfies its designated success condition by the end of the episode and no terminal event assigns a win to either side, according to the evaluation protocol.

ScoreRate is defined as an event-based success rate that measures how frequently task-scoring events occur, normalized at the episode level. For the attacker, we count scoring events as successful ring passes and, when required by the task definition, successful completion of the return-to-start stage. For the defender, we count scoring events as successful defensive outcomes such as hold success and block events. We then report the normalized frequency of these scoring events per episode in the cross-play matrix.

Overall, the final attacker wins about 0.66 against contemporary defenders and about 0.80 against past defenders, demonstrating convergence and robust performance.

4. Conclusions

This paper introduced *Beyond the Ring*, a competitive MARL framework for learning attack and

defense intelligence in drone soccer using a realistic Isaac Lab environment and an asymmetric attacker–defender task. With self-play MAPPO and EMA-normalized zero-sum rewards, two quadrotor agents learn increasingly strong strategies, exhibiting monotonic Elo gains and robust cross-play generalization. Future work will transfer these policies to real UAVs and extend the framework toward decoy and adversarial multi-UAV strategies around shared structures such as the drone-soccer ring [3–10].

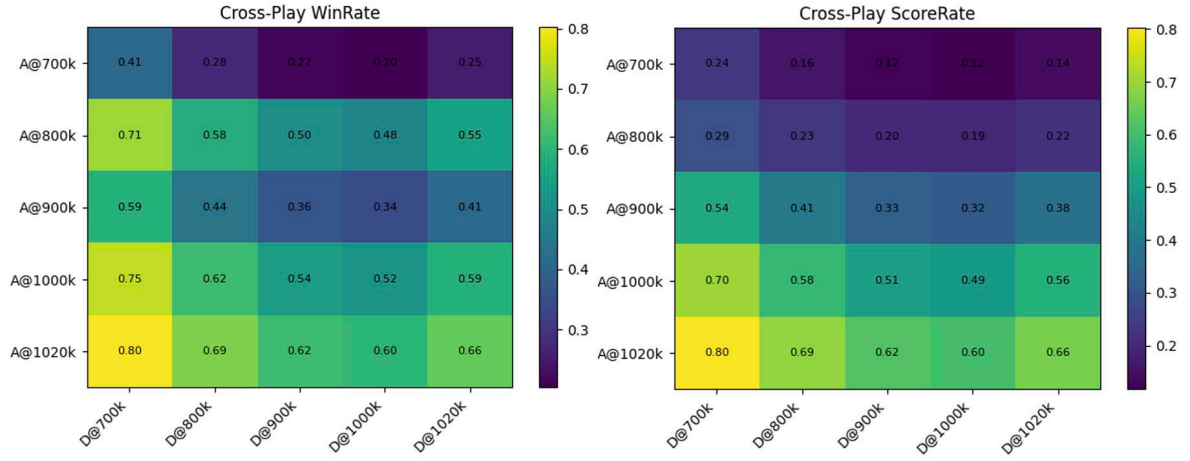

Fig. 4. Cross-play WinRate and ScoreRate.

Acknowledgements

This work was supported by the Future Challenge Defense Technology Research and Development Program through the Agency For Defense Development (ADD) grant funded by the Defense Acquisition Program Administration (DAPA) in 2025 (No.915134201).

References

[1]. K. Zhang, Z. Yang, T. Başar, Multi-agent reinforcement learning: A selective overview of theories and algorithms, Chapter 12, in Handbook of Reinforcement Learning and Control (K. G. Vamvoudakis, Y. Wan, F. L. Lewis, D. Cansever, Eds.), *Springer*, Cham, 2021, pp. 321-384.

[2]. J. Schulman, F. Wolski, P. Dhariwal, A. Radford, et al., Proximal policy optimization algorithms, *arXiv*, 2017, arXiv:1707.06347.

[3]. E. Kaufmann, L. Bauersfeld, A. Loquercio, M. Müller, et al., Champion-level drone racing using deep reinforcement learning, *Nature*, Vol. 620, 2023, pp. 982-987.

[4]. Y. Song, M. Steinweg, E. Kaufmann, D. Scaramuzza, Autonomous drone racing with deep reinforcement learning, in *Proceedings of the IEEE/RSJ International Conference on Intelligent Robots and Systems (IROS'21)*, 2021, pp. 1205-1212.

[5]. Y. Song, A. Romero, M. Müller, V. Koltun, et al., Reaching the limit in autonomous racing: Optimal control versus reinforcement learning, *Science Robotics*, Vol. 8, Issue 82, 2023, adg1462.

[6]. E. Kaufmann, A. Loquercio, R. Ranftl, A. Dosovitskiy, et al., Deep drone acrobatics, in *Proceedings of Robotics: Science and Systems Conference (RSS'20)*, 2020.

[7]. Z. Xu, C. Yu, R. Zhang, H. Yuan, et al., VolleyBots: A testbed for multi-drone volleyball game combining motion control and strategic play, *arXiv*, 2025, arXiv:2502.01932.

[8]. M. Samvelyan, T. Rashid, C. S. de Witt, G. Farquhar, et al., The StarCraft multi-agent challenge, in *Proceedings of the 18th International Conference on Autonomous Agents and Multiagent Systems (AAMAS'19)*, 2019, pp. 2186-2188.

[9]. W. Li, Z. Ding, S. Karten, C. Jin, FightLadder: A benchmark for competitive multi-agent reinforcement learning, *arXiv*, 2024, arXiv:2406.02081.

[10]. International Drone Soccer Federation (FIDA), Official drone soccer rules and regulations, https://dronesoccer.org/

(031)

Decentralized Potential-Field Control for Drone Swarms in Bounded Airspace

Marlon M. López-Flores [1], Fabio Suim Chagas [1], Fábio Luiz Júnior [1], Nina Machado Figueira [2] and Paulo F. F. Rosa [1]
[1] Military Engineering Institute, Artificial Intelligence, Robotics and Cybernetics Laboratory, Praça Gen. Tibúrcio, 80 – Urca, Rio de Janeiro, Brazil
[2] Escola de Comando e Estado-Maior do Exército – ECEME, Rio de Janeiro, Brazil
E-mail: marlon.michael@ime.eb.br, fsuim@ime.eb.br, fabioluiz@ime.eb.br, nina.figueira@eb.mil.br, rpaulo@ime.eb.br

Summary: This paper presents a decentralized potential-field controller for drone swarms operating in a bounded three-dimensional airspace that may contain a small number of non-cooperative agents. Each drone evaluates simple analytic potentials from locally sensed neighbors and hostiles. The control law combines (i) short-range repulsion parameterized by a protection radius between cooperatives, (ii) weaker cohesion that preserves swarm integrity, and (iii) a strong repulsive term from hostile agents, all saturated by platform speed and acceleration limits and constrained by periodic horizontal boundaries and clipped altitude. We test the method in a 500×500×200 m^3 domain with 200 cooperative drones and five hostile drones. Monte Carlo simulations over 100 trials show that agents remain inside the airspace, avoid hard-body collisions, maintain safe separation, and achieve average threat response times on the order of seven seconds, while relying only on local sensing and lightweight onboard computation.

Keywords: Unmanned aerial vehicles, Drone swarms, Potential fields, Decentralized control, Moving obstacle avoidance.

1. Introduction

Classic artificial potential fields enable reactive obstacle avoidance [1] and exact navigation with specially constructed potentials [2]. Our design adopts simple analytic terms suitable for decentralized swarm control.

The rapid expansion of unmanned aerial vehicle (UAV) operations – especially multi-UAV and swarm-based missions – intensifies the need for tactical deconfliction methods that remain effective when communication is limited and decisions must be made locally. Recent surveys of artificial-intelligence (AI) approaches for UAV deconfliction emphasize that, despite progress in optimization- and learning-based strategies, operational deployments still require lightweight mechanisms that can react in real time, scale with swarm size, and remain robust under sensing and connectivity constraints [1]. This need is particularly evident in drone logistics and emerging UAV traffic-management concepts, where AI-enabled autonomy must be paired with dependable low-level safety behaviors to maintain separation and handle unexpected non-cooperative traffic [2].

In addition to "will they collide?", safe swarm operation increasingly depends on "what is the risk if they do?" – especially in confined environments where interactions and post-contact dynamics may differ from open-air conditions. Physics-based simulation has been explored to quantify collision risk and study collision dynamics for autonomous drones in confined fluids using lattice Boltzmann methods, providing complementary insight to purely kinematic separation rules [3, 4]. These results motivate controllers that can enforce separation proactively while remaining computationally simple enough for onboard, distributed execution.

Among reactive approaches, artificial potential fields (APFs) remain attractive because they map relative geometry directly into control actions with minimal computation. Classic formulations demonstrated real-time obstacle avoidance by shaping repulsive and attractive potentials [5], while later work established conditions for exact navigation using specially constructed potential functions [6]. For multi-agent coordination, flocking theory provides a principled route to cohesion and collective motion through combinations of attraction/repulsion and (often) velocity alignment [7]. However, implementing full consensus-like alignment can increase sensing/communication requirements and may be unnecessary for short-horizon safety responses.

Recent swarm-navigation studies continue to build on APF principles for cluttered or adversarial settings. Hybrid potential-function methods have been proposed to prevent collisions with fixed obstacles while guiding swarm motion [8], and APF-based navigation has been combined with impedance control to improve traversal through cluttered environments [9]. Still, there is a practical gap for a controller that is (i) fully decentralized, (ii) explicitly handles non-cooperative moving agents, and (iii) is tailored to a bounded 3D operational volume with explicit kinematic constraints.

This paper addresses that gap by presenting a decentralized potential-field controller for drone swarms operating in a bounded three-dimensional airspace with a small number of non-cooperative agents. Each UAV computes closed-form repulsion

and cohesion terms from locally sensed neighbors, together with a strong repulsive response to detected hostiles, while respecting speed/acceleration limits and the airspace boundary model. The resulting method targets scalable onboard use and immediate safety response without reliance on centralized coordination.

The remainder of the paper is structured as follows. Section 2 defines the problem setup and assumptions. Section 3 details the proposed methodology, and Section 4 presents the algorithm. Section 5 reports the simulation results. Section 6 discusses the findings and their implications, and Section 7 concludes the paper and outlines directions for future work.

2. Problem Setup

We consider a leaderless swarm of N_c cooperative drones $i \in \mathcal{C} = \{1, \dots, N_c\}$ operating in a bounded 3D domain with N_h hostile agents $k \in \mathcal{H} = \{1, \dots, N_h\}$. Each cooperative has state $(\boldsymbol{x}_i, \boldsymbol{v}_i) \in \mathbb{R}^3 \times \mathbb{R}^3$ updated in discrete time with step Δt.

The workspace is

$$\Omega = [0, X_{\max}) \times [0, Y_{\max}) \times [0, Z_{\max}],$$

with periodic wrap-around in xy-plane and altitude clipping in z:

$$x \leftarrow x \bmod X_{\max}, y \leftarrow y \bmod Y_{\max}, z \leftarrow \text{clip}(z, 0, Z_{\max})$$

Cooperative motion is constrained by

$$\| \mathbf{v}_i \| \leq v_{\max}, \| \mathbf{a}_i \| \leq a_{\max},$$

implemented by vector-norm clamping.

Each agent senses cooperative neighbors within range R:

$$\mathcal{N}_i(t) = \{j \in \mathcal{C}, j \neq i : \| \mathbf{x}_j - \mathbf{x}_i \| \leq R\}$$

Neighbor queries are implemented via a KD-tree built each frame.

Drones have radius r and safety margin s. We use

$$d_{\text{col}} = 2r, \ \gamma = r + s,$$

where γ is a buffer used inside the repulsion law (distance lower bound) and is not a hard invariant under discrete-time integration and saturation.

Hostiles and sensing range. Hostiles have positions $\boldsymbol{h}_k(t)$. A sensing range $R$is used for detection events (for response-time measurement), while the avoidance term assumes access to all hostile positions in the simulation.

3. Methodology: Decentralized Potential-Field Controller

At each time step, each cooperative drone computes an acceleration command as the sum of: (i) short-range cooperative repulsion, (ii) weak cooperative cohesion, and (iii) hostile repulsion. Let $\varepsilon > 0$ avoid division by zero.

For drone i, define $\boldsymbol{d}_{ij} = \boldsymbol{x}_i - \boldsymbol{x}_j$, $r_{ij} = \| \boldsymbol{d}_{ij} \|$, and $r_{ij}^{\gamma} = \max(r_{ij}, \gamma)$. The cooperative contributions are

$$\mathbf{a}_i^{\text{rep}} = K_{PP} \sum_{j \in \mathcal{N}_i} \frac{\boldsymbol{d}_{ij}}{(r_{ij}^{\gamma})^3}, \mathbf{a}_i^{\text{att}} = K_{PA} \sum_{j \in \mathcal{N}_i} \frac{\boldsymbol{x}_j - \boldsymbol{x}_i}{r_{ij} + \varepsilon}$$

For $\boldsymbol{d}_{ik} = \boldsymbol{x}_i - \boldsymbol{h}_k$ and $r_{ik} = \| \boldsymbol{d}_{ik} \|$,

$$\mathbf{a}_i^{\text{host}} = K_{PH} \sum_{k \in \mathcal{H}} \frac{\boldsymbol{d}_{ik}}{r_{ik}^3},$$

i.e., summed over all hostiles in the reference implementation.

The commanded acceleration is

$$\tilde{\mathbf{a}}_i = \mathbf{a}_i^{\text{rep}} + \mathbf{a}_i^{\text{att}} + \mathbf{a}_i^{\text{host}}, \mathbf{a}_i = \text{sat}_{a_{\max}}(\tilde{\mathbf{a}}_i)$$

We update using a semi-implicit Euler step with speed saturation and boundary handling:

$$\mathbf{v}_i \leftarrow \text{sat}_{v_{\max}}(\mathbf{v}_i + \mathbf{a}_i \Delta t), \mathbf{x}_i \leftarrow \text{WRAP}(\mathbf{x}_i + \mathbf{v}_i \Delta t)$$

Hostiles perform a bounded random walk: with probability 0.02 per step, a random velocity increment is applied, then speed-limited and integrated with the same WRAP$(\cdot)$ operator.

A cooperative "detects" at the first frame when its nearest hostile enters range R. The response frame is the first subsequent frame where:

$$\| \mathbf{a}_i(t) - \mathbf{a}_i(t - \Delta t) \| > \tau \text{ (with } \tau = 0.1),$$

and the reported response time is the mean $(t_{\text{resp}} - t_{\text{detect}})\Delta t$ over drones that detect and respond.

Each trial simulates 200 steps (200 s). Initial cooperative positions are Sobol-sampled [10] in Ω; hostile initial positions are uniform random in Ω. Across trials, we report the mean and 95 % CI; trials run up to 100 and may stop early if all CI half-widths drop below 0.05. Metrics Min Sep. and Avg Threat Dist. are computed from the final positions at the end of the run.

4. The Algorithm

We presented a simplified version of the algorithm developed in this paper. We detail the discrete-time update used to propagate the cooperative swarm and the hostile agents in the bounded 3D domain. For clarity, we present the procedure in the same order as implemented: initialization, neighborhood construction, potential-field interaction computation and boundary enforcement.

Algorithm 1 defines the discrete-time closed-loop update used throughout the paper: a leaderless set of

N_c cooperative drones evolve inside the bounded 3D domain $\Omega = [0, X_{\max}) \times [0, Y_{\max}) \times [0, Z_{\max}]$ while avoiding N_h hostiles. The algorithm takes as input: time step Δt and horizon T; sensing radius R; interaction gains (K_{PP}, K_{PA}, K_{PH}); the short-range regularization scale γ; and kinematic limits $(V_{\max}, A_{\max})$ (with mass m).

Algorithm 1. Decentralized Potential-Field.

Require: N_c, N_h, $(X_{\max}, Y_{\max}, Z_{\max})$, Δt, $V_{\max}$, $A_{\max}$, m, R, γ, K_{PP}, K_{PA}, K_{PH}, p_{turn}, T

1: **Init:**
2: Initialize cooperative and hostiles drones
3: **for** $i \leftarrow 1$ **to** T **do**
4: $F_i \leftarrow K_{PP} \sum_{j \in N_i} \frac{x_i - x_j}{\max(\|x_i - x_j\|, \gamma)^3} + K_{PA} \sum_{j \in N_i} \frac{x_j - x_i}{\|x_j - x_i\| + 10^{-6}} + K_{PH} \sum_{k: \|x_i - h_k\| > 0} \frac{x_i - h_k}{\|x_i - h_k\|^3}$
5: $A_i \leftarrow \text{LIMIT}(F_i/m, A_{\max})$
6: Integrate
$\forall i$: $v_i \leftarrow \text{LIMIT}(v_i + A_i \Delta t, V_{\max})$;
$x_i \leftarrow \text{WRAP}(x_i + v_i \Delta t)$
7: **end for**
8: **return** $\{x_i\}_{i=1}^{N_d}, \{h_k\}_{k=1}^{N_h}$ (positions for visualization)
9: **Aux:** LIMIT clamps vector norm; WRAP is periodic in x, y and clips $z \in [0, Z_{\max}]$.

Line 1 initializes the state. Cooperative positions $\{x_i\}$ and hostile positions $\{h_k\}$ are sampled in Ω, and velocities are set to zero ($v_i \leftarrow 0$ for cooperatives, $u_h \leftarrow 0$ for hostiles). Line 2 then starts the main loop over $t = 1, \ldots, T$, and the update is synchronous: interaction terms are computed from the current step's states before advancing the dynamics. To enforce locality efficiently, Line 3 Loops over cooperative positions so that each cooperative i can query its neighbor set $\mathcal{N}_i(t) = \{j \neq i : \| p_j - p_i \| \leq R\}$.

In Line 4, each hostile executes a bounded random-walk: with probability p_{turn} a random 3D velocity perturbation is applied, then the resulting hostile speed is clamped to $V_{\max}$. The hostile position is integrated forward and mapped back into Ω using the same boundary operator as the cooperatives. This produces moving threats while keeping their motion kinematically plausible.

In Line 5, each cooperative i accumulates a net interaction vector F_i as the superposition of three potential-field components: (i) short-range repulsion from neighbors $j \in \mathcal{N}_i$ (separation), scaled as an inverse-cube law with $\max(\| x_i - x_j \|, \gamma)$ in the denominator to regularize close approaches; (ii) a weaker attraction toward neighbors (cohesion), implemented as a normalized direction term to avoid distance-dependent blow-up; and (iii) repulsion from hostiles, again using an inverse-cube decay (excluding the singular zero-distance case). In the reference implementation, this hostile term is summed over all hostiles (i.e., no explicit range truncation), so "locality" is enforced only for cooperative–cooperative interactions via $\mathcal{N}_i$.

Finally, Line 6 converts the interaction vector into an acceleration command by mass normalization and clamps it to the actuator bound, $A_i \leftarrow \text{LIMIT}(F_i/m, A_{\max})$. This saturation is essential because inverse-power potentials can demand unrealistically large accelerations during close encounters. In Line 7, cooperatives are propagated using a semi-implicit Euler step: velocities are updated with the saturated acceleration and then speed-limited to $V_{\max}$, after which positions are updated and projected back into the domain via WRAP(·). Here, WRAP implements the boundary model: periodic wrap-around in x and y (modulo $X_{\max}$ and $Y_{\max}$) and altitude clipping $z \in [0, Z_{\max}]$.

After completing T iterations, Lines 8–9 terminate and output the final (or logged) cooperative and hostile trajectories $\{x_i(t)\}$and $\{h_k(t)\}$, which are then used for visualization and for computing the reported metrics.

5. Simulation Scenario

We evaluate the decentralized potential-field controller (Algorithm 1) in a bounded three-dimensional workspace using Monte Carlo simulation. In each trial, cooperative and hostile initial positions are sampled uniformly at random within Ω, mentioned in Section 2 and the system is propagated for T discrete steps with time step Δt, enforcing the same boundary model as in Algorithm 1 (periodic wrap-around in xy-plane and altitude clipping in z) and the same kinematic saturations. Across independent trials (up to 100), we report the mean and 95 % confidence intervals of the performance metrics, with the full set of parameter values (e.g., swarm size, workspace dimensions, Δt, sensing range, and platform limits) summarized in Table 1.

Table 1. Simulation input parameters used to produce the reported metrics.

Parameter	Symbol	Value
N. coop. drones	N_c	200
N. hostiles	N_h	5
Workspace size	$X_{\max}, Y_{\max}, Z_{\max}$	500, 500, 200 (m)
Time step	Δt	1.0 (s)
Max.speed (coop.)	$V_{\max}$	5.0 (m/s)
Max.accel. (coop.)	$A_{\max}$	0.5 (m/s²)
Vision radius	R	150.0 (m)
Sep. threshold	D_{sep}	1.0 (m)
Collision factor	–	8.0
Drone mass	m	1.0 (kg)
Drone radius	r	0.50 (m)
Safety margin	λ	0.50 (m)
Protection radius	$\gamma = r + \lambda$	1.0 (m)
Random-turn prob.	p_{turn}	0.02
Steps (T)	–	200
Repul. coop. s.r.	K_{PP}	5.0
Attrac. coop. l.r.	K_{PA}	0.5
Repul. hostiles	K_{PH}	5.0

We simulate a leaderless swarm of $N_c = 200$ cooperative drones and $N_h = 5$ hostile agents in the rectangular domain $\Omega = [0, X_{\max}) \times [0, Y_{\max}) \times [0, Z_{\max}]$ for $T = 200$ discrete steps with $\Delta t = 1\,\mathrm{s}$ (total duration 200 s).

Cooperative motion is constrained by speed and acceleration saturations, and the boundary operator enforces periodic wrap-around in xy-plane and altitude clipping in z, consistent with Algorithm 1. At each step, cooperatives discover neighbors within sensing range R, compute the net potential-field acceleration as the sum of short-range cooperative repulsion, weak cooperative attraction (cohesion), and hostile repulsion, apply acceleration saturation, then integrate velocity (with speed saturation) and position using the same boundary operator.

Hostiles evolve according to the bounded random-walk model of Algorithm 1: with probability p_{turn} per step, a random 3D velocity increment is applied, then hostiles are speed-limited and integrated with the same boundary handling. Fig. 1 shows representative time snapshots of a run.

In each trial, cooperative initial positions are sampled to cover Ω (Sobol sampling), with zero initial velocities; hostile initial positions are sampled uniformly at random in Ω. We execute up to 100 trials and report the mean and 95 % confidence intervals across trials; trials may terminate early if the CI half-widths meet the stopping criterion.

Table 2 summarizes the resulting statistics. Min. Sep. is computed as the minimum cooperative–cooperative Euclidean distance at the final frame of each trial (end-of-run positions). Av. Threat Dist. is the mean (over cooperatives) of the distance to the nearest hostile, also evaluated at the final frame. Threat Resp. Time is computed online during the run: a drone "detects" when a hostile first enters range R, and its "response" is the first subsequent frame where the acceleration changes by more than the specified threshold; the reported response time is averaged over drones that both detect and respond.

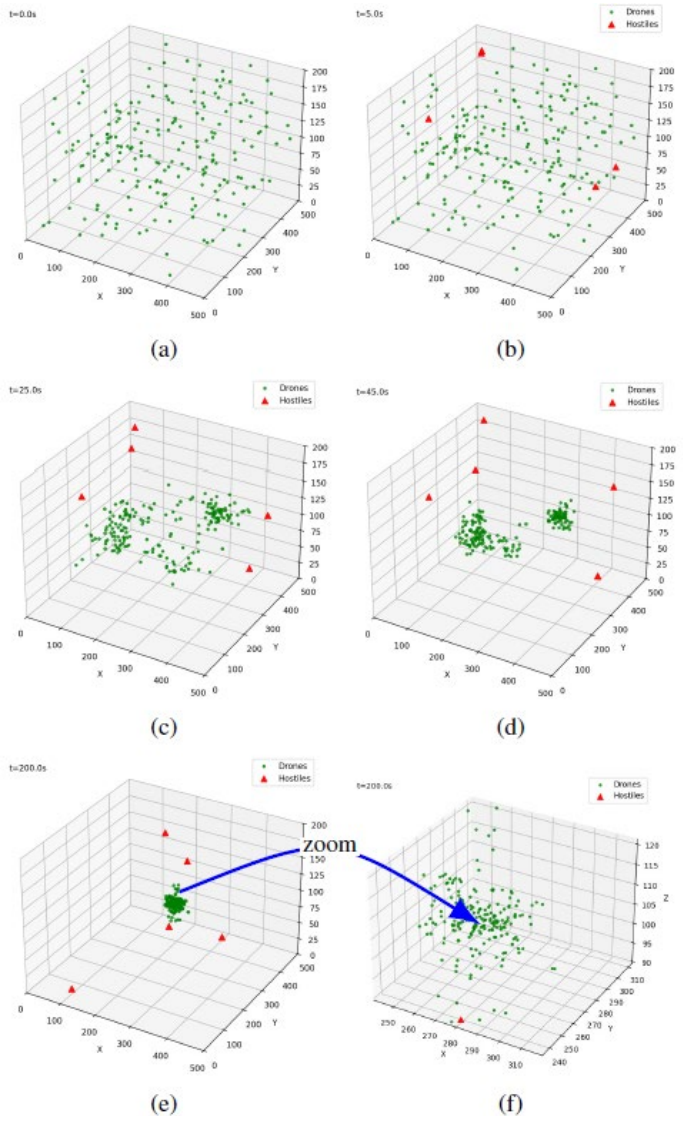

Fig. 1. Time snapshots of the 3D potential-field swarm in the bounded box Ω = [0,500) × [0,500) × [0,200] m with 200 cooperative drones (green) and 5 hostiles (red).

Table 2. Simulation Performance Metrics (100 Trials).

Metric	Mean	95 %CI	95 % CI Range	Trials
Min. Sep.	0.762	±0.063	[0.699, 0.825]	100
Av. Threat Dist.	140.441	±7.332	[133.109, 147.773]	100
Threat Resp. Time	7.144	±0.466	[6.678, 7.610]	100

6. Discussion

The proposed decentralized potential-field controller demonstrates that a large, leaderless swarm can be kept kinematically feasible (via speed/acceleration saturation) and spatially confined (via the WRAP operator) while reacting to a small set of moving non-cooperative agents in a bounded 3D box. Across 100 Monte Carlo trials in a $500 \times 500 \times 200\ \mathrm{m}^3$ domain with $N_c = 200$ cooperatives and $N_h = 5$ hostiles, the controller yields an average threat response time on the order of 7 s, with final-frame average nearest-hostile distance around 140 m.

Table 2 reports Min. Sep. ≈ 0.762 (95 % CI $[0.699, 0.825]$), which is below the protection radius $\gamma = 1.0\ \mathrm{m}$. This is consistent with the implementation and the clarified modeling: γ is used as a distance lower bound inside the repulsion law (to avoid singularities and set the buffer scale), but it is not enforced as a hard invariant under discrete-time integration and saturation. The hard-body collision threshold is smaller (center-to-center $d_{\mathrm{col}} = 1.0$), so separations below γ do not necessarily imply collisions; rather, they indicate buffer violations that can occur due to timestep discretization, simultaneous multi-agent interactions, and acceleration/speed clamping.

The reported response time is not a continuous-time latency; it is computed from discrete frames: detection occurs when a hostile first enters range R, and "response" is the first subsequent frame where the acceleration change exceeds a threshold ($\tau = 0.1$). With $\Delta t = 1\ s$, a mean of $\approx 7.1\ s$ corresponds to roughly seven simulation steps between those events, and is therefore sensitive to both the timestep and the chosen change threshold (as well as acceleration saturation at $A_{\max} = 0.5\ m/s^2$. This metric captures behavioral responsiveness of the closed-loop law under the stated kinematic limits, rather than sensor/compute latency.

Both Min. Sep. and Avg. Threat Dist. are evaluated at the final frame of each trial in the metrics implementation. As a result, these values reflect end-of-run configuration after 200 s, and may under-represent transient closest approaches occurring earlier in the run. For safety assessment in dense swarms, a natural extension is to also report time-series extrema (e.g., minimum separation over all frames) to better capture brief near-misses and "chattering" behavior typical of saturated potential fields.

Cooperative interactions are explicitly local: neighbors are queried within range R. However, the hostile repulsion term is summed over all hostiles in the reference implementation (no cutoff), while the sensing range R is used primarily to define detection events for the response-time metric. This is an important modeling choice: it makes hostile avoidance effectively nonlocal unless one assumes broadcast hostile positions or longer-range sensing. A straightforward variant is to enforce the same range-limited model for the hostile term (and report sensitivity), aligning the controller more strictly with decentralized observability.

The periodic wrap-around in xy-plane and altitude clipping in z simplify confinement and remove wall-induced congestion, but they are not physically realistic for bounded airspace enforcement. In particular, altitude clipping is a non-smooth projection that can distort local dynamics and bias distances for agents near $z = 0$ or $z = Z_{\max}$. Results should therefore be interpreted as performance under an idealized bounded domain; reflective boundaries or smooth barrier potentials are expected to change both density distribution and near-boundary safety statistics.

The controller is lightweight (closed-form potential terms plus vector-norm clamping) and the simulation uses KD-tree [11] neighbor queries to keep neighborhood discovery efficient at $N_c = 200$. This supports the intended use case of onboard decentralized evaluation with local neighbor sensing, while emphasizing that real-world deployment would additionally require (i) a consistent hostile sensing/communication assumption and (ii) boundary enforcement that matches operational constraints.

The current study intentionally focuses on a minimal potential-field design (no velocity alignment) and reports aggregate statistics under a fixed discretization and saturation regime. The most valuable next additions are: (1) baseline comparisons to standard flocking/consensus controllers (e.g., Olfati-Saber–style alignment), (2) timestep and saturation-activation analyses to rule out discretization artifacts, and (3) physically plausible boundary models (reflective or barrier-based) with time-series safety metrics (min-over-time separation and min-over-time distance to hostiles).

7. Conclusions and Future Works

This paper presented a lightweight decentralized potential-field controller for leaderless drone swarms operating inside a bounded 3D airspace with a small number of non-cooperative moving agents. Each cooperative UAV computes closed-form interaction terms from locally sensed neighbors (repulsion for separation and weak attraction for cohesion) and a hostile-repulsion term, while respecting speed and acceleration limits through vector-norm saturation and remaining inside the operational volume via the adopted boundary operator. In Monte Carlo simulation with 200 cooperative drones and five hostiles in a 500×500×200 m³ domain over 200 s, the method

exhibits consistent reactive behavior to threats, with an average threat response time on the order of seven seconds. The reported separation statistics reflect the discrete-time, saturation-limited dynamics and the fact that the protection radius parameter is used as a regularization/buffer scale inside the repulsion law rather than as a hard invariant.

For future work, we plane to (i) extend the evaluation beyond end-of-run summaries by reporting time-series safety metrics, such as minimum separation over all frames, near-miss counts under selected thresholds, and closest-approach statistics; (ii) enforce strict locality in hostile avoidance by applying a hard sensing cutoff to the hostile-repulsion term and quantifying any performance trade-offs relative to the current reference behavior; (iii) replace periodic wrap-around and hard altitude clipping with more realistic boundary models (e.g., reflective boundaries or smooth barrier potentials) and assess their impact on swarm density and near-boundary safety; and (iv) include baselines and controller variants, comparing against standard flocking/consensus approaches (e.g., velocity-alignment controllers) and testing hybrid designs that preserve decentralization while improving cohesion, reactivity, and interpretability.

Acknowledgements

This work was partially funded by the Project EVAAT_GCN (FINEP Convenio 01.24.0661.00 ref. 3311/24). Nina M. Figueira thanks Departamento de Educação e Cultura do Exército (DECEX) and Departamento de Ciência e Tecnologia (DCT).

References

[1]. F. S. Chagas, N. Ruseno, A. A. A. Bechina, Artificial intelligence approaches for UAV deconfliction: A comparative review and framework proposal, *Automation*, Vol. 6, Issue 4, 2025, 54.

[2]. F. S. Chagas, N. Ruseno, E. Koyuncu, A. A. A. Bechina, Integrating AI for autonomous UAV traffic management in drone logistic operations: Challenges, approaches, and future directions, *IFAC-PapersOnLine*, Vol. 59, Issue 10, 2025, pp. 1191-1196.

[3]. F. S. Chagas, M. M. López-Flores, P. F. F. Rosa, Assessing collision risk for autonomous drone swarms in confined fluids via lattice Boltzmann simulation, *Journal of Intelligent & Robotic Systems*, 2025 (under review).

[4]. F. S. Chagas, M. M. Lopez-Flores, P. F. F. Rosa, Collision dynamics of autonomous drones in confined fluid environments using the lattice Boltzmann method, in *Proceedings of the Brazilian Symposium on Robotics (SBR'25) and Workshop on Robotics in Education (WRE'25)*, 2025, pp. 135-140.

[5]. O. Khatib, Real-time obstacle avoidance for manipulators and mobile robots, in *Proceedings of the IEEE International Conference on Robotics and Automation (ICRA'85)*, 1985, pp. 500-505.

[6]. E. Rimon, D. E. Koditschek, Exact robot navigation using artificial potential functions, *IEEE Transactions on Robotics and Automation*, Vol. 8, Issue 5, 1992, pp. 501-518.

[7]. R. Olfati-Saber, Flocking for multi-agent dynamic systems: Algorithms and theory, *IEEE Transactions on Automatic Control*, Vol. 51, Issue 3, 2006, pp. 401-420.

[8]. T. Muslimov, E. Kozlov, R. Munasypov, Drone swarm movement without collisions with fixed obstacles using a hybrid algorithm based on potential functions, in *Proceedings of the International Russian Automation Conference (RusAut oCon'23)*, 2023, pp. 781-785.

[9]. R. A. Khan, M. Zafar, A. Batool, A. Fedoseev, et al., SwarmPath: Drone swarm navigation through cluttered environments leveraging artificial potential field and impedance control, in *Proceedings of the IEEE International Conference on Robotics and Biomimetics (ROBIO'24)*, 2024, pp. 402-407.

[10]. H. Niederreiter, Low-discrepancy and low-dispersion sequences, *Journal of Number Theory*, Vol. 30, Issue 1, 1988, pp. 51-70.

[11]. SciPy Community, cKDTree – SciPy v1.16.2 manual, https://docs.scipy.org/doc/scipy/reference/generated/scipy.spatial.cKDTree.html

(033)

GA-SDG: A ROS 2 Genetic Algorithm-Based Framework for High-Fidelity GNSS Spoofing Simulation and Dataset Generation in Support of IDS Research in UAS

Fahd Dehbi, Mohamed Zraib and Ahmed Chebak
Green Tech Institute, Mohamed VI Polytechnic University, Benguerir, Morocco
E-mail: fahd.dehbi@um6p.ma

Summary: Global Navigation Satellite System (GNSS) spoofing represents a critical security threat to unmanned aerial systems (UAS), as manipulated positioning data can mislead navigation and state-estimation processes and compromise mission objectives. The development and evaluation of effective spoofing detection mechanisms remain constrained by the limited availability of high-fidelity datasets. Real-world spoofing experiments require specialized hardware, advanced expertise, and are subject to strict regulatory and safety constraints, motivating the use of simulation-based alternatives. This paper introduces GA-SDG, a GNSS spoofing simulation and dataset generation framework built on open-source ROS 2–PX4–Gazebo stack. The framework integrates a Genetic Algorithm to generate time-varying spoofing trajectories with controllable geometry and difficulty, enabling systematic exploration of navigation-level spoofing behaviors. Designed to be modular, automated, and fully reproducible, GA-SDG provides a cost-effective simulation-based approach for generating diverse spoofing scenarios. It supports multiple attack configurations and produces synchronized datasets that capture spoofed navigation solutions together with internal autopilot and estimator states, making them suitable for behavior-based intrusion detection system benchmarking. The experimental evaluation of the framework is conducted in a Software-in-the-Loop (SITL) environment using a representative spoofing scenario, and the corresponding results are reported. Future work will extend the validation toward Hardware-in-the-Loop (HIL) and Field-in-the-Loop (FIL) experimentation and will consider additional attack types, including GNSS jamming.

Keywords: UAS cybersecurity, GNSS spoofing, ROS 2, Genetic Algorithms (GA), Spoofing simulation, Dataset generation, Intrusion Detection Systems (IDS).

1. Introduction

Unmanned Aerial Systems (UAS) are increasingly deployed across civilian, industrial, and governmental sectors, supporting applications such as surveillance, disaster assessment, precision agriculture, environmental monitoring, and critical infrastructure inspection. Autonomous and semi-autonomous UAV operations rely fundamentally on accurate navigation to operate safely and effectively [1]. Despite advances in sensor fusion, civilian UAVs still depend predominantly on GNSS as their primary source of position, velocity, and timing (PVT) [1, 2].

Civil GNSS signals are broadcast in open spectrum and remain largely unauthenticated, which makes them inherently vulnerable to intentional interference and cyberattacks [3, 4]. Among these threats, GNSS spoofing represents one of the most critical attack vectors against UAV navigation systems [5]. Spoofing consists of transmitting counterfeit GNSS-like signals that cause a receiver to compute false PVT solutions while maintaining nominal signal availability [3]. Unlike jamming, which degrades signal availability, spoofing can covertly manipulate a UAV's estimated navigation state, leading to trajectory deviation, premature landing, or loss of control without immediate alarms [1, 6].

Detecting such attacks is particularly challenging in the UAV context. Small and medium UAV platforms are resource-constrained in terms of energy, computation, and payload, which limits the feasibility of RF-centric detection approaches requiring additional hardware or software-defined radio instrumentation [7, 8]. Consequently, onboard intrusion detection systems (IDS) based on internal telemetry and behavioral consistency are often more practical than signature-based or RF-level approaches [7]. However, the development and validation of robust behavior-based IDS remain constrained by the limited availability of representative spoofing datasets.

Collecting real-world GNSS spoofing data typically requires complex and costly testbeds, specialized RF equipment, expert knowledge, controlled environments, and regulatory authorization, making such experiments inaccessible to most researchers [9]. Simulation-based approaches provide a safer alternative, but many existing frameworks rely on simplified drift injection or randomized offsets that do not capture the propagation of spoofed navigation solutions through onboard state estimation and control loops [10, 11].

In this context, GNSS threat simulation frameworks serve two essential purposes: (i) generating datasets representing nominal and adversarial conditions, and (ii) enabling verification and validation of GNSS intrusion detection and mitigation strategies under controlled and repeatable experiments [3]. Motivated by these requirements, this paper presents GA-SDG, a Genetic Algorithm–based GNSS spoofing simulation and dataset generation framework for UAS. GA-SDG models spoofing at the interface between the GNSS receiver and the onboard

autopilot by injecting coherent, time-varying navigation solutions rather than synthesizing radio-frequency signals. This abstraction targets the attack surface observable by onboard navigation systems while avoiding RF-level complexity. The framework integrates simulation, evolutionary optimization, and automated data acquisition to generate mission-relevant spoofing scenarios with controllable geometry and difficulty levels, supporting systematic dataset generation and IDS evaluation in software-based environments.

The key contributions of this study are:

1. **Spoofing attack simulation:** The framework provides a safe and customizable simulation testbench capable of generating both authentic and spoofed GNSS navigation scenarios;
2. **Genetic algorithm–based spoofing optimization:** The framework introduces genetic algorithm–driven support for generating coherent and stealthy GNSS spoofing scenarios with controllable spoofing mode and difficulty level;
3. **Dataset generation:** GA-SDG generates on-demand authentic and spoofed GNSS datasets that are spatially and temporally synchronized, integrating navigation outputs, estimator states, and control responses;
4. **Reproducibility and automation:** GA-SDG enables repeatable experiments through automated workflows and easy-to-use configuration tools, allowing researchers to customize mission scenarios and logged features without requiring extensive expertise in ROS 2 or PX4-SITL.

2. Related Works

This section surveys existing GNSS spoofing datasets and simulation frameworks, highlighting their limitations for UAV-centric research.

2.1. Existing Datasets

Existing GNSS spoofing research relies on a limited number of publicly accessible datasets, which can be classified according to their data abstraction level. Accordingly, available resources are commonly grouped into signal-centric (signal-level) and telemetry-centric (system-level) datasets.

Signal-centric datasets provide raw RF or receiver-level observables such as pseudoranges, carrier phase, Doppler frequency, and C/N_0. The Texas Spoofing Test Battery (TEXBAT), introduced by [12], is one of the earliest and most widely used benchmarks in this category. Building on TEXBAT, the Oak Ridge Spoofing and Interference Test Battery (OAKBAT) were proposed by [13] to improve reproducibility and metadata richness using synchronized GNSS simulators and SDR-based recordings. These datasets have supported numerous physical-layer spoofing detection studies [14-16], primarily focusing on legacy GNSS signals and RF-level detection techniques [9].

Despite their high-fidelity signal representations, TEXBAT and OAKBAT are not collected from UAV platforms operating in real flight conditions. TEXBAT relies on laboratory and vehicle-mounted receiver experiments, while OAKBAT is entirely laboratory-based. As a result, these datasets do not capture the propagation of spoofed measurements through UAV state estimation and control loops. Moreover, detection methods trained on signal-centric datasets typically assume access to low-level GNSS observables at deployment, often requiring specialized receivers or SDR front-ends, which limits applicability to lightweight and resource-constrained UAV platforms.

Telemetry-centric datasets provide higher-level navigation and sensor logs, including GPS, IMU, barometric, and control data recorded from UAV flights. The UA/MAVLink dataset introduced by [17] combines simulated and real UAV experiments under spoofing, jamming, and benign conditions. Subsequent studies, such as [18, 19], primarily relied on the live-flight subset due to realism limitations in the simulated data. Fully real datasets such as those used in [20] and [21] were constructed from onboard UAV logs and used for machine-learning-based spoofing detection, with attacks injected via software-level manipulation of GPS coordinates.

While telemetry-centric datasets better reflect UAV navigation behavior under attack, they remain limited in scale, diversity, and public availability. The UA/MAVLink dataset has been reported as imbalanced, with spoofing occurring over short intervals, and its simulated subset considered insufficiently realistic by multiple studies [18, 19, 22]. Notably, datasets used in [20, 21] are not publicly available.

2.2. Existing Simulation and Testbed Frameworks

Several simulation and testbed frameworks have been proposed for UAV cybersecurity analysis, each addressing different attack surfaces and levels of realism. UAVSim, introduced by [23], focuses on network-level cybersecurity and supports communication-centric attacks such as jamming and denial-of-service; however, its scope is limited to network behavior and does not model GNSS spoofing at the navigation or state-estimation level. To improve realism, more security-oriented frameworks have been proposed. The Software-/Hardware-in-the-Loop framework presented in [24] enables cyberattack injection within the PX4 control loop, allowing analysis of attack impacts under realistic execution conditions; nevertheless, attack scenarios are manually defined and not intended for systematic dataset generation. MIXED-SENSE, introduced by [11], further increases fidelity through mixed-reality sensor emulation and false data injection, but its reliance on specialized hardware and complex experimental setups limits reproducibility and ease of adoption.

More recent ROS 2–based simulation frameworks represent a modular and scalable direction for UAV security research. OpenUAV, presented by [25], provides an open-source, cloud-enabled testbed built on ROS, Gazebo, and PX4, with a focus on accessibility and large-scale UAV experimentation; however, it does not incorporate GNSS spoofing models or support labeled dataset generation for intrusion detection evaluation. The ROS 2–based CPS security framework proposed by [26] supports GPS spoofing and jamming through predefined or scripted sensor-level models, primarily for attack impact analysis rather than automated, IDS-oriented dataset generation. In parallel, OS-RFODG, presented by [27], focuses on reproducible multi-sensor dataset generation for localization and sensor-fusion research; however, GNSS data remains nominal and adversarial navigation manipulation is not considered.

Genetic algorithms (GAs) have also been explored as optimization mechanisms for deception and interference strategies. In [28], a GA is employed to tune spoofing parameters using fitness functions derived from GNSS/INS innovation consistency metrics, with the objective of manipulating the position solution while avoiding detection. While these metrics reflect local estimator consistency, the evaluation assumes that innovation behavior alone is a sufficient proxy for detectability, which does not fully capture the broader impact of spoofing overall system behavior. In a different context, [29] applies GA optimization to physical-layer jamming parameters using signal distortion and bit error rate metrics, demonstrating GA effectiveness for continuous parameter tuning but without addressing GNSS spoofing or UAV navigation dynamics.

2.3. Summary and Motivation

Existing GNSS spoofing datasets and simulation frameworks predominantly emphasize RF-level analysis, network-centric attacks, hardware-intensive realism, or nominal data generation, with limited support for systematic evaluation of navigation-level spoofing effects on UAV autopilot behavior. While the study [28] has demonstrated the use of a genetic algorithm to optimize covert GNSS spoofing parameters based on estimator-level innovation consistency, this approach is not integrated within closed-loop UAV mission execution and relies on a limited proxy for detectability. Consequently, an end-to-end framework enabling automated, repeatable, and mission-aware generation of GNSS spoofing trajectories evaluated through cumulative multi-signal anomaly behavior remains lacking, motivating the approach proposed in this work.

3. Methodology

To address the gaps identified in existing datasets and frameworks, this section introduces **GA-SDG**, a ROS 2–based simulation framework for GNSS spoofing simulation and dataset generation. The section first defines the GNSS spoofing threat model considered in this work, then presents the GA-SDG pipeline used to configure, execute, and record navigation-level spoofing scenarios in a reproducible manner.

3.1. Threat Model

We consider a GNSS spoofing attacker operating at the RF level whose goal is to capture the GNSS receiver and induce manipulated navigation solutions (PVT). Rather than modeling RF signal generation and receiver tracking, GA-SDG emulates the downstream effects of a successful spoofing attack by injecting forged navigation solutions at the interface between the GNSS receiver and the onboard autopilot, implemented in simulation through the Gazebo–PX4 bridge. The spoofing injection alters the position component of the navigation solution, while velocity and timing remain physically consistent with nominal sensor outputs. Receiver quality and health indicators are set to stable, plausible values, reflecting a clean receiver capture without exposed receiver-level faults. This threat model focuses on the attack surface observable by the autopilot, where navigation, estimation, and control rely solely on reported navigation solutions.

3.2. GA-SDG Pipeline

GA-SDG operates through five coordinated phases that are described in detail below.

Phase I: Pipeline controller

Phase I establishes the global experimental context and synchronizes all subsequent phases of GA-SDG. A dedicated pipeline controller node defines whether an experiment is authentic or spoofed, selects the spoofing geometry and difficulty level, and publishes a single, immutable objective specification that conditions calibration, optimization, and dataset generation.

GA-SDG supports two mutually exclusive operating modes:

(i) **Authentic dataset mode:** Spoofing and optimization are disabled. After Phase II completes, the framework records clean GNSS and autopilot telemetry under nominal flight conditions. These datasets serve as baseline references for IDS training, calibration validation, and benchmarking.

(ii) **Spoofed dataset mode:** The user specifies:

- a geometric spoofing mode (e.g., lateral-only, vertical-only, or full 3-D displacement in a path-aligned reference frame);
- a difficulty level, OVERT (simplified), EVASIVE (intermediate), or COVERT (stealthy), encoding the intended trade-off

between displacement magnitude and detectability.

These controller settings serve three practical purposes. First, they constrain the optimization search space, ensuring tractable and well-conditioned evaluation. Second, they align generated scenarios with mission-relevant manipulations (e.g., altitude-only perturbations targeting altitude-hold or terrain-following controllers). Third, they are propagated as metadata into the generated datasets, enabling structured analysis and reproducibility.

Phase II: Telemetry Discovery and Calibration

This phase identifies spoof-sensitive autopilot telemetry and derives the calibration parameters required by the Anomaly scoring monitor and the GA-driven optimization. Its output is a reduced, reproducible telemetry specification shared consistently across all downstream phases.

A. Automatic Telemetry Discovery

In earlier iterations of the framework, predefined parameter lists were used to identify spoofing-relevant telemetry. This approach lacked robustness across autopilot implementations and risked omitting informative signals. To overcome this limitation, GA-SDG implements an automatic discovery procedure.

All telemetry exposed by the autopilot through MAVROS (ROS–MAVLink bridge) or Micro XRCE-DDS (lightweight DDS middleware) is scanned and flattened into scalar signals. Irrelevant or non-informative streams (e.g., camera feeds, timestamps, counters) are filtered out. The resulting candidate pool includes GNSS navigation outputs, estimator innovations and covariances, estimator status flags, velocity components, attitude indicators, and other autopilot-observable state variables.

This discovery step produces a comprehensive set of candidate signals while minimizing manual bias and ensuring compatibility across autopilot stacks such as PX4 and ArduPilot.

B. Calibration

To characterize the response of each candidate signal to GNSS manipulation, GA-SDG applies controlled, ramp-limited GNSS perturbations ("spoofing pulses") along the North, East, and Down axes. Pulses are time-bounded and followed by settling windows to allow estimator reconvergence.

For each candidate signal, robust baseline statistics (e.g., baseline location, baseline scale, and nominal rate variability) are computed over nominal flight segments. Pulse-induced responses are then evaluated by comparing pre- and post-pulse windows, extracting magnitude deviations, rate excursions, persistence, and short-term trend indicators.

This calibration process captures both direct navigation effects (e.g., PVT offsets) and indirect estimator-level responses (e.g., innovation behavior), providing a quantitative mapping between navigation-solution manipulation and autopilot dynamics.

C. Feature Selection and Threshold Initialization

Following calibration, candidate signals are ranked according to their sensitivity to spoofing pulses relative to baseline variability and update rate. A configurable top-(K) subset is retained as the spoof-sensitive telemetry set used consistently by the Anomaly scoring monitor, the GA fitness evaluation, and the dataset generator.

For each selected signal (k), detector parameters are initialized directly from calibration results, including baseline statistics, level bounds, rate thresholds, and normalized weights. Boolean or discrete indicators are handled separately and monitored for logical consistency rather than numerical exceedance.

The output of this phase is a compact, reproducible spoof-sensitive telemetry specification that reduces online scoring dimensionality while ensuring that detection and optimization focus on signals that genuinely reflect autopilot-level consequences of GNSS spoofing. This specification is exported as metadata alongside the generated datasets, enabling reproducibility and fair IDS benchmarking.

Phase III: Genetic Algorithm Optimization

This phase constitutes the operational core of GA-SDG. It transforms the high-level adversarial objectives defined in Phase I (spoofing geometry and difficulty level) into optimized, time-varying spoofing trajectories. A Genetic Algorithm (GA) performs this search, while the Anomaly scoring monitor, configured using the spoof-sensitive telemetry and thresholds obtained in Phase II, provides quantitative supervision that shapes genome fitness.

A. Genetic Algorithms: Overview

Genetic Algorithms (GAs) are heuristic, population-based search methods inspired by the mechanisms of natural selection and natural genetics [30, 31]. Originating from Holland's foundational work Adaptation in Natural and Artificial Systems (1975), GAs emulate Darwinian "survival of the fittest," where stronger individuals are more likely to survive and reproduce [32]. In this framework, each candidate solution is encoded as a chromosome composed of genes, and its fitness quantitatively reflects its quality with respect to the optimization objective. Through iterative application of biologically inspired operators, selection, crossover, and mutation, GAs exploit historical information while maintaining controlled randomness, enabling systematic exploration of the search space [31, 32]. Because they operate without explicit gradient information and can evolve multiple candidate solutions simultaneously, GAs have become widely used as robust optimization

tools across engineering and computational intelligence applications [33].

B. GA Workflow

The GA operates in discrete evaluation epochs, each corresponding to a closed-loop flight execution under a single candidate spoofing genome.

At the beginning of an experiment, the GA reads the immutable objective specification produced in Phase I, including the path-aligned reference frame, enabled axes, sign constraints, spoofing mode, and difficulty level, together with genome bounds and GA hyperparameters. An initial population of real-valued genomes is randomly initialized within these objective-constrained limits.

At the beginning of an experiment, the GA reads the immutable objective specification produced in Phase I, including the path-aligned reference frame, enabled axes, sign constraints, spoofing mode, and difficulty level, together with genome bounds and GA hyperparameters. An initial population of continuous-valued genomes, each encoding a time-varying navigation bias trajectory, is randomly initialized within these objective-constrained limits. The selected difficulty level further defines a difficulty-aware alert-reduction target used during fitness evaluation, specifying the expected reduction in detector alert count (OVERT: 50 % reduction, EVASIVE: 75 % reduction, COVERT: 100 % reduction) relative to the baseline alert level observed at the beginning of the experiment.

For each generation, genomes are evaluated sequentially using a closed-loop SITL execution. A PX4 autopilot instance is simulated in Gazebo using a selected UAV model and terrain environment, while mission execution and vehicle state are supervised through QGroundControl (QGC). The desired flight path, altitude profile, and mission waypoints are defined once in QGC and kept identical across all epochs to ensure deterministic and comparable evaluations. During each epoch, the candidate genome injects a time-varying navigation bias into the GNSS solution, and the resulting vehicle behavior is continuously monitored through autopilot telemetry and estimator states.

The Anomaly scoring monitor, configured using the spoof-sensitive telemetry set and thresholds initialized in Phase II, evaluates the resulting telemetry online and produces an epoch-level report containing integrated anomaly penalty, alert count, and timing metrics. These quantities, together with the achieved displacement, are used to compute the genome fitness.

After all individuals in the current population have been evaluated, the GA updates the population according to the following steps:

- **Selection:** genomes are ranked by fitness and selected using rank-based selection with elitism;
- **Crossover:** offspring are generated by blending corresponding control points of selected parent genomes;
- **Mutation:** Gaussian perturbations are applied to control points, with mutation amplitude scaled according to the selected difficulty level;
- **Replacement:** the newly generated population fully replaces the previous one.

Mutation parameters are adaptively adjusted based on recent optimization success to balance exploration and convergence. The GA terminates when one of the following criteria is met: reaching a maximum number of generations, satisfying the displacement objective within difficulty-specific alert tolerance, or observing stagnation in fitness improvement. The best genome observed across all generations is retained and forwarded to the spoofing and dataset generation stages together with its associated detector behavior summary.

C. Detector–GA Interaction

The anomaly scoring monitor provides the quantitative supervision used to evolve genomes in GA-SDG. It operates on a set of spoof-sensitive telemetry signals and thresholds initialized during Phase II. For each monitored signal, the detector defines baseline statistics, admissible bounds, a r ate-of-change limit, and a relative importance weight. At runtime, the detector evaluates anomalies using two complementary criteria: (i) deviations of the signal value beyond its admissible range and (ii) abnormal short-term variations exceeding the allowed rate. These criteria are combined into a weighted penalty for each signal, and all penalties are aggregated into a global anomaly score that reflects the overall detectability of the injected spoofing behavior.

Over each evaluation epoch, the detector produces a report containing the integrated penalty, the peak score, alert count, and time-to-first-alert, together with a ranked attribution of the most contributing signals based on their integrated penalties. Alerts are triggered when a smoothed score exceeds a predefined threshold or when a hard cap on peak level exceedance is reached, with a short cooldown to avoid double counting.

The GA uses this detector report to compute genome fitness by rewarding achieved displacement while penalizing detectability, reflected by high integrated penalties, early alerts, and frequent alerts. This strict epoch-level synchronization ensures that all genomes are evaluated under identical monitoring logic, enabling reproducible selection pressure toward spoofing trajectories consistent with the selected spoofing mode and difficulty level.

Phase IV: Spoofing Execution

Phase IV operationalizes the optimized spoofing trajectory produced by the GA and deploys it deterministically within the closed-loop simulation. This phase ensures that the evolved adversarial behavior is replayed exactly as optimized, without further adaptation, while preserving estimator stability and repeatability.

Once GA optimization terminates, the best genome, selected according to the displacement–stealth trade-off encoded by the spoofing geometry and difficulty level, is forwarded to the spoofing executor. Spoofing execution begins only after all deployment gates are satisfied: publication of the final genome, activation of spoofing, availability of a valid GNSS fix, and reception of the immutable objective specification defined in Phase I.

At deployment start, the executor initializes the spoofed trajectory from the last valid GNSS position reported by the Gazebo GNSS sensor, ensuring continuity between nominal and spoofed navigation solutions. The genome encodes a sequence of control points representing a time-varying navigation bias, which is converted into per-axis bias rates and integrated at a fixed publish rate. The resulting bias progressively overrides the simulated Gazebo GNSS position output so that the autopilot consumes spoofed position values transparently.

Spoofing execution is governed by the immutable objective specification defined in Phase I, including the path-aligned reference frame, enabled axes, sign constraints, optional forward-only constraint, and difficulty level. Axis masking and sign enforcement are applied at every integration step to prevent leakage outside the intended spoofing geometry.

To preserve estimator stability and physical plausibility, the executor enforces rate limits on bias increments and applies a brief warm-up ramp at spoofing start. Velocity, timing, and receiver health indicators remain consistent with the nominal simulation, modeling the downstream effect of a successful receiver capture rather than RF-level manipulation.

The resulting spoofed GNSS solution is published as a replacement navigation fix, transparently consumed by the autopilot. Throughout deployment, the Anomaly scoring monitor remains active in deploy mode and produces windowed summaries characterizing alert behavior and estimator response under the executed spoofing trajectory.

Phase V: Dataset Generation

The final phase of GA-SDG records synchronized telemetry datasets for both authentic and spoofed operating modes using a unified, mode-agnostic logging mechanism.

Authentic dataset mode:

When the controller is configured in authentic mode, spoofing and optimization are disabled. Dataset recording starts automatically after calibration completes and logs clean GNSS and autopilot telemetry under nominal flight conditions. These datasets serve as baseline references for IDS training. By default, the recorder logs the same spoof-sensitive telemetry set used in spoofed experiments, enabling direct comparison between authentic and attacked scenarios. Optionally, users may extend logging to additional parameters for exploratory analysis.

Spoofed dataset mode:

In spoofed mode, dataset recording runs in parallel with spoofing execution. Logging is gated to ensure semantic consistency and begins only once spoofing is enabled and spoofed GNSS data are confirmed to be flowing. Telemetry is collected online from PX4 topics exposed through ROS 2 interfaces (e.g., Micro XRCE-DDS or MAVROS), using the calibrated spoof-sensitive parameter set.

All parameters are recorded as timestamped snapshots, preserving the native publish frequency of each telemetry stream and using sample-and-hold alignment to ensure that each record represents a coherent system state. Outputs are serialized as structured CSV files (and optionally rosbags), with explicit episode boundaries and schema versioning.

Each generated dataset is annotated with metadata specifying the operational mode (authentic or spoofed), spoofing geometry, and difficulty level. This explicit labeling ensures full reproducibility, supports machine-learning–based IDS training, and enables systematic comparison across spoofing strategies and parameterizations.

4. Implementation and Results

This section presents the implementation of GA-SDG in a SITL environment and reports representative results obtained from the execution of the framework. The objective is to demonstrate that GA-SDG can (i) simulate reproducible, closed-loop GNSS spoofing scenarios and (ii) produce synchronized, structured datasets.

4.1. Environment and Experimental Setup

GA-SDG was deployed in a PX4–ROS 2 SITL environment that emulates the full navigation pipeline of a multirotor UAV. The PX4 stack executes estimation, guidance, and control tasks, while Gazebo provides a physics-based 3D environment that generates sensor data, including GNSS measurements, consumed by the autopilot. ROS 2 ensures structured communication between modules and exposes PX4 telemetry through MAVROS and Micro XRCE-DDS, enabling direct access to GNSS, EKF, attitude, and control-loop signals for discovery, calibration, and spoofing injection.

For mission execution, waypoint-based trajectories are loaded into the system and followed autonomously by PX4 using Gazebo sensor feedback. To support spoofing experiments, the PX4/ROS 2 bridge was extended so that the Gazebo GNSS sensor stream is overridden when spoofing is enabled, allowing GA-SDG to inject manipulated positions directly at the

autopilot interface while preserving estimator timing and update rates.

The simulation environment runs on Ubuntu 22.04 with ROS 2 Humble, PX4 v1.14+, Gazebo 11+, and QGC v4.2, using an 8-core CPU, 16 GB RAM, and a 4 GB GPU. This configuration provides stable

4.2. Experimental Workflow Execution

To evaluate GA-SDG, we conducted a series of experiments covering both authentic scenarios and multiple spoofing geometries, including LATLON_RIGHT, LATLON_LEFT, ALT_UP, and ALT_DOWN, under identical mission and calibration conditions. Across all configurations, GA-SDG consistently produced optimized spoofing trajectories that achieved the intended displacement while respecting difficulty-specific alert constraints.

We report detailed results for one representative configuration, namely LATLON_RIGHT with the OVERT difficulty level, which prioritizes displacement effectiveness over stealth. This scenario was selected because it clearly illustrates the full GA-SDG pipeline – calibration, optimization, spoofing, and dataset generation – while remaining representative of the behavior observed across other geometries.

Following calibration, over 400 scalar PX4 telemetry signals were enumerated, from which 32 spoof-sensitive parameters were selected based on spoofing pulse sensitivity. These parameters were used consistently for alert monitoring, GA fitness evaluation, and dataset annotation.

During GA optimization, the baseline alert count under naïve spoofing was 19 alerts per epoch. Under the OVERT policy – corresponding to a 50 % alert-reduction target configurable by the user – the GA converged within six generations, producing lateral displacements between 9.5 m and 15.8 m while reducing alerts to 6–10 per epoch. The best genome achieved a 15.53 m lateral deviation with 8 alerts. Fig. 1 illustrates the evolution of drift vectors across generations, highlighting the convergence toward optimized spoofing trajectories under the imposed detectability constraints.

The optimized genome was then replayed deterministically during deployment, yielding a smooth divergence between real and spoofed GNSS trajectories while preserving estimator stability. The resulting drift behavior is shown in Fig. 2, where the spoofed trajectory diverges cleanly from the real GNSS path. Synchronized telemetry was recorded, generating structured datasets containing GNSS trajectories, EKF states and innovations, estimator covariances and control outputs, all annotated with spoofing geometry and difficulty level.

4.3. Reproducibility and Evolution

GA-SDG is designed to support reproducible experimentation within a ROS 2– and PX4-based simulation environment. The full workflow is executed using ROS 2 launch files that initialize the different phases and coordinate their actions. Once a phase is completed, transitions are handled automatically based on system state and evaluation outcomes. The framework is intended to evolve toward a more automated pipeline with a user interface for controlling experiment execution.

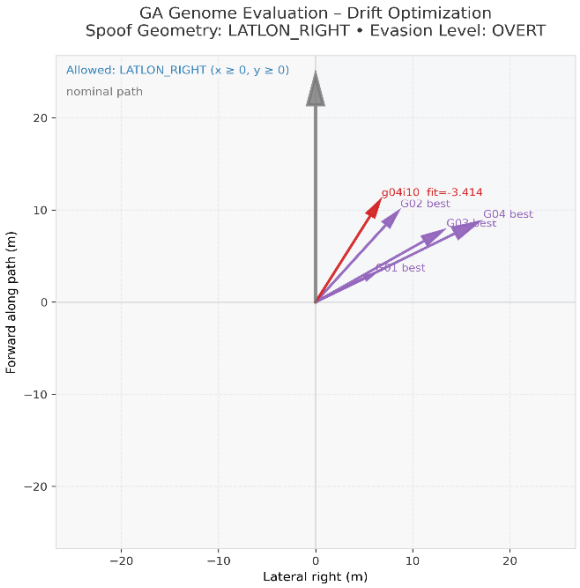

Fig. 1. GA Drift Optimization Result.

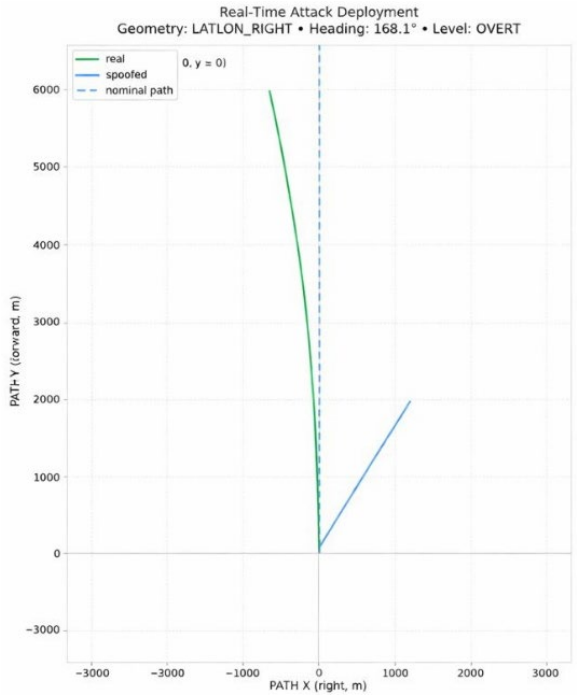

Fig. 2. Spoofing Result.

5. Discussions

The results presented in this work position GA-SDG as a valuable tool within the GNSS spoofing

research landscape. By operating at the navigation–autopilot interface rather than at the RF layer, the framework avoids regulatory and hardware constraints while still capturing the estimator- and control-level effects that govern UAV behavior under spoofing.

A central contribution of GA-SDG is the integration of evolutionary optimization for spoofing trajectory generation. The use of a Genetic Algorithm enables systematic exploration of time-varying navigation biases that balance displacement effectiveness and detectability, guided by a synchronized alert-monitoring module. Compared to fixed or handcrafted drift profiles, this approach supports more diverse and realistic adversarial behaviors and produces structured, time-aligned datasets suitable for IDS development and testing.

From a dataset perspective, GA-SDG produces rich, multi-layer telemetry that jointly captures spoofed navigation solutions, internal estimator states and innovations, control responses, and alert dynamics. This feature diversity enables IDS development based on autopilot-observable behavioral patterns rather than RF-level artifacts, improving generality across platforms and avoiding reliance on specialized receiver hardware.

While GA-SDG provides a flexible and reproducible framework for GNSS spoofing dataset generation, several limitations must be acknowledged. First, all experiments are conducted in SITL, and realism is inherently bounded by the fidelity of the Gazebo environment and PX4 sensor models. Second, the current evaluation focuses on a limited set of vehicle platforms and environmental conditions.

6. Conclusions

This work contributes to ongoing efforts in securing Unmanned Aerial Systems by addressing the growing threat of GNSS spoofing and the limited availability of realistic and accessible research resources. As UAS become increasingly deployed in safety-critical and civilian applications, understanding their behavior under adversarial navigation manipulation is essential. GA-SDG provides a dedicated framework for studying GNSS spoofing effects at the navigation-system level, enabling safe, reproducible experimentation and dataset generation. By bridging the gap between costly RF testbeds and oversimplified simulation approaches, this work supports more rigorous evaluation of intrusion detection and navigation-resilience strategies.

Future work will focus on extending GA-SDG toward hardware-in-the-loop validation to assess real-world transferability and platform-specific effects, as well as integrating GNSS jamming scenarios.

References

[1]. L. Al-Soufi, T. Demirsoy, E. Gelal Soyak, An implementation-based study of the detection of and recovery from GPS spoofing attacks for unmanned aerial vehicles, *International Journal of Advances in Engineering and Pure Sciences*, Vol. 36, Issue 3, 2024, pp. 211-223.

[2]. M. M. Abrar, R. Islam, S. Z. H. Shovon, M. A. Rahman, et al., GPS-IDS: An anomaly-based GPS spoofing attack detection framework for autonomous vehicles, *arXiv*, 2024, arXiv:2405.08359.

[3]. I. Iudice, D. Pascarella, G. Corraro, G. Cuciniello, A real/fast-time simulator for impact assessment of spoofing & jamming attacks on GNSS receivers, in *Proceedings of the 11th International Workshop on Metrology for AeroSpace (MetroAeroSpace'24)*, 2024, pp. 309-314.

[4]. P. Wang, Z. Yang, J. Li, L. Shi, Learning-based detection of GPS spoofing attack for quadrotors, *arXiv*, 2025, arXiv:2501.07597.

[5]. F. Dehbi, M. Zraib, A. Chebak, PASTAD: A context-aware threat modeling methodology for unmanned aerial systems, *Cyber Security and Applications*, Vol. 3, 2025, 100111.

[6]. A. Ghanbarzadeh, M. Soleimani, H. Soleimani, GNSS/GPS spoofing and jamming identification using machine learning and deep learning, Chapter 7, in Explainable Artificial Intelligence in Cyber Threat Intelligence (A. K. Luhach, A. Elci, Eds.), *Bentham Science Publishers*, Singapore, 2022, pp. 165-194.

[7]. G. Loukas, E. Karapistoli, E. Panaousis, P. Sarigiannidis, et al., A taxonomy and survey of cyber-physical intrusion detection approaches for vehicles, *Ad Hoc Networks*, Vol. 84, 2019, pp. 124-147.

[8]. F. Dehbi, M. Zraib, A. Chebak, Unmanned aerial systems architecture and security concerns: A cyber-physical system perspective, Chapter 29, in Cyber Security in Intelligent Computing and Communications (R. C. Poonia, S. K. Singh, L. S. S. Reddy, Eds.), *Springer*, Cham, 2025, pp. 333-344.

[9]. S. Islam, M. Z. H. Bhuiyan, M. Liaquat, I. Pääkkönen, et al., An open GNSS spoofing data repository: characterization and impact analysis with FGI-GSRx open-source software-defined receiver, *GPS Solutions*, Vol. 28, Issue 4, 2024, 176.

[10]. P. Draugelytė, I. Suzdalev, Blockchain-based secure communication for UAV networks: a decentralized approach to GNSS spoofing detection, *Aviation*, Vol. 29, Issue 3, 2025, pp. 191-200.

[11]. K. A. Pant, L.-Y. Lin, J. Kim, W. Sribunma, et al., MIXED-SENSE: A mixed reality sensor emulation framework for test and evaluation of UAVs against false data injection attacks, *arXiv*, 2024, arXiv:2407.09342.

[12]. T. E. Humphreys, J. A. Bhatti, D. P. Shepard, K. D. Wesson, The Texas spoofing test battery: Toward a standard for evaluating GPS signal authentication techniques, in *Proceedings of the 25th International Technical Meeting of the Satellite Division of The Institute of Navigation (ION GNSS'12)*, 2012, pp. 3569-3583.

[13]. A. Albright, S. Powers, J. Bonior, F. Combs, A tool for furthering GNSS security research: The Oak Ridge spoofing and interference test battery (OAKBAT), in *Proceedings of the 33rd International Technical Meeting of the Satellite Division of The Institute of Navigation (ION GNSS+ 2020)*, 2020, pp. 3697-3712.

[14]. C. Huang, H. Zhang, Y. Wang, X. Zhan, et al., To lock the authentic signals: mitigating GNSS spoofing with INS-aided tracking, *Information Fusion*, Vol. 126, 2026, 103596.

[15]. G. Marchand, A. Toumi, G. Seco-Granados, Machine learning assessment of anti-spoofing techniques for GNSS receivers, in *Proceedings of the 32nd International Technical Meeting of the Satellite Division of The Institute of Navigation (ION GNSS+ 2019)*, 2019, pp. 2409-2422.

[16]. X. Wei, C. Sun, X. Li, J. Ma, GNSS spoofing detection for UAVs using doppler frequency and carrier-to-noise density ratio, *Journal of Systems Architecture*, Vol. 153, 2024, 103212.

[17]. J. Whelan, T. Sangarapillai, O. Minawi, A. Almehmadi, et al., HITL UAV DoS GPS spoofing attacks (MAVLink), IEEE DataPort, 2020, https://ieee-dataport.org/open-access/hitl-uav-dos-gps-spoofing-attacks-mavlink

[18]. O. Jullian, B. Otero, M. Stojilović, J. J. Costa, et al., Deep learning detection of GPS spoofing, in Machine Learning, Optimization, and Data Science (G. Nicosia, et al., Eds.), *Springer*, Cham, 2022, pp. 527-540.

[19]. J. D. Yoo, G. M. Kim, M. G. Song, H. K. Kim, MeNU: Memorizing normality for UAV anomaly detection with a few sensor values, *Computers & Security*, Vol. 150, 2025, 104248.

[20]. X. Wei, Y. Wang, C. Sun, PerDet: Machine-learning-based UAV GPS spoofing detection using perception data, *Remote Sensing*, Vol. 14, Issue 19, 2022, 4925.

[21]. X. Wei, C. Sun, M. Lyu, Q. Song, et al., ConstDet: Control semantics-based detection for GPS spoofing attacks on UAVs, *Remote Sensing*, Vol. 14, Issue 21, 2022, 5587.

[22]. A. B. Mohammed, L. C. Fourati, Investigation on datasets toward intelligent intrusion detection systems for Intra and inter-UAVs communication systems, *Computers & Security*, Vol. 150, 2025, 104215.

[23]. A. Y. Javaid, W. Sun, M. Alam, UAVSim: A simulation testbed for unmanned aerial vehicle network cyber security analysis, in *Proceedings of the IEEE Globecom Workshops (GC Wkshps'13)*, 2013, pp. 1432-1436.

[24]. J. Goppert, A. Shull, N. Sathyamoorthy, W. Liu, et al., Software/hardware-in-the-loop analysis of cyberattacks on unmanned aerial systems, *Journal of Aerospace Information Systems*, Vol. 11, Issue 5, 2014, pp. 337-343.

[25]. M. Schmittle, A. Lukina, L. Vacek, J. Das, et al., OpenUAV: A *UAV testbed for the CPS and robotics community,* in *Proceedings of the ACM/IEEE 9th International Conference on Cyber-Physical Systems (ICCPS'18)*, 2018, pp. 130-139.

[26]. U. Patil, A. Gunasekaran, R. Bobba, H. Abbas, ROS2-based simulation framework for cyberphysical security analysis of UAVs, *arXiv*, 2024, arXiv:2410.03971.

[27]. I. Jarraya, A. B. Mohammed, M. A. Hamdi, L. C. Fourati, et al., OS-RFODG: Open-source ROS2 framework for outdoor UAV dataset generation, SSRN, 2025, https://ssrn.com/abstract = 5114884

[28]. H. Chen, Z. Wen, C. Lei, Optimization of covert spoofing parameters for loosely coupled GNSS/INS systems based on improved genetic algorithm, *Scientific Reports*, Vol. 15, Issue 1, 2025, 7285.

[29]. Y. Dang, D. Li, Y. Fu, Y. Liao, A jamming method for OAM communication system using genetic algorithm, *Physical Communication*, Vol. 73, 2025, 102835.

[30]. D. E. Goldberg, Genetic Algorithms in Search, Optimization, and Machine Learning, *Addison-Wesley*, Reading, 1989.

[31]. J. McCall, Genetic algorithms for modelling and optimisation, *Journal of Computational and Applied Mathematics*, Vol. 184, Issue 1, 2005, pp. 205-222.

[32]. K. F. Man, K. S. Tang, S. Kwong, Genetic algorithms: concepts and applications [in engineering design], *IEEE Transactions on Industrial Electronics*, Vol. 43, Issue 5, 1996, pp. 519-534.

[33]. S. Katoch, S. S. Chauhan, V. Kumar, A review on genetic algorithm: past, present, and future, *Multimedia Tools and Applications*, Vol. 80, Issue 5, 2021, pp. 8091-8126.

(035)

SkySim: A ROS2-Based Simulation Environment for Natural Language Control of Drone Swarms Using Large Language Models

Aditya Shibu [1], Marah Saleh [2], Mohamed Al-Musleh [2] and Nidhal Abdulaziz [3]
[1] School of Mathematical and Computer Sciences, [2] School of Textiles and Design
(AIM BeyonD Research Lab), [3] School of Engineering and Physical Sciences,
Heriot-Watt University Dubai Campus, UAE
E-mail: as2397@hw.ac.uk, Marah.Saleh@hw.ac.uk, M.Al-Musleh@hw.ac.uk, Nidhal.Abdulaziz@hw.ac.uk

Summary: Unmanned Aerial Vehicle (UAV) swarms offer versatile applications in logistics, agriculture, and surveillance, yet controlling them requires expert knowledge for safety and feasibility. Traditional static methods limit adaptability, while Large Language Models (LLMs) enable natural language control but generate unsafe trajectories due to lacking physical grounding. This paper introduces SkySim, a ROS2-based simulation framework in Gazebo that decouples LLM high-level planning from low-level safety enforcement. Using Gemini 3.5 Pro, SkySim translates user commands (e.g., "Form a circle") into spatial waypoints, informed by real-time drone states. An Artificial Potential Field (APF) safety filter applies minimal adjustments for collision avoidance, kinematic limits, and geo-fencing, ensuring feasible execution at 20 Hz.
Experiments with swarms of 3, 10, and 30 Crazyflie drones validate spatial reasoning accuracy (100 % across tested geometric primitives), real-time collision prevention, and scalability. SkySim empowers non-experts to iteratively refine behaviors, bridging AI cognition with robotic safety for dynamic environments. Future work targets hardware integration.

Keywords: Micro and mini drone control, Large Language Models (LLMs), UAV Swarms, Natural language control, ROS2, Gazebo simulation.

1. Introduction

Unmanned Aerial Vehicle (UAV) swarms are powerful tools capable of performing tasks across diverse domains, including logistics, agriculture, and surveillance [1]. However, designing complex movements or controlling these systems remains a complex challenge, requiring significant expert knowledge to ensure the balance between safety and physical feasibility [2]. Historically, UAV systems have relied on static control methods such as pre-programmed task flows and rule-based libraries, which restrict them to executing predefined actions and limit their adaptability in dynamic, real-world environments [3]. The emergence of Large Language Models (LLMs) offers a potential solution by allowing users to translate high-level human intentions into actionable control commands via Natural Language [1, 4]. Nevertheless, LLM-generated reference trajectories are inherently unsafe, as LLMs lack the real-world grounding necessary to understand physics or predict events like collisions, especially since even small errors in reasoning can lead to immediate failure in drone swarms [2, 4].

To realize the benefits of natural language control while maintaining physical security, a decoupled mechanism is needed to enforce safety constraints. In this paper we introduce **SkySim**, a ROS2 based simulation framework that bridges this gap by decoupling the LLM's high-level planning from a low-level, real-time safety filter. This system leverages the LLM's reasoning power to control a swarm of drones, while an optimization-based safety filter operates beneath it, ensuring trajectories are feasible, collision free, and safe for real-world deployment by applying minimal adjustments where constraints are violated. This architecture enables non-experts to iteratively refine swarm behaviors using natural language, without the burden of accounting for safety or low-level feasibility constraints.

1.1. Related Work

The integration of Large Language Models (LLMs) into Unmanned Aerial Vehicle (UAV) systems has emerged as a transformative approach to bridging the gap between high-level human intentions and actionable control commands. Recent literature demonstrates that LLMs enable users to issue natural language instructions that can be converted into executable trajectories, moving past the limitations of traditional static frameworks [1-3]. However, the reliability challenges and lack of real-world grounding in LLM-generated outputs require the development of hybrid architectures to ensure safety in mission critical applications [4-6].

A leading paradigm in this domain is the SwarmGPT framework [7], which pioneered the integration of LLMs for synchronized drone swarm choreography. SwarmGPT addresses fundamental safety challenges by augmenting the LLM with an optimization-based safety filter that minimally corrects generated trajectories to ensure they remain collision-free. However, this architecture is largely optimized for temporally coordinated choreography, focusing on the smoothness and aesthetic quality of the swarm's motion over time. It is less focused on zero-shot spatial reasoning, where the primary objective is to rapidly translate abstract natural

language commands into valid, arbitrary static geometries (e.g., 'form a Christmas Tree') without prior training on those specific shapes. Consequently, alternative strategies focusing on real-time reachable set generation and spatial optimization have emerged as crucial complements, highlighting the need for frameworks that can ensure safety during rapid, goal-oriented reconfiguration [8, 9].

Furthermore, the effectiveness of the safety filter relies heavily on the choice of collision avoidance algorithm [10]. While recent research highlights the efficacy of techniques such as Convolutional Neural Networks (CNNs) and Deep Reinforcement Learning (DRL) [11-14], these approaches often add significant computational overhead and training complexity. In an architecture where the high-level planner (LLM) is already subject to variable inference latency, adding a computationally intensive learning-based safety layer increases the risk of control loop delays, potentially leading to collisions during rapid and clustered maneuvers. In contrast, deterministic reactive models like Artificial Potential Fields (APF) offer a lightweight, distinct alternative [11]. By leveraging real-time state information, readily available via ground truth or motion capture systems, APF provides immediate, reflexive collision avoidance with negligible computational cost. This validates the decoupled "sense-plan-act" architecture that SkySim aims to achieve, where the LLM handles the high-level cognitive reasoning while a fast, deterministic APF layer enforces physical safety constraints in real-time.

2. System Architecture and Methodology

Our methodology is established on a modular, decoupled architecture implemented within the Robot Operating System (ROS2 Jazzy). To ensure system stability under variable network conditions, the framework strictly separates high-latency cognitive planning from low-latency real-time execution.

Fig. 1 illustrates this multi-layered architecture, detailing the asynchronous data flow between the Planning Layer (LLM-driven goal generation) and the Control Layer (20Hz safety enforcement).

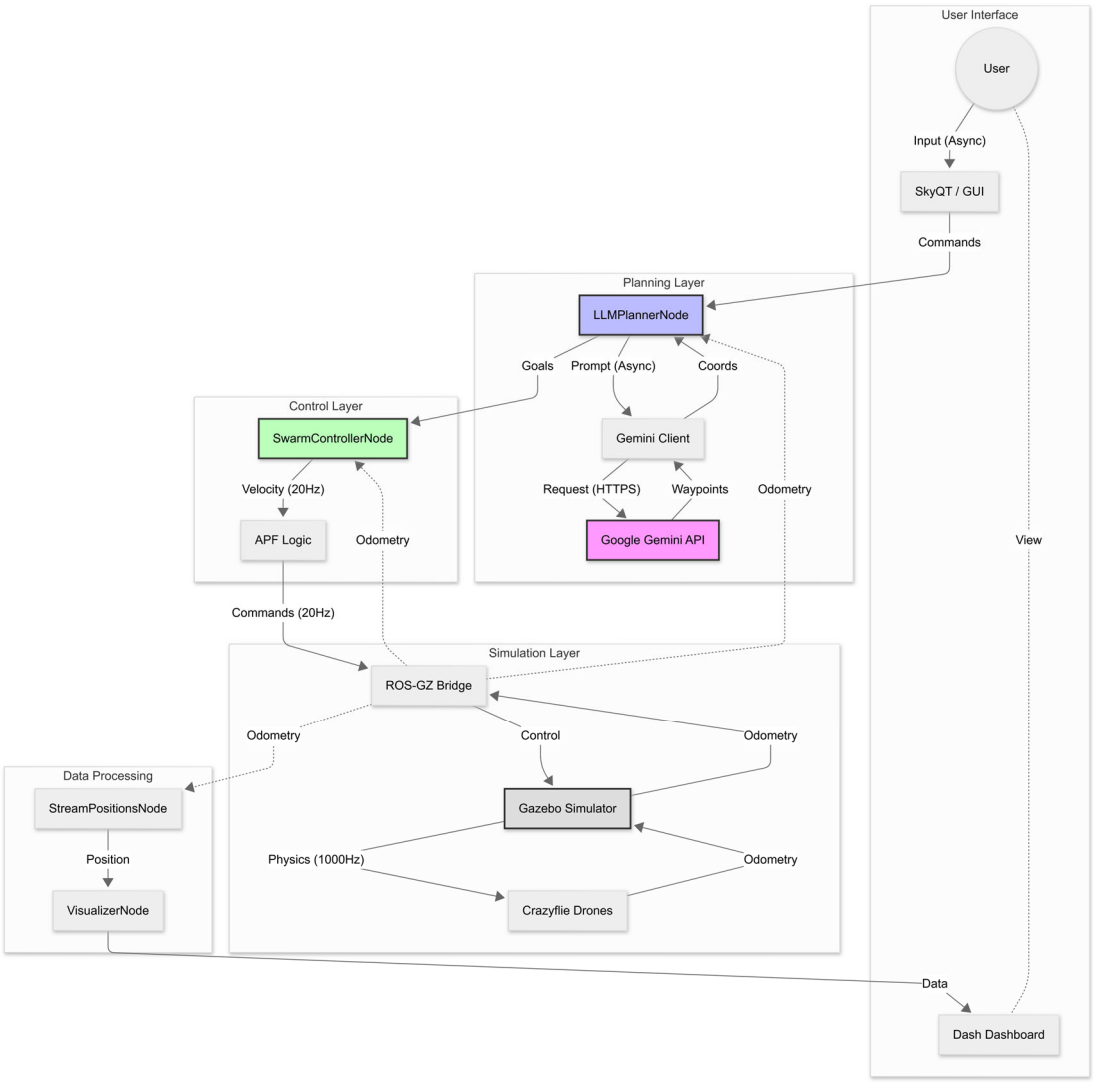

Fig. 1. SkySim system architecture.

2.1. Command Input and State Sensing

The process is initiated via a natural language command (e.g., "Form a circle around the center at a 2m height"). Upon receiving the input, the SkySim interface initiates the "sense" phase by subscribing to the current spatial coordinates of all agents via the ROS2 (/odom) topic.

The (/odom) topic is bridged directly from the Gazebo Simulation to the control node. This is done to emulate the high-precision, real-world motion capture systems (e.g., OptiTrack). This provides a noiseless, instantaneous snapshot of the current swarm topology.

2.2. State-Aware LLM-Based Planning

Contrary to standard LLM control pipelines, SkySim does not attempt to map text directly to discrete control primitives (e.g., throttle, pitch). Instead, it acts as a high-level spatial planner via the Gemini 3.5 Pro LLM (google.generativeai API).

To ensure deterministic and physically feasible outputs, the LLM is initialized with strict system instruction defining the swarm size *(N),* the coordinate system *(X = forward, Y = left, Z = up),* and the ground-collision constraints *(Z ≥ 0.5 m).*

When a user issues a command, the framework constructs a dynamic state-aware prompt by concatenating the system instructions, the instantaneous 3D positional telemetry of all the drones, and the natural language input.

Example Prompt Structure (N = 3)

System Instruction:

"You are a drone swarm controller for 3 drones. Generate target [x, y, z] coordinates to fulfill the command. Output only a valid python list of 3 lists. Keep *Z ≥ 0.5".*

Current Context:

Current Drone Positions: [[0.1, 0.0, 1.0], [0.0, 1.5, 1.1], [1.2, 1.1, 0.9]].

User Command:

"Form a triangle around the center."

The LLM is constrained to output a serialized configuration matrix, formatted as a raw Python list as shown in Eq. (1):

$$P_{goal} = [[x_1, y_1, z_1], \dots, [x_N, y_N, z_N]] \quad (1)$$

This string is deterministically parsed via Abstract Syntax Tree for validation. No additional formatting, markdown, or text explanations are permitted. In the event of an API timeout or malformed output schema, the system holds the position of the previous command to prevent undefined system states.

2.3. The Safety Filter and Safe Execution

The "act" phase is managed by the Safety Filter, which bridges the gap between static LLM waypoints and real-time dynamic feasibility. We model the multi-agent system using a single-integrator kinematic model, where the control input for agent *i* is its velocity vector, $u_i = \dot{p}_i$.

To enforce collision avoidance in real-time without the computational overhead of non-linear solvers (e.g., MPC), SkySim implements an Artificial Potential Field controller. The control loop operates at 20 Hz, continuously calculating the required velocity as a gradient of a composite potential function:

$$v_{total,i} = v_{att,i} + \sum_{j \neq i} v_{rep,ij} \quad (2)$$

1. Attractive Velocity (Goal Seeking): A proportional controller puts agent *i* toward the LLM-assigned waypoint $P_{goal,i}$ with a gain of $K_p = 1.0$:

$$v_{att,i} = K_p \cdot (P_{goal,i} - P_i) \quad (3)$$

2. Repulsive Velocity (Collision Avoidance): A hard safety constraint is enforced to prevent inter-agent collisions. If the Euclidean distance $d_{ij} = \| P_i - P_j \|$ between agent *i* and neighbour *j* falls below the safety radius $r_{min} = 0.8$ m (can be configured), a linear repulsive vector is activated:

$$v_{(rep,ij)} = \begin{cases} K_{rep} \cdot (r_{min} - d_{ij}) \cdot \hat{n}_{ij} \; if \; d_{ij} < r_{min} \\ 0 \; otherwise \end{cases}, \quad (4)$$

where $\hat{n}_{ij} = \frac{P_i - P_j}{d_{ij}}$ is the unit vector pointing away from the neighbour, and $K_{rep} = 2.0$ is the repulsion gain.

3. Kinematic and Boundary Constraints: To ensure absolute system safety, commands are sanitized via a two-stage constraint protocol before execution. First, the LLM Planner Node enforces a strict virtual geo-fence. Any LLM-generated waypoint that falls outside the defined spatial boundaries $(X, Y \in [10.0, 10.0]\, m, Z \in [0.2, 5.0]\, m)$ is immediately rejected, triggering a position-hold fallback to prevent the swarm from exiting the simulated range of a motion capture system.

Secondly, for waypoints within a valid workspace, the kinematic limits of the nano-quadrotors are enforced. The final resultant velocity command is saturated at $v_{max} = 0.5$ m/s before being published to the ROS2 (/cmd_vel) topic:

$$v_{cmd,i} = \min(|v_{total,i}|, v_{max}) \cdot \frac{v_{total,i}}{|v_{total,i}|} \quad (5)$$

This multi-tiered architecture guarantees that the swarm remains bounded within a safe operational volume and respects the physical motor limits at all times.

3. Experimental Evaluation and Results

To validate the safety, scalability, and cognitive capabilities of the SkySim framework, we conducted a series of simulation experiments using Gazebo

Harmonic Environment and ROS2 Jazzy. The swarm consists of simulated Crazyflie 2.1 Brushless. The positions of the drones are retrieved directly from the ground truth provided by Gazebo under the ROS2 (/odom) topic.

The evaluation focuses on three primary metrics: LLM spatial reasoning accuracy, real-time collision avoidance, and system scalability. Swarm sizes of (N = 3, 10, and 30) agents were tested to evaluate the framework under increased density.

3.1. Test Scenarios and Swarm Scalability

To evaluate the framework, we designed three distinct experimental scenarios to test LLM spatial reasoning, real-time safety, and boundary enforcement. The system was dynamically scaled across swarm sizes of (N = 3, 10, and 30) agents to evaluate the computational limits of the APF controller, the LLM context window, and the scalability aspect of the framework.

Scenario A: Geometric Formation Control (Spatial Reasoning)

The swarm was commanded to perform high-level topological tasks, including: “Form a circle with a radius of 2 meters.”, “Form a sphere of radius 2 meters.”, “Form a 5x6 grid at a height of 2 meters.”, “Form a 3D cube.”, and “Form a Christmas tree.”.

Gemini 3.5 Pro Preview successfully translated these abstract commands into valid N-dimensional spatial coordinates. Across all swarm sizes (N = 3 to 30), the LLM achieved a 100 % success rate on the defined geometric primitives, accurately calculating target coordinates for every test conducted. The system demonstrated robust scalability, with the LLM generating actionable plans within ≈ 50 seconds (for N = 30) and the APF controller successfully converging the agents to their target formations without collision.

Fig. 2. Drone formations generated via LLM prompts: (left) N = 3 triangle, (center) N = 10 circle with a radius 3 m, (right) N = 30 5×6 grid. Prompts:

- ***N* = 3: “**Form a triangle at height 2 m centered at zero”;
- ***N* = 10:** “Form a circle of radius 3 m at height 2 m centered at zero”;
- ***N* = 30:** *“*Form a 5×6 grid pattern at height 2 m*”.*

Scenario B: Static and Dynamic Collision Avoidance (APF Stress-Tests)

To evaluate the operational limits of the decoupled APF controller, we tested the medium swarm size (N = 10) under two distinct collision-avoidance tests.

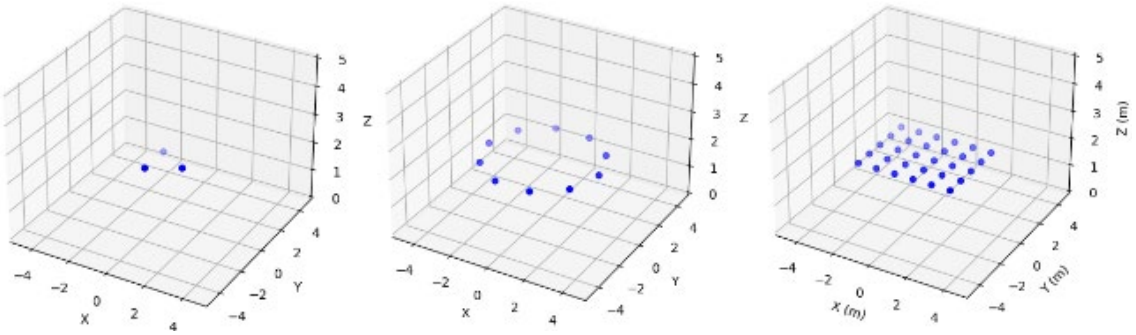

Fig. 2. The final positions of the drones after reaching the waypoints set by the LLM.

The Static Hazard (Unsafe Waypoint Test): An automated stress-test was triggered, commanding all of the swarm to converge on to a single point. Fig. 3. Shows the inter-agent separation distances. As illustrated, there is only a small moment where the Euclidean distance marginally drops below the 0.8-meter threshold. This brief moment of the safety boundary is the exact mechanism that triggers the APF, the resultant repulsive vector instantly dominated the attractive goal-seeking force. This shows that the APF successfully detected when the drones were converging and the repulsion forces dominated the attractive forces.

The Dynamic Hazard (Positional Swap Test): The swarm was given a natural language command “All drones swap positions with the drone directly opposite to you.” This command forces all agent trajectories to dynamically intersect simultaneously at the center of the workspace. Without the low-level safety filter, this would result in a catastrophic multi-agent collision. However, the repulsive vector fields (r_{min} = 0.8) dynamically routed the agents around each other in real-time, allowing the swarm to resolve the conflict and reach their target waypoints safely.

3.2. Safety and Feasibility Metrics

To strictly quantify the performance of the safety filter, we monitored two key metrics: Minimum Inter-Agent Distance (d_{min}) for collision verification and Swarm Velocity Profile across all unique agent pairs throughout the simulation runtime. We analyzed

this metric specifically during the formation of high-density structures: the $N = 10$ "Christmas Tree", N = 30 "Christmas Tree" (Complex 3D topology), and the N = 30 "Star" (high-density planar topology).

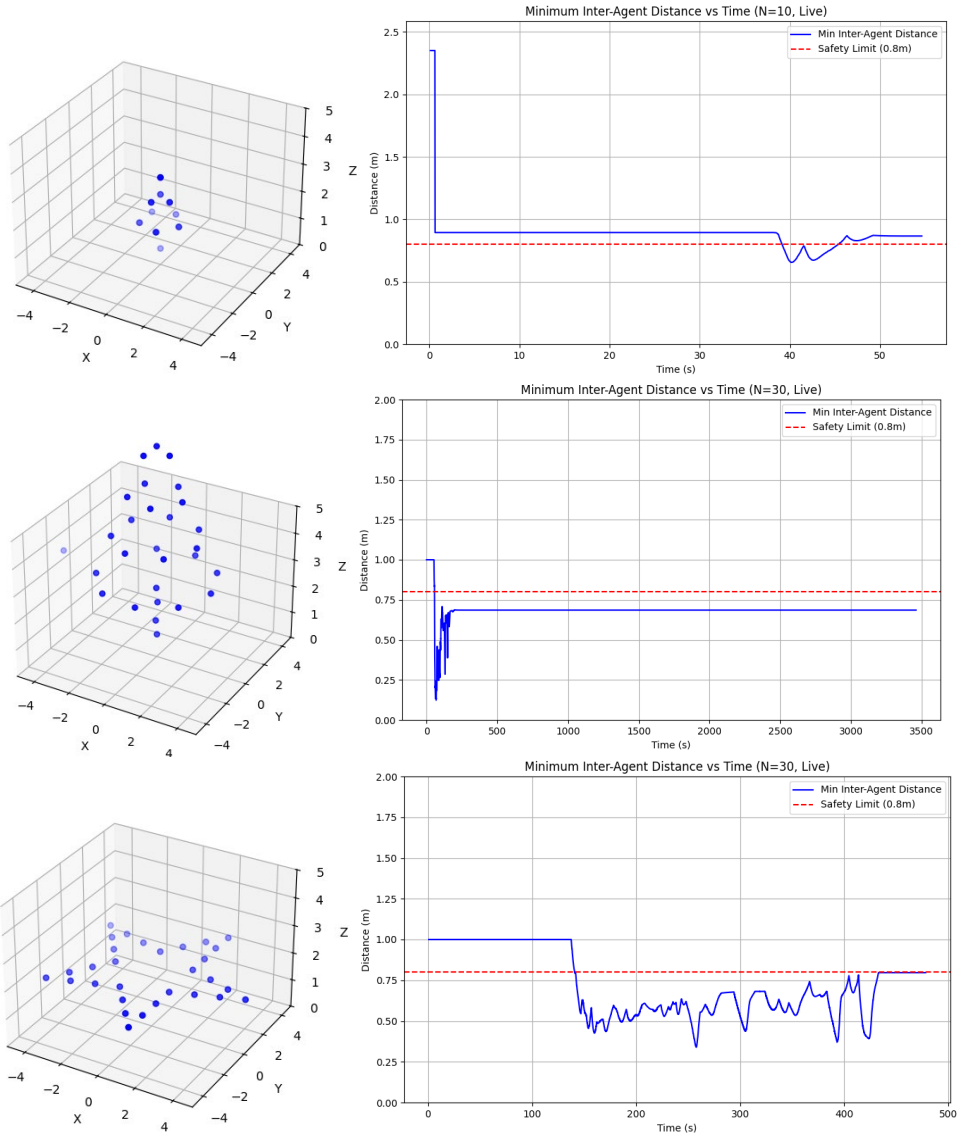

Fig. 3. (Left) 3D swarm snapshots. (Right) Minimum inter-agent distance over time. The red line (0.8m) indicates the APF activation buffer, no physical collisions occurred.

Fig. 3 presents the resulting formation snapshots alongside their distance profiles. It is important to note that the red dashed line at 0.8 m represents the APF activation threshold, not the physical collision boundary. As observed, d_{min} naturally dips below this conservative buffer to stabilize the dense formations, yet it remains strictly above the physical collision limit ($r_{drone} \approx 55$ mm [15]) at all times, validating real-time safety."

To ensure the generated trajectories were smooth and flyable, we analyzed the velocity profile of the N = 10 swarm during reconfiguration, as shown in Fig. 4. The profile demonstrates a smooth acceleration phase followed by a natural decay, with no high-frequency oscillations. the peak velocity ($\approx$ 0.42 m/s) remains strictly within the defined kinematic limit (v_{max} = 0.5 m/s), validating that the decoupled architecture produces physically feasible control commands.

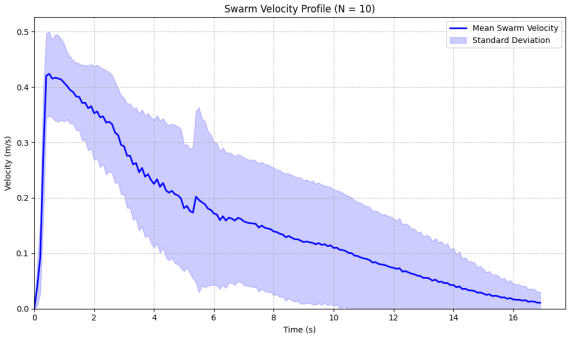

Fig. 4. Velocity Profile of drones in N = 10 configuration.

3.3. Latency Analysis

To evaluate the computational viability of the framework for large-scale operations, we measured the End-to-End planning latency, defined as the total time elapsed between issuing a natural language command and receiving the parsed coordinate list from the LLM.

Fig. 5 illustrates the latency distribution across varying swarm sizes ($N = 3, 4, 10, 30$).

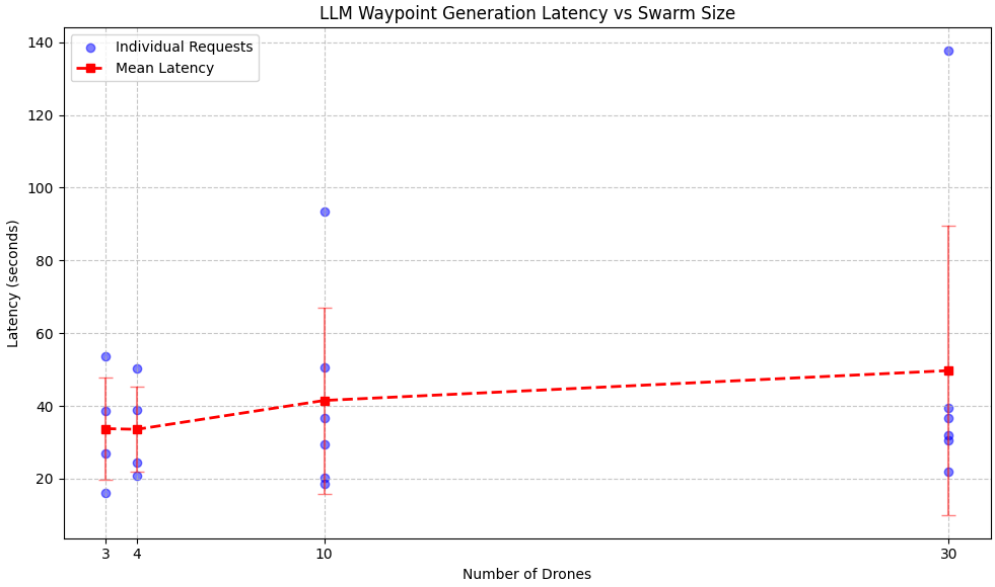

Fig. 5. End-to-end planning latency vs. Swarm Size.

The results highlight two critical performance characteristics:

Sub-Linear Scalability: The system demonstrates scalability with respect to swarm density. While the swarm size increased by a factor of 10 ($N = 3$ to $N = 10$), the mean planning latency only increased by approximately 45 % (34s to 50s). This indicates that the computational cost of processing the drone state data increases efficiently, proving that the system can handle larger swarms without a drastic increase in processing time.

Decoupled Safety: Significant variance is observed in the planning time (e.g., outliers at $N = 30$), which in a characteristic of cloud-based probabilistic models influenced by API server load and network jitter. However, this Planning Latency (seconds) is completely decoupled from the Control Loop Latency (milliseconds). As detailed in Fig. 1., the local safety filter operates continuously at 20Hz, ensuring that these variable planning delays never compromise the physical safety or stability of the swarm during the planning phase.

4. Discussion and Limitations

The experimental results validate SkySim's ability to translate natural language into safe, feasible swarm behaviors. Specifically, the 100 % success rate on tested geometric primitives demonstrates the LLMs's spatial reasoning, effectively outperforming static control libraries in terms of adaptability and ease of use.

Implications: The integration of the decoupled safety filter proved essential. While the LLM generated valid goal states, the brief dips in inter-agent distances highlight the APF's reactive nature. This mechanism effectively prevented collision across all $N = 3$, $N = 10$, and $N = 30$ trials, although at the cost of increased convergence time during high-density maneuvers. By decoupling high-level planning from low-level safety, SkySim mitigates risks in safety-critical domains, potentially allowing UAV applications in agriculture or disaster response where non-experts require complex, on-demand swarm behaviors without extensive programming knowledge.

Limitations: Despite these successes, several limitations in the current architecture must be addressed. The system's reliance on cloud-based inference (Google Gemini API). As shown in the latency analysis (Fig. 5), this introduces significant variance (outliers > 100s) driven by server load. While the local safety guarantees physical safety during these delays, the system is currently unsuitable for time-critical missions where millisecond-level reaction to new commands is required.

SkySim also relies on noiseless ground-truth state estimation from Gazebo. Real-world deployment will introduce sensor noise (e.g., from Optitrack [16] or GPS), communication packet loss, and environmental disturbances (e.g., weather conditions), which may degrade the precision of the APF repulsion vectors.

While the system scales sub-linearly, the LLM's context window limits the maximum swarm size. For $N > 30$, the prompt length required to encode every agent's position may exceed token limits, our validation was capped at $N = 30$ due to the local hardware resources required to maintain real-time fidelity for the physics engine and ROS2 node communication across all agents.

The deterministic APF controller, while fast is susceptible to local minima. In highly cluttered environments or complex obstacle fields, agents may become trapped in state equilibrium points before reaching their goal, a known limitation of reactive potential fields compared to predictive solvers.

Finally, the system is optimized for zero-shot static formations. It does not natively support continuous, time-bound trajectories (e.g., a" spinning sphere"), limiting its current scope of waypoint-based reconfiguration.

5. Conclusion and Future Works

This paper presented SkySim, a ROS2-based simulation environment that bridges the gap between natural language and LLM based cognition. By isolating the probabilistic LLM reasoning from a deterministic 20Hz safety filter, we demonstrated that non-experts can command complex swarm formations without compromising physical safety.

Future work will aim to focus on three key areas to address these identified limitations

1. Hardware Integration: We aim to transfer the stack to physical Crazyflie 2.1 Brushless drones [15] using OptiTrack motion capture system [16] to quantify the impact of real-world sensor noise.

2. Advanced Control Solvers: To overcome the local minima limitations of the APF, we will explore integrating Model Predictive Control (MPC) as a proactive safety layer that can handle dynamic constraints more effectively than a simple APF.

3. Multi-Modal Inputs: Future iterations will incorporate multi-modal capabilities, allowing the swarm to react to visual inputs or dynamic environmental changes, further extending the "sense-plan-act" loop beyond static coordinates.

4. Edge Deployment and Optimization: To eliminate the latency bottlenecks inherent to cloud-based inference, future iterations will transition from general-purpose cloud LLMs to Small Language Models (SLMs) deployed directly on local hardware. We plan to leverage efficient fine-tuning frameworks, such as Unsloth [17], to optimize these models specifically for swarm control vocabularies. This shift aims to reduce the end-to-end planning to sub-second levels, enabling the system in combination with MPC to support dynamic, high-speed maneuvers that are currently impossible with API-based delays.

References

[1]. G. Aikins, M. Dao, J. Moukpe, T. Eskridge, et al., LEVIOSA: Natural language-based uncrewed aerial vehicle trajectory generation, *Electronics*, Vol. 13, Issue 22, 2024, 4508.

[2]. Y. Ping, et al., Multimodal large language models-enabled UAV swarm: Towards efficient and intelligent autonomous aerial systems, *arXiv*, 2025, arXiv:2506.12710.

[3]. B. Han, Y. Chen, J. Li, J. Li, et al., SwarmChain: Collaborative LLM inference for UAV swarm control, *IEEE Internet of Things Magazine*, Vol. 8, Issue 5, 2025, pp. 64-71.

[4]. L. Yuan, C. Deng, D. Han, I. Hwang, et al., Next-generation LLM for UAV: From natural language to autonomous flight, *arXiv*, 2025, arXiv:2510.21739.

[5]. S. Sarkar, et al., Review of LLM based control, ResearchGate, 2025, https://www.researchgate.net/publication/390334927_Review_of_LLM_based_Control.

[6]. H. Kurunathan, H. Huang, K. Li, W. Ni, et al., Machine learning-aided operations and communications of unmanned aerial vehicles: A contemporary survey, *IEEE Communications Surveys & Tutorials*, Vol. 26, Issue 1, 2024, pp. 496-533.

[7]. M. Schuck, et al., SwarmGPT: Combining large language models with safe motion planning for drone swarm choreography, *arXiv*, 2025, arXiv:2412.08428.

[8]. P. Xie, S. Diaconescu, F. Stoican, A. Alanwar, Roundabout constrained convex generators: A unified framework for multiply-connected reachable sets, *arXiv*, 2025, arXiv:2511.07330.

[9]. Z. Wang, H. Ding, Opposition-based learning equilibrium optimizer with application in mobile robot path planning, *International Journal of Robotics and Automation Technology*, Vol. 10, 2025, pp. 64-74.

[10]. P. Mishra, B. Boopal, N. Mishra, Real-time 3D routing optimization for unmanned aerial vehicle using machine learning, *EAI Endorsed Transactions on Scalable Information Systems*, Vol. 11, Issue 4, 2024, e5.

[11]. J. Yasin, S. A. Mohamed, M. Haghbayan, J. Heikkonen, et al., Unmanned aerial vehicles (UAVs): Collision avoidance systems and approaches, *IEEE Access*, Vol. 8, 2020, pp. 105139-105155.

[12]. X. Dai, Y. Mao, T. Huang, N. Qin, et al., Automatic obstacle avoidance of quadrotor UAV via CNN-based learning, *Neurocomputing*, Vol. 402, 2020, pp. 346-358.

[13]. R. Bălaşa, M. C. Bîlu, C. Iordache, A proximal policy optimization reinforcement learning approach to unmanned aerial vehicles attitude control, *Land Forces Academy Review*, Vol. 27, Issue 4, 2022, pp. 400-410.

[14]. J. Hu, L. Wang, T. Hu, C. Guo, et al., Autonomous maneuver decision making of dual-UAV cooperative air combat based on deep reinforcement learning, *Electronics*, Vol. 11, Issue 3, 2022, 467.

[15]. Bitcraze AB, Crazyflie 2.1 brushless datasheet, https://www.bitcraze.io/documentation/hardware/crazyflie_2_1_brushless/crazyflie_2_1_brushless-datasheet.pdf

[16]. NaturalPoint, PrimeX 22 technical specifications, https://optitrack.com/cameras/primex-22

[17]. Unsloth AI, Unsloth documentation, https://unsloth.ai/docs

(039)

3D Reconstruction from UAV Integrated Sensors and Topology Optimization for Real-Time Simulation

Rodrigo Arantes-Oliveira [1], Gabriela Moutinho de Souza Dias [1], Nina Machado Figueira [2] and Paulo Fernando Ferreira Rosa [1]
[1] Instituto Militar de Engenharia-IME, Rio de Janeiro, Brazil
[2] Escola de Comando e Estado-Maior do Exército - ECEME, Rio de Janeiro, Brazil
E-mail: rodrigo.alves@ime.eb.br, rpaulo@ime.eb.br, gabriela@ime.eb.br, nina.figueira@eb.mil.br

Summary: Unmanned Aerial Vehicles (UAVs) equipped with integrated sensors such as high-resolution RGB cameras, RTK-GNSS receivers, and optional LiDAR modules enable the acquisition of centimetric 3D data for modeling real environments with high fidelity. Although photogrammetric software can reconstruct dense and detailed meshes, these raw models are not directly suitable for real-time simulation due to their excessive polygon count, irregular topology, and high memory requirements. This work presents a post-processing pipeline that converts UAV-derived reconstructions into efficient, visually faithful assets optimized for simulation engines. The topology-optimization stage is implemented in Blender through a combination of field-aligned remeshing, feature-preserving simplification, quad-dominant retopology, and high-to-low-poly texture baking. These operations collectively reduce geometric complexity while retaining the perceptual characteristics necessary for accurate visualization. A case study demonstrates substantial mesh reduction, consistent rendering performance, and improved suitability for mission-planning and training environments, addressing the gap between UAV mapping workflows and the operational needs of real-time simulation.

Keywords: UAV, Integrated sensors, 3D reconstruction, Topology optimization, Quad-remeshing, Mesh simplification, Real-time simulation.

1. Introduction

High-fidelity 3D reconstruction from UAVs has become a fundamental component of applications that demand precise environmental understanding, realistic visualization and detailed spatial analysis. UAV platforms equipped with integrated sensors such as high-resolution RGB cameras, RTK-GNSS receivers and optional LiDAR or thermal modules can capture centimetric-accuracy data, making them highly effective for documenting complex scenes and generating reliable geometric information. These capabilities support a variety of uses that benefit from realistic digital representations, including training environments, operational planning, simulation systems and decision-support workflows.

A systematic review of the literature shows that most studies emphasize acquisition strategies, sensor integration and photogrammetric reconstruction quality. Although these works advance image matching, dense point-cloud generation and multisensor fusion, far fewer address the steps required to convert photogrammetric outputs into assets suitable for real-time rendering. Among the 54 studies surveyed, there is limited discussion of topology optimization, quad-based retopology, UV organization, texture baking or LOD generation, exposing a clear gap between UAV reconstruction workflows and the needs of real-time applications.

Modern photogrammetric software can process these datasets into dense point clouds and highly detailed meshes. However, the raw outputs produced in this stage often contain millions of triangles, irregular topology and inconsistent surface structure. Such characteristics create excessive memory requirements and lead to low rendering performance, preventing direct use in real-time applications. Engines for simulation and interactive visualization rely on optimized geometry, coherent edge flow, efficient UV layouts and texture representations that minimize computational cost.

In response to these challenges, this work focuses on the transformation of photogrammetric outputs into lightweight and visually coherent assets. The proposed pipeline reorganizes geometry through polygon reduction, quad-based retopology, UV generation and texture baking, allowing high-frequency detail to be preserved while drastically reducing geometric complexity. By addressing the gap between UAV-based reconstruction workflows and the practical requirements of real-time rendering systems, the method produces simulation-ready models that maintain the fidelity necessary for accurate visualization and interactive performance.

2. Background and Proposed Research

The proposed workflow is structured into four stages that transform raw UAV data into simulation-ready assets. The overall objective of this research is to develop and validate a complete post-processing pipeline capable of converting high-density photogrammetric reconstructions into lightweight, visually coherent 3D models optimized for real-time simulation engines. This includes the integration of

UAV sensor data, reconstruction strategies, topology optimization methods and performance benchmarking to ensure that the final models maintain visual fidelity while significantly reducing computational cost (Fig. 1).

2.1. UAV Data Acquisition with RTK

Imagery is collected using an RTK-enabled UAV equipped with integrated RGB sensors and, when available, thermal and LiDAR modules when available. RTK georeferencing ensures centimetric positional accuracy and improves alignment consistency during reconstruction.

2.2. Sensor-Integrated 3D Reconstruction

Agisoft Metashape performs the processing of RGB, thermal, and LiDAR measurements resulting in a dense, high-resolution mesh that captures fine geometric detail but is unsuitable for real-time simulation due to excessive polygon count and very irregular topology.

2.3. Blender Add-On for Topology Optimization

A custom Blender add-on automates mesh optimization through the following steps:

a) *QEM-based simplification* reduces polygon count while preserving shape, sharp edges, and local features;
b) *Quad-based retopology* reorganized topology according to model characteristics;
c) *UV mapping* automatically generates seam lines based on sharp-edge detection, ensuring clean texture islands;
d) *Texture and normal-map baking* transfers high-poly detail onto the optimized quad mesh, preserving visual fidelity at significantly lower computational cost.

2.4. Real-Time Engine Benchmarking

The resulting assets are tested in real-time rendering engines (e.g., Unreal Engine, Unity) to evaluate frame-rate improvements, memory reduction, and LOD behavior under operational simulation conditions.

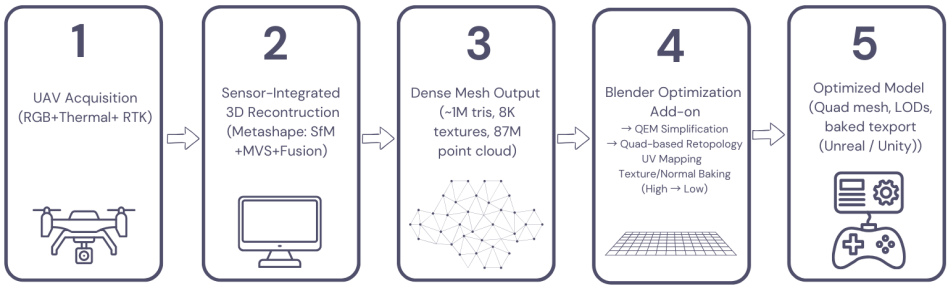

Fig. 1. Pipeline workflow.

3. Methodology

This section details the technical implementation and parametrization of the pipeline introduced in Section 2. While the previous section presents the conceptual workflow, the methodology focuses on how each stage was executed, including parameter choices, optimization criteria, and evaluation procedures, ensuring reproducibility and fair assessment of the proposed approach.

3.1. Input Data and Baseline Model Characterization

The methodology assumes that sensor-integrated UAV data have been acquired and reconstructed as described in Sections 2.1 and 2.2. The input to the optimization pipeline consists of dense triangular meshes generated in Agisoft Metashape from RGB imagery and, when available, LiDAR data. Prior to optimization, each reconstructed model was analyzed to establish a baseline reference. The following metrics were recorded: total polygon count, topological regularity and triangle valence distribution, texture configuration (resolution and number of tiles), and file size and memory footprint.

Baseline meshes typically ranged from approximately 1 million to over 18 million triangles, exhibiting highly irregular triangulation and fragmented texture layouts. These characteristics confirm their unsuitability for direct deployment in real-time simulation engines.

3.2. Geometric Simplification Strategy

Geometric simplification was applied as the first optimization stage using a Quadric Error Metrics (QEM)–based decimation algorithm. This step aims to reduce polygon density while preserving the global geometric structure of the model. Simplification parameters were defined according to scene characteristics: target triangle densities of 2–4 tris/m²

for terrain-dominated scenes and 4–8 tris/m² for architecturally complex scenes.

This controlled decimation stage provides an intermediate representation that significantly reduces computational cost while preserving sufficient geometric fidelity for subsequent retopology and texture processing.

3.3. Quad-Based Retopology and Topological Reorganization

Since QEM decimation does not address the irregular topology inherent to photogrammetric meshes, a dedicated retopology stage was introduced to reorganize the geometry into a quad-dominant structure better suited for UV mapping, texture baking, and LOD generation. Two automatic quad-remeshing strategies were evaluated: QuadriFlow, which favors homogeneous quad distribution and global regularity, and QuadWild, which incorporates feature-line detection to better preserve sharp edges and architectural details. Retopology was parameterized according to scene scale and geometric complexity, including a target quad count between 50k and 150k, adaptive density to allocate higher resolution to complex regions, and feature preservation enabled in both methods, with explicit feature-line guidance in QuadWild.

This stage produces structurally coherent meshes that significantly improve downstream UV organization, texture baking quality, and LOD generation.

3.4. UV Mapping and Texture Baking

UV coordinates were automatically generated on the retopologized meshes using an angle-based unwrapping strategy, prioritizing stretch minimization and atlas coherence. The UV mapping process considered scene-dependent parameters, including target Texel density and the number of UV sets, adjusted according to model scale and geometric complexity. To compensate for geometric detail loss introduced by simplification and retopology, texture baking was performed using the original high-resolution meshes as reference sources. The baking process employed a resolution of 4096 × 4096 pixels and generated albedo and normal maps, with normal maps computed using the MikkTSpace tangent basis to ensure compatibility with real-time engines such as Unreal Engine and Unity.

This procedure transfers high-frequency geometric information into texture space, enabling visually coherent rendering with substantially reduced polygonal complexity.

3.5. Automation and Benchmarking Procedure

All optimization stages were integrated into a custom Blender add-on developed using the Blender Python API. The add-on automates mesh simplification, quad-based retopology, UV generation, texture baking, and asset export, ensuring reproducibility and scalability across heterogeneous datasets. Final assets were evaluated in real-time rendering engines under controlled conditions. Performance metrics included draw calls, GPU memory consumption, per-model draw call count, and LOD transition behavior. These metrics were compared against baseline models to quantify the impact of the proposed pipeline on real-time rendering performance.

Performance tests were conducted on a workstation equipped with an NVIDIA RTX 4070 Ti (12 GB VRAM), 32 GB dual-channel DDR5 RAM (4800 MT/s), and an Intel Core i7-13700KF (13th Gen, 3.40 GHz). This hardware configuration provides sufficient computational capacity to reliably assess real-time rendering behavior and compare dense and optimized models.

3.6. Reproducibility Summary

For clarity and reproducibility, the core parameters of the methodology are summarized below:

A. Triangle density: 2–8 tris/m²;
B. Feature angle threshold: 45° to 66°;
C. Target quad count: 50k–150k;
D. Texel density;
E. Bake resolution: 4K;
F. Normal map basis: MikkTSpace.

4. Results

The workflow was evaluated using three datasets representing distinct sensing modalities and geometric complexities. LiDAR data of the Pão de Açúcar (50 cm resolution, 2024) provided high-accuracy geometry for UV generation and normal-map baking. RGB and thermal imagery from the Igreja do Outeiro da Glória enabled assessment of radiometric detail and baking quality on complex architectural surfaces. RGB imagery of the Ilha Rasa lighthouse served as a small-scale test case for evaluating simplification and quad-based retopology on compact structures. Together, these datasets cover LiDAR-only, RGB-only and RGB+thermal scenarios, demonstrating the robustness of the pipeline across diverse sensing conditions and geometric profiles.

4.1. Sugar Loaf LiDAR

The Sugar Loaf LiDAR dataset was used to evaluate the optimization pipeline under high-accuracy geometric conditions. The original LiDAR-derived mesh (Fig. 2) contains approximately 4.15 million triangles, representing large-scale terrain morphology at a native spatial resolution of 0.5 m. QEM-based simplification reduced the mesh to 10k triangles (Fig. 3), corresponding to a geometric reduction of 99.76 % and a simplification factor of approximately 415×, while preserving global topographic features.

QuadWild retopology further reorganized the surface into a structured quad layout equivalent to 22,8k triangles, achieving a 99.45 % reduction relative to the original mesh and a simplification factor of approximately 180×, while providing coherent edge flow and improved suitability for UV generation and texture baking.

Fig. 2. Sugar Loaf LiDAR model.

Fig. 3. Sugar Loaf decimated model without normal map baked.

Fig. 4. Sugar Loaf QuadWild model with normal map baked from LiDAR model.

The optimized model employs a single 4K baked normal map, achieving an effective Texel density of approximately 2355 px/m. Compared to the original LiDAR sampling rate (0.5 m), this represents an increase of more than three orders of magnitude in spatial detail representation. This transfer of high-frequency information into texture space enables visually coherent shading beyond the explicit LiDAR geometry, resulting in a visually enhanced yet computationally efficient terrain representation suitable for real-time rendering.

4.2. Igreja do Outeiro da Glória

The Outeiro da Glória dataset illustrates the effect of each optimization stage on geometric complexity and topological organization. The original photogrammetric model (Fig. 5), contains approximately 1.41 million triangles with a single 8K texture, preserving high-frequency detail but exhibiting a highly irregular triangulated topology. The decimated mesh (Fig. 6), reduces the count to 141389 triangles, maintaining the overall shape but still presenting irregular triangulation and softened architectural features. In contrast, the QuadWild (Fig. 7), and QuadriFlow (Fig. 8), retopologized versions convert the surface into structured quad layouts containing 52804 and 117214 quads, respectively, each one using a single 4K texture. QuadriFlow produces a more uniform quad distribution, while QuadWild more effectively preserves sharp features and architectural contours. These results highlight the trade-off between regularity and feature retention and demonstrate the benefits of quad-based representations for UV generation, normal-map baking and real-time rendering performance.

Fig. 5. Outeiro da Glória photogrammetric model.

Fig. 6. Outeiro da Glória decimated model.

Fig. 7. Outeiro da Glória QuadWild model.

Fig. 8. Outeiro da Glória QuadriFlow model.

Compared to the original mesh containing approximately 1.41 million triangles, the decimated model achieved a geometric reduction of 89.97 %. The QuadWild and QuadriFlow retopologized models achieved reductions of 96.26 % and 91.69 %, corresponding to simplification factors of 26.7× and 12.0×, respectively. Both quad-based models also reduced texture resolution from 8K to 4K, resulting in a 75 % decrease in texture memory usage. While QuadriFlow retained a higher polygon count and produced a more uniform quad distribution, QuadWild generated a lighter mesh with better preservation of sharp architectural features. Both quad-based models achieved UV packing efficiencies above 80 % within a single UV sheet, demonstrating improved UV organization and texture utilization compared to irregular triangulated meshes. These results quantitatively demonstrate the trade-off between topological regularity and feature retention, highlighting the advantages of quad-based remeshing for UV mapping, texture baking and real-time rendering.

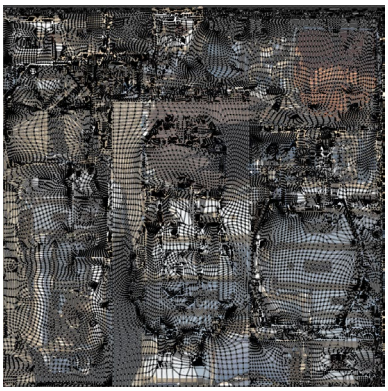

Fig. 9. Outeiro da Glória UV layout for QuadriFlow model.

4.2. Ilha Rasa Lighthouse

The Ilha Rasa lighthouse dataset provides a compact example of the pipeline's behavior on small architectural structures. The original mesh contains 302844 triangles with a single 8K texture (Fig. 10), preserving global shape but exhibiting irregular triangulation. QEM simplification reduces the model to 1299 triangles, maintaining the silhouette but losing mid-frequency detail (Fig. 11),. The QuadWild and QuadriFlow retopologized versions reorganize the surface into 15372 and 5006 quads, respectively, each using a 4K baked texture (Figs. 12 and 13). QuadriFlow yields a more uniform quad distribution, whereas QuadWild better preserves architectural contours. The baked textures achieve Texel densities of 0.903 px/cm (QuadriFlow) and 0.879 px/cm (QuadWild).

The QuadriFlow model achieved a geometric reduction of 98.35 %, while QuadWild achieved 94.93 %, corresponding to simplification factors of 60.5× and 19.7×, respectively. Both approaches reduced texture resolution from 8K to 4K, resulting in a 75 % decrease in texture memory usage. Compared to QuadWild, QuadriFlow produced a model approximately three times lighter, whereas QuadWild better preserved architectural features. Both QuadriFlow and QuadWild produced UV layouts occupying approximately 84.5 % of the available 0–1 UV space within a single UV sheet, indicating efficient packing with only 15.5 % unused area, which contributes to improved texture utilization and more consistent Texel distribution (Fig. 14). These results demonstrate that quad-based remeshing improves UV unwrapping, texture baking and LOD generation, enabling efficient representation of small-scale structures for real-time simulation.

Fig. 10. Ilha Rasa Lighthouse photogrammetric model.

Fig. 11. Ilha Rasa Lighthouse decimated model.

5. Conclusions

The results demonstrate that traditional photogrammetric and LiDAR-based reconstructions,

although geometrically accurate, are not directly suitable for real-time simulation due to excessive polygon density and irregular topology. The proposed workflow systematically addresses these limitations by restructuring geometry, optimizing UV layouts and transferring high-frequency detail to texture space. Across all evaluated datasets, the optimized models achieved orders-of-magnitude reductions in geometric complexity while maintaining visual fidelity and structural coherence. This confirms that quad-based representations constitute a critical intermediary between raw 3D reconstruction and real-time digital environments.

Fig. 12. Ilha Rasa Lighthouse QuadWild model.

Fig. 13. Ilha Rasa Lighthouse QuadriFlow model.

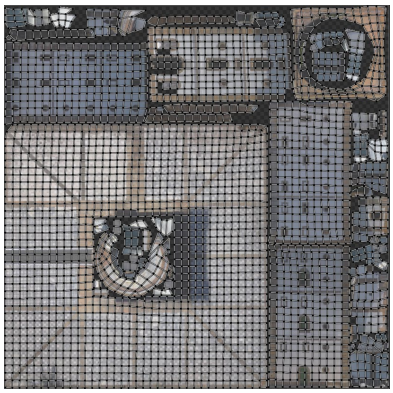

Fig. 14. Ilha Rasa Lighthouse UV layout for QuadriFlow model.

Acknowledgements

Rodrigo Arantes de Oliveira Alves Thanks Instituto Militar de Engenharia (IME), Centro de Análise de Sistemas Navais (CASNAV), Museu Nacional (UFRJ) and Instituto Pereira Passos (IPP). This work was partially funded by the EVAAT_GCN Project (FINEP Agreement 01.24.0661.00, ref. 3311/24). The first author is supported by a scholarship from the EVAAT_GCN Project.

References

[1]. N. Pietroni, S. Nuvoli, T. Alderighi, P. Cignoni, et al., Reliable feature-line driven quad-remeshing, *ACM Transactions on Graphics*, Vol. 40, Issue 4, 2021, 155.
[2]. J. Huang, Y. Zhou, M. Niessner, J. R. Shewchuk, et al., QuadriFlow: A scalable and robust method for quadrangulation, *Computer Graphics Forum*, Vol. 37, Issue 5, 2018, pp. 147-160.
[3]. W. Jakob, M. Tarini, D. Panozzo, O. Sorkine-Hornung, Instant field-aligned meshes, *ACM Transactions on Graphics*, Vol. 34, Issue 6, 2015, 189.
[4]. J. Huang, QuadriFlow: Scalable and robust quadrangulation library, https://github.com/hjwdzh/QuadriFlow
[5]. N. Pietroni, QuadWild: Robust automatic quadrangulation framework, https://github.com/nicopietroni/quadwild
[6]. Bern CGG Group, QuadWild-BIMDF: Robust quad layout and quadrangulation, https://github.com/cgg-bern/quadwild-bimdf
[7]. A. Takayama, mesh_simplification: Quadric Error Metric mesh decimation library, https://github.com/astaka-pe/mesh_simplification
[8]. Agisoft Metashape Professional – User Manual, Version 2.x, *Agisoft*, 2023.
[9]. Blender Foundation, Blender 4.x manual, https://www.blender.org
[10]. M. Tarini, Closed-form quadrangulation of n-sided patches, *Computers & Graphics*, Vol. 107, 2022, pp. 60-65.
[11]. D. Bommes, B. Lévy, N. Pietroni, E. Puppo, et al., Quad-mesh generation and processing: A survey, *Computer Graphics Forum*, Vol. 32, Issue 6, 2013, pp. 51-76.
[12]. P. Zhang, J. Solomon, E. Vouga, Octahedral frames for feature-aligned cross fields, *ACM Transactions on Graphics*, Vol. 39, Issue 3, 2020, 25.
[13]. M. Garland, P. S. Heckbert, Surface simplification using quadric error metrics, in *Proceedings of the 24th Annual Conference on Computer Graphics and Interactive Techniques (SIGGRAPH'97)*, 1997, pp. 209-216.
[14]. LiDAR Topographic Dataset of Rio de Janeiro, *Instituto Pereira Passos (IPP)*, Rio de Janeiro, 2024.
[15]. J. C. Araújo, J. C. S. Seoane, O. N. Grillo, E. E. S. Santos, et al., Low-cost digital elevation model for marine protected areas, *Revista Brasileira de Cartografia*, Vol. 71, Issue 1, 2019, pp. 176-206.

(040)

Autonomous UAVs for Disaster Response: Terrain-Aware Target Detection and Payload Delivery

Aryan Sirsavkar, Muzammil Shaikh, Anuj Kale, Abhijeet Thore and Mayur Patil
Pune Vidyarthi Griha's College of Engineering, Technology & Management, Department of Engineering,
1, Vidyanagari, Pune – 411007, India
Tel.: +91 8010076404
E-mail: aryansirsavkarc700@gmail.com

Summary: This work presents a modular, cost-efficient Unmanned Aerial System (UAS) for autonomous disaster response. The drone autonomously scans a user-defined area, detects disaster zones using a YOLOv8-based vision model, and performs payload drops without ground control. The onboard pipeline fuses LiDAR, PX4 telemetry, and GPS to reconstruct terrain undulations, allowing subsequent UAS to navigate at lower altitudes and improve detection rates. Target coordinates are calculated onboard using a heading-aware pixel-to-GPS conversion, enabling precise payload delivery. The system supports pre-flight model selection to detect different types of disaster zones. All computation runs on a Raspberry Pi 5, with *pymavlink* sending commands to the Pixhawk 4 for autonomous waypoint navigation. Peer-to-peer Wi-Fi Direct communication allows secure, infrastructure-free coordination. The system has been validated in SITL simulations and field tests, achieving 2 kg payload capacity and 25-minute flight endurance while maintaining modularity and ease of maintenance.

Keywords: Autonomous UAS, Disaster response, Terrain undulation mapping, Target detection, Payload delivery, LiDAR and telemetry data fusion, Onboard navigation.

1. Introduction and System Architecture

Rapid disaster response increasingly relies on autonomous aerial systems capable of delivering payloads and performing reconnaissance with minimal or no ground support. Conventional solutions often depend on human operators for navigation, have limited payload capacity, or rely solely on GPS-based waypoint guidance. These limitations can significantly reduce operational accuracy and efficiency, especially in complex environments such as collapsed structures, densely forested areas, or urban flood zones.

Additionally, many existing UAVs lack integrated perception systems, preventing adaptive navigation or real-time decision-making in dynamic disaster scenarios. To address these challenges, this work presents a modular Unmanned Aerial System (UAS) designed to autonomously detect disaster zones, navigate complex terrain, and execute precise payload delivery. The proposed UAS integrates a YOLOv8-derived onboard vision system, LiDAR-based terrain mapping, and PX4 telemetry to enable robust autonomous operations without human intervention. Fig. 1 illustrates the airframe design and payload integration, highlighting the compact arrangement that balances stability, sensor placement, and payload capacity.

Furthermore, the UAS incorporates advanced sensor fusion techniques to combine visual, LiDAR, and inertial data, improving situational awareness and navigational reliability. Its autonomous planning algorithms adapt to dynamic obstacles, shifting environmental conditions, and GPS-challenged scenarios or environments, ensuring continuous mission execution. The system's modular payload interface allows rapid configuration for tasks such as medical supply drops, debris inspection, and environmental monitoring, enhancing operational versatility in disaster response scenarios.

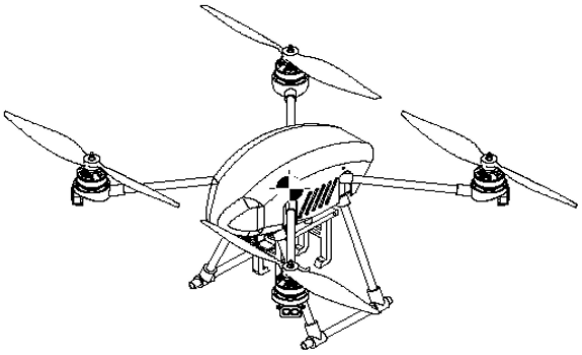

Fig. 1. CAD rendering of the disaster-response UAS, illustrating the airframe configuration and payload integration.

The airframe adopts a hybrid dihedral–anhedral configuration, providing passive aerodynamic stability and improved flight resilience under varying wind conditions or during abrupt maneuvers. The hybrid dihedral–anhedral configuration was selected to improve passive roll stability while preserving maneuverability under payload-induced inertia and wind disturbances, reducing control effort during low-altitude autonomous flight. Low-level flight control is managed by a Pixhawk 4 autopilot, which executes PID-based stabilization and navigation commands. PX4 position and altitude controllers were tuned using iterative flight testing under payload, prioritizing altitude-hold stability and disturbance rejection rather

than aggressive maneuvering. High-level decision-making and onboard perception are handled by a Raspberry Pi 5, which processes camera feeds, fuses LiDAR and telemetry data, and computes heading-aware pixel-to-GPS conversions for target localization. Commands are sent from the Pi to the Pixhawk via pymavlink [1], allowing precise waypoint execution without requiring low-level velocity commands—particularly advantageous for heavy payload missions or dynamic re-routing. The high-level, autonomy-focused system architecture of the operational UAS is depicted in Fig. 2, showing onboard sensing, processing, and flight-control modules.

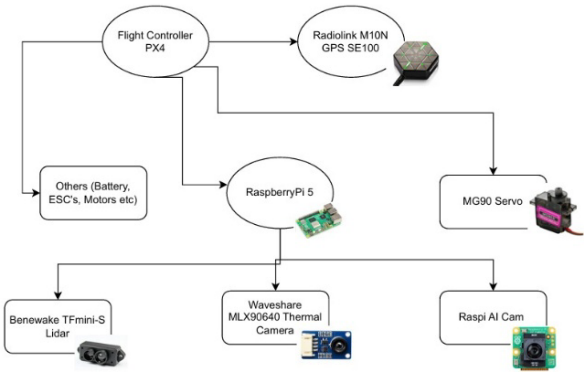

Fig. 2. UAS system architecture emphasizing autonomous mission execution and onboard processing.

This integrated architecture allows the UAS to operate autonomously in complex environments, combining stable flight, real-time perception, and responsive payload delivery.

This work specifically targets open-area disaster scenarios such as urban flooding, debris fields, wildfire perimeters, and collapsed low-rise structures, where partial GNSS availability, limited infrastructure, and time-critical payload delivery are primary operational constraints. Fully GPS-denied operation (e.g., indoor or subterranean environments) is outside the scope of this study and is considered future work.

2. Onboard Vision and Target Detection

Disaster zones are identified using a YOLOv8-derived custom model [2] running fully onboard the UAV. The model allows for pre-flight configuration, enabling it to detect different targets such as fire, debris, or waterlogging, depending on mission requirements. Camera feeds are continuously fused with telemetry and LiDAR data, providing terrain-aware perception that allows the UAV to maintain situational awareness and respond to environmental changes in real time.

The YOLOv8-derived model was trained on a custom dataset containing images of water bodies, debris zones, and fire-like regions, augmented using rotation, brightness variation, and scale jittering. Inference runs onboard the Raspberry Pi 5 at approximately 10 FPS (measured during flight tests). Detection accuracy is reported as per-target detection rate at an IoU threshold of 0.5 under outdoor lighting conditions.

Once a potential target is detected, its location in the camera frame is converted from pixel coordinates to global GPS coordinates using a heading-aware projection pipeline.

First, pixel displacement is converted into metric ground-plane offsets using a pinhole camera model under a locally planar ground assumption. Given the camera altitude above ground h, horizontal and vertical field of view (FOV_x, FOV_y), and image resolution (W, H), pixel offsets $(\Delta u, \Delta v)$from the image center are mapped to ground-plane coordinates as:

$$x_g = h \cdot \tan\left(\frac{FOV_x}{2}\right) \cdot \frac{2\Delta u}{W},$$
$$y_g = h \cdot \tan\left(\frac{FOV_y}{2}\right) \cdot \frac{2\Delta v}{H}$$

The resulting ground-plane offsets are then rotated into the North–East navigation frame using the UAV yaw angle ψobtained from PX4 telemetry:

$$\begin{bmatrix} north \\ east \end{bmatrix} = \begin{bmatrix} \cos\psi & -\sin\psi \\ \sin\psi & \cos\psi \end{bmatrix} \begin{bmatrix} x_g \\ y_g \end{bmatrix}$$

Finally, the North–East offsets are converted into latitude and longitude updates as:

$$\Delta lat = \frac{north}{R_{Earth}}, \Delta lon = \frac{east}{R_{Earth} \cdot \cos(lat)}$$

Prior camera calibration is used to minimize lens distortion effects. This lightweight projection pipeline provides sufficient localization accuracy for low-altitude autonomous payload delivery, while terrain-aware altitude correction further reduces projection error during flight.

```
def nudge_gps(lat, lon, h, dx, dy, w, H, m=2):
    hdg = math.radians(h)
    nx, ny = dx/(w/2), dy/(H/2)
    nx, ny = max(-1, min(1, nx)), max(-1, min(1, ny))
    move_x, move_y = nx*m, -ny*m
    north, east  = move_y*math.cos(hdg) + move_x*math.sin(hdg), move_y*math.sin(hdg) - move_x*math.cos(hdg)
    return lat + math.degrees(north/R_EARTH), lon + math.degrees(east/(R_EARTH*math.cos(math.radians(lat))))
```

Fig. 3. Pixel-to-GPS conversion for real-time target localization during autonomous UAV missions.

The UAV follows a sequential operational procedure. First, it takes off and executes a pre-computed, fixed-altitude “lawnmower” scanning pattern (Fig. 4). This systematic coverage ensures no area within the survey region is missed, which is critical for high-confidence disaster zone detection.

The fixed-altitude lawnmower pattern is used as an initial baseline coverage strategy to guarantee systematic area exploration under time constraints.

While adaptive altitude or uncertainty-aware search strategies may improve coverage in certain disaster types, the proposed system prioritizes reliable, repeatable coverage that can be executed onboard with limited computational overhead. Terrain-aware re-navigation and altitude reduction are introduced after initial mapping, partially addressing the limitations of fixed-altitude search.

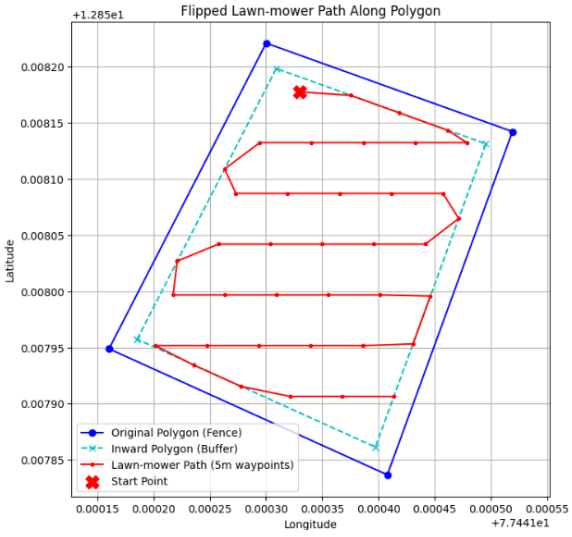

Fig. 4. Example pre-computed low-altitude scanning path illustrating waypoint coverage for autonomous target detection.

Upon reaching the target, the UAV executes the payload drop. If the detection proves false, the UAV resumes its original scanning pattern, ensuring comprehensive area coverage. This adaptive detection-to-action workflow allows the UAV to dynamically respond to confirmed targets while maintaining overall mission efficiency and coverage.

In summary, the integration of YOLOv8-based vision, telemetry, and LiDAR provides a robust onboard perception system, enabling precise target localization, navigation, and payload deployment without requiring human intervention. The real-time pixel-to-GPS conversion allows for accurate georeferencing of detected targets, which is critical for autonomous decision-making in disaster response scenarios.

During the mission, onboard camera and LiDAR continuously analyze the environment. When a potential disaster zone is detected, the UAV evaluates the confidence of the detection. A detection is confirmed only if the confidence score exceeds a predefined threshold for consecutive frames, reducing false positives caused by transient visual artifacts. If the disaster zone is confirmed, it temporarily leaves the pre-planned path to navigate directly over the target area using GPS coordinates derived from the pixel-to-GPS conversion.

A test scenario of target detection over a simulated disaster zone (pool) is shown in Fig. 5, illustrating the bounding box and heading-aware nudge until centered.

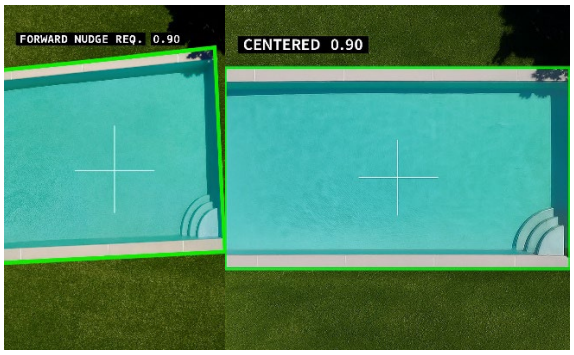

Fig. 5. Onboard target detection in a test scenario. The UAS identifies the pool (simulated disaster zone) with a bounding box, computes the heading-aware nudge to center over the target, and indicates when the UAV is aligned ("Centered").

3. Terrain Mapping and Navigation

LiDAR range measurements, GPS position, and PX4 attitude telemetry are fused onboard to construct a local terrain-undulation map that represents the surface topography of the mission area (Fig. 6). Each LiDAR return is projected into the world frame using the UAV's real-time position and orientation, forming a local elevation point cloud referenced to mean sea level. Outliers caused by spurious returns or dynamic objects are removed using range and height thresholding.

The filtered elevation data are stored as a 2.5D grid-based terrain map with fixed spatial resolution, which is incrementally updated during flight. Rather than performing full 3D SLAM, the system relies on continuous GNSS correction and PX4 state estimation to mitigate drift, enabling reliable terrain reconstruction in GPS-challenged, outdoor disaster environments while maintaining low computational load suitable for real-time execution on a Raspberry Pi 5.

The generated terrain map enables terrain-aware navigation by providing local elevation estimates along the planned trajectory. During subsequent passes, the UAV adapts its flight altitude to maintain a safe clearance above the mapped terrain, allowing lower-altitude operation where sensor resolution and target detection accuracy are improved. Elevation discontinuities or obstacles detected in the map trigger local path and altitude adjustments, enhancing flight safety in uneven or cluttered environments where GPS-only waypoint navigation may be insufficient [5].

Sensor fusion is performed through direct frame projection using PX4-provided pose estimates rather than probabilistic filters (e.g., EKF or ICP), prioritizing computational simplicity and robustness under outdoor GNSS-corrected flight.

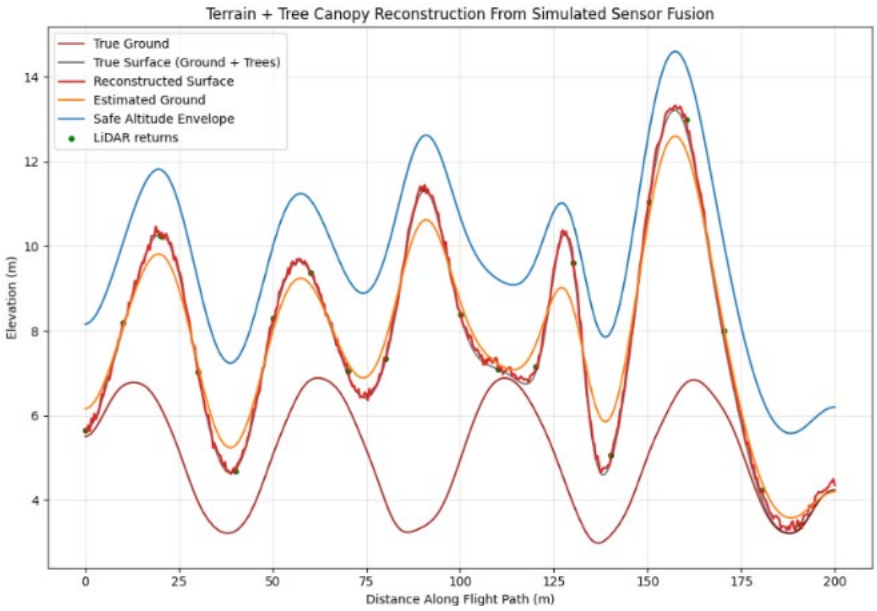

Fig. 6. Terrain-undulation map generated from fused LiDAR, GPS, and telemetry data, used by the UAS to navigate at lower altitudes and improve detection and payload delivery precision.

Terrain awareness also directly improves payload delivery accuracy. By accounting for local surface variations at the target location, the UAV can approach drop points with reduced vertical and lateral error, ensuring more consistent payload placement. Additionally, the terrain map supports scan-path refinement by locally modifying the fixed-altitude lawnmower pattern in regions with obstacles or significant elevation change, improving coverage efficiency while preserving autonomous mission execution [6].

4. Communication and Coordination

The proposed system architecture includes support for peer-to-peer communication using Wi-Fi Direct, enabling secure, infrastructure-free coordination between multiple UAVs when deployed in a fleet configuration [7]. The communication layer is designed to exchange target coordinates and mission status messages using NaCl-based encryption for lightweight confidentiality and integrity protection [8].

While the communication framework enables multi-UAV coordination, the experimental evaluation presented in this work was conducted using a single UAV. In this configuration, the communication subsystem was used to transmit mission updates and detected target coordinates to a ground monitoring interface, validating message generation, encryption, and transmission under real flight conditions.

In a multi-UAV deployment, the same communication mechanism allows any UAV to broadcast detected disaster locations to other agents in the fleet. This design enables dynamic task reallocation, such as redirecting a scanning UAV toward a newly identified target, improving overall mission responsiveness and coverage efficiency. Although fleet-level coordination was not experimentally validated in this study, the architecture is fully compatible with such extensions in future work.

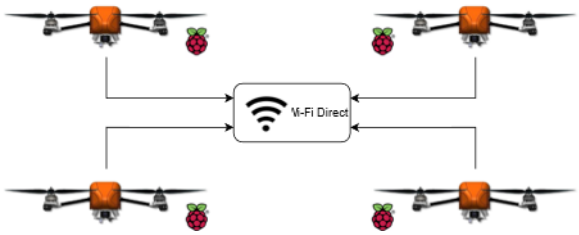

Fig. 7. UAS fleet coordination using a peer-to-peer Wi-Fi Direct network.

5. Validation and Experimental Results

The system has been validated through both SITL (Software-In-The-Loop) simulations [9-11] and extensive real-world field deployments, ensuring that both the software and hardware components perform reliably under realistic operating conditions. The SITL simulations (Fig. 8) allowed thorough pre-flight testing of autonomous navigation, sensor fusion, and multi-UAV coordination before committing to physical flights, reducing the risk of errors and system failures.

SITL experiments focused on validating autonomous waypoint tracking, perception-triggered rerouting, and payload-drop sequencing under nominal GPS conditions. Simulated missions included straight-line waypoint execution, lawnmower scanning, and target-diversion scenarios. Failure

modes such as communication loss or GPS denial were not modeled and are outside the scope of this study.

Fig. 8. Software-in-the-Loop (SITL) simulation of autonomous UAV mission for validation of flight control and payload delivery.

A total of 30 fully autonomous test flights were conducted in simulated disaster-response environments, implemented in real-world outdoor open areas with artificially introduced disaster cues and controlled obstacles. Test sites included obstacle-free fields and uneven terrain to evaluate overall operational performance under representative but repeatable conditions. These trials (Fig. 9) assessed payload handling, terrain-aware navigation, disaster-zone detection, and autonomous decision-making without human intervention.

Key system-level performance metrics included a 2 kg payload capacity, 25-minute average flight endurance, and an average per-target detection success rate of approximately 80 %, as defined by IoU-based overlap and temporal confidence criteria. These results demonstrate the effectiveness of the onboard vision pipeline and LiDAR-assisted terrain modeling in realistic outdoor conditions.

Fig. 9. Autonomous test flight demonstrating UAV maneuverability.

During field tests, the UAV demonstrated robust real-time adaptability. Upon identifying simulated disaster zones, the system autonomously modified its pre-planned lawnmower scanning trajectory to navigate directly over confirmed targets, validating the heading-aware pixel-to-GPS localization pipeline. Fig. 10 illustrates the UAV en route to a detected disaster zone while maintaining stable autonomous navigation, dynamic path adjustment, and continuous target tracking.

In 24 out of 30 test flights, the UAV executed payload delivery within a ±5 m radius of the detected target, meeting the defined mission success criteria. In the remaining 6 flights, the system intentionally aborted payload release and returned with the payload due to safety-triggered conditions such as excessive localization uncertainty, transient false detections, or wind-induced drift. These cases were classified as safe mission aborts rather than deployment failures, highlighting the robustness of the decision logic and fault-handling mechanisms.

Fig. 10. UAS en route to a confirmed disaster zone for payload delivery, demonstrating autonomous navigation and target tracking.

The terrain-mapping pipeline further enhanced operational accuracy by enabling low-altitude flight with improved sensor resolution. By referencing real-time terrain undulations, the UAV maintained safe clearance above obstacles while improving detection rates and payload delivery precision. This allowed for repeatable, high-confidence drops, even in complex or uneven environments where traditional GPS-only navigation would have resulted in errors.

Overall, the validation results confirm that the proposed UAS architecture effectively integrates autonomous sensing, terrain-aware navigation, and payload delivery into a single operational platform. The combined use of SITL-based simulation and outdoor field testing provides evidence of the system's reliability and operational readiness for disaster-response scenarios. While experimental validation in this work focuses on single-UAV missions, the architecture is designed to support future multi-UAV coordination once swarm-level testing is conducted.

Table 1. Performance Metrics.

Metric	Value
Total autonomous flights	30
Successful deliveries	24
Detection accuracy	~80 % (IoU ≥ 0.5)
Payload capacity	2 kg
Average flight endurance	25 min
Drop success radius	±5 m
Typical flight altitude	20 m AGL
Failure causes	Wind gusts, GPS drift, false detection
Wind Speed(avg.)	estimated 2–5 m/s

6. Conclusion

This work presents a fully autonomous, modular unmanned aerial system for rapid disaster-response missions, capable of scanning user-defined areas, detecting critical zones, and executing payload delivery without continuous ground intervention. The system integrates onboard vision-based detection, LiDAR-assisted terrain mapping, and heading-aware pixel-to-GPS localization to enable reliable low-altitude navigation and targeted payload deployment. SITL simulations and outdoor field tests demonstrate consistent autonomous operation and successful payload delivery under realistic conditions.

The key novelty of this work lies in the unified, fully onboard integration of terrain-aware navigation, real-time vision-based target localization, and autonomous payload delivery on a low-cost computational platform. Unlike existing approaches that rely on ground-station processing or treat perception, mapping, and delivery as separate modules, the proposed system forms a closed-loop autonomous pipeline capable of dynamic path deviation and terrain-informed deployment decisions. While swarm coordination was not experimentally validated, the communication architecture is designed to support secure peer-to-peer information sharing and scalable multi-UAV operations.

Future work will focus on experimental validation of cooperative multi-UAV missions, adaptive scan planning, and improved operation in GPS-challenged environments.

Acknowledgements

The authors gratefully acknowledge Pune Vidyarthi Griha's College of Engineering, Technology & Management (PVGCOETM) for funding and providing the facilities necessary for this project. We also acknowledge Team Squadrone, the college's drone club, including non-author members, for their guidance, collaboration, and contributions, which helped advance the UAS project. The team's enthusiasm and technical expertise greatly contributed to turning the concept into a functional autonomous UAV. Their support during iterative testing, problem-solving sessions, and system integration was invaluable in overcoming challenges and enhancing the reliability, performance, and overall capabilities of the UAV system.

References

[1]. A. Koubâa, A. Allouch, M. Alajlan, Y. Javed, et al., Micro Air Vehicle Link (MAVLink) in a nutshell: A survey, *IEEE Access*, Vol. 7, 2019, pp. 87658-87680.

[2]. S. Zang, G. Hong, Y. Liu, H. Gan, et al., MCD-YOLO: An improved YOLOv8-based approach for surface defect detection of marine machinery components, *Ocean Engineering*, Vol. 341, 2025, 122624.

[3]. J. Mao, L. Zhang, X. He, H. Qu, et al., Accurate geolocalization for UAVs using visual-inertial odometry and 2D georeference maps, in *Proceedings of the IEEE/RSJ International Conference on Intelligent Robots and Systems (IROS'22)*, 2022, pp. 11094-11101.

[4]. G. Sohn, I. Dowman, Terrain surface reconstruction by the use of tetrahedron model with the MDL criterion, in *Proceedings of the 20th ISPRS Congress*, 2004, pp. 336-341.

[5]. D. M. Cobby, D. C. Mason, I. J. Davenport, Image processing of airborne scanning laser altimetry data for improved river flood modelling, *ISPRS Journal of Photogrammetry and Remote Sensing*, Vol. 56, Issue 2, 2001, pp. 121-138.

[6]. C. Baillard, H. Maître, 3-D reconstruction of urban scenes from aerial stereo imagery: A focusing strategy, *Computer Vision and Image Understanding*, Vol. 76, Issue 3, 1999, pp. 244-258.

[7]. S. Benhadhria, M. Mansouri, A. Benkhlifa, I. Gharbi, et al., VAGADRONE: Intelligent and fully automatic drone based on Raspberry Pi and Android, *Applied Sciences*, Vol. 11, Issue 7, 2021, 3153.

[8]. D. J. Bernstein, T. Lange, P. Schwabe, The security impact of a new cryptographic library, in Progress in Cryptology – LATINCRYPT 2012 (A. Hevia, G. Neven, Eds.), *Springer*, Berlin, 2012, pp. 159-176.

[9]. N. Mastronarde, D. Russell, Z. Guan, G. Sklivanitis, et al., RF SITL: A software-in-the-loop channel emulator for UAV swarm networks, in *Proceedings of the IEEE International Conference on Sensing, Communication, and Networking (SECON'20)*, 2020, pp. 1-9.

[10]. M. Khaneghaei, D. Asadi, Ö. Tutsoy, Software-in-the-loop simulation for an autonomous multirotor flight planning and landing with ROS and Gazebo, in *Proceedings of the International Symposium on Autonomous Systems (ISAS'21)*, 2021, pp. 1-6.

[11]. S. M. Rahman, M. A. Hossain, H. Kim, Software-in-the-loop simulation for autonomous UAV mission validation using PX4 and Gazebo, in *Proceedings of the International Conference on Unmanned Aircraft Systems (ICUAS'21)*, 2021, pp. 142-148.

(042)

A UAV-Enabled Overhead Digital Twin for Real-Time AGV Traffic Management in Confined Environments

N. Bahnes
Computer sciences department, University of Abdelhamid Ibn Badis Mostaganem,
CSTL Laboratory, Ex Ines de Chimie Zaghloul, Mostaganem, Algeria
Tel.: + 00213 45 36 64 72
E-mail: nacera.bahnes@univ-mosta.dz

Summary: This paper presents an unmanned aerial vehicle (UAV) enabled overhead digital twin framework aimed at improving real-time traffic management for Automated Guided Vehicles (AGVs) operating in confined spaces. The proposed system leverages an UAV equipped with aerial vision sensors and lightweight onboard processing to provide a global view of the operating area. By combining aerial vision, lightweight onboard processing, and a synchronized digital twin environment, the system delivers continuous situational awareness, early congestion detection, and dynamic path optimization. This integration guarantees persistent situational awareness, supports early detection of congestion and conflict situation, and enables proactive planning and control strategies. The digital twin supports dynamic path planning and traffic optimization by simulating alternative routing strategies before deployment in the physical environment. By combining airborne sensing, real-time data processing, and digital twin-based simulation, the proposed framework enhances operational efficiency, improves AGV throughput, and increases system robustness in complex and space-constrained industrial settings.

Keywords: UAV, AGV, Traffic management, Digital twin, Wireless communication.

1. Introduction

Automated Guided Vehicles (AGVs) are increasingly deployed in industrial and logistics environments, where traffic coordination, safety, and operational efficiency are essential [1]. Their performance decreases in narrow aisles or cluttered indoor facilities where sensor occlusion restricts reliable tracking. Despite advances in localization and control, maintaining efficient AGV traffic flows in narrow aisles, densely packed storage areas, or dynamically evolving layouts remains challenging. Several studies are proposed to autonomous AGV navigation [2-4].

However, conventional AGV monitoring systems encounter challenges in confined or indoor environments due to occlusion, restricted sensor coverage, and inflexible infrastructure-based localization. Conventional solutions, such as embedded floor markers, fixed cameras or lidar technology, frequently necessitate costly installation and are vulnerable to blind spots.

To address this, unmanned aerial vehicles (UAVs) offer an opportunity for flexible, mobile, and unobstructed sensing, enabling continuous overhead visibility [5]. Coupled with a real-time digital twin, UAV-based sensing supports the generation of a synchronized virtual model of AGV operations, enabling improved traffic decision-making. UAVs offer a flexible alternative where a single overhead platform can provide adaptable, unobstructed visibility. The integration of aerial sensing with a real-time digital twin enables robust traffic analysis and control [6].

This study proposes a UAV-enabled overhead digital twin designed to provide real-time traffic monitoring, dynamic path management, and predictive collision avoidance. Through the integrating airborne sensing, computer vision, and digital twin simulation, the framework enhances situational awareness and improves throughput in indoor or GPS-denied spaces.

The proposed solution leverages a small autonomous UAV equipped with high-resolution cameras and onboard computing. Its main functions are:

- **Reduced Infrastructure:** No need for fixed overhead camera arrays or floor markers;
- **Improved Situational Awareness:** Continuous aerial coverage captures full AGV motion, even in narrow or dynamic layouts;
- **Real-Time Optimization:** Digital twin simulation supports predictive rerouting and congestion mitigation;
- **Scalable Deployment**: Multiple UAVs can coordinate to cover larger or multi-zone environments.

The rest of this paper is organized as follows: Section 2 presents background and problem situation. Section 3 describes the architecture of the proposed system. In Section 4, we outline Digital twin technologies. Section 5 presents discussion. Finally, we conclude this paper.

2. Background and Problem Situation

Automated Guided Vehicles (AGVs) have become a staple in industrial environments, such as warehouses and manufacturing facilities, due to their pivotal role

in ensuring the seamless and efficient management of materials. As AGV deployments increase in scale, there is a strong necessity for them to operate in confined environments characterised by narrow aisles, dense traffic, and frequent interactions with infrastructure and other vehicles [7]. In such conditions, effective real-time traffic management is essential to ensure safety, avoid congestion, and maintain high system throughput.

Existing AGV traffic management approaches typically rely on onboard sensing and fixed ground-based infrastructure, including magnetic guidance systems, LiDAR sensors, and static cameras [8]. Whilst the efficacy of these approaches is evident in structured and predictable settings, they frequently offer restricted global visibility and are susceptible to occlusions caused by static or moving obstacles such as shelving, machinery, or other AGVs [9]. Consequently, the maintenance of an accurate and up-to-date representation of the overall traffic state becomes challenging, particularly in dynamic or atypical environment.

Digital Twin (DT) technology has emerged as a promising paradigm for the monitoring and optimization of cyber-physical systems, achieved by synchronizing a virtual model with real-time operational data. In AGV systems, a digital twin can facilitate traffic supervision, performance analysis, and decision-making. However, the efficacy of such a digital twin is contingent upon the availability of comprehensive, reliable, and timely sensory data. In confined spaces, reliance on ground-based sensing frequently results in updates that are either incomplete or delayed, thereby constraining the digital twin's capacity to mirror the actual system state in real time.

The present paper addresses the problem of how to achieve accurate and real-time AGV traffic awareness in confined environments without extensive fixed infrastructure. The primary challenge in this regard is the procurement of a comprehensive, unobstructed, and adaptable global perspective on AGV traffic, with the capacity to reliably synchronise a digital twin and facilitate real-time traffic management operations. In order to address this issue, the utilisation of an Unmanned Aerial Vehicle (UAV) as a mobile overhead sensing platform integrated with a digital twin framework enables real-time monitoring and management of AGV traffic in confined industrial settings.

3. System Architecture

The proposed UAV-enabled overhead digital twin architecture is composed of three tightly integrated layers: 1) the UAV overhead sensing, 2) the real-time digital twin engine, and 3) the AGV traffic control layer. These components enable continuous perception, synchronized virtual modeling, and decision-making for AGV fleet management in confined environments. Fig. 1 illustrates the different layers of the proposed system, as well as the underlying the interactions between them.

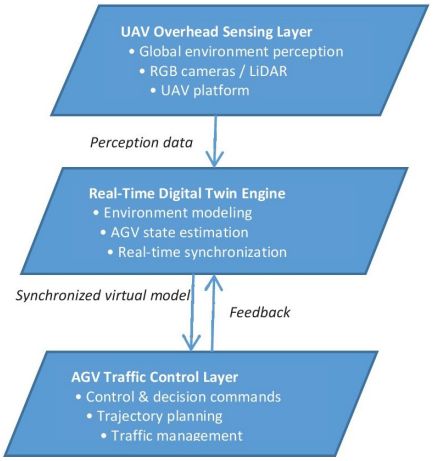

Fig. 1. The proposed UAV-enabled overhead digital twin layers.

3.1. UAV Overhead Sensing

A lightweight indoor-capable UAV captures continuous top-down imagery of the AGV fleet. This vantage point minimizes occlusion and reduces the number of sensors needed. The system uses a compact, collision-tolerant UAV designed for indoor operations. Key onboard components include: an RGB-D camera, Lightweight onboard computing, IMU and optical flow sensors for stable indoor navigation and obstacle-avoidance sensors (stereo, ToF, or lidar lite) for safe operation in cluttered areas.

Flight Strategy: The UAV follows a predefined or adaptive flight path that ensures maximum visibility over AGV corridors. Two modes are considered: Static Hover Mode (SHM) where the UAV such as quadrotor, hovers above a critical zone (e.g., an intersection) and Patrolling Mode (PM) in which the UAV autonomously circulates along a loop to cover larger facilities [10]. An onboard controller maintains safe altitude and ensures that the UAV does not interfere with human workers or AGVs. Flying above the operational area, the UAV provides a top-down perspective free of obstacles. This vantage point ensures complete visibility of AGV movements, reduced occlusion compared to static cameras and adaptable coverage depending on task zones.

Onboard Vision Processing: To reduce network load and latency, part of the image-processing pipeline runs on the UAV itself. Only the processed metadata (AGV positions, confidence scores, UAV state) is transmitted to the digital twin, ensuring efficient bandwidth usage.

3.2. Real-Time Digital Twin

Image streams are processed using onboard or edge-based vision models to detect and track AGV

positions. These positions feed a digital twin that mirrors the physical workspace and evaluates potential conflicts, bottlenecks, and route alternatives. The virtual environment includes the facility layout, AGV geometric models and kinematic constraints and dynamic obstacles (workers, mobile equipment). The digital twin continuously synchronizes with the physical system, ensuring high-fidelity representation. Incoming UAV data is fused with additional sources when available (AGV onboard odometry or wheel encoders, Indoor positioning systems (UWB, Wi-Fi), Static ceiling cameras). Data captured by the UAV is streamed to a digital twin platform, where:

- AGV locations are updated in real time;
- Path predictions are computed;
- Congestion and collision risks are detected;
- Dynamic rerouting strategies are simulated before execution.

The digital twin simulates short-term AGV motion by predicting: the potential collisions, congestion zones and delays caused by local traffic density. These predictions help evaluate possible rerouting decisions before sending commands to the physical AGVs.

3.3. Traffic Control Layer

Table 1 presents the aims and output of the main tasks of Digital twin for traffic control.

Table 1. Digital twin Tasks for traffic control.

Task	Aims & output
Trajectory Optimization	Graph-based routing for structured environments. Model-predictive control (MPC) for dynamic adjustment. Collision-free time windows to prevent bottlenecks.
Coordination Policies	Priority rules at intersections. Speed modulation instead of full stops. Virtual lane assignment in narrow aisles.
Communication Interface	Standard industrial protocols (MQTT, OPC-UA, ROS2). Real-time feedback loops enabling sub-second responsiveness. The returned AGV telemetry also feeds back into the digital twin, closing the control loop.

The digital twin computes optimized trajectories, speed adjustments, and collision-avoidance strategies and sends commands back to the AGVs. The UAV autonomously maintains safe altitude, avoids obstacles, and adapts its flight path to maximize visibility. The digital twin acts as a virtual replica of the physical environment, updated in real time using UAV-derived data. This layer translates the digital twin's insights into actionable commands for the AGV fleet.

3.4. System-Level Integration

All components are interconnected through a low-latency network. A cloud-edge hybrid architecture ensures:

- Edge processing for fast local decisions;
- Cloud-based analytics for long-term performance evaluation;
- High availability through redundancy and fail-safe UAV return-to-home routines.

4. Digital Twin Technologies

Computer Vision for AGV Detection: Advanced image processing and machine learning models identify and track AGVs, even under poor lighting or cluttered conditions. Techniques include object detection (e.g., YOLO-based models), optical flow estimation, and image-based SLAM for UAV localization.

Multi-Agent Traffic Control: The digital twin integrates AGV kinematics and motion constraints to evaluate the optimal paths, speed adjustments, Conflict resolution policies and queue management in narrow corridors.

UAV Autonomy and Safety: to operate in confined spaces, the UAV relies on obstacle avoidance sensors, stable hovering capability, battery-optimized flight scheduling and safety protocols ensuring non-interference with AGVs.

5. Discussion

In our proposal system, the UAV detects AGVs in the video frames (YOLO-lite [11], MobileNet-SSD [12], etc.), tracks them across frames and converts pixel coordinates to global. Data Fusion is ensured with the merge of UAV-derived positions and AGV odometry.

Visual data captured by the UAV are processed using computer vision techniques and continuously synchronized with a digital twin environment that mirrors the physical system in real time [13].

Digital Twin Synchronization mirrors the real-world AGV positions and maintains a geometric/kinematic model of the facility. In the control Layer, the temporary visual occlusions are eliminated by sending new trajectories to AGVs. This ensures smooth flow and resolves conflicts before they occur. UAV Autonomous Behavior ensures optimal visibility for perception and monitors battery and returns safely when necessary. Digital-twin system ensures the following aims:

- **Enhanced Operational Efficiency:** Real-time overhead monitoring helps identify bottlenecks and improve AGV routing, increasing throughput;

- **Improved Safety:** Early detection of potential collisions or unsafe behaviors fosters safer human-robot coexistence;
- **Flexibility in Dynamic Environments:** The system adapts easily to layout changes, temporary installations, or seasonal variations in workload;
- **Scalability:** Multiple UAVs can coordinate to monitor large or multi-floor environments, all feeding data into a unified digital twin.

6. Conclusion

The proposed UAV-enabled overhead digital twin offers an agile and cost-efficient solution for AGV traffic monitoring and control in confined industrial spaces. By integrating mobile aerial sensing with real-time simulation, the system enhances safety, efficiency, and adaptability. Unlike fixed camera arrays or complex localization grids, the UAV-based system requires only: a safe indoor flight corridor, wireless communication and digital twin software. This makes it ideal for rapidly changing industrial layouts or temporary installations.

A UAV-enabled overhead digital twin presents a novel and highly effective method for managing AGV traffic in confined environments. By combining aerial perception, real-time simulation, and advanced traffic control algorithms, the solution overcomes the limitations of traditional ground-based sensing and enhances both efficiency and safety. As industries continue to digitize and automate, such integrated cyber-physical systems will play an increasingly critical role in optimizing logistics and manufacturing operations.

Future work will explore multi-UAV collaboration and deeper fusion with indoor localization systems.

References

[1]. A. Lombard, F. Perronnet, A. A. Turki, A. Moudni, Decentralized management of intersections of AGVs, *IFAC-PapersOnLine*, Vol. 49, Issue 12, 2016, pp. 497-502.

[2]. I. S. Mohamed, K. Yin, L. Liu, Autonomous navigation of AGVs in unknown cluttered environments: Log-MPPI control strategy, *IEEE Robotics and Automation Letters*, Vol. 7, Issue 4, 2022, pp. 10240-10247.

[3]. A. K. Sivarathri, A. Shukla, Autonomous navigation of AGV by tracking the motion of UAV, in *Proceedings of the 20th IEEE/ASME International Conference on Mechatronic and Embedded Systems and Applications (MESA'24)*, 2024, pp. 1-8.

[4]. H. B. Choi, J. B. Kim, Y. H. Han, S. W. Oh, et al., MARL-based cooperative multi-AGV control in warehouse systems, *IEEE Access*, Vol. 10, 2022, pp. 100478-100488.

[5]. Y. Khosiawan, I. Nielsen, A system of UAV application in indoor environment, *Production & Manufacturing Research*, Vol. 4, Issue 1, 2016, pp. 2-22.

[6]. T. H. J. Uhlemann, C. Schock, C. Lehmann, S. Freiberger, et al., The digital twin: Demonstrating the potential of real time data acquisition in production systems, *Procedia Manufacturing*, Vol. 9, 2017, pp. 113-120.

[7]. P. Verma, Control strategies for the traffic management of AGV-based transportation systems, PhD Thesis, *Universitat Politècnica de Catalunya*, 2025.

[8]. K. Kuru, Planning the future of smart cities with swarms of fully autonomous unmanned aerial vehicles using a novel framework, *IEEE Access*, Vol. 9, 2021, pp. 6571-6595.

[9]. J. Lu, Review of AGV obstacle avoidance algorithm based on machine vision, *Science and Technology of Engineering, Chemistry and Environmental Protection*, Vol. 1, Issue 2, 2025.

[10]. O. Fedorovich, M. Lukhanin, D. Krytskyi, O. Prokhorov, Modeling strategies for conducting wave surveillance using a swarm of security drones, *Computation*, Vol. 13, Issue 8, 2025, 193.

[11]. S. Patil, S. M. Jaybhaye, M. M. Khalifa, S. Kharche, et al., Drone detection using YOLO, *AIP Conference Proceedings*, Vol. 2938, Issue 1, 2023, 020002.

[12]. D. S. Levkovits-Scherer, I. Cruz-Vega, J. Martinez-Carranza, Real-time monocular vision-based UAV obstacle detection and collision avoidance in GPS-denied outdoor environments using CNN MobileNet-SSD, in Advances in Soft Computing (I. Batyrshin, A. Gelbukh, G. Sidorov, Eds.), *Springer*, Cham, 2019, pp. 613-621.

[13]. S. Sepahvand, N. Amiri, H. Masnavi, I. Mantegh, et al., A novel fuzzy image-based UAV landing using RGBD data and visual SLAM, *Drones*, Vol. 8, Issue 10, 2024, 594.

(044)

A Lightweight Vision-Based GNSS Substitute for Small UAVs

L. Kempf [1,2] and K. B. Kochersberger [1]
[1] Virginia Tech, Uncrewed Systems Laboratory, 160 Inventive Lane, Blacksburg, VA 24061, USA
[2] Technical University of Darmstadt, Institute for Flight Systems and Automatic Control,
Otto-Berndt Strasse 2, 64287 Darmstadt, Germany
Tel.: +49 1590 1030037
Email: lkempf@vt.edu

Summary: While Global Navigation Satellite System (GNSS) technology combined with advanced augmentation techniques provides high accuracy, its reliance on signal integrity leaves safety-critical applications vulnerable to spoofing and jamming. To address this, a lightweight vision-based localization module is proposed as a self-contained GNSS substitute for small Uncrewed Aerial Vehicles (UAVs). It leverages offline satellite maps and an ensemble of Convolutional Neural Network (CNN) models to estimate 2D offsets and associated uncertainty for stable Extended Kalman Filter (EKF) fusion. The system is designed for seamless integration with PX4 and real-time operation on resource-limited platforms. Software-In-The-Loop (SITL) simulations over varied mission scenarios at Virginia Tech's Kentland Farm demonstrate an R95 accuracy of 4.5 m to 5.5 m, with effective drift bounding even in low-texture environments. Remaining challenges include uncertainty calibration, particularly over tree-covered regions, before transitioning to field testing.

Keywords: GNSS-denied navigation, Vision-based sensing, Cross-view geolocalization.

1. Introduction

Today, absolute 3D positioning with sub-meter accuracy is no longer a question of feasibility but of the performance demands of specific mission objectives. Standardized technology such as the Global Positioning System (GPS), supported by the Wide Area Augmentation System (WAAS), can now provide an R95 accuracy of 1.6 m, compared to over 20 m in 1995 [11, 12]. Advancements in navigation technology – particularly global radionavigation – have been driven by the fusion of multiple signals, sources, or sensors, with an Inertial Navigation System (INS) combined with a Global Navigation Satellite System (GNSS) receiver being the basic configuration.

However, GNSS depends entirely on signal quality, and with spoofing and jamming becoming major concerns for safety-critical applications, the need for a self-contained substitute has grown. In line with recent research trends, a vision-based localization module using offline satellite maps is proposed as a lightweight GNSS alternative for absolute positioning of small Uncrewed Aerial Vehicles (UAVs). It employs a Convolutional Neural Network (CNN) trained on georeferenced satellite imagery to estimate position and uncertainty. Initial Software-In-The-Loop (SITL) testing shows a baseline R95 accuracy of 5 m.

1.1. Scene-Referenced Navigation

Technologies for Terrain Referenced Navigation (TRN), such as Terrain Contour Matching (TERCOM) and the later Digital Scene Matching Area Correlation (DSMAC), originally evolved during the Cold War. While TERCOM matches radar and altimeter readings with a Digital Elevation Model (DEM), DSMAC uses an onboard camera to exploit the correlation of binary images and therefore works better for terrain with less variation in ground elevation.

Substantial advances in Artificial Intelligence (AI) have enabled a variety of even more powerful approaches, with the two predominant categories being Template and Feature Matching (TFM) and Semantic Mapping and Recognition (SMR). The latter targets content rather than structure alone, extracting more information from the processed data. Depending on the reference maps, the type and quantity of sensors used, and the complexity of the algorithm, final R95 accuracies can range from the sub-meter range to hundreds of meters. Table 1 compares a selection of relevant approaches. Note that all techniques have been evaluated under different conditions and rarely on the same datasets.

Table 1. Converted R95 accuracies assuming an isotropic Gaussian error with Rayleigh distribution.

Method	R95 accuracy in m
Object-to-pixel-level [9]	0.2 - 20
SAR range–doppler [4]	~ 2.5
Semantic monocular [5]	~ 10
DSMAC [6]	≤ 20
TERCOM [8]	~ 60
Magnetic anomalies [7]	200 - 800

1.2. Design Approach

Building upon established technology, what is the minimum effort needed to fly purely vision-based on an autonomous platform? As a response to the

limitations of existing techniques, the proposed approach promotes a modular system with sufficiently high absolute positioning accuracy to bound drift, uncertainty estimation for stable Extended Kalman Filter (EKF) fusion, and real-time capability on a small UAV platform with limited computational resources. It must scale to different mission scenarios, maintain reasonable robustness, and use simple, inexpensive sensors, as well as satellite imagery of moderate resolution. Only through recent advances in the commercial availability of imagery with multiple daily updates can the introduced navigation paradigm become a promising approach in future mission scenarios. Therefore, success ultimately depends on providers like Planet Labs PBC or BlackSky supplying new data at high frequencies and reasonable costs, with current trends being very promising [2, 3].

2. Methodology & Modeling

The localization module is designed to integrate directly with the widely accepted and highly compatible PX4 open-source autopilot, with the built-in EKF2 communicating with the module via ROS2. Fig. 1 shows the methodology blueprint of the localization module. An actively gimbaled, north-aligned RGB camera provides an observation. The observed scene is then compared to a window of the same extent as the camera frame extracted from a reference satellite map based on the last EKF position estimate. Both images are preprocessed and passed to the estimator ensemble, which outputs a mean 2D offset $\boldsymbol{\mu}_{\Delta x}$ alongside covariance $\boldsymbol{\Sigma}_{\Delta x}$. Using the built-in `VehicleOdometry` topic, EKF2 fuses the probabilistic estimate provided like it would fuse any other measurement and ensures correct allocation in time based on the reported timestamps.

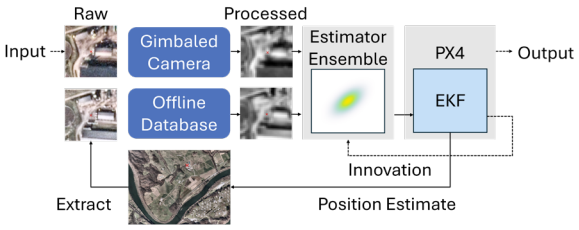

Fig. 1. Methodology blueprint.

2.1. Preconceived Limitations

While being designed to provide an absolute position reference not only when flying across geometrical human-made structures, but also for organic textures, any extreme alteration of the terrain or substantially compromised visibility (bright reflections, dark shadows, changed vegetation, clouds, fog, smoke) will put mission success at risk. The employed model ensemble is specialized to the defined mission settings and extended capabilities are only established through ensemble pooling. Using an RGB camera, nighttime operations are also currently excluded. Therefore, other ranges and resolutions of the electromagnetic spectrum, as well as additional filtering techniques are to be explored in the future.

Being intended for cruise flight – typically the most relevant segment for navigation problems – the initial localization module explicitly targets a constant altitude Above Ground Level (AGL) of 120 m that provides sufficient spatial context for absolute positioning. Object displacement from relief and realistic out-of-plane deviations in the camera angle (less than 7°) from uncompensated wind gusts will be modeled during SITL testing. This ensures robustness under nominal flight conditions. More variation during training can later enable true adaptability to greater AGL fluctuations or additional effects.

Another critical aspect of the localization module is the data used for training. The chosen sources and the ones thereby excluded determine the strengths and limitations of the employed models. It is therefore important to acknowledge the inherent bias from data availability and understand its effects on a later deployment of the technology. Overcast weather conditions or satellite constellation limitations are two very immediate factors to be aware of.

Since first testing is conducted in simulation and not on the final hardware stack, results should be treated carefully, in particular as regards latency. EKF2 accepts signals as old as 1000 ms, allowing for initial SITL testing without optimizing. However, a translation from Python, used for fast prototyping, to another more efficient language, such as C++ or Rust, may be necessary to meet the 10 Hz target data rate.

2.2. Estimator Ensemble

Employing three or more CNN models trained on the same dataset but with different sample shuffling, the variance across their predictions $\boldsymbol{\Sigma}_{\mu_{\Delta x}}$ provides an inexpensive estimate of systematic uncertainty from model disagreement. This can be combined with the average of the stochastic uncertainty $\overline{\boldsymbol{\Sigma}}_{\Delta x}$ of all models M to form the total effective covariance

$$\boldsymbol{\Sigma}_{eff,\Delta x} = \overline{\boldsymbol{\Sigma}}_{\Delta x} + \boldsymbol{\Sigma}_{\mu_{\Delta x}}, \tag{1}$$

with

$$\overline{\boldsymbol{\Sigma}}_{\Delta x} = \frac{1}{M}\sum_{i=1}^{M} \boldsymbol{\Sigma}_{\Delta x,i}, \tag{2}$$

$$\boldsymbol{\Sigma}_{\mu_{\Delta x}} = \frac{1}{M}\sum_{i=1}^{M} \left(\boldsymbol{\mu}_{\Delta x,i} - \overline{\boldsymbol{\mu}}_{\Delta x}\right)\left(\boldsymbol{\mu}_{\Delta x,i} - \overline{\boldsymbol{\mu}}_{\Delta x}\right)^{T} \tag{3}$$

The diagonal elements of the covariance then guide EKF updates and signal fusion on the PX4.

The final models follow a curriculum learning approach, with the first 10 epochs training only the means using the mean model, and the next 30 epochs

extending the output to uncertainties using the Gaussian model and a custom Negative Log Likelihood (NLL) loss. Fig. 2 shows the overall high-level architecture. This initial structure provides a reasonable baseline, with its simplicity allowing clearer interpretation of performance. Nevertheless, a more sophisticated CNN design could be introduced later to optimize estimate quality.

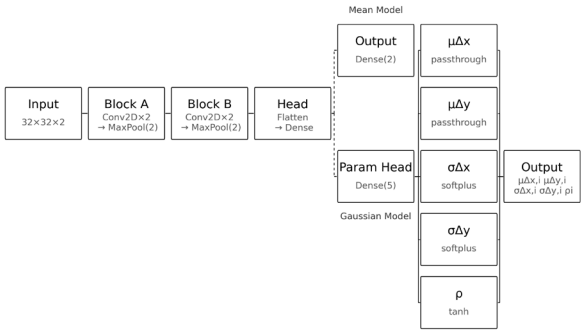

Fig. 2. CNN architecture.

2.3. Data Sampling

Even more important than the supervised training itself is the dataset used: from a pool of nine satellite images of Virginia Tech's Kentland Farm (Fig. 3) provided by BlackSky [1], six are selected based on their visual correspondence to the test mission. While the reference satellite map must reflect the latest changes in terrain (1), additional sources should be selected with training convergence in mind but still allow for natural fluctuation in lighting conditions (2-4). At the same time, robustness is maintained by also including more significant variation in vegetation and foliage (5, 6). This yields a 200,000-sample dataset of paired satellite windows and surrogate camera frames, downsampled from 1 m to 3.8 m for low-pass filtering and converted to greyscale. Within the defined sampling domain – enabling a later cross-area evaluation – window centers and associated offsets are randomly chosen. Offsets are bound to ±10 m (8.3 % of the frame size) on both Cartesian axes to optimally use the deliberately limited complexity of the CNN.

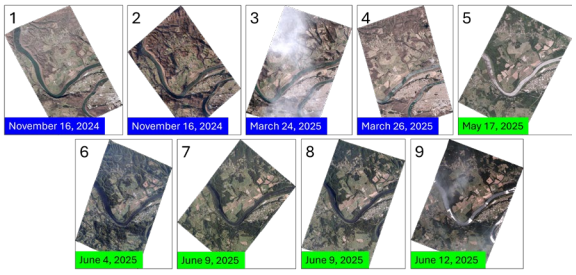

Fig. 3. Raw satellite images sorted by date. Blue labels show low vegetation coverage, and green labels show high vegetation coverage corresponding to seasonal change.

3. Results

For a first systematic evaluation of the localization module, SITL simulation with the X500 Quadrotor model in Gazebo Harmonic is performed on the reComputer J4012 by Seeed Technology [10]. Using a simulated camera view from a dedicated geo-mosaic of Kentland Farm, combined with a DEM for relief modeling, a variety of mission scenarios can be addressed (Fig. 4). The raw data was collected using a SenseFly eBee fixed-wing mapping drone

(a) Geo-mosaic image (b) DEM

Fig. 4. Geo-mosaic and associated DEM for camera simulation during SITL testing.

Starting with a reference mission, relevant modifications are explored. These include a disabled GNSS-signal for all subsequent test scenarios, cross-area evaluations on sections not used during training, a linear instead of a circular flight profile, as well as wind gust simulations. Fig. 5 shows the in-area mission, with at least 75 % of the terrain covered by pastures and farmland.

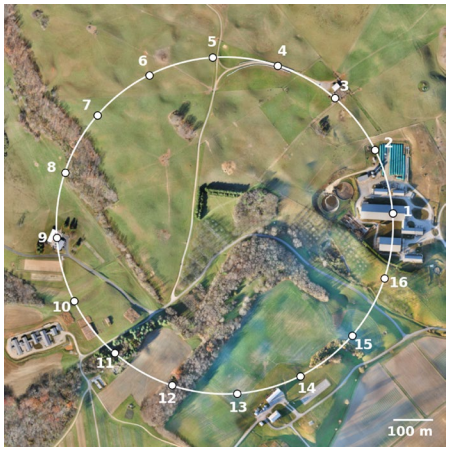

Fig. 5. Route of the reference mission. The Ground Control Points (GCPs) indicate the centers of the 200 m sampling radii for the employed training dataset.

Fig. 6 demonstrates a cumulative R95 accuracy of 5.2 m along the course of the mission, including the outlier about 400 s into the flight. With 1.3 m compared to a final resolution of 3.8 m, the mean bias stays in the sub-pixel range. However, the coverage statistics reveal the localization module's continuous overconfidence on unseen data, with significant

under-coverage compared to the expected percentages (hereafter denoted *exp*) for all three bands.

Fig. 7a uncovers the cause of the drift at GCP 12 (400 s into the flight) computing the relevant ground truth statistics: there is a significant bias in the negative x-direction from training-to-truth inconsistency. Although Fig. 6 revealed a significant under-coverage, Fig. 7b shows that the squared Mahalanobis distance has the correct order of magnitude in most regions, being a promising tendency in the data.

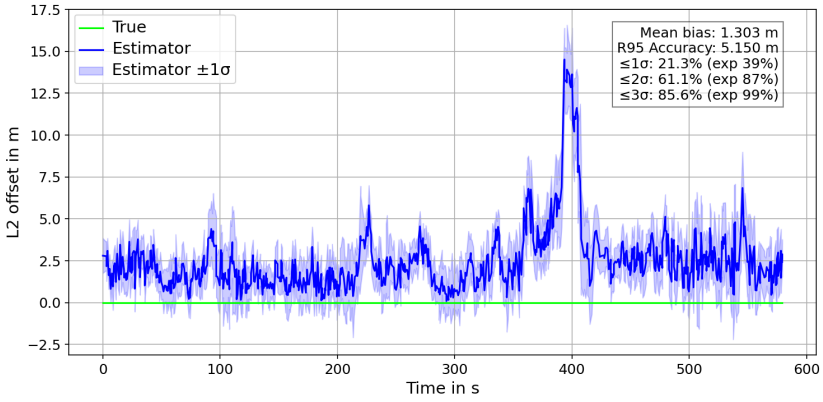

Fig. 6. L2 offset of the estimated position with respect to the truth, with the blue band around the estimator representing the radial standard deviation obtained by projecting the effective covariance $\boldsymbol{\Sigma}_{eff,\Delta x}$ onto the offset-direction unit vector.

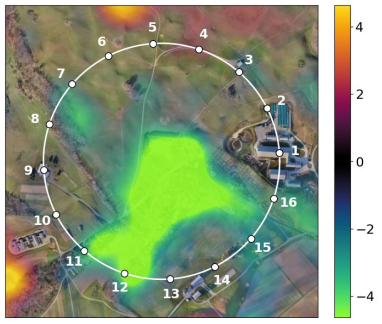

(a) X mean error in m

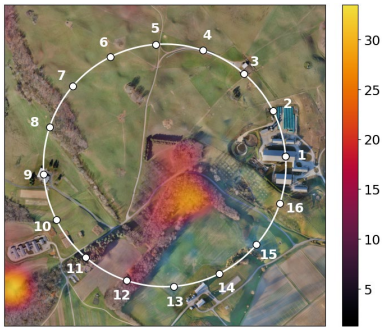

(b) Mean squared Mahalanobis (exp 2)

Fig. 7. Ground truth statistics for the reference mission, generated by performing repeated Monte Carlo simulations of the estimator ensemble on discrete grid cells across the geo-mosaic. Grid resolution is 60×60 m, with 30 runs per cell and a maximum offset of 5 m for regularization.

However, there are cases with critically high values, as seen in Fig. 8. When looking at the alternate mission location for cross-area evaluation, terrain with challenging textures – usually textures like trees that can change significantly from the training data to the observed truth during flight – lead to excessively high values. In contrast, the models still perform well on unseen areas if similarity is provided.

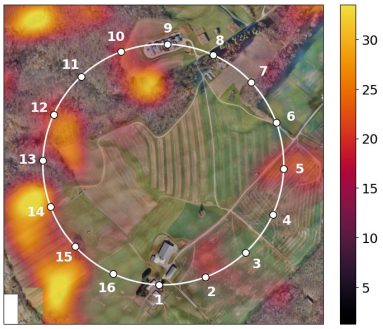

Fig. 8. Mean squared Mahalanobis for the alternate mission location (exp 2).

A significant inconsistency for an extended period will break the EKF logic and therefore induce a high risk of destabilization (Fig. 9).

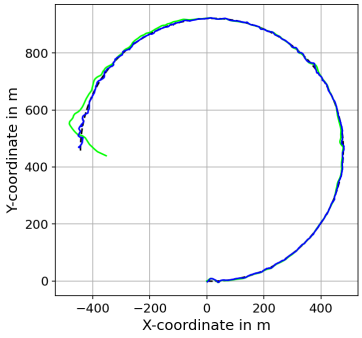

Fig. 9. Destabilization across forest.

Empirically tuning the `WindEffects` plugin in Gazebo, it shows that wind gusts have only a minor effect during nominal operation but generally lead to destabilization during a 10 s signal freeze, while Fig. 10 demonstrates recovery for windless conditions.

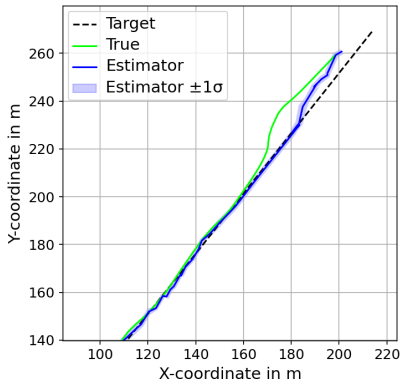

Fig. 10. Recovery after a signal loss around x = 150 m.

Overall R95 accuracy for the different test cases ranges from 4.5 m to 5.5 m. Flying across distinct human-made structures typically improves accuracy by about 50 %. In contrast, extended forest coverage imposes a high risk of destabilization without further measures taken.

Ground truth evaluation suggests that despite poor performance in some areas, the baseline uncertainty output by the estimator ensemble has the correct order of magnitude to provide long-term EKF consistency. Furthermore, using an ensemble instead of a single model is a promising approach, especially for distinct textures (Fig. 11). Terrain classification and specialized CNN models could be a cure for compromised coverage in more complex regions.

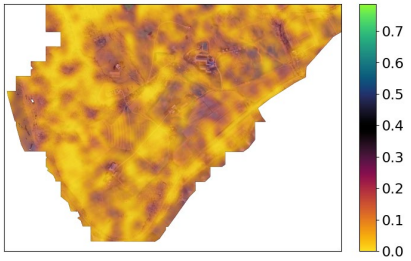

(a) 1σ coverage for a single mode (exp 39 %)

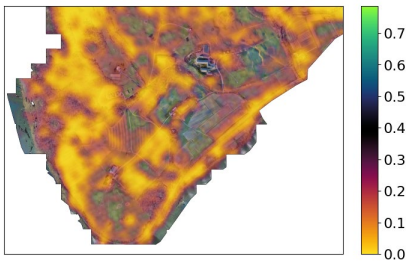

(b) 1σ coverage for the ensemble (exp 39 %)

Fig. 11. Coverage overview for a single model and the estimator ensemble.

While gust-induced fluctuations in pitch and roll of less than 7° are tolerated (max 3 % pixel shift), in-plane camera variation from yaw imposes a real challenge. The ensemble is not trained on off-axis distortions, which must be addressed by including an additional yaw Degree Of Freedom (DOF) in training to ensure robustness against magnetometer inaccuracies.

Also, the localization module does not perform any global search at this point. With the initial simplified CNN architecture, it has a very limited receptive field of ±10 m, providing a reference for absolute positioning only as long as sufficient ground features remain available, but destabilizing during extended sections with sparse textures. Visual Transformers (ViTs) could be used for an upstream global search.

With only 5.7 Hz on average (min 3 Hz, max 10 Hz), the target data rate of 10 Hz is not steadily met yet. Since model inference taking about 25 ms per run is not the only bottleneck, a transition to the Graphics Processing Unit (GPU) alone might not be sufficient. An additional code and language optimization is advised to minimize the overhead from statistical computations of the ensemble.

Instead of just using an RGB camera, Infrared (IR) could be used for nighttime missions and polarization information could be exploited to improve vision in foggy scenes. Additionally, an orthorectification algorithm is a cost-effective gimbal replacement for a future flight stack.

4. Conclusion & Outlook

While trees are identified as a major challenge, the proposed localization module can still effectively bound drift in low-texture areas if features persist across training and truth. However, sensitivity towards yaw must be addressed. Further ablation studies will allow for effective optimization, pushing the robustness of uncertainty coverage on unseen data beyond its current limitations before first flight tests.

Acknowledgements

The presented work is based on the first author's thesis submitted in partial fulfillment of the requirements for the degree of Master of Science in Mechanical Engineering at Virginia Tech and Technical University of Darmstadt. The research is funded by the National Science Foundation Center for Autonomous Air Mobility and Sensing and supported by a fellowship of the German Academic Exchange Service (DAAD).

References

[1]. BlackSky Technology Inc., BlackSky imagery and analytics: Satellite images of Kentland Farm (Virginia Tech), 2025, https://www.blacksky.com

[2]. BlackSky Technology Inc., Form 10-K for the fiscal year ended December 31, 2024, 2025, https://ir.blacksky.com

[3]. BryceTech, Smallsats by the numbers, 2025, https://brycetech.com/reports

[4]. C. Lindstrom, J. L. P. Barker, T. E. Humphreys, GPS-denied navigation aided by synthetic aperture radar using the range-Doppler algorithm, NAVIGATION: *Journal of the Institute of Navigation*, Vol. 69, Issue 3, 2022, navi.529.

[5]. C. Ouyang, Y. Wang, J. Chen, X. Wang, et al., A semantic vector map-based approach for aircraft positioning in GNSS/GPS denied large-scale environment, *Defence Technology*, Vol. 34, 2024, pp. 1-10.

[6]. J. C. O'Halloran, Jane's Weapons: Strategic 2015-2016, *IHS Global Inc*., Coulsdon, 2015.

[7]. M. Muradoglu, A. K. Mohammed, J. M. Baker, H. J. Liu, et al., Quantum-assured magnetic navigation achieves positioning accuracy better than a strategic-grade INS in airborne and ground-based field trials, *arXiv*, 2024, arXiv:2407.02685.

[8]. An Assessment of Minimum Deterrence Claims Regarding the Cost Benefit of Deep Nuclear Force Reductions, *National Institute for Public Policy*, Fairfax, 2015.

[9]. Q. Ye, J. Luo, Y. Lin, A coarse-to-fine visual geo-localization method for GNSS-denied UAV with oblique-view imagery, *ISPRS Journal of Photogrammetry and Remote Sensing*, Vol. 212, 2024, pp. 306-322.

[10]. Seeed Technology, NVIDIA Jetson Orin NX 16GB AI device – reComputer J4012, https://www.seeedstudio.com/reComputer-J4012-p-5586.html

[11]. Global Positioning System Precise Positioning Service Performance Standard, *United States Department of Defense*, 2007.

[12]. Global Positioning System Wide Area Augmentation System (WAAS) Performance Standard, *Federal Aviation Administration*, 2008.

(047)

The African Drone and Data Academy: Malawi's Talent Pipeline

K. Kochersberger [1], S. Muthukrishnan [2], N. Mkuwu [3], C. Chisenga [4] and M. Scheibenreif [5]
[1] Professor Mechanical Engineering, Virginia Tech, Blacksburg, Virginia, USA
[2] Director GIS and Remote Sensing Center, Furman University, Greenville, South Carolina, USA
[3] Senior Instructor, ADDA, Malawi University of Science and Technology (MUST), Tholo, Malawi
[4] Executive Dean, Ndata School of Climate and Earth Science, MUST, Tholo, Malawi
[5] Regional ADDA Manager, Impact YOMA Lead, UNICEF
Tel.: + 001 540-231-5589
E-mail: kbk@vt.edu

Summary: Established in 2020, the African Drone and Data Academy (ADDA) pioneers frontier technology education in the Global South. This paper details ADDA's six-year evolution, highlighting a blended curriculum merging regulatory-compliant flight operations, geospatial analysis, and entrepreneurship. To date, ADDA programs have enrolled 3979 students, with 1345 of them graduating from either synchronous online or in-person instructional programs. While Malawians represent the majority of the graduates at the ADDA, there are alumni from 31 African countries who have gained "Drones and Data for Good" competencies, fostering a diverse workforce with significant female participation. Graduates operationalize these skills in critical sectors, from humanitarian disaster response, exemplified by mapping Tropical Cyclone Freddy, to public health logistics. Beyond pedagogy, this article analyzes implementation challenges in resource-constrained environments, demonstrating how international higher education partnerships can leverage local talent to build scalable, sustainable ecosystems for technological innovation and economic development across Africa.

Keywords: Africa, Malawi, Drone, Education, Trusted operator.

1. Introduction

Inspired by the capabilities of drones and their potential to positively impact African communities, the African Drone and Data Academy (ADDA) admitted its first cohort of students in January, 2020 and is currently training the 17th in-person cohort – six years later. The ADDA represents a unique partnership between Virginia Tech, Furman University and the Malawi University of Science and Technology (MUST) to support certificate courses for post-baccalaureate science and engineering majors. Graduates of the program have found successful placement in a variety of government, non-government and commercial organizations, with applications ranging from agriculture to disaster risk management.

1.1. Drone Operations in Africa

The rapid growth of drone operations in Africa has been fueled by an unlikely alliance of tech entrepreneurs exploring leapfrog technologies, and countries eager to extend humanitarian services into rural and isolated communities. Stokenberga and Ochoa [1] identified five main areas of operation in Sub-Saharan Africa based on delivery and data collection services: medical goods delivery, food aid delivery, land mapping and risk assessment, agriculture and infrastructure inspections. Infrastructure that is in need of repair or simply does not exist has encouraged drone use for vaccine delivery, blood delivery, diagnostics, as well as on-demand stocking of essential medicines. Zipline started its drone-based medical supply delivery system in Rwanda in 2016 [2].

Deliveries of life-saving critical payloads such as units of blood are markedly superior to ground transportation when speed and cold chain continuity are factored in. However, a cost analysis still shows a significant gap in delivery methods, with a motorbike costing about $0.50 per (straight line distance) km whereas a drone flying 5000 annual flights would show a cost of $1.00 per km. Scaling a delivery operation can significantly lower cost (more flights, more aircraft), and with a focus on life-saving benefits of blood and "long-tail products" (small quantity, unpredictable demand), drone use in medicine will continue to grow [3].

In 2017, UNICEF opened the Humanitarian Drone Testing Corridor centered at Kasungu airport in Malawi to test drone concepts with reduced regulatory oversite from the Malawi Civil Aviation Authority [4]. The 80 km diameter test corridor became a resource for companies to test their technologies, and among the groups using the test corridor was Virginia Tech with a low-cost, easy-to-build drone called EcoSoar [5]. EcoSoar demonstrated low-cost delivery of dried blood spot samples, but the VT team also ran a workshop on drone construction and that led to a request from UNICEF to develop the ADDA.

The list of companies and organizations providing humanitarian drone services in Africa today is long. Zipline continues to expand, WingCopter has flown 130000 km and delivered 2300 kg of medical supplies [6], and Village Reach has made 5500 vaccine deliveries in Malawi and the Democratic Republic of the Congo [7]. Jedsy is building drones in Malawi [8]

and WeRobotics has created the Flying Labs network serving over 40 countries in drone training and operations ranging from emergency response to precision agriculture [9].

1.2. Drone Training

The African Drone and Data Academy was conceived as a post-baccalaureate program for science and engineering majors to expand their knowledge of operations and data. While this program was established in Malawi, it would serve pan-African students who earn internationally recognized certificates of drone knowledge and practical skills.

Originally defined as a drone technology program, UNICEF redirected the program development to include geospatial information systems (GIS) topics and applications with data. This inclusion better prepares students to immediately become productive with the skills and tools commonly used in drone operations.

2. ADDA Curriculum Development

The ADDA curriculum was developed by Virginia Tech and Furman University over a six-month period that preceded the first class offered in January, 2020. A requirement from UNICEF was to provide an accredited certificate of accomplishment that would follow the in-person training in drone flight operations. Students would be able to use this training to earn a Malawi Remote Pilot License; the ADDA became the first and only approved training organization in Malawi for remotely piloted aircraft (RPA) during the first year of operation.

Additionally, the curriculum incorporated geospatial sciences, encompassing GIS, photogrammetry, and remote sensing principles and applications, as a foundational component. This integration was designed to create a comprehensive learning and skills development ecosystem that extends beyond drone flight operations, addressing a broad spectrum of community needs. By embedding geospatial technologies into the program, ADDA filled a critical gap in regional capacity for spatial data analysis and decision-making, enabling graduates to apply advanced mapping and analytical techniques to sectors such as healthcare, environment, agriculture, disaster resilience, and infrastructure planning.

The program was deliberately structured for portability and replication elsewhere, underpinned by a curriculum that prioritizes robust foundational knowledge and applied competencies. Central to its design is a project-based pedagogical approach, which has been shown to enhance learner engagement, critical thinking, and problem-solving across diverse disciplinary contexts [10–12]. By embedding authentic, real-world projects, such as spatial modeling for hospital site selection, flood risk assessment, wildlife conservation, and agricultural monitoring, the curriculum fosters experiential learning that bridges theory and practice, equipping graduates to address complex challenges in humanitarian, environmental, and development domains.

2.1. Facilities

Partnering with the Malawi University of Science and Technology (MUST) was critical to support training, administration and student housing. The first class was actually taught at Daeyang University in Lilongwe to facilitate travel for the international students; subsequent cohorts were based at MUST in Thyolo. Early in the curriculum design it became apparent that creating A and B groups would improve the instructional efficiency so that while “A” was flying, “B” would receive lecture content or conduct laboratory activities. The groups would rotate and the instructors repeat the lessons.

The first cohort class was designed for 24 students (though 26 were admitted), but subsequent classes were designed around 16 students requiring four flight instructors and two ground instructors. Four pairs of students received flight training simultaneously, with one student flying the training drone while the other student observed. A football pitch-sized training area was adequate to run the four simultaneous flight operations (Fig. 1).

Indoors, a combined classroom / lab that could seat 16 students worked well, with additional space needed for storage and desk space for the instructors. Roughly 100 m^2 has been used now for several years with success (Fig. 2).

Fig. 1. Flight training site.

Fig 2. Indoor flex space.

2.2. Student Recruitment and Composition

Admission to the in-person program is highly competitive, with specific goals established for each cohort's composition. With the program based in Malawi and originally funded by the Malawi Country Office (MCO) of UNICEF, the majority of students enrolled in the certificate granting courses have been Malawian, with 30 other African nations represented. To promote gender equity, UNICEF mandated that at least 55 % of the graduates be female, a target consistently achieved across the certificate programs.

Applicants generally fell into two broad categories based on their academic background. The first group comprised largely of engineering students, including computer and electronics, civil, mechanical, telecommunications, biomedical, aeronautical, and mining, who were primarily attracted to the drone module, which focused on hardware and systems operations.

The second group was oriented toward data and geographic sciences, and typically came with backgrounds in GIS, environmental sciences, forestry, geology, mining, or land surveying and were primarily drawn to the data module of the program. While these two categories represented the majority of the applicants, the program also attracted individuals from non traditional fields such as social sciences or journalism, who sought to explore how drone and data technologies could be applied beyond strictly technical fields.

2.3. Funding

Donor funds were solicited and received by UNICEF to cover the costs of curriculum development in the startup phase as well as to provide grants to students during the operational phase. The 2021 – 2023 period of operation required a $1.91M budget that served 1345 students [13], with a per graduate cost of $1421. Fig. 3 shows expenses during this period.

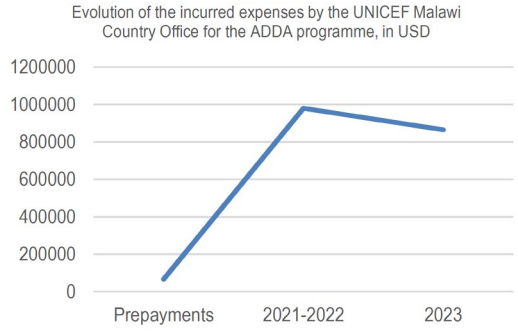

Fig. 3. Expenses for the first two years [13].

Funding beyond 2023 was secured through additional donor contributions and partial operational support from MCO, resulting in a reduced cost per graduate as the program matured. Virginia Tech continues to provide program accreditation, requiring a $60 fee for each Level 1 and 2 certificate issued.

2.4. Courses

The first ADDA Certificate of Drone and Data Technology (CDDT) course began in January, 2020 as a 10-week, in-person program. Instruction was provided by Virginia Tech and Furman University faculty and graduate students who were also evaluating the class to select four new ADDA instructors. Planned in-person cohorts were canceled due to the SARS-CoV-2 pandemic resulting in a new curricular challenge to create online course content and open ADDA courses to an international audience at low or no cost. For the next year, ADDA, VT and Furman provided the instructional support for several online cohorts. The first in-person class taught by the Malawian instructors did not happen until June, 2021.

In its final state, the ADDA offers two in-person courses (CDDT 2 and the Remote Pilot License, or RPL), and four online courses which are all managed and delivered by Malawian instructors (Table 1). The expansion of online courses during COVID represented a value-added change with new development of specialized curricula, specifically Earth Observation Technologies in Agriculture (ETAg) and Data Visualisation and Cartography (DVAC). Francophone versions of the classes have been also developed in anticipation of expansion to Niger and other French language countries.

Table 1. ADDA Courses.

Course	Modality	Accreditation	Period
CDDT 1	Online	Accredited	5 wks
CDDT 2	In-person	Accredited	6 wks
ETAg	Online	Self-enrolment	Self-paced
RPAT	Online	Self-enrolment	Self-paced
DVAC	Online	Self-enrolment	Self-paced
RPL	In-person	Malawi-approved	2 wks

2.4.1. Trusted Operator Drone Training

The Association of Uncrewed Vehicle Systems International (AUVSI) maintains a protocol for an accredited curriculum called the Trusted Operator program (TOP) [14]. The CDDT 1 course includes Level 1 TOP certification and is delivered in a synchronous online format. Level 1 training applies to routine flight operations (no waivers), aircraft weighing less than 2 kg, and a low complexity safety management system (SMS). The course includes elements of good flight operation practice but also covers the theory of flight, propulsion systems, flight control, radio communications and drone payloads.

Flight rules and regulations are presented through the American TV show "Jeopardy" format, which is embedded in the learning management system (LMS) Moodle to keep the class interesting. Video modules

were created to supplement the PDF course documents.

The in-person CDDT 2 class includes the TOP Level 1 and 2 certificates. The Level 2 class is in-person and covers operations that may need a waiver and/or require a visual observer to enhance safety. A more detailed SMS is used for complex flight operation scenarios. Laboratory experiences and training designed for professional preparation include propeller performance testing, flight controller error recognition, camera and digital radio operation, radiotelephony and participation in a team design project.

Approximately 3 hours of flight training per student is conducted with a quadcopter where students use an online flight management system developed by Virginia Tech called ADDAtracking. This Google-based system provides online checklists, logbooks, and all the documentation necessary to meet the TOP course requirements including online manuals and certification records.

The flight training curriculum is structured using FAA airman certification standards (ACS) format that defines measurable knowledge, risk management and skills for assessment of a student's competencies. Seven training activities are defined leading to a practical flight assessment (PFA):

1. Risk analysis;
2. Aircraft preflight;
3. Takeoff, hover and land;
4. Attitude awareness in hover;
5. Single command maneuvers;
6. Dual command maneuvers;
7. Flying patterns.

The PFA is flown in an open area with simple ground markers as shown in Fig. 4. The "H" markers outline the home zone while the numbered markers represent targets during flight maneuvers:

1. Maintain positional control in home zone for 30 s, 4 m AGL ± 2 m;
2. Move to pt. 4 and climb to 15 m ± 2 m;
3. Descend to 5 m ± 2 m from pt. 4 to pt. 6;
4. Starting at 6, fly a rectangular path to 1, 3, 4 and 6 while maintaining flight heading;
5. Move from 6 to 2;
6. Fly a horizontal circle yawing to center of circle around pt. 5 with a radius of 5 m;
7. From pt. 2. Yaw 180º (nose facing pilot) then roll to pt. 1. Yaw 180º (nose to pt. 4);
8. Move to home zone and land.

In addition to the maneuvers that are flown, the instructor also simulates an emergency such as low battery voltage and requires the student to exhibit proper actions to safely maneuver the aircraft.

Students completing the Level 2 course are eligible to receive the Malawi Remotely Piloted Aircraft license and use it in commercial flight activities.

2.4.2. Geospatial Technologies Curriculum

Geospatial technologies including GIS, Remote Sensing, and Photogrammetry, form an essential pillar of the African Drone and Data Academy curriculum and operational philosophy. As emphasized by the UNCTAD Technology and Innovation Report [15], it is imperative for developing nations to build the domestic capacity to "use, adopt, and adapt" frontier technologies to avoid widening inequalities and effectively meet local development needs. Accordingly, ADDA's integration of these disciplines is strategic, enabling the transformation of raw spatial data into actionable intelligence that supports humanitarian objectives. This approach directly addresses the region's "readiness gap" by establishing a comprehensive ecosystem for the acquisition of both theoretical knowledge and transferable technical skills.

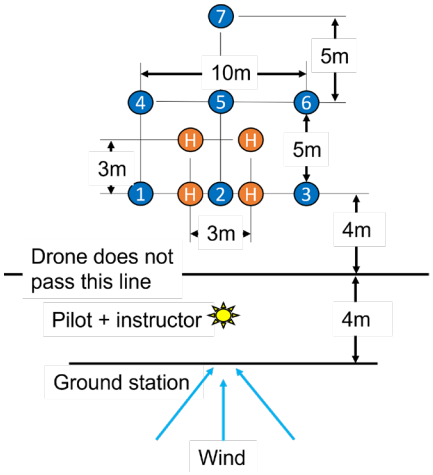

Fig. 4. Flight test area.

The data modules for CDDT Level 1 and Level 2 are structured to facilitate a balanced progression from theoretical conceptualization to practical application and experiential mastery. This pedagogical approach is supported by a robust suite of asynchronous resources. Video lectures provide systematic explications of core technologies, such as GIS principles, photogrammetry workflows, and remote sensing fundamentals, ensuring learners comprehend both the operational mechanics and the applied significance of these tools. These lectures are complemented by curated readings from authoritative sources, which engage students with conceptual frameworks, ethical considerations, and emerging trends in geospatial science. This dual modality of multimedia instruction and scholarly reading establishes a strong cognitive foundation, effectively preparing students for practical implementation.

3. Student Outcomes and Evaluation

The 2024 formative evaluation of the ADDA commissioned by UNICEF [13] is helpful in summarizing program outcomes. The UNICEF Innovation Unit has recognized innovation and digital

transformation as pivotal strategies that support vulnerable children and young people, and many of the Country program initiatives are addressed by ADDA.

Some of the main findings of the report include:

- The program has been successful in providing Malawian and African youth with the skills needed to innovate;
- ADDA has greatly enhanced the skills of postgraduate students and entrepreneurs in drone technology and geospatial data analysis. However, feedback suggests that adding modules on bid drafting, procurement processes, and entrepreneurship could further address existing gaps;
- ADDA enhanced MUST's institutional capacities, establishing it as a Centre of Excellence for drone technology. However, MUST faces internal and external challenges impacting its effectiveness and contribution to the ADDA program;
- The program improved DODMA (Dept. of Disaster Mgmt Affairs) by creating a rapid geospatial response unit that uses advanced drone technology and made disaster management more efficient and effective;
- Malawi's achievements in the drone sector position it as a global leader. The creation of a specialized drone testing corridor enabled innovation by allowing local and international entities to refine drone technologies, while ADDA enhances local capabilities, contributing to a self-sufficient workforce skilled in independent drone deployment, thus advancing Malawi's technological and industry growth.

In a survey of 79 ADDA graduates, 79 % felt that the ADDA performed well or extremely well in supporting national challenges of economic and social growth, and environmental health. Likewise, the vast majority of interviewees confirmed that the program positively impacts 21st century skills for the graduates.

One concern raised the by evaluators was the fact that the ADDA was created mainly to serve young adults and not children or youth. In response to this, a Junior Academy was created by MUST and it has been effective in offering programs to age 14 – 18 youth from diverse socio-economic backgrounds. The two-week academy introduces students to a wide range of STEM topics, giving them exposure to practical applications using drones.

3.1. Employment

A survey of 98 graduates of the ADDA Level 2 program (38 % of the total) conducted by UNICEF showed that 79 % were employed (Fig. 5), and 75 % of those employed were at an equal or higher salary than their peers because of ADDA training. Graduates reported 14 different sectors of employment, including precision agriculture (28 %), medical logistics (22 %), education (19 %), urban / rural / regional planning (16 %), environment / climate change, natural resources, mining, energy, civil engineering and transportation.

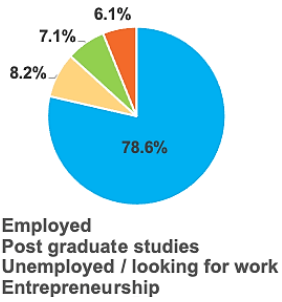

Fig. 5. Graduate employment.

3.2. Drones for Good

During the first in-person cohort (2020), ADDA and VT students conducted flood risk mapping at the Dzaleka Refugee camp to determine loss risk with camp expansion plans [16]. ADDA aircraft were used to image the 4.6 km^2 camp, and with soil maps and the 3D reconstruction of the terrain, the Soil and Water Assessment Tool (SWAT) provided building loss risk estimates. Dzaleka camp personnel were advised on the outcome of the analysis, and some of the students who participated eventually started a new drone imaging business.

The ADDA catalyzed the creation of the ADDA Centre of Excellence (ADDACoE) at MUST in 2023, providing a framework for technology training, entrepreneurship, and climate action and resilience activity. The Incubation Center under ADDACoE focuses on climate smart technologies and marginalized communities, with graduates participating in design projects and data collection campaigns. Recent graduates and instructors have deployed to collect imagery in the wake of major disasters, such as Cyclone Freddy, which supported the Malawi Emergency Operations Centre team in recovery decision-making.

4. The Future of the ADDA

ADDA exemplifies a successful model of South-South cooperation with significant potential for replication. The program's framework is currently being scaled to other nations, including Ethiopia and South Africa, fostering a pan-African ecosystem of experts capable of addressing continental challenges. This expansion illustrates how multi-stakeholder partnerships can effectively leapfrog traditional infrastructure gaps, positioning the Global South at the forefront of the Fourth Industrial Revolution while prioritizing sustainable, community-led development.

For those students looking to start a new business or find new employment, the challenges can be significant in a country such as Malawi. Access to

capital required to purchase computers and drones is difficult due to high inflation and a low foreign exchange reserve. Still, students find that ADDA credentials expand opportunity, including graduate school and lateral career moves not possible before training.

5. Conclusions

The ADDA continues to set a precedence for quality drone education in Africa, supporting a growing interest and need for drone services throughout the continent. Graduates have found success not only in the original use-case of medical supply delivery, but also in mining, agriculture and public safety. The model is replicable with the LMS Moodle, which has cost and enrolment benefits not available with other learning systems.

As with any course that requires hands-on skills, scaling remains a challenge. With a drone training student/teacher ratio of 1, the costs will always be high when earning the RPL. For beyond visual line-of-sight cargo operations where the aircraft is never manually flown, a student would be better served to learn flight risk management in all phases of flight with a good simulator. Perhaps there will be certification standards in the future to address this growing area of drone operations.

Acknowledgements

This work was funded by UNICEF. The information in this document expresses the personal views and opinions of the authors and does not necessarily represent UNICEF's position.

References

[1]. A. Stokenberga, M. Catalina Ochoa, Unlocking the Lower Skies: The Costs and Benefits of Deploying Drones Across Use Cases in East Africa, *World Bank Publications*, Washington, DC, 2021.

[2]. Zipline, Instant delivery for the planet, https://www.flyzipline.com/

[3]. C. Wright, S. Rupani, K. Nichols, Y. Chandani, M. Machagge, What should you deliver by unmanned aerial systems?, Technical Report, *JSI Research & Training Institute, Inc*., Arlington, 2018.

[4]. UNICEF, Malawi's unique drone corridor, https://www.unicef.org/innovation/drones/malawi-unique-drone-corridor

[5]. Z. Standridge, K. Kochersberger, Design, development, and range optimization of flying wing UAV, in *Proceedings of the AIAA/ASCE/AHS/ASC Structures, Structural Dynamics, and Materials Conference*, 2018, 0567.

[6]. Wingcopter, Malawi medical delivery project, https://wingcopter.com/project/malawi_medical_delivery

[7]. VillageReach, Transforming health care delivery to reach everyone, https://www.villagereach.org/

[8]. Jedsy, How Jedsy is helping the employment gap in Malawi, https://jedsy.com/blogs/news/how-jedsy-is-helping-the-employment-gap-in-malawi

[9]. Flying Labs, WeRobotics and Flying Labs, https://flyinglabs.org/

[10]. P. Solís, N. Huynh, D. Carpenter, M. Adames de Newbill, L. Ojeda, Using an authentic project-based learning framework to support integrated geography education linked to geospatial competencies, *Journal of Geography in Higher Education*, Vol. 41, Issue 4, 2017, pp. 532-547.

[11]. S. Han, R. Capraro, M. M. Capraro, How science, technology, engineering, and mathematics (STEM) project-based learning affects high, middle, and low achievers differently: The impact of student factors on achievement, *International Journal of Science and Mathematics Education*, Vol. 13, 2015, pp. 1089-1113.

[12]. P. C. Blumenfeld, E. Soloway, R. W. Marx, J. S. Krajcik, et al., Motivating project-based learning: Sustaining the doing, supporting the learning, *Educational Psychologist*, Vol. 26, Issue 3-4, 1991, pp. 369-398.

[13]. F. Fourestier, S. Guillot, A. Nyondo, A. Malunga, K. Valverde, Formative evaluation of the African Drone and Data Academy (ADDA) as a case study to enhance the youth and learning innovations portfolio in Malawi – 2019-2023, Technical Report, *Malawi Country Office UNICEF*, 2024.

[14]. AUVSI, Trusted Operator Program (TOP), https://www.auvsi.org/certification-training/trusted-operator-uas/

[15]. Technology and Innovation Report 2021: Catching Technological Waves – Innovation with Equity, in *Proceedings of the United Nations Conference on Trade and Development (UNCTAD'21)*, Geneva, 2021.

[16]. D. Whitehurst, B. Friedman, K. Kochersberger, V. Sridhar, J. Weeks, Drone-based community assessment, planning, and disaster risk management for sustainable development, *Remote Sensing*, Vol. 13, Issue 9, 2021, 1739.

(048)

UAV-Based Supervisory Coordination for Collision-Free Navigation of Automated Guided Vehicles in Confined spaces

N. Bahnes
Computer sciences department; University of Abdelhamid Ibn Badis Mostaganem, CSTL Laboratory,
Ex Ines de chimie zaghloul, Mostaganem, Algeria
Tel.: + 00213 45 36 64 72
E-mail: nacera.bahnes@univ-mosta.dz

Summary: The efficient management of Automated Guided Vehicles (AGVs) traffic in confined environments, such as warehouses, industrial facilities, and port terminals, poses a significant challenge due to space limitations, high traffic density, and stringent safety requirements. Ensuring collision-free and congestion-free is imperative in order to maintain productivity and reduce operational risks. The present paper puts forward an air–ground cooperative architecture in which Unmanned Aerial Vehicles (UAVs) act as intelligent supervisors for AGV traffic management. Through continuous aerial monitoring, UAVs maintain an up-to-date and global perspective of AGV movements within the environment, enabling the analysis of movement patterns and the prediction of potential conflicts or bottlenecks. The proposed system integrates decentralised local AGV coordination with centralised aerial supervision, combining the strengths of both approaches. This hybrid architecture has been demonstrated to enhance traffic fluidity, improve operational safety, and increase overall system efficiency, particularly in complex and dynamic industrial environments.

Keywords: UAV, AGV, Traffic management, Coordination, Collision free, Wireless communication.

1. Introduction

Automated Guided Vehicles (AGVs) are widely deployed in warehouses, ports, factories, and other confined environments for transport and logistics tasks [1]. While AGVs move in predefined routes in confined space [2], they offer autonomous navigation capabilities in restricted areas which introduce challenges including collisions, congestion, and deadlocks. Conventional centralized traffic management systems are constrained by communication bottlenecks and single points of failure. Conversely, purely decentralized AGV navigation can be unsuccessful in dense traffic or when local perception is inadequate.

The confluence of limited space, constricted pathways, and high vehicle density has been demonstrated to result in a marked escalation in the probability of conflict, particularly in scenarios where multiple automated vehicles are engaged in concurrent operations with dynamic task allocation. It has been shown that the combination of limited space, narrow paths, and high vehicle density leads to a marked escalation in the likelihood of conflict, particularly in scenarios involving multiple automated vehicles in simultaneous operations with dynamic task allocation [11].

Inspired by swarm robotics and air-ground cooperative systems [3, 9], we propose a solution based on unmanned aerial vehicles (UAV) as supervisors that oversee AGV operations from above. UAVs provide a global view of the workspace, detect potential conflicts, and issue real-time coordination instructions [10]. This architecture combines local autonomy of AGVs with aerial supervision, enabling adaptive, collision-free traffic management in confined spaces.

The rest of this paper is organized as follows: Section 2 presents related works, Section 3 and 4 describes conceptual solution and Traffic Management Strategy. After a discussion in Section 5, we conclude this paper.

2. Related Works

The centralized Automated Guided Vehicle (AGV) traffic management typically relies on a global map to optimize vehicle routing and scheduling. While such approaches are effective for small-scale deployments, they suffer from limited scalability and reduced robustness to communication constraints and dynamic environments [3]. As fleet sizes increase, centralized architectures become bottlenecks, both computationally and in terms of connectivity. To address these limitations, decentralized traffic management strategies have been proposed. These methods leverage local perception and inter-vehicle communication to enable self-organized coordination. Multi-robot coordination has been addressed using potential field approaches and consensus-based algorithms, which achieve coordination with reduced communication overhead [4]. However, purely decentralized approaches often struggle in environments with limited visibility or complex spatial layouts.

More recently, the use of Unmanned Aerial Vehicles (UAVs) has explored to support ground robot operations [12]. UAVs can provide a global perspective by generating real-time traffic maps,

identifying congested areas, and assisting in conflict detection and resolution among AGVs [5, 6]. Such air–ground hybrid systems enhance situational awareness, improve operational safety, and compensate for the limitations of onboard sensing in ground vehicles. In [7], a UAV performs object detection through semantic segmentation to extract information about ground obstacles and environmental features.

Despite these advances, several challenges remain unresolved. Coordinating multiple AGVs in dynamic and partially observable environments continues to be difficult, particularly under constrained communication conditions. Open research problems include the design of resilient communication protocols for confined industrial spaces, the establishment of formal safety guarantees in air–ground hybrid systems, the development of scalable and efficient conflict resolution mechanisms suitable for large fleets.

3. Conceptual Solution

Two kinds of issues occur when the AGV is supposed to be driven independently. The autonomous AGVs navigation challenge is the first issue, AGV collision is the second issue [8]. Prevently AGV collision is the main problem in confined space such as warehouses, manufacturing plants, and port terminals. Our work addresses this gap by proposing a UAV-based supervisory model for AGV traffic management.

Conventional ground-based coordination methodologies frequently depend on local sensing and predefined routes, which may prove inadequate in anticipating congestion or resolving conflicts in intricate and evolving environments [13]. It is imperative to acknowledge that even minor collisions or deadlocks have the potential to result in system downtime, diminished productivity, and the emergence of safety hazards. It is evident that effective collision prevention necessitates not only accurate real-time localisation but also predictive traffic management and global situational awareness. Addressing this problem is essential to ensure safe, reliable, and efficient AGV operations in confined and high-demand industrial settings.

3.1. Proposed Architectural

The proposed system is composed of three layers:

a) **Ground Layer (AGVs):** Each AGV navigates autonomously using onboard sensors (LiDAR, cameras) and performs basic obstacle avoidance. Local rules handle short-range collision avoidance and speed control.

b) **Aerial Layer (UAV):** UAV provides a global view of AGV positions and traffic patterns. It monitors trajectories, predicts conflicts, and issues high-level instructions for rerouting, pausing, or adjusting speeds. The UAV acts as edge coordinators, broadcasting traffic updates and priority commands.

c) **Communication Layer:** UAV and AGVs communicate through a low-latency wireless network (e.g., 5G or Ad-hoc mesh). Reliable and low-latency communication is essential to ensure timely coordination and safe system operation. This layer supports bidirectional exchange of state information, broadcast of traffic updates and priority commands and synchronization between local and global decision processes.

3.2. Conflict Detection and Resolution

A conflict is detected when the predicted distance between two or more AGVs falls below a predefined safety threshold or when traffic density exceeds a critical level in a given area. The problem of prevention collision or detection deadlock is one of the first problems that should be addressed in the free movement of an unmanned vehicles in confined space.

a) **Detection*:*** An UAV tracks AGV positions in real-time, estimating potential trajectory intersections within a prediction horizon;

b) **Resolution*:*** When a potential collision is detected, the UAV assigns temporary priorities (pause, reroute, priority) and broadcast instructions;

c) **Feedback*:*** AGVs acknowledge commands and adjust their paths accordingly, maintaining local autonomy while following global coordination.

3.3. Coordination Algorithm

To manage conflict situation inter-AGVs in confined space, the UAV ensures coordination between AGVs by executing the algorithm illustrated in Fig. 1. After predicting a future collision, the UAV send a priority command to organize a safe traffic. AGV receives instructions and update local trajectories and its current state (pause or move).

Algorithm. UAV coordination.
1. For each time step:
2. Collect AGV positions and velocities
3. Predict potential collisions in next t seconds
4. If collision predicted:
5. Determine conflict resolution
6. Send instructions to the concerned AGV

Fig. 1. UAV coordination algorithm.

This approach ensures distributed decision-making at the AGV level while providing global guidance from UAVs.

4. Traffic Management Strategy

The proposed traffic management strategy is based on a cooperative interaction between decentralized

AGV-level control and centralized UAV-based supervision. In this section, we explain the mains tasks of the proposed traffic management of AGV in a confined space.

4.1. Local AGV Behavior and Command Dissemination

At the ground level, local traffic management is governed by a set of reactive rules that include: short-range collision avoidance, local obstacle avoidance, dynamic speed regulation based on proximity and relative velocity of neighboring AGVs and compliance with high-level commands received from the UAV. Each AGV operates autonomously using onboard sensing and local decision-making. AGVs rely on sensors such as LiDAR and cameras to perceive their immediate surroundings and detect nearby obstacles, including other vehicles and static elements of the environment.

High-level commands generated by the UAV are disseminated to the relevant AGVs via the communication layer. Upon receiving a command, each AGV integrates it into its local planning and control framework while respecting its own safety constraints.

These local behaviors ensure fast response times and guarantee safety even in the presence of communication delays or temporary loss of aerial supervision. Importantly, AGVs retain full autonomy to execute emergency maneuvers when necessary.

4.2. Global Traffic Monitoring and State Estimation

The UAV continuously monitors the traffic area using onboard sensors and communication with AGVs. Each AGV periodically transmits its state information, including position, velocity and/or planned trajectory to the UAV. By aggregating this information, the UAV constructs a global traffic model that provides: a real-time map of AGV positions, predicted short-term trajectories, estimation of traffic density in different zones and identification of critical areas prone to congestion.

This global situational awareness enables the UAV to reason beyond local interactions, thereby enabling anticipation of impending traffic-related challenges.

4.3. Trajectory Prediction and Conflict Detection

Based on the estimated global state, the UAV performs trajectory prediction over a finite time horizon. Using traffic model and motion constraints of AGVs, future positions are extrapolated to identify potential conflicts such as imminent collisions, deadlocks at intersections and congestion caused by merging flows or narrow passages. This predictive capability allows the system to take preventive actions rather than reactive ones.

4.4. High-Level Decision Making and Coordination

The UAV does not issue low-level control commands; rather, it provides strategic guidance that preserves AGV autonomy while ensuring global coherence. The objective of decision-making policies is to minimise travel time, reduce stop-and-go behaviour, and maintain system-wide safety.

When a potential conflict or congestion is detected, the UAV generates high-level coordination decisions aimed at resolving the issue with minimal disruption to overall traffic flow. These decisions include: rerouting selected AGVs through alternative paths, temporarily pausing low-priority AGVs, adjusting speed profiles to smooth traffic flow and assigning dynamic priorities at intersections or bottlenecks.

4.5. Robustness and Adaptability

The hybrid nature of the proposed strategy enhances system robustness. Local AGV behaviours guarantee safe operation in the event of communication delays or UAV unavailability, while aerial supervision improves efficiency during normal operation. The system is inherently adaptable to dynamic changes such as varying traffic density, unexpected obstacles, or AGV failures.

This distributed execution mechanism ensures that global coordination goals are achieved without compromising local responsiveness. In the event of conflicting instructions or unforeseen obstacles, local safety rules always take precedence.

5. Discussion

The UAV-supervised model combines the strengths of centralized and decentralized coordination: AGVs retain local autonomy for flexibility and low-latency response, while UAV provide global situational awareness to prevent collisions. The advantages of the proposed traffic management based on UAV include scalability, resilience, and adaptability to dynamic environments. The limitations of the proposed solution are the dependency on reliable UAV sensing and communication, as well as the need for formal safety verification. The integration of AI-based prediction and reinforcement learning could further enhance adaptive coordination.

We can simulate the proposal system using ROS2, Gazebo, or omnet++ with veins, where:

- The AGVs modeled as ground robots with basic navigation model;

- The UAVs modeled as quadrotors with communication module providing a top-down view;
- The communication layer simulated using ROS2 topics or a mesh network plugin;
- The conflict detection and resolution implemented as a ROS2 node on the UAV agent.

Simulation allows us to test scalability, robustness, and the effectiveness of the UAV-based supervision before real-world deployment. Performance metrics are collision rate, average travel time, path efficiency, system robustness under communication delays or lost packets rate.

6. Conclusion and Future Work

This paper presents a UAV-based supervisory system for managing AGVs in confined space. The proposed architecture enables collision-free, efficient traffic flow by combining local autonomy with aerial supervision. The UAV acts as a proactive coordinator, mitigating conflicts and congestion at a system-wide level, while AGVs ensure real-time responsiveness through decentralized decision-making. The integration of predictive global supervision with reactive local control is a key process of the proposed traffic management strategy which aims at achieving a balanced approach towards safety, efficiency, and scalability.

Future work will investigate the use of multiple UAVs, learning-based traffic prediction methods, integration of the edge computing and 5G networks for low-latency control and large-scale real-world validation.

References

[1]. M. Ntotis, I. Vlachos, Automated guided vehicles (AGVs) in warehousing industry: A literature review, in *Proceedings of the International Conference on Industrial Engineering and Operations Management*, 2022, pp. 1553-1562.

[2]. A. Lombard, F. Perronnet, A. A. Turki, A. Moudni, Decentralized management of intersections of AGVs, *IFAC-PapersOnLine*, Vol. 49, Issue 12, 2016, pp. 497-502.

[3]. M. A. Rahman, M. M. Rashid, M. S. Hossain, E. Hassan, et al., Decentralized multi-agent coordination for autonomous vehicles in constrained environments, *Journal of Intelligent & Robotic Systems*, Vol. 105, Issue 2, 2022, 66.

[4]. M. Brambilla, E. Ferrante, M. Birattari, M. Dorigo, Swarm robotics: A review from the swarm engineering perspective, *Swarm Intelligence*, Vol. 7, Issue 1, 2013, pp. 1-41.

[5]. J. P. Queralta, J. Taipalmaa, B. C. Pullinen, V. K. Sarker, et al., Collaborative unmanned aerial and ground vehicles: Technologies, challenges, and opportunities, *IEEE Access*, Vol. 8, 2020, pp. 133045-133096.

[6]. Y. Zhang, Y. Wang, G. Li, S. Jin, et al., Air–ground cooperative traffic management for intelligent logistics, *Robotics and Autonomous Systems*, Vol. 141, 2021, 103736.

[7]. G. Niu, L. Wu, Y. Gao, M. O. Pun, Unmanned aerial vehicle (UAV)-assisted path planning for unmanned ground vehicles (UGVs) via disciplined convex-concave programming, *IEEE Transactions on Vehicular Technology*, Vol. 71, Issue 7, 2022, pp. 6996-7007.

[8]. A. K. Sivarathri, A. Shukla, Autonomous navigation of AGV by tracking the motion of UAV, in *Proceedings of the 20th IEEE/ASME International Conference on Mechatronic and Embedded Systems and Applications (MESA'24)*, 2024, pp. 1-8.

[9]. H. B. Choi, J. B. Kim, Y. H. Han, S. W. Oh, et al., MARL-based cooperative multi-AGV control in warehouse systems, *IEEE Access*, Vol. 10, 2022, pp. 100478-100488.

[10]. Y. Khosiawan, I. Nielsen, A system of UAV application in indoor environment, *Production & Manufacturing Research*, Vol. 4, Issue 1, 2016, pp. 2-22.

[11]. A. J. M. Muzahid, S. F. Kamarulzaman, M. A. Rahman, S. A. Murad, et al., Multiple vehicle cooperation and collision avoidance in automated vehicles: Survey and an AI-enabled conceptual framework, *Scientific Reports*, Vol. 13, Issue 1, 2023, 603.

[12]. J. Chen, X. Zhang, B. Xin, H. Fang, Coordination between unmanned aerial and ground vehicles: A taxonomy and optimization perspective, *IEEE Transactions on Cybernetics*, Vol. 46, Issue 4, 2016, pp. 959-972.

[13]. A. Eskandarian, C. Wu, C. Sun, Research advances and challenges of autonomous and connected ground vehicles, *IEEE Transactions on Intelligent Transportation Systems*, Vol. 22, Issue 2, 2021, pp. 683-711.

(050)

Secure Edge AI for Autonomous Decision-Making in Unmanned Aerial Systems

S. Silva
University of Maia, Department of Communication Sciences and Information Technologies,
4475-690 Maia, Portugal
E-mail: D012196@umaia.pt

Summary: This work presents a security-aware Edge AI framework designed to strengthen autonomous decision-making in Unmanned Aerial Systems (UAS). As UAVs increasingly rely on onboard artificial intelligence to interpret sensor data, select flight trajectories, and react to environmental conditions, they also become more vulnerable to cyber-physical threats such as data manipulation, GPS spoofing, and adversarial perturbations. To address these vulnerabilities, the proposed approach integrates lightweight deep learning models optimized for embedded processors with a multilayer cybersecurity architecture. The system includes integrity verification of sensor streams, adversarial robustness modules, and secure decision-validation routines that prevent unsafe actions even under attempted compromise. Real-time tests demonstrate that secure onboard inference maintains autonomy performance while significantly reducing susceptibility to spoofing and data-injection attacks. The results highlight the importance of combining Edge AI with built-in security mechanisms to enhance the resilience, safety, and reliability of next-generation unmanned systems operating in contested or communication-limited environments.

Keywords: Edge AI, Unmanned aerial systems, Cybersecurity, Autonomous decision-making, Embedded intelligence, Adversarial robustness, Safety and resilience.

1. Introduction

The autonomy of Unmanned Aerial Systems (UAS) has advanced rapidly with the integration of onboard Artificial Intelligence (AI), enabling complex tasks with limited human input [1].

However, reliance on digital sensors, communication links, and machine learning models also increases exposure to cyber-physical threats that can compromise safety and reliability [2-4].

GPS spoofing, data injection, and adversarial visual perturbations may lead to incorrect decisions or loss of control [5].

To address these risks, security mechanisms must be embedded directly into Edge AI processing to ensure resilient autonomous operation solutions capable of verifying data integrity, detecting anomalies, and validating decisions are critical in remote or contested environments with limited communication support [6].

This work proposes a secure Edge AI architecture that enhances UAS autonomy and resilience by combining lightweight embedded deep learning models with dedicated cybersecurity layers.

2. Methodology

The proposed approach integrates secure Edge AI capabilities into the autonomous decision-making pipeline of a UAS. The methodology is structured into three main components: (i) onboard perception and inference, (ii) security and integrity verification, and (iii) autonomous decision validation. All components are optimized to operate in real time on embedded hardware with limited computational resources.

2.1. Onboard Perception and Edge AI Inference

The onboard perception module performs obstacle detection and free-space assessment from monocular RGB imagery using a compressed CNN based on Nano YOLOv5 optimized for embedded deployment. The model processes 416×416 images and outputs obstacle bounding boxes with confidence scores. Training combines the VisDrone dataset with in-house outdoor flight data (70/15/15 split), using brightness variation, Gaussian noise, and motion blur for augmentation. Real-time performance on an NVIDIA Jetson Nano is achieved through post-training INT8 quantization, ~35 % structured channel pruning, and TensorRT optimization. The model achieves mAP@0.5 = 71.4 %, precision = 0.76, recall = 0.69, and an inference rate of 18–22 FPS, depending on scene complexity.

2.2. Cybersecurity and Data Integrity Layer

A dedicated integrity-monitoring layer evaluates the consistency of GNSS, IMU, and vision-based estimates using an Extended Kalman Filter (EKF).

Anomaly detection is based on innovation residuals $\mathrm{r}_k = \mathrm{z}_k - h(\hat{\mathrm{x}}_{k|k-1})$ and χ^2 gating $r_k^T S_k^{-1} r_k > \chi^2_{0.95}$, triggering integrity alerts upon threshold violation.

Monitored features include GNSS drift, velocity inconsistencies, IMU bias variation, and vision-inertial

disagreement, with detection latency measured from attack onset.

2.3. Secure Decision-Making and Validation Layer

AI generated navigation commands are validated by a safety filter based on rule enforcing flight envelope constraints, obstacle clearance, and integrity alerts. Commands associated with detected anomalies are rejected, triggering a reactive control module that executes safe fallback actions (hover, loiter, or return-to-home), thereby preventing unsafe maneuvers while preserving mission continuity. Fig. 1 summarizes the overall system architecture.

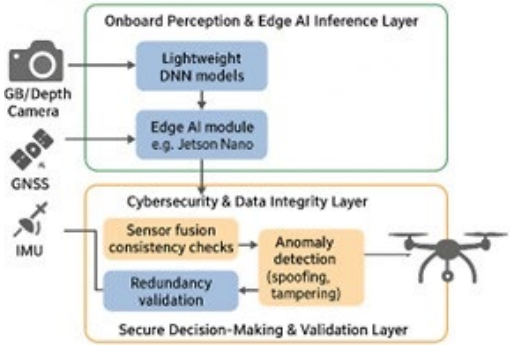

Fig. 1. Architecture of Secure Edge AI for UAS.

3. Experiences Setup and Preliminary Results

3.1. Experimental Platform

Experiments were conducted on a quadrotor UAS equipped with an NVIDIA Jetson Nano, a flight controller based on PX4, RGB camera, GNSS receiver, and IMU. Edge AI inference was executed using TensorRT, and integrity monitoring ran as a companion process on the same embedded platform.

3.2. Test Scenarios

Three adversarial scenarios were evaluated: GPS spoofing via gradual GNSS position drift injection, visual perturbations based on FGSM applied to camera frames, and sensor data injection through falsified IMU readings at the middleware level. Ground truth was obtained from unaltered sensor logs and reference flights assisted by the capture motion.

3.3. Preliminary Results

Each scenario was evaluated over 20 flight trials of approximately 5 minutes each. Table 1 summarizes detection performance with mean ± standard deviation.

An ablation study comparing no security, only the integrity, filter of safety, and the full system shows that the full configuration reduces unsafe commands by over 85 %, with false alarms below 6 %. Safety filtering activates within 200 ms and limits the mission-time degradation under benign conditions to under 3 %.

Table 1. Performance of Secure Edge AI Under Threat.

Threat	Detect. (%)	FPR (%)	Latency (ms)	FPS
GPS Spoofing	92±3	4.1	180	20
Visual Perturbation	88±4	5.3	210	18
Sensor Data Injection	90±2	4.7	165	22

4. Conclusions

This work demonstrates that integrating formal integrity monitoring and secure decision validation with Edge AI significantly enhances the resilience of autonomous UAS. By combining lightweight deep learning perception with anomaly detection based on sensor-fusion detection and safety filtering, the proposed framework mitigates GPS spoofing, sensor manipulation, and adversarial visual attacks while preserving real-time autonomy. The results highlight the importance of security-aware Edge AI for safe deployment of unmanned systems in contested environments or with limited communication.

References

[1]. A. Hakeem, M. Sabir, R. M. Alhebshi, A. G. Almakky, et al., Integrating artificial intelligence for improved security of IoT-drones through cyber-physical attack detection, *Frontiers in Computer Science*, Vol. 7, 2025, 1545282.

[2]. L. Alhoraibi, D. Alghazzawi, R. Alhebshi, Detection of GPS spoofing attacks in UAVs based on adversarial machine learning model, *Sensors*, Vol. 24, Issue 18, 2024, 6156.

[3]. A. Al-Sabbagh, A. El-Bokhary, S. El-Koussa, A. Jaber, et al., Enhancing UAV security against GPS spoofing attacks through a genetic algorithm-driven deep learning framework, *Information*, Vol. 16, Issue 2, 2025, 115.

[4]. T. Ma, X. Zhang, Z. Miao, Detection of UAV GPS spoofing attacks using a stacked ensemble method, *Drones*, Vol. 9, Issue 1, 2025, 2.

[5]. T. Hickling, N. Aouf, P. Spencer, Robust adversarial attacks detection based on explainable deep reinforcement learning for UAV guidance and planning, *IEEE Transactions on Intelligent Vehicles*, Vol. 8, Issue 10, 2023, pp. 4381-4394.

[6]. L. Al-Soufi, T. Demirsoy, E. Gelal Soyak, An implementation-based study of the detection of and recovery from GPS spoofing attacks for unmanned aerial vehicles, *International Journal of Advances in Engineering and Pure Sciences*, Vol. 36, Issue 3, 2024, pp. 211-223.

(052)

Comparative and Joint Optimization of Rotor Speed and Trajectory for Energy-Efficient Electric Unmanned Aerial Vehicle (UAV) Helicopters

E. Chijioke and M. Żugaj
Warsaw University of technology, PL. Politechniki 1, 00-661 Warsaw, Poland
Tel.: + 48 222347220
E-mail: emeka.chijioke.dokt@pw.edu.pl

Summary: This research investigates energy-efficient mission execution for electric unmanned helicopters, whose endurance is limited by battery capacity. A baseline simulation with constant rotor speed (Stage 1) quantifies energy consumption across hover, ascent, cruise, and descent. Stage 2 introduces variable rotor speed optimization, implemented via a MATLAB/Simulink control model that dynamically adjusts rotor speed according to flight mode. Stage 3 performs trajectory optimization at constant rotor speed to isolate the impact of trajectory shaping on energy usage. Finally, Stage 4 combines rotor speed scheduling and trajectory optimization to capture coupled effects. Using a MATLAB/Simulink and FLIGHTLAB simulation framework, power usage, battery depletion, and cumulative energy are quantified. Results indicate that cruise dominates total energy consumption due to duration, while hover is the most power-intensive phase. This staged methodology demonstrates that joint optimization can significantly reduce total mission energy and improve endurance.

Keywords: Rotor speed optimization, Trajectory optimization, Energy consumption, State of charge, Simulation based evaluation, Battery depletion.

1. Introduction

Unmanned aerial vehicles (UAVs), particularly electric powered helicopters, are increasingly used in planning, environmental monitoring, inspection, and emergency response due to their agility and ability to hover and takeoff vertically. However, their operational endurance remains constrained by the low energy density of onboard batteries relative to the high continuous power required for rotor propulsion. Extending flight time without increasing battery mass has therefore become a critical research objective.

The energy demand of an electric helicopter is strongly influenced by both its rotor speed and the trajectory it follows. Rotor speed controls the lift and thrust that keep the helicopter aloft and maintain stable flight. Prior research has shown that adjusting the rotor's revolutions per minute (RPM) across different mission phases can reduce overall power consumption by more effectively balancing aerodynamic lift and drag [1]. In particular, operating at a lower RPM during phases such as descent or downward pitching flight can yield substantial energy savings while still preserving adequate stability and controllability.

Similarly, optimizing the trajectory can contribute significantly to reducing energy consumption. Well planned trajectories minimize aerodynamic penalties such as wind drag, unnecessary altitude changes, and inefficient maneuvering especially during forward flights. Studies show that selecting routes that avoid regions of high aerodynamic resistance and strategically using tailwinds can lower the total energy required to complete a mission [2]. Such energy-efficient trajectories are often generated through advanced path planning techniques which include dynamic modeling and model predictive control that accounts for factors such as distance, altitude, and prevailing wind conditions [3, 4]. When combined with rotor speed management strategies, these methods provide a holistic framework for reducing overall energy consumption by improving both aerodynamic efficiency and propulsion demands.

Reference [5] focuses on energy consumption characterization of a small electric unmanned helicopter under prescribed flight conditions and fixed rotor speed values, with the primary goal of understanding how rotor RPM influences energy usage and control performance. In that work, the rotor speed is treated as a global parameter, and the analysis is conducted by sweeping discrete constant RPM values across individual flight phases and maneuvers and the study does not attempt to optimize rotor speed and trajectory parameters jointly. Instead, [5] provides an important baseline assessment of how energy consumption scales with RPM and maneuver type. In contrast, the present paper advances beyond baseline energy analysis by introducing a structured, multistage optimization framework that explicitly exploits phase dependent rotor speed scheduling and trajectory tailoring to minimize total mission energy consumption. Rather than treating rotor speed as a fixed or uniformly adjusted parameter, this work allows the main rotor RPM to vary independently across hover, ascent, cruise, and descent phases, enabling the identification of optimal RPM combinations that are not observable under constant RPM assumptions. Furthermore, once the optimal variable rotor speed schedule is identified, the trajectory itself is systematically optimized by adjusting specific phase airspeed commands while

preserving mission constraints such as total altitude change and phase durations.

The key novelty of this paper relative to [5] is the staged optimization framework that first treats rotor speed and flight trajectory as separate design variables before combining them in a unified assessment. The study first isolates rotor speed effects by holding the trajectory parameters constant, then isolates trajectory effects by holding rotor speed constant, and finally performs a joint rotor speed and trajectory optimization. This staged methodology enables clear attribution of energy savings and exposes coupled effects between rotor speed selection and flight conditions that are not captured when each parameter is varied independently, as in [5]. The results demonstrate that comparable or greater energy reductions can be achieved through coordinated rotor speed scheduling and modest trajectory reshaping than through RPM reduction alone. Additionally, this paper shift from component or maneuver level analysis to mission level energy optimization which constitutes a further distinction from [5].

Small variations in RPM can generate disproportionately substantial changes in power demand, especially in hover and ascent where induced power is highest. Likewise, the trajectory's geometry, which includes altitude, forward velocity, and vertical rate, significantly affects aerodynamic drag, rotor inflow, and mission duration. Despite this, most operational UAV helicopters rely on fixed RPM operation and standardized trajectory that do not consider energy optimization.

To address these limitations, current work develops a MATLAB based simulation and postprocessing framework to evaluate how rotor speed scheduling and trajectory shaping influence total mission energy over a complete hover, ascent, cruise and descent flight profile. The framework quantifies propulsion power demand, battery depletion, and cumulative energy consumption across multiple rotor speed schedules using a coupled flight dynamics and drive system power consumption model.

The objective is to identify control and path planning approaches that reduce energy use without compromising flight stability or mission performance.

The main contributions of this study are:

1. Establishing a baseline simulation to quantify energy consumption under constant rotor speed;
2. Implementing variable rotor speed optimization with mode dependent control;
3. Performing trajectory optimization to evaluate trajectory shaping on energy consumption;
4. Conducting joint rotor speed and trajectory optimization to evaluate coupled effects;
5. Demonstrating, through simulation, the energy savings and mission endurance improvements achievable through integrated optimization. In summary the optimization is performed as a constrained parametric search over phase scheduled setpoints.

2. Methodology

The simulation workflow integrates MATLAB/ Simulink for supervisory scheduling and command shaping used for the rotor speed and trajectory studies with FLIGHTLAB's nonlinear six degree of freedom (6DoF) rotorcraft model to capture high fidelity flight dynamics and aerodynamics. The time series outputs which are altitude, airspeed, vertical speed, rotor speed, power, and cumulative energy are interpolated to a common time base for multiple run comparison.

The proposed methodology combines a systematic experimental framework with a physics based helicopter simulation environment to assess how rotor speed scheduling and trajectory geometry influence total mission energy. This approach makes it possible to distinguish energy savings that arise from improved aerodynamics from those associated with power system operating behavior.

The study adopts a four stage procedure that progressively isolates and then couples the dominant contributors to electrical energy use in an electric UAV helicopter. Each stage builds on the previous one so that the effect of rotor speed scheduling and the effect of trajectory design can be examined independently before being optimized together.

Stage 1: Baseline with Constant Rotor Speed

The first stage establishes a reference mission in which the main rotor speed is held constant throughout hover, ascent, cruise, and descent. Mission parameters are selected to model an average, standard operational flight or mission, the hover segment is long enough to exercise power margins, the ascent and descent rates reflect operational practice, and the cruise airspeed is chosen within the vehicle's efficient envelope. This baseline simulation provides the quantitative yardstick for all subsequent comparisons, yielding time histories of shaft power, cumulative energy, and battery depletion against which optimized strategies are assessed.

Stage 2: Rotor Speed Optimization

In the second stage, rotor speed is scheduled by flight mode using a MATLAB/Simulink implementation that selects distinct RPM commands for hover, ascent, cruise, and descent. The airframe trajectory is held fixed to the baseline so that any change in energy can be attributed to propulsion control rather than path changes. The scheduler is optimized to reduce induced power in hover and ascent while preserving sufficient thrust authority, and to exploit lower power settings in cruise and descent where the aerodynamic requirements allow. The outcome of this stage is an energy-efficient RPM profile that improves electrical efficiency without altering the mission geometry.

Stage 3: Trajectory Optimization with Constant Rotor Speed

The third stage examines the influence of trajectory design while holding rotor speed constant at the baseline value. The optimization tunes key path parameters, the altitude history, the choice of cruise airspeed, and the nominal ascent rates to reshape the mission in ways that reduce energy use. By fixing rotor speed, this stage isolates the impact of trajectory design and mission timing on power peaks and total energy consumption, independent of propulsion scheduling.

Stage 4: Joint Optimization of Rotor Speed and Trajectory

The final stage couples propulsion and trajectory by optimizing the mode dependent rotor speed schedule and the trajectory simultaneously. This joint formulation captures interactions between vehicle motion and powerplant operation, for example, the ability to trade a slightly longer but less power intensive climb against a reduced RPM setpoint, thereby uncovering combinations that are unavailable when each variable is tuned in isolation. The result is a mission configuration that minimizes total energy use and extends endurance relative to both the baseline and the single variable optimizations. Intermediate optimization results are not shown due to space limitations. An overview of the methodology workflow is shown in Fig. 1.

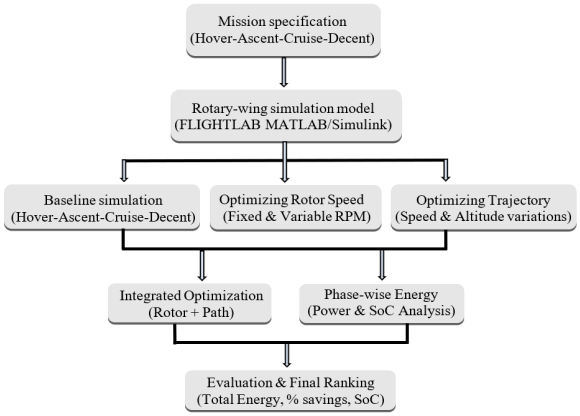

Fig. 1. Process flow chart.

2.1. Optimization Problem Formulation

In this paper, the term optimization refers to a constrained mission level parametric search performed using the nonlinear helicopter simulation model. The mission is divided into hover, ascent, cruise, and descent phases with fixed durations, and candidate control schedules are defined using phase dependent setpoints. Each candidate schedule is simulated, the corresponding cumulative electrical energy consumption is computed, and the schedule yielding the minimum feasible energy is selected.

For the variable rotor speed stage, the decision variables are the phase scheduled rotor speeds:

$$X_\Omega = [\Omega_{hover}, \Omega_{ascent}, \Omega_{cruise}, \Omega_{descent}]^T \quad (1)$$

For the flight path stage, rotor speed is held fixed at the optimal energy schedule obtained previously, and the decision variables include the phase scheduled true airspeeds (TAS) and the cruise altitude (h_{cruise}):

$$X_V = [V_{ascent}, V_{cruise}, V_{descent}, h_{cruise}]^T \quad (2)$$

For the combined stage, the rotor speed schedule and flight path parameters are optimized jointly:

$$X = \left[X_\Omega{}^T, X_V{}^T\right]^T \quad (3)$$

The objective in all stages is to minimize total mission energy consumption at the end of the fixed duration mission:

$$\min_x J(X) = E(t_{end}), \quad (4)$$

where $E(t_{end})$ is the cumulative electrical energy consumed at the mission completion time t_{end} for all comparisons, expressed in watt-hours (Wh). The total mission duration is fixed; therefore, the optimization reduces energy expenditure by modifying the selected decision variables X without altering the total flight time.

The mission is divided into four phases, hover, ascent, cruise, and descent which are defined by fixed phase durations, $t_{hover} = 40$ s, $t_{ascent} = 30$ s, and $t_{cruise} = 70$ s, after which the descent phase continues until $t = 200$ s. Rotor speed scheduling is parameterized using four constant setpoints, one per flight phase. The commanded rotor speed is limited to a maximum slew rate $| d\Omega/dt | \leq 10$ RPM/s to reflect actuator constraints and then passed through a first order filter $G(s) = 1/(s+1)$ to capture the lag due to rotor inertia and aerodynamic response. A similar rate limiting strategy is applied to the commanded airspeed and altitude trajectories, with bounds of $| dV/dt | \leq 12\ ft/s^2$ and $| dh/dt | \leq 5\ ft/s$ respectively, ensuring smooth, physically plausible transitions between phase setpoints. The performance metric used for comparison across candidates is the final cumulative energy consumption at mission completion. Battery depletion is defined directly as the time integral of battery power. Candidate solutions are accepted only if the mission is completed successfully while maintaining stable tracking of the prescribed altitude and airspeed profiles and avoiding nonphysical transients at phase transitions.

3. Simulation and Co-Simulation Framework

A MATLAB/Simulink and FLIGHTLAB simulation framework is used to model the UAV's dynamics and energy consumption. The environment

couples detailed rotorcraft dynamics with aerodynamic and induced power calculations and includes a battery model to track energy use. Within this setup, a mode dependent rotor speed controller was designed to adjust the commanded RPM in real time according to the current flight phase. The combined framework provides the quantities required for the analysis, namely the instantaneous power consumption, the cumulative energy drawn over the mission, and the resulting battery depletion throughout the mission profile.

4. Vehicle and Energy Model Description

This study considers an electric unmanned helicopter [5] modeled within a 6DoF flight dynamics framework coupled with a rotorcraft energy consumption model. The vehicle parameters are held constant across all simulation cases, with a fixed vehicle mass of 7.23 kg. The simulation captures the coupled translational and rotational motion of the fuselage, rotor aerodynamic response across flight regimes, and closed loop control system interactions. Rotor aerodynamic loads and main rotor power are evaluated using a lookup table based rotor model parameterized by rotor angular speed and shaft torque, enabling computationally efficient yet physically representative estimation of the main rotor power demand across the simulated flight envelope.

Steady sate trim conditions are computed at the beginning of each mission phase, providing consistent initial conditions for the hover, ascent, cruise, and descent segments. Throughout all simulations, rotor speed scheduling is constrained within predefined bounds derived from trim feasibility and actuator limits.

Phase durations are held fixed across all cases, providing a consistent mission structure and allowing direct comparison of energetic outcomes between constant rotor speed baseline simulation, variable rotor speed schedules, and optimized trajectory configurations.

The electrical energy consumption is evaluated from the power drawn by the propulsion drive system using an efficiency mapped representation adopted from the referenced drive system modeling approach [5]. Specifically, the main rotor operating point is defined by rotor speed and shaft torque, where the rotor speed is expressed in RPM and the torque is computed from the measured rotor power and angular speed. These variables are then used as inputs to a two dimensional (2D) lookup table implemented in Simulink as an n-D Lookup Table block. The lookup returns the corresponding electrical power demand $P_e(t)$, representing the electrical power drawn from the battery to support the rotor operating point after accounting for drivetrain and motor losses. The cumulative mission energy is obtained by integrating this electrical power over time and converting it to Wh:

$$E(t) = \frac{1}{3600}\int_0^t P_e(\tau)\, d\tau, \tag{5}$$

where $E(t)$ denotes the cumulative electrical energy consumption.

The state of charge (S oC) is reported as a normalized remaining energy metric based on the cumulative energy consumption:

$$SoC(t) = 100\left(1 - \frac{E(t)}{E_{cap}}\right), \tag{6}$$

$$E_{\text{cap}} = E_{\text{capbaseline}}(t_{end}), \tag{7}$$

where E_{cap} is the baseline derived reference capacity equal to the final cumulative energy consumption of the baseline case at t_{end}. Consequently, the reported S oC depends only on integrated energy draw and not on battery voltage, current dynamics, internal resistance variation, discharge rate effects, or temperature dependence. This normalization enforces full depletion at 0 % S oC for the baseline case and enables a consistent comparison of mission completion margins across all candidate schedules. Comparative analysis is performed using both cumulative energy and phase wise energy breakdowns to quantify how energy demand is distributed across hover, ascent, cruise, and descent.

Environmental conditions are held constant across all simulations to isolate the effects of rotor speed scheduling and flight path optimization. Standard atmospheric properties are assumed, with no wind or gust disturbances applied. This ensures that observed differences in energy consumption are attributable to the imposed rotor speed and trajectory variations rather than external environmental variation. The vehicle and energy model parameters used in simulation are summarized in Table 1.

Table 1. The vehicle and battery parameters.

Parameter	Value / Description
UAV mass	7.23 kg
Diameter of main rotor	1.78 m
Main rotor blade count	2
Tail rotor blade count	2
Diameter of tail rotor	0.158 m
Rotor response dynamics	First order transfer function, $G(s) = 1/(s+1)$ with rate limiter constraints
Flight dynamics	Nonlinear 6DOF rigid body model
Phase duration	$t_{hover} = 40$ s, $t_{ascent} = 30$ s, $t_{cruise} = 70$ s, $t_{end} = 200$ s
Trim methodology	Phase wise steady state trim
Baseline RPM	1000 RPM
Variable RPM range	850–1000 RPM
Battery capacity	The final cumulative baseline energy, E_{cap}
Energy integration	Time integration of electrical power
Atmospheric model	Standard atmosphere
Wind and turbulence	None

5. Results

To keep the results free of startup transients such as trim convergence, actuator rate limits, and first order rotor response, the analysis begins at $t_z = 30$ s. After this point the vehicle is in the steady sequence of hover, ascent, cruise, and descent, so only physically representative behavior is evaluated.

Table 2 specifies the reference mission for the helicopter, detailing the timeline alongside commanded airspeeds (V_z), altitude (H_z), target altitudes (h_z), the intended climb rate (CR), and descent objectives.

Table 2. Baseline Mission Profile Parameters.

P_z	t_z (s)	Δt_z (s)	V_z (ft/s)	H_z (ft)	h_z
Hover	0	40	0	34	hold
Ascent	40	30	60	80	hold
Cruise	70	70	60	80	CR, +2 ft/s
Descent	140	60	55	34	34 ft

Table 3 summarizes the final best candidates identified across the staged optimization workflow and compares them against the 1000 RPM baseline. The baseline uses a constant rotor speed with the nominal trajectory (60–60–55 ft/s, 80 ft). Rotor speed optimization reduces energy by scheduling RPM per phase while keeping the baseline trajectory unchanged (925–870–870–850). Trajectory optimization keeps the energy optimal RPM schedule fixed and improves the flight speed schedule to (50–45–40 ft/s, 80 ft). The joint optimization, adjusts both the RPM schedule and the trajectory, yielding a slightly different optimal RPM profile (935–880–870–850) with the same optimized trajectory. Altogether, the table provides a compact comparison of decision variables and final selected strategies for each stage.

Table 3. Summary of baseline and best optimization cases for rotor speed scheduling and trajectory strategy.

Case	RPM Schedule (Ω_h, Ω_a, Ω_c, Ω_d)	Trajectory (V_a, V_c, V_d, h_c)
Baseline	1000	60–60–55 ft/s, 80 ft
RPM Opt.	925-870-870-850	60–60–55 ft/s, 80 ft
Path Opt.	925-870-870-850	50–45–40 ft/s, 80 ft
Joint Opt.	935-880-870-850	50–45–40 ft/s, 80 ft

Fig. 2 presents the baseline flight profile, showing altitude, forward airspeed, and vertical speed over time with dashed lines marking phase changes at 40 s, 70 s, and 140 s. The altitude trace holds 34 ft in hover, climbs smoothly to 80 ft after the first transition, remains level through cruise, and then descends back toward the starting height 34 ft.

The airspeed history is near zero in hover, rises during ascent, and stabilizes at the 60 ft/s cruise setpoint. At the start of descent, it decreases to 55 ft/s, consistent with the mission specification. The vertical speed subplot complements these results, the rates are near zero in hover and cruise, positive at approximately 3 ft/s during ascent, and approximately −2 ft/s during descent, yielding smooth phase transitions.

Taken together, the three traces confirm that the reference mission was executed as intended, with the controller tracking altitude and speed commands accurately across hover, ascent, cruise, and descent. This baseline serves as a credible reference for subsequent energy optimization studies.

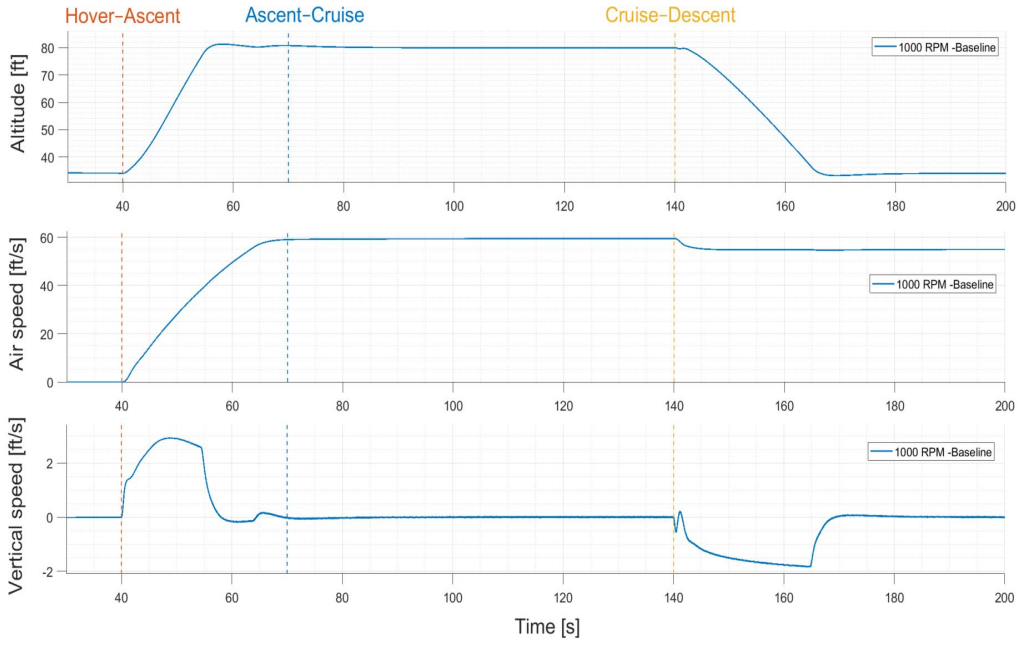

Fig. 2. Baseline mission flight profile and trajectory characteristics.

Fig. 3 presents the phase resolved electrical energy consumption for the baseline case operating at a constant main rotor speed of 1000 RPM over the complete hover–ascent–cruise–descent mission. The results show a clear partitioning of energy demand by flight segment, hover consumes approximately 9.0 Wh, ascent consumes 5.9 Wh, cruise consumes 11.7 Wh, and descent consumes 9.5 Wh, giving a total mission energy of 36.1 Wh. The cruise phase is the dominant contributor, accounting for the largest single portion of the mission energy because it is sustained over the longest interval while maintaining forward flight power requirements. Hover and descent exhibit comparable energy usage, reflecting the continuous power needed to support weight and manage vertical flight tasks, whereas ascent is lower in this breakdown because it occupies a shorter duration in the fixed mission timeline. Altogether, this baseline establishes a consistent reference for quantifying the benefits of variable rotor speed scheduling and trajectory shaping, since any reduction in total energy in subsequent cases can be directly attributed to changes in rotor operating point or commanded airspeed and altitude schedules under the same mission structure.

Fig. 4 compares the mission energy usage for the baseline and the best cases obtained from three successive improvement stages. The upper subplot shows the cumulative battery energy depletion (Wh), while the lower subplot shows the corresponding S oC computed from the same cumulative energy.

The baseline case exhibits the steepest increase in depletion throughout the mission, reaching full depletion by the end of the 200 s window, which confirms that the baseline configuration is energy limited under the assumed mission duration and reference schedule. In contrast, all three optimized cases reduce the depletion slope across the mission phases, leading to a substantially lower final energy use and therefore a higher remaining S oC at mission completion.

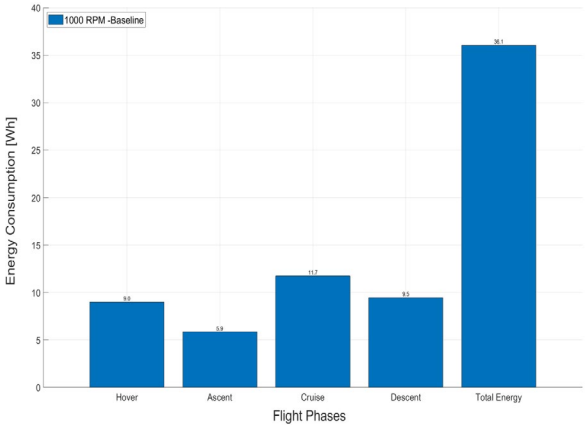

Fig. 3. Baseline mission energy consumption by flight phase for constant rotor speed operation at 1000 RPM.

Among the optimized runs, rotor speed optimization provides a clear improvement over the baseline by lowering the propulsion electrical demand, while trajectory optimization produces an even lower cumulative depletion trend. The joint optimization closely follows the lowest curve and results in the strongest overall energy reduction, indicating that coordinating rotor operating point selection with the flight speed schedule yields the most favorable outcome.

Fig. 5 compares the phase wise and total mission energy consumption of the baseline mission and the best performing solutions from each optimization stage. Across all flight phases, the baseline configuration exhibits the highest energy demand. Rotor speed optimization consistently lowers the energy consumption relative to the baseline, with clear reductions observed throughout the mission. Trajectory optimization achieves the largest overall improvement, indicating that trajectory shaping strongly influences mission energy. The joint optimization follows the same phase wise trends as the trajectory optimized case and remains closely aligned with it, reflecting that most of the energy benefit is captured through trajectory refinement, with only minor additional gains achievable when rotor speed scheduling is coupled with trajectory optimization.

Table 4 summarizes the total mission energy consumption for the baseline configuration and the best solutions obtained through rotor speed, trajectory, and joint optimizations. The baseline mission requires 36.1 Wh, while rotor speed optimization reduces the total energy to 28.18 Wh, yielding 21.85 % savings. Trajectory optimization further decreases the energy demand to 27.05 Wh, corresponding to 24.99 % savings. The joint optimization provides the lowest reported energy consumption at 27.04 Wh, achieving 25.01 % savings. Although the difference between the trajectory and joint optimization is small, the table confirms a consistent ranking in which coupling rotor speed scheduling with trajectory shaping delivers the best overall mission efficiency.

6. Conclusions

This study proposes a stepwise framework for optimizing the energy use of electric UAV helicopters. The process begins with a rigorously defined baseline against which improvements are measured. It then examines the two main optimization variables independently, first, the rotor speed scheduling and then trajectory design to quantify their separate contributions to energy demand. In the final stage, both variables were optimized together to seek the most efficient mission profile.

The results demonstrate that both optimization strategies yield substantial reductions in total mission energy relative to the baseline configuration. Rotor speed optimization alone achieves meaningful energy savings, primarily during hover and ascent phases, while trajectory optimization provides the largest overall reduction by improving energy efficiency across all mission segments. The joint optimization

achieves the lowest total energy consumption, but only a marginal improvement beyond trajectory optimization, indicating diminishing returns from additional rotor speed scheduling once the trajectory is near optimal. Overall, these findings emphasize the primary role of trajectory design in energy-efficient rotorcraft operations, while rotor speed variation serves as a secondary refinement for further, limited gains.

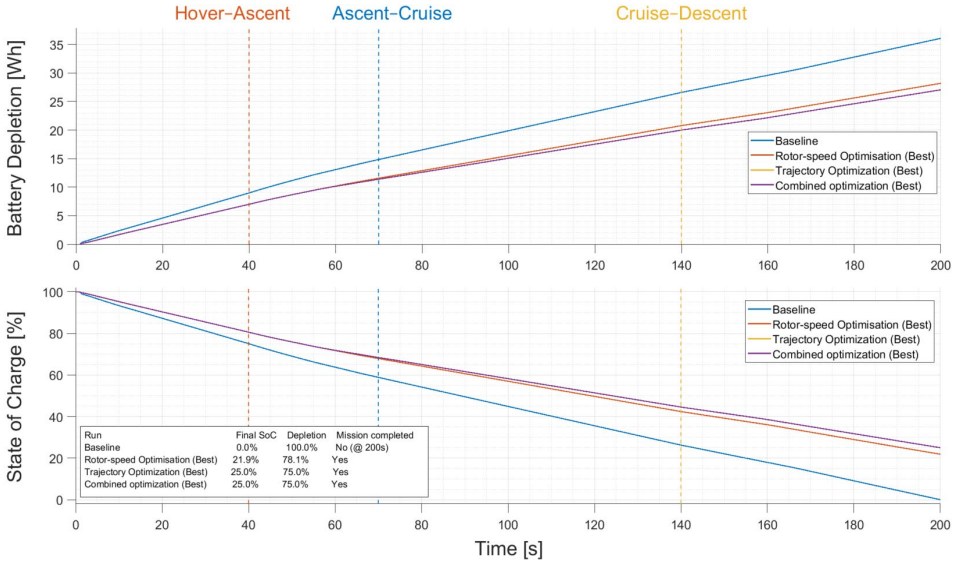

Fig. 4. Cumulative battery depletion and state of charge for the baseline mission and optimized cases.

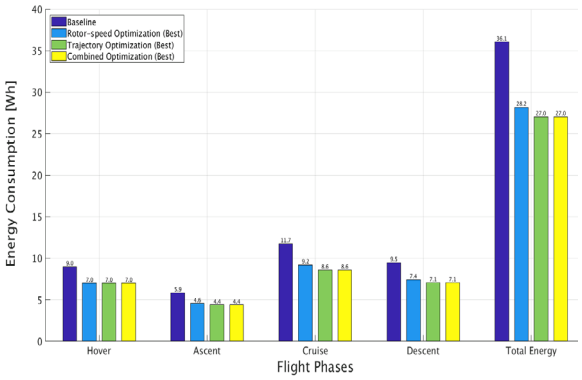

Fig. 5. Phase wise and total mission energy consumption for the baseline and best optimization cases.

Table 4. Total mission energy and savings for baseline and optimized cases.

Case	Total Energy (Wh)	Energy Saved (%)
Baseline	36.1	0.0
RPM Opt.	28.18	21.85
Path Opt.	27.05	24.99
Joint Opt.	27.04	25.01

Acknowledgements

The authors acknowledge the simulation infrastructure and computational resources used in this study.

References

[1]. W. Rex, T. Pflumm, M. Hajek, Enhanced efficiency and flight envelope by variable main rotor speed for different helicopter configurations, in *Proceedings of the 42nd European Rotorcraft Forum*, 2016, pp. 722-735.

[2]. H. Rienecker, V. Hildebrand, H. Pfifer, Energy optimal 3D flight path planning for unmanned aerial vehicle in urban environments, *CEAS Aeronautical Journal*, Vol. 14, 2023, pp. 621-636.

[3]. L. Deori, S. Garatti, M. Prandini, A model predictive control approach to aircraft motion control, in *Proceedings of the American Control Conference (ACC'15)*, 2015, pp. 2299-2304.

[4]. G. Su, X. Cheng, X. Liu, J. Jiang, Flight path optimization with optimal control method, *arXiv*, 2024, arXiv:2405.08306.

[5]. M. Żugaj, E. Mohammed, S. Głębocki, R. Żbikowski, An unmanned helicopter energy consumption analysis, *Energies*, Vol. 16, Issue 4, 2023, 1969.

(055)

A Lightweight Sensor-Fusion Framework for Low-Cost UAV-Based Air-Quality Mapping Including Calibration and Uncertainty Assessment

M. S. Saha, S. Baccar and M. Kadi
IRSEEM, ESIGELEC, University of Rouen Normandy, Rouen, France
E-mail: Moni-Sankar.Saha@esigelec.fr, Sahbi.Baccar@esigelec.fr, Moncef.Kadi@esigelec.fr

Summary: Unmanned Aerial Vehicles (UAVs) equipped with low-cost sensors are emerging as practical tools for environmental monitoring, offering rapid deployment and access to areas difficult to measure using ground instruments. This paper presents a lightweight multi-sensor UAV platform based on the ESP32 microcontroller. The system integrates four sensing modules: an MPU6050 IMU (Inertial Measurement Unit) for attitude estimation, a NEO-6M GPS receiver for geolocation, an MQ135 gas sensor for air-quality assessment, and an ESP32-CAM for visual documentation. A unified synchronization framework is implemented to merge heterogeneous sensor streams, while calibration routines address IMU bias, gas-sensor stabilization, and GPS noise. Measurement uncertainty is analyzed following GUM (The Guide of the Expression of Uncertainty in Measurement) principles. Experimental flight tests demonstrate stable operation, accurate trajectory–attitude reconstruction, and repeatable pollutant-level variations correlated with UAV motion. The platform provides a low-cost and portable solution for multi-modal environmental measurements.

Keywords: UAV instrumentation, ESP32, Sensor fusion, IMU calibration, Gas sensing, GPS tracking, Environmental monitoring.

1. Introduction

UAVs enable flexible and spatially distributed measurements in environments that are difficult or inefficient to assess with fixed ground instrumentation. Their ability to follow custom flight paths and capture georeferenced data makes them valuable for air-quality monitoring, environmental sensing, and autonomous inspection tasks [1].

Low-cost embedded systems now allow multiple sensors to be integrated into lightweight airborne platforms. However, accurate measurement extraction remains challenging due to IMU drift, gas-sensor warm-up effects, GPS fluctuations, vibration, and asynchronous sampling. These factors introduce uncertainty in reconstructed physical quantities and must be compensated for to ensure reliable measurements.

This work presents a compact ESP32-based multi-sensor payload for small multirotor UAVs. The platform incorporates four sensing modules, summarized in Fig. 1, enabling measurements of UAV attitude, position, environmental gases, and visual events.

A unified acquisition and synchronization framework merges data from sensors with different sampling rates, and calibration methods address bias, drift, and noise. Flight experiments verify stable operation and demonstrate the platform's suitability for low-cost environmental and measurement applications. The rest of this paper is organized as follows. Section 2 describes the hardware integration and individual sensor evaluations. Section 3 presents the overall UAV system architecture. Section 4 introduces the data synchronization and sensor-fusion framework.

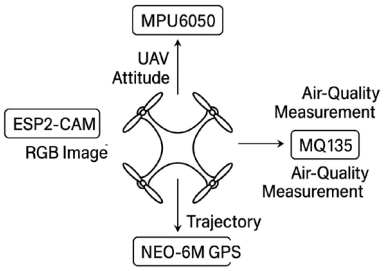

Fig. 1. Overview of the UAV Environmental Monitoring System with Onboard IMU, MQ135 Gas Sensor, NEO-6M GPS, and ESP32-CAM.

2. Standalone Sensor Tests and Calibration

Prior to multi-sensor fusion, each module was evaluated independently to verify functionality, quantify noise, and derive calibration parameters. This section details the test protocols, metrics, and governing equations for the IMU (MPU6050), gas sensor (MQ135), GPS (Neo-6M), and ESP32-CAM.

2.1. IMU-Based Stability Assessment

The MPU6050 IMU was tested independently on the ESP32 platform to assess short-term mechanical stability. Data were recorded for 50 s at 20 Hz, with the sensor placed on a flat surface and manually tilted

between 10–15 s. The measured tri-axial acceleration and angular-rate signals are shown in Fig. 2.

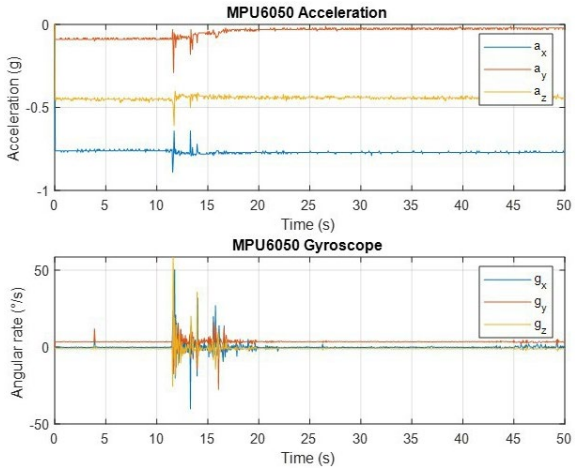

Fig. 2. Standalone MPU6050 response showing tri-axial acceleration (top) and angular rate (bottom). Static intervals demonstrate stability; peaks (10–15 s) correspond to manual perturbations.

2.1.1. Static Stability

During static intervals (0–10 s and 20–50 s), the accelerometer outputs remain nearly constant, with $a_z \approx -0.95g$ and $a_x, a_y \approx 0g$. The acceleration magnitude,

$$\| \mathbf{a} \| = \sqrt{a_x^2 + a_y^2 + a_z^2} \approx 1g, \quad (1)$$

deviates by less than $\pm 0.05g$, indicating good alignment with gravity and low noise.

2.1.2. Dynamic Response

Tilting the sensor (10–15 s) produces transient changes in a_x and a_y, while a_z decreases proportionally to the tilt angle. Simultaneously, the gyroscope records angular-rate peaks up to $\pm 50°/s$, confirming adequate sensitivity to short-duration maneuvers. The instantaneous angular-rate magnitude is

$$\| \boldsymbol{\omega} \| = \sqrt{g_x^2 + g_y^2 + g_z^2} \quad (2)$$

Static gyro bias and drift stability are quantified by

$$b_{\omega,i} = \frac{1}{N} \sum g_i(k), \sigma_{\omega,i} = \\ = \sqrt{\frac{1}{N-1} \sum (g_i - b_{\omega,i})^2}, \quad (3)$$

where N denotes the total number of IMU samples acquired during the static interval. The measured drift remains below $0.05°/s$.

2.1.3. Stability Summary

Table 1 summarizes the computed metrics. The accelerometer maintains a near-constant norm, while the gyroscope exhibits low drift and rapid recovery, confirming that the IMU provides sufficient stability for UAV-based sensor fusion and environmental measurements.

Table 1. Summary of MPU6050 Stability Metrics.

Parameter	Symbol	Value	Interpretation
Accel. magnitude	$\| \mathbf{a} \|$	$1.00 \pm 0.03g$	Correct gravity alignment
Accel. variance	σ_a^2	$< 0.002g^2$	High static stability
Gyro bias	$b_{\omega,i}$	$< 0.05°/s$	Negligible drift
Gyro std. dev.	$\sigma_{\omega,i}$	$0.8°/s$	Low-frequency noise
Gyro peak	$\| \boldsymbol{\omega} \|_{\max}$	$50°/s$	Dynamic sensitivity
Recovery time	t_r	< 3 s	Fast stabilization

Overall, the IMU exhibits stable bias, low noise, and reliable dynamic response, ensuring accurate orientation estimation when fused with GPS and gas-sensing data during UAV operation.

2.2. MQ135 Response and Calibration Analysis

Fig. 3 illustrates the temporal response of the MQ135 gas sensor interfaced with the ESP32. The output voltage V_{out} was recorded during transitions from clean air to gas exposure and back to baseline; gray points represent raw ADC samples, and the blue curve shows moving-average filtered data.

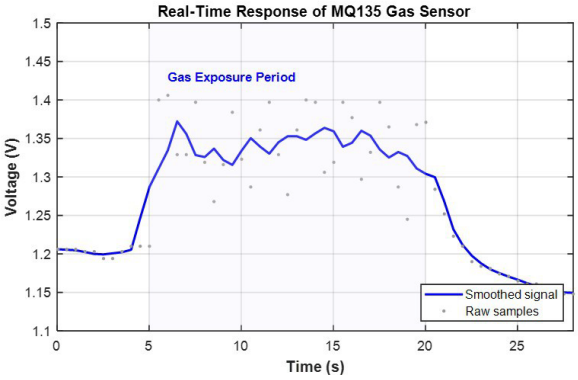

Fig. 3. Real-time MQ135 sensor response showing gas exposure and recovery. Smoothed curve overlaid on raw ADC samples.

The MQ135 operates as a variable resistor R_S in a voltage-divider configuration, with output voltage

$$V_{\text{out}} = V_{\text{CC}} \cdot \frac{R_L}{R_S + R_L}, \quad (4)$$

where $V_{CC} = 3.3$ V. Gas exposure (5–20 s) reduces R_S due to adsorption on the SnO_2 layer, increasing V_{out}, while desorption after removal causes voltage recovery.

The dynamic behavior is modeled as

$$V(t) = V_0 + \Delta V\left(1 - e^{-t/\tau_r}\right), \quad (5)$$

during the response phase, and

$$V(t) = V_s, e^{-t/\tau_d} + V_\infty, \quad (6)$$

during recovery, with time constants $\tau_r \approx 2.5$ s and $\tau_d \approx 6.0$ s.

The steady-state voltage increased from $V_0 \approx 1.20$ V to $V_s \approx 1.38$ V, yielding

$$\Delta V_{rel} = \frac{V_s - V_0}{V_0} \times 100, \quad (7)$$

which confirms the high sensitivity and suitability of the ESP32-MQ135 module for UAV-based environmental sensing.

2.3. Neo-6M GPS Receiver Evaluation

The Neo-6M GPS module was first evaluated under static open-sky conditions to assess short-term positioning accuracy and fix stability. Fig. 4 shows the latitude–longitude scatter recorded over a 10 min acquisition at 1 Hz. National Marine Electronics Association (NMEA) data were parsed in MATLAB to extract position, altitude, and Horizontal Dilution of Precision (HDOP) information.

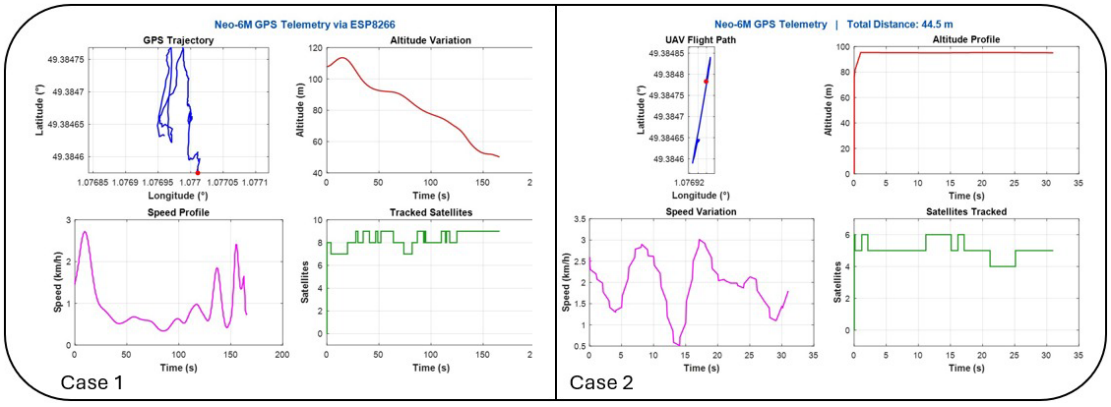

Fig. 4. Comparative GPS trajectories for Case 1 (200 s static/slow-motion) and Case 2 (30 s short displacement), showing horizontal position clusters, altitude variations, and reconstructed path length.

The great-circle distance between each GPS fix (φ, λ) where φ denotes the geodetic latitude and λ the geodetic longitude, expressed in degrees. and a reference position (φ_0, λ_0) was computed using the Haversine formula [2].

$$d = 2R\arcsin\sqrt{\sin^2\frac{\Delta\varphi}{2} + \cos\varphi_0\cos\varphi\sin^2\frac{\Delta\lambda}{2}}, \quad (8)$$

with $R = 6371$ km. Position precision was quantified using

$$\mathrm{CEP}_{50} = 0.59\sigma_x + 0.59\sigma_y, \mathrm{RMS}_{3D} = \\ = \sqrt{\sigma_x^2 + \sigma_y^2 + \sigma_h^2} \quad (9)$$

The module achieved $\mathrm{CEP}_{50} = 2.8$ m and $\mathrm{RMS}_{3D} < 5$ m, with altitude varying within ± 3 m, consistent with manufacturer specifications.

2.3.1. GPS Flight Data Comparison

Fig. 4 present two representative datasets acquired during low-altitude flights. These experiments were used to assess repeatability of the Neo-6M position and velocity estimates.

Case 1: 200 s Static/Slow-Motion Test. The horizontal trajectory forms a compact cluster with 5–8 m dispersion, mainly due to satellite geometry and receiver jitter. Altitude decreases gradually from 115 m to 70 m, reflecting the internal barometric correction model. Ground speed remains within 1–3 km/h, and satellite availability (7–9) ensures favorable Geometric Dilution of Precision (GDOP) (<1.5).

Case 2: 30 s Short Displacement Test. The UAV was manually displaced by approximately 40–50 m. The reconstructed distance (44.5 m), computed using the segment-wise Haversine expression agrees with the ground truth. Altitude remains stable (90–100 m), and the trajectory shows reduced noise due to the short acquisition time and improved satellite lock.

Comparison. Case 2 exhibits higher localization confidence, with smaller trajectory dispersion and speed standard deviation ($\sigma_v < 0.5$ km/h), whereas Case 1 shows larger drift due to prolonged integration time. These results confirm that the ESP32–Neo-6M subsystem provides sufficiently accurate short-range

localization for UAV-based geo-tagging and air-quality mapping.

2.4. Fire Detection Module Based on ESP32-CAM and MATLAB Processing

The ESP32-CAM provides continuous RGB video frames that are processed in MATLAB to detect fire in real time. A hybrid fire-detection model is implemented, combining color constraints, chromaticity normalization, and a probabilistic Gaussian classifier. This ensures robustness against motion blur, illumination variations, and sensor noise.

2.4.1. Color Normalization and Chromaticity Features

For each frame, the RGB pixel vector $I(x,y) = [R,G,B]$ is converted to normalized chromaticity coordinates

$$r = \frac{R}{R+G+B}, g = \frac{G}{R+G+B}, b = \frac{B}{R+G+B}, \quad (10)$$

where fire-colored regions typically satisfy

$$r > g > b \quad (11)$$

Two pixels with the same color but different brightness may have very different raw RGB values. To remove this effect, we normalize the RGB vector:

$$\mathbf{c} = \frac{1}{\sqrt{R^2+G^2+B^2}}\begin{bmatrix}R\\G\\B\end{bmatrix} \quad (12)$$

2.4.2. Hybrid Fire Classification

A pixel is first evaluated by deterministic color rules:

$$R > T_R, G > T_G, B < T_B, R > G > B \quad (13)$$

To detect fire regions, an initial binary mask $M_1(x,y)$ is generated using empirical RGB thresholds $T_R = 0.6$, $T_G = 0.2$, and $T_B = 0.3$. To improve robustness against illumination changes, the normalized chromaticity vector $\mathbf{v} = [r,g,b]^T$ is evaluated using a Gaussian fire-likelihood model [3]:

$$P_{\text{fire}}(\mathbf{v}) = \exp\left[-\frac{1}{2}(\mathbf{v}-\mu)^T\Sigma^{-1}(\mathbf{v}-\mu)\right] \quad (14)$$

The Gaussian parameters were estimated from 12 manually annotated fire images comprising approximately 18000 fire pixels captured under varying illumination conditions. The sample mean and covariance were computed using maximum likelihood estimation. With mean and covariance

$$\mu = \begin{bmatrix}0.60\\0.32\\0.08\end{bmatrix}, \Sigma = \begin{bmatrix}0.015 & 0.002 & 0.001\\0.002 & 0.010 & 0.001\\0.001 & 0.001 & 0.005\end{bmatrix}$$

Pixels satisfying $P_{\text{fire}} > 0.35$ form the probabilistic mask $M_2(x,y)$. The final segmentation is obtained by combining both models:

$$M(x,y) = M_1(x,y)\, M_2(x,y) \quad (15)$$

The detected fire area is computed as

$$N_{\text{fire}} = \sum_{x,y} M(x,y), \quad (16)$$

and a fire alarm is raised when $N_{\text{fire}} \geq 4000$ for QVGA resolution.

To suppress transient false alarms, a temporal exponential filter is applied:

$$S(k) = \alpha N_{\text{fire}}(k) + (1-\alpha)S(k-1), \quad \alpha = 0.25, \quad (17)$$

and the normalized fire-confidence score is defined as

$$C_{\text{fire}} = \frac{S(k)}{76800}, \quad (18)$$

where $76800 = 320 \times 240$ is the total number of pixels in a QVGA frame.

2.4.3. Experimental Summary

In the sequence shown in Fig. 5, the system detected $N_{\text{fire}} = 4228$ fire pixels with a confidence level of $C_{\text{fire}} = 0.055$, exceeding the alarm threshold. The results confirm that the ESP32-CAM, combined with the hybrid detection algorithm, reliably identifies fire events despite motion, vibration, and low-cost camera limitations.

Fig. 5. Fire-region segmentation mask from the proposed hybrid model.

2.5. Summary and Pass/Fail Criteria

Each sensor is in terms of GUM if: (i) the IMU maintains $\| \mathbf{a} \| \approx 1g$ and low gyro bias, (ii) the MQ135 produces consistent R_S/R_0 variation, (iii) the GPS maintains consumer-grade precision (CEP $_{50}$ and

Haversine error within limits), and (iv) the ESP32-CAM maintains stable timing and adequate image sharpness S. These metrics ensure reliable fusion in Section 5.

3. System Design and Architecture

The proposed UAV-based measurement platform integrates an ESP32 microcontroller with multiple sensing modules for geo-referenced environmental monitoring. The system comprises three main units: (i) the UAV carrier, (ii) the ESP32-based multi-sensor payload incorporating the Neo-6M GPS, MPU6050 IMU, MQ135 gas sensor, and ESP32-CAM, and (iii) the ground station for data logging and supervisory control. The hardware prototype is shown in Fig. 6.

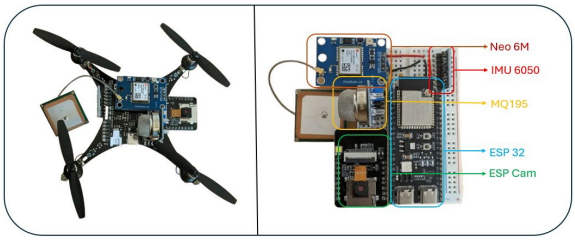

Fig. 6. Prototype of the ESP32-based multi-sensor UAV module integrating GPS, IMU, gas sensor, and camera.

3.1. UAV Platform

A commercial quadrotor platform is used as the aerial carrier due to its mechanical stability and sufficient payload capacity. The onboard flight controller provides real-time telemetry (attitude, altitude, and velocity) via MAVLink, supporting later geo-referencing and motion compensation. The UAV is powered by a Li-Po battery with a regulated power distribution module, while vibration-damping mounts reduce mechanical disturbances transmitted to the sensor payload.

3.2. Correlation of Gas Sensor Output with Altitude

The MQ135 response was analyzed as a function of UAV altitude. As shown in Fig. 7, the sensor voltage (sampled at 10 Hz) increases between 10-12 m, consistent with the imposed altitude-dependent gas and temperature gradients. The observed dispersion (в‰€ В±50 mV) is mainly due to ADC noise and short-term sensor fluctuations, remaining acceptable for low-cost sensing.

These results confirm that the ESP32-based acquisition chain provides stable and monotonic measurements correlated with flight telemetry, enabling altitude-aware air-quality profiling.

3.3. Geo-Referenced Air-Quality Mapping

Geo-referenced MQ135 measurements were obtained by fusing the sensor output with latitude–longitude data from the NEO-6M GPS. Fig. 8 presents the resulting 2D heatmap, where each 10 Hz sample is color-coded according to its MQ135 voltage level, representing relative gas concentration along the UAV path [5].

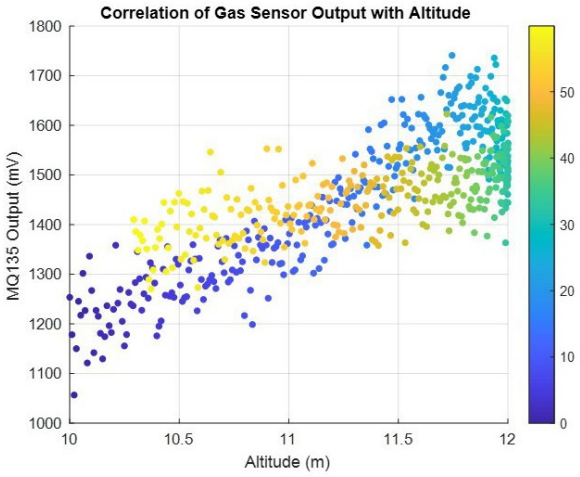

Fig. 7. Correlation between MQ135 output and altitude during flight.

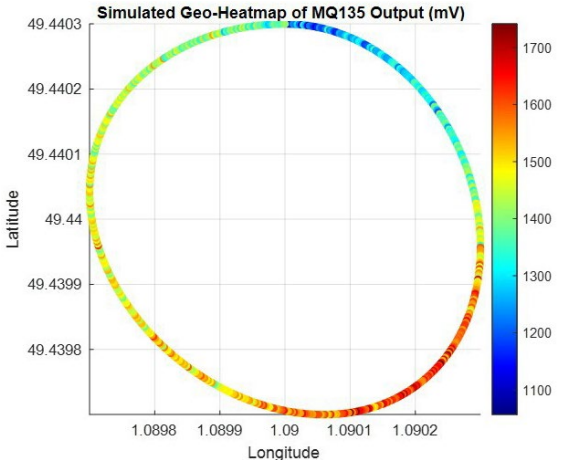

Fig. 8. Geo-referenced MQ135 measurements during circular UAV flight.

The measured flight traces a circular trajectory of approximately 60 m diameter around (49.440 ° N, 1.090 ° E). Distinct spatial variations appear along the loop, with higher voltage values (yellow/red) indicating localized concentration peaks or turbulence-induced effects, and lower values (blue) corresponding to cleaner regions. This demonstrates the platformвЂ™s ability to resolve meter-scale air-quality gradients.

The coherent spatial pattern further confirms correct synchronization between the ESP32 sensor

stream and the GPS telemetry, validating the suitability of low-cost UAV systems for geo-referenced environmental monitoring.

3.4. System Stability and IMU Analysis

Figs. 9 and 10 show the time-domain response of the MPU6050 IMU during a 60 s measured flight, sampled at 10 Hz and covering both steady and maneuvering intervals.

1) **Gyroscope Response:** The RSS angular velocity in Fig. 9 remains around 2.2 °/s, with peaks below 4 °/s, reflecting minor attitude corrections during circular flight. The absence of large transients indicates good rotational stability and limited vibration coupling to the sensing modules.

2) **Accelerometer Response:** Fig. 10 shows the acceleration magnitude close to 1 g, with deviations of about ± 0.05 g due to vertical motion and vibration, confirming proper IMU calibration and stable translation.

Overall, the IMU data confirm stable flight conditions suitable for reliable environmental measurements.

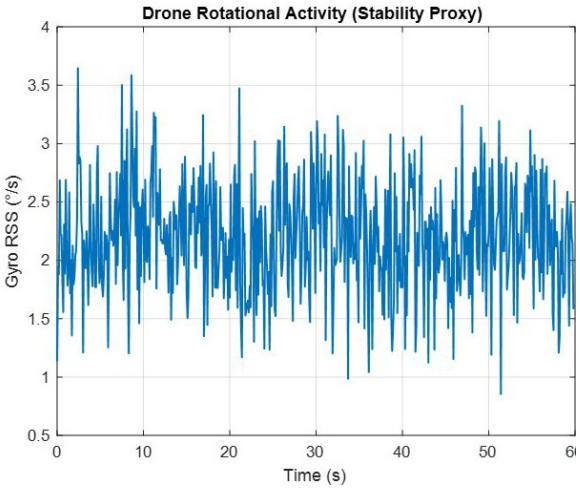

Fig. 9. MPU6050 gyroscope RSS showing 1-4°/s bounded variations and stable attitude behavior.

4. Sensor Fusion and Data Synchronization

The fusion framework [6]in this section builds upon the independent sensor evaluations already performed in Section 3, where the MPU6050, MQ135, NEO-6M, and ESP32-CAM were each tested separately. These preliminary tests provided baseline calibration parameters, noise characteristics, and timing behavior for every module. As a result, the fusion and synchronization pipeline introduced here relies directly on the validated sensor outputs from Section 2, integrating them into a unified spatiotemporal representation suitable for UAV-based environmental measurement.

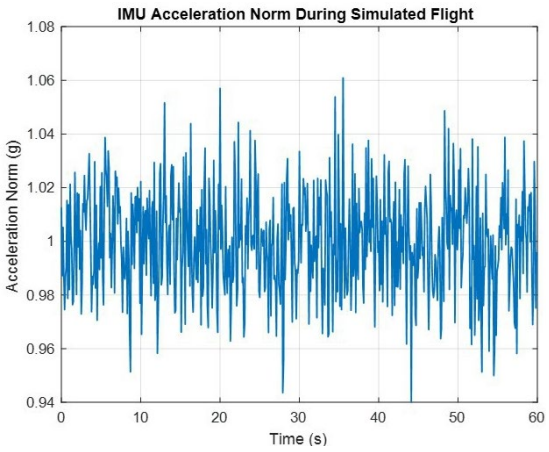

Fig. 10. MPU6050 acceleration norm staying near 1 g, indicating stable platform behavior.

4.1. Overview of the Fusion Algorithm

Fig. 11 presents the proposed sensor-fusion and synchronization pipeline. The process begins with the independent acquisition of raw data streams from the MPU6050, MQ135, and Neo-6M. Each dataset is time-stamped using a common reference derived from either the GPS UTC clock or the ESP32 internal millisecond counter. Since the sampling rates differ ($f_{\mathrm{IMU}} \approx 50$ Hz, $f_{\mathrm{gas}} \approx 10$ Hz, $f_{\mathrm{GPS}} \approx 1$ Hz), all signals are resampled to the IMU time base by means of linear interpolation, ensuring a unified temporal frame.

The synchronized signals are then processed by a complementary filter that merges the high-frequency angular-rate data from the gyroscope with the low-frequency orientation estimate obtained from the accelerometer. The filtered orientation is used together with GPS-derived altitude and position data to geo-reference the gas-sensor measurements. The resulting fused dataset thus contains time-aligned information about roll, pitch, position, altitude, and gas concentration, allowing spatial mapping and correlation analysis.

4.2. Mathematical Model

At each discrete sampling instant t_k, the fused roll ($\hat{\theta}_k$) and pitch ($\hat{\phi}_k$) angles are computed using a complementary filter that blends the short-term stability of the gyroscope with the long-term reference of the accelerometer:

$$\hat{\theta}_k = \alpha\left(\hat{\theta}_{k-1} + \omega_x \Delta t\right) + (1-\alpha)\tan^{-1}\left(\frac{a_y}{a_z}\right),$$
$$\hat{\phi}_k = \alpha\left(\hat{\phi}_{k-1} + \omega_y \Delta t\right) + (1-\alpha)\tan^{-1}\left(\frac{-a_x}{\sqrt{a_y^2 + a_z^2}}\right), \quad (19)$$

where ω_x, ω_y denote the gyroscope angular rates, a_x, a_y, a_z the accelerometer readings, and α a tunable filter coefficient ($0.95 \leq \alpha \leq 0.99$).

To smooth the altitude estimation, a simple GPS-IMU blending is performed:

$$\hat{h}_k = \beta\, h_{\mathrm{GPS},k} + (1-\beta)\, h_{\mathrm{IMU},k-1}, \qquad (20)$$

where $h_{\mathrm{GPS},k}$ is the altitude provided by the GPS and $h_{\mathrm{IMU},k}$ is the incremental altitude variation derived from the IMU vertical acceleration. Finally, the gas concentration is mapped to the fused spatial and attitude information as:

$$C_{\mathrm{gas},k} = f\left(V_{\mathrm{MQ135},k}, \hat{h}_k, \hat{\theta}_k, \hat{\phi}_k\right), \qquad (21)$$

where $V_{\mathrm{MQ135},k}$ is the measured voltage of the gas sensor and $f(\cdot)$ represents the empirical calibration function relating sensor voltage to concentration.

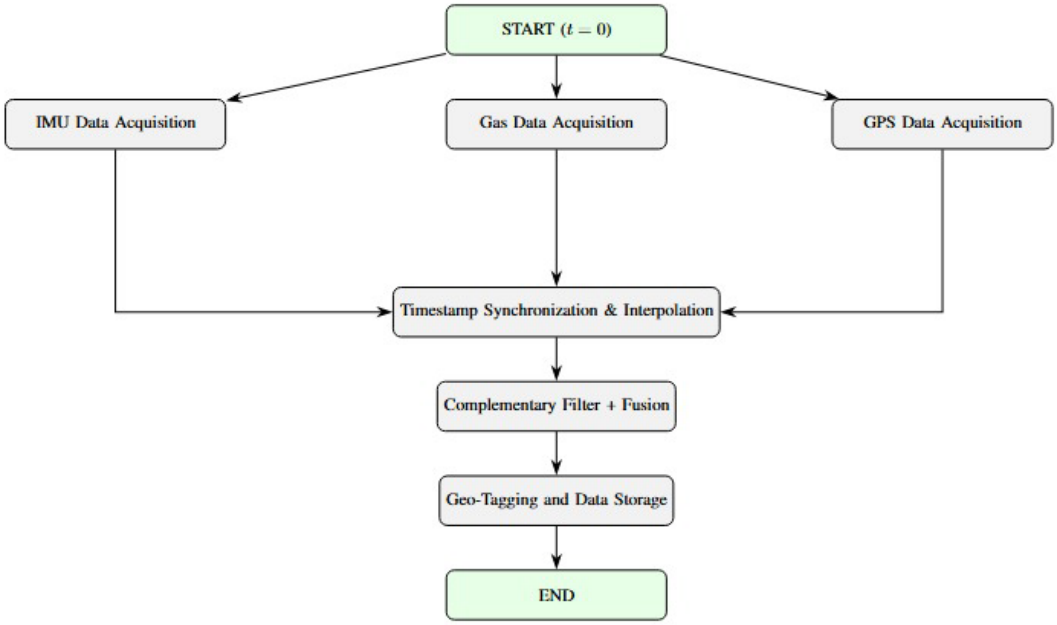

Fig. 11. Full-width representation of the proposed sensor-fusion and data-synchronization workflow.

4.3. Implementation and Validation

The proposed fusion algorithm was first implemented and validated in MATLAB, using measured data streams corresponding to asynchronous IMU, GPS, and gas-sensor signals. Linear interpolation was employed to resample the GPS and gas measurements to the IMU time base, while the complementary filter was executed in real time using a sampling interval of 20 ms. The correlation coefficient between the fused altitude and the gas-sensor voltage reached values above 0.85, confirming the consistency of the synchronization and the effectiveness of the proposed algorithm in capturing dynamic environmental variations during measured flight conditions.

5. Conclusion

This paper presented a lightweight and low-cost UAV-based multi-sensor platform for geo-referenced air-quality monitoring using an ESP32 microcontroller. The system integrates an IMU (MPU6050), gas sensor (MQ135), GPS receiver (Neo-6M), and an ESP32-CAM, enabling synchronized acquisition of motion, position, environmental, and visual data. Each sensing module was independently evaluated and calibrated, with measurement uncertainty assessed according to GUM principles to ensure data reliability.

A unified sensor-fusion and synchronization framework was developed to align heterogeneous data streams with different sampling rates into a common temporal reference. Experimental and measured flight results demonstrated stable UAV dynamics, accurate trajectory reconstruction, and consistent correlations between gas-sensor output, altitude, and spatial position. Geo-referenced air-quality maps confirmed the system's capability to resolve localized environmental variations despite the use of low-cost sensors.

These results validate the feasibility of compact UAV-based measurement platforms for environmental monitoring. Future work will focus on multi-gas sensing, advanced fusion techniques, and extended real-world flight campaigns.

Acknowledgment

We thank the U-SPACE project for funding this research, supported by a collaboration between the Normandy Region and IRSEEM/ESIGELEC.

References

[1]. M. Y. Alzahrani, Enhancing drone security through multi-sensor anomaly detection and machine learning, *SN Computer Science*, Vol. 5, Issue 5, 2024, 651.

[2]. A. Andreou, C. X. Mavromoustakis, J. M. Batalla, E. K. Markakis, et al., UAV trajectory optimisation in smart cities using modified A* algorithm combined with haversine and vincenty formulas, *IEEE Transactions on Vehicular Technology*, Vol. 72, Issue 8, 2023, pp. 9757-9769.

[3]. X. Chen, B. Hopkins, H. Wang, L. O'Neill, et al., Wildland fire detection and monitoring using a drone-collected RGB/IR image dataset, *IEEE Access*, Vol. 10, 2022, pp. 121301-121317.

[4]. M. J. Fadhil, S. K. Gharghan, T. R. Saeed, LoRa sensor node mounted on drone for monitoring industrial area gas pollution, *Engineering and Technology Journal*, Vol. 42, Issue 2, 2024, pp. 248-260.

[5]. G. Tassielli, R. Beltramo, S. Duglio, L. Cananà, et al., Integration of drones in environmental management systems: determining an appropriate sensors configuration based on the specific application under analysis, in Resilienza e Sostenibilità nel Cambiamento Globale, *Università del Salento*, Lecce, 2025, pp. 96-105.

[6]. H. Lee, S. Han, J. I. Byeon, S. Han, et al., CNN-based UAV detection and classification using sensor fusion, *IEEE Access*, Vol. 11, 2023, pp. 68791-68808.

2nd International Conference on Drones and Unmanned Systems (DAUS' 2026)
25-27 February 2026, Salzburg, Austria

ReFair: A Framework for Retention Depolarization in Recommender Systems

Junaid Ahmed Iqbal
E-mail: admitsiqbal@gmail.com

Summary: Retention disparities among user groups in recommender systems exacerbate polarization, undermining long-term user engagement and diversity. Addressing this challenge, we propose ReFair, a novel computational framework designed to enhance recommendation algorithms while enforcing retention fairness across the user population. ReFair employs a model-based reinforcement learning approach, iteratively alternating between environment learning for user retention dynamics and fairness-constrained policy optimization. Our method incorporates uncertainties in dynamic estimations to ensure robust performance. Empirical evaluations on real-world datasets demonstrate ReFair's ability to improve long-term user satisfaction and reduce retention polarization effectively. This work introduces new possibilities for fairness in recommender systems, advancing both theoretical and practical objectives.

Keywords: Retention Fairness, Recommender Systems, Model-Based Reinforcement Learning, User Engagement Dynamics, Algorithmic Bias Mitigation, Fair AI, Retention Depolarization

1. Introduction

To effectively respond to shifting consumer interests, evolving content trends, and fluctuating market dynamics, contemporary large-scale recommender systems frequently revise their algorithms by integrating continuously gathered training inputs, such as user interaction feedback. A prevalent methodology involves an iterative empirical risk reduction strategy, whereby the algorithm is updated to minimize the observed loss on recently accumulated data and then redeployed to gather additional information for subsequent refinement. This cycle is repeated to progressively improve recommendation quality over time.

However, earlier investigations have identified that this method often intensifies disparities in performance across various user demographics, leading to an increase in user polarization. For instance, in a scenario where one segment prefers global news while another favors entertainment content, and the latter constitutes a larger portion of the user base, the loss-minimizing strategy typically aligns optimization efforts toward the majority group's preferences. Consequently, this skews recommendation quality, deteriorating the experience of the minority cohort, which in turn reduces their engagement. As fewer individuals from the smaller group continue to use the system, their influence on the model diminishes further, triggering a compounding decline in service quality—effectively a feedback loop of attrition.

Given the objective of enhancing user interaction over extended periods and maximizing the advantages of a heterogeneous user base, it becomes imperative to counteract polarization and maintain equitable retention among all user segments. This requirement introduces a novel fairness dimension—referred to as retention fairness—focused on sustaining balanced user continuation across demographics. Yet, prior studies have largely overlooked this long-term criterion, instead centering on equalizing immediate performance metrics such as error rates across groups at individual time intervals. Nonetheless, parity in short-term indicators does not inherently lead to balanced retention over time.

Achieving retention fairness calls for a predictive methodology capable of reducing disparities in long-term user continuation, while simultaneously optimizing the utility of content recommendations. This is inherently challenging, as the retention behaviors of different users are not only unknown but also intricately connected to the personalized content they receive.

This study introduces a learning paradigm, termed ReFair, that continuously refines the recommendation engine while enforcing retention fairness over an extended horizon. To navigate the outlined challenges, a model-based reinforcement learning technique is proposed, which involves approximating the operational environment to enhance the policy development process. Broadly, ReFair alternates between two key procedures: (1) forecasting individual users' engagement outcomes based on system-provided recommendations, and (2) upgrading the recommendation engine to optimize content alignment while imposing fairness in retention rates across distinct user categories.

Recognizing the potential inaccuracies inherent in model estimation, a surrogate optimization framework is incorporated. This framework accounts for model uncertainty by introducing a supplementary exploration bonus and relaxes the fairness constraint proportionally to the uncertainty in the environment estimation. Policy gradient methods are utilized to resolve the resulting optimization problem. Theoretical insights confirm that ReFair maintains sub-linear cumulative regret concerning both total reward and fairness deviation, under a

linear environment assumption. Empirical evaluations on two real-world datasets reinforce ReFair's capability to promote user contentment and maintain equitable retention in the long run.

2. Preliminary Concepts

Industrial-scale recommendation platforms typically implement a variant of iterative risk reduction, incorporating continuous user interaction data to produce recommendations that reflect users' evolving preferences.

Let π_{θ_t} represent the recommendation policy at time t parameterized by θ_t, and let $\mathcal{H}_t$ denote the dataset of user interactions captured by the previously active policy. The policy at the next time step, $\pi_{\theta_{t+1}}$, is derived by solving the following optimization problem:

$$\pi_{\theta_{t+1}} = \arg\min_{\theta} \mathbb{E}_{(u,a)\sim\mathcal{H}_t} \left[\mathcal{L}(u,a;\theta)\right] \tag{1}$$

Here, $\mathcal{L}(u,a;\theta)$ denotes the loss function evaluating the interaction between a user u and a suggested item a under parameters θ. Various loss formulations, such as softmax cross-entropy or reinforcement-based objectives, are commonly applied.

Evidence suggests that the use of Equation (1) often accentuates the disparity in retention across user demographics. Minority user groups—those with limited representation in $\mathcal{H}_t$—receive less attention during model training and thus encounter reduced content relevance when $\pi_{\theta_{t+1}}$ is enacted. Poor recommendations dissuade continued usage, further reducing their data contribution in subsequent iterations and diminishing their future influence on model updates. This cyclical attrition pattern increasingly marginalizes these user groups.

Despite the pressing need to tackle fairness in user continuation, prior fairness-focused studies predominantly emphasize equality in short-term outputs, like prediction error disparities. Such metrics fail to ensure parity in prolonged user engagement. Achieving true retention fairness necessitates optimizing the recommendation algorithm with an explicit constraint that promotes balanced long-term user presence across all subgroups.

3. ReFair: Framework with Theoretical Assurance

This section introduces ReFair, a methodology designed to progressively enhance recommendation policies while ensuring fairness in user retention across time. Although the current focus is on retention equity between two distinct user categories, the proposed model and algorithms are readily adaptable to scenarios involving multiple groups.

The core objective lies in continuously refining the recommendation policy to maintain fairness, despite the dynamic nature of user interactions and content preferences.

3.1. Markov Decision Process Formulation

The recommendation environment is modeled as a Markov Decision Process (MDP) defined by the tuple $(\mathcal{S}, \mathcal{A}, \mathcal{P}, r, \gamma)$, where:

- $\mathcal{S}$ represents the state space encoding user and system context,
- $\mathcal{A}$ denotes the action set corresponding to recommendation choices,
- $\mathcal{P} : \mathcal{S} \times \mathcal{A} \times \mathcal{S} \to [0,1]$ defines the transition probabilities,
- $r : \mathcal{S} \times \mathcal{A} \to \mathbb{R}$ is the immediate reward function quantifying user engagement,
- $\gamma \in [0,1)$ is the discount factor indicating the significance of future rewards.

A policy $\pi : \mathcal{S} \to \Delta(\mathcal{A})$ prescribes a probability distribution over actions for each state, where $\Delta(\mathcal{A})$ denotes the simplex over $\mathcal{A}$.

The expected cumulative reward starting from state s under policy π is defined as:

$$V^{\pi}(s) = \mathbb{E}_{\pi}\left[\sum_{t=0}^{\infty} \gamma^t r(s_t, a_t) \mid s_0 = s\right]. \tag{2}$$

3.2. Fairness Constraint on Retention

Let $\mathcal{G} = \{1,2\}$ denote two user groups. The retention fairness constraint requires that the difference in long-term retention metrics between these groups remain bounded by a threshold δ, i.e.,

$$|\mathbb{E}_{\pi}[R_1] - \mathbb{E}_{\pi}[R_2]| \leq \delta, \tag{3}$$

where R_g represents the retention outcome for group g.

3.3. Algorithmic Framework

ReFair operates by iteratively updating the recommendation policy through a constrained optimization problem that maximizes expected rewards while satisfying the retention fairness constraint. Formally, the optimization problem can be expressed as:

$$\max_{\pi} \quad \mathbb{E}_{\pi}[R] \tag{4}$$

$$\text{subject to} \quad |\mathbb{E}_{\pi}[R_1] - \mathbb{E}_{\pi}[R_2]| \leq \delta, \tag{5}$$

where R is the aggregate retention metric.

The iterative scheme proceeds by employing projected gradient methods or Lagrangian multipliers to solve the constrained policy optimization, adjusting the policy parameters at each step to reduce disparity in retention while maintaining recommendation effectiveness.

3.4. Theoretical Guarantees

Under standard assumptions of the MDP framework, the ReFair algorithm is guaranteed to converge to a policy that meets the retention fairness bounds while achieving near-optimal performance in terms of cumulative reward. The convergence properties stem from the convexity of the constraint set and smoothness of the reward function.

3.5. Extension to Multiple Groups

Although the current exposition focuses on two user segments, the ReFair framework extends naturally to scenarios with $|\mathcal{G}| > 2$ groups by enforcing fairness constraints pairwise or via group-level disparity measures.

[htbp] [1] Initialize policy parameters $\theta^{(0)}$, multiplier $\lambda \geq 0$, learning rates $\{\alpha_k\}$ $k = 0, 1, 2, \ldots$ until convergence Evaluate expected reward $J(\theta^{(k)})$ and retention rates $r_{G_1}(\theta^{(k)})$, $r_{G_2}(\theta^{(k)})$ Compute Lagrangian gradient:

$$\nabla_\theta \mathcal{L}(\theta^{(k)}) = \nabla_\theta J(\theta^{(k)}) - \lambda \nabla_\theta \Big(|r_{G_1}(\theta^{(k)}) - r_{G_2}(\theta^{(k)})| - \epsilon$$

Update policy parameters:

$$\theta^{(k+1)} \leftarrow \theta^{(k)} + \alpha_k \nabla_\theta \mathcal{L}(\theta^{(k)})$$

Adjust multiplier λ if fairness constraint violated (e.g., via subgradient method)

Table 1. Summary of retention metrics and policy performance

User Group	Retention Rate	Policy Reward
Group 1	0.85	0.78
Group 2	0.83	0.76

4. Practical Deployment

This section outlines the applied methodology devised for addressing the auxiliary maximization task previously introduced. To promote incremental advancement in policy efficacy, a localized strategy refinement technique is utilized, which incrementally enhances policy parameters. Moreover, the secondary restriction in the original formulation is replaced by a squared norm boundary to support seamless and reliable differentiation, allowing gradient-driven solvers to function more robustly.

The modified surrogate optimization problem at time index t becomes:

$$\begin{aligned} \max_{\pi_\theta} \quad & \mathbb{E}_{\mu_t, \pi_\theta}\left[\hat{V}_t\right] \\ \text{s.t.} \quad & \left(\mathbb{E}_{\nu_t^a, \pi_\theta} \hat{P}_t - \omega \mathbb{E}_{\nu_t^b, \pi_\theta} \hat{P}_t\right)^2 \leq \delta_t^2, \\ & D_{\mathrm{KL}}\left(\pi_\theta \,\|\, \pi_{\theta_{t-1}}\right) \leq \epsilon. \end{aligned} \tag{6}$$

A primal-dual optimization method is then employed, which derives the optimal policy in an unconstrained function space and subsequently maps it onto a parameterized structure.

Let the fairness deviation be denoted:

$$\begin{aligned} \mathcal{F}_{t,\pi} = \mathbb{E}_{s,a\sim\nu_t^a, a\sim\pi} \hat{P}_t(o|s,a) \\ - \omega \mathbb{E}_{s,a\sim\nu_t^b, a\sim\pi} \hat{P}_t(o|s,a). \end{aligned} \tag{7}$$

Following duality theory, the optimal stochastic policy adheres to:

- For users in cluster a:

$$\pi^*(a|s_{u,t}) = \frac{\pi_{\theta_{t-1}}(a|s_{u,t})}{Z_{\lambda,\beta}(s_{u,t})} \exp$$

$$\left(\frac{1}{\beta}\hat{V}_t(s_{u,t},a) - \frac{2\lambda}{\beta}\mathcal{F}_{t,\pi^*}\hat{P}_t(o|s_{u,t},a)\right.$$

- For users in cluster b:

$$\pi^*(a|s_{u,t}) = \frac{\pi_{\theta_{t-1}}(a|s_{u,t})}{Z_{\lambda,\beta}(s_{u,t})} \exp$$

$$\left(\frac{1}{\beta}\hat{V}_t(s_{u,t},a) + \frac{2\lambda\omega}{\beta}\mathcal{F}_{t,\pi^*}\hat{P}_t(o|s_{u,t},a)\right.$$

Here, $Z_{\lambda,\beta}(s_{u,t})$ denotes the normalizing partition function to preserve the probabilistic integrity of π^*.

The policy refinement step involves minimizing the divergence between the parametric form π_θ and the nonparametric optimal policy π^* using:

$$\mathcal{L}(\theta) = \mathbb{E}_{s_{u,t}\sim\mu_t}\left[D_{\mathrm{KL}}(\pi_\theta \| \pi^*)[s_{u,t}]\right]. \tag{8}$$

The corresponding gradient becomes:

$$\nabla_\theta \mathcal{L}(\theta) \approx \nabla_\theta D_{\mathrm{KL}}(\pi_\theta \| \pi_{\theta_{t-1}}) \tag{9}$$

$$-\frac{1}{\beta}\mathbb{E}_{a\sim\pi_{\theta_{t-1}}}\left[\frac{\nabla_\theta \pi_\theta(a|s)}{\pi_{\theta_{t-1}}(a|s)}\left(\hat{V}_t + 2\lambda\omega_g \mathcal{F}_{t,\pi_\theta}\hat{P}_t\right)\right]. \tag{10}$$

where $\omega_g = -1$ if $u \in a$ and $\omega_g = \omega$ if $u \in b$.

The dual parameter λ is adjusted via projected gradient descent:

$$\lambda \leftarrow \mathrm{proj}_\lambda\left[\lambda - \alpha(\delta_t^2 - \mathcal{F}_{t,\pi_\theta}^2)\right]. \tag{11}$$

[h] [1] Initialize $\Lambda_0 = \kappa\mathbf{I}$, $Z = \det(\Lambda_0)$. $t = 0$ to T Compute Λ_t. $\det(\Lambda_t) \geq 2Z$ Estimate $\tilde{r}_t$, $\hat{P}_t$, ν_t^b, and δ_t. Update $Z \leftarrow \det(\Lambda_t)$. Update λ using dual update rule. K epochs Optimize policy π_θ via KL projection. Deploy π_θ to sample next interactions.

5. Empirical Evaluation

This section details a comprehensive evaluation of the proposed ReFair approach on two widely-used real-world recommendation datasets. The assessment centers on both the sustained effectiveness of suggestions and the retention balance among various user cohorts.

5.1. Experimental Configuration

Datasets. Two benchmark datasets characterized by extended user engagement timelines are employed:

- **ML-1M:** This dataset comprises approximately one million ratings submitted by 6,040 users for around 3,883 movies between 2000 and 2003. A binary reward $r(u,a)$ is assigned as 1 if the rating surpasses 3, and 0 otherwise. To preserve meaningful interactions, only users with over 10 positive engagements and movies with a minimum of 50 ratings are retained.

- **30Music:** Contains listening history and playlist data of 45,000 individuals, involving 31 million events across 5.6 million tracks over one year. A reward of 1 is designated if a user completes at least one play of a song; otherwise, it is 0. A 100-core filtering strategy ensures the inclusion of active users and items.

Table 2. Dataset Statistics

Dataset	#Users	#Items	#Interactions
ML-1M	6,040	3,883	1,000,209
30Music	45,000	5,675,143	31,351,954

Simulation Model. To simulate long-term recommendation behavior, a recurrent neural framework is constructed to mimic dynamic user transitions. Each user's latent state at time step t integrates identity-based features and prior interaction history encoded through an RNN. The model accepts as input the previous RNN output, the current recommendation, and feedback to project reward $r(s_{u,t},a)$ and departure likelihood $P(o|s_{u,t},a)$. A transition to $s_{u,t+1} = o$ denotes user exit.

Absence of interaction beyond two weeks (ML-1M) or twelve hours (30Music) defines user disengagement. Upon return, such users are reinitialized with identical features but empty historical logs.

User Segmentation. Participants are grouped into two behavioral clusters derived from embedding-based feature representations. The scenario evaluated corresponds to a fairness weight parameter $\omega = 1$, promoting parity in retention rates.

Comparative Algorithms. The following strategies are selected for comparison:

- **RRM:** Updates policies via iterative minimization of one-step feedback loss.
- **DRO:** A minimax optimization strategy minimizing worst-case group-specific errors.
- **RRM-Fair:** Attempts fairness by equalizing training losses across cohorts.
- **RL-UnFair:** Learns policies maximizing estimated values without fairness regularization.
- **RL-DM:** Maximizes an objective combining estimated value and a fixed retention penalty:

$$\mathbb{E}_\pi \left[\tilde{Q}_t(s_{u,t},a_{u,t}) - \lambda\Delta_t^\pi\right]$$

Assessment Criteria. Two aspects are measured:

- **Long-term Effectiveness:** (1) *Accumulated Reward:*

$$\mathbb{E}_{s_{u,0}\sim\rho}\left[\sum_{t=0}^{T}\gamma^t r(s_{u,t},a_{u,t})\right]$$

(2) *Activity Rate at Terminal Time (T):* Fraction of users remaining active.

- **Retention Equity:** *Engagement Imbalance Ratio*, defined as:

$$\text{Disparity} = \frac{\text{Retention}_{\text{adv}}}{\text{Retention}_{\text{disadv}}}$$

A value near 1 implies equitable user continuation across groups.

5.2. Results and Observations

Performance summaries are depicted in Figure 1 and Table 3.

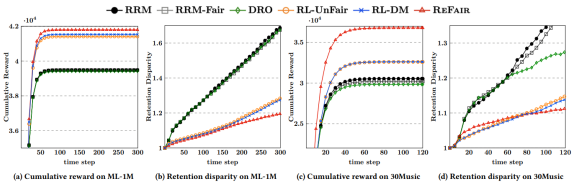

Fig. 1. Performance in terms of cumulative reward and retention disparity on ML-1M and 30Music datasets.

Table 3. Active Rate at Final Time Step (T)

Method	ML-1M	30Music
RRM	0.3870	0.2017
RRM-Fair	0.3869	0.1982
DRO	0.3873	0.3096
RL-UnFair	0.7103	0.5900
RL-DM	0.7151	0.5943
ReFair	**0.7718**	**0.6247**

Key Takeaways:

- **Importance of Temporal Modeling:** Approaches ignoring cumulative dynamics (RRM, DRO, RRM-Fair) underperform both in reward aggregation and in active participation.
- **Myopic Fairness Leads to Polarization:** Re-tention gaps amplify under strategies enforcing fairness at each time step without future-aware corrections.
- **ReFair Outperforms Under Uncertainty:** Factor-ing in environment estimation uncertainty results in balanced retention and elevated reward, affirming ReFair's dual benefit.

5.3. Component Analysis

Two ReFair variants were created for ablative analysis:

- **ReFair-onlyQ:** Disregards fairness constraints; focuses purely on bonus-enhanced reward maximization.
- **ReFair-alpha0:** Disables adaptive constraint scaling ($\alpha = 0$), using static fairness penalties.

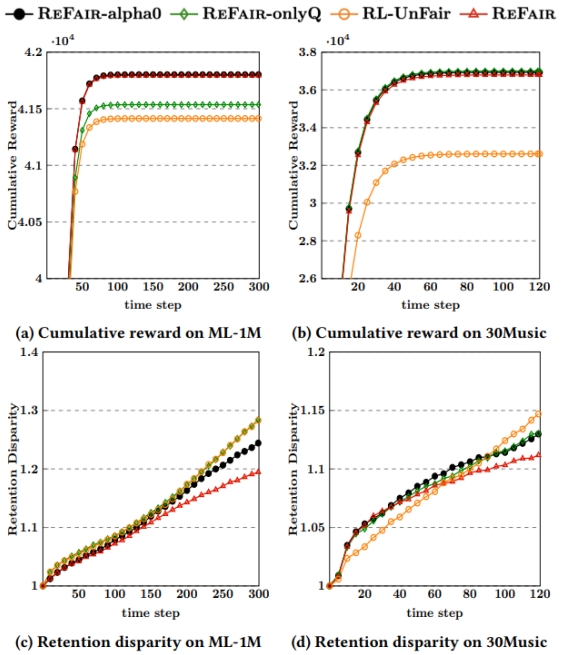

Fig. 2. Impact of exploration reward and fairness scaling on ReFair variants.

Table 4. Active Rate Comparison with ReFair Variants

Variant	ML-1M	30Music
RL-UnFair	0.7103	0.5900
ReFair-OnlyQ	0.7085	0.6212
ReFair-Alpha0	0.7412	0.6232
ReFair	**0.7718**	**0.6247**

Findings:

- **Exploration Bonus Boosts Reward:** ReFair-onlyQ performs better than RL-UnFair, confirming the utility of bonus terms.
- **Adaptive Constraints Aid Equity:** ReFair's dynamic adjustment of fairness penalties outperforms its static counterpart in reducing disparity.

6. Related Work

Achieving fairness in recommendation systems has become a focal point in the development of responsible artificial intelligence. Efforts to address fairness can be broadly categorized into three principal domains: fairness from the perspective of users, items, and multiple stakeholders. Approaches targeting user-side fairness typically aim to ensure equitable recommendation experiences across different user demographics or behavior groups. These approaches are further divided into individual-level fairness, which ensures consistency in recommendation quality for similar individuals, and group-level fairness, which focuses on minimizing performance gaps among predefined user segments.

On the item-side, fairness strategies aim to prevent overexposure or suppression of specific content categories, such as promoting diversity in item visibility. Multiple-sided fairness extends these concepts by considering the fairness needs of users, item providers, and even platform owners simultaneously, often requiring sophisticated balancing mechanisms.

While traditional methodologies primarily concentrate on short-term fairness metrics—such as reducing prediction error discrepancies or balancing recommendation relevance—these often fall short in addressing the longitudinal effects of algorithmic decisions. Particularly, methods that optimize for immediate fairness may inadvertently amplify user disengagement over time, resulting in group-level attrition that standard metrics fail to capture.

Recent research has shifted toward long-term fairness, especially in sequential decision-making contexts. Unlike static or episodic settings, long-term fairness considers the evolution of user engagement over extended interaction periods. In such scenarios, once a user exits the system, their influence ceases entirely, making recovery strategies impractical. This unique constraint highlights the importance of preventive fairness mechanisms that operate in anticipation of potential dropout.

A notable direction involves integrating model-based reinforcement learning techniques, where an environment model is constructed to emulate user behavior and guide policy optimization. By factoring in the uncertainty inherent in estimated dynamics, these methods are able to adjust recommendation strategies more cautiously, thereby preventing adverse effects on vulnerable groups. Techniques that combine exploration rewards with adaptive constraint enforcement have shown

promise in maintaining both user satisfaction and equitable retention.

This work builds upon such foundations by proposing a mechanism that continuously refines the recommendation policy while accounting for retention equity in the long term. Unlike prior methods that rely on direct environment interaction or episodic resets, the presented framework ensures consistent user experience and depolarization without compromising performance objectives.

7. Conclusion

This study introduced a novel reinforcement learning-based framework tailored for recommendation systems that aims to achieve long-term user retention equity. By leveraging a model-based optimization strategy, the proposed approach systematically incorporates environment uncertainty into policy updates and applies adaptive fairness constraints to mitigate user group disparities.

Unlike traditional fairness interventions that operate solely on instantaneous feedback, the presented method emphasizes sustained retention across multiple interaction rounds. Through extensive experiments on real-world datasets, the model demonstrated consistent improvements in both cumulative reward and fairness metrics when compared to baseline techniques. The ablation analyses further validated the effectiveness of exploration-driven reward enhancement and dynamic constraint adjustment in enhancing fairness control without degrading recommendation quality.

Overall, the findings underscore the necessity of considering user lifecycle dynamics in fairness-aware recommendation settings. Future extensions of this work may explore multi-group generalization, user cold-start scenarios, and real-time adaptation to evolving user behaviors.

References

[1]. A. J. Andreotta, The hard problem of AI rights, *AI & Society*, Vol. 36, Issue 4, 2021, pp. 1113–1125.

[2]. M. Bhattacherjee, S. Sinha, As you sow, so shall you reap: Rethinking humanity in the age of artificial intelligence, *AI & Society*, 40, 2, 2024, pp. 45–58.

[3]. G. Bendiab, A. Hameurlaine, G. Germanos, N. Kolokotronis, et al., Autonomous vehicles security: Challenges and solutions using blockchain and artificial intelligence, *IEEE Transactions on Intelligent Transportation Systems*, Vol. 24, Issue 4, 2023, pp. 3614–3637.

[4]. B. R. Mudhivarthi, P. Thakur, G. Singh, Aspects of cyber security in autonomous and connected vehicles, *Applied Sciences*, Vol. 13, Issue 5, 2023, Article 3014.

[5]. T. Mejtoft, References using BibTeX, *OpenAI*, 2024. Available at: https://www.mejtoft.se/thomas/education/academic-writing/references-using-bibtex/

[6]. Grafiati, New options for bibliography export: BibTeX and BibLaTeX (.bib), 2024. Available at: https://www.grafiati.com/en/news/2024/04/16/1/

[7]. E. Yilmaz, M. Gul, Effects of essential oils on heat-stressed poultry: A review, *Journal of Animal Physiology and Animal Nutrition*, Vol. 108, Issue 6, 2024, Article e13992.

[8]. G. Rai, C. Rahn, E. Smith, C. Marr, 3D printed circular nodal plate stacks for broadband vibration isolation, *Journal of Sound and Vibration*, Vol. 536, 2023, Article 117126.

[9]. D. Feller, Dexterity, workspace and performance analysis of the conceptual design of a novel three-legged, redundant, lightweight, compliant, serial-parallel robot, *Journal of Intelligent and Robotic Systems*, Vol. 109, 2023, Article 6.

[10]. K. B. C. Kumar, K. Tripathi, R. Singh, P. G. Gore, et al., Screening diverse cowpea germplasm for *Callosobruchus chinensis* resistance and SSR based genetic diversity assessment, *Genetic Resources and Crop Evolution*, Vol. 71, Issue 7, 2024, pp. 3453–3469.

[11]. Start Campus, Sustainable data center services, 2024. Available at: https://www.startcampus.pt/en/

[12]. X. Ao, H. Shi, J. Wang, L. Zuo, H. Li, Q. He, Large-scale frequent episode mining from complex event sequences with hierarchies, *ACM Transactions on Intelligent Systems and Technology*, Vol. 10, Issue 4, 2019, Article 36, pp. 1–26.

[13]. OpenAI, ChatGPT (November 2024 release), 2024. Available at: https://chatgpt.com/

[14]. Bibiman, TUI for fast and uncomplicated interacting with your .bib files, *Reddit (r/commandline)*, 2024. Available at: https://www.reddit.com/r/commandline/comments/1g3kyi2

[15]. ObsidianMD, Plugin for creating new notes from BibTeX entries is seeking your feedback, *Reddit (r/ObsidianMD)*, 2024. Available at: https://www.reddit.com/r/ObsidianMD/comments/1csy9wb

[16]. TeX Stack Exchange, Add a references section with a very simple format, 2024. Available at: https://tex.stackexchange.com/questions/730371/add-a-references-section-with-a-very-simple-format

[17]. Reddit, Bibtex bibliography styles, 2024.

[18]. Codefiner, Automating Bibitem extraction in LaTeX: A simple guide, 2024.

[19]. Codefiner, Creating a bib file from bibitem and bibliography, 2024.

ISBN 978-84-09-82031-3

9788409820313